Study and optimisation of the process of carbon dioxide hydrogenation towards gaseous and liquid hydrocarbons

Carlotta Panzone

▶ To cite this version:

Carlotta Panzone. Study and optimisation of the process of carbon dioxide hydrogenation towards gaseous and liquid hydrocarbons. Chemical engineering. Université de Lyon, 2021. English. NNT : 2021LYSE1340 . tel-03789618

HAL Id: tel-03789618
https://theses.hal.science/tel-03789618

Submitted on 27 Sep 2022

N° d'ordre NNT : 2021LYSE1340

THÈSE de DOCTORAT DE L'UNIVERSITÉ DE LYON
opérée au sein de :
l'Université Claude Bernard Lyon 1

Ecole Doctorale 206
Ecole Doctorale de Chimie de Lyon

Spécialité de doctorat : Procédés

Soutenue publiquement le 17/12/2021, par :
Carlotta PANZONE

Etude et optimisation du procédé d'hydrogénation du dioxyde de carbone en hydrocarbures gazeux et liquides

---

Devant le jury composé de :

JULCOUR Carine Directrice de Recherche, CNRS Toulouse UMR 5503 - LGC	**Présidente**
ROGER Anne-Cécile Professeure des Universités, Université de Strasbourg UMR 7515 - ICPEES	**Rapporteure**
THYBAUT Joris Professeur, Université de Gand (Belgique) - LCT	**Rapporteur**
POSTOLE Georgeta Maître de conference, Université Lyon 1 UMR 5256 - IRCELYON	**Examinatrice**
TRONCONI Enrico Professeur, Politecnico de Milan (Italie) - Département d'Energie	**Examinateur**
FONGARLAND Pascal Professeur des Universités, Université Lyon 1 UMR 5128 - CP2M	**Directeur de thèse**
BENGAOUER Alain Ingénieur de Recherche, CEA Grenoble	**Co-Directeur de thèse**
CHAPPAZ Alban Ingénieur de Recherche, CEA Grenoble	**Invité**
PHILIPPE Régis Chargé de Recherche, CNRS Lyon UMR 5128 - CP2M	**Invité**

Aknowledgments

Les travaux de recherche présentés dans cette thèse ont été réalisés au sein du LRP (Laboratoire Réacteurs et Procédés) au CEA-LITEN de Grenoble et du CP2M (Laboratoire de Catalyse, Polymérisation, Procédés et Matériaux) à Lyon. Je tiens donc à remercier les deux laboratoires pour leur accueil et pour m'avoir permis de mener ce travail au sein de leurs unités. En particulier, je remercie les chefs du laboratoire LRP, Frédéric Ducros d'abord et Laurent Bedel après, pour leur accompagnement et leur soutien.

Tout d'abord, je tiens à remercier mon directeur de thèse, professeur Pascal Fongarland, pour sa disponibilité, son soutien et ses conseils. Merci pour la confiance que tu m'as accordée et pour la motivation et la positivité que tu m'as toujours transmises.

Je remercie également mes encadrants au CEA : Alain Bengaouer et Alban Chappaz. Merci Alain pour tous ce que j'ai appris en travaillant avec toi. Merci pour le temps que tu m'as accordé et pour tous tes sages conseils qui m'ont permis d'apprendre à me poser les bonnes questions. Merci de même à Alban, pour tous tes conseils, ton aide et ta bienveillance.

Je tiens à remercier aussi mes encadrants au CP2M, Régis Philippe et Clémence Nikitine, pour votre soutien et vos conseils.

Je tiens à souligner que ça a été un plaisir de travailler avec vous tous, vous avez pu me guider en me laissant garder mon autonomie. Je vous remercie pour la confiance que vous m'avez accordée et pour les discussions très intéressantes qu'on a eues.

I would also like to thank all the people that have been part of this thesis jury, giving raise to very interesting discussions. Thanks to Professor Joris Thybaut of the LCT of Ghent University and to Professor Anne-Cécile Roger of the ICPEES of Strasbourg for accepting to dedicate some of their time to review this work. I also wish to thank Carine Julcour of LGC of Toulouse for chairing the jury and Professor Enrico Tronconi of Politecnico di Milano and Georgeta Postole of IRCELYON, as well, for accepting to be examiners of this work.

Je remercie aussi toutes les personnes qui ont contribué à la réussite de ce travail.

Merci à Fréd et Fabrice pour votre aide avec le montage expérimental. Merci à Fréd également pour ta patience, ta disponibilité constante et ton amabilité. Merci à Laurent pour tes conseils et ton aide sur l'analytique et pour tes idées souvent très géniales. Merci à Stéphanie pour ton aide avec la synthèse du catalyseur et les caractérisations.

Merci à Michel pour ton aide et surtout pour ta bonne humeur. Merci également à Benoît pour ton aide sur les caractérisations et ta disponibilité.

Je remercie aussi Jean-François Meunier du LCC Toulouse pour les analyses Mössbauer, Ruben Vera de l'Université de Lyon pour les analyses DRX, Laurent Veyre du CP2M pour les analyses TEM, Pascale Mascunan et ses collaborateurs de l'IRCELYON pour leur aide avec les analyses ICP et Sebastien Thiery du LRP pour les analyses ATG.

Merci à toutes les personnes que j'ai eu le plaisir de croiser pendant ce parcours. Merci à l'« équipe méthanation » (ou « SECCSY ? ») du LRP qui m'a très bien accueilli et accompagné pendant ces trois ans. Merci à Geneviève pour ta bonne humeur et à Albin pour ton amabilité et ton calme. Merci à Isabelle pour avoir été ma première co-bureau et m'avoir aidé à m'intégrer dans l'équipe, mais surtout pour nous n'avoir pas abandonné après ta thèse ! Merci pour ta bonne humeur et pour tes conseils.

Merci à tous les doctorants (et non) du premier étage du G1. Merci pour les repas, les pauses café et nos sorties après-boulot, mais surtout pour les blagues et les rires.

Merci en particulier à Antoinette pour avoir vécu avec moi ce parcours et m'avoir toujours soutenu au moment des mauvaises et des bonnes nouvelles. Merci pour ton souris, ton calme et ta gentillesse. Ça a été un énorme plaisir d'avoir abordé ce parcours avec toi. Merci à Robin pour avoir partagé le bureau avec nous et pour avoir soutenu mes sorties piscine (même si ça n'a pas duré longtemps !). Merci aussi à Chaimae et Kanthika, avec qui on a atteint un nombre incroyable de doctorantes dans l'équipe ! Kanthika, prends soin de la manip !

Merci aussi à toute l'équipe du CP2M pour votre accueil. Merci à tous ceux qui ont partagé le bureau avec moi pendant mes différentes missions à Lyon : merci à Valérie pour ton aide, ta patience et ton amabilité, merci à Victoria pour ta bonne humeur et ta vitalité et merci à Vincent pour m'avoir prêté ta GC. Je tiens à remercier aussi Laura (ta machine à café m'a sauvé !), Mathis et Amaury pour m'avoir accompagné pendant les repas le midi et Aline et Dolorès pour vos conseils et votre amabilité. Merci à tous les autres docs, post-docs et permanents pour les très bons moments que j'ai passés à Lyon.

Enfin, j'adresse mes sincères remerciements à mes amis pour leur soutien et leur amitié. Merci tout d'abord à « mes colocs » Quentin, Carole, Aurélie et Anthony pour les bons moments passés ensemble et pour votre aide avec le Français et la vie en France. On a survécu « au fou », rien ne peut plus nous arrêter dans la vie ! Grazie anche a tutti gli italiani che hanno contribuito a farmi sentire a casa in terra straniera: grazie ad Annalisa, Alberto, Andrea, Alessandro, Aurelio e Giusy.

Un gros merci à Jérémy pour avoir été à mes côtés à la fin de ce parcours et m'avoir soutenu et supporté dans mes moments bons et moins bons. Merci pour toute la sérénité que tu m'as apporté.

Grazie anche ai miei amici di sempre, Chiara, Esther, Arianna, Giada, Cane e Gianluca per avermi sempre fatto sentire la vostra amicizia e il vostro sostegno, da lontano o da vicino. A Chiara, un grazie particolare per il suo aiuto con la chimica a me oscura !

Infine, grazie ai miei genitori e a mio fratello per il sostegno che mi avete sempre dato di fronte alle mie scelte e per la vicinanza che mi dimostrate nonostante la distanza.

Thanks to all.

Résumé en français

La thèse, intitulée “ Etude et optimisation du procédé d'hydrogénation du CO_2 vers des hydrocarbures gazeux et liquides ”, consiste en l'étude expérimentale et la modélisation de la réaction catalytique d'hydrogénation de CO_2 pour la production d'hydrocarbures gazeux et liquides. Les objectifs principaux de la thèse sont les suivants :

- Le développement d'un modèle cinétique détaillé capable de décrire la vitesse de la réaction et la distribution des hydrocarbures dans différentes conditions opératoires.
- Le développement d'un modèle mathématique pour décrire le comportement du réacteur d'hydrogénation de CO_2 dans différentes conditions en tenant compte des phénomènes de transfert de chaleur et de masse entre la phase gazeuse et le catalyseur solide.
- L'étude du procédé globale pour comprendre et améliorer son efficacité énergétique et de matière.
- La compréhension du mécanisme réactionnel et des possibles voies de formation des différents produits, ainsi que des sites actifs impliqués.

Introduction.

Dans le contexte actuel de la transition énergétique, des nouvelles technologies se développent comme alternatives au pétrole dans différents domaines de l'énergie. La technologie Power-to-Liquid permet de produire des hydrocarbures synthétiques à partir de CO_2 et représente en même temps une technologie d'utilisation du CO_2 (contribuant à la réduction de la concentration de CO_2 dans l'atmosphère) et une solution pour le stockage de l'électricité renouvelable sous forme de vecteurs énergétiques liquides (limitant les problèmes de stockage et transport propres aux produits gazeux). La technologie de conversion directe du CO_2 en hydrocarbures gagne donc de l'intérêt et pourrait représenter une technologie de production d'hydrocarbures synthétiques pour le secteur des transports, notamment l'aviation, et l'industrie chimique. La plupart des travaux publiés dans la littérature sur l'hydrogénation de CO_2 vers des hydrocarbures ont été focalisés principalement sur le développement d'un catalyseur optimal pour maximiser la sélectivité vers les hydrocarbures visés. En particulier, l'ajout de promoteurs (comme du K et du Cu) aux catalyseurs à base de fer permet d'augmenter la production de chaines longues et la conversion du CO_2. A contrario, peu des travaux ont été dédiés à la modélisation de cette réaction : la plupart des modèles cinétiques qui ont été développés sont très simples et ne permettent pas de prédire la distribution des hydrocarbures. En conséquence, on a identifié d'une part la nécessité de développer un modèle mathématique détaillé qui soit capable de décrire le comportement du réacteur et d'autre part la nécessité d'évaluer le rendement énergétique et matière du procédé et de comprendre comment il pourrait être amélioré pour une éventuelle application à l'échelle industrielle.

Resultats experimentaux.

La plupart des essais expérimentaux ont été conduits dans un réacteur tubulaire à lit fixe à l'échelle du laboratoire, rempli avec un catalyseur à base de Fe, synthétisé par imprégnation du support Al_2O_3 et dopé avec du potassium. Un protocole analytique a été développé pour permettre l'identification et la quantification de la plupart des produits obtenus, en phase gaz, ainsi qu'en phases liquides (organique et aqueuse). Différentes conditions opératoires ont été testées, en variant le GHSV, la température du four, la pression totale et le ratio H_2/CO_2 en entrée du réacteur. Les résultats obtenus dans les conditions de référence (2080 Nml/g/h, 300°C, 15 bar, $H_2/CO_2=3$) sont montrés dans la Figure 1. On peut observer qu'une conversion de CO_2 autour de 30% a été obtenue, avec une sélectivité de CO autour de 10%. Le méthane représente 35% et les oléfines C_2-C_4 31% des produits obtenus (CO exclu). Globalement, les oléfines linéaires (majoritairement à chaines courtes) représentent le produit principal. Au contraire, les paraffines sont produites en quantités inférieures. Une fraction significative est représentée par les oxygénés, acides et alcools principalement. Des chaines ramifiées et des composés aromatiques ont également été observées en petites quantités (ils sont regroupés dans la catégorie « others »).

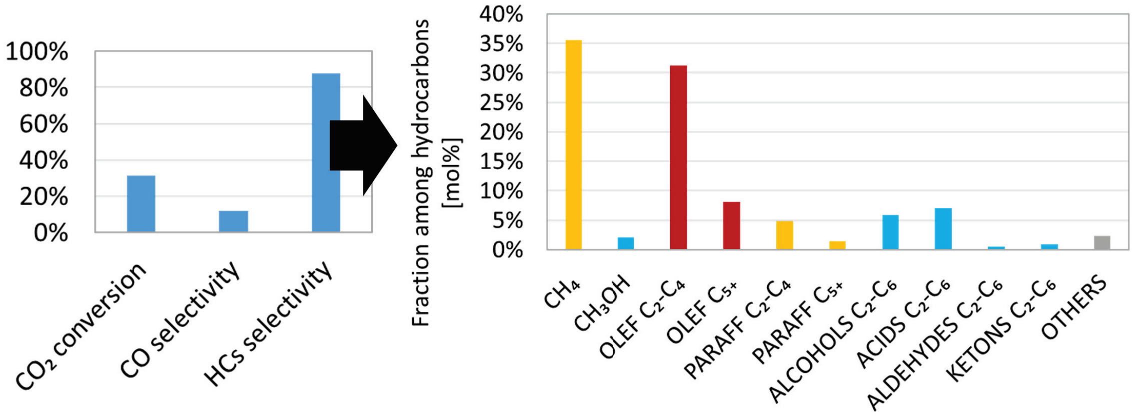

Figure 1. Résultats des essais expérimentaux obtenus en conditions de référence (2080 Nml/g/h, 300°C, 15 bar, $H_2/CO_2=3$).

Développement du modèle macro-cinétique.

A partir des données expérimentales obtenues, un modèle macro-cinétique a été développé pour décrire le comportement de la réaction dans les différentes conditions testées. L'objectif est de développer un modèle qui soit assez détaillé pour décrire la formation des principaux produits observés (oléfines linéaires, paraffines linéaires et oxygénés), tout en restant assez simple pour pouvoir être introduit dans des modèles de réacteur plus complexes. Pour le développement du modèle on a donc choisi des lois cinétiques pour décrire les lois de vitesse de RWGS et FT basés sur des travaux antérieurs (Riedel et al., 2001). A ces lois cinétiques on a rajouté des paramètres qui permettent de décrire la distribution selon le nombre de carbone (α_1 et α_2) et la nature chimique du produit (O, P, OX). Les paramètres cinétiques du modèle ont été dérivés via la méthode des moindres carrés à l'aide du logiciel Matlab. Une partie des résultats obtenus, comparés aux données expérimentales, est présentée dans la Figure 2. On peut observer que le modèle est capable de décrire avec une bonne précision les données expérimentales, même s'il nécessite encore quelques améliorations, notamment dans la description de la formation de méthane et des oléfines à chaines courtes dans certaines conditions. Néanmoins, ce modèle permettra la simulation des comportements cinétiques dans des modèles de réacteur ou de procédés plus complexes.

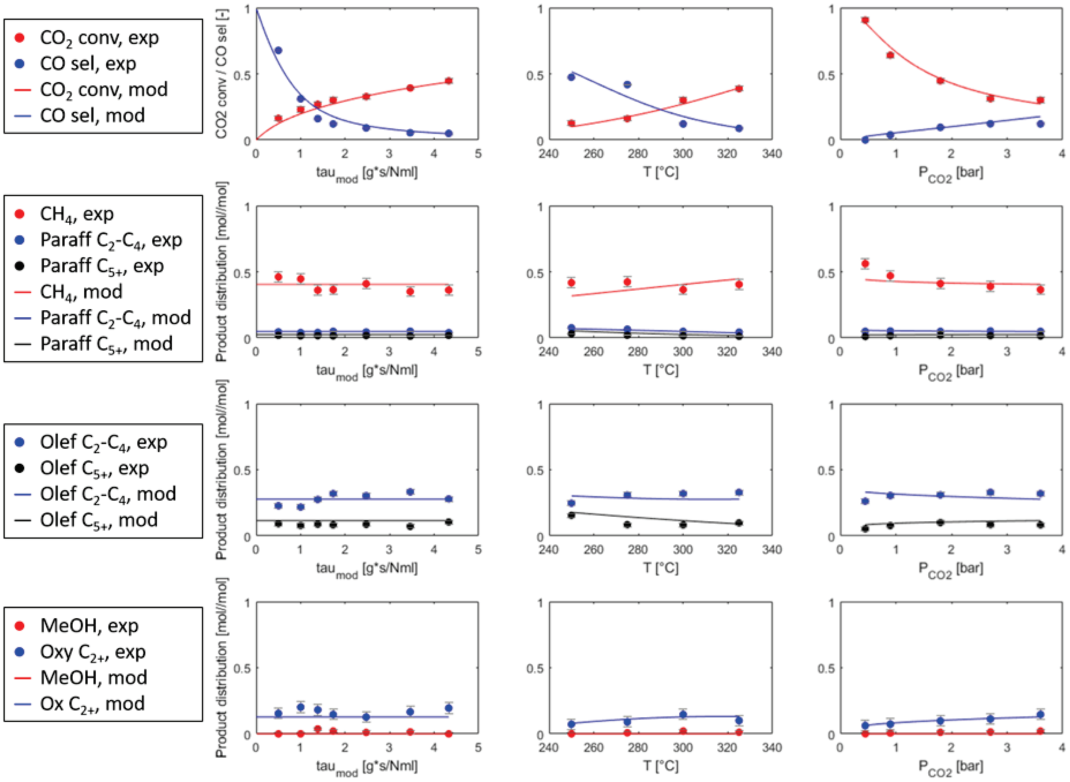

Figure 2. Résultats du modèle cinétique comparés aux données expérimentales. Les lignes représentent les résultats du modèle, les points les données expérimentales.

Développement du modèle micro-cinétique.

En suivant une procédure identique à celle utilisée pour développer le modèle macro-cinétique, deux modèles cinétiques basés sur des hypothèses mécanistiques ont été développés et comparés. Le but de cette approche est de comprendre au moins partiellement comment les différents produits sont formés. En particulier, la formation d'oxygénés est investiguée. Le premier modèle est basé sur l'hypothèse que les oxygénés d'une part et les paraffines et oléfines d'autre part se forment sur les mêmes sites actifs, notamment des carbures de fer, considérés comme la phase active pour la réaction FT. Le deuxième modèle au contraire est basé sur l'hypothèse que les oxygénés se forment sur des sites actifs différents de ceux où les paraffines et les oléfines sont formés.

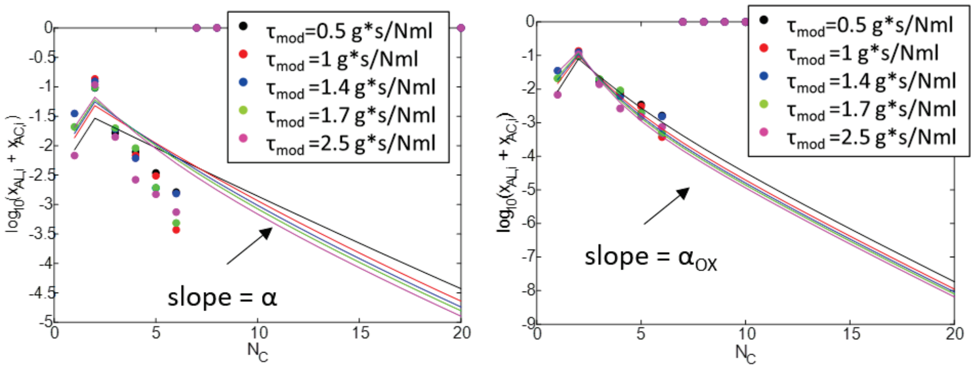

Figure 3. Distribution ASF des oxygénés prédit par le modèle mono-site (à gauche) et par le modèle multi-site (à droite).

La Figure 3 montre la distribution ASF pour les oxygénés prédite par les deux modèles et comparée aux résultats expérimentaux. L'étude menée montre que le modèle basé sur l'hypothèse selon laquelle les oxygénés sont formés sur des sites actifs différents de ceux des oléfines et paraffines permet de mieux prédire la distribution des oxygénés observée expérimentalement. Par contre, ce modèle présente une erreur statistique plus élevée que le modèle mono-site et ressent de la grande quantité de paramètres cinétiques. Une amélioration des deux modèles est donc nécessaire pour mieux comprendre la formation des oxygènes.

Développement du modèle réacteur et étude du procédé.
Le modèle macro-cinétique développé a été inclus dans un modèle idéal de réacteur à piston, homogène en 1D, pour étudier les profils de température et de concentration le long du réacteur. Ce modèle a été comparé à un modèle plus complexe, hétérogène, qui prend en compte la présence de deux phases : le fluide et le catalyseur solide. Cette comparaison montre des différences très limitées entre les deux modèles et a permis de vérifier qu'aucune limitation de transport de masse ni de chaleur n'intervient dans le système.

Ensuite, on a étudié des possibles voies d'optimisation du procédé, par exemple par l'utilisation d'un réacteur membranaire qui permettrait d'éliminer l'eau produite pendant la réaction, évitant ainsi une cause probable de désactivation du catalyseur. On a montré que l'utilisation d'un réacteur membranaire avec l'hydrogène comme gaz de balayage permet d'augmenter la conversion de CO_2 sans modifier significativement les sélectivités en hydrocarbures et en CO.

Enfin, le procédé a été simulé pour estimer son efficacité énergétique et comprendre comment l'optimiser. Une voie possible est l'utilisation de deux réacteurs en série afin d'augmenter la conversion du CO_2, suivis par un système de séparation par des membranes polymériques où les réactifs qui n'ont pas réagi sont séparés des produits valorisables et recyclés en entrée du réacteur. Un système de ce type permet d'obtenir une phase vapeur riche en méthane qui pourrait être injectée dans les réseaux de gaz naturel et une phase organique riche en oléfines qui peut être raffinée pour obtenir différents types de produits (combustibles ou matières premières pour l'industrie chimique). L'efficacité énergétique estimée est autour de 66%.

Conclusions et perspectives.
En conclusion, ce travail montre une étude complète de la réaction d'hydrogénation du CO_2 vers les hydrocarbures, de la synthèse du catalyseur et son étude expérimentale dans un réacteur à l'échelle du laboratoire aux simulations à l'échelle du procédé, en passant par l'étude du mécanisme de la réaction et la dérivation de modèles cinétiques et leur utilisation dans un modèle de réacteur. Des progrès ont été accompli dans le développement de modèles macro et micro cinétiques de la réaction, qui peuvent être appliqués dans des modèles de réacteur plus complexes ou dans des simulations des procédés.

Des possibles voies pour améliorer le procédé ont aussi été proposées, par exemple l'utilisation de réacteurs membranaires pour éviter la désactivation des catalyseurs et donc augmenter la conversion du CO_2 et le rendement en hydrocarbures.

Enfin, de nombreuses améliorations sont nécessaires avant l'implémentation de ce type de procédé à l'échelle industrielle. Entre autres, une connaissance approfondie du mécanisme de réaction peut aider à optimiser la composition du catalyseur afin d'améliorer la sélectivité vers les produits visés ; une étude expérimentale des réacteurs membranaires est aussi nécessaire pour valider le modèle réalisé et pour comprendre les effets de l'élimination de l'eau sur la distribution des hydrocarbures.

Abstract

This thesis is focused on the study of the carbon dioxide hydrogenation reaction towards gaseous and liquid hydrocarbons over a supported Fe-K/Al_2O_3 catalyst. The subject is part of the framework of the Power-to-X technologies that aim at storing surplus electric power derived from renewable energy into the form of gaseous and liquid chemical compounds. In particular, the electricity is used to perform the water electrolysis to produce hydrogen, then the obtained hydrogen is used to convert carbon dioxide into hydrocarbons. These hydrocarbons can have applications as feedstock in the chemical industry or as fuels in the transport field. The carbon dioxide hydrogenation is a catalytic reaction, generally performed over Fe-based catalysts, consisting in two steps: first, carbon dioxide is converted into carbon monoxide via the reverse water-gas shift reaction (RWGS), and then it is further transformed into hydrocarbons via the Fischer-Tropsch synthesis (FT). One of the main constraints of this reaction is its low selectivity, as a variety of hydrocarbons can be obtained. For an eventual application of this process at the industrial scale, it is necessary to deeper understand and better describe the selectivity of the reaction to optimize the productivity of the desired products. In this work, we have carried out an experimental study of the reaction in a lab-scale fixed bed reactor and developed an analytic protocol that allows the quantification of all the products obtained. Moreover, we have developed a macro-kinetic model that describes with a semi-empirical approach the formation of all the products considered; and a micro-kinetic model, that contributes to give insights about the reaction mechanism. Finally, we have modelled a scaled-up reactor with a heterogeneous and a pseudo-homogeneous approach and we have simulated the global process to estimate its carbon and energy efficiencies.

Contents

Nomenclature

Latin letters.

a	Attraction parameter of cubic equations of state [m^3/mol^2]
A_i	Peak area of i in the gas-chromatograph [-]
A_{log}	Mean logarithmic area [m^2]
A_r	Lateral area of the reactor [m^2]
a_{RWGS} or a_{FT}	Inhibition terms for H_2O referred to CO [MPa^{-1}]
a_s	Specific external surface area of a catalyst particle [m^2/m$^3{}_{\text{pellet}}$]
A_{sh}	Lateral area of the shell [m^2]
ASF	Anderson-Schulz-Flory
b	Volume of inert material as fraction of total solid volume [-] or Co-volume of cubic equations of state [m^3/mol]
b_{RWGS} or b_{FT}	Inhibition terms for CO_2 referred to CO [MPa^{-1}]
C	Volumetric concentration [mol/m^3]
c_{ij}	Elements of covariance matrix [-]
c_P	Heat capacity at constant pressure [J/mol/K]
c_{RWGS} or c_{FT}	Inhibition terms for H_2 referred to CO [MPa^{-1}]
cov	Covariance matrix [-]
D	Diffusion coefficient [m^2/s]
d	Diameter [m]
D_{ax}	Axial dispersion coefficient in the catalyst pores [m^2/s]
D_{eff}	Effective diffusion coefficient in the catalyst pores [m^2/s]
D_{Kn}	Knudsen diffusion coefficient in the catalyst pores [m^2/s]
d_i	Critical Kelvin's diameter [m]
D_{ij}	Binary diffusion coefficient between i and j [m^2/s]
D_m	Molecular diffusion coefficient in the bulk [m^2/s]
d_P	Catalytic particle diameter [m]
d_r	Reactor diameter [m]
e	Thickness [m]
E_a	Apparent activation energy of the reaction [J/mol]
F	General function [-]
F_0	Inlet total mole flow [mol/s]
f_i	Fugacity of compound i [MPa]
F_i	Mole flow of i [mol/s]
$F^{'}$	First derivative of the function F [-]

FID	Flame ionization detector
FT	Fischer-Tropsch synthesis
GC	Gas-chromatography
GHG	Greenhouse emissions
$GHSV$	Gas hourly space velocity [Nml/g_{cat}/h]
h	Heat transfer coefficient [W/m^2/K]
H	Henry coefficient [bar]
h_C	Heat transfer coefficient with the cooling fluid [W/m^2/K]
HHV	Higher heat value [J/g]
h_{OV}	Overall heat transfer coefficient between catalytic bed and reactor wall [W/m^2/K]
h_{perm}	Heat transfer coefficient between retentate and permeate sizes [W/m^2/K]
J	Jacobian matrix [-]
J_i	Diffusion flow [mol/s/m^2] or Permeation flow across the membrane [mol/s/m^2]
k_{0i}^*	Modified pre-exponential factor of kinetic constant [mol/kg/s/MPa^2]
k_{0i}	Pre-exponential factor of kinetic constant [mol/kg/s/MPa^2]
k_{ax}	Axial thermal conductivity of the packed bed [W/m/K]
K_{eq}	Equilibrium constant of RWGS [-]
k_G	Mass transfer coefficient between bulk and particle [m/s]
K_i	Equilibrium constant between liquid and vapour phases [-]
k_{ij}	Binary interaction parameters [-]
k_t	Heat transfer coefficient between bulk and particle [W/m^2/K]
L_{bed}	Catalytic bed length [m]
LHV	Lower heat value [J/g]
LVE	Liquid-vapour equilibrium
M	Molar mass [kg/mol]
m	Mass [g]
$\dot{m}$	Total mass flow [g/s]
m_{cat}	Mass of catalyst [g]
$MRF_{i,j}$	Mole response factor of i referred to j [-]
n	Reaction order [-]
N	Maximum C number considered
$\bar{n}_C$	Carbon number of the pseudo-solvent
N_0	Inlet total mass flux [kg/s/m^2]
n_{exp}	Number of experimental points considered
n_{gas}	Number of species detected in gas phase
n_{par}	Number of kinetic parameters
n_{var}	Number of response variables
n_{wat}	Number of species detected in water phase
O	Fraction of olefins for a given C number i [-]
OX	Fraction of oxygenates for a given C number i [-]
p	Total pressure [Pa]
P	Fraction of paraffins for a given C number i [-]
p_c	Critical pressure [Pa]
p_i	Partial pressure of i [Pa]
p_r	Reduced pressure [-]
PtL	Power-to-Liquid
q	Heat transferred by conduction [W]

Q	Heat source [W/m^3]
Q_{H_2}	Permeance of hydrogen [mol/(m^2.s.Pa)]
Q_{H_2O}	Permeance of water [mol/(m^2.s.Pa)]
Q_m	Membrane heat density [W/m^3]
Q_r	Reaction heat density [W/m^3]
Q_0	Heat density exchanged between reactive and permeative zones [W/m^3]
R	Ideal gas constant [J/mol/K]
r_1	Reaction rate of C_1 compounds [mol/kg/s]
r_i	Reaction rate [mol/kg/s]
R_P	Radius of the catalyst particle [m]
$resnorm$	Squared norm of the residual [-]
$RF_{i,j}$	Mass response factor of i referred to j [-]
$R_{v,i}^{obs}$	Observed volumic reaction rate per unit of catalyst pellet volume [mol/m$^3_{\text{pellet}}$/s]
$RWGS$	Reverse water-gas shift
S_i	Selectivity of product i [-]
S_r	Reactor cross-sectional surface [m^2]
SW	Ratio between sweep gas flow and inlet retentate flow [-]
T	Temperature [K]
T_{bed}	Bed temperature [K]
T_c	Critical temperature [K]
T_C	Cooling fluid temperature [K]
T_P	Catalyst particle temperature [K]
T_r	Reduced temperature [K]
TCD	Thermal conductivity detector
ToS	Time on Stream [h]
u	Surface velocity [m/s]
v	Molar volume [cm^3/mol]
$\dot{V}$	Mole flow [Nml/s]
V_{cat}	Volume of catalyst [m^3]
V_r	Reactor volume [m^3]
x	Mole fraction [-]
x_i	Mole fraction of i in liquid phase [-]
y_i	Mole fraction of i in vapour phase [-]
X_i	Fraction of product i among hydrocarbons [-]
z	Bed length coordinate [m]
Z	Compressibility factor [-]
z_i	Mole fraction of i [-]
WI	Wobbe Index [kWh/m^3]
$\mathcal{J}_i$	Poyinting factor [-]

Greek letters.

α	Chain-growth probability [-]
α_{bed}	Heat transfer coefficient through the catalytic bed [W/m^2/K]
α_{rad}	Equivalent radial heat transfer coefficient in the catalytic bed [W/m^2/K]
α_V	Fraction of vapour phase in the system [-]
$\alpha_{w,int}$	Heat transfer coefficient in the inner side of the reactor wall [W/m^2/K]

$\alpha_{w,out}$	Heat transfer coefficient through the reactor wall [W/m^2/K]
γ	Activity coefficient [-]
ΔH^r	Enthalpy of reaction [J/mol]
ΔT_{film}	Temperature difference over the film surrounding the catalyst particles [K]
ϵ	Porosity [-]
η_C	Carbon conversion [-]
η_{PtX}	Energy efficiency of Power-to-X process [-]
κ	Permeability [darcy]
λ	Mean free path of a gas molecule [m] or Thermal conductivity [W/m/K]
λ_m	Thermal conductivity of membrane [W/m/K]
λ_{rad}	Radial effective thermal conductivity of the bed [W/m/K]
λ_s	Thermal conductivity of steel [W/m/K]
μ	Viscosity [Pa.s]
ν	Fuller's volume [-]
ν_{ij}	Stoichiometric coefficient of i in reaction j [-]
ρ	Density [kg/m^3]
σ	Surface tension [N/m]
τ	Tortuosity [-]
τ_{mod}	Modified contact time [g.s/Nml]
ϕ	Ratio of pressure in permeate side and in retentate side [-]
Φ	Weisz-Prater modulus [-]
Φ_i	Fugacity coefficient [-]
χ_i	Conversion of reactant i [-]
ω	Mass fraction [-]
ω_c	Critical acentric factor [-]

Adimensional numbers.

Bo	Bodenstein number	$= \frac{ud}{D}$
Ca	Carberry number	$= \frac{R_v^{obs}}{k_G a_s C_b}$
Kn	Knudsen number	$= \frac{\lambda}{d_{pores}}$
Nu	Nusselt number	$= \frac{hd}{\lambda}$
Pr	Prandtl number	$= \frac{c_P \mu}{\lambda}$
Re_P	Reynolds number	$= \frac{\rho u d}{\mu}$
Sc	Schmidt number	$= \frac{\mu}{\rho D}$
Sh	Sherwood number	$= \frac{d k_G}{D}$

Subscripts and superscripts.

0	inlet
b	bulk
bed	bed
C	cooling fluid
cat	catalyst
$calc$	calculated
CHO	aldehyde
CO	ketone
$COOH$	carboxylic acid
exp	experimental
HCs	hydrocarbons
IN	inlet
inj	injected
L	liquid phase
m	membrane
mix	gaseous mixture
OH	alcohol
oth	others (branched chains or aromatics)
OUT	outlet reactor
P	catalyst particle or permeate side
$prod$	products
r	reactor
R	retentate side
ref	reference
S	at particle surface
sat	saturated
sh	shell
$solv$	solvent
tot	total
SW	sweep gas
V	vapour phase
w	wall
wat	water phase
σ	saturated
∞	at infinite dilution
$-$	alkane
$=$	alkene

Introduction

In the last decades, the increase of global population and the increase of the energy consumption, have led to the increase of the greenhouse gas emissions in the atmosphere, causing the global warming of the planet. In order to avoid disastrous consequences on our planet, different international agreements, such as the Paris agreement in 2016, have fixed the objective to keep the greenhouse gases concentration under 450 ppm before 2100. In this way, the increase of the average temperature of the planet could be kept below 2°C, limiting the disastrous consequences on the planet. With the aim to reduce greenhouse gases emissions, the transition from fossil fuels to renewable sources is necessary in every economic sector.

In this context, novel technologies - based on renewable sources - are developing as an alternative to fossil fuels. However, renewable energies present a problem connected to their intermittent nature. This causes periods with higher demand than production and periods with higher production than demand. In these periods of excess production, it is necessary to store the produced electricity into another form, so that it can be used when required. The renewable electricity storage can be done in many different ways, such as hydraulic storage, electrochemical storage, or chemical storage.

In this work, we are interested in the chemical storage of renewable electricity in the form of gaseous and liquid hydrocarbons. This technology, known as Power-to-X, allows the storage of renewable electricity in the form of hydrocarbons: first H_2 is produced from water via electrolysis and then it is converted into fuels, via CO_2 hydrogenation. Transport and storage of H_2 is known to be complicated and expensive because of its low energy density per volume unit. Thus, its conversion into other kinds of chemical compounds could contribute to avoid these problems. Moreover, the synthetic hydrocarbons obtained from this process could be suitable for applications as fuels for the transport sector, especially aviation, and as feedstock for the chemical industry.

Despite the advantages of this technology, its deployment at the industrial scale is still far, as H_2 production via water electrolysis still has a very high impact on the final cost of the fuels and CO_2 capture technologies still need some improvements, as well as the CO_2 hydrogenation reaction.

In this work, we are focusing on the CO_2 hydrogenation reaction. This reaction includes two steps, the reverse water-gas shift that converts CO_2 into CO, followed by the Fischer-Tropsch synthesis that further converts CO into hydrocarbons:

$$nCO_2 + nH_2 \leftrightarrow nCO + nH_2O$$

$$nCO + 2nH_2 \leftrightarrow (-CH_2-)_n + nH_2O$$

These two reactions are very different from each other: the first one is an endothermic and fast reaction, favoured at high temperature; the second one is an exothermic and slower reaction, favoured at low temperature and high pressure.

This process is currently performed at pilot scale in the so-called indirect way, where the two reactions are separated in two different reactors, so that they can be optimized. This process, however, requires cooling and eventually compression between the two steps, thus from an energetic point of view, it may be advantageous to perform both reactions in the same reactor, in the so-called direct way. In order to perform both reactions in the same reactor, a suitable catalyst is needed and the operating conditions have to be optimized. Other limitations of this reaction are the very low selectivity, as many hydrocarbons are obtained as products, and the formation of water as co-product that can lead to fast deactivation of the catalyst.

Most of the work published in the literature on the hydrogenation of CO_2 to hydrocarbons is focused primarily on the development of an optimal catalyst that maximizes the selectivity to the targeted hydrocarbons. In particular, the addition of promoters (such as K and Cu) to iron-based catalysts has been observed to increase the production of long-chain hydrocarbons and the conversion of CO_2.

Conversely, only few works have been dedicated to the modelling of this reaction. In view of industrial applications, having mathematical models that describe the reaction behaviour is very important, as it allows to study the scale-up of the reaction and the phenomena that could be involved. Most of the models that are available in the literature are very simple and do not allow to predict the hydrocarbons distribution.

Our work has the aim to understand if the direct pathway of the CO_2 hydrogenation towards hydrocarbons can be energetically competitive, compared to the indirect pathway, and to evaluate its feasibility. To do that, it is very important to understand the behaviour of the reaction, its mechanism and its limitations. Moreover, it is crucial to develop tools for the modelling and the study of the reaction in scaled-up systems and different configurations.

The work presented in this manuscript is the result of a collaboration between the CEA-LITEN of Grenoble (the *Laboratory Reactors and Processes - LRP*) and the CP2M (*Laboratory of Catalysis, Polymers, Processes and Materials*) of Lyon (UMR 5128). It includes an experimental study of the reaction and a detailed mathematical modelling:

- an experimental study of the reaction in a laboratory-scale reactor and in a scaled-up reactor for the comprehension of the reaction behaviour and mechanism;
- the development of a detailed macro-kinetic model that describes the reaction rates and the hydrocarbons distribution under different operating conditions;
- the development of a detailed micro-kinetic model that is based on hypothesis about the reaction mechanism and provides insights about the formation pathways of olefins, paraffins ans oxygenates;
- the development of a mathematical model that describes the behaviour of a scaled-up reactor for the CO_2 hydrogenation under different conditions, taking into account the heat and mass transfer phenomena between the gas and the solid catalyst;
- the simulation of the overall process and the estimation of mass and energy efficiencies.

The manuscript is structured in 6 chapters:

- the 1st chapter deals with the state-of-the-art of the hydrogenation of carbon dioxide towards hydrocarbons. We review the most important work made about this reaction and we identify which advancements are needed.

The analysis of the context of the work and the state-of-the-art has been the subject of a review:

Panzone, C., Philippe, R., Chappaz, A., Fongarland, P. and Bengaouer, A. 2020. 'Power-to-Liquid Catalytic CO_2 Valorization into Fuels and Chemicals: Focus on the Fischer-Tropsch Route'. *Journal of CO2 Utilization* 38: 314–47.

- the 2nd chapter describes the experimental procedures followed for the synthesis of the catalyst and for the experimental study of the reaction. The chapter is structured in 4 main parts that refer to: 1. the synthesis and caracterisation of the catalyst; 2. the experimental study in the laboratory-scale reactor of CP2M; 3. the experimental liquid co-feeding study in the same laboratory-scale reactor of CP2M; 4. the experimental study in the scaled-up reactor of CEA.

- the 3rd chapter presents the results of the experimental studies whose procedures were described in Chapter 2. First the characterisation of the catalyst is presented, then the experimental kinetic study of the CO_2 hydrogenation in absence of transfer limitations is shown, to conclude with the results of the co-feeding study and the scaled-up reactor study.

- the 4th chapter is focused on the development of a detailed macro-kinetic model that describes the reaction rates of the main compounds and is validated on the experimental data obtained in the laboratory-scale reactor of CP2M.

The contents of the third and fourth chapters have been the subject of a paper, recently accepted by the *Industrial & Engineering Chemistry Research* journal:

Panzone, C., Philippe, R., Nikitine, C., Vanoye, L., Bengaouer, A., Chappaz, A. and Fongarland, P. 2021. 'Catalytic and Kinetic Study of the CO_2 Hydrogenation Reaction over a Fe-K/Al_2O_3 Catalyst towards Liquid and Gaseous Hydrocarbons Production.'

- the 5th chapter shows the development of a micro-kinetic model based on hypothesis on the reaction mechanism and gives insights about the mechanism of formation of the different species and the active sites involved. This Chapter is presented in form of a paper that will be soon submitted:

Panzone, C., Philippe, R., Nikitine, C., Vanoye, L., Bengaouer, A., Chappaz, A. and Fongarland, P. 'Development and validation of a detailed micro-kinetic model for the CO_2 hydrogenation reaction towards hydrocarbons over a Fe-K/Al_2O_3 catalyst.'

- finally, the 6th chapter focuses on the scale-up of the process. First, a scaled-up reactor model is presented and validated on the experimental data obtained during the experimental campaign performed in CEA. Then, a membrane reactor model is presented, as a solution to improve the hydrocarbons yield by removing water produced during the reaction. Finally, the global process is simulated and the carbon and energy efficiencies are estimated.

The manuscript ends with conclusions and perspectives of the work.

The results of this work have been presented to the following international conferences:

1. **CAMURE-11, 11th International Symposium on Catalysis in Multiphase Reactors, March 2021, Online event - Oral communication**

   Panzone, C., Philippe, R., Chappaz, A., Nikitine, C., Vanoye, L., Bengaouer, A. and Fongarland, P. ‘Catalytic and kinetic study of the CO_2 hydrogenation reaction over a K-Fe/Al_2O_3 catalyst for gaseous and liquid hydrocarbons production.’

2. **EUBCE, 29th European Biomass Conference and Exhibition, April 2021, Online event - Oral communication**

   Panzone, C., Philippe, R., Nikitine, C., Vanoye, L., Bengaouer, A., Chappaz, A. and Fongarland, P. ‘Study of Catalytic Performances and Kinetics of CO_2 Hydrogenation Reaction over a K-Fe/Al_2O_3 Catalyst for Gaseous and Liquid Hydrocarbons Production.’

   Winner of the Student Award.

3. **ECCE, 13th European Congress of Chemical Engineering, September 2021, Online event - Oral communication**

   Panzone, C., Philippe, R., Chappaz, A., Nikitine, C., Vanoye, L., Bengaouer, A. and Fongarland, P. ‘Kinetic study and reactor modelling of the CO_2 hydrogenation reaction for hydrocarbons production.’

a

CHAPTER 1

State-of-the-art of CO_2 hydrogenation towards hydrocarbons.

1.1 General introduction.

1.1.1 Context.

1.1.1.1 The energy sector.

The increase of the global population since the Sixties (see Figure 1.1), together with the increase of the quality of life have contributed to the increase of the global energy consumption that passed from 43000 TWh in 1965 to 154600 TWh in 2020. (https://ourworldindata.org/energy) The increase of the global energy consumption by world region is presented in Figure 1.2 and shows that the main energy consumers are currently Asia, North America and Europe. The energy consumption in Europe is almost stable since the late Nineties and has been showing a slight decrease over the last ten years.

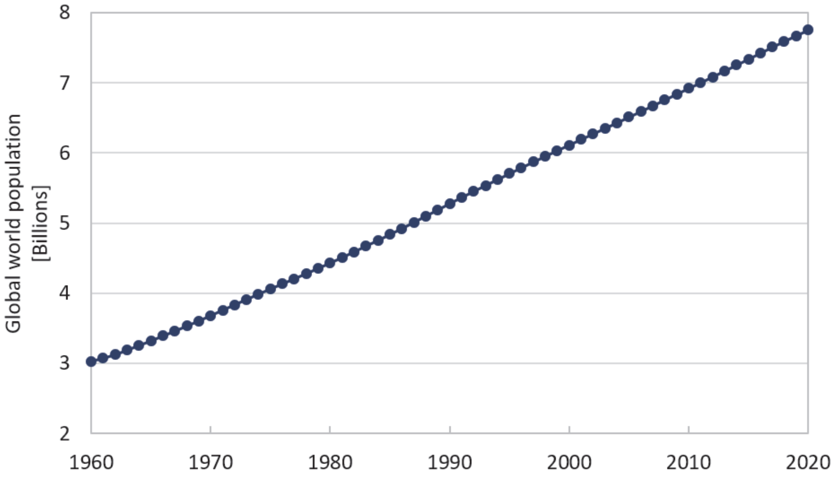

Figure 1.1: World population from 1960 to 2020. Data from https://ourworldindata.org/world-population-future-eductation now/.

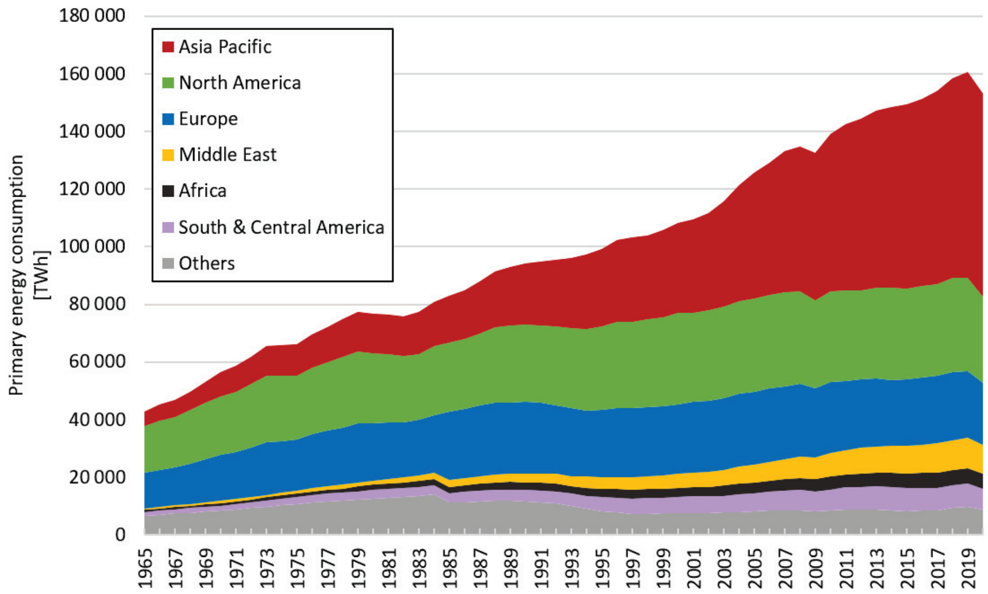

Figure 1.2: Primary energy consumption by world region from 1965 to 2020. Data from https://ourworldindata.org/energy.

Predictions expect a further increase of the global population with a resulting additional rise of the energy consumption. (Siegemund et al., 2017) Energy consumption is currently based mainly on fossil fuels (see Figure 1.3) that constitute the 84% of the global energy consumption in the world. (https://ourworldindata.org/energy)

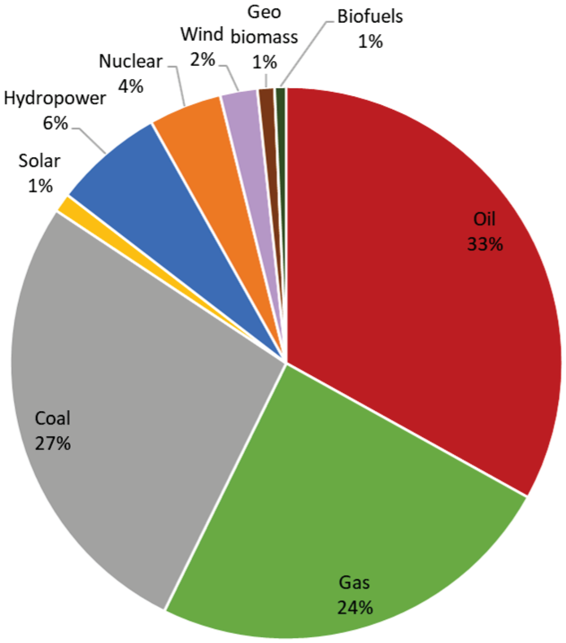

Figure 1.3: World energy consumption by source in 2019. Data from https://ourworldindata.org/energy.

This kind of fuels, beside being non-renewable, involve the release of greenhouse gases (GHG) in the atmosphere. The repartition of GHG emissions by gas expressed in percentage of CO_2-equivalents is shown in Figure 1.4. (https://ourworldindata.org/greenhouse-gas emissions) CO_2

thus represents the gas with the highest impact on climate change.

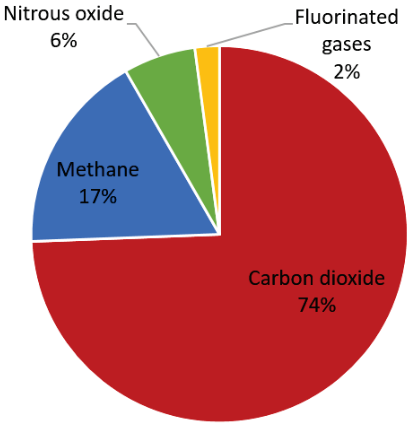

Figure 1.4: Global greenhouse gas emissions by gas. Greenhouse gas emissions are converted to CO_2-equivalents by multiplying each gas emissions by the corresponding 100-year global warming potential (GWP). Data from https://ourworldindata.org/greenhouse-gas emissions.

The CO_2 concentration in the atmosphere has increased from 317 ppm in 1960 to 414 ppm in 2020. (https://climate.nasa.gov/) This increase has been accompanied by a gradual increase of the mean surface temperature of the Earth, that in 2020 reached an increase of 1°C compared to the pre-industrial level (see Figure 1.5).

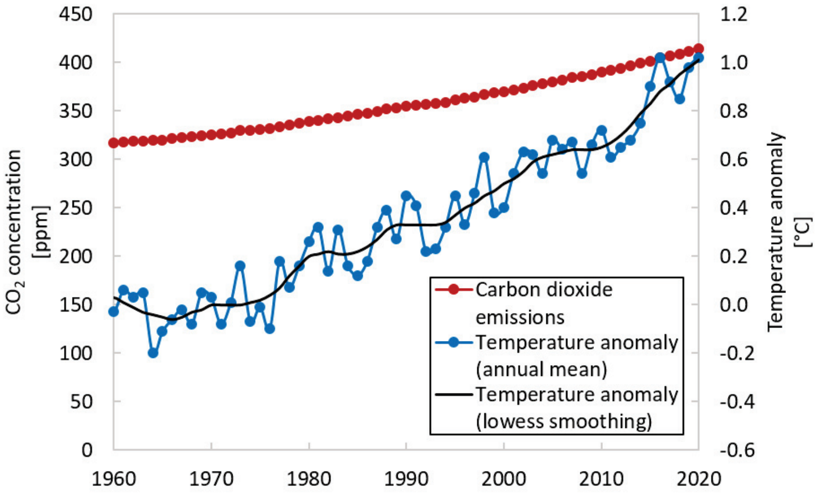

Figure 1.5: Increase of the CO_2 concentration in the atmosphere and of the global land-ocean temperature anomaly (compared to average temperature of the period 1951-1980). Data from https://climate.nasa.gov/.

This level of CO_2 in the atmosphere is expected to rise by 20% in the next 20 years if measures are not taken to decrease the CO_2 emissions. (Siegemund et al., 2017) The Intergovernmental Panel on Climate Change (IPCC) has determined a critical threshold of 450 ppm that does not have to be overcome before 2100. (IPCC, 2014) This level of CO_2 is likely to guarantee the global warming below 2°C. For this scenario, reductions of GHG emissions from 40 to 70% by 2050 (in reference to 2010) are required and zero or below CO_2 emissions are required by 2100.

The IPCC has identified four different scenarios depending on the effort that is made to reduce CO_2 emissions. Figures 1.6-1.8 show some results of the different scenarios analysed. In the worst scenario considered, named RCP8.5, with no additional effort to constrain emissions, CO_2 emissions would continue to increase until values over 100 Gt_{CO2}/year in 2100, and the average surface temperature would increase over 4°C compared to the pre-industrial level. This would have disastrous consequences on the whole planet. An increase of 4°C of the average surface temperature would imply an increase of more than 7°C in some parts of the planet, above all at the North Pole, as shown in the image on the right of Figure 1.8. This also entails significant increase of the mean sea level, reduction of the sea ice extent and acidification of the oceans. In the best possible scenario, RCP2.6, zero emissions of CO_2 would be achieved in 2100 and average temperature increase would be limited below 1°C. However, even in this scenario, consequences at the North Pole would be serious, with an increase of the temperature higher than 3°C.

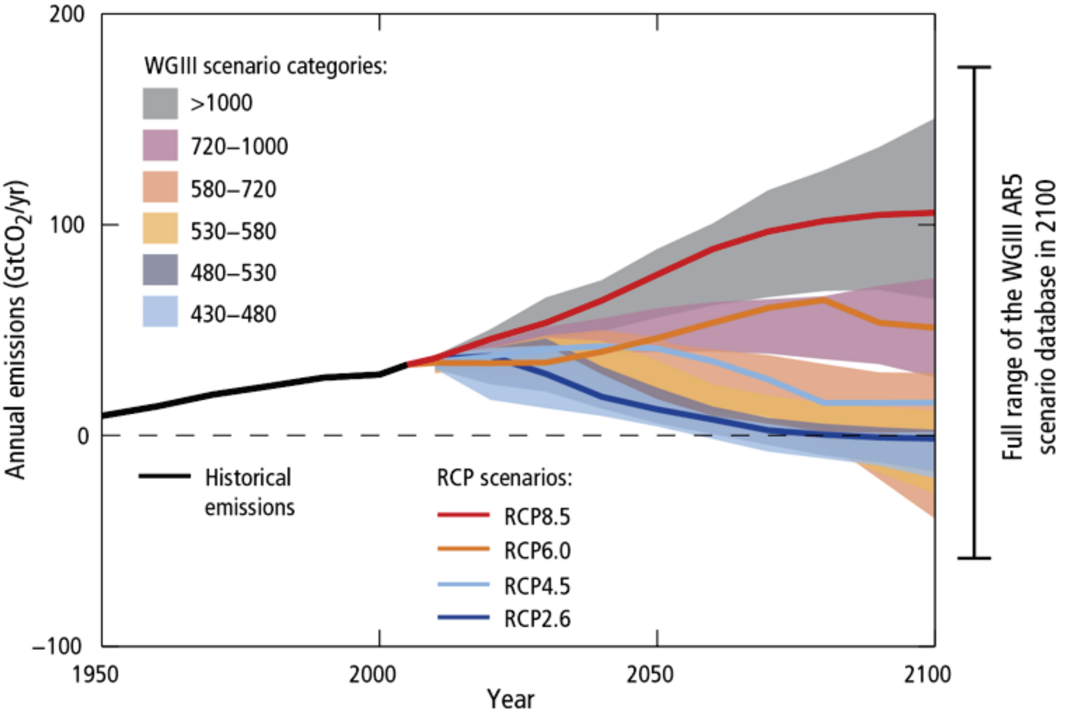

Figure 1.6: Annual anthropogenic CO_2 emissions predicted according to different proposed scenarios. Figure adapted from IPCC (2014).

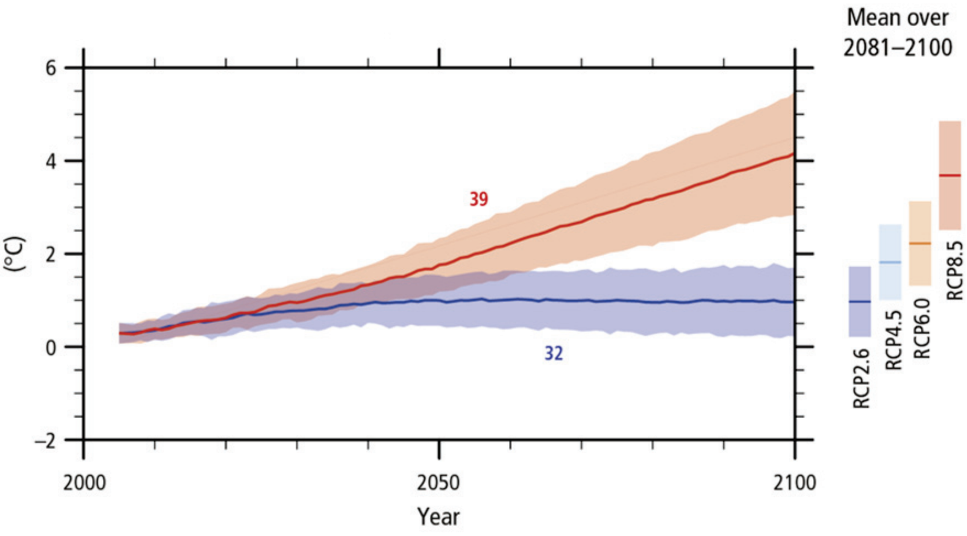

Figure 1.7: Global average surface temperature change (compared to the period 1986-2005). Figure adapted from IPCC (2014).

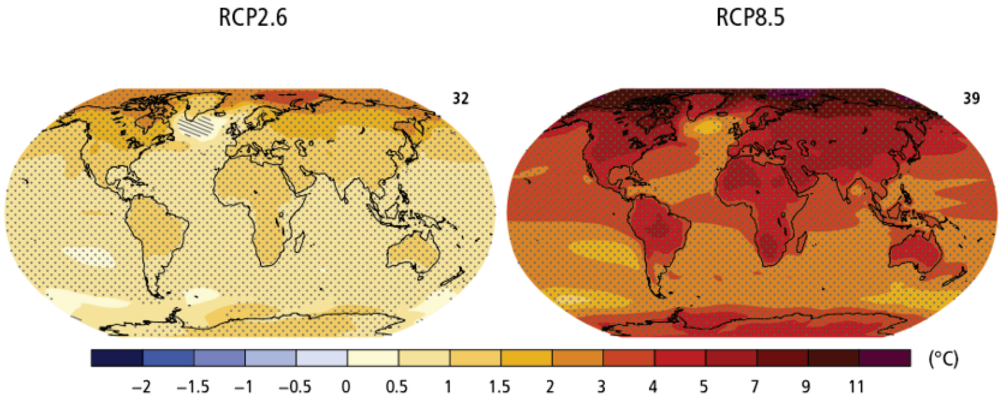

Figure 1.8: Change in average surface temperature for the period 2081-2100 compared to the period 1986-2005. Figure on the left refers to scenario RCP2.6, figure on the right to RCP8.5. Figure adapted from IPCC (2014).

Scenarios like the RCP2.6 consider substantial net negative emissions of CO_2 by 2100, around 2 Gt_{CO2}/year on average. This means that the effort to reduce the CO_2 emissions, besides the development of alternative fuels not based on fossil sources, should include neutral CO_2 emissions and thus the development of technologies for capture and storage or utilisation of CO_2. Therefore, it is necessary to transform the whole economic sector, by changing the way fuels are produced and consumed and by developing new technologies for the CO_2 capture.

Figure 1.9 presents the evolution of the European CO_2 emissions by sector. These data reveal that transport is currently the sector responsible for the highest GHG emissions. Figure 1.10 shows the emissions from transport sector: almost 80% of the emissions derived from transport are caused by road transport, while only 12% and 9% derive from aviation and shipping, respectively. (IEA, 2020) It is thus clear that a strong effort should be focused on the reduction of CO_2 emissions deriving from the transport sector.

The reduction of GHG emissions through the substitution of fossil fuels by renewable sources is the objective of the energy transition which is currently ongoing in the whole world.

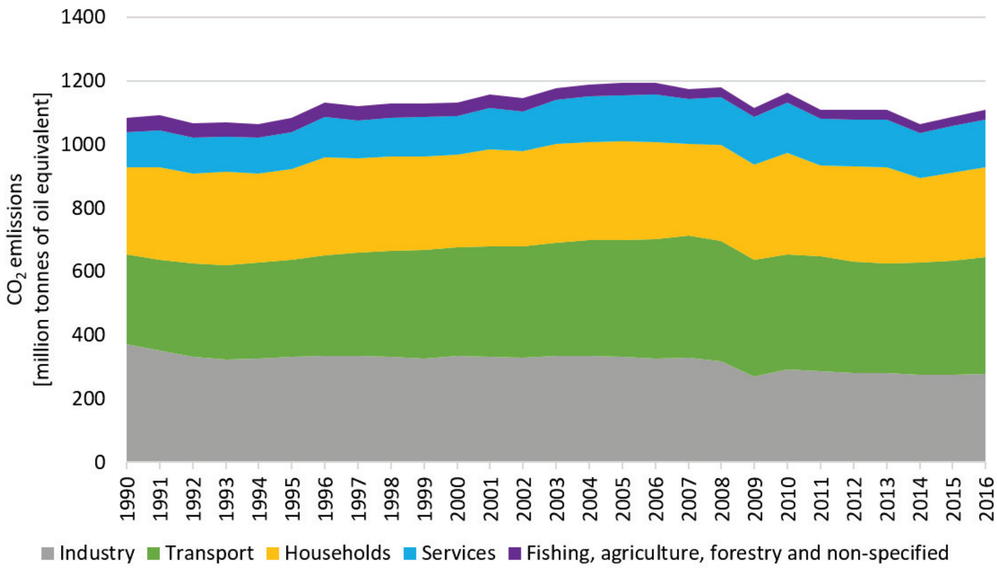

Figure 1.9: CO_2 emissions by sector in Europe in the period from 1990 to 2016. Data from https://www.eea.europa.eu/.

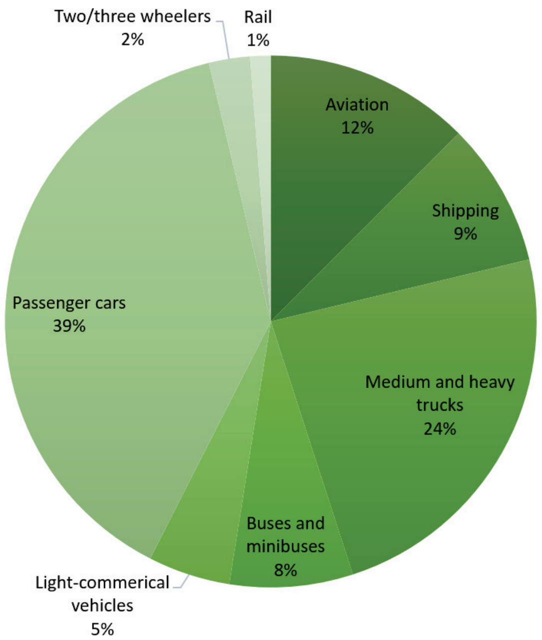

Figure 1.10: Shares of CO_2 emissions from transport sector by transport type. Data from IEA (2020).

1.1.1.2 The energy transition.

The energy transition represents the gradual substitution of the current system of production, distribution and consumption of energy, which is based on fossil sources and emits GHGs, by renewable energy sources, with the aim to reduce the CO_2 emissions and to mitigate climate change.

In the energy transition context, renewable energies play a very important role. The global consumption of renewable energy has been increasing very rapidly, especially over the last 10 years, as shown in Figure 1.11. Currently, about 18000 TWh, or the 11%, of the global energy consumption derives from renewable energy. In Europe, more than 10% of the total energy consumption comes from renewable energies, in particular from hydropower and wind power. If only

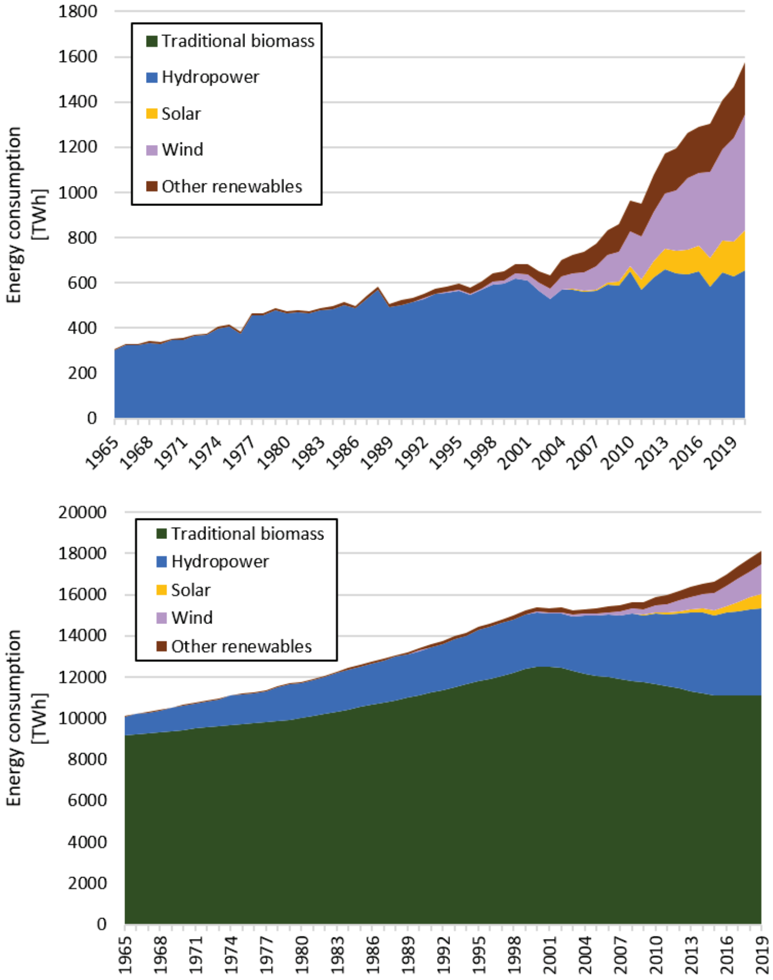

Figure 1.11: Consumption of renewable energy in Europe (up) and in the world (down). Data from https://ourworldindata.org/grapher/renewable-energy consumption.

electricity generation is taken into account, the percentage of renewable energy used becomes higher. In Europe, renewable sources represent the 37.5% of the total electricity production, while fossil fuels represent the 38%, as shown in Figure 1.12.

The main issue connected to the use of renewable energies is their intermittence, meaning that electricity is not always produced when it is needed. The production of electricity from renewable sources is strongly dependent on meteorological conditions, with periods where the production is higher than the demand and periods where the production does not satisfy the demand. Therefore, during excess production periods, it becomes necessary to convert the electricity into storable forms of energy.

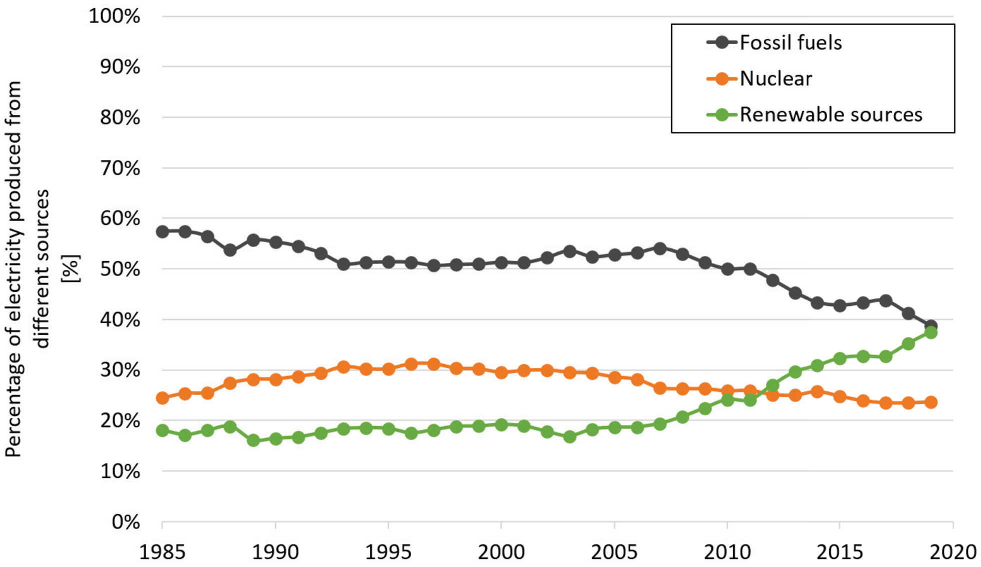

Figure 1.12: Share of production of electricity by sources. Data from https://ourworldindata.org/electricity mix.

1.1.1.3 Energy storage.

Energy can be stored in different ways. Figure 1.13 classifies different energy storage systems according to their volumetric and gravimetric energy densities. Some energy storage systems are already proven, such as pumped hydropower or electrochemical storage. Hydraulic storage offers high efficiency and capacity but is limited by geographical constraints, while electrochemical storage in batteries is limited in terms of power and energy density. Different kinds of batteries exist: lead acid battery is currently the most developed technology on the market; nickel metal hydrides battery has the advantage to require minimal maintenance and not contain hazardous products; lithium ion battery has high gravimetric energy density, but presents safety constraints and is quite expensive. (Gallandat et al., 2017) Other storage systems are still under development, such as compressed air or chemical storage. Chemical storage in form of gaseous or liquid hydrocarbons presents high value of both volumetric and gravimetric energy density, representing a good solution for renewable energy storage.

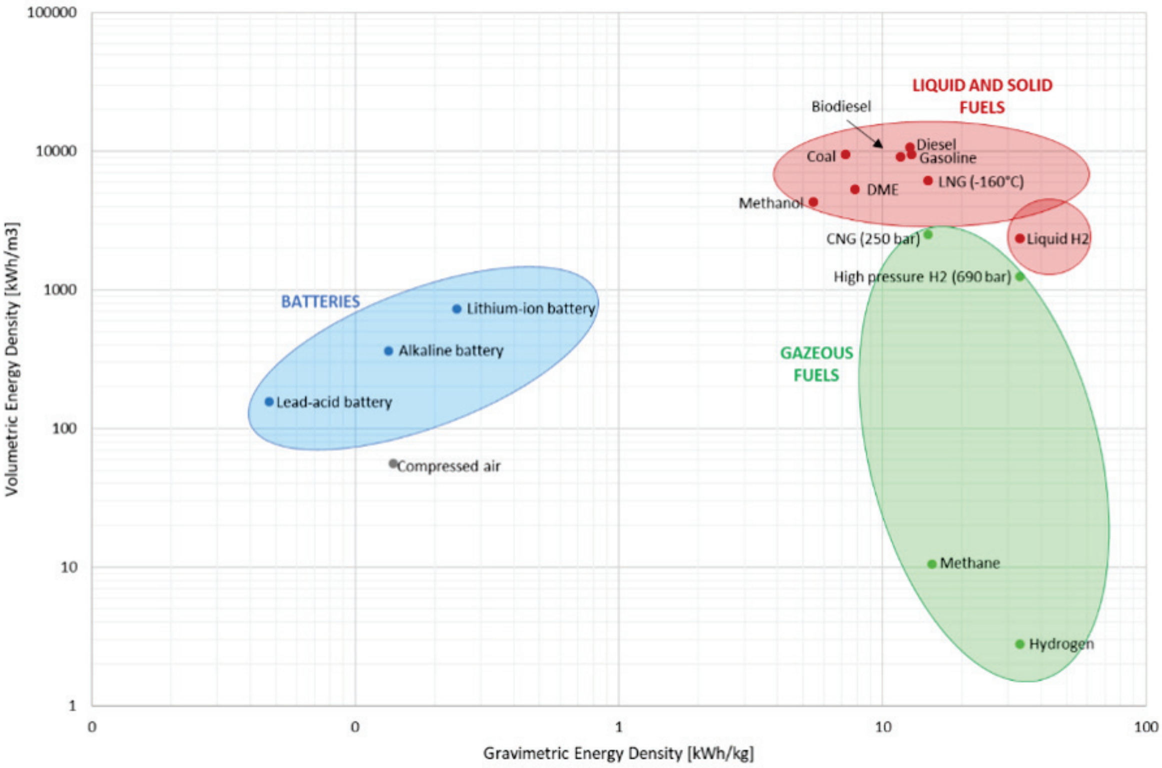

Figure 1.13: Volumetric and gravimetric energy densities of different energy storage systems. Figure from Panzone et al. (2020).

1.1.1.4 Chemical storage.

Chemical storage of renewable energy could be in form of gas, such as hydrogen or methane, or in form of liquid, such as methanol, DME, formic acid, or liquid hydrocarbons.

All these technologies, known as Power-to-X technologies, are based on the idea that excess electricity derived from renewable energy can be converted into H_2 via water electrolysis. H_2 could be directly used as a fuel for mobility, heat and power generation, or as raw material for the chemical industry. Hydrogen has a high mass energy density and a clean combustion, but its low volumetric energy density makes difficult and expensive its transport and storage. Hydrogen can thus be further converted into other chemical compounds by reaction with CO_2. This allows to overcome the problem of itermittence of renewable energies, as electricity is stored in form of one or several chemical compounds, and to contribute to reduce the CO_2 emissions via carbon capture and utilization (CCU). CO_2 hydrogenation reactions can lead to the formation of different products, according to the catalyst used and the operating conditions adopted. Figure 1.14 illustrates different possible pathways of CO_2 hydrogenation and their possible applications.

Conversion of H_2 to CH_4 through the Sabatier reaction is generally performed over Ni catalysts (Wang et al., 2011; Chang et al., 2002; Champon et al., 2019) and involves a slight loss of the process efficiency (a decrease from 75% for Power-to-Hydrogen to 65% for Power-to-Methane). (Ducamp et al., 2018) Methane can be used as a substitute of natural gas.

CO_2 could also be converted into liquid compounds. The energy storage in form of liquid chemicals has many advantages: transport and storage of liquid compounds is much easier than that of gaseous, their energy density per unit volume is higher and the mass loss during long-term storage is lower. Moreover, their extraction from the reactor is generally easier and does not need expensive separation systems. (Varone and Ferrari, 2015; Gallandat et al., 2017; König et al., 2015b)

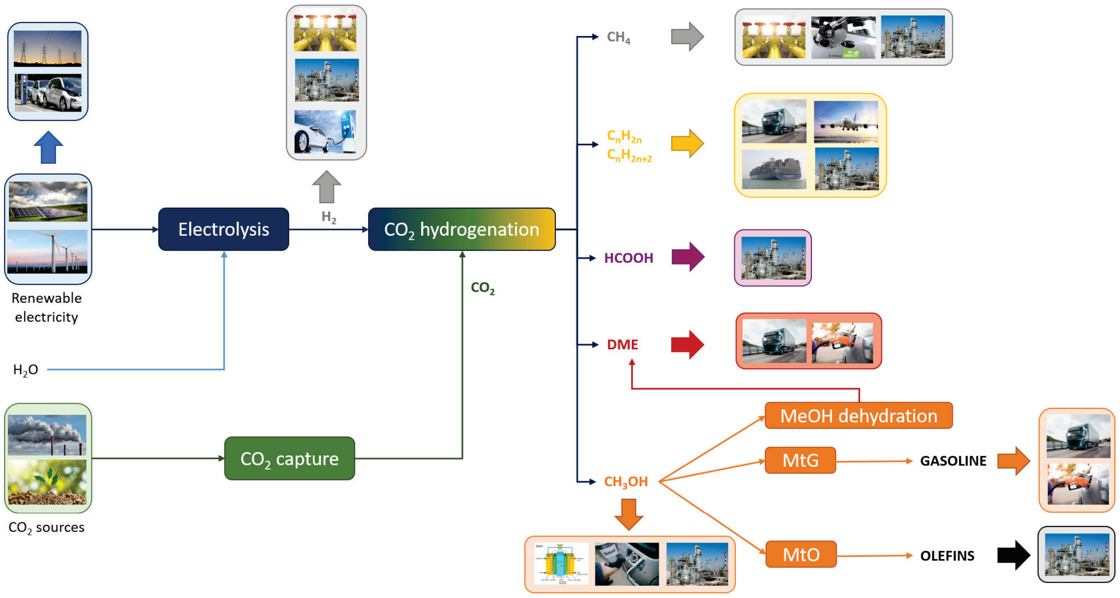

Figure 1.14: Power-to-X technologies and their applications.

Methanol can be obtained from CO_2 over Cu-based catalysts. It can be used as fuel in the direct methanol fuel cells (DMFC) (McGrath et al., 2004) or in modified diesel engines (Bromberg and Cohn, 2010), as its combustion is cleaner than that of petrol and does not involve the emission of NO_x and SO_x. Methanol is also extensively used in the chemical industry. Processes to convert methanol into gasoline (MtG) (Mignard and Pritchard, 2006) or olefins (MtO) (Goeppert et al., 2014) have already been developed at industrial scale. DME can be obtained from methanol via dehydration over acid catalysts or directly from CO_2 over bi-functional catalysts. (Li et al., 2018a; Larmier et al., 2017; An et al., 2017; Vanoye et al., 2013) It can be used as a substitute for diesel, as it has a high cetane number and cleaner combustion. Formic acid can be obtained from CO_2 via homogeneously catalysed reaction, over Ru-based catalysts. (Jessop et al., 2004; Filonenko et al., 2014; Wang et al., 2015b) Formic acid is largely used in industry, in particular in pharmaceutical, paper production, garments finishing, leather and rubber industries.

CO_2 can also be converted into liquid hydrocarbons, a mixture of olefinic and paraffinic chains of different lengths that can be post-processed to obtain gasoline, diesel, kerosene... and applied in the transport field. Alternatively, the pool of hydrocarbons obtained can have applications in the chemical and petrochemical industry. The advantage of this pathway compared to other Power-to-Liquid (PtL) pathways is that these liquid fuels could be easily integrated with the existent infrastructure or used in the transport field, without the need of huge investments or technological renovations. Moreover, the technological transformation is made upstream the consumers, resulting in a high level of popular acceptance. (Varone and Ferrari, 2015; Gallandat et al., 2017; König et al., 2015b; Schmidt et al., 2018)

We have shown previously that the transport field is the highest contributor to GHG emissions and that alternative fuels as substitutes of those derived from fossil sources are needed. A recent report of the International Energy Agency (IEA) shows predictions of the future energetic mix of the transport sector. (IEA, 2020) Figure 1.15 summarizes some of the results presented in the IEA report. According to this scenario, the transport energy transition will pass primarily by electricity and biofuels that will mainly substitute gasoline; later, hydrogen and synthetic fuels will also become a significant part of the mix. Decarbonized electricity will become the most important form of energy by 2070, especially for passenger cars and light-duty vehicles. For heavy-duty vehicles, electricity and hydrogen will represent the main form of energy by 2070, while for maritime transport ammonia will contribute for more than the half of the demand. The aviation sector is the most difficult to renovate and kerosene from fossil fuels will still be an important energy source in 2070. In parallel, biofuels and synthetic fuels will gradually substitute fossil-derived kerosene, becoming more than the 75% of the global energy demanded for the aviation transport by 2070.

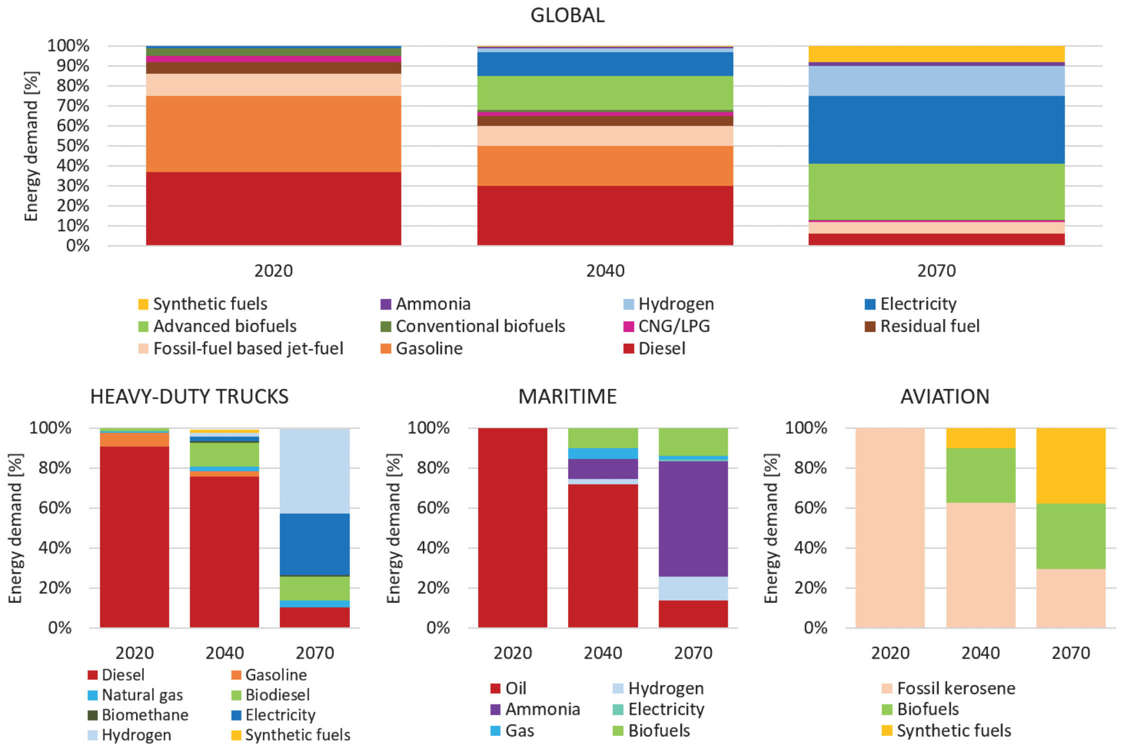

Figure 1.15: Energy consumption of the transport sector by fuel in 2020 and predictions for 2040 and 2070. Data from IEA (2020).

Therefore, according to this scenario, synthetic fuels obtained from CO_2 hydrogenation will be part of the energetic mix and necessary for the aviation transport by 2070. This technology is still at very early stage of development, thus a significant effort is essential to contribute to its development.

As it is the purpose of our work, in the following we will focus only on the synthesis of hydrocarbons via CO_2 hydrogenation.

1.1.2 The CO_2 hydrogenation to hydrocarbons concept.

The process of hydrogenation of CO_2 into liquid fuels consists in the conversion of CO_2 and H_2 into hydrocarbons (see Figure 1.16). The process needs electricity to convert water into H_2 via electrolysis. Ideally, if renewable electricity is used, this technology allows to create a zero net CO_2 emissions cycle (where all CO_2 emitted is reconverted) and provides a possible solution for the intermittence problem of renewable energy.

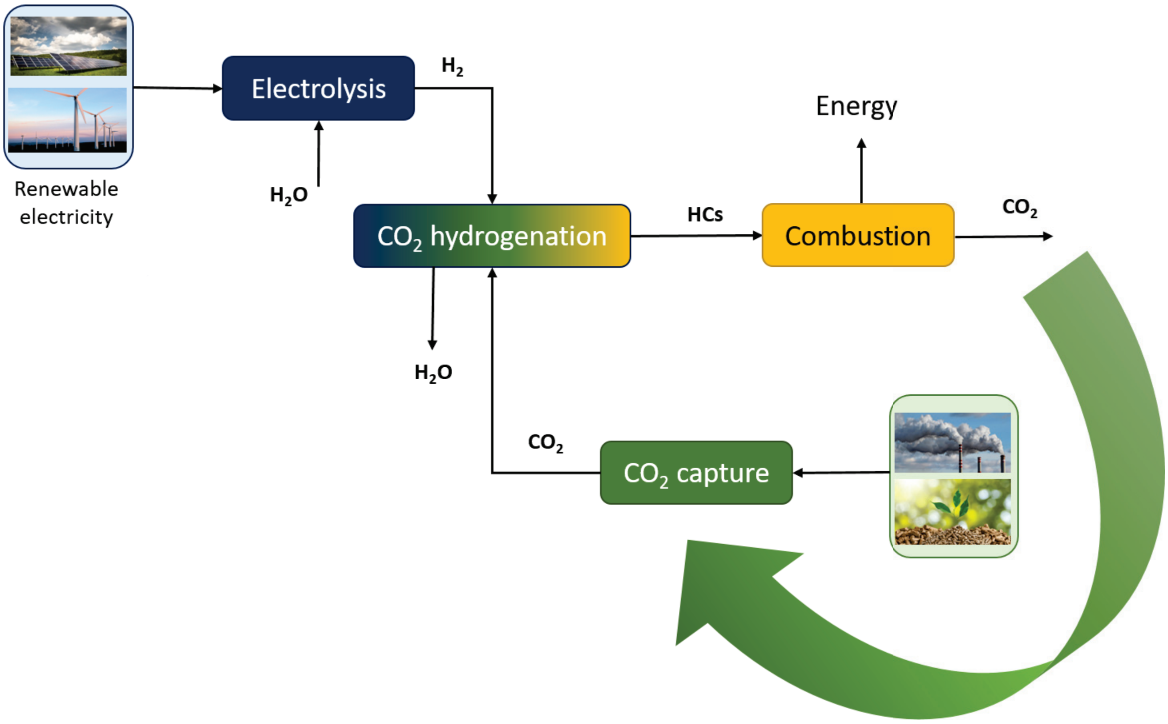

Figure 1.16: Concept of Power-to-Liquid for the production of synthetic liquid fuels.

In this Section, the possible technologies for CO_2 capture and for H_2 production via electrolysis are discussed.

1.1.2.1 CO_2 capture.

CO_2 capture technologies allow the separation of CO_2 from concentrated sources, so that it can be used for other purposes, such as injection in natural reservoirs (Carbon capture and Storage - CCS) or its valorization (Carbon Capture and Utilisation - CCU).

Possible sources of CO_2 could be represented by the exhaust gases of industrial processes. Global CO_2 emissions from the industry sector in 2018 have been estimated to be around 8.5 Gt. (https://www.eea.europa.eu/) Figure 1.17 shows the repartition of the direct CO_2 emissions from different industrial sectors. The main carbon emitting industries are cement, iron and steel and chemical and petrochemical sectors. However, the concentration of CO_2 in the exhaust gases coming from these sectors is relatively low (see Table 1.1). Natural gas processing, ammonia production, ethylene oxide production and hydrogen production by steam-methane reforming on the contrary give very concentrated CO_2 sources. Thus, even if they constitute only a small part of the CO_2 emissions, they could still represent an important source of CO_2 with high purity and thus lower separation cost. (Leeson et al., 2017)

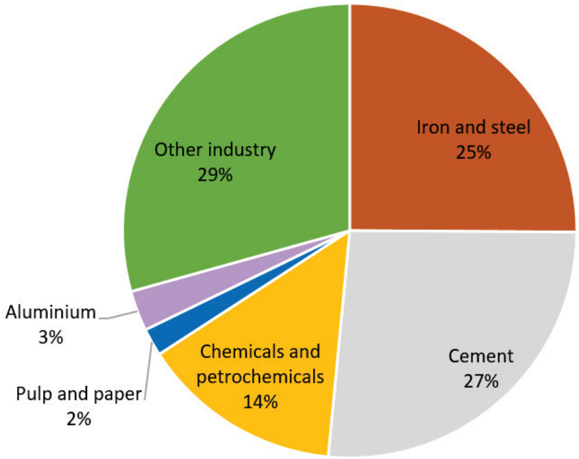

Figure 1.17: Direct CO_2 emissions by industrial sectors. Percentages are referred to the total direct CO_2 emissions from industry. Data from https://www.iea.org/data-and-statistics/charts/industry-direct-co2-emissions-in-the-sustainable-development-scenario 2000-2030.

Table 1.1: CO_2 content of flue gases from different industrial processes. Data from Bains et al. (2017).

CO_2 source	**CO_2 content**
Petroleum power plant	3-8%
Natural gas power plant	3-5%
Coal power plant	10-15%
Cement production	14-33%
Petroleum refineries	3-20%
Iron and steel manufacturing	16-42%
Ethylene production	7-12%
Ethylene oxide production	30-100%
Ammonia processing	98-100%
Natural gas processing	96-99%
Hydrogen production	30-100%
Ethanol production	98-99%

Alternatively, biomass and low-value wastes can represent a source of CO_2 as well. Biomass-derived syngas contains a quantity of CO_2 between 10 and 35%. The global amount of CO_2 emitted by biomass burning (including fires and agriculture and energy sectors) has been estimated to be 13.4 Gt/year, where the 25% of those emissions are from biofuels burning and charcoal making and burning. (Andreae, 2019) Biogas obtained by anaerobic digestion of solid wastes contains 50-65% of methane and 30-40% of CO_2, which is generally removed to increase the energy density of the biogas. CO_2 available for capture from biogas plants has been estimated to reach values higher than 19.4 Mt/year. (Li et al., 2017)

Three approaches are generally adopted for the capture of CO_2 from concentrated sources. They are graphically described in Figure 1.18. The most common process used in industries, the post-combustion process, consists in performing the capture from large volumes of flue gases at low CO_2 concentrations (3-14%), without modifying the combustion process. Another option is the pre-combustion process, where the combustion technology is changed in order to directly create concentrated CO_2 streams. First, syngas is produced from fossil fuel and then CO is converted to CO_2 via WGS and then removed. The big advantage is that CO_2 concentration is much higher. The third option is oxy-combustion, which uses pure or highly enriched oxygen for fossil fuel combustion. Highly concentrated CO_2 gases (85–95%) are directly obtained from the combustion and no nitrogen is present.

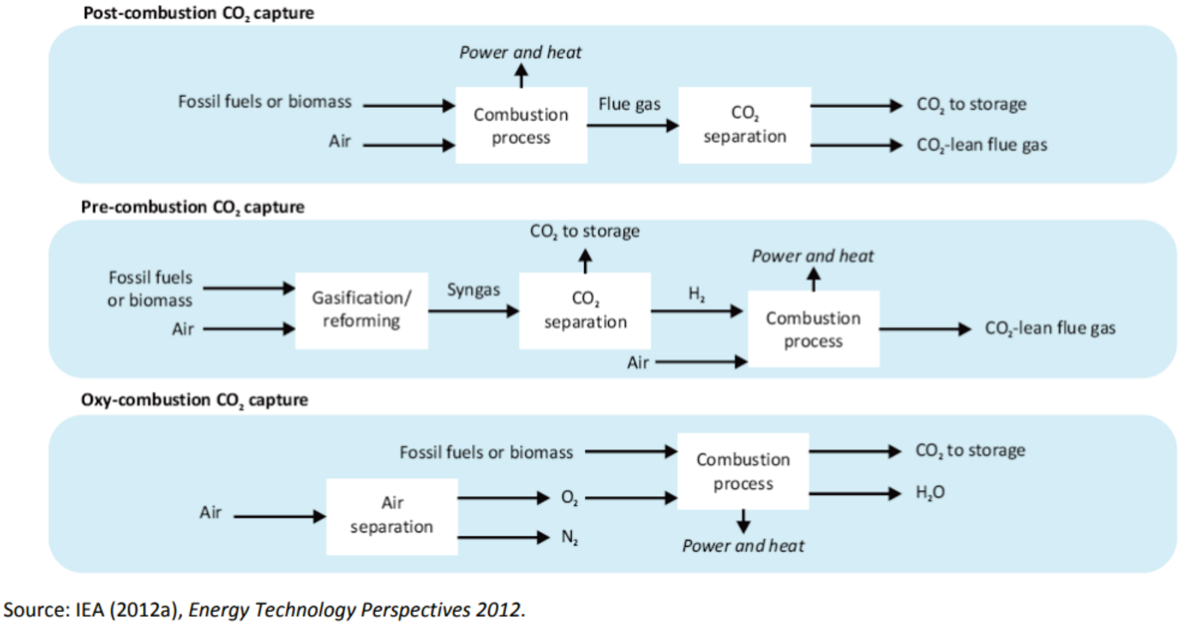

Figure 1.18: CO_2 capture approaches. Figure from IEA (2016).

The main technologies used for the CO_2 capture are summarized in Figure 1.19 according to their technology readiness level. Currently, the most used technology is the absorption with monoethanolamine (MEA) or diethanolamine (DEA). The absorption leads to the formation of carbamates and bicarbonates. The reaction is then reversed to separate CO_2 from the absorbent. The H_2S eventually present in the flue gas can deactivate the amine, while oxygen can form stable salts with the amine solutions. Despite these limitations, amine absorption is currently the most suitable technology for CO_2 separation from flue gases. (Kohl and Nielsen, 1997; Aresta, 2003; Olah et al., 2009, 2011) Cryogenic separation of CO_2 consists in the partial liquefaction of the flue gas at temperature and pressure above the triple point of CO_2 (-56.6°C, 5.18 bar). To obtain a pure gas, a distillation process could be necessary. This process is very energy expensive and economically convenient only for highly concentrated flue gases (CO_2 concentration in the gas >75%). (Aresta, 2003; Olah et al., 2011) CO_2 can also be captured by adsorption technologies. Typically, microporous solids with pore diameters up to a few tens of Å are used, such as silica gel, alumina, activated carbon or zeolites. The main issues of this technology are the fast decline in adsorption capacity when temperature increases and the difficult applications for low-concentrated sources. (Olah et al., 2011) Calcium looping is a developing promising technology for CO_2 capture. It is based on the use of a CaO-based sorbent. First the flue gas reacts with CaO at moderate temperature (650-700°C) to form $CaCO_3$. The desorption step is performed at higher temperatures (900-950°C), allowing the decomposition of $CaCO_3$ into CaO and CO_2. This technology has the advantage to use a cheap sorbent and to introduce a very low penalty on a power station (about 6-8%). Its application would be particularly suitable for the cement industry. However, it is still at early stages of development, as some problems of loss of the sorbent reactivity still have to be solved. (Blamey et al., 2010; Dean et al., 2011) Separation of CO_2 via polymeric membrane can have applications in power plant flue gases. However, the efficiency of this process needs to be improved, because these membranes still have very low selectivity to permeation and the driving force is low, due to the low partial pressure difference. (Aresta, 2003)

Figure 1.20 compares the avoidance costs of different CO_2 capture technologies applied to different industrial sources, according to the results obtained by the study of Leeson et al. (Leeson et al., 2017) The avoidance cost takes into account both the CO_2 capture cost and the CO_2 emissions reduction. A small value of this parameter represents a technology that with a small increase of the power cost can lead to a high reduction of CO_2 emissions. From this study it appears that capturing CO_2 from highly concentrated sources leads to lower avoidance costs, as expected. Moreover, oxy-fuel technology appears to currently be the most competitive technology for each industrial sector analysed. The only exception is the cement industry where the calcium looping technology was found to have significantly lower avoidance cost.

Developing technologies aim at capturing CO_2 directly from air (about 400 ppm). Direct air capture (DAC) is a technology that can sequester previously emitted carbon dioxide from atmosphere, where the concentration is orders of magnitude lower than that of point sources. The lower concentration in air increases thermodynamic limitations and moving great quantity of air into an adsorbing system requires high energy and material costs. Despite all these issues, air capture is gaining a lot of interest as it allows negative global CO_2 emissions. Moreover, since CO_2 concentration in air is at the equilibrium, DAC systems could be placed anywhere. (Olah et al., 2009; Keith, 2009) The technology is based on a medium that has affinity to the CO_2, in order to create a covalent bond with the partially acidic C atom of the CO_2 molecule. The most common used medium for DAC is solid sorbents containing amines, which are able to capture CO_2 by chemisorption. To collect CO_2, a desorption process is necessary by application of vacuum and/or heat. The temperature-vacuum swing adsorption (TVSA) process applies both heat and vacuum, allowing the operation of desorption at a lower temperature. Some improvements are needed for a better use of this technology: the development of adsorbent properties is necessary to increase the CO_2 working capacity; the adsorption chamber design also requires an improvement, because the system needs large quantities of air due to the very low concentration of CO_2; moreover, the DAC uses ambient air which is very dependent on the weather conditions, so a process control is needed in order to optimize the energy consumption. (Vázquez et al., 2018)

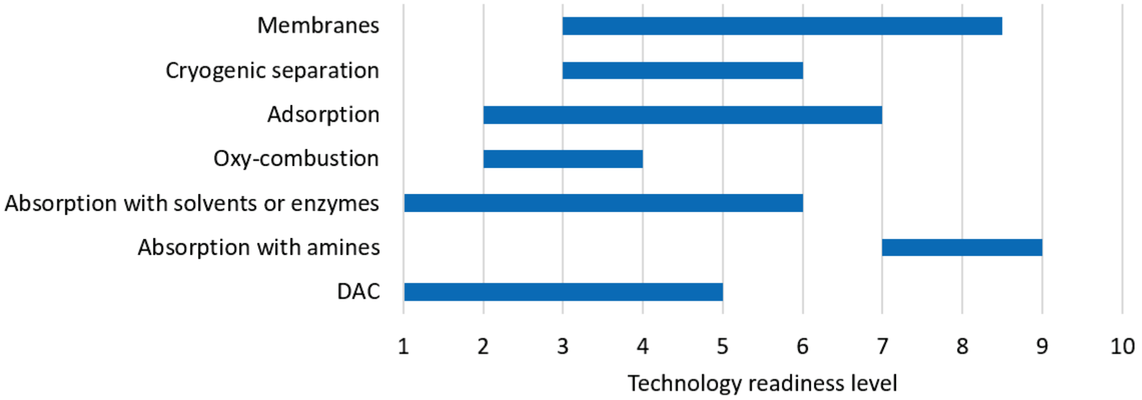

Figure 1.19: CO_2 capture technologies and their technology readiness level. Data from UNECE (2021).

In conclusion, different sources and different technologies are available or are under development for the CO_2 capture. Some of them, such as absorption with ethanolamines, are currently used in industrial applications, even if they still present some limitations. Other technologies are still in course of development and are generally difficult to apply with low CO_2 concentrated sources. The development of the direct air capture technology is an important challenge, as such a technology would significantly contribute to achieve neutral CO_2 emissions.

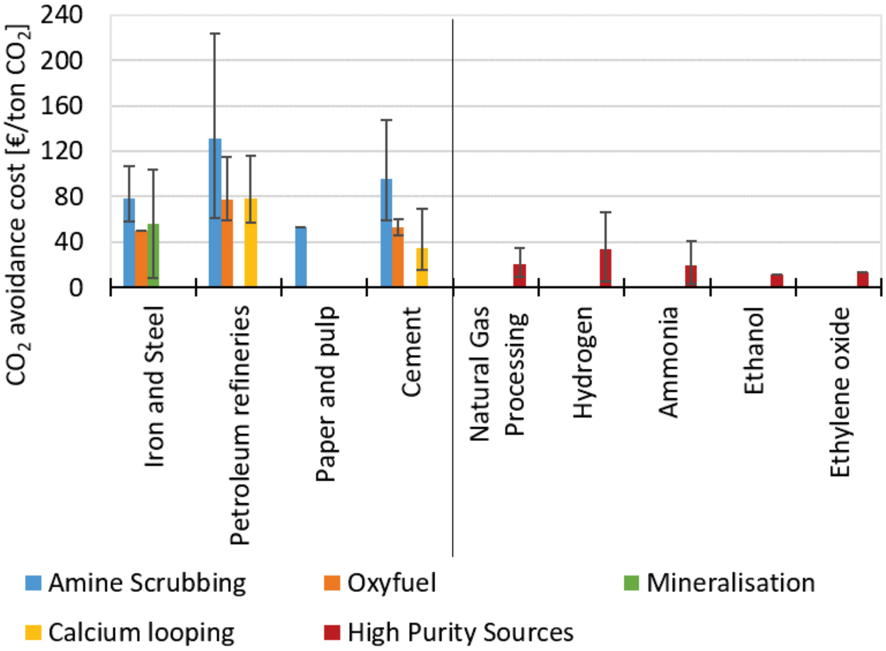

Figure 1.20: CO_2 avoidance cost of different technologies applied to different industry sectors. Figure from Panzone et al. (2020) with data from Leeson et al. (2017).

1.1.2.2 H_2 production.

Hydrogen is conventionally produced by steam reforming of methane, coal gasification, or partial oxidation of heavy oil, but these methods are all based on the consumption of fossil fuels and lead to the emission of CO_2 in the atmosphere. Figure 1.21 shows the distribution of the current world hydrogen production according to the different sources. (IRENA, 2018) Water electrolysis could be a sustainable way to produce hydrogen. Water electrolysis is an electrochemical process that splits the water molecule into H_2 and O_2. At the anode, the oxidation reaction generates the electrons which are consumed at the cathode to reduce water and form hydrogen.

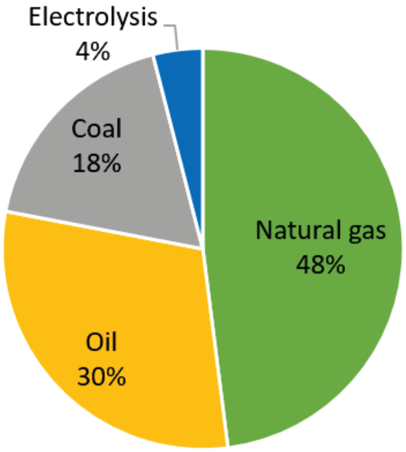

Figure 1.21: H_2 global production by sources. Data from IRENA (2018).

Different electrolysis technologies are under development and they are compared in Table 1.2. Alkaline electrolysis (AE) is the first technology that has been developed and it is currently a mature technology. It uses as electrolyte a solution of potassium hydroxide and operates at low temperatures. The polymer electrolyte membrane (PEM) electrolysis uses as electrolyte a polymeric membrane that allows the conduction of protons. It is a technology in early-commercialization stage for high power applications and it has been developed for flexible energy storage applications. Its compact system design and high voltage efficiency at larger current densities make this technology very interesting. Although this type of electrolysis is currently more expensive than alkaline, PEM electrolysis cost is expected to decrease by 1/4 if large-scale applications are reached. (Ursua et al., 2012; Vázquez et al., 2018) New technologies are being developed, such as solid oxide electrolysis (SOEC) which is a very promising solution, as it can electrochemically reduce H_2O to produce H_2 at high efficiency (>80%) by working at high temperatures. Moreover, these cells can work both as electrolysis cells or as fuel cells, only inverting the current direction; furthermore, H_2 and O_2 are physically separated within the cell and they have extremely high purity, eliminating the need of a purification step. (Varone and Ferrari, 2015; Chiang et al., 2014; Ursua et al., 2012; Aicart, 2014; Buttler, 2018) SOEC cells can also be used as co-electrolysis cells, because of their ability to directly reduce H_2O and CO_2 into syngas.

Table 1.2: Comparison of water electrolysis technologies. Table adapted from Panzone et al. (2020).

	AE	**PEM**	**SOEC**
Temperature	20-80°C	20-200°C	500-1000°C
Pressure	3-30 bar	10-50 bar	1-10 bar
Current density	0.2-0.8 A/cm^2	0.8-2 A/cm^2	1-2 A/cm^2
Electricity consumption	4.3-6.5 kWh/Nm^3	4.3-6.5 kWh/Nm^3	3.7 kWh/Nm^3
Efficiency	65-82%	65-78%	85-90%
Capacity	150 MW	150 kW (stacks) 1 MW (systems)	Lab scale
Flexibility	20-100 (% of nominal load)	0-100 (% of nominal load)	-100/+100 (% of nominal load)
Investment cost	80-1500 USD/kW	1500-3800 USD/kWh	
Life time	60000-90000 h	20000-60000 h	1000 h
Maturity	Mature	Early market	Pre-industrial

In conclusion, water electrolysis is certainly the most suitable technology for the production of H_2 without the use of fossil sources. Currently, alkaline electrolysis is the most developed and the less expensive technology but the PEM and SOEC electrolysis, which are currently at a less mature stage and more expensive compared to the AE, have higher potential, thanks to their higher flexibility and the possibility to operate at higher current density. Further improvements in these technologies could allow the reduction of the capital cost and the increase of their efficiency.

1.1.2.3 FT vs MeOH pathways.

The reaction between hydrogen and carbon dioxide to yield hydrocarbons can follow two different pathways:

- the FT pathway, if the intermediate product of the hydrocarbons synthesis is CO (or a syngas);
- the MeOH pathway, if the intermediate product of the hydrocarbons synthesis is methanol.

Both pathways can occur in one step or two steps, as illustrated in Figure 1.22. When the one-step (direct) process is performed, liquid hydrocarbons are directly formed from H_2 and

CO_2, while when the two-step (indirect) process is carried out, two different units are needed: in the FT pathway, RWGS is performed to produce syngas and then syngas reacts in a traditional FT synthesis to form hydrocarbons; in the two-step methanol pathway, methanol is first formed from CO_2 and H_2 and then liquids are produced through a Methanol-to-Liquid process.

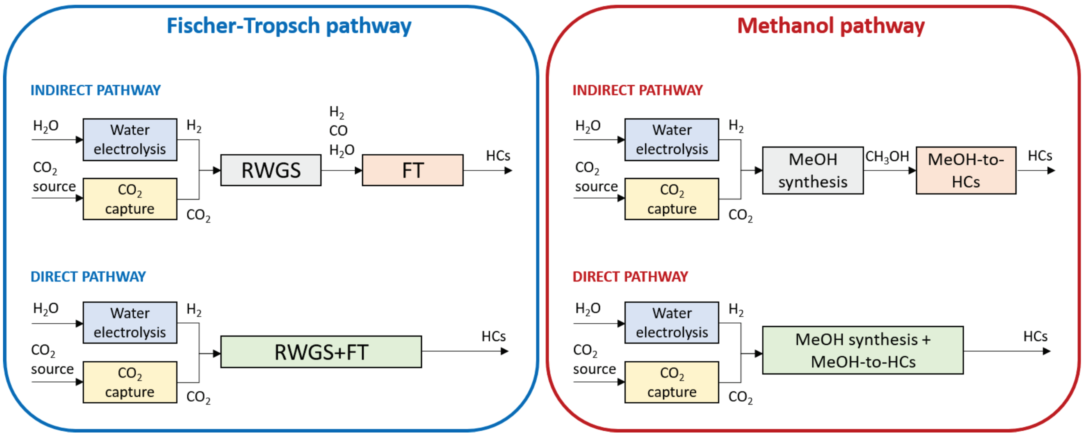

Figure 1.22: Schematic description of the Fischer-Tropsch and Methanol direct and indirect pathways.

Many advances have been made in the production of hydrocarbons via the methanol pathway. In the indirect route, methanol is produced from CO_2 over metallic catalysts. Cu is the main active catalyst for this reaction, often promoted with different elements (Zn, Zr, V, Ga, B, Cr, Mo) and supported on oxides (SiO_2, Al_2O_3, TiO_2, CeO_2). (Sun and Sermon, 1994; Koeppel et al., 1992; Wambach et al., 1999) Methanol is then converted to the desired hydrocarbons over acidic catalysts (such as acidic zeolites). (Westgård Erichsen et al., 2013; Álvaro Muñoz et al., 2013) Several processes have already been commercialized, such as the Methanol-to-Gasoline (MtG) by Mobil (Chang, 1983), the Topsøe TIGAS process (Topp-Jørgensen, 1988), the Methanol-to-Olefins (MtO) by UOP/Hydro and the Methanol-to-Propylene (MtP) by Lurgi (Koempel and Liebner, 2007). The conversion of methanol into diesel or kerosene is also being studied and could constitute a valid solution for the aviation transport. The formation of diesel or kerosene involves a first step of conversion into light olefins, followed by oligomerization. (Avidan, 1988)

More recently, research has been focused on the direct conversion of CO_2 to hydrocarbons via methanol pathway over bi-functional catalysts, containing both metallic and acidic sites. (Fujiwara et al., 1995; Park et al., 1998; Angelo, 2014; Kobl, 2015; Ahouari et al., 2015; Wang et al., 2016a; Gao et al., 2017) Indium oxide catalysts supported on zeolites have been reported to have high selectivity towards the formation of long hydrocarbons. (Gao et al., 2017; Numpilai et al., 2019b) Products obtained from methanol pathways contain mainly aromatics and branched aliphatics, making it suitable for direct application as gasoline (with high octane number 90–95). (Wang et al., 2016b; Li et al., 2018b)

The indirect Fischer-Tropsch pathway (including the RWGS step, followed by the FT synthesis unit) has been widely studied and some applications at pilot plants scale already exist. (Vázquez et al., 2018; Sunfire, 2017) RWGS is generally performed over metal catalysts such as Ni, Fe or Cu at high temperatures (400-800°C). FT is performed over Ru, Co (for low-temperature) or Fe (for high temperature) at temperatures between 180 and 250°C and pressures between 20 and 30 bars. The direct conversion of CO_2 to hydrocarbons via FT pathway would allow to avoid compression and cooling between the two steps, but is very challenging because it requires an optimal catalyst, active for both reaction steps, and optimized operating conditions. Iron has been identified as the most suitable catalyst, as we will discuss in the next section.

Products obtained from FT pathways mainly consist in a mixture of hydrocarbons of different lengths. Selectivity towards gasoline and diesel products is generally limited. (Wang et al., 2016b; Li et al., 2018b) However, the wide range of products obtained makes this pathway more versatile, with possible applications in the transport field but also in the chemical and petrochemical industries. Thus, even if the FT route requires higher energy and higher hydrogen quantity compared to the methanol route, the lower cost of catalyst and the versatility of its applications make this pathway very interesting. A technical-economic analysis applied to the aviation sector has shown that MeOH and FT pathways have very similar efficiencies and specific jet fuel production cost, with FT-derived jet fuel only 7% more expensive than methanol-derived fuel. (Schmidt et al., 2018) The results of this study are summarized in Table 1.3.

Table 1.3: Comparison of production cost and efficiency of MeOH ad FT pathways applied to the aviation sector. Data from Schmidt et al. (2018).

	LT electrolysis		HT electrolysis	
	FT pathway	MeOH pathway	FT pathway	MeOH pathway
Jet fuel cost [€/L]	1.10	0.98	0.93	0.94
Efficiency [%]	53	54	64	63

In conclusion, the FT direct route still needs some improvements in increasing the selectivity towards the desired products, with simultaneous minimization of the undesired products, such as CO and CH_4. However, it could have a good potential for applications in the aviation field or in the chemical and petrochemical industry. As this work is focused on the study of the direct FT pathway, in the following our attention will be given only to this route.

1.2 Review of the most used catalysts and their performances in different operating conditions.

The direct hydrogenation of CO_2 to hydrocarbons generally takes place with two reactions in series:

$$nCO_2 + nH_2 \leftrightarrow nCO + nH_2O \quad \Delta H_r^{298K} = 41kJ/mol \tag{1.1}$$

$$nCO + 2nH_2 \leftrightarrow (-CH_2-)_n + nH_2O \quad \Delta H_r^{298K} = -166kJ/mol \tag{1.2}$$

A small part of hydrocarbons can also be formed by the direct hydrogenation of CO_2 as primary products.

$$nCO_2 + 3nH_2 \leftrightarrow (-CH_2-)_n + 2nH_2O \quad \Delta H_r^{298K} = -125kJ/mol \tag{1.3}$$

The first step that converts CO_2 into CO via the reverse water-gas shift is a reversible and endothermic reaction that rapidly reaches the equilibrium. It is favoured at high temperatures and not influenced by pressure. The second step consists in the conversion of CO to organic products, via Fischer-Tropsch synthesis. This is an exothermic reaction and involves a decrease of the number of product molecules, so it is favoured at high pressures. Thus, optimal conditions for the process have to be found, so that both reactions can occur. Figure 1.23 shows the composition obtained at thermodynamic equilibrium for the RWGS as function of the temperature. At low temperatures, the hydrocarbons formation reactions are favoured and the most favoured product is methane. To shift the equilibrium towards the formation of CO, higher temperatures are needed. However, the equilibrium does not need to be completely shifted towards the formation of CO, as it is further converted into hydrocarbons via FT, contributing to the shift of the equilibrium towards further formation of CO. The equilibrium can also be shifted by the presence of water, which is formed as by-product and can contribute to limit the CO_2 conversion.

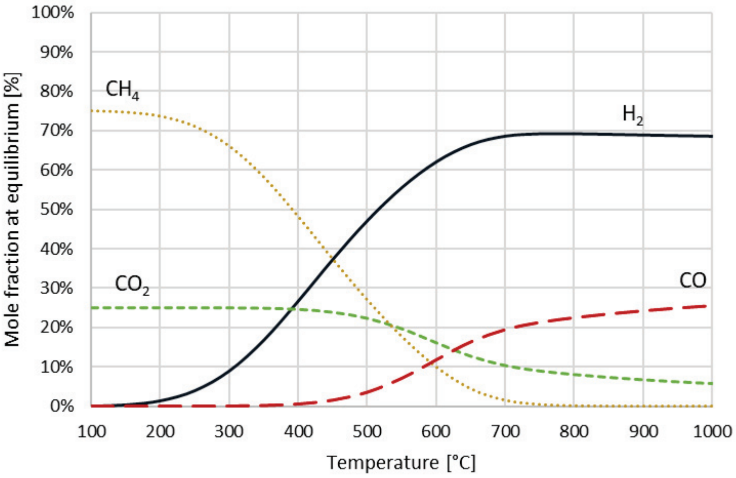

Figure 1.23: Composition at thermodynamic equilibrium of RWGS simulated at 1 bar and H_2/CO_2=3. Adapted from Panzone et al. (2020).

Hence, a catalyst is needed in order to reach high conversion of CO_2 and avoid limitations due to the thermodynamic equilibrium. A suitable catalyst for CO_2 hydrogenation has to be active for both the RWGS and the FT reactions. For this reason, Fe-based catalysts are generally favoured over Co, Ni or Ru, because of their higher activity towards RWGS and selectivity towards C_{2+} hydrocarbons. However, the performances of the catalysts can be affected by the presence of promoters and supports, that can influence the hydrocarbons distribution. In the next section we review the most used catalysts for the CO_2 hydrogenation.

1.2.1 Iron-based catalysts.

Iron-based catalysts are commonly used for the CO_2 hydrogenation, because of their relatively high selectivity to long hydrocarbons and their ability to reduce the methane formation. Among the products obtained with these catalysts, olefins have been observed as the most important one, especially the short fraction C_2-C_4, while paraffins are generally obtained in smaller quantities. Oxygenated products are also observed (mainly alcohols) in the products pool. The performances of the best Fe-based catalysts reported in literature are summarized in Table 1.4.

The main part of these Fe-based catalysts are used in combinations with other elements that act as promoters. Some authors obtained good performances by using an Fe-based catalyst without the need to add promoters, but only using a proper method for the catalyst synthesis. (Albrecht et al., 2017) They obtained a stable catalyst able to give a high selectivity towards C_2-C_{18} hydrocarbons (65%) for CO_2 conversion of 23%. However, in general, non-doped Fe-based catalysts have shown low selectivity towards the long hydrocarbons chains and important formation of methane. (Riedel et al., 1999; Wang et al., 2013; Choi et al., 2017; Hwang et al., 2019)

Promoters can act as structural or electronic promoters and are generally catalytically or chemically active. Among the promoters that are generally used, potassium is probably the one with the most positive effects, thanks to its electronic role. It is able to promote the CO adsorption and thus to weaken the bond between C and O, leading to a promotion of the CO dissociation instead of its desorption. Moreover, it favours the CO_2 dissociation, thus increasing the rate of carburization of metallic iron and promoting the supply of CO as feedstock for the chain-growth. These aspects result in an increase of the chain-growth activity that leads to higher selectivity towards long chain hydrocarbons. Moreover, K is able to limit the H_2 adsorption, thus lowering the activity towards the secondary hydrogenation of olefins and thus resulting in higher selectivity towards alkenes and less methane formation. (Lee et al., 1989; Martinelli et al., 2014; Fischer et al., 2016; Amoyal et al., 2017; Visconti et al., 2017) The degree of alkalization is very important and seems to highly influence the effects of the K promotion. It has been reported that high content of K ($> 5-6\ wt\%$) can have a negative effect on the catalytic performances because the C deposition is favoured, leading to faster deactivation of the catalyst. (Wang et al., 2013; Schulz, 2014) The limit value on the K content can depend on different parameters, such as the synthesis method, and has to be determined case by case. The K/Fe mass ratio generally adopted varies between 0.1 and 0.4. However, in some cases higher ratios have been used. For example, Xie et al. used a catalyst containing a K/Fe ratio of 0.67 that showed relatively high values of CO_2 conversion and good selectivity towards C_2-C_4 chains. (Xie et al., 2017) Very good performances were obtained by Jiang et al. with a Fe-K catalyst with K/Fe ratio of 0.24. The formation of CO and CH_4 was limited, while the selectivity towards C_{5+} hydrocarbons was enhanced (63%). (Jiang et al., 2018) Very high selectivity towards long chains ($S_{C_{5+}} = 57\%$) were obtained with the Fe-K catalyst synthetized by Hwang et al. (Hwang et al., 2019) Values of the chain-growth probability α for these catalysts are reported around 0.67. (Visconti et al., 2017; Hwang et al., 2019)

Another important element used as promoter for Fe-based catalysts is copper. It is considered to be responsible of promoting the carburization process of iron oxides and to increase the dispersion of the catalytic particles. Moreover, it is able to increase the surface basicity, leading to decreased methane formation. The strong surface interaction between Fe and Cu results in an increase of the CO_2 conversion and the C_{5+} hydrocarbons selectivity. Cu also promotes the RWGS reaction, favouring the decrease of CO selectivity. (Dorner et al., 2010a; Pastor-Pérez et al., 2017) The addition of copper has also been reported to favour the secondary hydrogenation of olefins, leading to enhanced formation of paraffins. (Liu et al., 2018) Some interesting results have been obtained over the Fe-Cu catalyst synthesised by Choi et al. (Choi et al., 2017) that led to the minimization of the formation of methane and to high selectivity towards long chains ($S_{C_{5+}} = 66\%$ CO-free).

The combination of K and Cu as promoters for Fe-based catalysts can lead to improved catalytic performances. (Kim et al., 2006; Sai Prasad et al., 2008; Hwang et al., 2019) Hwang et al. were able to obtain high selectivity towards C_{5+} hydrocarbons and a value of the chain-growth probability α of 0.72, with low methane formation. (Hwang et al., 2019)

Many other elements have been used to promote Fe-based catalysts. Among them, chromium is known to especially increase the C_2-C_4 alkenes formation (Sai Prasad et al., 2008), while zirconium has been shown to promote the CO_2 and CO adsorptions, thus increasing the CO_2 conversion, but to reduce the H_2 adsorption, thus increasing methane selectivity. (Wambach et al., 1999; Su et al., 2015) Manganese has a role similar to that of copper: it favours the catalyst reduction and the carburization process and increases the surface basicity, promoting the chemisorption of acid molecules such as CO_2. This results in higher CO_2 conversions. (Kuei et al., 1991) Molybdenum increases the electron deficiency of the surface iron, favouring its activity for the RWGS. (Kharaji et al., 2013) These promoters, though able to increase the CO_2 conversion, generally lead to the production of a lot of CO and CH_4. (Lee et al., 1991; Kuei et al., 1991) Cerium is known to catalyse both RWGS and WGS, but its influence in Fe-based catalyst was observed to be only an acceleration of the carburization process. (Pérez-Alonso et al., 2008) Cesium can facilitate the CO_2 adsorption and inhibit the formation of methane. (Pastor-Pérez et al., 2017) Ruthenium was found to increase CO_2 conversion and to reduce methane selectivity. (Sai Prasad et al., 2008) Zinc can increase the selectivity towards light olefins. (Sai Prasad et al., 2008; Zhang et al., 2015)

Combinations of different promoters with Fe-based catalysts have been tested in literature, but the main part of them led to very high selectivity towards methane. Su et al. (Su et al., 2015) were able to enhance the formation of light chains C_2-C_4 ($S_{C_2-C_4} = 60\%$), with limited formation CO ($< 10\%$), by using a catalyst containing Fe promoted with Zr and K. Recently, a K-Mn-Fe-Ti catalyst was reported to have very high selectivity towards long hydrocarbons ($> 51\%$ of the total products were C_{5+}) with limited formation of CO and methane. (Zhao et al., 2021)

The performances of a catalyst are also significantly influenced by the presence and the nature of supports. Supports provide stability and help to reach a better distribution of the active phase. Alumina and titania have been observed to have better performances then silica, as supports, because of their ability to inhibit the formation of methane. (Sai Prasad et al., 2008; Rodemerck et al., 2013; Wang et al., 2013) Alumina has been reported to provide resistance to sintering. Moreover, in presence of K it can form a catalytically active phase, the potassium alanate $KAlH_4$, that can reversibly adsorb hydrogen at moderate temperatures, leading to lower methane selectivity and higher alkenes selectivity. (Dorner et al., 2010b; Ares et al., 2009)

Zeolites have been used as supports for Fe-base catalysts. HY-zeolites have been observed to lead to high formation of methane, while alkalized structures can increase the formation of C_{5+} hydrocarbons. (Nam et al., 1999; Riedel et al., 1999) Iron catalysts supported on zeolites show in general worse performances than Fe-based catalysts supported on alumina or titania, which can be due to pore blockage and drastic decrease of the surface area when iron is added to the zeolite. (Riedel et al., 1999) However, Wei et al. reported very positive performances of a Na-Fe catalyst supported on HZSM-5 zeolites. (Wei et al., 2017) Very high selectivity towards the C_{5+} fraction were observed ($S_{C_{5+}} = 74\%$) with a value of α of 0.70 and limited methane formation.

Catalyst particle size and active phase dispersion are two other parameters that significantly influence the stability and activity of a catalyst. FT synthesis is known to be a very structure-sensitive process and iron particle size is known to influence the reaction rate and the products distribution, as reported by many authors. (Nakhaei Pour et al., 2011; Torres Galvis et al., 2012; Nakhaei Pour et al., 2014; Nakhaei Pour and Housaindokht, 2014; Liu et al., 2015, 2017) The activity of catalysts during CO_2 hydrogenation has also been observed to be influenced by the catalytic particle size. Over a Fe/Cu/K catalyst, it was observed that reducing the particle size from 38 to 14 nm led to the increase of both the catalytic activity and the amount of reactants that can be adsorbed, resulting in higher values of kinetic rates. (Nakhaei Pour and Housaindokht, 2017) Furthermore, over a Fe-K/Al_2O_3 catalyst, the selectivity towards long hydrocarbons was found to be maximized when iron oxide particle had sizes in the range 5-8 nm. Too small particle sizes were found to be not effective for the chain-growth, while too large particle sizes could decrease the iron dispersion. (Xie et al., 2017)

Table 1.4: Summary of performances obtained in literature with different Fe-based catalysts. Underline values of selectivity indicate hydrocarbons fractions (CO-free).

Catalyst	χ_{CO_2} %	S_{CO} %	S_{CH_4} %	$S_{C_2-C_4}$ %	$S_{C_{5+}}$ %	Olefins content	α	T [°C]	p [MPa]	GHSV [mL/g_{cat}/h]	H_2/CO_2	Reference
Fe	23%	21%	14%	65%		O/P=1.4		300	1	1140	3	(Albrecht et al., 2017)
Fe	30%	23%	20%	57%		O/P=1		300	1.5	1170	3	(Skrypnik et al., 2021)
Fe	42%	12%	16%	40%	32%	O/P=1.6		320	3	7200	3	(Liu et al., 2021)
Fe/SiO_2	7%	71%	$\underline{80.9\%}$	$\underline{19.6\%}$	$\underline{0.42\%}$	O%=0.64%		300	1	1896	3	(Riedel et al., 1999)
Fe/TiO_2	11.5%	36%	$\underline{51.7\%}$	$\underline{41.6\%}$	$\underline{6.9\%}$	O%=2.7%		300	1	1896	3	(Riedel et al., 1999)
Fe/Al_2O_3	22.8%	11%	$\underline{43.2\%}$	$\underline{48.1\%}$	$\underline{8.8\%}$	O%=0.58%		300	1	1896	3	(Riedel et al., 1999)
Fe/ZrO_2	32%	25%	$\underline{70\%}$	$\underline{29.1\%}$	$\underline{0.9\%}$			340	2	1200	3	(Wang et al., 2013)
Fe/NaY	21%	29.5%	$\underline{14.6\%}$	$\underline{40.6\%}$	39.8%	O%=71.4%		300	1	1900	3	(Nam et al., 1999)
Fe/NaY	20.8%	29%	$\underline{14.6\%}$	$\underline{45.6\%}$	$\underline{39.9\%}$	O%=71.0%		300	1	1896	3	(Riedel et al., 1999)
Fe/HY	10.1%	3%	$\underline{72.6\%}$	$\underline{25.8\%}$	$\underline{1.5\%}$	O%=0.36%		300	1	1896	3	(Riedel et al., 1999)
Fe/LiY	17%	44%	$\underline{17.9\%}$	$\underline{43.4\%}$	$\underline{38.8\%}$	O%=60%		300	1	1896	3	(Riedel et al., 1999)
Fe/KY	17.9%	31%	$\underline{12.5\%}$	$\underline{42.5\%}$	$\underline{44.5\%}$	O%=75.9%		300	1	1896	3	(Riedel et al., 1999)
Fe/RbY	17.2%	31%	$\underline{9.5\%}$	$\underline{35.8\%}$	$\underline{54.4\%}$	O%=79.6%		300	1	1896	3	(Riedel et al., 1999)
$Na-Fe_3O_4/HZMS-5$	34%	15%	$\underline{8\%}$	$\underline{18\%}$	$\underline{74\%}$		0.70	320	3	4000	3	(Wei et al., 2017)
$K-Fe/C-H-ZSM5$	37.2%	18.1%	$\underline{11.1\%}$	$\underline{49.0\%}$	$\underline{39.9\%}$	O%=1.3%		320	2	1200	2.5	(Guo et al., 2021)
$K-Fe/C-K-ZSM5$	34.5%	18.8%	$\underline{11.0\%}$	$\underline{18.9\%}$	$\underline{70.1\%}$	O%=3.5%		320	2	1200	2.5	(Guo et al., 2021)
$K-Fe/C-H-ZSM5*$	33.7%	18.3%	$\underline{12.1\%}$	$\underline{38.0\%}$	$\underline{49.9\%}$	O%=0.4%		320	2	1200	2.5	(Guo et al., 2021)
$K-Fe$	45%	12%	16%	41%	30%		0.67	300	0.6	2700	≈ 3	(Visconti et al., 2017)
$K-Fe$	38%	23%	12%	37%	31%		0.66	300	0.6	2700	≈ 3	(Visconti et al., 2017)
$K-Fe$	37.8%	7.3%	8.3%	21.4%	62.9%	O%=75.6		300	2.5	560	≈ 3	(Jiang et al., 2018)
$K-Fe$	21%	27%	14%	1.6%	57.4%		0.68	300	2.5	5002	≈ 3	(Hwang et al., 2019)
$K-Fe/Al_2O_3$	34.6%	41.8%	$\underline{32.5\%}$	$\underline{20.0\%}$	$\underline{5.4\%}$			400	3	3600	≈ 3	(Liu et al., 2018)
$K-Fe/Al_2O_3$	42%	33%	$\underline{19.8\%}$	$\underline{33.1\%}$	$\underline{15.3\%}$			400	3	3600	≈ 3	(Xie et al., 2017)
$K-Fe/Al_2O_3$	36%	16%	10%	46%	27%			300	1	2000	≈ 3	(Lee et al., 2003)
$K-Fe/Al_2O_3$ + PVA	35%	21%	$\underline{12\%}$	$\underline{41.2\%}$	$\underline{25\%}$			300	1	2000	≈ 3	(Lee et al., 2003)
$K-Fe/Al_2O_3$ + FA	41%	19%	$\underline{10\%}$	$\underline{26\%}$	$\underline{56\%}$			300	1	2000	≈ 3	(Lee et al., 2003)
$Cu-Fe$	38%	8%	36.8%	42.1%	5.3%		0.42	300	2.5	5001	≈ 3	(Hwang et al., 2019)
$Cu-Fe$	17%	32%	$\underline{3\%}$	$\underline{31\%}$	$\underline{66\%}$	O/P=7.3		300	1	1800	3	(Choi et al., 2017)
$Cu-K-Fe$	38%	10%	9.2%	26.3%	47.4%		0.72	300	2.5	5003	≈ 3	(Hwang et al., 2019)
$Cu-K-Fe-Al$	13.2%	28%	16.3%	28.4%	27.2%	O/P=1.17		265	1.27	1800	3	(Sai Prasad et al., 2008)
$Cu-K-Fe-Al$	15.6%	22.8%	9.9%	19.29%	39.4%	O/P=4.38		265	1.27	1800	3	(Sai Prasad et al., 2008)
$Cu-K-Fe-Al$	16.9%	18%	9.4%	25.2%	47.3%	O/P=6.23		265	1.27	1800	3	(Sai Prasad et al., 2008)
$Cu-K-Fe-Al$	14.4%	20.9%	8.7%	25.5%	44.8%	O/P=12.61		265	1.27	1800	3	(Sai Prasad et al., 2008)
$Cu-K-Fe-Al$	41%	6%	$\underline{15\%}$	$\underline{37.6\%}$	$\underline{19.7\%}$	O%=79%		300	1	1800	3	(Hong et al., 2001)

Cu – K – Fe – Al	36%	9.6%	11%	35%	54%	O%=76%		300	1	2000	3	(Kim et al., 2006)
Cu – K – Fe/Al_2O_3	42%	26.5%	27.8%	32%	13.8%			400	3	3600	3	(Liu et al., 2018)
Ce – Fe	25%	21.3%	37.7%	35.6%	4.5%			300	1	15500	3	(Pérez-Alonso et al., 2008)
K – Zr – Fe	49.8%	7.1%	19.6%	61.2%	19.2%	O/P=6.24		320	2	1000 h^{-1}	3	(Su et al., 2015)
K – Zr – Fe	54.4%	3%	19.8%	61.9%	18.2%	O/P=6.44		320	2	1000 h^{-1}	3	(Su et al., 2015)
K – Zr – Fe	51.6%	6.1%	21.8%	60.6%	17.7%	O/P=5.09		320	2	1000 h^{-1}	3	(Su et al., 2015)
K – Zr – Fe	43.4%	9.9%	24.74%	60.81%	14.46%	O/P=3.28		320	2	1000 h^{-1}	3	(Su et al., 2015)
K – Mn – Fe/Al_2O_3	41.4%	11.5%	26%	64.2%		O/P=4.2		290	1.38	5400	3	(Dorner et al., 2010a)
K – Mn – Fe/Al_2O_3	46.2%	43.4%	24.4%	32%		O/P=4.8		300	1.9	2700	3	(Willauer et al., 2013)
La – Cu – K – Fe/Al_2O_3	32%	15%	20%	39%	26%			300	1	1320	3	(Rodemerck et al., 2013)
La – Cu – K – Fe/TiO_2	27%	32%	7%	21%	40%			300	1	1320	3	(Rodemerck et al., 2013)
Mn – K – Fe/Al_2O_3	42%	23%	36.1%	29.8%	11.1%			400	3	3600	3	(Liu et al., 2018)
Mo – K – Fe/Al_2O_3	39%	31%	31.1%	28.7%	8.9%			400	3	3600	3	(Liu et al., 2018)
Zn – K – Fe/Al_2O_3	39%	33%	35.8%	24.1%	6.8%			400	3	3600	3	(Liu et al., 2018)
Zr – K – Fe/Al_2O_3	40%	28.9%	37.5%	26%	7.6%			400	3	3600	3	(Liu et al., 2018)
Cr – K – Fe/Al_2O_3	36%	36.1%	35.2%	23.7%	5%			400	3	3600	3	(Liu et al., 2018)
Fe – Mn	28.8%	4.9%	35.0%	39.5%	20.0%	O/P=0.43		320	5	24000	2.79	(Zhao et al., 2021)
K – Mn – Fe – Ti	34.9%	9.7%	9.2%	27.2%	51.0%	O/P=2.68		320	5	24000	2.79	(Zhao et al., 2021)
K – Fe/C	35.6%	20.9%	15.3%	43.9%	40.8%	O%=70%		320	2	4800	2.5	(Guo et al., 2021)
Fe – C – ZnO – Na	38%	19%	27%	73%		O/P=7	0.65	320	1.5	10000	3	(Tu et al., 2021)

1.2.2 Cobalt-based catalysts.

Cobalt-based catalysts, which are commonly used in the traditional FT synthesis, are not very performing in presence of CO_2, as they are almost inactive for the RWGS and WGS. Thus, the CO partial pressure at the catalyst surface during the reaction remains very low, hindering the establishment of a FT regime and making the catalyst act as a methanation one. (Visconti et al., 2016) Using Co catalysts for CO_2 hydrogenation generally leads to very high formation of methane and short chains. The performances of some catalysts reported in literature are summarized in Table 1.5.

As for Fe-based catalysts, many promoters can be added to Co-based catalysts to improve their performances, in particular to help the suppression of methane formation. Shi et al. have shown that the addition of 4.2%(mol) of K to a $CuCo/TiO_2$ catalyst could decrease the methane formation and lead to higher selectivity towards C_{5+} products and higher values of α. (Shi et al., 2018) Co-based catalysts supported on micro-porous metal-organic framework MIL-53(Al) were shown to act as bi-functional catalyst and limit the methane formation. (Tarasov et al., 2018)

The most promising application of Co catalysts could be in bi-metallic Fe-Co catalysts. The effect of Fe-Co catalysts in CO hydrogenation has been investigated by different authors and different works observed an improvement of activity and selectivity. (Tihay et al., 2002; Ishihara et al., 1987) Satthawong et al. studied the effects of adding Co to Fe-based catalysts during CO_2 hydrogenation and showed that the increase of Co content in the catalyst could improve the CO_2 conversion, but led to very important formation of CH_4 and very low values of α. (Satthawong et al., 2013) It was also shown that the addition of K on Co-Fe bimetallic catalysts can contribute to limit the methane formation and to enhance the formation of longer hydrocarbons.

In conclusion, a lot of work has been and still is focused on the development of an effective catalyst for CO_2 hydrogenation with the ability to convert a good extent of CO_2, by limiting the formation of CH_4 and CO and by maximizing the formation of long hydrocarbons. We have summarized the properties and the performances of the most used catalysts for this application and we have evidenced that Fe-based catalysts are the most promising.

One of the catalysts that has been studied the most is the Fe-K/Al_2O_3 because of its relative simplicity of synthesis and its ability to limit the methane formation in favour of olefins production. (Lee et al., 2003; Kim et al., 2006; Xie et al., 2017; Liu et al., 2018) The alumina-supported form of Fe-K catalysts has been observed to be more stable and to be more active than their bulk form. (Kim et al., 2006) The presence of K is crucial to minimize the methane formation on this kind of catalyst (Riedel et al., 1999) and Cu can also be added to decrease the formation of methane and CO. With these Fe-based catalysts promoted with K and eventually Cu values of α in the range 0.66-0.72 can be obtained.

In the following, we will focus only on the CO_2 hydrogenation over iron catalysts, as we have shown that they are the most appropriate for this reaction and as our work is based on a Fe catalyst.

In the next section we will summarize the most used operating conditions at which these catalysts have been tested and the effects of the operating conditions on the catalytic performances.

Table 1.5: Summary of performances obtained in literature with different Co-based catalysts.

Catalyst	χ_{CO_2} %	S_{CO} %	CH_4 fraction %	C_2-C_4 fraction %	C_{5+} fraction %	Olefins content	α	T [°C]	p [MPa]	GHSV [mL/g_{cat}/h]	H_2/CO_2	Reference
$Co/\gamma-Al_2O_3$	33%						0.25	220	2	4800	2.45	(Visconti et al., 2016)
Co/Al_2O_3	48.8%	2%	97%	1%		O/P=0	0.00	300	1.1	3600	3	(Satthawong et al., 2013)
$K-Co/Al_2O_3$	60.6%	1%	96%	3%		O/P=0	0.10	300	1.1	3600	3	(Satthawong et al., 2013)
$Co-Cu/TiO_2$	23%	1.3%	89.5%	5.6%	4.9%	O/P=0.01	0.34	250	5	3000	3.04	(Shi et al., 2018)
$K-Co-Cu/TiO_2$	21%	4.7%	62%	24.3%	13.8%	O/P=0.02	0.47	250	5	3000	3.04	(Shi et al., 2018)
$K-Co-Cu/TiO_2$	13.8%	19.7%	45%	33.3%	21.3%	O/P=0.14	0.52	250	5	3000	3.04	(Shi et al., 2018)
$K-Co-Cu/TiO_2$	13%	35.1%	34%	30.8%	35.1%	O/P=0.33	0.63	250	5	3000	3.04	(Shi et al., 2018)
$K-Co-Cu/TiO_2$	12.8%	35.9%	34.6%	34.6%	30.8%	O/P=0.46	0.60	250	5	3000	3.04	(Shi et al., 2018)
$K-Co-Cu/TiO_2$	11.9%	45.9%	35%	33.9%	31.1%	O/P=0.41	0.61	250	5	3000	2.70	(Shi et al., 2018)
$Co-MIL-53(Al)$	25.3%	6.6%	35.2%	29.8%	35%	O%=20-25%		260	3	$800h^{-1}$	2.70	(Tarasov et al., 2018)
$Co-MIL-53(Al)$	30.4%	5.9%	44.6%	24.6%	30.8%	O%=20-25%		300	3	$800h^{-1}$	2.70	(Tarasov et al., 2018)
$Co-MIL-53(Al)$	37.5%	3.3%	53.2%	24.1%	22.7%	O%=20-25%		340	3	$800h^{-1}$	2.70	(Tarasov et al., 2018)
$Fe-Co/Al_2O_3$	20.3%	28%	33%	39%		O/P=0	0.37	300	1.1	3600	3	(Satthawong et al., 2013)
$Fe-Co/Al_2O_3$	25.2%	13%	44%	43%		O/P=0	0.36	300	1.1	3600	3	(Satthawong et al., 2013)
$Fe-Co/Al_2O_3$	26.8%	10%	54%	36%		O/P=0	0.31	300	1.1	3600	3	(Satthawong et al., 2013)
$Fe-Co/Al_2O_3$	33.1%	1%	87%	12%		O/P=0	0.04	300	1.1	3600	3	(Satthawong et al., 2013)
Co/Fe@C	58.9%	0%	69.2%	29.3%	1.5%			300	1	4000		(Cui et al., 2021)
$Fe-Co-K/Al_2O_3$	35.8%	13%	16%	71%		O/P=0.6	0.57	300	1.1	3600	3	(Satthawong et al., 2013)
$Fe-Co-K/Al_2O_3$	33.7%	14%	18%	68%		O/P=0.7	0.52	300	1.1	3600	3	(Satthawong et al., 2013)
$Fe-Co-K/Al_2O_3$	32%	38%	15%	47%		O/P=0.2	0.40	300	1.1	3600	3	(Satthawong et al., 2013)
$Fe-Co-K/Al_2O_3$	50.3%	1%	63%	36%		O/P=0	0.20	300	1.1	3600	3	(Satthawong et al., 2013)
$Fe-Co-K/Al_2O_3$	37.4%	15.8%	34.5%	48%	17.6%	O/P=3.93		320	2	7200	3	(Numpilai et al., 2019a)
$Fe-Co-K/Al_2O_3$	41%	12.4%	33.7%	48%	18.7%	O/P=6.38		320	2	7200	3	(Numpilai et al., 2019a)
$Fe-Co-K/Al_2O_3$	41.6%	12.1%	32.2%	47%	20.6%	O/P=6.82		320	2	7200	3	(Numpilai et al., 2019a)

1.2.3 Effects of operating conditions on the catalytic performances.

Different authors have reported results obtained by varying different operating parameters, such as reaction temperature and total pressure, contact time and molar H_2/CO_2 inlet ratio. Table 1.6 summarizes the conditions used for different studies and their effects on the hydrocarbons distribution.

Table 1.6: Summary of operating conditions tested in literature and their effects on the hydrocarbons distribution. ↔ indicates a value almost constant. Arrows between parenthesis indicate values that did not change significantly or not monotonically.

Parameter	Range	χ_{CO_2}	S_{CO}	S_{CH_4}	$S_{C_{2+}}$	α	Olefins	Reference
T [°C]	300-350	↑	↓	↔	↑			(Albrecht et al., 2017)
	245-297	↑	(↑)	↔	↑	↑		(Iglesias Gonzalez et al., 2015)
	270-300	↑	(↓)	↓	↑	↑	↑	(Visconti et al., 2017)
	230-260	↑	↓	↓			↑	(Ning et al., 2017)
	260-340	↑	↓	↑		↓		(Jiang et al., 2018)
	300-400	↑		↓		(↑)	(↑)	(Riedel et al., 2001)
	300-400	↑						(Mokou et al., 2015)
H_2/CO_2	3-6	↑	↓	↑	↓			(Albrecht et al., 2017)
	4-8	↑	(↓)					(Iglesias Gonzalez et al., 2015)
	1-3	↑	↓	↑	↑	↑	↓	(Visconti et al., 2017)
	1-3	↑	↓	↑			↓	(Yao et al., 2011)
GHSV [Nml/g/h]	1200-18000	↓	↑	↑	↓	↓		(Iglesias Gonzalez et al., 2015)
	2700-16000	↓	↑	↓	↓	↔	↔	(Visconti et al., 2017)
	168-85700	↓	↑		↓	↓	↑	(Riedel et al., 2001)
	1800-3600	↓	↓	↔	↑			(Mokou et al., 2015)
	169.2-334.8	↓	↑	(↓)	↓	↑		(Willauer et al., 2013)
p [MPa]	1-2	↑	↔					(Iglesias Gonzalez et al., 2015)
	0.1-0.6	↑	↓	↑		↑	↑	(Visconti et al., 2017)
	1-3	(↑)	↔	↔	↔			(Jiang et al., 2018)
	0.1-1	↑	↓	↓	↑	↑	↓	(Lee et al., 1991)

The effects of temperature have been investigated in the range between 230 and 400°C. Temperature has an obvious effect of increasing CO_2 conversion and reducing the CO formation. Increasing the reaction temperature has in fact a kinetic effect, that leads to an increase of the kinetic constants, thus the reaction rates; and a thermodynamic effect, since the RWGS equilibrium is shifted towards the conversion of CO_2 to CO. The effect on hydrocarbons distribution are less clear. Temperature is known to favour the desorption of hydrocarbons and at the same time to favour the CO dissociation and the consequent formation of carbides and decreases the H_2/CO surface ratio. All this contributes to promote the chain-growth process and to obtain higher values of α, as observed by some authors. (Visconti et al., 2017; Iglesias Gonzalez et al., 2015; Riedel et al., 2001)

At relatively high temperatures (>297°C or >400°C) some authors observed deactivation of the catalyst, that could be explained by the presence of high partial pressures of water, formed by the enhanced RWGS equilibrium shift. (Riedel et al., 2001; Iglesias Gonzalez et al., 2015)

The effects of the molar H_2/CO_2 inlet ratio have been studied in the range between 1 and

8. An increase of the H_2/CO_2 ratio is observed to significantly increase the CO_2 conversion and to decrease the CO selectivity. This is due to the increased H_2 content in the feed that favours the CO hydrogenation rate, promoting the formation of hydrocarbons. The selectivity towards methane is observed to increase and the olefin content to decrease. (Visconti et al., 2017; Yao et al., 2011; Albrecht et al., 2017) The chain-growth probability has been observed to increase when the H_2/CO_2 ratio was increased. (Visconti et al., 2017) The higher H surface coverage and CO faster hydrogenation rate can explain the increase of the chain-growth monomer formation and thus the increase of α.

The effects of space velocity have been studied in a very wide range (168-85700 $\mathrm{Nml/g_{cat}/h}$). The increase of space velocity leads to a decrease of the CO_2 conversion and to an increase of the CO selectivity. The general trend is a decrease of the chain-growth probability, with enhanced formation of shorter hydrocarbons and methane. (Iglesias Gonzalez et al., 2015; Riedel et al., 2001) Some authors however observed very light influence of space velocity on hydrocarbons distribution. (Visconti et al., 2017)

Pressure is a parameter that does not have evident effects on the catalytic performances. The RWGS is not influenced by the total pressure, as it does not involve any change in the number of moles. The FT reaction rate seems to be influenced more by the CO dissociation rate than the CO molecules concentration, thus the effect of pressure should not have significant effects, at least at sufficiently high values. (Jiang et al., 2018) An increase of pressure from 0.1 to 1.5 MPa has been observed to increase the CO_2 conversion and to contribute to shift from the RWGS regime to an FT one. (Visconti et al., 2017; Lee et al., 1991) Over a certain value (between 0.6 and 1.1 MPa) the effects of an increase pressure become negligible. (Visconti et al., 2017; Iglesias Gonzalez et al., 2015)

1.3 Review of the information available about the reaction mechanism.

We have shown in the previous section that a lot of work has been done to develop an optimal catalyst able to convert CO_2 to a good extent preferably into long-chain hydrocarbons. However, we have observed that the formation of long hydrocarbons (C_{5+}) is significantly harder than in the case of CO hydrogenation and C_2-C_4 products are generally the most abundant fraction. Moreover, the formation of methane is very relevant and very hard to contain. It is thus very important to understand the mechanism of the reaction. Information about the reaction mechanism could be used to understand how to better design the catalyst so that methane formation could be minimized and long hydrocarbons production enhanced.

In this section we review the information existing about the CO_2 hydrogenation reaction mechanism, investigating the possible active sites and how the different products can be formed.

1.3.1 Advances on the reaction mechanisms for the CO_2 hydrogenation reaction.

1.3.1.1 Active sites.

The main part of the information about the CO_2 hydrogenation mechanism derive from the works of Schulz and Visconti and their collaborators. (Schulz and Claeys, 1999; Schulz et al., 2005; Schulz, 2014; Riedel et al., 2003; Martinelli et al., 2014; Visconti et al., 2017)

Over Fe-based catalysts, differently from what happens on Co, many species are involved in the catalysis of the reaction. It is commonly believed that three types of active sites are involved in the CO_2 hydrogenation catalysis (Martinelli et al., 2014; Schulz, 2014; Visconti et al., 2017):

- the Fe_3O_4 sites are responsible for the RWGS reaction activity and eventually for the production of oxygenates products;

- the Fe carbides (in particular the Hägg phase Fe_5C_2) are responsible for the chain-growth process through the formation of the C-C bond and for the formation of primary products;
- the metallic iron Fe(0) that is responsible for the olefin re-adsorption and their secondary hydrogenations.

The relative amount of these active sites can influence the final composition of the product and it depends on process conditions and catalyst reduction conditions. CO is known to promote the carburization process of iron oxides and Fe into carbides, promoting the chain-growth process. CO_2 on the contrary favours the decarburization process, causing a decrease of the carbides sites amount. (Visconti et al., 2017) It has however been shown that, even with CO_2 feeds, a highly carburized catalyst can be obtained, thanks to the "construction" process to which it undergoes that allows the conversion of metallic and oxide species into carbides. (Schulz and Claeys, 1999; Riedel et al., 2003; Sai Prasad et al., 2008; Schulz, 2014) The "construction" of the active catalyst consists in the increase of the number of sites specifically active for the CO conversion towards hydrocarbons. Five different episodes have been discriminated for the CO_2-hydrogenation over Fe catalysts, as shown in Figure 1.24: at the beginning, in episode I, carbon deposition on the catalyst surface and carbiding of the catalyst are the dominant events and no hydrocarbons are formed. The fresh catalyst, mainly made of α-iron, Fe_3O_4 and a small amount of Fe_2O_3, does not show any activity for FT. A very small activity for the RWGS reaction allows the formation of small quantities of CO, which is converted into carbides species according to an associative/dissociative chemisorption and a carbiding mechanism:

$$CO \rightarrow CO_{ads}$$

$$CO_{ads} \rightarrow C_{ads} + O_{ads}$$

$$C_{ads} \rightarrow C_{carbure}$$

In episode II, the carbiding process reaches a pseudo-stationary state and RWGS activity develops. In episode III, FT activity starts to slowly develop and RWGS activity accelerates, while carbides formation declines. The RWGS activity rapidly increases only when FT activity starts to develop: to explain this observation, it has been proposed that RWGS needs the presence of some water and thus it can occur only when the FT synthesis has provided enough H_2O. (Schulz and Claeys, 1999) From episode IV, the FT activity is completely developed and it reaches the steady-state in episode V. Thus, FT can occur only when the carbiding of the catalyst is complete (in other words, when the metal α-Fe phase disappeared, forming the carbide phase Fe_5C_2) and RWGS has provided enough CO. At the end of episode IV, until episode V, a change in BET area, pore volume and pore diameter has been observed when using bulk iron catalysts. These changes are related to the accumulation of liquid organic products that fill the pores, without causing an activity decline.

With CO feed, the same episodes are observed, but they are less extended in time because the carbiding process is faster. CO is in fact directly available on the surface and does not need to be generated from the RWGS reaction. An additional episode, corresponding to the catalyst deactivation, is observed during the CO hydrogenation. The deactivation seems to be connected to the process of carbiding/C formation, that occurs at high rates in alkalized catalysts in presence of CO. This is not observed with CO_2 because of the lower CO partial pressure. The very slight difference between the two hydrogenations suggests that the composition of the feed gas has no crucial effect on the product distribution. (Schulz and Claeys, 1999; Riedel et al., 2003)

1.3.1.2 Formation of products.

The mechanism of the CO_2 hydrogenation involves the breaking of the C-O bond, first the bond of CO_2 to form CO and then that of CO that leads to the formation of the C monomer responsible

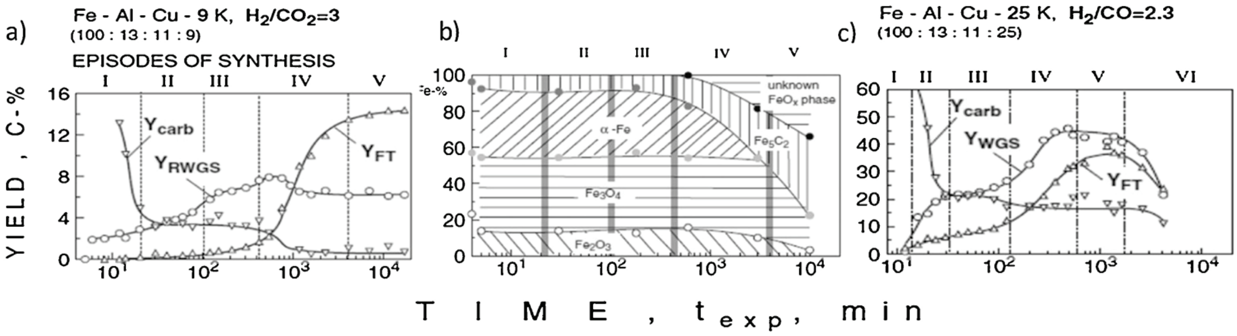

Figure 1.24: Catalyst construction process: a) evolution of Fischer-Tropsch, RWGS and carbides formation yields during CO_2 hydrogenation over Fe-based catalyst; b) evolution of iron phase composition during CO_2 hydrogenation over Fe-based catalyst; c) evolution of Fischer-Tropsch, RWGS and carbides formation yields during CO hydrogenation on the same Fe-based catalyst. Figure adapted from Riedel et al. (2003).

for the chain-growth. (Shafer et al., 2019) The catalyst's surface coverage of $CO/CO_2/H_2$ has an influence on the composition of the final product. Furthermore, over Fe-K catalysts, K has been reported to have a role in controlling the rate of CO dissociation into C. (Visconti et al., 2017; Amoyal et al., 2017; Jiang et al., 2018; Schulz, 2014) The CO dissociation forms a C adsorbed species as intermediate that can undergo different reactions, as shown in Figure 1.25:

- if it reacts with hydrogen, it can form the $-CH_x$ monomer, responsible for the chain-growth, thus enhancing the formation of long hydrocarbons;
- if it reacts with the metal iron, it can form iron carbides, the active phase for chain-growth, thus enhancing again the formation of long hydrocarbons;
- if it reacts with other adsorbed C, it can form a carbon phase that deposits on the catalyst surface, causing its deactivation.

K controls the rate of CO decomposition and can thus influence the further reaction of the adsorbed C and the type of products formed. Too high content of K favours the carbon deposition, thus increasing the deactivation (Jiang et al., 2018; Schulz, 2014), while optimal contents of alkali favour the chain-growth. K in fact favours the CO dissociation rate, increasing the rate of formation of adsorbed C and thus their surface concentration. Therefore, the formation of the C-C bond is enhanced and so is the formation rate of long hydrocarbons. Moreover, the presence of K reduces the H_2 adsorption rate, reducing the concentration of adsorbed H on the catalytic surface and thus leading to decreased methane formation. Catalyst with high (but not too much) alkali level were observed to have less metallic iron at the end of the "construction" and the formation of secondary products was limited. (Dorner et al., 2010b; Jiang et al., 2018; Schulz, 2014)

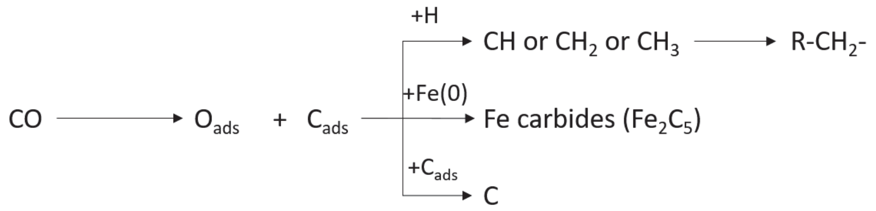

Figure 1.25: Possible reaction pathways of the adsorbed C intermediate.

Chain-growth can theoretically occur with linear growth or branching, both addressed as primary reactions. (Schulz et al., 2005; Schulz, 2014) Linear chain-growth is the reaction between the alkylene and a methyl species to form an alkyl intermediate, which is attached to the site with its α-carbon atom. The chain branching follows the same mechanism but the alkyl intermediate is attached to the site with its β-carbon atom. A further growth of this intermediate causes the formation of a branched chain. The branching growth probability is significantly lower than the linear growth probability, as shown in Figure 1.26. This is due to spatial constraints that are more important for the branching growth than for the linear one. Moreover, these spatial constraints increase with the increase of the chain length, leading to a decrease of the branching growth probability with increasing carbon number (for N_C>4). (Riedel et al., 2003; Sai Prasad et al., 2008; Schulz et al., 2005; Schulz, 2014) Carbon number of 3 presents an exception to this trend, as its branching probability has a relatively high value.

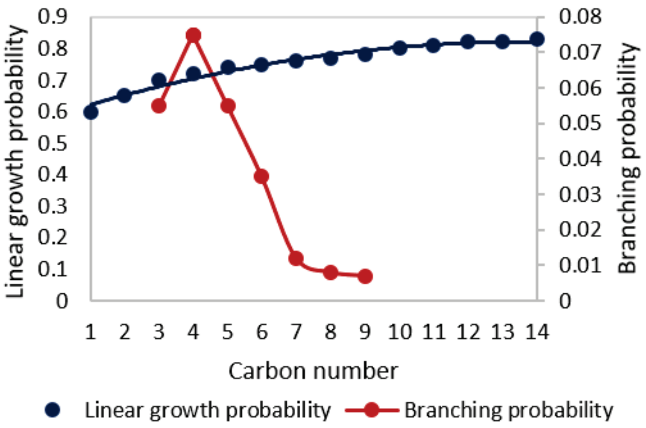

Figure 1.26: Probability of linear chain-growth and probability of branching as functions of carbon number. Adapted from Schulz (2014).

Olefins can be in principle formed as primary products or as secondary products. (Schulz, 2014; Schulz et al., 2005; Schulz and Claeys, 1999) The formation of primary olefins and paraffins occur over the chain-growth sites. Then, two competitive reactions can occur on the same active sites: the dissociative desorption to give α-olefins and the associative desorption to give n-paraffins (see Figure 1.27). Over Fe catalysts and during CO_2 hydrogenation, the formation of α-olefins as primary products appears to be prevalent (70-80% of primary products were found to be olefins). (Riedel et al., 2003; Schulz, 2014; Schulz et al., 2005; Schulz and Claeys, 1999) α-olefins can undergo secondary hydrogenation, isomerization or double bond shift reactions. Those reactions occur on hydrogenation sites, typically α-iron and lead to the formation of paraffins, as shown in Figure 1.28. The tendency of the olefins to undergo hydrogenation reactions depends on their carbon number: the longer the olefin chain, the slower the molecule's diffusion rate and the higher the conversion to the corresponding paraffin. (Visconti et al., 2017) Ethylene represents an exception, because of its high reactivity for secondary reactions. (Riedel et al., 2003; Schulz, 2014) Formation of secondary products from rehydrogenation of olefins has been reported to be minor over alkalised Fe catalysts. (Schulz et al., 1999; Riedel et al., 2003)

REACTIONS OF FORMATION OF PRIMARY OLEFINS AND PARAFFINS

DISSOCIATIVE DESORPTION $R-CH_2-CH_2(ads) \rightarrow R-CH=CH_2+H(ads)$

ASSOCIATIVE DESORPTION $R-CH_2-CH_2(ads)+H(ads) \rightarrow R-CH_2-CH_3$

Figure 1.27: Mechanism of formation of primary olefins and primary paraffins. Adapted from Schulz et al. (2005).

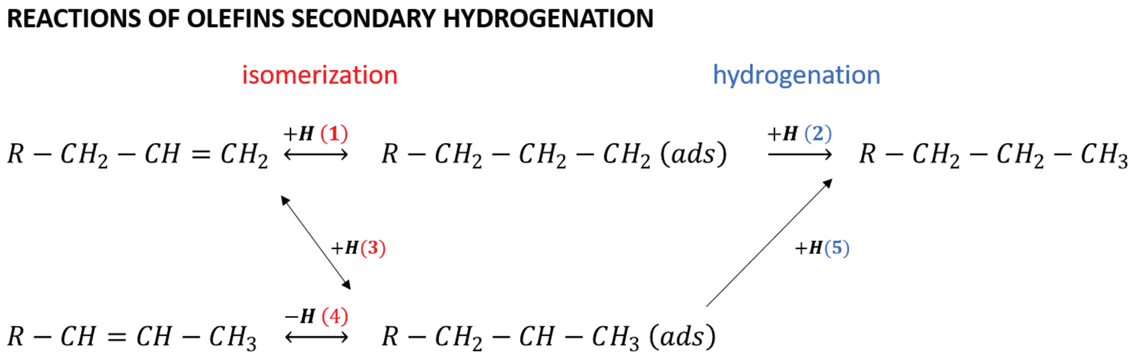

Figure 1.28: Description of the formation of secondary products. Adapted from Schulz et al. (2005).

Oxygenates are frequent by-products of the FT process and they can be formed both as primary or secondary products. Riedel et al. proposed that oxygenates form from a first dissociation of adsorbed CO that forms adsorbed O. (Riedel et al., 2003) The subsequent reaction of adsorbed O with adsorbed H leads to the production of adsorbed OH groups that react with the hydrocarbon growing species, leading to the formation of oxygenates. This mechanisms is described by Eqs. 1.4-1.6.

$$CO_{ads} \rightarrow C_{ads} + O_{ads} \tag{1.4}$$

$$O_{ads} + H_{ads} \rightarrow OH_{ads} \tag{1.5}$$

$$R - CH_2 - CH_{ads} + OH_{ads} \rightarrow R - CH_2 - CH - OH_{ads} \rightarrow R - CH_2 - CH = O \tag{1.6}$$

Other mechanisms have been proposed, such as the CO insertion (in analogy to what happens over Co catalysts) and secondary olefin hydroformilation. (Schulz et al., 1999) Among alcohols, methanol is generally produced in very low quantities, because of the low activity for methanol production of Fe catalysts and because of non-favouring thermodynamically conditions. On the contrary, oxygenates with 2 carbon atoms are very abundant, due to the high reactivity of ethylene.

Thus, we have summarized the most important results derived from mechanistic studies performed on the CO_2 hydrogenation over Fe catalysts. In addition, as the CO_2 hydrogenation reaction is a two-step reaction that passes by the formation of CO via RWGS and then converts the formed CO into hydrocarbons via the FT synthesis, many information can be derived from the wide work that already exists on the reaction mechanism of the FT synthesis. In the next section we will focus on the results reported in literature on the reaction mechanism of the FT reaction.

1.3.2 Mechanism of the FT reaction.

The FT synthesis is a polymerization reaction that occurs with stepwise chain-growth (Dry, 1996), but unlike other polymerization reactions, the feed should be first converted into monomer and initiator, before polymerizing into the final hydrocarbon. Thus, for the understanding of the reaction mechanism, it is essential to identify the nature and the formation pathways of the initiator and the monomer. Though lot of effort has been dedicated to this purpose, the reaction mechanism of the FT reaction is still extensively debated. Many authors have reviewed the most important works that investigate the mechanism of FT. (Novak et al., 1981; Van der Laan and Beenackers, 1999; Maitlis, 2004; Mousavi et al., 2015; Saeidi et al., 2017; Mahmoudi et al., 2017) Here, we give an overview of the mechanisms proposed for the FT reaction over Fe catalysts.

Many mechanisms have been proposed for the FT synthesis. The two most accepted ones are the carbide and the CO-insertion mechanisms.

The carbide mechanism.

According to the carbide mechanism (represented in Figure 1.29), CH_2 is the monomer that is formed from the reduction of iron carbides, produced via the reaction of CO with the active metal phase. (Fischer and Tropsch, 1926) Strong evidence exist about the involvement of carbides in the FT synthesis. (Ponec, 1978; Biloen and Sachtler, 1981) An initiator is needed for the polymerization of the CH_2 monomer. Different hypothesis exist about which species act as initiators. According to the alkyl mechanism, an alkyl species CH_3 is the initiator of the polymerization. Then, chain-growth can occur via consecutive insertion of the CH_2 surface species into the growing hydrocarbon chain. (Brady and Pettit, 1980) This simple mechanism can easily describe the formation of linear alkanes and alkenes and it is generally recognized for the formation of those species. However, the formation of branched chains and oxygenates cannot be explained by the alkyl mechanism, thus more complex mechanisms have been proposed.

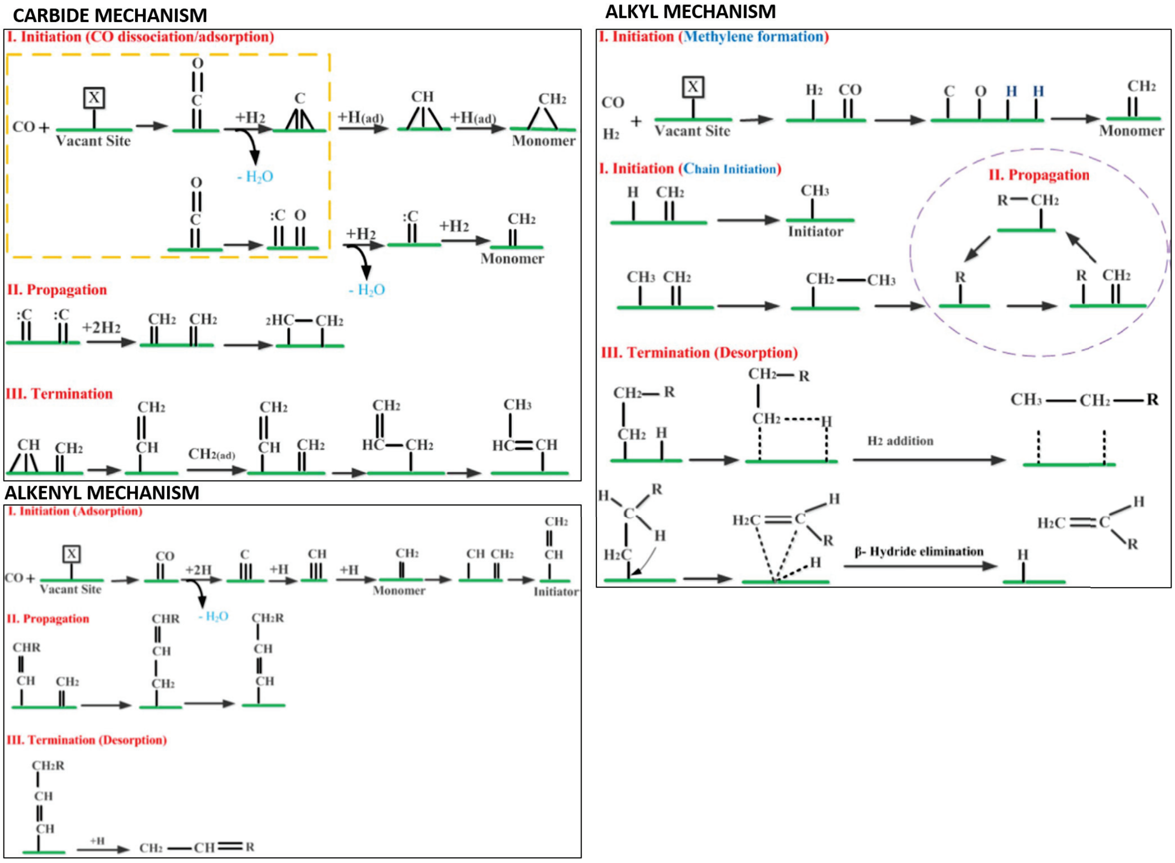

Figure 1.29: Schematic representation of carbide mechanism, alkyl mechanism and alkenyl mechanism. Figures from Saeidi et al. (2017).

The alkenyl mechanism considers as initiator a vinyl surface species $-CH = CH_2$ which is formed from the reaction of the species CH and CH_2. (Maitlis, 2004) Reaction of the vinyl species with the monomer CH_2 forms an allyl species $-CH_2CH = CH_2$ that can undergo isomerization and form an alkenyl species $-CH = CHCH_3$, from which alkenes are formed. This mechanism has some limitations, such as that it does not explain the formation of branched products and considers the formation of alkanes only as secondary products.

The alkylidene-hydride-methylidyne mechanism proposes that CH and H act as monomer instead of CH_2. (Ciobıcă et al., 2002) In this way, the formation of methyl branched hydrocarbons is possible, as well as the formation of alkanes as primary products. Thus, the alkylidene-hydride-methylidyne mechanism is currently the most general mechanism discussed so far to explain the FTS mechanism. (Saeidi et al., 2017)

The CO-insertion mechanism.

In CO insertion mechanism (represented in Figure 1.30), the CO absorbed on active metal surface is considered as the monomer. (Pichler and Schulz, 1970) The chain-growth is considered to occur in two steps: first, a CO adsorbed species dissociates and another CO inserts into a hydrocarbon fragment species; then, the CO bond of the inserted CO cleaves, leading to chain-growth of the hydrocarbon chain. This mechanism remains postulated rather than validated as experimental data are missing to prove it in heterogeneous catalysis. (Hindermann et al., 1993; Schulz and Claeys, 1999)

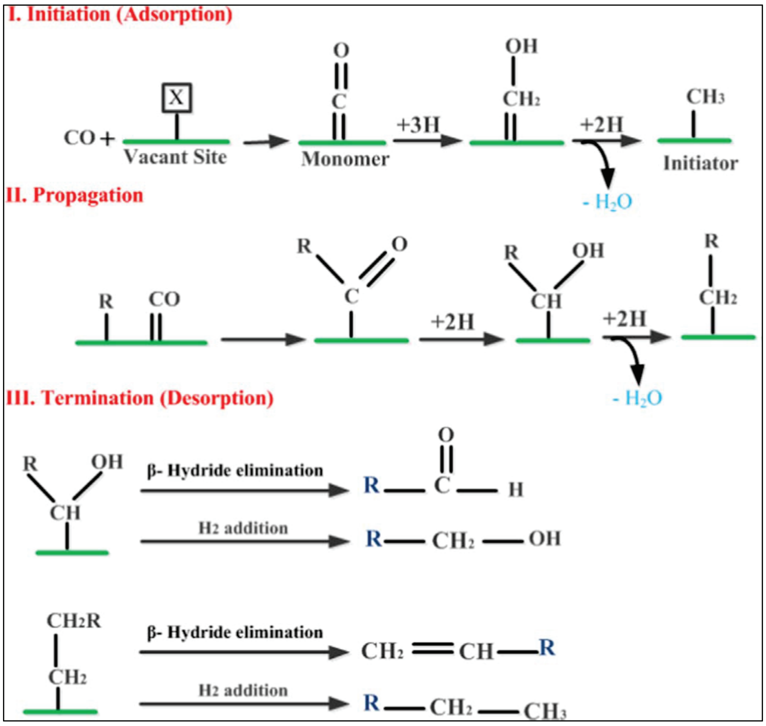

Figure 1.30: Schematic representation of the CO insertion mechanism. Figure from Saeidi et al. (2017).

Other mechanisms proposed for the FT reaction.

Many other mechanisms have been proposed to describe the FT reaction. The enolic mechanism assumes that the species $CHOH$ acts as monomer and initiates the reaction. $CHOH$ is formed by hydrogenation of the chemisorbed CO, while chain-growth occurs via condensation reactions between enolic species. (Huff Jr and Satterfield, 1984) Major debate is addressed to this mechanism: some authors reported that alcohols and aldehydes can initiate the reaction over Fe catalysts (Kokes et al., 1957); others reported that alcohols can initiate but not propagate the reaction (Tau et al., 1992); others identified the monomer in an alkoxide structure but not $CHOH$ (Blyholder and Wyatt, 1966; Blyholder and Neff, 1966; Benziger and Madix, 1980, 1982). The formate mechanism proposes that CO is the monomer that gives chain-growth via insertion into the $O-R$ bond of a surface hydroxyl group to form a $COOR$ species. Over Co catalysts, the chain-growth probability α was found to be proportional to the partial pressure of CO, but with a relationship that strongly depends on the support properties. (Frennet and Hubert, 2000; Schweicher et al., 2012) The formate mechanism would not be able to take into account the type of support, thus it is generally not considered as an accurate mechanism.

More complex mechanisms have been proposed, combining different mechanisms in order to explain the formation of different species. The CO insertion-carbide mechanism for example assumes that CO insertion and alkyl mechanisms take place simultaneously. (Gaube and Klein, 2010) This mechanism could explain the observed double-α ASF distribution and the formation of oxygenated compounds.

Another important aspect that is debated about the FT reaction mechanism is the CO dissociation that can be direct or H-assisted. One of the main limit of carbides mechanisms is that direct CO dissociation rates is limiting because of the high activation energy barrier. Assuming that CO dissociation is H-assisted would avoid this limitation, as the activation energy barrier would be decreased. However, assuming that CO dissociation is H-assisted would exclude any interaction between the metal and support, which has been observed to influence the reaction mechanism.

1.3.2.1 Distribution of hydrocarbons products of the FT synthesis.

To describe the distribution of hydrocarbons obtained as products during the FT synthesis, an important parameter is the chain-growth probability α defined as the fraction of the chain propagation rate $r_{P,n}$ to the total turnover rate $r_{P,n}+r_{T,n}$:

$$\alpha_n = \frac{r_{P,n}}{r_{P,n}+r_{T,n}} \tag{1.7}$$

This definition derives from the approach developed by Schulz (Schulz, 1935) and Flory (Flory, 1936) for polymerization reactions and adapted to Fischer-Tropsch by Herington (Herington, 1946) and Anderson (Friedel and Anderson, 1950; Anderson et al., 1951; Storch, 1951; Anderson, 1956). The ideal Anderson-Schulz-Flory (ASF) distribution is based on the hypothesis that the chain-growth probability α is not dependent on the chain length and can be written as:

$$z_n = (1-\alpha)\,\alpha^{n-1} \tag{1.8}$$

where z_n is the mole fraction of components with carbon number n. This is a simple way to represent the hydrocarbons distribution according to their carbon number. The value of chain-growth probability can influence the hydrocarbons selectivity, as shown in Figure 1.31-b. The ideal model applies to the obtained experimental values if the logarithm of the mole fractions z_n plotted as function of the carbon number shows a straight line, as shown in Figure 1.31-a.

Deviations from the ideal ASF distribution are often observed, such as positive C_1 deviations, negative C_2 deviations and long-chain hydrocarbons positive deviations.

Positive deviations of C_1 are generally observed together with negative deviations of C_2, especially over Ru and Co catalysts. (Henrici-Olivé and Olivé, 1976; Patzlaff et al., 2002; Van der Laan and Beenackers, 1999; Iglesia et al., 1991) The reason of the observed positive deviations of methane are still debated in literature. Different explications have been proposed, such as the presence of different active sites, very active for methane formation (Schulz et al., 1988), or an increased termination probability (Wojciechowski, 1988; Sarup and Wojciechowski, 1988), or by a separate reaction pathway that would lead to the formation of methane from secondary hydrogenolysis by demethylation, especially at high temperatures (>275°C) (Komaya and Bell, 1994; Kuipers et al., 1996).

Negative deviations of C_2 have been observed over Co and Ru catalysts, but also over Fe catalysts promoted with K. (Kuipers et al., 1995; Dictor and Bell, 1986; Patzlaff et al., 1999)

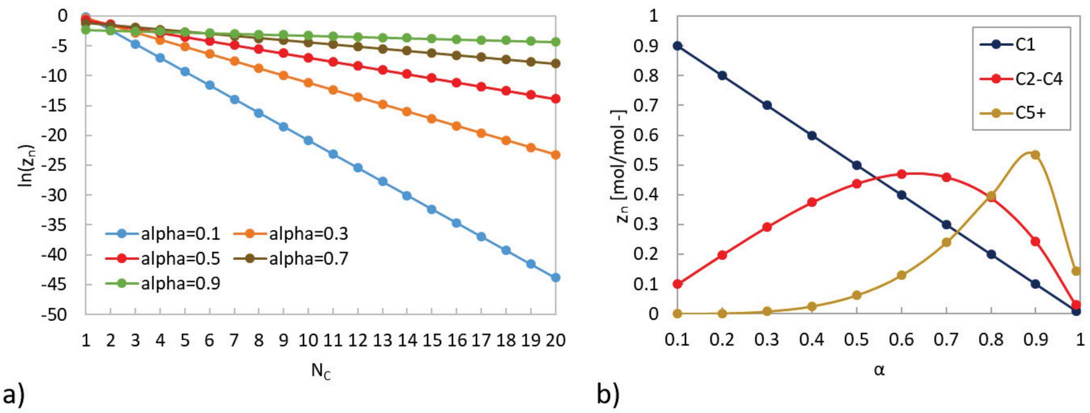

Figure 1.31: a) ASF distribution of compounds C_1-C_{20}: logarithm of the mole fraction of compounds with carbon number n as function of carbon number; b) Mole percentage of C_1, C_2-C_4 and C_{5+} hydrocarbons fraction as functions of α, estimated from the ideal ASF distribution.

The high reactivity of ethylene seems to represent the cause of such a deviation, as ethylene is supposed to re-adsorb on the catalytic surface and to contribute to the formation of longer hydrocarbons. (Iglesia et al., 1991; Komaya and Bell, 1994; Patzlaff et al., 1999, 2002)

Deviations of long hydrocarbons (C_{10+}) from the ideal ASF distribution are found especially over iron catalysts. (Donnelly et al., 1988; Dictor and Bell, 1986; Patzlaff et al., 1999; Van der Laan and Beenackers, 1999) These deviations have been interpreted in different ways. Some authors assumed the existence of two different active sites, each one characterized by its own chain-growth probability. (Madon, 1981; Donnelly et al., 1988) This led to the development of double-ASF distributions. Other explanations were given, such as different chain termination reactions (Wojciechowski, 1988; Sarup and Wojciechowski, 1988), or re-adsorption of olefins and their secondary hydrogenations (Kuipers et al., 1995; Schulz and Claeys, 1999; Patzlaff et al., 2002).

The double-ASF distribution is often used to describe the deviations of long hydrocarbons from the ideal distribution. This method, proposed by Satterfield and collaborators (Donnelly et al., 1988), is based on the superposition of two independent ideal ASF distributions, each characterised by a value of chain-growth probability α. The two α are both assumed to be independent on the carbon number.

$$z_n = A\alpha_1^{n-1} + B\alpha_2^{n-1} \tag{1.9}$$

At the intersection point ξ the contributions of the two terms of the previous equation are equal:

$$A\alpha_1^{n-1} = B\alpha_2^{n-1} \quad at\ n = \xi \tag{1.10}$$

Methane and ethane are generally considered to not obey to the ASF distribution, thus the double-ASF distribution is applied to products with $n > 2$. (Patzlaff et al., 1999; Tavasoli et al., 2010; Nakhaei Pour et al., 2013) The sum of mole fractions over all carbon numbers equals unity, thus if C_1 and C_2 fractions are excluded, the following equation is obtained:

$$\sum_{i=3}^{N} z_i = 1 - z_1^{exp} - z_2^{exp} = \sum_{i=1}^{N} \left(A\alpha_1^{i-1} + B\alpha_2^{i-1}\right) - A\left(1+\alpha_1\right) - B\left(1+\alpha_2\right) \tag{1.11}$$

The mathematical procedure proposed by Donnelly et al. (Donnelly et al., 1988) arrives at:

$$A = (1 - z_1^{exp} - z_2^{exp}) \left[\frac{\alpha_1^2}{1-\alpha_1} + \left(\frac{\alpha_1}{\alpha_2}\right)^{\xi-1} \left(\frac{\alpha_2^2}{1-\alpha_2}\right)\right]^{-1} \tag{1.12}$$

and finally at:

$$\frac{z_i}{1 - z_1^{exp} - z_2^{exp}} = \left[\alpha_1^{i-1} + \left(\frac{\alpha_1}{\alpha_2}\right)^{\xi-1} \alpha_2^{i-1}\right] \left[\frac{\alpha_1^2}{1-\alpha_1} + \left(\frac{\alpha_1}{\alpha_2}\right)^{\xi-1} \frac{\alpha_2^2}{1-\alpha_2}\right]^{-1} \tag{1.13}$$

Parameters α_1, α_2 and ξ are determined by least squares method. The mole fraction of products formed with the chain-growth probability α_1 can thus be estimated as:

$$\mu_1 = \frac{1-\alpha_2}{1-\alpha_1}\alpha_1^2 \left[\frac{1-\alpha_2}{1-\alpha_1}\alpha_1^2 + \left(\frac{\alpha_1}{\alpha_2}\right)^{\xi-1}\alpha_2^2\right]^{-1} \tag{1.14}$$

The mole fraction of products formed with the chain-growth probability α_2 equals:

$$\mu_2 = 1 - \mu_1 \tag{1.15}$$

The double-ASF distribution as function of μ_1 or μ_2 can thus be expressed as follows (Förtsch et al., 2015):

$$z_n = (1-\mu_2)(1-\alpha_1)\alpha_1^{n-1} + \mu_2(1-\alpha_2)\alpha_2^{n-1} \tag{1.16}$$

Other more complex models with chain-length dependent chain-growth probability have been developed, either based on olefins re-adsorption (Schulz and Claeys, 1999) or on chain-length dependent desorption (Botes, 2007). These models are not covered here, but a comprehensive review can be found in the paper by Förtsch et al. (Förtsch et al., 2015)

1.3.2.2 Role of H_2O in the FT mechanism.

As we have already asserted several times, water is believed to have a role in the deactivation of iron catalysts. Water is the co-product of both RWGS and FT, thus it is always present in the reactor with varying content.

Many experiments with addition of water to the feed have been performed over different catalysts and in different reaction systems for the FT synthesis. The results observed are sometimes contrasting, indicating that water effects are significantly dependent on the type of catalyst and of reactors used. For example, Karn et al. observed that the addition of 10-30% of H_2O to a syngas in a fixed-bed reactor led to only slight changes in CO conversion over a Fe-based catalyst. (Karn et al., 1961) These changes were reported to be reversible for low concentrations of water. However, when catalysts were exposed at high concentrations of water for long time, the loss of activity was permanent. This was correlated to sintering. (Satterfield et al., 1986) Satterfield et al., using a slurry reactor with Fe catalysts, observed that the addition of 20% of H_2O to the inlet H_2/CO gas with 0.96 molar ratio led to accelerated deactivation rate of the FT catalyst. Methane and oxygenates selectivity were observed to increase, as well as the activity towards the WGS. When the H_2/CO molar ratio was set to 0.52, no effects were observed on the FT rate. (Satterfield et al., 1986) Reymond et al. reported that at atmospheric pressure and with differential conversion, the addition of 0.6% of H_2O to a $9H_2/1CO$ syngas led to a significant decrease of the products formation rate, without changing their distribution. (Reymond et al., 1980) Water co-feeding studies over Fe-K catalysts were performed by Pendyala et al. in a CSTR reactor. (Pendyala et al., 2010) They observed that at high temperatures (270°C) the addition of water to the feed had a positive effect on CO conversion, while when temperature was decreased to 230°C, deactivation of the catalyst and drop of CO conversion were observed. The addition of water at 230°C led to oxidation of iron carbides into Fe_3O_4, reducing the FT activity.

In conclusion, it has been shown that high partial pressures of water can be detrimental for the catalysts and for its catalytic performances, as water can contribute to the re-oxidation of iron carbides. However, these effects are strongly dependent on the type of catalyst, the reactor used and the operating conditions.

From the point of view of the CO_2 hydrogenation, understanding the role of water can be very important, as higher concentration can be reached during the reaction compared to the FT synthesis. Water can have a role in the catalyst deactivation in conditions of strong CO_2 conversion, as it has already been reported by different authors. (Iglesias Gonzalez et al., 2015; Riedel et al., 2001)

1.3.2.3 Role of olefins in the FT mechanism.

FT synthesis leads to the formation of olefins as primary products, especially over iron-based catalysts. The role of alkenes in FT synthesis has been debated for many years, as they can either be chain initiators or essentially inert except for hydrogenation. During the FT synthesis, olefins can be involved in many kinds of secondary reactions that can influence the final composition of the pool of products obtained. In particular, olefins can undergo 1) secondary hydrogenations to form the corresponding paraffin; 2) reincorporation into the growing chain to form longer hydrocarbons; 3) hydrogenolysis to form shorter chains; 4) isomerization. It is thus important to understand the role of olefins and the reaction pathways they can undergo. This will help in understanding how to enhance the selectivity of the FT process towards the desired products.

Many studies have been conducted with co-feeding ethylene or longer alkenes during the FT synthesis over different catalysts.

Ethylene is known to be very active for secondary reactions. Generally, when it is added to the FT feed, it is observed to convert to high extent into ethane. However, it also acts as a propagator and initiator for chain-growth, leading to the formation of longer hydrocarbons and decreasing the methane selectivity. (Tau et al., 1990; Hanlon and Satterfield, 1988; Snel and Espinoza, 1987; Molina et al., 1980; Kim, 1983) Methane selectivity is inhibited by the ethylene presence because of the scavenge of the adsorbed H from the catalyst surface for hydrogenation. (Snel and Espinoza, 1987; Boelee et al., 1989; Jordan and Bell, 1986; Yang et al., 2020) Boelee et al. reported that the reincorporation of ethylene rate depends on the $p_{C_2H_4}/p_{CO}$ ratio. (Boelee et al., 1989) This could explain why some authors found not very significant ethylene reincorporation (Satterfield, 1983) or an increase in olefin selectivity (Snel and Espinoza, 1987) at very high $p_{C_2H_4}/p_{CO}$ ratios.

The reactions of higher olefins is more difficult to understand. Some authors observed that the added α-olefins undergo mainly secondary hydrogenations into the corresponding paraffin or isomerization into the corresponding β-olefin. (Hanlon and Satterfield, 1988) Others observed that secondary hydrogenation rates are strongly dependent on the C number of the alkene: chains with higher C numbers have higher tendency to undergo secondary hydrogenations to the corresponding paraffin, because of an increased residence time in the reactor. (Tau et al., 1990)

In conclusion, these studies showed that 1-alkenes, except for ethylene, undergo secondary hydrogenation to form the corresponding paraffins, but it seems that they don't have a role in the chain-growth. Ethylene, on the contrary, is much more active and can have a role in enhancing the formation of long chains and in suppressing the methane formation. However, the only interest of adding olefins to the feed is to suppress the methane formation, as adding olefins strongly decreases the actual olefins formation rate.

1.3.2.4 Role of alcohols in the FT mechanism.

The formation of oxygenates products during the FT synthesis has been observed especially over iron catalysts. The role of alcohols in the reaction mechanism has been widely studied in the past, to understand if these species can be re-adsorbed on the catalytic sites and have an active role in the chain-growth. The main part of the works have been done by co-feeding ethanol or propanol to the syngas.

Ethanol co-feeding to the syngas was observed not to have any influence on the CO conversion (Kokes et al., 1957; Hanlon and Satterfield, 1988), but to decrease the hydrogenating activity of the catalyst, leading to lower methane selectivity and higher olefins/paraffins ratios. (Kokes et al., 1957; Hanlon and Satterfield, 1988; Kummer et al., 1951) The non-influence on CO conversion rate was explained by a weaker adsorption of ethanol compared to CO or by the adsorption of ethanol on different sites than those where CO is adsorbed. (Hanlon and Satterfield, 1988) The decrease of hydrogenating activity could be due to an inhibition of H_2 adsorption by ethanol and suggests that ethanol and α-olefins are competitively adsorbed on the same active sites, leading to inhibition of secondary hydrogenations. (Hanlon and Satterfield, 1988) Satterfield and collaborators observed that the loss of hydrogenation activity did not influence the value of α, suggesting that the mechanism of formation of CH_4 is different than that of formation of longer hydrocarbons. (Satterfield et al., 1986; Hanlon and Satterfield, 1988) Therefore, no incorporation of ethanol to form longer hydrocarbons was observed in these studies. However, other studies showed that part of the ethanol added was incorporated and acted as chain initiator to form longer hydrocarbons. This incorporation was found to be stronger at lower pressures. (Kummer et al., 1951; Kokes et al., 1957; Hall et al., 1960) Ethanol was also observed to influence oxygenates selectivity. Acetaldehyde and ethyl ethanoate formations increased when ethanol partial pressure in the feed was increased. (Tau et al., 1987; Hanlon and Satterfield, 1988) Acetaldehyde is probably formed from ethanol dehydrogenation and subsequent reaction of acetaldehyde with ethanol could explain the formation of ethyl ethanoate. Acetone formation was also reported by Hanlon et al. who suggested that ethanol is bonded to the active sites with its oxygenated carbon and reacts with surface methylene species to form acetone. (Hanlon and Satterfield, 1988)

From these experiments, it can thus be concluded that ethanol in some conditions can be incorporated and eventually contribute to the formation of hydrocarbons.

1.3.3 Mechanism of the hydrogenation reaction with with CO/CO_2 mixtures.

Since we have analysed the mechanism of the hydrogenation of CO, it is interesting to investigate the most common differences between CO and CO_2 hydrogenations.

First of all, CO_2 hydrogenation requires additional moles of H_2 per mole of CO_2 and produces higher quantities of H_2O as co-product. Generally, products obtained are lighter (C_2-C_4 hydrocarbons) and the conversion rates are lower. (Choi et al., 2017) However, the endothermic RWGS step makes the CO_2 hydrogenation less exothermic than the CO hydrogenation, making temperature control easier. (Srinivas et al., 2007)

Iron catalysts can hydrogenate both CO and CO_2, but they are generally less active with CO_2 because of the slower carbiding activity of the catalyst in presence of CO_2. (Schulz et al., 1999; Visconti et al., 2009, 2016; Riedel et al., 1999) Many authors agree that lighter hydrocarbons and methane are considerably formed during CO_2 hydrogenation. (Visconti et al., 2009, 2016; Kaiser et al., 2013; Yao et al., 2011; Pérez-Alonso et al., 2008; Ando et al., 2000) This has been explained by the higher H/C surface ratio, due to the low partial pressure of CO and the low adsorption strength of CO_2. This leads to higher methane formation. Moreover, the higher concentration of CO_2 and H_2O on the catalytic surface favours the decarburization of iron carbides into iron oxides or metallic iron. (Visconti et al., 2016) Other studies showed that the CO_2 hydrogenation led to product distributions very close to those obtained with CO. (Riedel et al., 1999; Schulz et al., 1999; Gnanamani et al., 2011) The only difference was the conversion rate that with CO was 43% higher. It was thus suggested that the chain-growth process and the methane formation are independent on the partial pressure of CO. The discrepancies observed in these results compared to those reported by Visconti's group (Visconti et al., 2009, 2016) can be attributed to the catalyst composition, as higher K content increases the activity towards the RWGS and thus the rate of CO formation and carburization. (Riedel et al., 1999; Kaiser et al., 2013)

The hydrogenation of CO/CO_2 mixtures has also been investigated by many authors. Adding CO_2 to CO feed could be beneficial for the hydrocarbons yield, as the presence of CO_2 in the feed contributes to limit the formation of CO_2 as co-product, without modifying the hydrocarbons distribution. (Visconti et al., 2016; Martinelli et al., 2014; Krishnamoorthy et al., 2002) The CO_2 in the feed in fact contributes to shift the WGS equilibrium towards the reversed reaction, approaching the net rate of WGS to negligible values. However, the absence of WGS implies the non-consumption of the produced water, which is known to be a poison for the catalyst. Thus, the CO_2 content in the feed needs to be optimised so that the WGS rate is reduced but not completely cancelled. When adding CO to CO_2 feeds, CO_2 was observed to be converted at lower rates compared to when only CO_2 feeds were used. No changes in hydrocarbons distribution were observed. (Visconti et al., 2016; Riedel et al., 1999) Results obtained by Riedel et al. are reported in Figure 1.32. (Riedel et al., 1999) It was thus supposed that the adsorption competition between CO and CO_2 is gained by CO, leading to lower conversion rates of CO_2. On the contrary, other authors have observed an increase of the methane selectivity and a global shift towards the formation of lighter hydrocarbons (Kaiser et al., 2013) and an increase of the olefin/paraffin ratio (Yao et al., 2011) when CO_2 content in the feed was increased. Results obtained by Kaiser et al. are reported in Figure 1.33. (Kaiser et al., 2013) Again, the lower K content of this catalyst, and thus its lower activity for the RWGS, was considered as an explanation for this apparently contradictory result.

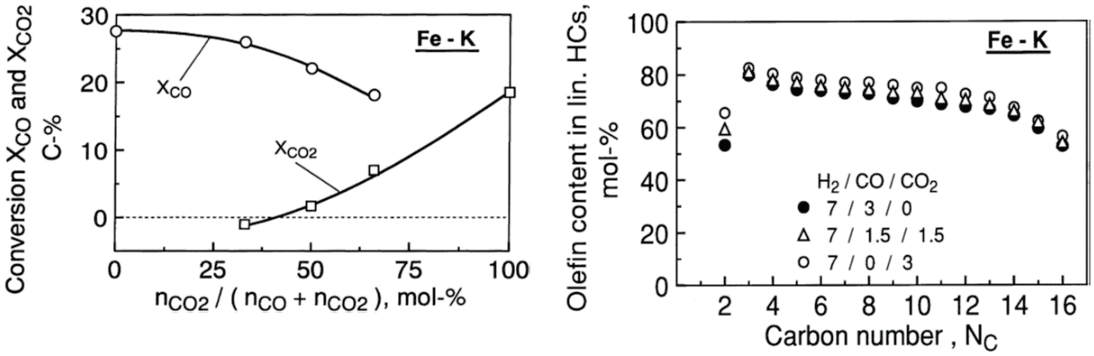

Figure 1.32: Results obtained by Riedel et al. over a $100Fe/13Al_2O_3/10Cu/10K$ catalyst at 523 K, 1 MPa, $H_2/C=7/3$ and 30 $Nml_{syngas}/min/g_{Fe}$. Left figure shows the evolution of CO and CO_2 conversion as function of the CO_2 content in the feed. Figure on the right shows the olefins fraction at different CO_2 content in the feed. Figure from Riedel et al. (1999).

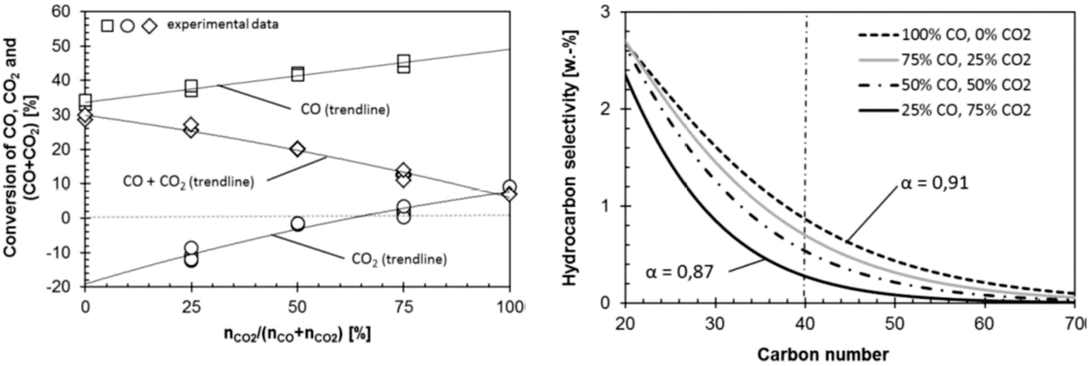

Figure 1.33: Results obtained by Kaiser et al. over a $100Fe/25SiO_2/5Cu/5K_2O$ catalyst at 233°C, 2.5 MPa, $H_2/C=3$ and $18x10^3$ $kg.s/m^2$. Left figure shows the evolution of CO, CO_2 and total C conversions as function of the CO_2 content in the feed. Figure on the right shows the ASF distribution of products at different CO_2 content in the feed. Figure from Kaiser et al. (2013).

1.3.4 Reaction mechanisms proposed for the (R)WGS reaction.

Advances about the reaction mechanism of the reversible water-gas shift reaction can be useful to understand the global mechanism of the CO_2 hydrogenation reaction.

The WGS mechanism is still object of some controversies. Two mechanisms have been proposed for the WGS reaction over metal catalysts in non-FT conditions: the direct oxidation (redox) and the formate mechanisms. Rethwisch and Dumesic suggested that the direct oxidation mechanism is prevalent over unsupported magnetite catalysts, while over supported iron catalysts a formate mechanism prevails. (Rethwisch and Dumesic, 1982) The redox mechanism suggests that water first dissociates at the reduced catalytic sites forming H_2, while the sites are oxidized. Then CO is oxidized to CO_2 and the sites are simultaneously reduced. This mechanism has the characteristic feature that products can be generated also in absence of one of the reactants. (Kul'kova and Temkin, 1949) The associative mechanism, on the contrary, involves the formation of a formate species ($-COOH$) as intermediate. (Armstrong and Hilditch, 1920) This adsorbed species can be formed through the reaction of CO with water or with a hydroxyl species, formed via decomposition of water. The formate intermediate is then reduced to CO_2. The formate mechanism has been found to be the most accurate to describe the reaction mechanism under FT-conditions over iron catalysts. (Nakhaei Pour et al., 2010; Van der Laan and Beenackers, 2000; Lox and Froment, 1993)

Studies on the RWGS suggest that the redox mechanism is commonly the dominant one over metal oxides. (Amoyal et al., 2017; Daza and Kuhn, 2016; Chou et al., 2019) The redox mechanism proposed by Amoyal et al. is illustrated in Figure 1.34. (Amoyal et al., 2017) For the redox mechanism, the CO_2 dissociation is commonly considered as rate determining step. (Chou et al., 2019) This is especially true in the case of potassium-promoted iron-based catalysts, as the addition of K contributes to reduce the CO adsorption's activation energy. (Amoyal et al., 2017) Formate mechanism was found to be suitable to describe the behaviour of the RWGS over a Fe/Cu/K catalyst. (Nakhaei Pour and Housaindokht, 2017) Over Fe/Al_2O_3 and $Fe\text{-}K/Al_2O_3$ it was suggested that simple redox or associative mechanisms are not sufficient to describe the behaviour of the reaction in every condition, but that a more complex mechanism (a combination of the two pathways) may be better. (Loiland et al., 2016)

In conclusion, a lot of effort has been dedicated to the investigation of the reaction mechanism of such a complex reaction. Many phenomena are involved that lead to the formation of a wide range of species and the mechanism seems to be strongly influenced by different parameters, such as catalyst composition and operating conditions.

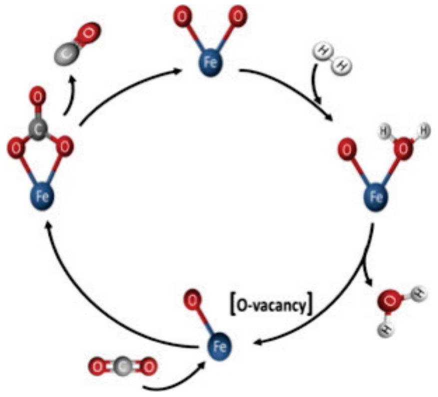

Figure 1.34: Redox mechanism of the RWGS over Fe catalysts. Figure from Amoyal et al. (2017).

1.4 Review of models proposed in literature for the CO_2 hydrogenation reaction.

As we have already discussed, most of the effort dedicated to the CO_2 hydrogenation has been directed to the development of an optimal catalyst. On the contrary, work on kinetic and reactor modelling for the CO_2 hydrogenation is poor.

In this section, we analyse the work that has been done in the development of kinetic models to describe the reaction rates for the CO_2 hydrogenation.

1.4.1 Kinetic models.

Only few studies are available up to now about kinetic modelling of CO_2 hydrogenation and they present quite simple models that take into account only few products. (Riedel et al., 2001; Willauer et al., 2013; Iglesias Gonzalez et al., 2015; Nakhaei Pour and Housaindokht, 2017; Najari et al., 2019b)

One of the first questions that have to be answered when developing a kinetic model for the CO_2 hydrogenation is whether to consider the two-step pathway (RWGS + FT) or the direct one (direct hydrogenation of CO_2 into hydrocarbons). The kinetic constants for the direct hydrogenation of CO_2 were found to be negligible compared to those for the two-step pathway, indicating that the two-step pathway is the dominant mechanism. (Riedel et al., 2001; Nakhaei Pour and Housaindokht, 2017) Thus, direct hydrogenation is generally neglected.

In most of the models developed, the kinetic laws are in the form of Eqs. 1.17-1.18, including the thermodynamic equilibrium for the RWGS and the inhibition effects of H_2O and CO_2 adsorption, as first proposed by Riedel et al. (Riedel et al., 2001) in analogy to previous approaches for the FT kinetic modelling. (Kuo, 1982; Leib and Kuo, 1984; Zimmerman and Bukur, 1990)

$$r_{RWGS} = k_{RWGS} \frac{p_{CO_2} p_{H_2} - p_{CO} p_{H_2O}/K_{eq}}{p_{CO} + a_{RWGS} p_{H_2O} + b_{RWGS} p_{CO_2}} \tag{1.17}$$

$$r_{FT} = k_{FT} \frac{p_{CO} p_{H_2}}{p_{CO} + a_{FT} p_{H_2O} + b_{FT} p_{CO_2}} \tag{1.18}$$

The kinetic constants are expressed according to the Arrhenius law:

$$k_i = k_{i0} exp\left(-\frac{E_A}{RT}\right) \tag{1.19}$$

Furthermore, in the most part of the existing models, only one compound is considered as representative of the whole pool of hydrocarbons obtained (propane or propylene in general).

(Riedel et al., 2001; Willauer et al., 2013; Iglesias Gonzalez et al., 2015) The model from Iglesias et al. also takes into account the formation of methane, considered separately from the formation of longer hydrocarbons. (Willauer et al., 2013) Some more complex models consider the formation of different products. For example, Najari et al. could predict the formation of olefins and paraffins from C_1 to C_4 (Najari et al., 2019b), while Zhang et al. considered the formation of CH_4, C_3H_6 and $C_{11}H_{24}$. (Zhang et al., 2019)

Table 1.7 summarizes the kinetic laws and the corresponding kinetic parameters obtained for the CO_2 hydrogenation. Values of kinetic constants $k_{i,0}$ obtained from different studies are very hardly comparable, as their order of magnitude varies in a very wide range. Concerning the effects of inhibition due to adsorption, the inhibition effect of water appears to be more important than that of CO_2, even if this latter cannot be neglected. This applies especially to highly alkalised catalysts (Riedel et al., 2001; Willauer et al., 2013), as K is known to favour the CO_2 adsorption. The CO_2 inhibition terms obtained for highly alkalised catalysts is in fact more important than for catalysts with less K. (Iglesias Gonzalez et al., 2015) The activation energies obtained are in a quite wide range. Results from Riedel and Willauer show activation energies of RWGS lower than those of FT, suggesting that the FT step is the rate-determining step. (Riedel et al., 2001; Willauer et al., 2013) Less alkalised catalysts, less active towards RWGS, resulted in higher RWGS activation energy. (Iglesias Gonzalez et al., 2015)

The most detailed model available up to now is the one developed by Najari et al. that considers the formation of olefins and paraffins until 4 carbon atoms. (Najari et al., 2019b) They obtained higher pre-exponential factor for olefins compared to the corresponding paraffins and decreasing pre-exponential factors with increasing carbon umbers. Values of activation energies were found to be higher than those generally reported.

In conclusion, some kinetic models of the CO_2 hydrogenation have been developed but no detailed models exist able to describe the formation of the main part of the products observed. Moreover, the existing models provide kinetic parameters that are sometimes inconsistent. This can be explained by the differences in catalyst composition, as promoters (such as K) can significantly influence the kinetic behaviour. Furthermore, all these approaches are macro-kinetic, thus only partially based on mechanistic assumptions. The kinetic laws adopted in these studies account for many phenomena, thus the interpretation of the kinetic parameters values is not always evident.

Further work is needed with the aim to develop a detailed kinetic model that describes the formation of different categories of products. A model of this kind can be used to predict the hydrocarbons distribution in different conditions, or in different reactor systems and eventually for a future scale-up of the process.

Table 1.7: Summary of kinetic laws and parameters obtained for CO_2 hydrogenation by different authors.

Product	Reaction rate equation	a_{i,H_2O} [MPa]	b_{i,CO_2} [MPa]	k_{i0} [mol/s/g/MPa]	$E_{A,i}$ [kJ/mol]	Reference
CO	$r_{RWGS} = k_{RWGS}\dfrac{p_{CO_2}p_{H_2} - p_{CO}p_{H_2O}/K_{eq}}{p_{CO} + a_{RWGS}p_{H_2O} + b_{RWGS}p_{CO_2}}$	65	7.4	$1.51x10^{7}$	55	(Riedel et al., 2001)
C_3H_8	$r_{FT} = k_{FT}\dfrac{p_{CO}p_{H_2}}{p_{CO} + a_{FT}p_{H_2O} + b_{FT}p_{CO_2}}$	33	2.7	$2.58x10^{8}$	72	
C_3H_8 from DH	$r_{DH} = k_{DH}\dfrac{p_{CO}p_{H_2}}{p_{CO} + a_{DH}p_{H_2O} + b_{DH}p_{CO_2}}$	90	66	39.6	20	
CO	$r_{RWGS} = k_{RWGS}\dfrac{p_{CO_2}p_{H_2} - p_{CO}p_{H_2O}/K_{eq}}{p_{CO} + a_{RWGS}p_{H_2O} + b_{RWGS}p_{CO_2}}$	65	7.4	$1.51x10^{7}$	55	(Willauer et al., 2013)
CH_4	$r_{METH} = k_{METH}\dfrac{p_{CO}p_{H_2}}{p_{CO} + a_{METH}p_{H_2O} + b_{METH}p_{CO_2}}$	33	2.7	$5.15x10^{2}$	72	
C_3H_6	$r_{FT} = k_{FT}\dfrac{p_{CO}p_{H_2}}{p_{CO} + a_{FT}p_{H_2O} + b_{FT}p_{CO_2}}$	33	2.7	$1.29x10^{3}$	72	
CO	$r_{RWGS} = k_{RWGS}\dfrac{p_{CO_2}p_{H_2} - p_{CO}p_{H_2O}/K_{eq}}{p_{CO} + a_{RWGS}p_{H_2O} + b_{RWGS}p_{CO_2}}$	128	0.8	$1.6x10^{-3}$	138.9	(Iglesias Gonzalez et al., 2015)
C_3H_8	$r_{FT} = k_{FT}\dfrac{p_{CO}p_{H_2}}{p_{CO} + a_{FT}p_{H_2O} + b_{FT}p_{CO_2}}$	152	0.5	$2.6x10^{-3}$	94.6	
CO	$r_{RWGS} = k_{RWGS}\dfrac{p_{CO_2}p_{H_2} - p_{CO}p_{H_2O}/K_{eq}}{p_{CO} + a_{RWGS}p_{H_2O} + b_{RWGS}p_{CO_2}}$	53.5	4.6	$6.19x10^{7}$	136	(Najari et al., 2019b)
CH_4		43.0	3.4	$3.82x10^{7}$	135	
C_2H_4		41.2	3.1	$4.09x10^{8}$	146	
C_2H_6		85.9	2.3	$4.93x10^{7}$	135	
C_3H_6	$r_i = k_i\dfrac{p_{CO}p_{H_2}}{p_{CO} + a_ip_{H_2O} + b_ip_{CO_2}}$	15.9	4.0	$2.54x10^{8}$	147.1	
C_3H_8		55.6	3.2	$1.42x10^{6}$	127	

C_4H_8		30.9	4.9	1.40x10^{5}	111	
C_4H_{10}		87.9	3.7	84.4	81	
C_nH_{2n} from DH		74.3	62.0	36.6	150	
CO	$r_{RWGS} = k_1\left(p_{CO_2}p_{H_2} - p_{CO}p_{H_2O}/K_1\right)$			2.02x10^{-3}	27.3	(Zhang et al., 2019)
CH_4	$r_{CH_4} = k_4\left(p_{CO}p_{H_2}^3 - p_{CH_4}4p_{H_2O}/K_4\right)$			6.13x10^{-5}	22.8	
C_3H_6	$r_{C_3H_6} = k_3\left(p_{CO}p_{H_2}^2 - p_{C_3H_6}^{1/3}p_{H_2O}/K_3\right)$			5.90x10^{-5}	14.4	
$C_{11}H_{24}$	$r_{C_{11}H_{24}} = k_2\left(p_{CO}p_{H_2}^{23/11} - p_{C_{11}H_{24}}^{1/11}p_{H_2O}/K_2\right)$			8.78x10^{-6}	4.1	

1.5 Final considerations on the process and solutions to improve the efficiency.

The main part of the studies on CO_2 hydrogenation have been performed in fixed-bed reactors at laboratory scale. Only few information is available about the process at bigger scale. In this section, state-of-the-art about the process configuration and propositions to improve the process efficiency is analysed.

1.5.1 Process configurations.

Only few pilot plants have been developed so far to convert CO_2 into hydrocarbons. The SOLETAIR pilot plant, created in Finland in 2017, demonstrated the production of gas, liquid and solid fuels for applications as fuels or chemicals from water, air and solar energy with an energy efficiency of 47%. (Vázquez et al., 2018) The pilot plant developed by Sunfire demonstrated the production of e-diesel from water, air and wind or solar energy. (Sunfire, 2017) An alternative pathway based on co-electrolysis of water and air-captured CO_2 would increase the efficiency up to 80%. (Sunfire, 2019)

These pilot plants, as well as other proposed process concepts (Kaiser et al., 2013; König et al., 2015a), are based on a two-step synthesis, meaning that CO_2 is first converted into CO via RWGS and then CO is converted to hydrocarbons via FT in a separate reactor. Thus, each reaction can occur in its optimal conditions and with an optimal catalyst, but this requires cooling and eventually compression of the exit gas after RWGS. Recirculation of the non-reacted gases is often needed to increase the conversion and avoid excessive reactor length.

Configuration with a single reactor where both reactions can occur would contribute to increase the energy efficiency of the process, because it would eliminate the need to cool and compress the gas that exits the RWGS reactor. However, with only one reactor, the conversion would be too low, thus a gas recycle or many reactors in series would be required to increase the conversion. (Srinivas et al., 2007)

We have already discussed how water can represent a problem for the CO_2 hydrogenation, because of its tendency to deactivate the iron-based catalysts, by oxidizing the iron carbides. (Vázquez et al., 2018; Kaiser et al., 2013; Martinelli et al., 2014) It is thus very important to remove water produced during the reaction, in order to improve process conversion and efficiency. Selective removal of H_2O during CO_2 hydrogenation can be performed in different ways, such as interstage cooling and condensation, adsorption or membranes. The use of perm-selective membranes for in-situ water removal seems a promising approach to increase the CO_2 hydrogenation performances and avoid the limitations due to the co-production of water. We discuss recent progress in the development of membranes for water removal and of membrane reactors in the following.

1.5.2 Membrane reactors.

For applications in the CO_2 hydrogenation, water perm-selective membranes are required to have some properties at the operating conditions needed for the reaction:

- high selectivity towards water permeation. Generally, permeances higher than $1x10^{-7}$ mol/s/Pa/m^2 are considered as acceptable. (Rohde et al., 2008)
- high perm-selectivity towards water. The perm-selectivity between i and j is defined as the ratio of the permeance of i and that of j. High perm-selectivity towards water means that the membrane has to be permeative towards water, while simultaneously retaining the permeation of other compounds, such as hydrogen, carbon dioxide, carbon monoxide and hydrocarbons.

- high mechanical and thermal stability at the reaction conditions, that require relatively high temperature and slightly acidic water medium.

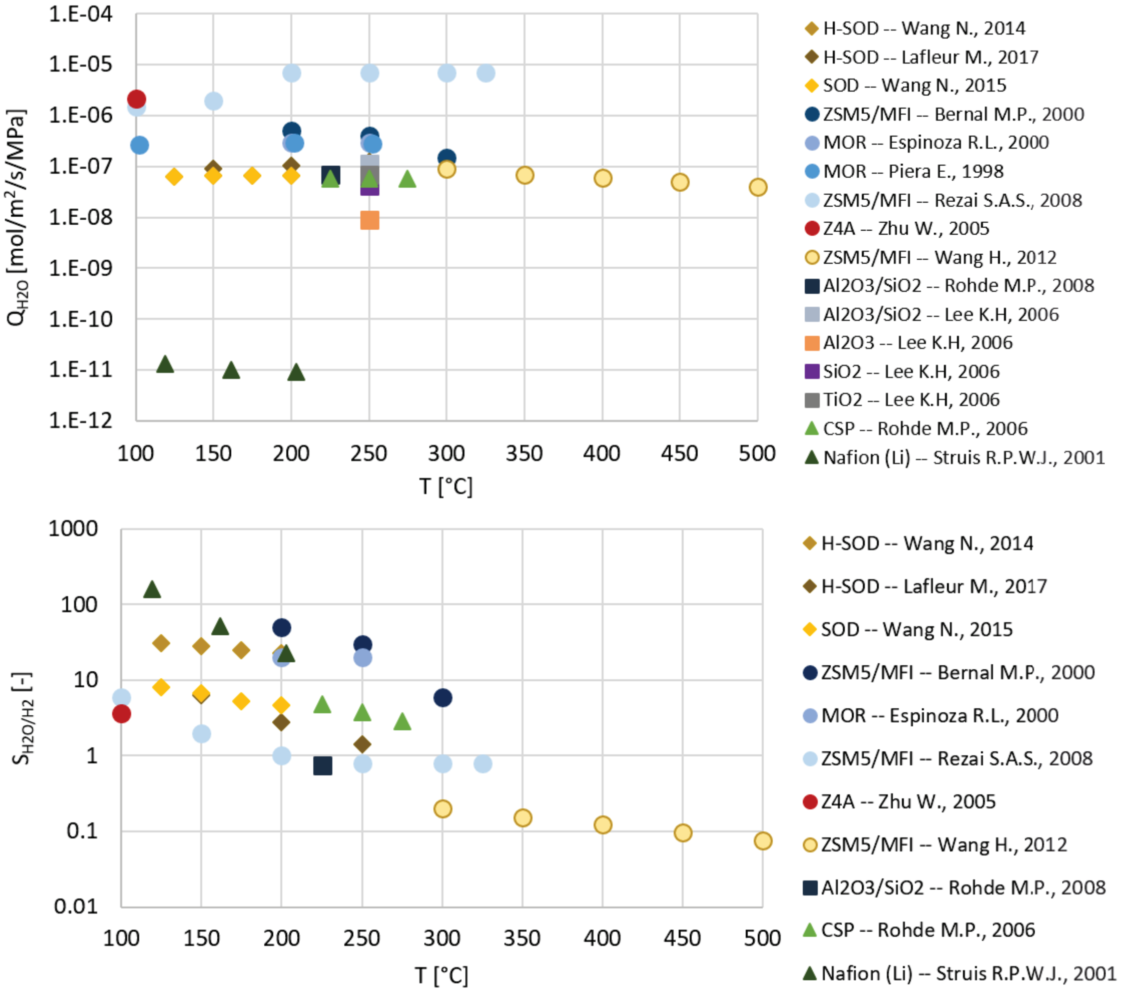

Figure 1.35: Summary of literature data about water permeances (up) and perm-selectivity compared to hydrogen (down) of different kinds of membranes and at different temperatures. ◆ (H-)SOD zeolite membranes, • other zeolite membranes (ZSM5/MFI, MOR, Z4A), ■ amorphous membranes, ▲ polymeric membranes. Cited references: Wang et al. (2014); Lafleur et al. (2017); Wang et al. (2015a); Bernal et al. (2000); Espinoza et al. (2000); Piera et al. (1998); Rezai et al. (2008); Zhu et al. (2005); Wang and Lin (2012); Rohde et al. (2008); Lee et al. (2006); Rohde et al. (2006); Struis and Stucki (2001).

Hydrophilic membranes for water removal have already been applied at pilot scales, in applications such as natural gas dehydration, air dehydration and organic compounds dehydration by pervaporisation. (Rohde et al., 2008) However, these applications are operated at relatively low temperatures. Hydrophilic membranes suitable for applications at high temperatures (>150°C) are quite limited. We have summarized in Figure 1.35 data of literature about water permeances (Q_{H_2O}) and perm-selectivity compared to hydrogen (S_{H_2O/H_2}) of different kinds of membranes at different temperatures. For a wider number of data refer to Rohde et al. (2008) or van Kampen et al. (2019). From these data, we can observe that amorphous microporous membranes (■) and polymeric membranes (▲) present relatively low water permeability ($< 10^{-7}$ mol/s/m^2/Pa) and that their H_2O/H_2 perm-selectivity significantly drops at temperatures higher than 200°C. (Unruh et al., 2004; Kölsch et al., 2000; Lee et al., 2006; Struis and Stucki, 2001; Rohde et al., 2006) On the contrary, microporous zeolite membranes (● and ◆) present the best behaviour in terms of water permeability and water perm-selectivity, as well as thermal and mechanical stability at high temperatures. These membranes are made of crystalline structure with uniform pores distribution and their hydrophilicity can be regulated by changing the Si/Al ratio of the material lattice. Water permeances reported for zeolite membranes can be up to 10^{-6} mol/s/Pa/m^2 (Zhu et al., 2005) or even 10^{-5} mol/s/Pa/m^2 for the ZSM5/MFI membrane tested by Rezai et al. (Rezai et al., 2008) These values do not significantly drop at higher temperatures. The H_2O/H_2 perm-selectivity is much more influenced by temperature. For low temperatures, H_2O/H_2 perm-selectivity higher than 20 are found for zeolite membranes. This value considerably decreases when temperature is increased. Zeolite membranes used for water removal applications have pore diameters higher than the kinetic diameter of water and hydrogen, thus separation of these molecules occurs through adsorption-controlled and diffusion-controlled permeation. As the loading of water in the zeolite that blocks the permeation of the weakly adsorbed hydrogen decreases with the increase of temperature, this explains why the increase of temperature results in a decrease of the H_2O/H_2 perm-selectivity. (Rohde et al., 2008) However, some zeolites, such as ZSM5 and MOR, still exhibit acceptable values of H_2O/H_2 perm-selectivity (>10) at high temperatures (>200°C). (Espinoza et al., 2000; Bernal et al., 2000) Generally, only the H_2O/H_2 perm-selectivity is considered, because other compounds perm-selectivity (such as CO, CO_2 or hydrocarbons) are lower and thus neglected. H-SOD zeolite membranes have recently received a lot of attention because of their relatively high water permeance (around 10^{-7} mol/s/Pa/m^2) and their good perm-selectivity towards water (> 10). However, not many data are available for their applications at temperatures higher then 200°C and their performances rapidly deteriorate when temperatures are increased. (Wang et al., 2014; Lafleur et al., 2017; Wang et al., 2015a)

The first use of hydrophilic membranes for H_2O removal applications in the FT process was reported by Espinoza et al. who performed permeation tests in non-reactive conditions with different zeolite membranes, showing that the use of these membranes could extend the catalyst life and improve the reactor utilization. (Espinoza et al., 2000) Unruh et al. observed a significant increase of the CO_2 conversion via in-situ H_2O removal using a membrane made of $Si(OH)_x$ layers over Al_2O_3. (Unruh et al., 2004) The need of a very performant membrane was evidenced by Rhode et al. that showed that with tetraethyl orthosilicate (TEOS) coated ceramic membrane the selectivity towards hydrocarbons could not be significantly increased, because of the loss of reactants and CO to which the membrane is permeable. With ceramic supported polymer membrane (CSP), the effect of water removal on the HCs selectivity was much positive, as higher water perm-selectivity could be obtained even at higher temperature. (Rohde et al., 2008) Promising candidates for water removal in CO_2 hydrogenation however were found to be the hydroxyl sodalite (H-SOD) membranes, as they exhibit high selectivity of H_2O/H_2 at least at temperatures below 200°C. (Rohde et al., 2008) Najari et al. in a theoretical study showed that in-situ water removal with H-SOD membrane can increase hydrocarbon yields. However, hydrocarbons yield and distribution are highly influenced by a combination of different factors, such as sweep ratio, pressures ratio and the nature of the sweep gas. (Najari et al., 2019a)

The membrane in fact is swept with a sweep gas at lower pressure to maintain a driving force across the membrane. The ratio ϕ between the pressure in the permeate side and that in the retentate influences the driving force across the membrane and can thus influence the water removal. The nature of the sweep gas can influence the water separation and the final hydrocarbons distribution, especially with membranes that are permeable to other compounds such as CO_2 or H_2. An inert gas such as N_2 can be used as sweep gas, but when the membrane perm-selectivity is poor, the performances of the reactor could drop below those of the packed bed without membrane, because of the loss of reactants across the membrane. The loss of reactants can be avoided by using H_2/CO_2 mixtures as sweep gas that allows to reach improved conversions and HCs yields. (Rohde et al., 2005) The ratio between the sweep flow and the retentate feed flow (SW) can also influence the water removal. Generally, it is kept low, to reduce the compression costs. However, an increase of the SW ratio could help to increase the driving force across the membrane, thus improving the water removal.

The effects of water removal via membrane permeation are thus promising. However, few works are available in literature and experimental data are especially missing. The main limit of the current studies is that they are not able to predict how the hydrocarbons distribution is influenced when a membrane reactor is used and for this experimental data are needed. Optimization of some parameters such as reaction temperature, sweep ratio and pressures ratio could contribute to obtain improved performances, in terms of CO_2 conversion and HCs yield, thus membrane reactors seem a promising solution to improve such a process.

1.6 Conclusions of the state-of-the-art and objectives of our work.

1.6.1 Focus of previous works.

We have analysed in this Chapter the available work about the CO_2 hydrogenation. This analysis allow us to choose the direction of our work.

We have shown that synthetic liquid fuels will probably be part of the energetic mix by the next 50 years, especially as fuels for the aviation sector. However, this technology is still at very early development stage and many advancements have to be made before a development at early demonstration stage could be done.

The work about CO_2 hydrogenation to hydrocarbons has been focusing mainly on the development of an optimal catalyst: the addition of promoters to the iron active phase and the handling of the synthesis steps can allow the synthesis of an optimal catalyst, able to convert CO_2 towards hydrocarbons, limiting the formation of CO and CH_4. The selectivity towards long chains (C_{5+}) is however very hard to achieve, even with very performing catalyst. Water production during the reaction represents one of the main limitations to the achievement of high conversions of CO_2.

On the other side, less effort has been dedicated to the kinetic experimental study of the reaction and to the development of kinetic models for the reaction. Some models exist, but they are all quite simple and not able to predict the distribution of the hydrocarbons obtained. Having a kinetic model that can predict the product distribution with good accuracy would be very important for an eventual future development of the process at industrial scale.

At process scale, not a lot of work exist. The only existing industrial demonstrators are based on a two-step pathway (RWGS and FT in two separated reactors) and theoretical simulations of the global process also consider the two-step way.

Therefore, there is the need to 1) develop a mathematical model that describes the reactor behaviour in different conditions and with a good level of detail; 2) understand how the process could be improved, in terms of CO_2 conversion and, more importantly, of long hydrocarbons yield.

1.6.2 Objectives of our work.

We have thus decided to focus our attention to the modelling of the reaction and the optimisation of the process. The aim of our work is to understand the reaction behaviour, provide all the tools needed for its modelling and understand how the global efficiency can be improved. In particular, the objectives of the work are the following:

- First, we want to develop a kinetic model that describes with enough detail the behaviour of the reaction in different conditions. The model should be able to predict the conversion of CO_2 and the formation of CO, but also the distribution of the obtained hydrocarbons products, their chain length and their chemical nature.

The development of a kinetic model is based on an experimental study that allows to understand the reaction behaviour and that provides experimental data, used for the validation of the model. As the work about the catalyst development is extensive and our means are limited, we have chosen to synthesize a catalyst that other authors showed to have good performances. Our work does not include the optimisation of the catalyst or of its synthesis procedure.

- Secondly, we want to gain some insights about the reaction mechanism. Determining the reaction mechanism in fact is crucial to understand how to better formulate the catalyst composition to limit the formation of undesired products. Completely understanding the mechanism of such a complex reaction is quite ambitious: the FT reaction mechanism is still widely debated after decades of study on the subject.

  However, we want to contribute to answer some questions about the reaction mechanism: which are the pathways followed for the formation of the different species? Which are the active sites involved in the catalysis of the reaction and what is their role? Is there a co-existence of multiple reaction pathways that lead to chain-growth?

- Then, we want to simulate the behaviour of a reactor for the CO_2 hydrogenation in different operating conditions and at different scale. To do that, we have to develop a mathematical model that includes 1) the heat transfer study, to verify the efficiency of thermal exchanges; 2) the mass transfer between the bulk phase and the solid catalytic pellets; 3) the kinetic model.

  The validation of such a reactor model requires an experimental study. The experimental study is performed in a fixed-bed reactor mildly scaled-up compared to the lab-scale reactor used for the kinetic study and with an oil-circulation cooling system.

- Finally, we want to study the global process to understand its eventual feasibility at industrial scale. Would the process be energetically efficient compared to the indirect pathway? How can the process be optimized? How the products can be valorised?

  For this purpose, simulations of the process, including the downstream separation of the obtained products, are performed with the aim to estimate the global energy efficiency. Solutions to remove the water formed during the reactions, which is one of the main limitations to reach high conversion, are tested, such as water removal trough perm-selective membranes.

References

H. Ahouari, A. Soualah, A. Le Valant, L. Pinard, and Y. Pouilloux. Hydrogenation of CO_2 into hydrocarbons over bifunctional system Cu–ZnO/Al_2O_3+HZSM-5: Effect of proximity between the acidic and methanol synthesis sites. *Comptes Rendus Chimie*, 18(12):1264–1269, 2015. ISSN 16310748. doi: 10.1016/j.crci.2015.07.005. URL `https://linkinghub.elsevier.com/retrieve/pii/S1631074815002040`.

J. Aicart. *Modélisation et validation expérimentale d'un co-électrolyseur de la vapeur d'eau et du dioxyde de carbone à haute température*. PhD Thesis, Grenoble, 2014.

M. Albrecht, U. Rodemerck, M. Schneider, M. Bröring, D. Baabe, and E. V. Kondratenko. Unexpectedly efficient CO_2 hydrogenation to higher hydrocarbons over non-doped Fe_2O_3. *Applied Catalysis B: Environmental*, 204:119–126, 2017. ISSN 09263373. doi: 10.1016/j.apcatb.2016.11.017. URL `https://linkinghub.elsevier.com/retrieve/pii/S092633731630875X`.

M. Amoyal, R. Vidruk-Nehemya, M. V. Landau, and M. Herskowitz. Effect of potassium on the active phases of Fe catalysts for carbon dioxide conversion to liquid fuels through hydrogenation. *Journal of Catalysis*, 348:29–39, 2017. ISSN 00219517. doi: 10.1016/j.jcat.2017.01.020. URL `https://linkinghub.elsevier.com/retrieve/pii/S0021951717300325`.

B. An, J. Zhang, K. Cheng, P. Ji, C. Wang, and W. Lin. Confinement of Ultrasmall Cu/ZnO_x Nanoparticles in Metal–Organic Frameworks for Selective Methanol Synthesis from Catalytic Hydrogenation of CO_2. *Journal of the American Chemical Society*, 139(10):3834–3840, 2017. ISSN 0002-7863. doi: 10.1021/jacs.7b00058. URL `https://doi.org/10.1021/jacs.7b00058`.

R. B. Anderson. Catalysts for the Fischer-Tropsch Synthesis. *Catalysis*, IV:257–371, 1956. ISSN 00959553. doi: 10.1002/jps.3030451217. URL `http://linkinghub.elsevier.com/retrieve/pii/S0095955315340919`.

R. B. Anderson, R. A. Friedel, and H. H. Storch. Fischer-Tropsch Reaction Mechanism Involving Stepwise Growth of Carbon Chain. *The Journal of Chemical Physics*, 19(3):313–319, 1951. ISSN 0021-9606. doi: 10.1063/1.1748201. URL `https://doi.org/10.1063/1.1748201`. Publisher: American Institute of Physics.

H. Ando, Y. Matsumura, and Y. Souma. Active phase of iron catalyst for alcohol formation in hydrogenation of carbon oxides. *Applied Organometallic Chemistry*, 14(12):831–835, 2000.

M. O. Andreae. Emission of trace gases and aerosols from biomass burning – an updated assessment. *Atmos. Chem. Phys.*, 19(13):8523–8546, 2019. ISSN 1680-7324. doi: 10.5194/acp-19-8523-2019. URL `https://www.atmos-chem-phys.net/19/8523/2019/`.

L. Angelo. *Développement de catalyseurs pour la synthèse de méthanol produit par hydrogénation du dioxide de carbone*. PhD thesis, Université de Strasbourg, Strasbourg, 2014.

J. R. Ares, K.-F. Aguey-Zinsou, F. Leardini, I. J. Ferrer, J.-F. Fernandez, Z.-X. Guo, and C. Sánchez. Hydrogen Absorption/Desorption Mechanism in Potassium Alanate ($KAlH_4$) and Enhancement by $TiCl_3$ Doping. *The Journal of Physical Chemistry C*, 113(16):6845–6851, 2009. ISSN 1932-7447, 1932-7455. doi: 10.1021/jp807184v. URL `http://pubs.acs.org/doi/10.1021/jp807184v`.

M. Aresta, editor. *Carbon Dioxide Recovery and Utilization*. Springer Netherlands, Dordrecht, 2003. ISBN 978-90-481-6335-9 978-94-017-0245-4. doi: 10.1007/978-94-017-0245-4. URL `http://link.springer.com/10.1007/978-94-017-0245-4`.

E. F. Armstrong and T. P. Hilditch. A Study of Catalytic Actions at Solid Surfaces. V. The Rate of Change Conditioned by a Nickel Catalyst and Its Bearing on the Law of Mass Action. *Proceedings of the Royal Society of London. Series A, Containing Papers of a Mathematical and Physical Character*, 98(688):27–40, 1920. ISSN 09501207. URL `http://www.jstor.org/stable/93902`. Publisher: The Royal Society.

A. Avidan. Gasoline and Distillate Fuels From Methanol. In D. Bibby, C. Chang, R. Howe, and S. Yurchak, editors, *Studies in Surface Science and Catalysis*, volume 36, pages 307–323. Elsevier, 1988. ISBN 0167-2991. doi: 10.1016/S0167-2991(09)60524-3. URL http://www.sciencedirect.com/science/article/pii/S0167299109605243.

P. Bains, P. Psarras, and J. Wilcox. CO_2 capture from the industry sector. *Progress in Energy and Combustion Science*, 63:146–172, 2017. ISSN 03601285. doi: 10.1016/j.pecs.2017.07.001. URL https://linkinghub.elsevier.com/retrieve/pii/S0360128517300114.

J. Benziger and R. Madix. Reactions and reaction intermediates on iron surfaces: I. Methanol, ethanol, and isopropanol on Fe(100). *Journal of Catalysis*, 65(1):36–48, 1980. ISSN 0021-9517. doi: 10.1016/0021-9517(80)90276-6. URL https://www.sciencedirect.com/science/article/pii/0021951780902766.

J. Benziger and R. Madix. Reactions and reaction intermediates on iron surfaces: III. Reactions of aldehydes and ketones on Fe(100). *Journal of Catalysis*, 74(1):55–66, 1982. ISSN 0021-9517. doi: 10.1016/0021-9517(82)90008-2. URL https://www.sciencedirect.com/science/article/pii/0021951782900082.

M. Bernal, E. Piera, J. Coronas, M. Menéndez, and J. Santamarıa. Mordenite and ZSM-5 hydrophilic tubular membranes for the separation of gas phase mixtures. *Catalysis Today*, 56(1-3):221–227, 2000. ISSN 09205861. doi: 10.1016/S0920-5861(99)00279-5. URL https://linkinghub.elsevier.com/retrieve/pii/S0920586199002795.

P. Biloen and W. Sachtler. Mechanism of Hydrocarbon Synthesis over Fischer-Tropsch Catalysts. In D. Eley, H. Pines, and P. B. Weisz, editors, *Advances in Catalysis*, volume 30, pages 165–216. Academic Press, 1981. ISBN 0360-0564. doi: 10.1016/S0360-0564(08)60328-4. URL https://www.sciencedirect.com/science/article/pii/S0360056408603284.

J. Blamey, E. Anthony, J. Wang, and P. Fennell. The calcium looping cycle for large-scale CO_2 capture. *Progress in Energy and Combustion Science*, 36(2):260–279, 2010. ISSN 0360-1285. doi: 10.1016/j.pecs.2009.10.001. URL http://www.sciencedirect.com/science/article/pii/S0360128509000574.

G. Blyholder and L. D. Neff. Structures of Some C_xH_yO Compounds Adsorbed on Iron. *The Journal of Physical Chemistry*, 70(3):8, 1966.

G. Blyholder and W. V. Wyatt. Infrared Spectra and Structures of Some C_xH_yO Compounds Adsorbed on Silica-Supported Iron, Cobalt, and Nickel. *The Journal of Physical Chemistry*, 70(6):6, 1966.

J. Boelee, J. Cüsters, and K. Van Der Wiele. Influence of reaction conditions on the effect of Co-feeding ethene in the Fischer-Tropsch synthesis on a fused-iron catalyst in the liquid phase. *Applied Catalysis*, 53(1):1–13, 1989. ISSN 0166-9834. doi: 10.1016/S0166-9834(00)80005-6. URL http://www.sciencedirect.com/science/article/pii/S0166983400800056.

F. G. Botes. Proposal of a New Product Characterization Model for the Iron-Based Low-Temperature FischerTropsch Synthesis. *Energy & Fuels*, 21(3):1379–1389, 2007. ISSN 0887-0624. doi: 10.1021/ef060483d. URL https://doi.org/10.1021/ef060483d. Publisher: American Chemical Society.

R. C. Brady and R. Pettit. Reactions of diazomethane on transition-metal surfaces and their relationship to the mechanism of the Fischer-Tropsch reaction. *Journal of the American Chemical Society*, 102(19):6181–6182, 1980. ISSN 0002-7863. doi: 10.1021/ja00539a053. URL https://doi.org/10.1021/ja00539a053.

L. Bromberg and D. Cohn. Alcohol Fueled Heavy Duty Vehicles Using Clean, High Efficiency Engines. SAE International, 2010. doi: 10.4271/2010-01-2199. URL https://doi.org/10.4271/2010-01-2199.

A. Buttler. Current status of water electrolysis for energy storage, grid balancing and sector coupling via power-to-gas and power-to-liquids. A review. *Renewable and Sustainable Energy Reviews*, 2018.

I. Champon, A. Bengaouer, A. Chaise, S. Thomas, and A.-C. Roger. Carbon dioxide methanation kinetic model on a commercial Ni/Al_2O_3 catalyst. *Journal of CO2 Utilization*, 34:256–265, 2019. ISSN 2212-9820. doi: 10.1016/j.jcou.2019.05.030. URL `http://www.sciencedirect.com/science/article/pii/S2212982019301799`.

C. D. Chang. Hydrocarbons from Methanol. *Catalysis Reviews*, 25(1):1–118, 1983. ISSN 0161-4940. doi: 10.1080/01614948308078874. URL `https://doi.org/10.1080/01614948308078874`.

F.-W. Chang, M.-T. Tsay, and M.-S. Kuo. Effect of thermal treatments on catalyst reducibility and activity in nickel supported on RHA–Al_2O_3 systems. *Thermochimica Acta*, 386(2):161–172, 2002. ISSN 0040-6031. doi: 10.1016/S0040-6031(01)00771-7. URL `http://www.sciencedirect.com/science/article/pii/S0040603101007717`.

A. W. Chiang, W.-C. Liu, P. Charusanti, and M.-J. Hwang. Understanding system dynamics of an adaptive enzyme network from globally profiled kinetic parameters. *BMC Systems Biology*, 8(1):4, 2014. ISSN 1752-0509. doi: 10.1186/1752-0509-8-4. URL `http://bmcsystbiol.biomedcentral.com/articles/10.1186/1752-0509-8-4`.

Y. H. Choi, Y. J. Jang, H. Park, W. Y. Kim, Y. H. Lee, S. H. Choi, and J. S. Lee. Carbon dioxide Fischer-Tropsch synthesis: A new path to carbon-neutral fuels. *Applied Catalysis B: Environmental*, 202:605–610, 2017. ISSN 09263373. doi: 10.1016/j.apcatb.2016.09.072. URL `https://linkinghub.elsevier.com/retrieve/pii/S0926337316307603`.

C.-Y. Chou, A. J. Loiland, and F. R. Lobo. Reverse Water-Gas Shift Iron Catalyst Derived from Magnetite. *Catalysts*, 9(9), 2019. ISSN 2073-4344. doi: 10.3390/catal9090773.

I. Ciobıcă, G. Kramer, Q. Ge, M. Neurock, and R. van Santen. Mechanisms for Chain Growth in Fischer–Tropsch Synthesis over Ru(0001). *Journal of Catalysis*, 212(2):136–144, 2002. ISSN 0021-9517. doi: 10.1006/jcat.2002.3742. URL `http://www.sciencedirect.com/science/article/pii/S0021951702937425`.

Y. Cui, L. Guo, W. Gao, K. Wang, H. Zhao, Y. He, P. Zhang, G. Yang, and N. Tsubaki. From Single Metal to Bimetallic Sites: Enhanced Higher Hydrocarbons Yield of CO_2 Hydrogenation over Bimetallic Catalysts. *ChemistrySelect*, 6(21):5241–5247, 2021. ISSN 2365-6549, 2365-6549. doi: 10.1002/slct.202101072. URL `https://onlinelibrary.wiley.com/doi/10.1002/slct.202101072`.

Y. A. Daza and J. N. Kuhn. CO_2 conversion by reverse water gas shift catalysis: comparison of catalysts, mechanisms and their consequences for CO_2 conversion to liquid fuels. *RSC Advances*, 6(55):49675–49691, 2016. ISSN 2046-2069. doi: 10.1039/C6RA05414E. URL `http://xlink.rsc.org/?DOI=C6RA05414E`.

C. Dean, J. Blamey, N. Florin, M. Al-Jeboori, and P. Fennell. The calcium looping cycle for CO_2 capture from power generation, cement manufacture and hydrogen production. *Chemical Engineering Research and Design*, 89(6):836–855, 2011. ISSN 0263-8762. doi: 10.1016/j.cherd.2010.10.013. URL `http://www.sciencedirect.com/science/article/pii/S0263876210003047`.

R. A. Dictor and A. T. Bell. Fischer-Tropsch synthesis over reduced and unreduced iron oxide catalysts. *Journal of Catalysis*, 97(1):121–136, 1986. ISSN 0021-9517. doi: 10.1016/0021-9517(86)90043-6. URL `https://www.sciencedirect.com/science/article/pii/0021951786900436`.

T. J. Donnelly, I. C. Yates, and C. N. Satterfield. Analysis and prediction of product distributions of the Fischer-Tropsch synthesis. *Energy & Fuels*, 2(6):734–739, 1988. ISSN 0887-0624. doi: 10.1021/ef00012a003. URL `https://pubs.acs.org/doi/abs/10.1021/ef00012a003`.

R. W. Dorner, D. R. Hardy, F. W. Williams, and H. D. Willauer. Heterogeneous catalytic CO_2 conversion to value-added hydrocarbons. *Energy & Environmental Science*, 3(7):884, 2010a. ISSN 1754-5692, 1754-5706. doi: 10.1039/c001514h. URL `http://xlink.rsc.org/?DOI=c001514h`.

R. W. Dorner, D. R. Hardy, F. W. Williams, and H. D. Willauer. K and Mn doped iron-based CO_2 hydrogenation catalysts: Detection of $KAlH_4$ as part of the catalyst's active phase. *Applied Catalysis A: General*, 373(1-2):112–121, 2010b. ISSN 0926860X. doi: 10.1016/j.apcata.2009.11.005. URL `http://linkinghub.elsevier.com/retrieve/pii/S0926860X09007716`.

M. E. Dry. Practical and theoretical aspects of the catalytic Fischer-Tropsch process. *Applied Catalysis A: General*, 138(2):319–344, 1996. ISSN 0926860X. doi: 10.1016/0926-860X(95)00306-1. URL `https://linkinghub.elsevier.com/retrieve/pii/0926860X95003061`.

J. Ducamp, A. Bengaouer, P. Baurens, I. Fechete, P. Turek, and F. Garin. Statu quo sur la méthanation du dioxyde de carbone : une revue de la littérature. *Comptes Rendus Chimie*, 21(3-4):427–469, 2018. ISSN 16310748. doi: 10.1016/j.crci.2017.07.005. URL `https://linkinghub.elsevier.com/retrieve/pii/S1631074817301571`.

R. Espinoza, E. du Toit, J. Santamaria, M. Menendez, J. Coronas, and S. Irusta. Use of membranes in fischer-tropsch reactors. In A. Corma, F. V. Melo, S. Mendioroz, and J. L. G. Fierro, editors, *Studies in Surface Science and Catalysis*, volume 130, pages 389–394. Elsevier, 2000. ISBN 0167-2991. doi: 10.1016/S0167-2991(00)80988-X. URL `http://www.sciencedirect.com/science/article/pii/S016729910080988X`.

G. A. Filonenko, R. vanPutten, E. N. Schulpen, E. J. M. Hensen, and E. A. Pidko. Highly Efficient Reversible Hydrogenation of Carbon Dioxide to Formates Using a Ruthenium PNP-Pincer Catalyst. *ChemCatChem*, 6(6):1526–1530, 2014. ISSN 18673880. doi: 10.1002/cctc.201402119. URL `http://doi.wiley.com/10.1002/cctc.201402119`.

F. Fischer and H. Tropsch. Über die direkte Synthese von Erdöl-Kohlenwasserstoffen bei gewöhnlichem Druck. (Erste Mitteilung). *Berichte der deutschen chemischen Gesellschaft (A and B Series)*, 59(4):830–831, 1926. ISSN 03659488. doi: 10.1002/cber.19260590442. URL `https://onlinelibrary.wiley.com/doi/10.1002/cber.19260590442`.

N. Fischer, R. Henkel, B. Hettel, M. Iglesias, G. Schaub, and M. Claeys. Hydrocarbons via CO_2 Hydrogenation Over Iron Catalysts: The Effect of Potassium on Structure and Performance. *Catalysis Letters*, 146(2):509–517, 2016. ISSN 1011-372X, 1572-879X. doi: 10.1007/s10562-015-1670-9. URL `http://link.springer.com/10.1007/s10562-015-1670-9`.

P. J. Flory. Molecular Size Distribution in Linear Condensation Polymers. *Journal of the American Chemical Society*, 58(10):1877–1885, 1936. ISSN 0002-7863, 1520-5126. doi: 10.1021/ja01301a016. URL `https://pubs.acs.org/doi/abs/10.1021/ja01301a016`.

A. Frennet and C. Hubert. Transient kinetics in heterogeneous catalysis by metals. *Journal of Molecular Catalysis A: Chemical*, 163(1-2):163–188, 2000. ISSN 13811169. doi: 10.1016/S1381-1169(00)00385-X. URL `https://linkinghub.elsevier.com/retrieve/pii/S138111690000385X`.

R. A. Friedel and R. B. Anderson. Composition of Synthetic Liquid Fuels. I. Product Distribution and Analysis of C_5—C_8 Paraffin Isomers from Cobalt Catalyst. *Journal of the American Chemical Society*, 72(3):1212–1215, 1950. ISSN 0002-7863. doi: 10.1021/ja01159a039. URL `https://doi.org/10.1021/ja01159a039`. Publisher: American Chemical Society.

M. Fujiwara, R. Kieffer, H. Ando, and Y. Souma. Development of composite catalysts made of Cu-Zn-Cr oxide/zeolite for the hydrogenation of carbon dioxide. *Applied Catalysis A: General*, 121(1):113–124, 1995.

D. Förtsch, K. Pabst, and E. Groß-Hardt. The product distribution in Fischer–Tropsch synthesis: An extension of the ASF model to describe common deviations. *Chemical Engineering Science*, 138:333–346, 2015. ISSN 00092509. doi: 10.1016/j.ces.2015.07.005. URL `https://linkinghub.elsevier.com/retrieve/pii/S0009250915004893`.

N. Gallandat, J. Bérard, F. Abbet, and A. Züttel. Small-scale demonstration of the conversion of renewable energy to synthetic hydrocarbons. *Sustainable Energy & Fuels*, 1(8):1748–1758, 2017. ISSN 2398-4902. doi: 10.1039/C7SE00275K. URL `http://xlink.rsc.org/?DOI=C7SE00275K`.

P. Gao, S. Li, X. Bu, S. Dang, Z. Liu, H. Wang, L. Zhong, M. Qiu, C. Yang, J. Cai, W. Wei, and Y. Sun. Direct conversion of CO_2 into liquid fuels with high selectivity over a bifunctional catalyst. *Nature Chemistry*, 9(10):1019–1024, 2017. ISSN 1755-4330, 1755-4349. doi: 10.1038/nchem.2794. URL `http://www.nature.com/doifinder/10.1038/nchem.2794`.

J. Gaube and H.-F. Klein. Further support for the two-mechanisms hypothesis of Fischer-Tropsch synthesis. *Applied Catalysis A: General*, 374(1-2):120–125, 2010. doi: 10.1016/j.apcata.2009.11.039. URL `https://www.scopus.com/inward/record.uri?eid=2-s2.0-74049106279&doi=10.1016%2fj.apcata.2009.11.039&partnerID=40&md5=4302b37e105b313c89d742162625111d`.

M. K. Gnanamani, W. D. Shafer, D. E. Sparks, and B. H. Davis. Fischer–Tropsch synthesis: Effect of CO_2 containing syngas over Pt promoted Co/γ-Al_2O_3 and K-promoted Fe catalysts. *Catalysis Communications*, 12(11):936–939, 2011. ISSN 15667367. doi: 10.1016/j.catcom.2011.03.002. URL `https://linkinghub.elsevier.com/retrieve/pii/S1566736711000732`.

A. Goeppert, M. Czaun, J.-P. Jones, G. K. Surya Prakash, and G. A. Olah. Recycling of carbon dioxide to methanol and derived products – closing the loop. *Chem. Soc. Rev.*, 43(23):7995–8048, 2014. ISSN 0306-0012, 1460-4744. doi: 10.1039/C4CS00122B. URL `http://xlink.rsc.org/?DOI=C4CS00122B`.

L. Guo, S. Sun, J. Li, W. Gao, H. Zhao, B. Zhang, Y. He, P. Zhang, G. Yang, and N. Tsubaki. Boosting liquid hydrocarbons selectivity from CO_2 hydrogenation by facilely tailoring surface acid properties of zeolite via a modified Fischer-Tropsch synthesis. *Fuel*, 306:121684, 2021. ISSN 00162361. doi: 10.1016/j.fuel.2021.121684. URL `https://linkinghub.elsevier.com/retrieve/pii/S0016236121015659`.

W. K. Hall, R. J. Kokes, and P. H. Emmett. Mechanism Studies of the Fischer-Tropsch Synthesis: The Incorporation of Radioactive Ethylene, Propionaldehyde and Propanol. *Journal of the American Chemical Society*, 82(5):1027–1037, 1960. ISSN 0002-7863. doi: 10.1021/ja01490a005. URL `https://doi.org/10.1021/ja01490a005`.

R. T. Hanlon and C. N. Satterfield. Reactions of selected 1-olefins and ethanol added during the Fischer-Tropsch synthesis. *Energy & Fuels*, 2(2):196–204, 1988. ISSN 0887-0624, 1520-5029. doi: 10.1021/ef00008a017. URL `https://pubs.acs.org/doi/abs/10.1021/ef00008a017`.

G. Henrici-Olivé and S. Olivé. The Fischer-Tropsch Synthesis: Molecular Weight Distribution of Primary Products and Reaction Mechanism. *Angewandte Chemie International Edition in English*, 15(3):136–141, 1976. doi: 10.1002/anie.197601361. URL `https://www.scopus.com/inward/record.uri?eid=2-s2.0-84982487173&doi=10.1002%2fanie.197601361&partnerID=40&md5=7f85ce6ed84df05c37d673c620348167`.

E. Herington. The Fischer-Tropsch synthesis considered as a polymerization reaction. *Chemistry & Industry*, 65, 1946.

J. P. Hindermann, G. J. Hutchings, and A. Kiennemann. Mechanistic Aspects of the Formation of Hydrocarbons and Alcohols from CO Hydrogenation. *Catalysis Reviews*, 35(1):1–127, 1993. ISSN 0161-4940. doi: 10.1080/01614949308013907. URL `https://doi.org/10.1080/01614949308013907`. Publisher: Taylor & Francis.

J.-S. Hong, J. S. Hwang, K.-W. Jun, J. C. Sur, and K.-W. Lee. Deactivation study on a coprecipitated Fe-Cu-K-Al catalyst in CO_2 hydrogenation. *Applied Catalysis A: General*, 218:53–59, 2001.

https://climate.nasa.gov/.

https://ourworldindata.org/electricity mix.

https://ourworldindata.org/energy.

https://ourworldindata.org/grapher/renewable-energy consumption.

https://ourworldindata.org/greenhouse-gas emissions.

https://ourworldindata.org/world-population-future-eductation now/.

https://www.eea.europa.eu/.

https://www.iea.org/data-and-statistics/charts/industry-direct-co2-emissions-in-the-sustainable-development-scenario 2000-2030.

G. A. Huff Jr and C. N. Satterfield. Intrinsic kinetics of the Fischer-Tropsch synthesis on a reduced fused-magnetite catalyst. *Industrial & Engineering Chemistry Process Design and Development*, 23 (4):696–705, 1984.

S.-M. Hwang, S. J. Han, J. E. Min, H.-G. Park, K.-W. Jun, and S. K. Kim. Mechanistic insights into Cu and K promoted Fe-catalyzed production of liquid hydrocarbons via CO_2 hydrogenation. *Journal of CO2 Utilization*, 34:522–532, 2019. ISSN 22129820. doi: 10.1016/j.jcou.2019.08.004. URL https://linkinghub.elsevier.com/retrieve/pii/S2212982019306018.

IEA. 20 years of carbon capture and storage. Technical report, 2016. URL https://www.iea.org/reports/20-years-of-carbon-capture-and-storage.

IEA. Energy Technology Perspectives 2020. Technical report, 2020.

E. Iglesia, S. C. Reyes, and R. J. Madon. Transport-enhanced α-olefin readsorption pathways in Ru-catalyzed hydrocarbon synthesis. *Journal of Catalysis*, 129(1):238–256, 1991.

M. Iglesias Gonzalez, C. de Vries, M. Claeys, and G. Schaub. Chemical energy storage in gaseous hydrocarbons via iron Fischer–Tropsch synthesis from H_2/CO_2 —Kinetics, selectivity and process considerations. *Catalysis Today*, 242:184–192, 2015. ISSN 09205861. doi: 10.1016/j.cattod.2014.05.020. URL https://linkinghub.elsevier.com/retrieve/pii/S0920586114003903.

IPCC. Climate Change 2014: Synthesis Report. Contribution of Working Groups I, II and III to the Fifth Assessment Report of the Intergovernmental Panel on Climate Change. [Core Writing Team R.K. Pachauri and L.A. Meyer (eds.)]. Technical report, IPCC, Geneva, Switzerland, 2014.

IRENA. Hydrogen from renewable power: Technology outlook for the energy transition. Technical report, 2018.

T. Ishihara, K. Eguchi, and H. Arai. Hydrogenation of carbon monoxide over SiO_2-supported Fe-Co, Co-Ni and Ni-Fe bimetallic catalysts. *Applied Catalysis*, 30(2):225–238, 1987. ISSN 0166-9834. doi: 10.1016/S0166-9834(00)84115-9. URL https://www.sciencedirect.com/science/article/pii/S0166983400841159.

P. G. Jessop, F. Joó, and C.-C. Tai. Recent advances in the homogeneous hydrogenation of carbon dioxide. *Coordination Chemistry Reviews*, 248(21-24):2425–2442, 2004. ISSN 00108545. doi: 10.1016/j.ccr.2004.05.019. URL https://linkinghub.elsevier.com/retrieve/pii/S0010854504001389.

F. Jiang, B. Liu, S. Geng, Y. Xu, and X. Liu. Hydrogenation of CO_2 into hydrocarbons: enhanced catalytic activity over Fe-based Fischer–Tropsch catalysts. *Catalysis Science & Technology*, 8(16): 4097–4107, 2018. ISSN 2044-4753, 2044-4761. doi: 10.1039/C8CY00850G. URL http://xlink.rsc.org/?DOI=C8CY00850G.

D. S. Jordan and A. T. Bell. Influence of ethylene on the hydrogenation of carbon monoxide over ruthenium. *The Journal of Physical Chemistry*, 90(20):4797–4805, 1986. ISSN 0022-3654, 1541-5740. doi: 10.1021/j100411a018. URL https://pubs.acs.org/doi/abs/10.1021/j100411a018.

P. Kaiser, R. Unde, C. Kern, and A. Jess. Production of Liquid Hydrocarbons with CO_2 as Carbon Source based on Reverse Water-Gas Shift and Fischer-Tropsch Synthesis. *Chemie Ingenieur Technik*, 85(4):489–499, 2013. ISSN 0009286X. doi: 10.1002/cite.201200179. URL http://doi.wiley.com/10.1002/cite.201200179.

F. Karn, J. Schultz, and R. B. Anderson. Kinetics of the Fischer-Tropsch synthesis on iron catalysts. III. Influence of water vapor. *Actes Congrés International Catalyse*, 26(2):2439–2452, 1961.

D. W. Keith. Why Capture CO_2 from the Atmosphere? *Science*, 325(5948):1654–1655, 2009. ISSN 0036-8075, 1095-9203. doi: 10.1126/science.1176731. URL http://www.sciencemag.org/cgi/doi/10.1126/science.1176731.

A. G. Kharaji, A. Shariati, and M. A. Takassi. A Novel γ-Alumina Supported Fe-Mo Bimetallic Catalyst for Reverse Water Gas Shift Reaction. *Chinese Journal of Chemical Engineering*, 21(9):1007–1014, 2013. ISSN 10049541. doi: 10.1016/S1004-9541(13)60573-X. URL https://linkinghub.elsevier.com/retrieve/pii/S100495411360573X.

C. J. Kim. Reducing methane production in Fischer-Tropsch reactions, 1983. URL `https://patents.google.com/patent/US4547525A/en`.

J.-S. Kim, S. Lee, S.-B. Lee, M.-J. Choi, and K.-W. Lee. Performance of catalytic reactors for the hydrogenation of CO_2 to hydrocarbons. *Catalysis Today*, 115(1-4):228–234, 2006. ISSN 09205861. doi: 10.1016/j.cattod.2006.02.038. URL `http://linkinghub.elsevier.com/retrieve/pii/S0920586106001179`.

K. Kobl. *Aspects mécanistiques et cinétiques de la production catalytique de méthanol à partir de CO_2/H_2*. PhD thesis, Université de Strasbourg, 2015.

H. Koempel and W. Liebner. Lurgi's Methanol To Propylene (MTP®) Report on a successful commercialisation. In F. Bellot Noronha, M. Schmal, and E. Falabella Sousa-Aguiar, editors, *Studies in Surface Science and Catalysis*, volume 167, pages 261–267. Elsevier, 2007. ISBN 0167-2991. doi: 10.1016/S0167-2991(07)80142-X. URL `http://www.sciencedirect.com/science/article/pii/S016729910780142X`.

R. A. Koeppel, A. Baiker, and A. Wokaun. Copper/zirconia catalysts for the synthesis of methanol from carbon dioxide: influence of preparation variables on structural and catalytic properties of catalysts. *Applied Catalysis A: General*, 84(1):77–102, 1992.

A. L. Kohl and R. B. Nielsen. Chapter 10 - Control of Nitrogen Oxides. In A. L. Kohl and R. B. Nielsen, editors, *Gas Purification (Fifth Edition)*, pages 866–945. Gulf Professional Publishing, Houston, 1997. ISBN 978-0-88415-220-0. doi: 10.1016/B978-088415220-0/50010-0. URL `http://www.sciencedirect.com/science/article/pii/B9780884152200500100`.

R. J. Kokes, W. K. Hall, and P. H. Emmett. Fischer-Tropsch Synthesis Mechanism Studies. The Addition of Radioactive Ethanol to the Synthesis Gas. *Journal of the American Chemical Society*, 79(12): 2989–2996, 1957. ISSN 0002-7863. doi: 10.1021/ja01569a002. URL `https://doi.org/10.1021/ja01569a002`.

T. Komaya and A. T. Bell. Estimates of rate coefficients for elementary processes occurring during Fischer-Tropsch synthesis over $RuTiO_2$. *Journal of Catalysis*, 146(1):237–248, 1994. ISSN 0021-9517. doi: 10.1016/0021-9517(94)90027-2. URL `https://www.sciencedirect.com/science/article/pii/0021951794900272`.

S. Krishnamoorthy, A. Li, and E. Iglesia. Pathways for CO_2 formation and conversion during Fischer–Tropsch synthesis on iron-based catalysts. *Catalysis Letters*, 80(1-2):77–86, 2002.

C.-K. Kuei, W.-S. Chen, and M.-D. Lee. Hydrogenation of Carbon Dioxide on Iron Manganese Catalysts. *Journal of the Chinese Chemical Society*, 38(2):127–139, 1991.

E. Kuipers, C. Scheper, J. Wilson, I. Vinkenburg, and H. Oosterbeek. Non-ASF Product Distributions Due to Secondary Reactions during Fischer–Tropsch Synthesis. *Journal of Catalysis*, 158(1):288–300, 1996. ISSN 0021-9517. doi: 10.1006/jcat.1996.0028. URL `https://www.sciencedirect.com/science/article/pii/S0021951796900287`.

E. W. Kuipers, I. H. Vinkenburg, and H. Oosterbeek. Chain Length Dependence of α-olefin Readsorption in Fischer-Tropsch synthesis. *Journal of Catalysis*, 152:137–146, 1995. doi: https://doi.org/10.1006/jcat.1995.1068. URL `https://www.sciencedirect.com/science/article/pii/S0021951785710688?via%3Dihub`.

N. Kul'kova and M. Temkin. Kinetics of the reaction of conversion of carbon monoxide by water vapors (shift-reaction). *Zh. Fiz. Khim.*, 23, 1949.

J. T. Kummer, H. H. Podgurski, W. B. Spencer, and P. H. Emmett. Mechanism Studies of the Fischer—Tropsch Synthesis. The Addition of Radioactive Alcohol. *Journal of the American Chemical Society*, 73(2):564–569, 1951. ISSN 0002-7863. doi: 10.1021/ja01146a018. URL `https://doi.org/10.1021/ja01146a018`.

J. Kuo. Slurry Fischer-Tropsch/Mobil two-stage process of converting syngas to high octane gasoline. Quarterly report, 1 January-31 March 1982. Technical report, United States, 1982. URL `https://www.osti.gov/servlets/purl/6831733`.

P. Kölsch, M. Sziládi, M. Noack, J. Caro, L. Kotsis, I. Kotsis, and I. Sieber. Keramische Membran zur Wasserabtrennung aus Lösungsmitteln. *Chemie Ingenieur Technik*, 72(10):1167–1173, 2000. Publisher: John Wiley & Sons, Ltd.

D. H. König, N. Baucks, R.-U. Dietrich, and A. Wörner. Simulation and evaluation of a process concept for the generation of synthetic fuel from CO_2 and H_2. *Energy*, 91:833–841, 2015a. ISSN 0360-5442. doi: 10.1016/j.energy.2015.08.099. URL http://www.sciencedirect.com/science/article/pii/S0360544215011767.

D. H. König, M. Freiberg, R.-U. Dietrich, and A. Wörner. Techno-economic study of the storage of fluctuating renewable energy in liquid hydrocarbons. *Fuel*, 159:289–297, 2015b. ISSN 00162361. doi: 10.1016/j.fuel.2015.06.085. URL https://linkinghub.elsevier.com/retrieve/pii/S0016236115006651.

M. Lafleur, F. Bougie, N. Guilhaume, F. Larachi, P. Fongarland, and M. C. Iliuta. Development of a water-selective zeolite composite membrane by a new pore-plugging technique. *Microporous and Mesoporous Materials*, 237:49–59, 2017. ISSN 13871811. doi: 10.1016/j.micromeso.2016.09.004. URL https://linkinghub.elsevier.com/retrieve/pii/S1387181116303857.

K. Larmier, W.-C. Liao, S. Tada, E. Lam, R. Verel, A. Bansode, A. Urakawa, A. Comas-Vives, and C. Copéret. CO_2-to-Methanol Hydrogenation on Zirconia-Supported Copper Nanoparticles: Reaction Intermediates and the Role of the Metal–Support Interface. *Angewandte Chemie International Edition*, 56(9):2318–2323, 2017. ISSN 1433-7851. doi: 10.1002/anie.201610166. URL https://doi.org/10.1002/anie.201610166.

K.-H. Lee, M.-Y. Youn, and B. Sea. Preparation of hydrophilic ceramic membranes for a dehydration membrane reactor. *Desalination*, 191(1-3):296–302, 2006. ISSN 00119164. doi: 10.1016/j.desal.2005.07.026. URL https://linkinghub.elsevier.com/retrieve/pii/S0011916406001962.

M.-D. Lee, J.-F. Lee, and C.-S. Chang. Hydrogenation of Carbon Dioxide on Unpromoted and Potassium-Promoted Iron Catalysts. *Bulletin of the Chemical Society of Japan*, 62(8):2756–2758, 1989.

M.-D. Lee, J.-F. Lee, C.-S. Chang, and T.-Y. Dong. Effects of addition of chromium, manganese, or molybdenum to iron catalysts for carbon dioxide hydrogenation. *Applied catalysis*, 72(2):267–281, 1991.

S.-C. Lee, J.-H. Jang, B.-Y. Lee, M.-C. Kang, M. Kang, and S.-J. Choung. The effect of binders on structure and chemical properties of Fe-K/γ-Al_2O_3 catalysts for CO_2 hydrogenation. *Applied Catalysis A: General*, 253(1):293–304, 2003. ISSN 0926860X. doi: 10.1016/S0926-860X(03)00540-4. URL http://linkinghub.elsevier.com/retrieve/pii/S0926860X03005404.

D. Leeson, N. Mac Dowell, N. Shah, C. Petit, and P. Fennell. A Techno-economic analysis and systematic review of carbon capture and storage (CCS) applied to the iron and steel, cement, oil refining and pulp and paper industries, as well as other high purity sources. *International Journal of Greenhouse Gas Control*, 61:71–84, 2017. ISSN 1750-5836. doi: 10.1016/j.ijggc.2017.03.020. URL http://www.sciencedirect.com/science/article/pii/S175058361730289X.

T. Leib and J. Kuo. Modeling of the Fischer–Tropsch synthesis in slurry bubble column reactors. 1984. URL https://www.scopus.com/inward/record.uri?eid=2-s2.0-0021602226&partnerID=40&md5=54847c10245384eab3b182b3f924a929.

H. Li, Y. Tan, M. Ditaranto, J. Yan, and Z. Yu. Capturing CO_2 from Biogas Plants. *13th International Conference on Greenhouse Gas Control Technologies, GHGT-13, 14-18 November 2016, Lausanne, Switzerland*, 114:6030–6035, 2017. ISSN 1876-6102. doi: 10.1016/j.egypro.2017.03.1738. URL http://www.sciencedirect.com/science/article/pii/S1876610217319409.

J. Li, L. Wang, Y. Cao, C. Zhang, P. He, and H. Li. Recent advances on the reduction of CO_2 to important C_{2+} oxygenated chemicals and fuels. *Chinese Journal of Chemical Engineering*, 26(11):2266–2279, 2018a. ISSN 10049541. doi: 10.1016/j.cjche.2018.07.008. URL https://linkinghub.elsevier.com/retrieve/pii/S1004954118304397.

W. Li, H. Wang, X. Jiang, J. Zhu, Z. Liu, X. Guo, and C. Song. A short review of recent advances in CO_2 hydrogenation to hydrocarbons over heterogeneous catalysts. *RSC Advances*, 8(14):7651–7669, 2018b. ISSN 2046-2069. doi: 10.1039/C7RA13546G. URL http://xlink.rsc.org/?DOI=C7RA13546G.

J. Liu, A. Zhang, X. Jiang, M. Liu, Y. Sun, C. Song, and X. Guo. Selective CO_2 Hydrogenation to Hydrocarbons on Cu-Promoted Fe-Based Catalysts: Dependence on Cu–Fe Interaction. *ACS Sustainable Chemistry & Engineering*, 6(8):10182–10190, 2018. ISSN 2168-0485, 2168-0485. doi: 10.1021/acssuschemeng.8b01491. URL `http://pubs.acs.org/doi/10.1021/acssuschemeng.8b01491`.

J. Liu, K. Li, Y. Song, C. Song, and X. Guo. Selective Hydrogenation of CO_2 to Hydrocarbons: Effects of Fe_3O_4 Particle Size on Reduction, Carburization, and Catalytic Performance. *Energy & Fuels*, 35(13):10703–10709, 2021. ISSN 0887-0624, 1520-5029. doi: 10.1021/acs.energyfuels.1c01265. URL `https://pubs.acs.org/doi/10.1021/acs.energyfuels.1c01265`.

J.-X. Liu, P. Wang, W. Xu, and E. J. Hensen. Particle Size and Crystal Phase Effects in Fischer-Tropsch Catalysts. *Engineering*, 3(4):467–476, 2017. ISSN 2095-8099. doi: 10.1016/J.ENG.2017.04.012. URL `https://www.sciencedirect.com/science/article/pii/S2095809917306069`.

Y. Liu, J.-F. Chen, and Y. Zhang. The effect of pore size or iron particle size on the formation of light olefins in Fischer–Tropsch synthesis. *RSC Advances*, 5(37):29002–29007, 2015. ISSN 2046-2069. doi: 10.1039/C5RA02319J. URL `http://xlink.rsc.org/?DOI=C5RA02319J`.

J. A. Loiland, M. J. Wulfers, N. S. Marinkovic, and R. F. Lobo. Fe/γ-Al_2O_3 and Fe–K/γ-Al_2O_3 as reverse water-gas shift catalysts. *Catalysis Science & Technology*, 6(14):5267–5279, 2016. ISSN 2044-4753. doi: 10.1039/C5CY02111A. URL `http://dx.doi.org/10.1039/C5CY02111A`.

E. S. Lox and G. F. Froment. Kinetics of the Fischer-Tropsch reaction on a precipitated promoted iron catalyst. 2. Kinetic modeling. *Industrial & Engineering Chemistry Research*, 32(1):71–82, 1993.

R. Madon. Fischer-Tropsch synthesis on a precipitated iron catalyst. *Journal of Catalysis*, 69(1):32–43, 1981. ISSN 00219517. doi: 10.1016/0021-9517(81)90125-1. URL `https://linkinghub.elsevier.com/retrieve/pii/0021951781901251`.

H. Mahmoudi, M. Mahmoudi, O. Doustdar, H. Jahangiri, A. Tsolakis, S. Gu, and M. Lech Wyszynski. A review of Fischer Tropsch synthesis process, mechanism, surface chemistry and catalyst formulation. *Biofuels Engineering*, 2(1):11–31, 2017. doi: 10.1515/bfuel-2017-0002. URL `https://www.degruyter.com/view/journals/bfuel/2/1/article-p11.xml`.

P. Maitlis. Fischer-Tropsch, organometallics, and other friends. *Journal of Organometallic Chemistry*, 689(24 SPEC. ISS.):4366–4374, 2004. doi: 10.1016/j.jorganchem.2004.05.037. URL `https://www.scopus.com/inward/record.uri?eid=2-s2.0-9944229887&doi=10.1016%2fj.jorganchem.2004.05.037&partnerID=40&md5=e590b86c11e5128a9ff986d2582d4f12`.

M. Martinelli, C. G. Visconti, L. Lietti, P. Forzatti, C. Bassano, and P. Deiana. CO_2 reactivity on Fe–Zn–Cu–K Fischer–Tropsch synthesis catalysts with different K-loadings. *Catalysis Today*, 228:77–88, 2014. ISSN 09205861. doi: 10.1016/j.cattod.2013.11.018. URL `https://linkinghub.elsevier.com/retrieve/pii/S0920586113006226`.

K. McGrath, G. Prakash, and G. Olah. *Direct methanol fuel cells*, volume 10. 2004.

D. Mignard and C. Pritchard. Processes for the Synthesis of Liquid Fuels from CO_2 and Marine Energy. *Chemical Engineering Research and Design*, 84(9):828–836, 2006. ISSN 02638762. doi: 10.1205/cherd.05204. URL `http://linkinghub.elsevier.com/retrieve/pii/S026387620672963X`.

C. Mokou, L. Beisswenger, H. Vogel, S. Klemenz, and B. Albert. Iron-catalyzed hydrogenation of carbon dioxide to hydrocarbons/fuels in condensed phase. In *Energy (IYCE), 2015 5th International Youth Conference on*, pages 1–6. IEEE, 2015.

W. Molina, V. Perrichon, R. P. A. Sneeden, and P. Turlier. Hydrocondensation of CO on iron-alumina catalysts. Influence of ethylene. *Reaction Kinetics and Catalysis Letters*, 13(1):69–75, 1980. ISSN 1588-2837. doi: 10.1007/BF02077689. URL `https://doi.org/10.1007/BF02077689`.

S. Mousavi, A. Zamaniyan, M. Irani, and M. Rashidzadeh. Generalized kinetic model for iron and cobalt based Fischer–Tropsch synthesis catalysts: Review and model evaluation. *Applied Catalysis A: General*, 506:57–66, 2015. ISSN 0926-860X. doi: 10.1016/j.apcata.2015.08.020. URL `http://www.sciencedirect.com/science/article/pii/S0926860X15301150`.

S. Najari, G. Gróf, and S. Saeidi. Enhancement of hydrogenation of CO_2 to hydrocarbons via In-Situ water removal. *International Journal of Hydrogen Energy*, 44(45):24759–24781, 2019a. ISSN 0360-3199. doi: 10.1016/j.ijhydene.2019.07.159. URL http://www.sciencedirect.com/science/article/pii/S0360319919327491.

S. Najari, G. Gróf, S. Saeidi, and F. Gallucci. Modeling and optimization of hydrogenation of CO_2: Estimation of kinetic parameters via Artificial Bee Colony (ABC) and Differential Evolution (DE) algorithms. *International Journal of Hydrogen Energy*, 44(10):4630–4649, 2019b. ISSN 03603199. doi: 10.1016/j.ijhydene.2019.01.020. URL https://linkinghub.elsevier.com/retrieve/pii/S036031991930093X.

A. Nakhaei Pour and M. R. Housaindokht. Studies on product distribution of nanostructured iron catalyst in Fischer–Tropsch synthesis: Effect of catalyst particle size. *Journal of Industrial and Engineering Chemistry*, 20(2):591–596, 2014. ISSN 1226-086X. doi: 10.1016/j.jiec.2013.05.019. URL https://www.sciencedirect.com/science/article/pii/S1226086X13002256.

A. Nakhaei Pour and M. R. Housaindokht. A new kinetic model for direct CO_2 hydrogenation to higher hydrocarbons on a precipitated iron catalyst: Effect of catalyst particle size. *Journal of Energy Chemistry*, 26(3):359–367, 2017. ISSN 20954956. doi: 10.1016/j.jechem.2016.12.006. URL https://linkinghub.elsevier.com/retrieve/pii/S2095495616301607.

A. Nakhaei Pour, M. R. Housaindokht, S. F. Tayyari, and J. Zarkesh. Kinetics of the water-gas shift reaction in Fischer-Tropsch synthesis over a nano-structured iron catalyst. *Journal of Natural Gas Chemistry*, 19(4):362–368, 2010. ISSN 1003-9953. doi: 10.1016/S1003-9953(09)60085-2. URL https://www.sciencedirect.com/science/article/pii/S1003995309600852.

A. Nakhaei Pour, M. R. Housaindokht, E. G. Babakhani, M. Irani, and S. M. K. Shahri. Size dependence on reduction kinetic of iron based Fischer–Tropsch catalyst. *Journal of Industrial and Engineering Chemistry*, 17, 2011.

A. Nakhaei Pour, H. Khodabandeh, M. Izadyar, and M. R. Housaindokht. Mechanistic double ASF product distribution study of Fischer–Tropsch synthesis on precipitated iron catalyst. *Journal of Natural Gas Science and Engineering*, 15:53–58, 2013. ISSN 1875-5100. doi: 10.1016/j.jngse.2013.09.005. URL http://www.sciencedirect.com/science/article/pii/S1875510013000814.

A. Nakhaei Pour, M. R. Housaindokht, M. Irani, and S. M. Kamali Shahri. Size-dependent studies of Fischer–Tropsch synthesis on iron based catalyst: New kinetic model. *Fuel*, 116:787–793, 2014. ISSN 0016-2361. doi: 10.1016/j.fuel.2013.08.080. URL https://www.sciencedirect.com/science/article/pii/S0016236113008235.

S.-S. Nam, H. Kim, G. Kishan, M.-J. Choi, and K.-W. Lee. Catalytic conversion of carbon dioxide into hydrocarbons over iron supported on alkali ion-exchanged Y-zeolite catalysts. *Applied Catalysis A: General*, 179(1-2):155–163, 1999.

W. Ning, C. Chen, T. Wang, Y. Jin, and X. Yang. An Introductive Study about CO_2 Hydrogenation into Hydrocarbons Using Iron Catalysts. *Advances in Chemical Engineering and Science*, 07(01):1–9, 2017. ISSN 2160-0392, 2160-0406. doi: 10.4236/aces.2017.71001. URL http://www.scirp.org/journal/doi.aspx?DOI=10.4236/aces.2017.71001.

S. Novak, R. J. Madon, and H. Suhl. Models of hydrocarbon product distributions in Fischer–Tropsch synthesis. I. *The Journal of Chemical Physics*, 74(11):6083–6091, 1981. ISSN 0021-9606. doi: 10.1063/1.441051. URL https://doi.org/10.1063/1.441051.

T. Numpilai, N. Chanlek, Y. Poo-Arporn, S. Wannapaiboon, C. K. Cheng, N. Siri-Nguan, T. Sornchamni, P. Kongkachuichay, M. Chareonpanich, G. Rupprechter, J. Limtrakul, and T. Witoon. Pore size effects on physicochemical properties of Fe-Co/K-Al_2O_3 catalysts and their catalytic activity in CO_2 hydrogenation to light olefins. *Applied Surface Science*, 483:581–592, 2019a. doi: https://doi.org/10.1016/j.apsusc.2019.03.331. URL https://www.sciencedirect.com/science/article/pii/S0169433219309705?via%3Dihub.

T. Numpilai, C. Wattanakit, M. Chareonpanich, J. Limtrakul, and T. Witoon. Optimization of synthesis condition for CO_2 hydrogenation to light olefins over In_2O_3 admixed with SAPO-34. *Energy Conversion and Management*, 180:511–523, 2019b. ISSN 01968904. doi: 10.1016/j.enconman.2018.11.011. URL https://linkinghub.elsevier.com/retrieve/pii/S019689041831255X.

G. A. Olah, A. Goeppert, and G. K. S. Prakash. Chemical Recycling of Carbon Dioxide to Methanol and Dimethyl Ether: From Greenhouse Gas to Renewable, Environmentally Carbon Neutral Fuels and Synthetic Hydrocarbons. *The Journal of Organic Chemistry*, 74(2):487–498, 2009. ISSN 0022-3263, 1520-6904. doi: 10.1021/jo801260f. URL http://pubs.acs.org/doi/abs/10.1021/jo801260f.

G. A. Olah, G. K. S. Prakash, and A. Goeppert. Anthropogenic Chemical Carbon Cycle for a Sustainable Future. *Journal of the American Chemical Society*, 133(33):12881–12898, 2011. ISSN 0002-7863, 1520-5126. doi: 10.1021/ja202642y. URL http://pubs.acs.org/doi/abs/10.1021/ja202642y.

C. Panzone, R. Philippe, A. Chappaz, P. Fongarland, and A. Bengaouer. Power-to-Liquid catalytic CO_2 valorization into fuels and chemicals: focus on the Fischer-Tropsch route. *Journal of CO2 Utilization*, 38:314–347, 2020. ISSN 2212-9820. doi: 10.1016/j.jcou.2020.02.009. URL http://www.sciencedirect.com/science/article/pii/S2212982019309916.

Y.-K. Park, K.-C. Park, and S.-K. Ihm. Hydrocarbon synthesis through CO_2 hydrogenation over $CuZnOZrO_2$/zeolite hybrid catalysts. *Catalysis today*, 44(1-4):165–173, 1998.

L. Pastor-Pérez, F. Baibars, E. Le Sache, H. Arellano-García, S. Gu, and T. Reina. CO_2 valorisation via Reverse Water-Gas Shift reaction using advanced Cs doped Fe-Cu/Al_2O_3 catalysts. *Journal of CO2 Utilization*, 21:423–428, 2017. ISSN 22129820. doi: 10.1016/j.jcou.2017.08.009. URL https://linkinghub.elsevier.com/retrieve/pii/S221298201730433X.

J. Patzlaff, Y. Liu, C. Graffmann, and J. Gaube. Studies on product distributions of iron and cobalt catalyzed Fischer–Tropsch synthesis. *Applied Catalysis A: General*, 186(1-2):109–119, 1999. ISSN 0926860X. doi: 10.1016/S0926-860X(99)00167-2. URL https://linkinghub.elsevier.com/retrieve/pii/S0926860X99001672.

J. Patzlaff, Y. Liu, C. Graffmann, and J. Gaube. Interpretation and kinetic modeling of product distributions of cobalt catalyzed Fischer–Tropsch synthesis. *Catalysis Today*, 71(3-4):381–394, 2002. ISSN 09205861. doi: 10.1016/S0920-5861(01)00465-5. URL https://linkinghub.elsevier.com/retrieve/pii/S0920586101004655.

V. R. R. Pendyala, G. Jacobs, J. C. Mohandas, M. Luo, H. H. Hamdeh, Y. Ji, M. C. Ribeiro, and B. H. Davis. Fischer–Tropsch Synthesis: Effect of Water Over Iron-Based Catalysts. *Catalysis Letters*, 140 (3):98–105, 2010. ISSN 1572-879X. doi: 10.1007/s10562-010-0452-7. URL https://doi.org/10.1007/s10562-010-0452-7.

H. Pichler and H. Schulz. Neuere Erkenntnisse auf dem Gebiet der Synthese von Kohlenwasserstoffen aus CO und H_2. *Chemie Ingenieur Technik - CIT*, 42(18):1162–1174, 1970. ISSN 0009-286X, 1522-2640. doi: 10.1002/cite.330421808. URL http://doi.wiley.com/10.1002/cite.330421808.

E. Piera, M. A. Salomón, J. Coronas, M. Menéndez, and J. Santamarıa. Synthesis, characterization and separation properties of a composite mordenite/ZSM-5/chabazite hydrophilic membrane. *Journal of Membrane Science*, 149(1):99–114, 1998. ISSN 03767388. doi: 10.1016/S0376-7388(98)00184-7. URL https://linkinghub.elsevier.com/retrieve/pii/S0376738898001847.

V. Ponec. Some Aspects of the Mechanism of Methanation and Fischer-Tropsch Synthesis. *Catalysis Reviews*, 18(1):151–171, 1978. doi: 10.1080/03602457808067530. URL https://www.scopus.com/inward/record.uri?eid=2-s2.0-0018057506&doi=10.1080%2f03602457808067530&partnerID=40&md5=55d2c150d07118d0d9f5f7be888530dc.

F. Pérez-Alonso, M. Ojeda, T. Herranz, S. Rojas, J. González-Carballo, P. Terreros, and J. Fierro. Carbon dioxide hydrogenation over Fe–Ce catalysts. *Catalysis Communications*, 9(9):1945–1948, 2008. ISSN 15667367. doi: 10.1016/j.catcom.2008.03.024. URL http://linkinghub.elsevier.com/retrieve/pii/S156673670800112X.

D. Rethwisch and J. Dumesic. Adsorptive and Catalytic Properties of Supported Metal Oxides - III. Water-Gas Shift over Supported Iron and Zinc Oxides. *Journal of Catalysis*, 101:35–42, 1982.

J. Reymond, P. Mériaudeau, B. Pommier, and C. Bennett. Further results on the reaction of H_2/CO on fused iron by the transient method. *Journal of Catalysis*, 64(1):163–172, 1980. ISSN 0021-9517. doi: 10.1016/0021-9517(80)90489-3. URL https://www.sciencedirect.com/science/article/pii/0021951780904893.

S. A. S. Rezai, J. Lindmark, C. Andersson, F. Jareman, K. Möller, and J. Hedlund. Water/hydrogen/hexane multicomponent selectivity of thin MFI membranes with different Si/Al ratios. *Microporous and Mesoporous Materials*, 108(1-3):136–142, 2008. ISSN 13871811. doi: 10.1016/j.micromeso.2007.04.002. URL https://linkinghub.elsevier.com/retrieve/pii/S1387181107002107.

T. Riedel, M. Claeys, H. Schulz, G. Schaub, N. Sang-Sung, J. Ki-Won, K. Gurram, and L. Kyu-Wan. Comparative study of Fisher-Tropsch sythesis with H_2/CO and H_2/CO_2 syngas using Fe- and Co-based catalysts. *Applied Catalysis A: General*, 186:201–213, 1999.

T. Riedel, G. Schaub, K.-W. Jun, and K.-W. Lee. Kinetics of CO_2 Hydrogenation on a K-Promoted Fe Catalyst. *Industrial & Engineering Chemistry Research*, 40(5):1355–1363, 2001. ISSN 0888-5885, 1520-5045. doi: 10.1021/ie000084k. URL http://pubs.acs.org/doi/abs/10.1021/ie000084k.

T. Riedel, H. Schulz, G. Schaub, K.-W. Jun, J.-S. Hwang, and K.-W. Lee. Fischer–Tropsch on iron with H_2/CO and H_2/CO_2 as synthesis gases: the episodes of formation of the Fischer–Tropsch regime and construction of the catalyst. *Topics in Catalysis*, 26(1-4):41–54, 2003.

U. Rodemerck, M. Holeňa, E. Wagner, Q. Smejkal, A. Barkschat, and M. Baerns. Catalyst Development for CO_2 Hydrogenation to Fuels. *ChemCatChem*, 5(7):1948–1955, 2013. ISSN 18673880. doi: 10.1002/cctc.201200879. URL http://doi.wiley.com/10.1002/cctc.201200879.

M. Rohde, G. Schaub, J. F. Vente, and H. v. Veen. Fischer-Tropsch Synthesis with In-situ H_2O Removal by a New Hydrophilic Membrane - An Experimental and Modelling Study. In *Proceedings of the DGMK/SCI-conference "Synthesis gas chemistry"*, Deutsche Wissenschaftliche Gesellschaft fuer Erdoel, Erdgas und Kohle e.V., Hamburg (Germany), 2006. Ernst, S.; Jess, A.; Nees, F.; Perego, C.; Rupp, M.; Santacesaria, E. (eds.). URL https://www.osti.gov/etdeweb/servlets/purl/20840774.

M. Rohde, G. Schaub, S. Khajavi, J. Jansen, and F. Kapteijn. Fischer–Tropsch synthesis with in situ H_2O removal – Directions of membrane development. *Microporous and Mesoporous Materials*, 115(1-2):123–136, 2008. ISSN 13871811. doi: 10.1016/j.micromeso.2007.10.052. URL https://linkinghub.elsevier.com/retrieve/pii/S1387181108000772.

M. P. Rohde, D. Unruh, and G. Schaub. Membrane application in Fischer–Tropsch synthesis reactors - Overview of concepts. *International Conference on Gas-Fuel 05*, 106(1):143–148, 2005. ISSN 0920-5861. doi: 10.1016/j.cattod.2005.07.124. URL http://www.sciencedirect.com/science/article/pii/S0920586105005031.

S. Saeidi, S. Najari, F. Fazlollahi, M. K. Nikoo, F. Sefidkon, J. J. Klemeš, and L. L. Baxter. Mechanisms and kinetics of CO_2 hydrogenation to value-added products: A detailed review on current status and future trends. *Renewable and Sustainable Energy Reviews*, 80:1292–1311, 2017. ISSN 1364-0321. doi: 10.1016/j.rser.2017.05.204. URL http://www.sciencedirect.com/science/article/pii/S1364032117308390.

P. S. Sai Prasad, J. W. Bae, K.-W. Jun, and K.-W. Lee. Fischer–Tropsch Synthesis by Carbon Dioxide Hydrogenation on Fe-Based Catalysts. *Catalysis Surveys from Asia*, 12(3):170–183, 2008. ISSN 1571-1013, 1574-9266. doi: 10.1007/s10563-008-9049-1. URL http://link.springer.com/10.1007/s10563-008-9049-1.

B. Sarup and B. W. Wojciechowski. Studies of the Fischer-Tropsch synthesis on a cobalt catalyst I. Evaluation of product distribution parameters from experimental data. *The Canadian Journal of Chemical Engineering*, 66(5):831–842, 1988. ISSN 0008-4034. doi: 10.1002/cjce.5450660518. URL https://doi.org/10.1002/cjce.5450660518. Publisher: John Wiley & Sons, Ltd.

C. Satterfield. Olefin addition in Fischer-Tropsch synthesis on an iron catalyst. *Journal of Catalysis*, 80 (2):486–490, 1983. ISSN 00219517. doi: 10.1016/0021-9517(83)90277-4. URL `https://linkinghub.elsevier.com/retrieve/pii/0021951783902774`.

C. N. Satterfield, R. T. Hanlon, S. E. Tung, Z. M. Zou, and G. C. Papaefthymiou. Effect of water on the iron-catalyzed Fischer-Tropsch synthesis. *Industrial & Engineering Chemistry Product Research and Development*, 25(3):407–414, 1986. ISSN 0196-4321. doi: 10.1021/i300023a007. URL `https://doi.org/10.1021/i300023a007`.

R. Satthawong, N. Koizumi, C. Song, and P. Prasassarakich. Bimetallic Fe–Co catalysts for CO_2 hydrogenation to higher hydrocarbons. *Journal of CO2 Utilization*, 3-4:102–106, 2013. ISSN 22129820. doi: 10.1016/j.jcou.2013.10.002. URL `https://linkinghub.elsevier.com/retrieve/pii/S2212982013000498`.

P. Schmidt, V. Batteiger, A. Roth, W. Weindorf, and T. Raksha. Power-to-Liquids as Renewable Fuel Option for Aviation: A Review. *Chemie Ingenieur Technik*, 90(1-2):127–140, 2018. ISSN 0009286X. doi: 10.1002/cite.201700129. URL `http://doi.wiley.com/10.1002/cite.201700129`.

G. V. Schulz. Über die Beziehung zwischen Reaktionsgeschwindigkeit und Zusammensetzung des Reaktionsproduktes bei Makropolymerisationsvorgängen:. *Zeitschrift für Physikalische Chemie*, 30B(1): 379–398, 1935. doi: 10.1515/zpch-1935-3027. URL `https://doi.org/10.1515/zpch-1935-3027`.

H. Schulz. Selforganization in Fischer–Tropsch synthesis with iron- and cobalt catalysts. *Catalysis Today*, 228:113–122, 2014. ISSN 09205861. doi: 10.1016/j.cattod.2013.11.060. URL `https://linkinghub.elsevier.com/retrieve/pii/S0920586113006895`.

H. Schulz and M. Claeys. Kinetic modelling of Fischer–Tropsch product distributions. *Applied Catalysis A: General*, 186(1):91–107, 1999. ISSN 0926-860X. doi: 10.1016/S0926-860X(99)00166-0. URL `http://www.sciencedirect.com/science/article/pii/S0926860X99001660`.

H. Schulz, K. Beck, and E. Erich. Mechanism of the Fischer Tropsch Process. In D. Bibby, C. Chang, R. Howe, and S. Yurchak, editors, *Studies in Surface Science and Catalysis*, volume 36, pages 457–471. Elsevier, 1988. ISBN 0167-2991. doi: 10.1016/S0167-2991(09)60540-1. URL `https://www.sciencedirect.com/science/article/pii/S0167299109605401`.

H. Schulz, G. Schaub, M. Claeys, and T. Riedel. Transient initial kinetic regimes of Fischer–Tropsch synthesis. *Applied Catalysis A: General*, 186(1-2):215–227, 1999.

H. Schulz, T. Riedel, and G. Schaub. Fischer–Tropsch principles of co-hydrogenation on iron catalysts. *Topics in Catalysis*, 32(3-4):117–124, 2005. ISSN 1022-5528, 1572-9028. doi: 10.1007/s11244-005-2883-8. URL `http://link.springer.com/10.1007/s11244-005-2883-8`.

J. Schweicher, A. Bundhoo, and N. Kruse. Hydrocarbon Chain Lengthening in Catalytic CO Hydrogenation: Evidence for a CO-Insertion Mechanism. *Journal of the American Chemical Society*, 134(39):16135–16138, 2012. ISSN 0002-7863, 1520-5126. doi: 10.1021/ja3068484. URL `https://pubs.acs.org/doi/10.1021/ja3068484`.

W. D. Shafer, G. Jacobs, U. M. Graham, H. H. Hamdeh, and B. H. Davis. Increased CO_2 hydrogenation to liquid products using promoted iron catalysts. *Journal of Catalysis*, 369:239–248, 2019. ISSN 00219517. doi: 10.1016/j.jcat.2018.11.001. URL `https://linkinghub.elsevier.com/retrieve/pii/S0021951718304317`.

Z. Shi, H. Yang, P. Gao, X. Li, L. Zhong, H. Wang, H. Liu, W. Wei, and Y. Sun. Direct conversion of CO_2 to long-chain hydrocarbon fuels over K–promoted CoCu/TiO_2 catalysts. *Catalysis Today*, 311:65–73, 2018. ISSN 09205861. doi: 10.1016/j.cattod.2017.09.053. URL `https://linkinghub.elsevier.com/retrieve/pii/S0920586117306685`.

S. Siegemund, M. Trommler, O. Kolb, V. Zinnecker, P. Schmidt, W. Weindorf, W. Zittel, T. Raksha, and J. Zerhusen. «E-FUELS» STUDY - The potential of electricity-based fuels for low-emission transport in the EU. *Deutsche Energie-Agentur GmbH (dena)*, 2017.

A. S. Skrypnik, Q. Yang, A. A. Matvienko, V. Y. Bychkov, Y. P. Tulenin, H. Lund, S. A. Petrov, R. Kraehnert, A. Arinchtein, J. Weiss, A. Brueckner, and E. V. Kondratenko. Understanding reaction-induced restructuring of well-defined $Fe_xO_yC_z$ compositions and its effect on CO_2 hydrogenation. *Applied Catalysis B: Environmental*, 291:120121, 2021. ISSN 09263373. doi: 10.1016/j.apcatb.2021.120121. URL https://linkinghub.elsevier.com/retrieve/pii/S0926337321002472.

R. Snel and R. L. Espinoza. Secondary reactions of primary products of the Fischer-Tropsch synthesis: Part 1. The role of ethene. *Journal of Molecular Catalysis*, 43(2):237–247, 1987. ISSN 0304-5102. doi: 10.1016/0304-5102(87)87011-6. URL https://www.sciencedirect.com/science/article/pii/0304510287870116.

S. Srinivas, R. K. Malik, and S. M. Mahajani. Fischer-Tropsch synthesis using bio-syngas and CO_2. *Energy for Sustainable Development*, 11(4):66–71, 2007.

H. H. Storch. *The Fischer-Tropsch and related syntheses, including a summary of theoretical and applied contact catalysis*. Number xii, 610 p. Wiley, New York, 1951. URL //catalog.hathitrust.org/Record/001515058.

R. Struis and S. Stucki. Verification of the membrane reactor concept for the methanol synthesis. *Applied Catalysis A: General*, 216(1-2):117–129, 2001. ISSN 0926860X. doi: 10.1016/S0926-860X(01)00548-8. URL https://linkinghub.elsevier.com/retrieve/pii/S0926860X01005488.

X. Su, J. Zhang, S. Fan, Q. Ma, and T.-S. Zhao. Effect of preparation of Fe–Zr–K catalyst on the product distribution of CO_2 hydrogenation. *RSC Advances*, 5(98):80196–80202, 2015.

Y. Sun and P. A. Sermon. Evidence of a metal-support interaction in sol-gel derived Cu-ZrO_2 catalysts for CO hydrogenation. *Catalysis Letters*, 29(3):361–369, 1994. ISSN 1572-879X. doi: 10.1007/BF00807115. URL https://doi.org/10.1007/BF00807115.

Sunfire. First commercial plant for the production of blue crude planned in Norway., 2017. URL https://www.sunfire.de/en/news/detail/first-commercial-plant-for-the-production-of-blue-crude-planned-in-norway.

Sunfire. Breaktrough for Power-To-X: Sunfire puts first co-electrolysis into operation and starts scaling., 2019. URL https://www.sunfire.de/en/news/detail/breakthrough-for-power-to-x-sunfire-puts-first-co-electrolysis-into-operation-and-starts-scaling.

A. Tarasov, V. Isaeva, O. Tkachenko, V. Chernyshev, and L. Kustov. Conversion of CO_2 into liquid hydrocarbons in the presence of a Co-containing catalyst based on the microporous metal-organic framework MIL-53(Al). *Fuel Processing Technology*, 176:101–106, 2018. ISSN 03783820. doi: 10.1016/j.fuproc.2018.03.016. URL https://linkinghub.elsevier.com/retrieve/pii/S0378382018302571.

L.-M. Tau, R. Robinson, R. D. Ross, and B. H. Davis. Oxygenates formed from ethanol during Fischer-Tropsch synthesis. *Journal of Catalysis*, 105(2):335–341, 1987. ISSN 00219517. doi: 10.1016/0021-9517(87)90062-5. URL https://linkinghub.elsevier.com/retrieve/pii/0021951787900625.

L. M. Tau, H. A. Dabbagh, and B. H. Davis. Fischer-Tropsch synthesis: carbon-14 tracer study of alkene incorporation. *Energy & Fuels*, 4(1):94–99, 1990. ISSN 0887-0624, 1520-5029. doi: 10.1021/ef00019a017. URL https://pubs.acs.org/doi/abs/10.1021/ef00019a017.

L.-M. Tau, H. A. Dabbagh, J. Halasz, and B. H. Davis. Fischer—Tropsch synthesis: Incorporation of 14C-labeled normal and isoalcohols. *Journal of Molecular Catalysis*, 71(1):37–55, 1992. ISSN 0304-5102. doi: 10.1016/0304-5102(92)80006-3. URL https://www.sciencedirect.com/science/article/pii/0304510292800063.

A. Tavasoli, A. N. Pour, and M. G. Ahangari. Kinetics and product distribution studies on ruthenium-promoted cobalt/alumina Fischer-Tropsch synthesis catalyst. *Journal of Natural Gas Chemistry*, 19(6):653–659, 2010. ISSN 1003-9953. doi: 10.1016/S1003-9953(09)60133-X. URL http://www.sciencedirect.com/science/article/pii/S100399530960133X.

F. Tihay, A. C. Roger, G. Pourroy, and A. Kiennemann. Role of the Alloy and Spinel in the Catalytic Behavior of FeCo/Cobalt Magnetite Composites under CO and CO_2 Hydrogenation. *Energy & Fuels*, 16(5):1271–1276, 2002. ISSN 0887-0624, 1520-5029. doi: 10.1021/ef020059m. URL `http://pubs.acs.org/doi/abs/10.1021/ef020059m`.

J. Topp-Jørgensen. Topsøe Integrated Gasoline Synthesis – The Tigas Process. In D. Bibby, C. Chang, R. Howe, and S. Yurchak, editors, *Studies in Surface Science and Catalysis*, volume 36, pages 293–305. Elsevier, 1988. ISBN 0167-2991. doi: 10.1016/S0167-2991(09)60523-1. URL `http://www.sciencedirect.com/science/article/pii/S0167299109605231`.

H. M. Torres Galvis, J. H. Bitter, T. Davidian, M. Ruitenbeek, A. I. Dugulan, and K. P. de Jong. Iron Particle Size Effects for Direct Production of Lower Olefins from Synthesis Gas. *Journal of the American Chemical Society*, 134(39):16207–16215, 2012. ISSN 0002-7863, 1520-5126. doi: 10.1021/ja304958u. URL `https://pubs.acs.org/doi/10.1021/ja304958u`.

W. Tu, C. Sun, Z. Zhang, W. Liu, H. S. Malhi, W. Ma, M. Zhu, and Y.-F. Han. Chemical and structural properties of Na decorated Fe_5C_2-ZnO catalysts during hydrogenation of CO_2 to linear α-olefins. *Applied Catalysis B: Environmental*, 298:120567, 2021. ISSN 09263373. doi: 10.1016/j.apcatb.2021.120567. URL `https://linkinghub.elsevier.com/retrieve/pii/S0926337321006937`.

UNECE. Carbon capture, use and storage (CCUS). Technical report, 2021. URL `https://unece.org/sites/default/files/2021-03/CCUS%20brochure_EN_final.pdf`.

D. Unruh, M. Rohde, and G. Schaub. Improving carbon utilization in biomass conversion to synthetic hydrocarbons via Fischer-Tropsch Synthesis. In S.-E. Park, J.-S. Chang, and K.-W. Lee, editors, *Studies in Surface Science and Catalysis*, volume 153, pages 91–96. Elsevier, Jan. 2004. ISBN 0167-2991. doi: 10.1016/S0167-2991(04)80225-8. URL `http://www.sciencedirect.com/science/article/pii/S0167299104802258`.

A. Ursua, L. M. Gandia, and P. Sanchis. Hydrogen Production From Water Electrolysis: Current Status and Future Trends. *Proceedings of the IEEE*, 100(2):410–426, 2012. ISSN 0018-9219. doi: 10.1109/JPROC.2011.2156750. URL `http://ieeexplore.ieee.org/document/5898382/`.

G. Van der Laan and A. A. Beenackers. Kinetics and Selectivity of the Fischer–Tropsch Synthesis: A Literature Review. *Catalysis Reviews*, 41(3-4):255–318, 1999. ISSN 0161-4940. doi: 10.1081/CR-100101170. URL `https://doi.org/10.1081/CR-100101170`.

G. P. Van der Laan and A. A. Beenackers. Intrinsic kinetics of the gas–solid Fischer–Tropsch and water gas shift reactions over a precipitated iron catalyst. *Applied Catalysis A: General*, 193(1-2):39–53, 2000.

J. van Kampen, J. Boon, F. van Berkel, J. Vente, and M. van Sint Annaland. Steam separation enhanced reactions: Review and outlook. *Chemical Engineering Journal*, 374:1286–1303, 2019. ISSN 13858947. doi: 10.1016/j.cej.2019.06.031. URL `https://linkinghub.elsevier.com/retrieve/pii/S1385894719312884`.

L. Vanoye, A. Favre-Réguillon, P. Munno, J. Rodríguez, S. Dupuy, S. Pallier, I. Pitault, and C. De Bellefon. Methanol dehydration over commercially available zeolites: Effect of hydrophobicity. *Catalysis Today*, 215:239–242, 2013. ISSN 09205861. doi: 10.1016/j.cattod.2013.01.012. URL `https://linkinghub.elsevier.com/retrieve/pii/S092058611300103X`.

A. Varone and M. Ferrari. Power to liquid and power to gas: An option for the German Energiewende. *Renewable and Sustainable Energy Reviews*, 45:207–218, 2015. ISSN 13640321. doi: 10.1016/j.rser.2015.01.049. URL `https://linkinghub.elsevier.com/retrieve/pii/S1364032115000593`.

C. G. Visconti, L. Lietti, E. Tronconi, P. Forzatti, R. Zennaro, and E. Finocchio. Fischer–Tropsch synthesis on a Co/Al_2O_3 catalyst with CO_2 containing syngas. *Applied Catalysis A: General*, 355 (1-2):61–68, 2009. ISSN 0926860X. doi: 10.1016/j.apcata.2008.11.027. URL `http://linkinghub.elsevier.com/retrieve/pii/S0926860X08007308`.

C. G. Visconti, M. Martinelli, L. Falbo, L. Fratalocchi, and L. Lietti. CO_2 hydrogenation to hydrocarbons over Co and Fe-based Fischer-Tropsch catalysts. *Catalysis Today*, 277:161–170, 2016. ISSN 09205861. doi: 10.1016/j.cattod.2016.04.010. URL https://linkinghub.elsevier.com/retrieve/pii/S0920586116302632.

C. G. Visconti, M. Martinelli, L. Falbo, A. Infantes-Molina, L. Lietti, P. Forzatti, G. Iaquaniello, E. Palo, B. Picutti, and F. Brignoli. CO_2 hydrogenation to lower olefins on a high surface area K-promoted bulk Fe-catalyst. *Applied Catalysis B: Environmental*, 200:530–542, 2017. ISSN 09263373. doi: 10.1016/j.apcatb.2016.07.047. URL https://linkinghub.elsevier.com/retrieve/pii/S0926337316305896.

F. V. Vázquez, J. Koponen, V. Ruuskanen, C. Bajamundi, A. Kosonen, P. Simell, J. Ahola, C. Frilund, J. Elfving, M. Reinikainen, N. Heikkinen, J. Kauppinen, and P. Piermartini. Power-to-X technology using renewable electricity and carbon dioxide from ambient air: SOLETAIR proof-of-concept and improved process concept. *Journal of CO2 Utilization*, 28:235–246, 2018. ISSN 22129820. doi: 10.1016/j.jcou.2018.09.026. URL https://linkinghub.elsevier.com/retrieve/pii/S2212982018305213.

J. Wambach, A. Baiker, and A. Wokaun. CO_2 hydrogenation over metal/zirconia catalysts. *Physical Chemistry Chemical Physics*, 1:5071–5080, 1999.

F. Wang, S. He, H. Chen, B. Wang, L. Zheng, M. Wei, D. G. Evans, and X. Duan. Active Site Dependent Reaction Mechanism over Ru/CeO_2 Catalyst toward CO_2 Methanation. *Journal of the American Chemical Society*, 138(19):6298–6305, 2016a. ISSN 0002-7863, 1520-5126. doi: 10.1021/jacs.6b02762. URL http://pubs.acs.org/doi/10.1021/jacs.6b02762.

H. Wang and Y. S. Lin. Effects of water vapor on gas permeation and separation properties of MFI zeolite membranes at high temperatures. *AIChE Journal*, 58(1):153–162, 2012. ISSN 00011541. doi: 10.1002/aic.12622. URL https://onlinelibrary.wiley.com/doi/10.1002/aic.12622.

J. Wang, Z. You, Q. Zhang, W. Deng, and Y. Wang. Synthesis of lower olefins by hydrogenation of carbon dioxide over supported iron catalysts. *Catalysis Today*, 215:186–193, 2013. ISSN 09205861. doi: 10.1016/j.cattod.2013.03.031. URL https://linkinghub.elsevier.com/retrieve/pii/S0920586113001442.

N. Wang, Y. Liu, A. Huang, and J. Caro. Supported SOD membrane with steam selectivity by a two-step repeated hydrothermal synthesis. *Microporous and Mesoporous Materials*, 192:8–13, 2014. ISSN 13871811. doi: 10.1016/j.micromeso.2013.08.013. URL https://linkinghub.elsevier.com/retrieve/pii/S1387181113003892.

N. Wang, Y. Liu, A. Huang, and J. Caro. Hydrophilic SOD and LTA membranes for membrane-supported methanol, dimethylether and dimethylcarbonate synthesis. *Microporous and Mesoporous Materials*, 207:33–38, 2015a. ISSN 13871811. doi: 10.1016/j.micromeso.2014.12.028. URL https://linkinghub.elsevier.com/retrieve/pii/S1387181114007276.

W. Wang, S. Wang, X. Ma, and J. Gong. Recent advances in catalytic hydrogenation of carbon dioxide. *Chemical Society Reviews*, 40(7):3703–3727, 2011.

W.-H. Wang, Y. Himeda, J. T. Muckerman, G. F. Manbeck, and E. Fujita. CO_2 Hydrogenation to Formate and Methanol as an Alternative to Photo- and Electrochemical CO_2 Reduction. *Chem. Rev.*, page 38, 2015b.

Z. Wang, T. He, J. Li, J. Wu, J. Qin, G. Liu, D. Han, Z. Zi, Z. Li, and J. Wu. Design and operation of a pilot plant for biomass to liquid fuels by integrating gasification, DME synthesis and DME to gasoline. *Fuel*, 186:587–596, 2016b. ISSN 00162361. doi: 10.1016/j.fuel.2016.08.108. URL https://linkinghub.elsevier.com/retrieve/pii/S0016236116308560.

J. Wei, Q. Ge, R. Yao, Z. Wen, C. Fang, L. Guo, H. Xu, and J. Sun. Directly converting CO_2 into a gasoline fuel. *Nature Communications*, 8:15174, 2017. ISSN 2041-1723. doi: 10.1038/ncomms15174. URL http://www.nature.com/doifinder/10.1038/ncomms15174.

M. Westgård Erichsen, S. Svelle, and U. Olsbye. The influence of catalyst acid strength on the methanol to hydrocarbons (MTH) reaction. *Catalysis Today*, 215:216–223, 2013. ISSN 09205861. doi: 10.1016/j.cattod.2013.03.017. URL https://linkinghub.elsevier.com/retrieve/pii/S0920586113001132.

H. D. Willauer, R. Ananth, M. T. Olsen, D. M. Drab, D. R. Hardy, and F. W. Williams. Modeling and kinetic analysis of CO_2 hydrogenation using a Mn and K-promoted Fe catalyst in a fixed-bed reactor. *Journal of CO2 Utilization*, 3-4:56–64, 2013. ISSN 22129820. doi: 10.1016/j.jcou.2013.10.003. URL `https://linkinghub.elsevier.com/retrieve/pii/S2212982013000504`.

B. W. Wojciechowski. The Kinetics of the Fischer-Tropsch Synthesis. *Catalysis Reviews*, 30(4):629–702, 1988. ISSN 0161-4940. doi: 10.1080/01614948808071755. URL `https://doi.org/10.1080/01614948808071755`. Publisher: Taylor & Francis.

T. Xie, J. Wang, F. Ding, A. Zhang, W. Li, X. Guo, and C. Song. CO_2 hydrogenation to hydrocarbons over alumina-supported iron catalyst: Effect of support pore size. *Journal of CO2 Utilization*, 19:202–208, 2017. ISSN 22129820. doi: 10.1016/j.jcou.2017.03.022. URL `https://linkinghub.elsevier.com/retrieve/pii/S2212982016304760`.

J. Yang, C. Ledesma Rodriguez, Y. Qi, H. Ma, A. Holmen, and D. Chen. The effect of co-feeding ethene on Fischer-Tropsch synthesis to olefins over Co-based catalysts. *Applied Catalysis A: General*, 598:117564, 2020. ISSN 0926-860X. doi: 10.1016/j.apcata.2020.117564. URL `http://www.sciencedirect.com/science/article/pii/S0926860X20301575`.

Y. Yao, X. Liu, D. Hildebrandt, and D. Glasser. Fischer–Tropsch Synthesis Using $H_2/CO/CO_2$ Syngas Mixtures over an Iron Catalyst. *Industrial & Engineering Chemistry Research*, 50(19):11002–11012, 2011. ISSN 0888-5885, 1520-5045. doi: 10.1021/ie200690y. URL `http://pubs.acs.org/doi/abs/10.1021/ie200690y`.

J. Zhang, S. Lu, X. Su, S. Fan, Q. Ma, and T. Zhao. Selective formation of light olefins from CO_2 hydrogenation over Fe–Zn–K catalysts. *Journal of CO2 Utilization*, 12:95–100, 2015. ISSN 22129820. doi: 10.1016/j.jcou.2015.05.004. URL `https://linkinghub.elsevier.com/retrieve/pii/S2212982015300032`.

L. Zhang, S. Xia, L. Chen, Y. Ge, C. Wang, and H. Feng. Entropy generation rate minimization for hydrocarbon synthesis reactor from carbon dioxide and hydrogen. *International Journal of Heat and Mass Transfer*, 137:1112–1123, 2019. ISSN 00179310. doi: 10.1016/j.ijheatmasstransfer.2019.04.022. URL `https://linkinghub.elsevier.com/retrieve/pii/S0017931018338250`.

H. Zhao, L. Guo, W. Gao, F. Chen, X. Wu, K. Wang, Y. He, P. Zhang, G. Yang, and N. Tsubaki. Multi-Promoters Regulated Iron Catalyst with Well-Matching Reverse Water-Gas Shift and Chain Propagation for Boosting CO_2 Hydrogenation. *Journal of CO2 Utilization*, 52:101700, 2021. ISSN 22129820. doi: 10.1016/j.jcou.2021.101700. URL `https://linkinghub.elsevier.com/retrieve/pii/S2212982021002675`.

W. Zhu, L. Gora, A. van den Berg, F. Kapteijn, J. Jansen, and J. Moulijn. Water vapour separation from permanent gases by a zeolite-4A membrane. *Journal of Membrane Science*, 253(1-2):57–66, 2005. ISSN 03767388. doi: 10.1016/j.memsci.2004.12.039. URL `https://linkinghub.elsevier.com/retrieve/pii/S0376738805000232`.

W. H. Zimmerman and D. B. Bukur. Reaction kinetics over iron catalysts used for the fischer-tropsch synthesis. *The Canadian journal of chemical engineering*, 68(2):292–301, 1990.

T. Álvaro Muñoz, C. Márquez-Álvarez, and E. Sastre. Enhanced stability in the methanol-to-olefins process shown by SAPO-34 catalysts synthesized in biphasic medium. *Catalysis Today*, 215:208–215, Oct. 2013. ISSN 09205861. doi: 10.1016/j.cattod.2013.03.015. URL `https://linkinghub.elsevier.com/retrieve/pii/S0920586113001119`.

CHAPTER 2

Experimental methodologies.

2.1 Introduction.

The main objective of the thesis is to develop the basis for the modelling of the CO_2 hydrogenation reaction towards hydrocarbons. The first step for the model development is to develop a kinetic model. In order to do that, it is required to collect experimental data on which the model is then validated. The CO_2 hydrogenation reaction has been widely studied experimentally, but not lot of works presented detailed kinetic studies with variation of operating parameters in large ranges. Thus, we have decided to perform a kinetic study to experimentally investigate the reaction in a laboratory-scale fixed-bed reactor and in different operating conditions. Another problem of the experimental studies reported in literature is that products obtained in liquid phases, and in particular in the water phase, are generally neglected. If we want to develop a model that is able to predict with good accuracy the formation of different kinds of products, we have to be able to accurately analyse the products experimentally obtained from the reaction. We have thus focused a lot of attention to the development of an optimal analytic protocol, first to identify all the products obtained from the reaction and then to quantify the main part of them.

Another objective of the thesis is to gain insights about the reaction mechanism. The experimental kinetic study can give us some information about the reaction mechanism, such as which products are favoured, if the reaction occurs in one or two steps... However, additional studies of co-injection of some products or co-products (alkanes, alcohols, CO, water...) in the inlet gas would provide very useful information about the reaction mechanism. Co-injection studies have been performed for the FT reaction (as we have described in section 1.3.2), but not for the CO_2 hydrogenation. We have thus decided to adapt our experimental set-up for the co-injection of liquids and to perform some experiments to investigate the role of water and alcohols in the reaction.

Finally, the last objective of the thesis is to develop a reactor model and to simulate the global process. In order to validate such a model at reactor scale, we need experimental data obtained in an upscaled reactor, to verify that the kinetic model developed before is still valid when we change the reactor scale. We have thus performed some experiments in a higher scale reactor. This reactor is also equipped with a cooling system that allows a better control of the reactor temperature. Moreover, in the experimental set-up used, a CO line was already installed and this allowed us to perform experiments with co-injection of CO and thus to verify if the kinetic model developed before is still valid for CO/CO_2 mixtures. This is useful to simulate conditions of recycle of the unreacted gases that we will consider in the process simulations.

This chapter is thus focused on the experimental procedures followed to obtain the experimental data during the three different experimental studies just described.

2.2 Catalyst synthesis and characterization.

2.2.1 The choice of the catalyst.

As discussed in Chapter 1, iron-based catalysts are globally recognized as the most performing catalysts for the CO_2 hydrogenation. (Visconti et al., 2016; Rodemerck et al., 2013; Weatherbee and Bartholomew, 1984; Yan et al., 2000) The addition of promoters, such as potassium, can increase their performances towards the production of longer-chains hydrocarbons. (Visconti et al., 2016; Rodemerck et al., 2013; Baussart et al., 1987; Martinelli et al., 2014; Amoyal et al., 2017; Visconti et al., 2017) Among the different catalysts that have already been used to study the reaction in literature, we have chosen to synthesize a Fe-K catalyst supported on alumina, which is a good compromise between catalyst activity and feasibility of the synthesis process.

The K/Fe mass ratio was chosen equal to 0.35 with 20% of Fe, as in the works of Kim and Hwang. (Kim et al., 2006; Hwang et al., 2001)

2.2.2 Protocol of synthesis of the catalyst.

The catalyst used in this work is thus an iron-based catalyst promoted with K, that we synthesized by wet impregnation of the alumina support. A γ-Al_2O_3 (Puralox SCCa 150-200 from Sasol) is used as support. The support is impregnated with a water solution of K_2CO_3 and $Fe(NO_3)_3 9H_2O$ in order to reach the nominal composition of $20Fe/7K/100Al_2O_3$. Information about the chemicals used are reported in Table A.1. The solution is dried in a rotary evaporator for 3 hours at 50°C and atmospheric pressure, then temperature is increased to 80°C and vacuum is created (200 mbar) and kept for 4.5 hours. After collection, the solid product is dried at 100°C for 12 hours under controlled air flow (675 Nml/min). Finally, the catalyst is calcined at 500°C under air flow for 12 hours. A summary of the synthesis protocol is reported in Figure 2.1. This protocol was taken from the work of Kim (Kim et al., 2006) and modified to reach better stability of the catalyst.

The catalyst is then sieved and only particles between 70 and 160 µm are selected to grant an homogeneous distribution of the particle size to avoid too high pressure drops. Too big particles are excluded to avoid limitations of internal mass or heat transport. Before use in the reactor, the catalyst is reduced ex-situ at 450°C for 24 hours under 40% H_2/N_2 flow.

The catalyst used during the thesis comes from a single batch of calcined catalyst. Small quantities of this catalyst were reduced from time to time and used in the reaction.

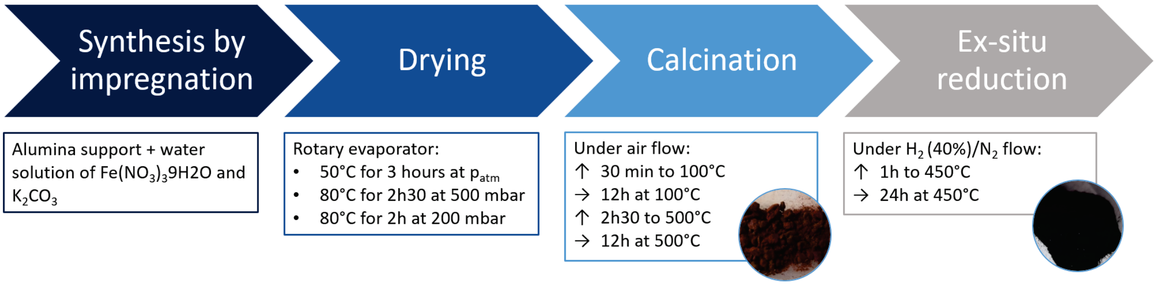

Figure 2.1: Description of the optimized protocol for catalyst synthesis.

2.2.3 Catalyst characterization.

Catalysts were characterized by using different techniques, described in the following.

2.2.3.1 Brunauer-Emmett-Teller (BET) Surface Area Analysis and Barrett-Joyner-Halenda (BJH) Pore Size and Volume Analysis.

BET and BJH are techniques used to determine specific surface area and pore size distribution of porous materials, thanks to nitrogen multilayer adsorption. Analysis were performed in CEA with the use of a Micromeritics TRI STAR 2. The sample needs to be pretreated before the analysis, in order to remove all contaminants. The solid is pretreated at 350°C for 4 hours under vacuum. After pretreatment the solid is cooled under vacuum to cryogenic temperature. Nitrogen is used as adsorptive and dosed to the solid in controlled increments. Once pressure is equilibrated, the quantity of gas adsorbed at each pressure is calculated, obtaining an adsorption isotherm. From the adsorption isotherm, the quantity of gas required to form a mono-layer over the external surface of the solid is obtained and then the surface area can be calculated using the Brunauer, Emmett and Teller equation. (Brunauer et al., 1938) Gas pressure is further increased incrementally so that gas can condense in pores. When all pores are filled with liquid, the gas pressure is reduced incrementally, allowing the condensed gas to evaporate from the system. Information about pore volume and pores size can be obtained from adsorption and desorption isotherms, by using the Barrett, Joyner and Halenda method. (Barrett et al., 1951)

2.2.3.2 Laser granulometry analysis.

Laser granulometry allows the measurement of particle size distribution of a solid sample. The analysis was performed at CEA using a MALVERN Mastersizer 2000 on a sample suspended in ethanol as liquid dispersant. This technique is based on diffraction and scattering of a light from a laser, which is scattered by the particles. According to the size and the chemical nature of the material, the interaction of the light with the particles is different and the diffraction detected is different. The diffraction pattern obtained is used to measure the particle size.

2.2.3.3 Inductively coupled plasma - Optical Emission Spectrometry (ICP-OES).

The catalyst composition was determined by ICP-OES. This technique is ideal for the analysis of metals in solutions. It uses a plasma induced by a high frequency generator as source of radiation. Analysis were performed at Ircelyon. The sample is first dissolved in a mixture of acids (sulphuric acid, nitric acid and hydrofluoric acid), then nebulized in an inductively coupled Ar plasma at very high temperatures (9000 K) where it is vaporized and analyte species are atomized, ionized and thermally excited. An optical emission spectrometer is used to detect and quantify the analytes, by measuring the intensity of the radiation generated at the characteristic wavelength specific for the considered element. From the measure of radiation intensity, concentrations can be obtained by comparison with calibration samples.

2.2.3.4 Temperature programmed reduction (TPR).

Temperature-programmed reduction is a widely used technique to study the reducibility of metal oxides surface. A reducing gas flows over the sample and a TCD detector is used to measure changes in thermal conductivity of gas stream. TPR experiments were carried out in CEA using a Autochem II-HP by Micromeritics. The sample was reduced under 5% H_2/Ar from 30 to 900°C with a ramp of 10°C/min.

2.2.3.5 X-ray diffraction (XRD).

X-ray diffraction is a technique used to study the crystallographic structure of a solid. It is based on irradiation of the material with X-rays that are generated in a cathode tube and directed to the sample. While the sample and the detector are rotated, the intensity and scatter angles of the reflected X-rays are recorded. Peaks appear when the geometry of the incident

X-rays impinging the samples satisfies the Bragg equation. (Bragg and Bragg, 1913) XRD analysis were performed in Centre de Diffractométrie Henri Longchambon in University of Lyon, using a Bruker D8-Advance diffractometer, equipped with a Bragg-Brentano $\theta - \theta$ goniometer, a Cu anti-cathode X-ray tube (40 kV, 40 mA) and a linear energy dispersive detector (Bruker LynxEye-XE). The angular range considered goes from 5 to 70° and it is measured in 45 minutes.

2.2.3.6 Mössbauer spectroscopy.

Mössbauer spectroscopy is a widely used technique for Fe samples, as it can give information about its valence state and can help in the identification of oxide phases based on their magnetic properties. It is based on a combination of the Mössbauer effect and Doppler shifts. It consists in measuring the difference between energy levels of the atomic nucleus which depend on the number and state of the surrounding electrons. These energy levels are determined by measuring absorption of γ-rays. Mössbauer spectroscopy was performed at the Laboratoire de Chimie de Coordination (LCC) in Toulouse using a constant-acceleration conventional spectrometer with a 1.85 GBq source of ^{57}Co in Rh matrix. Spectra were obtained at 80 and 300 K. Lorentzian curves were assumed for deconvolution of spectra based on least-square fitting techniques by Recoil Mössbauer Analysis Software and four parameters were identified: chemical shift (δ), quadrupole splitting (Δ), magnetic field (H) and percentage of site population (R). Responses were identified by comparison with literature data.

2.2.3.7 Transmission electron microscopy (TEM).

Transmission electron microscopy is a technology based on an accelerated beam of electrons that passes through a thin material and allows to gain information about the structure and the morphology of the material.

TEM images of the catalyst have been obtained by using a JEOL 2100F microscope working at 200 kV and used in the traditional TEM mode or in STEM-HAADF mode. Samples have been deposed after sieving on a Cu grid, coated with an ultra-fin carbon layer. For the EDS spectroscopy, a detector by Oxford Instruments has been used.

2.2.3.8 Thermogravimetric analysis (TGA).

Thermogravimetric analysis is an analytic method that allows to gain information about physical-chemical phenomena of a sample, by measuring the mass changes over time while the sample is exposed to changes of temperatures.

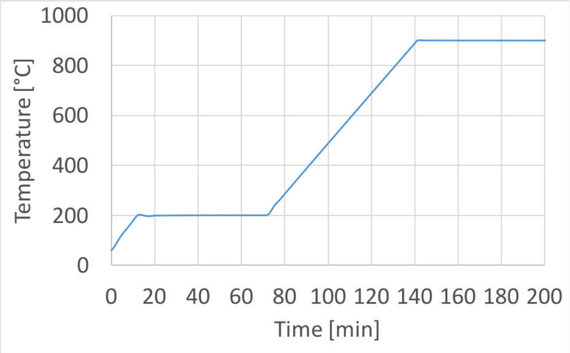

Figure 2.2: Temperature profile of the thermogravimetric analysis.

The analysis was performed using a thermobalance Setsys by SETARAM, under a flow of 50 Nml/min of compressed air. The temperature profile of the analysis is reported in Figure 2.2. Temperature was increased to 200°C with a ramp of 10°C/min and kept to 200°C for 1 h. Then, the temperature was further increased to 900°C with the same temperature ramp. The mass changes of the sample were measured during the analysis.

2.3 Experimental study in laboratory-scale fixed-bed reactor.

2.3.1 Literature overview about kinetic studies and objectives of the kinetic experimental study.

As already discussed in Chapter 1, not a lot of information is available about experimental kinetic studies of the CO_2 hydrogenation reaction over Fe-based catalysts. The effects of contact time and temperature were studied by different authors. (Riedel et al., 2001; Willauer et al., 2013; Nakhaei Pour and Housaindokht, 2017; Najari et al., 2019). Iglesias et al. also studied the effect of H_2/CO_2 ratio. (Iglesias Gonzalez et al., 2015) These studies, even if compounds until 20 C atoms are considered, do not give enough details about the hydrocarbons distribution (for example no information about the O/P ratio is given). A more detailed study of the effects of operating parameters is given by Visconti et al. (Visconti et al., 2017) where effects of temperature, total pressure, contact time and H_2/CO_2 ratio are analysed and hydrocarbons distribution is also discussed.

However, these studies are not detailed enough for our purpose. Water phase is generally not analysed, but in our case we observed it to be an important part of the obtained products, thus it cannot be neglected. Moreover, in order to have good experimental data, exploitable for the development of a detailed kinetic model, it is necessary to have an effective analytic protocol that allows the quantification of all the main products obtained in both gaseous and liquid phases, by distinguishing alkanes and alkenes, as well as linear and branched chains.

Thus, the reaction was experimentally studied in a laboratory-scale fixed-bed reactor with the aims to: 1) verify the stability of the catalyst during long-term runs; 2) develop an analytic protocol that allows the identification and quantification of the products obtained in all the phases; 3) study the effects of different operating parameters on the catalytic performances; 4) obtain experimental data to develop a kinetic model; 5) acquire information about the reaction mechanism.

2.3.2 Experimental protocol.

2.3.2.1 Description of the experimental set-up.

The experimental bench used for the lab-scale kinetic study was assembled at CP2M (Laboratory of Catalysis, Polymers, Processes and Materials) in University of Lyon.

A flow diagram of the experimental bench is shown in Figure 2.3. It is divided into four zones:

1. Gas feeding
2. Reactor
3. Heavy products condensation
4. Analytic chain

The feed gases (CO_2, H_2 and N_2) flows are regulated by mass flow regulators from Bronkhorst (1) able to regulate gas flows until 150 Nml/min. Gas bottles are supplied by AirLiquide and have purities $\geqslant$99.999%. Gases are then mixed together and pre-heated by passing through an electric resistance (6), before entering in the reactor.

The reactive zone consists in an oven that allows the regulation of temperature via electric resistances (9). The reactor is a stainless steel tube with 6 mm inner diameter and total length

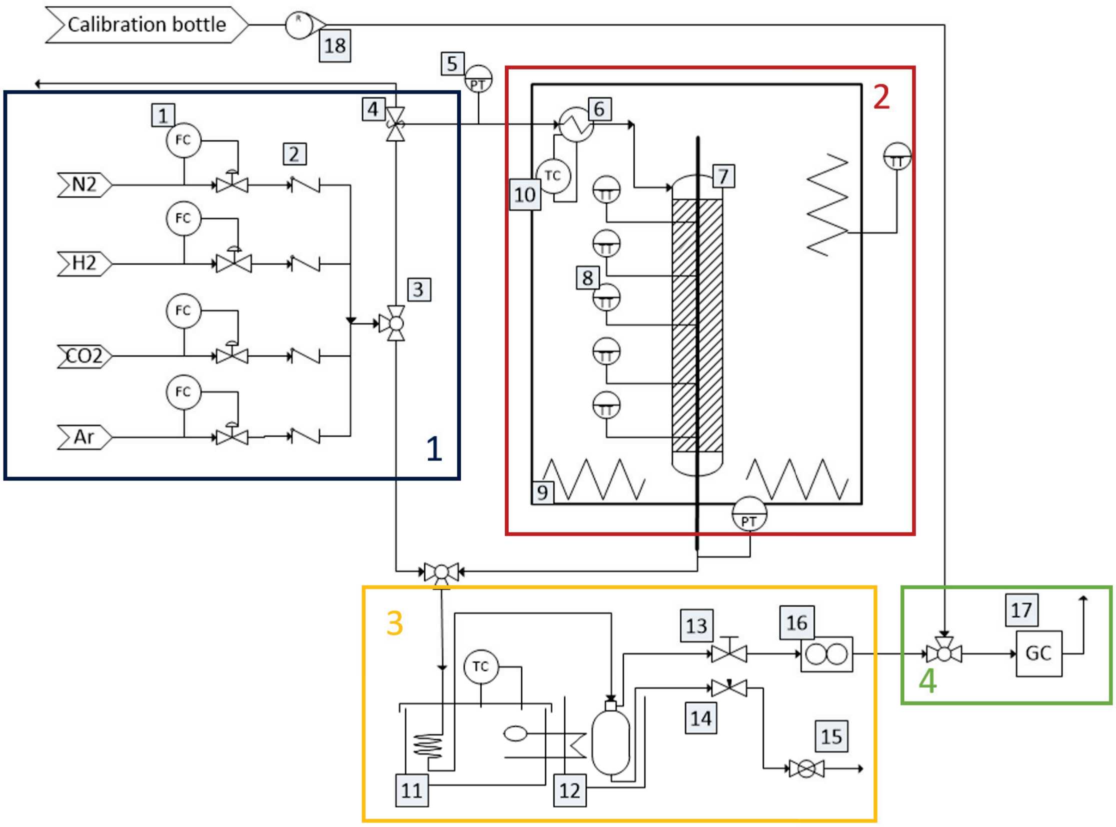

Figure 2.3: Process flow diagram of the experimental set-up. 1. Flows controller; 2. Check valves; 3. Three-way globe valve; 4. Security valve; 5. Pressure indicator; 6. Heater; 7. Fixed-bed reactor; 8. Temperature indicator; 9. Electric resistance; 10. Temperature controller; 11. Thermoregulated bath (water+ethylene glycol); 12. Cold trap; 13. Membrane pressure regulator; 14. Needle valve; 15. Bleed valve; 16. Coriolis mass flowmeter; 17. Gas chromatogram; 18. Rotameter.

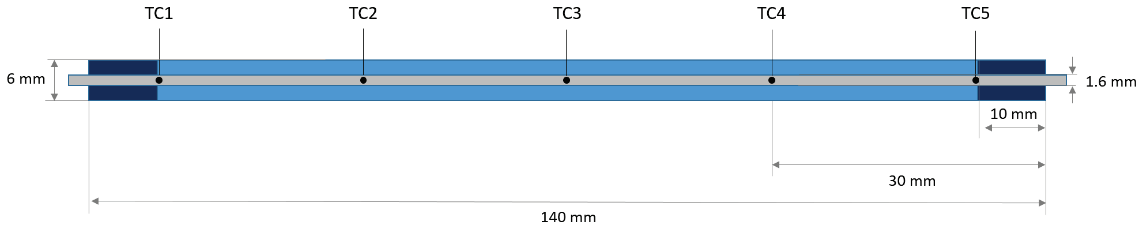

Figure 2.4: Scheme of reactor configuration in a typical run.

of 140 mm. The reactor is filled up with a variable mass of catalyst according to the experiment. The catalyst is in its pre-reduced form. SiC (with particle size of 100 µm) is added as inert to complete the total length of the reactor. A thermowell containing a thermocouple with multiple points of measure (5 points of measure, each 30 mm) provided by TC Direct (external diameter of 1.6 mm) is placed inside the reactor to follow the temperature axial profile along the reactor. A scheme of the reactor structure is given in Figure 2.4. Reactor pressure is controlled with a diaphragm pressure regulator (13) provided by Swagelok, able to work between 0 and 34.4 barg. Pressure is measured at the inlet and outlet of the reactor with pressure transmitters (5) provided by DeltaOHM, with a maximum operating pressure of 60 bara.

Outlet gas passes through the condensation unit (11) carried out by means of an LT eco-cool

150 temperature-regulated bath by Grant, filled up with a mixture of water and ethylene-glycol. In this unit, temperature is set at 5°C so that the heaviest products and water can condense. Pressure is the same as that at the reactor outlet. Liquid products are collected in a cold trap (12) that has a volume of 150 ml and is emptied each 10 to 50 hours, according to the experiment conditions. The two-phase solution obtained is passed through a separating funnel to separate water and organic phases.

Both phases are then analysed by GC. The non-condensed gases pass through a Coriolis Mini Cori-Flow M13 mass flow-meter by Bronkhorst (16) and are analysed with an on-line GC system (17) Agilent 6890 GC. Details about the chemicals used are given in Appendix A. Description of the analytic protocol is given in the next section.

2.3.2.2 Analytic protocol.

As explained before, the products of the reaction are collected in three phases (gaseous, organic and water phases). These phases are all analysed by gas chromatography. On the first experiments, sample were analysed via gas chromatography–mass spectrometry (GC-MS) that allows the identification of the peaks.

Gaseous products.

Gaseous products are analysed with an on-line GC, equipped with a Supelco Carboxen-1010 PLOT Capillary GC Column for the analysis of the non-condensable gases detected with TCD and an Agilent JW CP-PoraBOND Q GC Column for the analysis of the light gaseous HCs detected with FID. N_2 is used as internal standard, while He is the carrier gas. The method used for the analysis is described in detail in Appendix B.

The peaks observed in chromatograms correspond to the different products obtained. Peaks were identified by GC-MS. Figure 2.5 reports the chromatograms for the gaseous phase. Non-condensable products (H_2, N_2, CO, CH_4 and CO_2) are detected by TCD, while light gases (from C_2 to C_9), as well as some short oxygenates, are detected from FID. Among the FID detected products, for each C number the highest peak corresponds to the linear olefin, the one right next to it corresponds to the linear paraffin. The peaks between one linear olefin and the following one represent branched chains (both olefinic and paraffinic) or oxygenated products (such as alcohols or ketons).

Liquid products.

The liquid organic phase is analysed by off-line GC equipped with FID detector. For each sample, 500 µl of methyl-cyclohexane are added as internal standard to 500 µl of phase. An Optima 5-HT GC Column is used to separate heavy HCs.

Compounds in water phase are separated by using an Agilent JW DB-HeavyWAX GC Column. For each sample, 500 µl of water phase are added to 500 µl of acetonitrile as internal standard.

In some operating conditions at low conversion, the liquid obtained was not enough to separate the two phases by decanting. In these cases, methyl-cyclohexane is added as solvent to the liquid phase, so that organic compounds can dissolve into it, then the two phases are separated by decanting and analysed by GC.

Figure 2.6 reports the chromatograms of the organic and water phases. In the liquid organic phase, a variety of peaks are detected. Again, the highest peaks represent linear olefins and linear paraffins. The small peaks between them can represent branched olefins and paraffins or aromatics chains.

In water phase, mainly linear aldehydes, ketons, alcohols and carboxylic acids from C_1 to C_6 are observed. Some branched oxygenates were also observed and are represented by the small non-identified peaks in Figure 2.6-b).

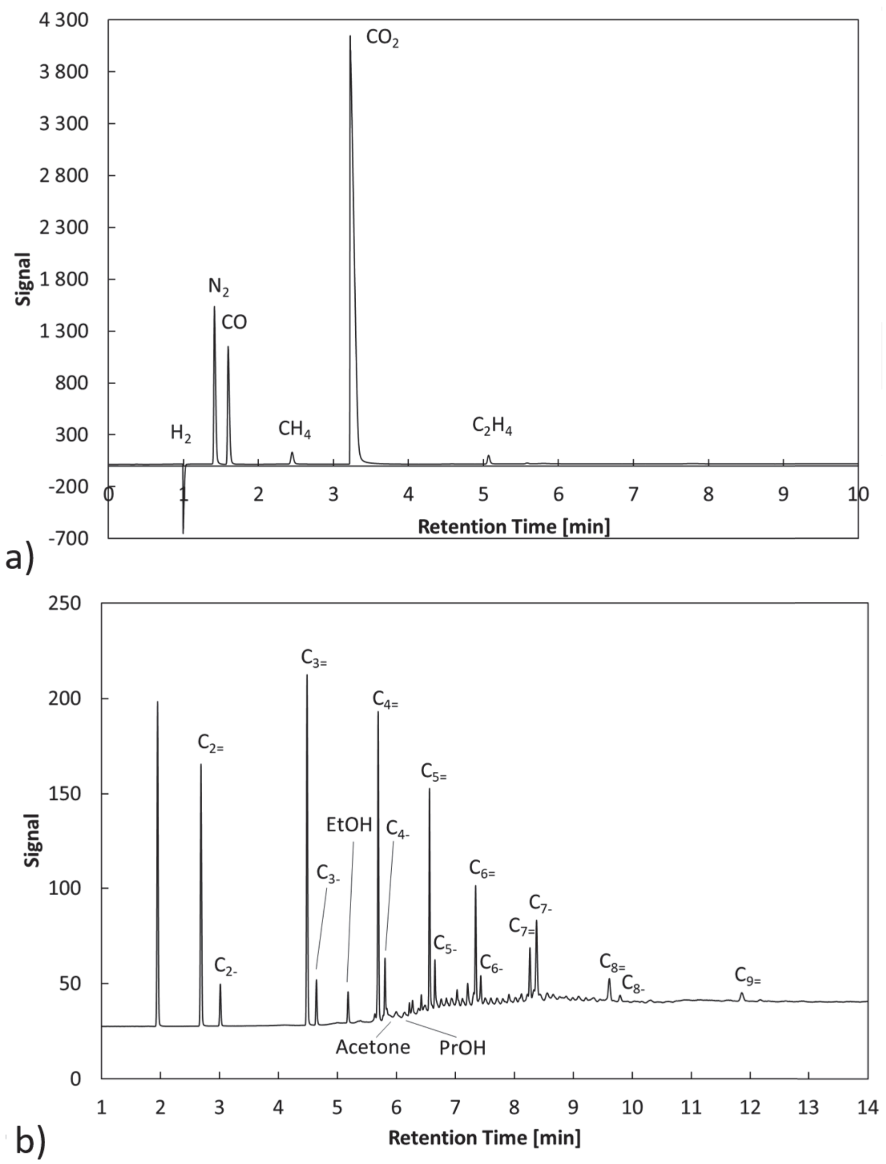

Figure 2.5: Chromatograms of the gaseous phase: a) products detected by TCD; b) products detected by FID.

A two-dimensional gas chromatography analysis was also performed on one sample of organic and water phases and species were identified by mass spectrometry. The analysis was performed by the CATREN team in Ircelyon. Two columns were used, the first with medium polarity and the second one completely apolar. Details about the experimental conditions applied are reported in Appendix B. The chromatograms of organic and water phases are reported respectively in Figures 2.7 and 2.8.

For the organic phase, the x axis represents the separation as function of the C number (according to temperature gradient of the oven), while the y axis represents the separation according to the polarity of the molecule. We observe different categories of products: alkanes, alkenes, aromatics, ketons, alcohols and carboxylic acids. For non-oxygenated products, chains from 9 to 32 C atoms are observed. Heavier compounds are not eluted because the maximum temperature limit of the column is attained. For hydrocarbons and ketons, branched and linear species are identified. In particular, branched chains are eluted before the linear chains with the same C number, as it is expected. Among aromatics, different kinds of molecules have been identified: the aromatic rings are branched to ramified and linear chains; saturated cycles and

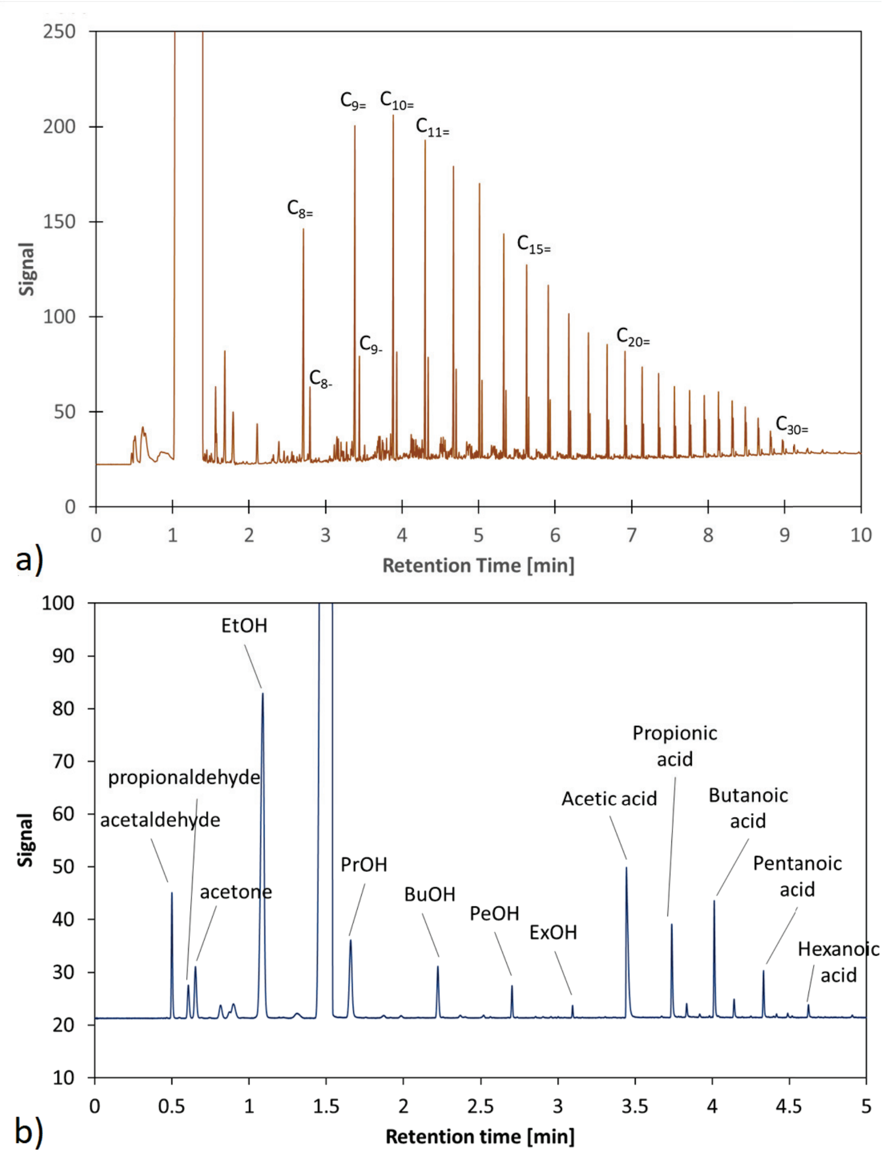

Figure 2.6: Chromatograms of a) organic phase; b) water phase.

double bonds can also be found on different aromatic species.

In water phase small oxygenated molecules are the main product, in particular short carboxylic acids, ketons and esters. Shorter molecules were not separated and were eluted within ethanol.

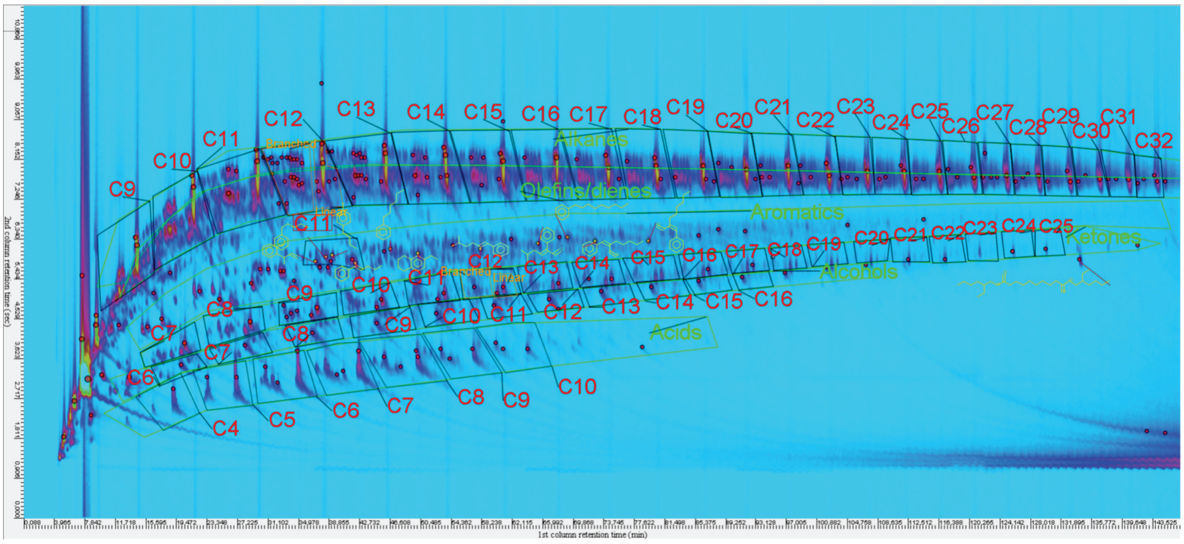

Figure 2.7: Chromatogram of the organic phase obtained after separation of products with a two-dimensional GC system.

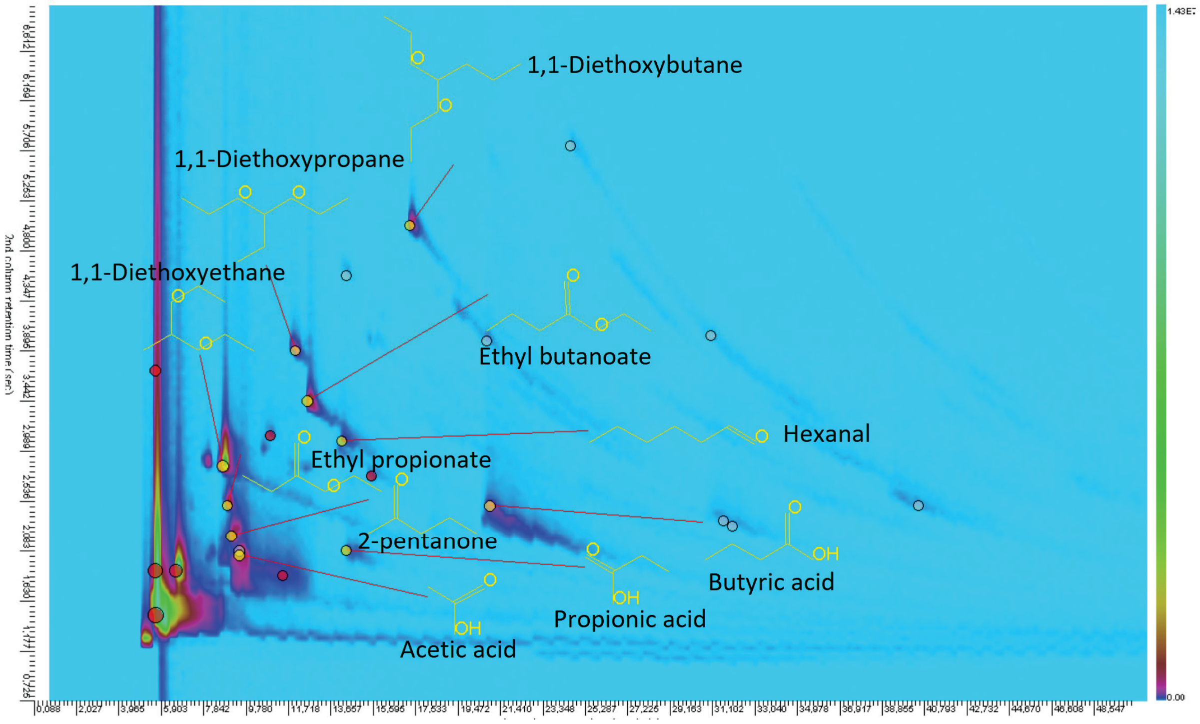

Figure 2.8: Chromatogram of the water phase obtained after separation of products with a two-dimensional GC system.

2.3.2.3 Data exploitation.

Gas phase.

For the quantification of the molar flows of the compounds observed in gaseous phase, N_2 is used as reference. Thus, the mole flow of each compound is calculated from Eq. 2.1:

$$F_{i,OUT} = MRF_{i,N_2}\frac{A_i}{A_{N_2}}F_{N_2,IN} \tag{2.1}$$

where A_i and A_{N_2} are respectively the peak areas of compound i and N_2, $F_{N_2,IN}$ is the mole flow of N_2 and MRF_{i,N_2} is the molar response factor of compound i referred to N_2. Response factors are estimated from calibration (details are given in Appendix B). Mass flows are then calculated with Eq. 2.2:

$$\dot{m}_{i,OUT} = F_{i,OUT} M_i \tag{2.2}$$

where M_i is the molar mass of compound i.

because of the utilisation of He as vector gas, the sensitivity to H_2 is low and its peaks are small and hard to integrate. Moreover, the relation between peak area and H_2 concentration resulted to be not linear in the range of conditions used, thus H_2 flow is estimated from Eq. 2.3:

$$\dot{m}_{H_2} = \dot{m}_{tot} - \sum_{i=1}^{n_{gas}} \dot{m}_i \tag{2.3}$$

where $\dot{m}_{tot}$ represents the total gaseous mass flow measured by the Coriolis flow-meter at the reactor outlet after condensation and $\dot{m}_i$ is the mass flow of compound i in gas phase. This generates high incertitudes on H_2 quantification, as it accumulates the error of every species in gaseous phase. Moreover, part of the total water is not condensed and exits with the gaseous phase; this water is not quantified in any ways, as our GC detectors could not detect it. The so-estimated H_2 mass flow thus includes the mass of eventual non-identified products and non-condensed water.

Liquid phases.

The quantification of products in organic and water phases follows the same procedure, with response factors referred to the solvent added (methyl-cyclohexane for organic phase and acetonitrile for water phase) and mass flows calculated with Eq. 2.4:

$$m_{i,OUT} = RF_{i,solv} \frac{A_i}{A_{solv}} m_{solv,inj} \frac{m_{phase,tot}}{m_{phase,inj}} \tag{2.4}$$

where $m_{i,OUT}$ is the mass of compound i at the reactor outlet, $m_{solv,inj}$ is the mass of solvent injected and $m_{phase,tot}$ and $m_{phase,inj}$ are the mass of water or organic phase respectively total and injected. The mass of water in water phase $m_{H_2O,wat}$ is estimated from Eq. 2.5:

$$m_{H_2O,wat} = m_{wat} - \sum_{i=1}^{n_{wat}} m_{i,wat} \tag{2.5}$$

where m_{wat} is the total water phase mass and $m_{i,wat}$ is the mass of compound i in water phase.

With this experimental protocol, we are able to obtain a quite detailed quantification of the products and mass balances are closed within a relative error $\leqslant 15\%$ for total mass and $\leqslant 10\%$ on C mass (see Figure 2.9). The error is calculated as follows:

$$error\% = |m_{OUT} - m_{IN}|/m_{IN} \tag{2.6}$$

The highest error is on total H mass, due to the high incertitudes related to water and hydrogen mass estimations. However, as C and global mass balances have relatively low errors and, considered the number of species involved, we can consider the analytic protocol as acceptable.

From the obtained mole flows, CO_2 conversion, CO selectivity and total HCs selectivity can be calculated according to Eqs. 2.7-2.9:

$$\chi_{CO_2} = \frac{F_{CO_2,IN} - F_{CO_2,OUT}}{F_{CO_2,IN}} \tag{2.7}$$

$$S_{CO} = \frac{F_{CO,OUT}}{F_{CO_2,IN} - F_{CO_2,OUT}} \tag{2.8}$$

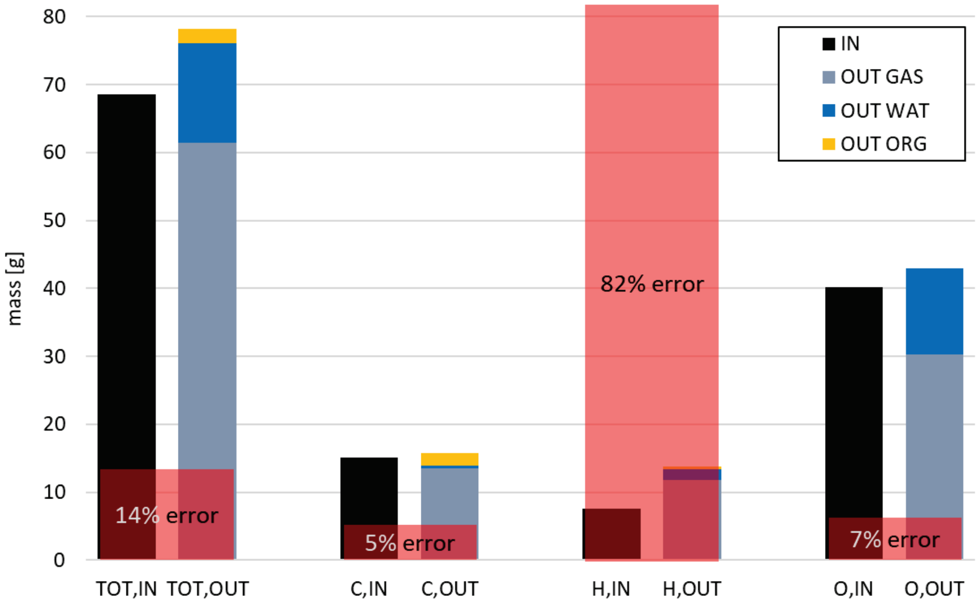

Figure 2.9: Global mass balance and elemental mass balance over C, H and O.

$$S_{HCs} = \frac{\sum_i iF_{i,OUT}}{F_{CO_2,IN} - F_{CO_2,OUT}} \tag{2.9}$$

To describe the HCs distribution, lumped molar fractions X_i (of methane, methanol, C_2-C_4 olefins, C_{5+} olefins, C_2-C_4 paraffins, C_{5+} paraffins, C_2-C_6 oxygenates) are calculated among the HCs pool, according to Eq. 2.10:

$$X_i = \frac{F_{i,OUT}}{F_{HCs,OUT}} \tag{2.10}$$

where $F_{HCs,OUT}$ is the mole flow of all products excluding CO.

2.3.3 Choice of operating conditions.

To have enough information to develop a kinetic model and to gain insights about the reaction mechanism, it is important to investigate the effects of a variety of operating parameters. From previous studies, it appears that contact time, temperature and partial pressures of H_2 and CO_2 predominantly control the synthesis rate and the hydrocarbons distribution. Total pressure is found to have less influence.

Fixed-bed reactors at laboratory-scale for the CO_2 hydrogenation over Fe-based catalyst are generally operated at the conditions reported in Table 2.1. (Sai Prasad et al., 2008; Visconti et al., 2011; Hwang et al., 2019; Choi et al., 2017; Hong et al., 2001; Kim et al., 2006; Riedel et al., 1999; Wang et al., 2013; Hwang et al., 2001; Liu et al., 2018; Xie et al., 2017; Lee et al., 2003; Rodemerck et al., 2013)

We have chosen as reference conditions 300°C, 15 bars, H_2/CO_2 ratio of 3 and GHSV of 2000 Nml/g_{cat}/h (Condition 1 of Table 2.2). GHSV is expressed here as the volume flow of reactants in Nml/h per mass of catalyst.

We decided then to investigate the effects of the following operating parameters: temperature, total pressure, H_2/CO_2 ratio and contact time (which is expressed as τ_{mod}, defined as the reciprocal of the GHSV, as in Eq. 2.11).

$$\tau_{mod} = \frac{m_{cat}}{\dot{V}_{IN}} \tag{2.11}$$

Table 2.1: Experimental conditions generally applied for the CO_2 hydrogenation over Fe-based catalyst.

Parameter	Unit	Range
T	°C	265-500
H_2/CO_2	mol/mol	3
p	bar	6-20
GHSV	$Nml/g_{cat}/h$	1200-5000

For each condition tested, only one parameter is varied while all the others are kept constant. The set of conditions tested is reported in Table 2.2. Contact time is varied by changing the GHSV in the range between 500 and 7000 $Nml/g_{cat}/h$. Temperature is varied between 250 and 350°C and total pressure between 10 and 25 bar. The H_2/CO_2 ratio is varied between 3 and 24, by changing the H_2 or CO_2 partial pressures and keeping constant the total pressure, while using N_2 to fill up the total flow.

Table 2.2: Experimental conditions applied in the work.

Condition	GHSV [Nml/g/h]	T [°C]	P_{tot} [bar]	p_{H2} [bar]	p_{CO2} [bar]	H_2/CO_2 ratio [-]	N_2 fraction [mol/mol]
1	2000	300	15	10.8	3.6	3	0.04
2	500	300	15	10.8	3.6	3	0.04
3	800	300	15	10.8	3.6	3	0.04
4	1000	300	15	10.8	3.6	3	0.04
5	1400	300	15	10.8	3.6	3	0.04
6	1800	300	15	10.8	3.6	3	0.04
7	2500	300	15	10.8	3.6	3	0.04
8	3600	300	15	10.8	3.6	3	0.04
9	7000	300	15	10.8	3.6	3	0.04
10	2000	250	15	10.8	3.6	3	0.04
11	2000	275	15	10.8	3.6	3	0.04
12	2000	325	15	10.8	3.6	3	0.04
13	2000	350	15	10.8	3.6	3	0.04
14	2000	300	15	10.8	0.45	24	0.25
15	2000	300	15	13.5	0.90	15	0.04
16	2000	300	15	10.8	0.90	12	0.22
17	2000	300	15	7.2	0.90	8	0.46
18	2000	300	15	10.8	1.80	6	0.16
19	2000	300	15	10.8	2.70	4	0.10
20	2000	300	10	7.2	2.40	3	0.04
21	2000	300	20	14.4	4.80	3	0.04
22	2000	300	25	18.0	6.00	3	0.04

Each experimental campaign consists in:

- reactor loading with a mass of catalyst between 1.5 and 4 g;
- activation of the catalyst under H_2/CO_2 flow for 48 hours in the following conditions: H_2/CO_2 molar inlet ratio of 3, 15 bars, 300°C and 2000 $Nml/g_{cat}/h$, with 4% of N_2;
- catalytic tests at different operating conditions.

Each test is run for 20 to 24 hours, so that stationary state is reached and enough liquid phase is produced. Then, the system is put under N_2 flow for 1 hour, so that all the liquid can be collected in the cold trap. Finally, the liquid is collected by emptying the cold trap and the two phases are separated by decanting and respectively analysed. Operating conditions are then changed to start a new test. Periodically, a test in reference conditions is performed to verify that the catalyst is still active and in its stationary regime. Once the catalyst starts to lose its activity, the reaction is stopped, the reactor is de-charged and a new campaign is started.

To obtain trusted and reliable results, every operating condition set should be repeated at least twice. However, considering that each test requires at least 24 hours, it was not possible to repeat each condition more than one time. For some of them, a short experiment (2 to 3 hours) was conduced, waiting for the stationary state to be reached and analysing only the gaseous phase.

Uncertainties were calculated as standard deviations on the average values. For conditions that were not repeated, standard deviations of the reference point were applied. Table 2.3 reports the values of standard deviations calculated on the mole flows of each compound considered for the tests in reference conditions. We can observe that the highest standard deviation is the one relative to H_2 because of the way H_2 mass is estimated, as explained above. All the other standard deviations are <1%, indicating the good repeatability of the experiments.

Table 2.3: Standard deviations (absolute) calculated on mole flows of each compound considered for the tests in reference conditions. Values that equal zero represent non detected compounds in that particular test.

	C4.6-P1 [mol/h]	C4.7-P1 [mol/h]	C6.1-P1 [mol/h]	C5.1-P1 [mol/h]	C5.2-P1 [mol/h]	Standard deviation [%]
N_2	$1.23x10^{-2}$	$1.32x10^{-2}$	$1.32x10^{-2}$	$1.33x10^{-2}$	$1.33x10^{-2}$	0.04%
H_2	$3.35x10^{-1}$	$3.39x10^{-1}$	1.74	$2.65x10^{-1}$	$2.67x10^{-1}$	64.49%
H_2O	$4.57x10^{-2}$	$4.66x10^{-2}$	$3.21x10^{-2}$	$3.93x10^{-2}$	$3.49x10^{-2}$	0.64%
CO_2	$5.43x10^{-2}$	$5.39x10^{-2}$	$5.73x10^{-2}$	$5.52x10^{-2}$	$5.62x10^{-2}$	0.14%
CO	$2.66x10^{-3}$	$2.96x10^{-3}$	$2.64x10^{-3}$	$2.90x10^{-3}$	$3.52x10^{-3}$	0.04%
CH_4	$1.78x10^{-3}$	$1.73x10^{-3}$	$2.28x10^{-3}$	$2.65x10^{-3}$	$1.93x10^{-3}$	0.04%
$C_{2,=}$	$6.87x10^{-4}$	$6.47x10^{-4}$	$6.77x10^{-4}$	$8.53x10^{-4}$	$5.64x10^{-4}$	0.01%
$C_{2,-}$	$1.13x10^{-4}$	$1.05x10^{-4}$	$1.20x10^{-4}$	$1.47x10^{-4}$	$1.03x10^{-4}$	0.00%
$C_{3,=}$	$5.95x10^{-4}$	$5.52x10^{-4}$	$5.88x10^{-4}$	$7.23x10^{-4}$	$4.59x10^{-4}$	0.01%
$C_{3,-}$	$8.13x10^{-5}$	$7.77x10^{-5}$	$8.54x10^{-5}$	$9.61x10^{-5}$	$6.37x10^{-5}$	0.00%
C3	$2.00x10^{-5}$	$1.48x10^{-5}$	0	$1.90x10^{-5}$	$1.79x10^{-5}$	0.00%
$C_{4,=}$	$3.42x10^{-4}$	$3.18x10^{-4}$	$3.32x10^{-4}$	$4.01x10^{-4}$	$2.50x10^{-4}$	0.01%
$C_{4,-}$	$5.51x10^{-5}$	$5.25x10^{-5}$	$5.58x10^{-5}$	$6.28x10^{-5}$	$4.10x10^{-5}$	0.00%
$C_{4,oth}$	0	0	0	0	0	0.00%
$C_{5,=}$	$1.94x10^{-4}$	$1.68x10^{-4}$	$1.82x10^{-4}$	$2.25x10^{-4}$	$1.40x10^{-4}$	0.00%
$C_{5,-}$	$3.37x10^{-5}$	$3.20x10^{-5}$	$3.19x10^{-5}$	$3.81x10^{-5}$	$2.53x10^{-5}$	0.00%
$C_{5,oth}$	$2.73x10^{-5}$	$1.91x10^{-5}$	$2.23x10^{-5}$	$3.01x10^{-5}$	$1.77x10^{-5}$	0.00%
$C_{6,=}$	$9.24x10^{-5}$	$8.29x10^{-5}$	$7.02x10^{-5}$	$1.06x10^{-4}$	$5.49x10^{-5}$	0.00%
$C_{6,-}$	$1.47x10^{-5}$	$1.38x10^{-5}$	$1.25x10^{-5}$	$1.58x10^{-5}$	$9.67x10^{-6}$	0.00%
$C_{6,oth}$	$7.88x10^{-5}$	$1.29x10^{-5}$	$1.69x10^{-4}$	$2.54x10^{-4}$	$1.52x10^{-4}$	0.01%
$C_{7,=}$	$8.72x10^{-5}$	$2.93x10^{-5}$	$2.71x10^{-5}$	$5.86x10^{-5}$	$3.24x10^{-5}$	0.00%
$C_{7,-}$	$2.16x10^{-5}$	$5.36x10^{-6}$	$5.68x10^{-6}$	$4.77x10^{-6}$	$6.41x10^{-6}$	0.00%
$C_{7,oth}$	$3.89x10^{-5}$	$1.11x10^{-5}$	$5.60x10^{-6}$	$2.49x10^{-5}$	$1.41x10^{-5}$	0.00%
$C_{8,=}$	$6.82x10^{-5}$	$2.74x10^{-5}$	$1.32x10^{-5}$	$3.38x10^{-5}$	$2.21x10^{-5}$	0.00%
$C_{8,-}$	$1.29x10^{-5}$	$4.41x10^{-6}$	$3.10x10^{-6}$	$6.57x10^{-6}$	$5.23x10^{-6}$	0.00%
$C_{8,oth}$	$4.21x10^{-5}$	$1.11x10^{-5}$	$4.24x10^{-6}$	$2.06x10^{-5}$	$1.18x10^{-5}$	0.00%
$C_{9,=}$	$5.56x10^{-5}$	$2.17x10^{-5}$	$1.11x10^{-5}$	$2.35x10^{-5}$	$2.25x10^{-5}$	0.00%
$C_{9,-}$	$1.14x10^{-5}$	$1.48x10^{-7}$	$1.78x10^{-6}$	$3.88x10^{-6}$	$3.88x10^{-6}$	0.00%
$C_{9,oth}$	$4.58x10^{-5}$	$1.38x10^{-5}$	$4.22x10^{-6}$	$7.54x10^{-5}$	$1.23x10^{-5}$	0.00%

$C_{10,=}$	4.14x10^{-5}	1.53x10^{-5}	6.45x10^{-6}	2.41x10^{-5}	1.48x10^{-5}	0.00%
$C_{10,-}$	1.20x10^{-5}	4.17x10^{-6}	2.24x10^{-7}	2.52x10^{-6}	4.43x10^{-6}	0.00%
$C_{10,oth}$	4.51x10^{-5}	1.15x10^{-5}	6.26x10^{-6}	6.44x10^{-5}	1.18x10^{-5}	0.00%
$C_{11,=}$	3.29x10^{-5}	1.22x10^{-5}	6.11x10^{-6}	1.15x10^{-4}	1.25x10^{-5}	0.00%
$C_{11,-}$	9.33x10^{-6}	2.48x10^{-6}	1.36x10^{-6}	3.52x10^{-5}	2.72x10^{-6}	0.00%
$C_{11,oth}$	3.31x10^{-5}	6.58x10^{-6}	2.96x10^{-6}	2.28x10^{-4}	3.01x10^{-5}	0.01%
$C_{12,=}$	2.81x10^{-5}	8.37x10^{-6}	4.23x10^{-6}	1.34x10^{-4}	8.15x10^{-6}	0.01%
$C_{12,-}$	7.60x10^{-6}	2.08x10^{-6}	1.09x10^{-6}	3.48x10^{-5}	2.06x10^{-6}	0.00%
$C_{12,oth}$	2.61x10^{-5}	4.66x10^{-6}	2.93x10^{-6}	1.34x10^{-4}	4.97x10^{-6}	0.01%
$C_{13,=}$	1.84x10^{-5}	6.22x10^{-6}	3.39x10^{-6}	1.09x10^{-4}	6.46x10^{-6}	0.00%
$C_{13,-}$	5.64x10^{-6}	1.48x10^{-6}	9.64x10^{-7}	3.72x10^{-5}	1.62x10^{-6}	0.00%
$C_{13,oth}$	1.88x10^{-5}	3.18x10^{-6}	1.64x10^{-6}	8.88x10^{-5}	3.09x10^{-6}	0.00%
$C_{14,=}$	1.44x10^{-5}	4.78x10^{-6}	2.58x10^{-6}	9.58x10^{-5}	5.31x10^{-6}	0.00%
$C_{14,-}$	4.51x10^{-6}	1.16x10^{-6}	7.19x10^{-7}	2.48x10^{-5}	1.34x10^{-6}	0.00%
$C_{14,oth}$	1.31x10^{-5}	2.27x10^{-6}	1.24x10^{-6}	6.67x10^{-5}	2.42x10^{-6}	0.00%
$C_{15,=}$	1.10x10^{-5}	3.41x10^{-6}	1.97x10^{-6}	7.18x10^{-5}	4.31x10^{-6}	0.00%
$C_{15,-}$	4.18x10^{-6}	1.01x10^{-6}	5.97x10^{-7}	2.08x10^{-5}	1.15x10^{-6}	0.00%
$C_{15,-}$	9.31x10^{-6}	1.49x10^{-6}	8.23x10^{-7}	4.61x10^{-5}	1.51x10^{-6}	0.00%
$C_{16,=}$	8.36x10^{-6}	2.66x10^{-6}	1.61x10^{-6}	5.26x10^{-5}	3.47x10^{-6}	0.00%
$C_{16,-}$	3.54x10^{-6}	7.50x10^{-7}	4.91x10^{-7}	1.56x10^{-5}	1.10x10^{-6}	0.00%
$C_{16,oth}$	6.13x10^{-6}	9.83x10^{-7}	5.80x10^{-7}	3.06x10^{-5}	1.20x10^{-6}	0.00%
$C_{17,=}$	6.58x10^{-6}	2.05x10^{-6}	1.30x10^{-6}	3.96x10^{-5}	2.84x10^{-6}	0.00%
$C_{17,-}$	2.80x10^{-6}	6.06x10^{-7}	4.00x10^{-7}	1.19x10^{-5}	8.86x10^{-7}	0.00%
$C_{17,oth}$	4.37x10^{-6}	4.26x10^{-7}	2.91x10^{-7}	2.33x10^{-5}	1.02x10^{-6}	0.00%
$C_{18,=}$	5.54x10^{-6}	1.62x10^{-6}	1.07x10^{-6}	2.74x10^{-5}	2.34x10^{-6}	0.00%
$C_{18,-}$	2.35x10^{-6}	5.61x10^{-7}	3.36x10^{-7}	9.07x10^{-6}	7.07x10^{-7}	0.00%
$C_{18,oth}$	3.12x10^{-6}	3.01x10^{-7}	1.47x10^{-6}	1.65x10^{-5}	6.32x10^{-7}	0.00%
$C_{19,=}$	4.41x10^{-6}	1.29x10^{-6}	7.59x10^{-7}	2.19x10^{-5}	1.98x10^{-6}	0.00%
$C_{19,-}$	1.89x10^{-6}	3.68x10^{-7}	2.34x10^{-7}	7.24x10^{-6}	6.18x10^{-7}	0.00%
$C_{19,oth}$	2.27x10^{-6}	1.92x10^{-7}	0	1.27x10^{-5}	2.35x10^{-7}	0.00%
$C_{20,=}$	5.47x10^{-6}	1.01x10^{-6}	6.28x10^{-7}	1.80x10^{-5}	1.71x10^{-6}	0.00%
$C_{20,-}$	0	3.14x10^{-7}	1.88x10^{-7}	6.07x10^{-6}	5.23x10^{-7}	0.00%
$C_{20,oth}$	1.66x10^{-6}	1.52x10^{-7}	0	1.02x10^{-5}	1.81x10^{-7}	0.00%
$C_{21,=}$	4.33x10^{-6}	7.98x10^{-7}	5.41x10^{-7}	1.48x10^{-5}	1.44x10^{-6}	0.00%
$C_{21,-}$	0	3.07x10^{-7}	1.85x10^{-7}	5.28x10^{-6}	4.30x10^{-7}	0.00%
$C_{21,oth}$	1.24x10^{-6}	5.38x10^{-8}	0	2.09x10^{-5}	1.11x10^{-7}	0.00%
$C_{22,=}$	3.70x10^{-6}	6.42x10^{-7}	4.62x10^{-7}	4.65x10^{-6}	1.21x10^{-6}	0.00%
$C_{22,-}$	0	3.06x10^{-7}	1.69x10^{-7}	4.40x10^{-7}	3.83x10^{-7}	0.00%
$C_{22,oth}$	8.44x10^{-7}	5.27x10^{-8}	2.14x10^{-8}	1.69x10^{-5}	4.32x10^{-8}	0.00%
$C_{23,=}$	2.83x10^{-6}	5.00x10^{-7}	3.96x10^{-7}	4.05x10^{-6}	1.01x10^{-6}	0.00%
$C_{23,-}$	0	2.48x10^{-7}	1.50x10^{-7}	3.52x10^{-7}	3.31x10^{-7}	0.00%
$C_{23,oth}$	5.19x10^{-7}	5.75x10^{-8}	0	1.34x10^{-5}	4.16x10^{-8}	0.00%
$C_{24,=}$	2.27x10^{-6}	3.91x10^{-7}	4.96x10^{-7}	3.72x10^{-6}	8.17x10^{-7}	0.00%
$C_{24,-}$	2.86x10^{-7}	2.21x10^{-7}	0	8.78x10^{-7}	2.74x10^{-7}	0.00%
$C_{24,oth}$	2.12x10^{-7}	5.02x10^{-8}	0	3.30x10^{-6}	0	0.00%
$C_{25,=}$	2.34x10^{-6}	5.13x10^{-7}	4.32x10^{-7}	6.28x10^{-6}	6.24x10^{-7}	0.00%
$C_{25,-}$	0	0	0	3.00x10^{-6}	2.26x10^{-7}	0.00%
$C_{25,oth}$	5.02x10^{-7}	4.68x10^{-8}	0	3.63x10^{-6}	0	0.00%
$C_{26,=}$	1.88x10^{-6}	3.96x10^{-7}	3.64x10^{-7}	4.76x10^{-6}	4.52x10^{-7}	0.00%
$C_{26,-}$	0	4.21x10^{-8}	0	2.68x10^{-6}	1.93x10^{-7}	0.00%
$C_{27,=}$	1.37x10^{-6}	2.87x10^{-7}	3.08x10^{-7}	3.22x10^{-6}	3.24x10^{-7}	0.00%

$C_{27,-}$	0	0	0	$2.34\text{x}10^{-6}$	$1.68\text{x}10^{-7}$	0.00%
$C_{28,=}$	$1.15\text{x}10^{-6}$	$2.11\text{x}10^{-7}$	$2.58\text{x}10^{-7}$	0	$2.43\text{x}10^{-7}$	0.00%
$C_{28,-}$	$4.80\text{x}10^{-7}$	$3.47\text{x}10^{-8}$	0	0	$1.54\text{x}10^{-7}$	0.00%
$C_{29,=}$	$9.99\text{x}10^{-7}$	$1.29\text{x}10^{-7}$	$2.16\text{x}10^{-7}$	0	$1.98\text{x}10^{-7}$	0.00%
$C_{29,-}$	$4.28\text{x}10^{-7}$	$3.25\text{x}10^{-8}$	0	0	$1.52\text{x}10^{-7}$	0.00%
$C_{30,=}$	$9.99\text{x}10^{-7}$	$7.98\text{x}10^{-8}$	0	0	0	0.00%
$C_{30,-}$	0	$2.92\text{x}10^{-8}$	0	0	0	0.00%
$C_{1,OH}$	$8.44\text{x}10^{-5}$	$1.01\text{x}10^{-4}$	$3.28\text{x}10^{-5}$	$2.05\text{x}10^{-4}$	$1.56\text{x}10^{-4}$	0.01%
$C_{2,OH}$	$2.62\text{x}10^{-4}$	$2.31\text{x}10^{-4}$	$1.57\text{x}10^{-4}$	$6.57\text{x}10^{-4}$	$1.35\text{x}10^{-4}$	0.02%
$C_{3,OH}$	$5.69\text{x}10^{-5}$	$4.77\text{x}10^{-5}$	$5.05\text{x}10^{-5}$	$1.06\text{x}10^{-4}$	$4.33\text{x}10^{-5}$	0.00%
$C_{4,OH}$	$6.50\text{x}10^{-6}$	$5.19\text{x}10^{-6}$	$2.51\text{x}10^{-6}$	$1.04\text{x}10^{-5}$	$2.34\text{x}10^{-6}$	0.00%
$C_{5,OH}$	$1.69\text{x}10^{-6}$	0	$1.27\text{x}10^{-6}$	$4.20\text{x}10^{-6}$	$3.54\text{x}10^{-6}$	0.00%
$C_{6,OH}$	0	0	$9.63\text{x}10^{-7}$	$3.00\text{x}10^{-6}$	$6.74\text{x}10^{-7}$	0.00%
$C_{2,COOH}$	$1.86\text{x}10^{-4}$	$2.45\text{x}10^{-4}$	$4.14\text{x}10^{-5}$	$1.82\text{x}10^{-4}$	$1.09\text{x}10^{-4}$	0.01%
$C_{3,COOH}$	$3.87\text{x}10^{-5}$	$4.84\text{x}10^{-5}$	$1.17\text{x}10^{-5}$	$3.44\text{x}10^{-5}$	$2.28\text{x}10^{-6}$	0.00%
$C_{4,COOH}$	$3.36\text{x}10^{-5}$	$3.89\text{x}10^{-5}$	$8.40\text{x}10^{-6}$	$2.72\text{x}10^{-5}$	$8.39\text{x}10^{-6}$	0.00%
$C_{5,COOH}$	$8.86\text{x}10^{-6}$	$9.38\text{x}10^{-6}$	$4.36\text{x}10^{-6}$	$6.70\text{x}10^{-6}$	0	0.00%
$C_{6,COOH}$	$2.43\text{x}10^{-6}$	$2.37\text{x}10^{-6}$	0	$9.79\text{x}10^{-6}$	0	0.00%
$C_{2,CHO}$	$2.57\text{x}10^{-5}$	$2.46\text{x}10^{-5}$	$5.59\text{x}10^{-5}$	$2.52\text{x}10^{-5}$	$1.20\text{x}10^{-5}$	0.00%
$C_{4,CHO}$	0	0	$3.20\text{x}10^{-5}$	0	0	0.00%
$C_{5,CHO}$	0	0	$7.07\text{x}10^{-6}$	0	0	0.00%
$C_{2,CO}$	$4.62\text{x}10^{-5}$	$4.43\text{x}10^{-5}$	$1.25\text{x}10^{-5}$	$7.33\text{x}10^{-5}$	$4.33\text{x}10^{-5}$	0.00%

2.3.3.1 Verifying that kinetic regime is dominant.

In order to determine the intrinsic kinetics of the reaction, it is necessary to work in the conditions where the kinetic regime is dominant. That means that inter-phase and intra-phase concentration and temperature gradients need to be absent, the reactor has to be in isothermal conditions and the flow pattern has to be ideal.

Isothermality of the reactor. The isothermality of the reactor is verified experimentally. A typical axial temperature profile along the reactor during stationary regime can be found in Fig. 3.12. It can be observed that the maximum measured ΔT is <5°C, thus the reactor can be considered isothermal.

Plug-flow operation. To ensure a plug-flow pattern, axial dispersion should be excluded. To verify the absence of axial dispersion, the Mears and Gierman criterion (Mears, 1971b; Gierman, 1988) is used (Eq. 2.12):

$$\frac{L_{bed}}{d_P} >> \frac{8}{Bo} n\, ln\left(\frac{1}{1-\chi_{CO2}}\right) \tag{2.12}$$

where Bo is the Bodenstein number, defined as in Eq. 2.13 and calculated from the correlation of Eq. 2.14. (Wakao et al., 1979)

$$Bo = \frac{u_0 d_P}{D_{CO_2,ax}} \tag{2.13}$$

$$\frac{1}{Bo} = \frac{\epsilon_{bed} D_{CO_2,m}}{\tau_{bed} d_P u_0} + 0.5 \tag{2.14}$$

The estimation of diffusion coefficients is described in Appendix C. Table 2.4 reports the values of calculated criteria for CO_2 in reference conditions, showing that the calculated values are far from the limit ones and thus plug-flow operation is allowed.

Absence of diffusion limitations. The absence of diffusional limitations were verified by the use of several criteria developed for catalytic reactions in fixed bed reactors. The general condition for considering that transport limitations are negligible is that the effect on the concentration gradient is less than 5%.

To verify that internal mass transfer limitations can be neglected, the Weisz-Prater criterion (Froment, 1962) was used. The Weisz modulus Φ is calculated from Eq. 2.15 as an estimation of the extent of the mass diffusion limitation in the catalyst pores.

$$\Phi = \left(\frac{n+1}{2}\right) \frac{R^{obs}_{v,CO2}\left(\dfrac{d_P}{6}\right)^2}{D_{CO2,eff}C^p_{CO2}} \tag{2.15}$$

The description of the estimation of the diffusion coefficient and the values of parameters used for the calculation of the criterion are reported in Appendix C. The deviation due to internal limitation is less than <5% if $\Phi < 0.08$, as it is the case for our system (see Table 2.4).

To verify that external mass transfer limitations can be neglected, the Mears criterion (Mears, 1971a) is used. The Carberry number Ca is calculated from Eq. 2.16 as an estimation of the extent of mass transfer limitation over the gaseous film that surrounds the catalyst particles.

$$Ca = \frac{R^{obs}_{v,CO2}}{k_{G,CO2}a_s C_{CO2,b}} \tag{2.16}$$

The estimation of the external mass transfer coefficient is described in Appendix C. The external mass transfer is considered negligible, as the Ca number is $< 0.05/n$ (see Table 2.4), indicating that the resistance due to external mass transfer is less than 5% of the resistance due to chemical reaction.

To verify that external heat transfer limitations can be neglected, the Mears criterion (Mears, 1971a) is used. It consists of calculating the temperature difference over the film that surrounds the catalytic particles according to Eq. 2.17:

$$\Delta T_{film} = \frac{R^{obs}_{v,CO2}\left|\Delta H^r\right| d_P}{6k_t} \tag{2.17}$$

The estimation of the external heat transfer coefficient is described in Appendix C. The external heat transfer is considered negligible, as ΔT_{film} respects the condition to be lower than $(0.05RT_G^2)/E_a$ (see Table 2.4).

To verify that internal heat transfer limitations can be neglected, the Mears criterion (Froment, 1962) was used. It consists of calculating the temperature difference between catalytic particle surface and particle center, according to Eq. 2.18:

$$\Delta T_{int} = \frac{R^{obs}_{v,CO2}\left|\Delta H^r\right| d_P^2}{60\lambda_P} \tag{2.18}$$

The estimation of the particle thermal conductivity λ_P is described in Appendix C. The internal heat transfer is considered negligible, as the ΔT_{int} is $< (0.05RT)/E_a$ as required from the criterion (see Table 2.4).

Finally, the radial heat transport limitation in the catalyst bed is verified according to the following criterion (Mears, 1971a):

$$\Delta T_{rad} = \frac{R^{obs}_{v,CO2}\left|\Delta H^r\right|(1-\epsilon_{bed})(1-b)\,d_r^2}{32\alpha_{bed}} \tag{2.19}$$

The estimation of the effective radial thermal conductivity in the bed α_{bed} is described in Appendix C. The radial heat transfer is considered negligible, as the ΔT_{rad} is $< (0.05RT_w)/E_a$ as required from the criterion (see Table 2.4).

Table 2.4 reports values of calculated criteria for the compound CO_2 in reference conditions and their corresponding limit values. Detailed procedure followed for the estimation of criteria, as well as values of criteria obtained in the other operating conditions are reported in Appendix C.

Table 2.4: Calculated values of criteria used to verify that kinetic regime is dominant. Values are referred to experiments in reference conditions and to the reactant CO_2.

Criterion		Value		Limit value
External mass transfer	Ca	$2.01\text{x}10^{-4}$	$<$	0.16
Internal mass transfer	Φ	$1.81\text{x}10^{-4}$	$<$	0.08
Axial dispersion	L_{bed}/d_p	731.71	$>$	1.12
External heat transfer	ΔT_{film}	$1.03\text{x}10^{-1}$	$<$	8.64
Internal heat transfer	ΔT_{int}	$6.14\text{x}10^{-4}$	$<$	8.64
Radial heat transfer	ΔT_{rad}	$7.90\text{x}10^{-4}$	$<$	8.64

2.4 Modification of the experimental set-up for liquid co-feeding.

Water is one of the co-products of this reaction and it is believed to be one of the causes of deactivation of potassium-promoted iron catalysts, because of the tendency of water to promote oxidation of iron carbides and metallic iron. (Pendyala et al., 2010; Satterfield et al., 1986) The role of water on iron catalyst deactivation has been widely investigated for the FT reaction from syngas (Pendyala et al., 2010; Satterfield et al., 1986), but no studies exist at our knowledge for the CO_2 hydrogenation.

During our experimental study, it was observed that the catalyst was deactivated by high temperatures, by high τ_{mod} and by long run times. The cause of deactivation could be related - at least partially - to the exposition to high partial pressure of water. Thus, an experimental investigation of the effect of water on the catalyst deactivation could give interesting insights about reaction mechanism and catalyst deactivation.

Moreover, to gain further understanding of the reaction mechanism, investigation of the role of 1-alkenes and alcohols would be relevant. For the FT reaction from syngas, many studies have been performed with co-injection of ethylene or longer α-olefins and ethanol in the feed gas. (Boelee et al., 1989; Muleja et al., 2019; Gaube and Klein, 2008; Kummer and Emmett, 1953) However, at our knowledge, no studies with co-injection of the above cited compounds exist for the CO_2 hydrogenation over iron catalysts.

Thus, the experimental set-up described above was modified for the campaign of experiments with co-feeding of liquids. The objectives of these experiments were:

- to study the effects of alcohols injection in the feed on the catalytic performances to understand their role in the reaction mechanism;
- to investigate the role of water in catalytic deactivation.

Study with α-olefins could not be performed because of technical issues due to the compatibility of materials.

A flow diagram of the experimental bench with liquid injection system is shown in Figure 2.10. A stainless steel syringe (19) with a volume of 8 ml is used to fill up a reservoir (21) with the liquid of interest. The reservoir can be isolated thanks to two valves (21) and it can be pressurised with N_2. The liquid flow is then regulated with a thermal liquid mass flowmeter provided by Bronkhorst (23), able to regulate until 0.9 g/h (referred to water flow) and suitable to work with water and ethanol. The liquid flow passes through an electric resistance (24) regulated at 300°C where the liquid is vaporized. The obtained gas is then mixed with the other feed gases before entering the reactor.

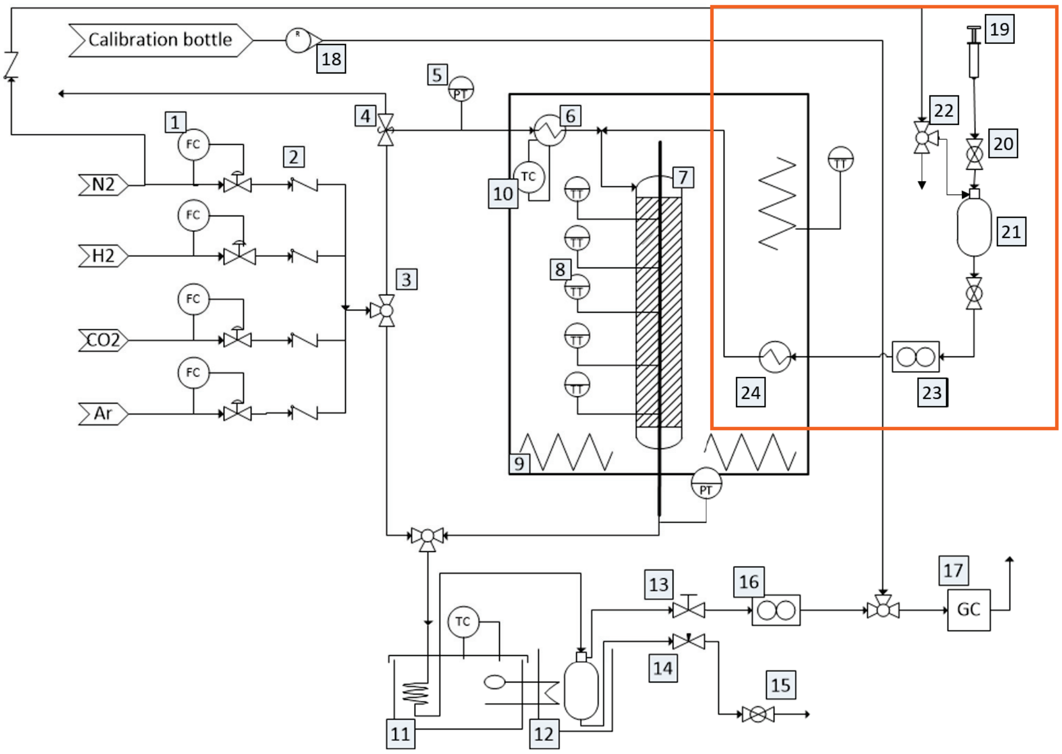

Figure 2.10: Process flow diagram of the experimental set-up. 1. Flows controller; 2. Check valves; 3. Three-way globe valve; 4. Security valve; 5. Pressure indicator; 6. Heater; 7. Fixed-bed reactor; 8. Temperature indicator; 9. Electric resistance; 10. Temperature controller; 11. Thermoregulated bath (water+ethylene glycol); 12. Cold trap; 13. Membrane pressure regulator; 14. Needle valve; 15. Bleed valve; 16. Coriolis mass flowmeter; 17. Gas chromatogram; 18. Rotameter; 19. Injection syringe; 20. Globe valve; 21. Liquid reservoir; 22. Three-way valve; 23. Liquid mass flow controller; 24. Electric resistance.

It is important to highlight that this system is not optimal: the electric resistance can give an uneven vaporization of the liquid, especially for large flows, leading to an uneven flow of gas. Moreover, both water and ethanol are almost completely condensed in the cold trap and thus collected only as liquid products at the end of the experiment. Thus, it is not possible to follow their concentration in real time, meaning that we do not really know what happens with the liquid injection and during the reaction.

The C and total mass balances for experiments with liquid flows until 0.50 $g_{H_2O,eq}$/h are closed within an error <15%, that we consider acceptable. For experiments conducted with higher flows, the error on C balance was >30%, indicating that the liquid vaporization was probably not uniform, thus these results were discarded.

2.5 Experimental scale-up in a fixed-bed reactor with cooling system.

2.5.1 Objectives.

The majority of the experimental studies conducted in literature for the CO_2 hydrogenation have been performed in lab-scale reactors. In this work, we are interested in developing a reactor model and in simulating the global process, in order to estimate an energy efficiency. It is thus necessary to have experimental data for the reaction performed in an upscaled reactor. These data will be used to validate the mathematical model at reactor scale. Furthermore, the fixed-bed reactor used in CP2M has an important limit in the temperature regulation: the reactor is placed in an oven and only the temperature of the oven can be regulated thanks to electric resistances placed on the walls. The temperature inside the reactor is measured by a thermocouple, but it cannot be regulated. The uniform distribution of the heat is assured by a fan system. The reactor used for the experimental study at higher scale has a cooling system that allows a better control of the reactor temperature. A cooling fluid circulates in the external coating of the reactor, ensuring a more efficient evacuation of the heat produced by the reaction.

Another objective of these experiments is to investigate the role of CO when it is added to a CO_2/H_2 mixture over Fe catalysts. The objective here is not to comprehensively investigate the role of CO in hydrogenation reactions, which has already been extensively treated in literature (Riedel et al., 1999; Schulz et al., 1999; Visconti et al., 2016; Riedel et al., 2003), but to understand if small contents of CO in the feed could influence the reaction performances. Furthermore, the results obtained with CO co-injection will be used to verify if the kinetic model developed is still valid for CO/CO_2 mixtures and to understand the effect of CO for the study of recycles at process scale.

2.5.2 Description of the experimental set-up.

The experimental set-up, named SynToMe, is available at Laboratoire Réacteurs et Procédés (LRP) in CEA-LITEN. It is made of 5 parts:

1. gas feeding
2. compression system
3. reactor
4. condensation zone
5. analytic chain

A graphical description of the set-up is given in Figure 2.11.

The gas feeding zone includes five gas lines for CO_2, H_2, CO, CH_4 and N_2. Each line is equipped with a check valve (1), a mass flow controller (2) and an electro-pneumatic valve (3). Flow controllers work in given ranges: 0-30 Nl/min for Ar and H_2, 0-15 Nl/min for CO_2 and CO and 0-5 Nl/min for CH_4.

Inlet gases are fed into the compression system where the gas mixture can be compressed at pressures until 100 bars. This system is made of a pneumatic air booster piston cylinder, fed by the compressed air line. An upstream buffer volume of 1 l at 20 bars ensures the proper functioning of flow-meters in continuous regime. A second buffer volume of 1 l at 100 bars is placed downstream, to smooth out the piston mode operation. After compression, the gas flow is measured by a Coriolis flow-meter (5) and the gas is heated up to the desired temperature (between 200 and 300°C) by passing through an electric resistance (6) before entering in the reactor.

The reactor (8) consists in a stainless steel tube with inner diameter of 10.2 mm and a total length of 400 mm. A thermocouple rod with external diameter of 2 mm containing 6 thermocouples is placed inside the reactor, allowing the measurement of the temperature axial profile. The reactor configuration is shown in Figure 2.12. The reactor was filled with 13.3 g of the above cited $Fe\text{-}K/Al_2O_3$ catalyst and two inert bed layers were created at the reactor inlet and outlet with the same Al_2O_3 used as catalyst support. The reactor is equipped with a temperature regulation system (9), allowing the flow of a heat-transfer fluid in the cooling circuit of the reactor. The heat-transfer fluid is the thermofluid DW-Therm HT from Huber Peter with a boiling point of 335°C. Pressure is measured at the reactor inlet and outlet thanks to pressure captors P1 and P2 (7 and 13).

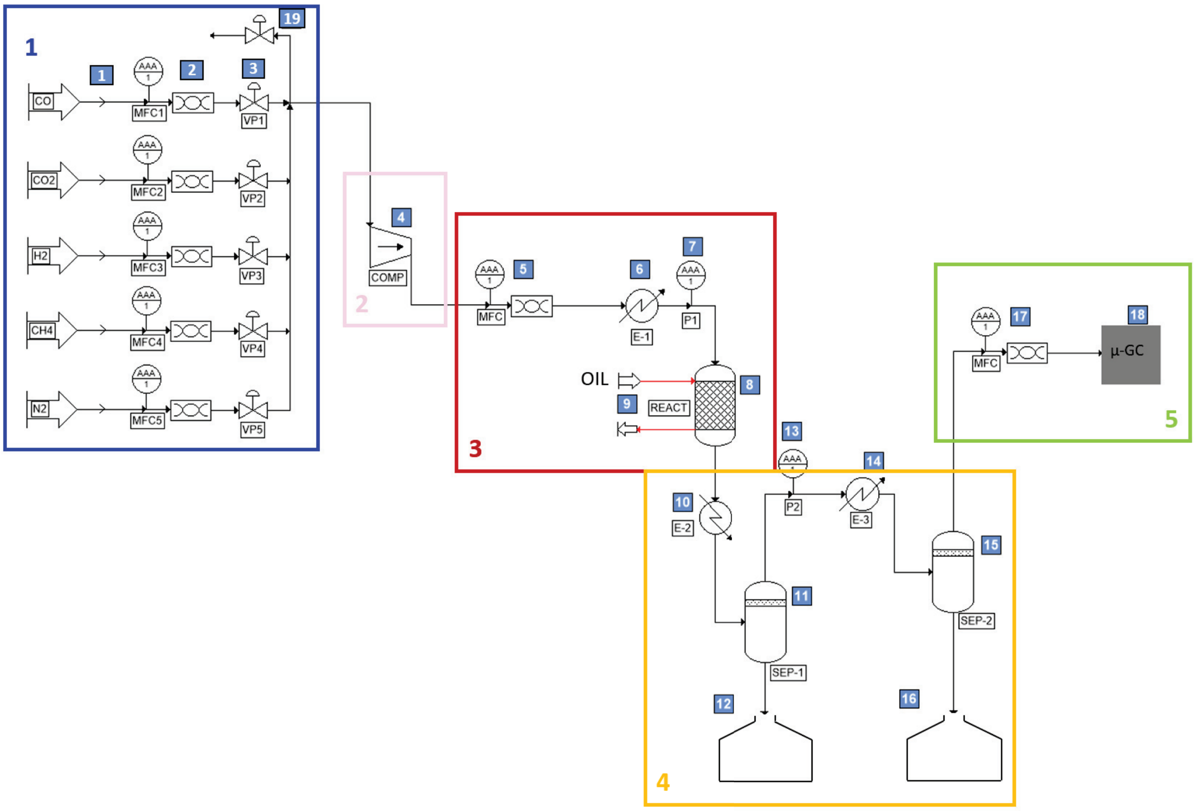

Figure 2.11: Process flow diagram of the SynToMe experimental set-up. 1) Check valve; 2) Mass flow controller; 3) Electro-pneumatic valve; 4) Compression system; 5) Mass flow indicator; 6) Pre-heater; 7) Pressure indicator; 8) Reactor; 9) Temperature regulation system; 10) Gas-oil exchanger; 11) First separator; 12) Liquid reservoir; 13) Pressure indicator; 14) Heat exchanger; 15) Second separator; 16) Liquid reservoir; 17) Mass flow controller; 18) µ-GC; 19) Release valve.

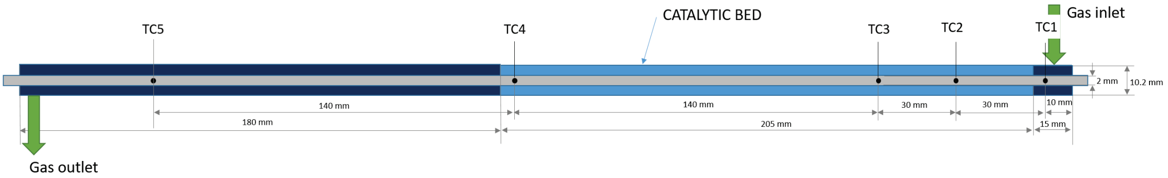

Figure 2.12: Reactor scheme used in the SynToME set-up.

Products are then passed through a two-step condensation system. The first condenser (10) is a gas/oil exchanger, regulated at 150°C, able to condense the heaviest hydrocarbons. These are collected into a reservoir (22) with level detector and posed on a balance. This first condensation step is not extremely useful for our experiments, since we did not produce high quantities of heavy products. However, it is necessary to avoid condensation of waxes in the system pipes that could cause plugging. The second condensation step (14) consists in a double-wall cylinder where temperature is regulated at 2°C, to condense water and light hydrocarbons. The actual temperature of liquids condensed cannot be calculated, but the external wall temperature is measured to be around 16°C and the temperature of gases after the cyclone is measured to be around 20°C. Thus, the actual temperature of condensing liquid is supposed to be higher than 2°C. Liquids are separated with a cyclone separator (15) and collected in a reservoir (16), posed on a balance, so that liquid production can be quantified. The reservoir is emptied at the end of every experiment. Products that do not condense, after measurement of the gas flow with a

Coriolis flow-meter (17), are sent to a µ-GC system (18) allowing the measurement of the outlet gas composition.

2.5.3 Analytic protocol and data exploitation.

The µ-GC system is equipped with two columns: a Supelco Mol Sieve 5A PLOT Capillary GC column which is able to separate H_2, N_2, CH_4 and CO; and an Agilent Plot U Capillary GC column to separate CO_2 and light hydrocarbons. Products are detected with TCD detectors. Ar is used as vector gas for the first column in order to have a good sensitivity to H_2 detection; He is used for the second column. The µ-GC system does not allow the establishment of temperature ramps, thus the analysis cannot detect hydrocarbons higher than C_3. The analytic method for the analysis of gaseous phase is described in Appendix B. As shown in Figure 2.13, representing a typical gas-chromatogram of the experiments, only CO_2, H_2, N_2, CO, CH_4, C_2H_4, C_2H_6, C_3H_6 and C_3H_8 are clearly detected. Liquids were analysed with the same equipment and the same procedure described before for the experiments conduced in CP2M.

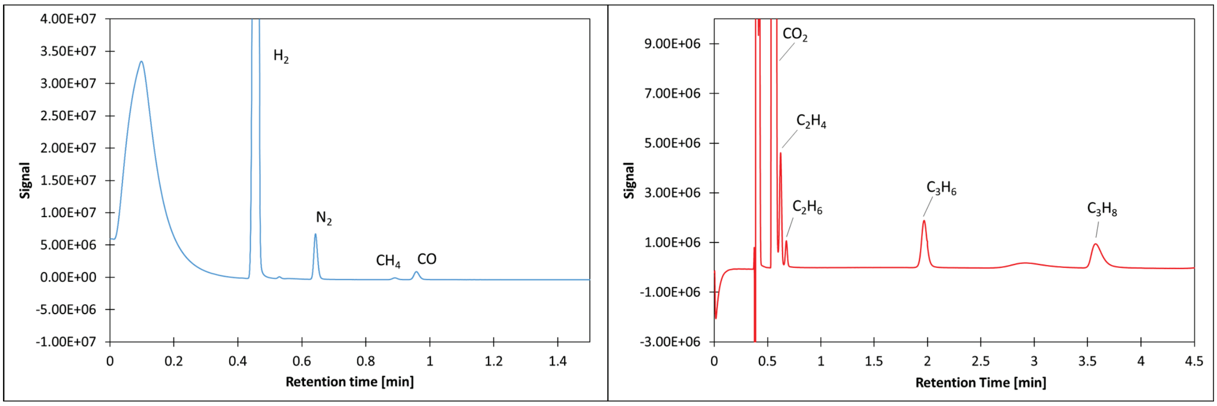

Figure 2.13: Chromatograms of gaseous products detected with µ-GC system for Mol Sieve column (left) and Plot U column (right).

Figure 2.14 shows the mass fraction of the hydrocarbons observed in the reactor outlet after analysis of the three phases. It appears that the main part of the products from C_3 to C_9 were lost during the analysis. Moreover, we observe much more paraffins than expected, especially for high C number. This is due to the previous experiments conduced in the SynToMe set-up, that led to the production of long-chain waxes. These products were condensed on the walls of the pipes and the condenser. Our experiments, producing alcohols that act as solvents for these waxes, led to the dissolution of these products into our reaction products, thus resulting in an increase of the paraffins fraction in the liquid organic phase. These two opposite effects (the loss of C_3-C_9 products and the increase of paraffin fraction from previous experiments) lead to very low errors in the total mass balance and the C balance, as shown in Figure 2.15.

Despite the low error on total balances, we cannot consider this protocol to be accurate. Moreover, our focus during these experiments was directed mainly on comparing the performances of the cooled reactor with the lab-scale reactor. At this point, we already have all the information needed to develop a kinetic model which is able to describe the products distribution. Thus, we neglect the hydrocarbons distribution and we only consider CO_2 conversion and CO and total hydrocarbons selectivity.

Mole flows of compounds (including H_2) were calculated as previously described, from Eqs. 2.1 and 2.2. From mole flows, reactants conversion and CO selectivity were calculated according to Eqs. 2.7-2.9.

In the case of CO co-feeding a global C conversion and CO conversion were also estimated

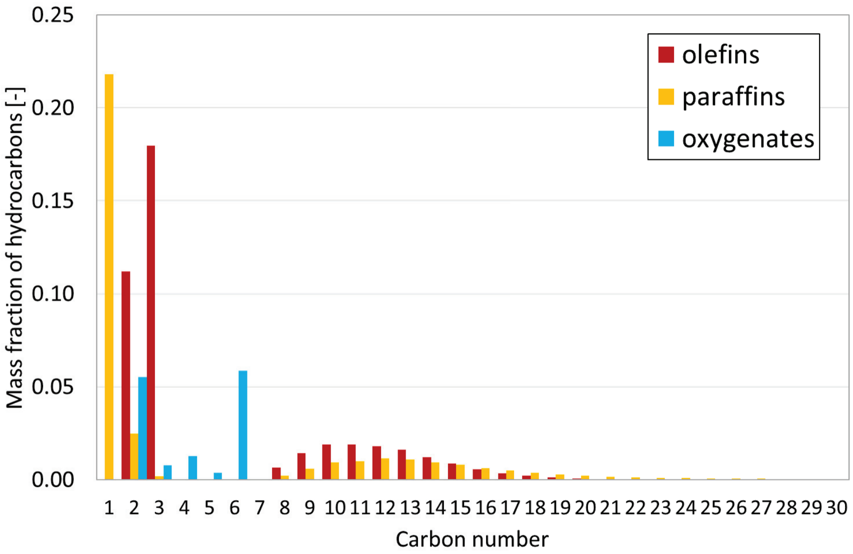

Figure 2.14: Mass fraction of olefins, paraffins and oxygenates as function of C number, observed at the reactor outlet.

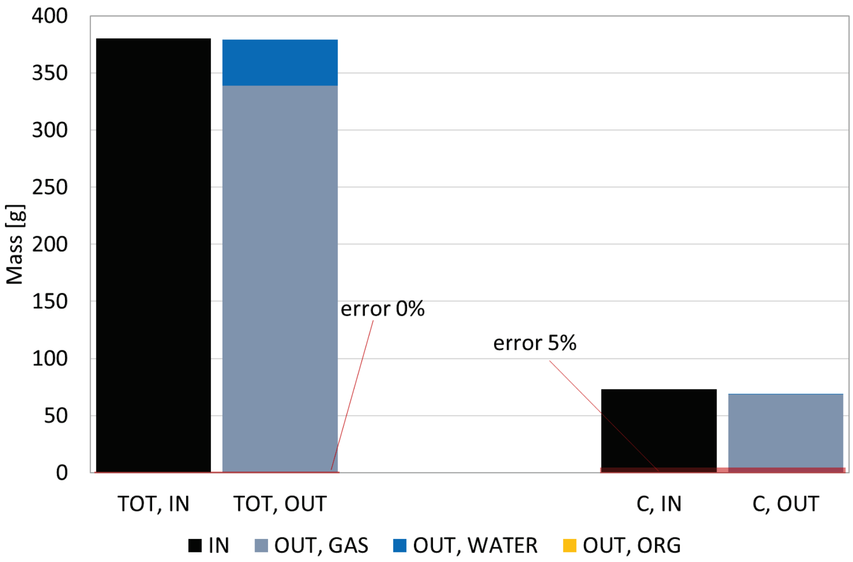

Figure 2.15: Total mass balance and C mass balance between reactor inlet and outlet.

from Eqs. 2.20-2.21.

$$\chi_C = \frac{(F_{CO_2,IN} + F_{CO,IN}) - (F_{CO_2,OUT} + F_{CO,OUT})}{(F_{CO_2,IN} + F_{CO,IN})} \tag{2.20}$$

$$\chi_{CO} = \frac{F_{CO}, IN - F_{CO,OUT}}{F_{CO,IN}} \tag{2.21}$$

2.5.4 Operating conditions.

The experimental conditions adopted for this study are reported in Table 2.5. Contact time was varied by changing the GHSV between 2700 and 10100 Nml/g_{cat}/h. Moreover, CO co-feeding effects were investigated by varying its inlet composition between 1 and 5%. Point 1 of

Table 2.5 represents the reference conditions. It was not possible to use the same conditions as in the previous experimental study (GHSV=2000 Nml/g/h), because of intrinsic limitations of the experimental set-up. The minimum theoretical mass flow that can be set in the system is in fact equal to 0.2 g/min, which corresponds to a GHSV of about 1100 Nml/g/h. However the set-up is adapted to work at 60 bars, thus when it works at 15 bars it is far from its optimum working window. The actual minimum mass flow that we were able to set was 0.46 g/min that corresponds to a GHSV of 2700 Nml/g/h. This problem could of course be prevented by using a greater quantity of catalyst in the reactor, but at this point of the study we did not have more catalyst left and synthesize another batch of catalyst would have required preliminary tests to verify that the catalyst activity was repeatable and comparable to the one of the previously used batch. When the flow was regulated in order to have a GHSV of 6735 Nml/g/h, the system stabilised much faster, thus this GHSV was chosen as reference condition.

For each experimental point, kinetic regime conditions were verified by using the same criteria as in Section 2.3.3.1.

Table 2.5: Operating conditions applied for the experiments in the CEA bench.

Condition	GHSV [Nml/g/h]	T [°C]	p_{tot} [bar]	p_{H2} [bar]	p_{CO2} [bar]	p_{N2} [bar]	p_{CO} [bar]	$CO/(CO + CO_2)$ [-]
1	6735	300	15	10.125	3.375	1.5	0.00	0
2	2700	300	15	10.125	3.375	1.5	0.00	0
3	10100	300	15	10.125	3.375	1.5	0.00	0
4	6735	300	15	10.125	3.075	1.5	0.30	0.91
5	6735	300	15	10.125	2.625	1.5	0.75	0.78
6	6735	300	15	10.125	1.875	1.5	1.50	0.84

2.6 Conclusions.

The main part of the experimental study was focused on studying the reaction in lab-scale fixed-bed reactor with the objective to investigate the effects of operating parameters and to collect enough experimental points to develop a kinetic model. We have dedicated significant effort to the development of an analytic protocol that allows an accurate analysis of the distribution of products obtained from the reaction. Product obtained in liquid phase, especially in water phase, are generally neglected in literature. However, we have shown that oxygenates products found in the water phase cannot be neglected, as they represent a significant fraction of the obtained hydrocarbons. Performing a detailed analysis of the products implies though to increase the reaction duration, as the catalyst is not very productive towards the formation of long chain hydrocarbons and enough time has to be waited before having enough liquid to analyse. We have found that performing tests of about 20 hours was the good compromise between reaction time and analysis accuracy. This of course reduced the number of experimental tests that could be performed. Nevertheless, we could still collect enough experimental data to develop detailed kinetic models that will be treated in the next chapters.

The experimental studies with liquid co-feeding and in the cooled reactor have to be considered as more preliminary, because of matters of timing and equipments. The water and ethanol co-feeding studies were performed to understand the role of water in the catalyst deactivation and to understand the role of alcohols in the reaction mechanism. The injection system though was not optimal and it could only work for small flows. Despite that, we were able to obtain some reasonable results that could be the base for future investigation. Few experimental conditions were tested in the upscaled reactor, because of a matter of timing and of not optimal dimensioning of the set-up for the purpose of the experiments. We could still obtain enough experimental data to validate our reactor model and to have some information about the effects of CO when added to CO_2/H_2 mixtures.

The experimental results obtained will be shown and discussed in the next chapter.

References

M. Amoyal, R. Vidruk-Nehemya, M. V. Landau, and M. Herskowitz. Effect of potassium on the active phases of Fe catalysts for carbon dioxide conversion to liquid fuels through hydrogenation. *Journal of Catalysis*, 348:29–39, 2017. ISSN 00219517. doi: 10.1016/j.jcat.2017.01.020. URL https://linkinghub.elsevier.com/retrieve/pii/S0021951717300325.

E. P. Barrett, L. G. Joyner, and P. P. Halenda. The Determination of Pore Volume and Area Distributions in Porous Substances. I. Computations from Nitrogen Isotherms. *Journal of the American Chemical Society*, 73(1):373–380, 1951. ISSN 0002-7863, 1520-5126. doi: 10.1021/ja01145a126. URL https://pubs.acs.org/doi/abs/10.1021/ja01145a126.

H. Baussart, R. Delobel, M. Le Bras, and J.-M. Leroy. Hydrogenation of CO_2 over Co/Cu/K catalysts. *Journal of the Chemical Society, Faraday Transactions 1: Physical Chemistry in Condensed Phases*, 83(6):1711–1718, 1987.

J. Boelee, J. Cüsters, and K. Van Der Wiele. Influence of reaction conditions on the effect of Co-feeding ethene in the Fischer-Tropsch synthesis on a fused-iron catalyst in the liquid phase. *Applied Catalysis*, 53(1):1–13, 1989. ISSN 0166-9834. doi: 10.1016/S0166-9834(00)80005-6. URL http://www.sciencedirect.com/science/article/pii/S0166983400800056.

W. H. Bragg and W. L. Bragg. The reflection of X-rays by crystals. *Proceedings of the Royal Society of London*, 88(605):428–438, 1913. doi: 10.1098/rspa.1913.0040. URL https://doi.org/10.1098/rspa.1913.0040. Publisher: Royal Society.

S. Brunauer, P. H. Emmett, and E. Teller. Adsorption of Gases in Multimolecular Layers. *Journal of the American Chemical Society*, 60(2):309–319, 1938. ISSN 0002-7863, 1520-5126. doi: 10.1021/ja01269a023. URL https://pubs.acs.org/doi/abs/10.1021/ja01269a023.

Y. H. Choi, Y. J. Jang, H. Park, W. Y. Kim, Y. H. Lee, S. H. Choi, and J. S. Lee. Carbon dioxide Fischer-Tropsch synthesis: A new path to carbon-neutral fuels. *Applied Catalysis B: Environmental*, 202:605–610, 2017. ISSN 09263373. doi: 10.1016/j.apcatb.2016.09.072. URL https://linkinghub.elsevier.com/retrieve/pii/S0926337316307603.

G. Froment. Design of fixed-bed catalytic reactors based on effective transport models. *Chemical Engineering Science*, 17(11):849–859, 1962. ISSN 00092509. doi: 10.1016/0009-2509(62)87017-1. URL https://linkinghub.elsevier.com/retrieve/pii/0009250962870171.

J. Gaube and H.-F. Klein. Studies on the reaction mechanism of the Fischer–Tropsch synthesis on iron and cobalt. *Journal of Molecular Catalysis A: Chemical*, 283(1):60–68, 2008. ISSN 1381-1169. doi: 10.1016/j.molcata.2007.11.028. URL http://www.sciencedirect.com/science/article/pii/S1381116907006711.

H. Gierman. Design of laboratory hydrotreating reactors: Scaling Down of Trickle-flow Reactors. *Applied Catalysis*, 43(2):277–286, 1988. ISSN 0166-9834. doi: 10.1016/S0166-9834(00)82732-3. URL https://www.sciencedirect.com/science/article/pii/S0166983400827323.

J.-S. Hong, J. S. Hwang, K.-W. Jun, J. C. Sur, and K.-W. Lee. Deactivation study on a coprecipitated Fe-Cu-K-Al catalyst in CO_2 hydrogenation. *Applied Catalysis A: General*, 218:53–59, 2001.

J. S. Hwang, K.-W. Jun, and K.-W. Lee. Deactivation and regeneration of Fe-K/alumina catalyst in CO_2 hydrogenation. *Applied Catalysis A: General*, 208:217–222, 2001.

S.-M. Hwang, S. J. Han, J. E. Min, H.-G. Park, K.-W. Jun, and S. K. Kim. Mechanistic insights into Cu and K promoted Fe-catalyzed production of liquid hydrocarbons via CO_2 hydrogenation. *Journal of CO2 Utilization*, 34:522–532, 2019. ISSN 22129820. doi: 10.1016/j.jcou.2019.08.004. URL https://linkinghub.elsevier.com/retrieve/pii/S2212982019306018.

M. Iglesias Gonzalez, C. de Vries, M. Claeys, and G. Schaub. Chemical energy storage in gaseous hydrocarbons via iron Fischer–Tropsch synthesis from H_2/CO_2 —Kinetics, selectivity and process considerations. *Catalysis Today*, 242:184–192, 2015. ISSN 09205861. doi: 10.1016/j.cattod.2014.05.020. URL https://linkinghub.elsevier.com/retrieve/pii/S0920586114003903.

J.-S. Kim, S. Lee, S.-B. Lee, M.-J. Choi, and K.-W. Lee. Performance of catalytic reactors for the hydrogenation of CO_2 to hydrocarbons. *Catalysis Today*, 115(1-4):228–234, 2006. ISSN 09205861. doi: 10.1016/j.cattod.2006.02.038. URL `http://linkinghub.elsevier.com/retrieve/pii/S0920586106001179`.

J. T. Kummer and P. H. Emmett. Fischer—Tropsch Synthesis Mechanism Studies. The Addition of Radioactive Alcohols to the Synthesis Gas. *Journal of the American Chemical Society*, 75(21):5177–5183, 1953. ISSN 0002-7863. doi: 10.1021/ja01117a008. URL `https://doi.org/10.1021/ja01117a008`.

S.-C. Lee, J.-H. Jang, B.-Y. Lee, M.-C. Kang, M. Kang, and S.-J. Choung. The effect of binders on structure and chemical properties of Fe-K/γ-Al_2O_3 catalysts for CO_2 hydrogenation. *Applied Catalysis A: General*, 253(1):293–304, 2003. ISSN 0926860X. doi: 10.1016/S0926-860X(03)00540-4. URL `http://linkinghub.elsevier.com/retrieve/pii/S0926860X03005404`.

J. Liu, A. Zhang, X. Jiang, M. Liu, Y. Sun, C. Song, and X. Guo. Selective CO_2 Hydrogenation to Hydrocarbons on Cu-Promoted Fe-Based Catalysts: Dependence on Cu–Fe Interaction. *ACS Sustainable Chemistry & Engineering*, 6(8):10182–10190, 2018. ISSN 2168-0485, 2168-0485. doi: 10.1021/acssuschemeng.8b01491. URL `http://pubs.acs.org/doi/10.1021/acssuschemeng.8b01491`.

M. Martinelli, C. G. Visconti, L. Lietti, P. Forzatti, C. Bassano, and P. Deiana. CO_2 reactivity on Fe–Zn–Cu–K Fischer–Tropsch synthesis catalysts with different K-loadings. *Catalysis Today*, 228:77–88, 2014. ISSN 09205861. doi: 10.1016/j.cattod.2013.11.018. URL `https://linkinghub.elsevier.com/retrieve/pii/S0920586113006226`.

D. E. Mears. Diagnostic criteria for heat transport limitations in fixed bed reactors. *Journal of Catalysis*, 20(2):127–131, 1971a. ISSN 0021-9517. doi: 10.1016/0021-9517(71)90073-X. URL `https://www.sciencedirect.com/science/article/pii/002195177190073X`.

D. E. Mears. The role of axial dispersion in trickle-flow laboratory reactors. *Chemical Engineering Science*, 26(9):1361–1366, Sept. 1971b. ISSN 0009-2509. doi: 10.1016/0009-2509(71)80056-8. URL `https://www.sciencedirect.com/science/article/pii/0009250971800568`.

A. A. Muleja, J. Gorimbo, and C. M. Masuku. Effect of Co-Feeding Inorganic and Organic Molecules in the Fe and Co Catalyzed Fischer–Tropsch Synthesis: A Review. *Catalysts*, 9(9), 2019. ISSN 2073-4344. doi: 10.3390/catal9090746.

S. Najari, G. Gróf, S. Saeidi, and F. Gallucci. Modeling and optimization of hydrogenation of CO_2: Estimation of kinetic parameters via Artificial Bee Colony (ABC) and Differential Evolution (DE) algorithms. *International Journal of Hydrogen Energy*, 44(10):4630–4649, 2019. ISSN 03603199. doi: 10.1016/j.ijhydene.2019.01.020. URL `https://linkinghub.elsevier.com/retrieve/pii/S036031991930093X`.

A. Nakhaei Pour and M. R. Housaindokht. A new kinetic model for direct CO_2 hydrogenation to higher hydrocarbons on a precipitated iron catalyst: Effect of catalyst particle size. *Journal of Energy Chemistry*, 26(3):359–367, 2017. ISSN 20954956. doi: 10.1016/j.jechem.2016.12.006. URL `https://linkinghub.elsevier.com/retrieve/pii/S2095495616301607`.

V. R. R. Pendyala, G. Jacobs, J. C. Mohandas, M. Luo, H. H. Hamdeh, Y. Ji, M. C. Ribeiro, and B. H. Davis. Fischer–Tropsch Synthesis: Effect of Water Over Iron-Based Catalysts. *Catalysis Letters*, 140 (3):98–105, 2010. ISSN 1572-879X. doi: 10.1007/s10562-010-0452-7. URL `https://doi.org/10.1007/s10562-010-0452-7`.

T. Riedel, M. Claeys, H. Schulz, G. Schaub, N. Sang-Sung, J. Ki-Won, K. Gurram, and L. Kyu-Wan. Comparative study of Fisher-Tropsch sythesis with H_2/CO and H_2/CO_2 syngas using Fe- and Co-based catalysts. *Applied Catalysis A: General*, 186:201–213, 1999.

T. Riedel, G. Schaub, K.-W. Jun, and K.-W. Lee. Kinetics of CO_2 Hydrogenation on a K-Promoted Fe Catalyst. *Industrial & Engineering Chemistry Research*, 40(5):1355–1363, 2001. ISSN 0888-5885, 1520-5045. doi: 10.1021/ie000084k. URL `http://pubs.acs.org/doi/abs/10.1021/ie000084k`.

T. Riedel, H. Schulz, G. Schaub, K.-W. Jun, J.-S. Hwang, and K.-W. Lee. Fischer–Tropsch on iron with H_2/CO and H_2/CO_2 as synthesis gases: the episodes of formation of the Fischer–Tropsch regime and construction of the catalyst. *Topics in Catalysis*, 26(1-4):41–54, 2003.

U. Rodemerck, M. Holeña, E. Wagner, Q. Smejkal, A. Barkschat, and M. Baerns. Catalyst Development for CO_2 Hydrogenation to Fuels. *ChemCatChem*, 5(7):1948–1955, 2013. ISSN 18673880. doi: 10.1002/cctc.201200879. URL `http://doi.wiley.com/10.1002/cctc.201200879`.

P. S. Sai Prasad, J. W. Bae, K.-W. Jun, and K.-W. Lee. Fischer–Tropsch Synthesis by Carbon Dioxide Hydrogenation on Fe-Based Catalysts. *Catalysis Surveys from Asia*, 12(3):170–183, 2008. ISSN 1571-1013, 1574-9266. doi: 10.1007/s10563-008-9049-1. URL `http://link.springer.com/10.1007/s10563-008-9049-1`.

C. N. Satterfield, R. T. Hanlon, S. E. Tung, Z. M. Zou, and G. C. Papaefthymiou. Effect of water on the iron-catalyzed Fischer-Tropsch synthesis. *Industrial & Engineering Chemistry Product Research and Development*, 25(3):407–414, 1986. ISSN 0196-4321. doi: 10.1021/i300023a007. URL `https://doi.org/10.1021/i300023a007`.

H. Schulz, G. Schaub, M. Claeys, and T. Riedel. Transient initial kinetic regimes of Fischer–Tropsch synthesis. *Applied Catalysis A: General*, 186(1-2):215–227, 1999.

C. G. Visconti, E. Tronconi, L. Lietti, P. Forzatti, S. Rossini, and R. Zennaro. Detailed Kinetics of the Fischer–Tropsch Synthesis on Cobalt Catalysts Based on H-Assisted CO Activation. *Topics in Catalysis*, 54(13):786, 2011. ISSN 1572-9028. doi: 10.1007/s11244-011-9700-3. URL `https://doi.org/10.1007/s11244-011-9700-3`.

C. G. Visconti, M. Martinelli, L. Falbo, L. Fratalocchi, and L. Lietti. CO_2 hydrogenation to hydrocarbons over Co and Fe-based Fischer-Tropsch catalysts. *Catalysis Today*, 277:161–170, 2016. ISSN 09205861. doi: 10.1016/j.cattod.2016.04.010. URL `https://linkinghub.elsevier.com/retrieve/pii/S0920586116302632`.

C. G. Visconti, M. Martinelli, L. Falbo, A. Infantes-Molina, L. Lietti, P. Forzatti, G. Iaquaniello, E. Palo, B. Picutti, and F. Brignoli. CO_2 hydrogenation to lower olefins on a high surface area K-promoted bulk Fe-catalyst. *Applied Catalysis B: Environmental*, 200:530–542, 2017. ISSN 09263373. doi: 10.1016/j.apcatb.2016.07.047. URL `https://linkinghub.elsevier.com/retrieve/pii/S0926337316305896`.

N. Wakao, S. Kaguei, and T. Funazkri. Effect of fluid dispersion coefficients on particle-to-fluid heat transfer coefficients in packed beds. *Chemical Engineering Science*, 34(3):325–336, 1979. ISSN 00092509. doi: 10.1016/0009-2509(79)85064-2. URL `https://linkinghub.elsevier.com/retrieve/pii/0009250979850642`.

J. Wang, Z. You, Q. Zhang, W. Deng, and Y. Wang. Synthesis of lower olefins by hydrogenation of carbon dioxide over supported iron catalysts. *Catalysis Today*, 215:186–193, 2013. ISSN 09205861. doi: 10.1016/j.cattod.2013.03.031. URL `https://linkinghub.elsevier.com/retrieve/pii/S0920586113001442`.

G. D. Weatherbee and C. H. Bartholomew. Hydrogenation of CO_2 on group VIII metals: IV. Specific activities and selectivities of silica-supported Co, Fe, and Ru. *Journal of Catalysis*, 87(2):352–362, 1984.

H. D. Willauer, R. Ananth, M. T. Olsen, D. M. Drab, D. R. Hardy, and F. W. Williams. Modeling and kinetic analysis of CO_2 hydrogenation using a Mn and K-promoted Fe catalyst in a fixed-bed reactor. *Journal of CO2 Utilization*, 3-4:56–64, 2013. ISSN 22129820. doi: 10.1016/j.jcou.2013.10.003. URL `https://linkinghub.elsevier.com/retrieve/pii/S2212982013000504`.

T. Xie, J. Wang, F. Ding, A. Zhang, W. Li, X. Guo, and C. Song. CO_2 hydrogenation to hydrocarbons over alumina-supported iron catalyst: Effect of support pore size. *Journal of CO2 Utilization*, 19:202–208, 2017. ISSN 22129820. doi: 10.1016/j.jcou.2017.03.022. URL `https://linkinghub.elsevier.com/retrieve/pii/S2212982016304760`.

S.-R. Yan, K.-W. Jun, J.-S. Hong, M.-J. Choi, and K.-W. Lee. Promotion effect of Fe–Cu catalyst for the hydrogenation of CO_2 and application to slurry reactor. *Applied Catalysis A: General*, 194:63–70, 2000.

CHAPTER 3

Results of the experimental kinetic study.

3.1 Introduction.

As mentioned before, to develop a kinetic model of the CO_2 hydrogenation, it is primary to understand how the reaction behaves experimentally. We have thus conducted an experimental study in a lab-scale reactor according to the procedure explained in the previous Chapter. Here, we focus on the results of this study.

The objectives of this Chapter are focused on providing information about the catalytic behaviour, studying the catalytic performances in different operating conditions and analysing the properties of the catalyst before and after the reaction. Moreover, in this Chapter we aim at understanding how different operating conditions - such as contact time, temperature, total pressure and H_2/CO_2 ratio - can influence the CO_2 conversion and the hydrocarbons distribution. Furthermore, the results of the experimental study with co-injection of ethanol and water to the reactor feed are analysed, with the aim to understand the role of these compounds in the reaction mechanism. We will conclude with the experimental results obtained when scaling-up the system to a cooled reactor, with the aim to compare these results with those obtained in the lab-scale reactor.

All these data can provide significant information about the reaction mechanism, allowing to investigate eventual ways to improve the reaction performances. As a second purpose, these data will be used for the validation of the kinetic models and reactors models that have been developed and will be explained in the following Chapters.

3.2 Catalyst characterization.

As described before, the obtained catalyst was characterized by different techniques to obtain information about its composition, its textural properties and its crystallite structure.

3.2.1 Textural properties and particle size.

Textural properties were obtained by BET and BJH analysis. The typical N_2 adsorption-desorption isotherm and the corresponding pore size distribution are shown in Figure 3.1 for the fresh catalyst. The isotherm is a type IV, indicating a mesoporous structure, with average pore size of the order of 10 nm. Table 3.1 reports the obtained properties for the catalyst in its fresh, reduced and used forms, as well as for the alumina support. The support has a BET surface area of 205 m^2/g and average pore diameter of 9.2 nm. Impregnation of the support with Fe and K precursors led to an important decrease of the porosity, with BET surface decreased to

86 m^2/g and pore diameter reduced to 7 nm. This is caused by the coverage of active metals on the surface of the alumina support. Reduction of the catalyst and then use in the reaction led to a further decrease of the BET surface area, probably caused by sintering or by carbon deposition on the catalyst surface as previously reported by Riedel et al. (Riedel et al., 2003)

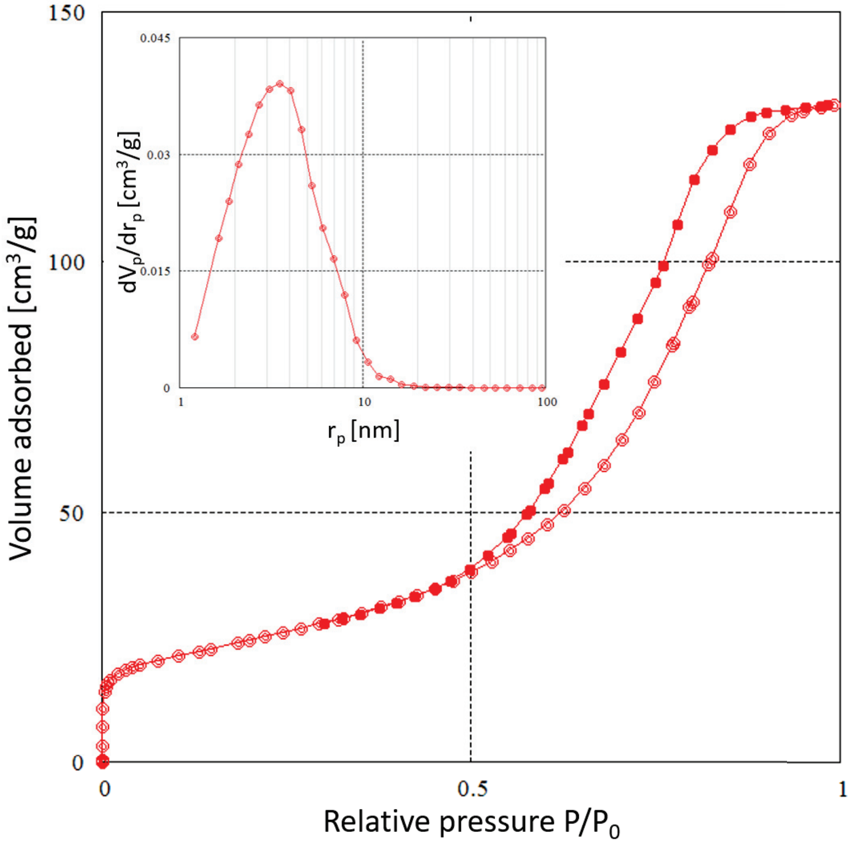

Figure 3.1: N_2 adsorption-desorption isotherm and corresponding pore size distribution for the fresh catalyst.

Table 3.1: Textural properties of the catalyst in its different synthesis phases.

	Surface area [m^2/g]	**Average pore diameter** [nm]	**Pore volume** [cm^3/g]
Support	205	9.2	0.44
Fresh catalyst	86	7.1	0.21
Reduced catalyst	75	10.6	0.20
Spent catalyst	43	8.1	0.14

Particle size was measured with laser granulometry. Figure 3.2 shows the typical size distribution obtained for the fresh catalyst. The main peak is observed around 150 µm. Another minor peak is observed at smaller particle size (around 25 µm). In Table 3.2 values of average particle diameter are reported for fresh, reduced and spent catalysts. Average particle diameter decreased from 150 to 139 µm after impregnation of the support and then further decreased after reduction to 126 µm. After the reaction, no significant changes in particle size are observed.

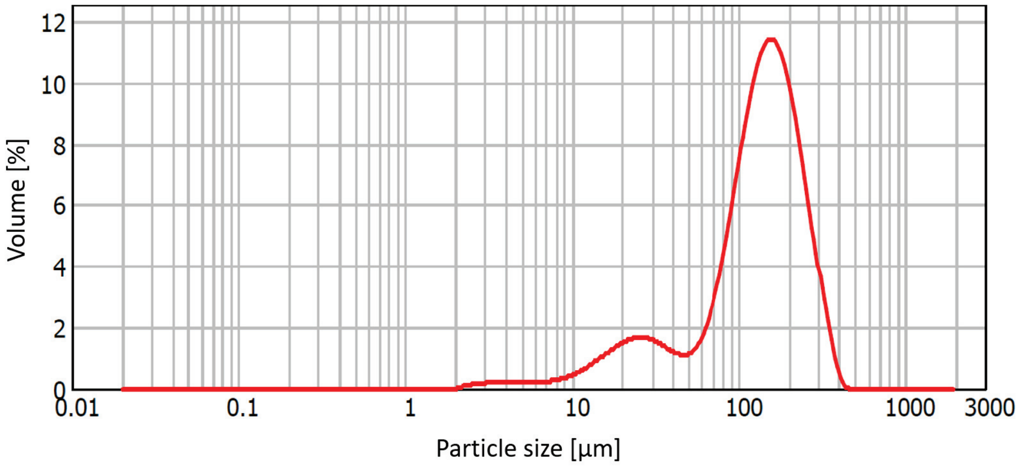

Figure 3.2: Particle size distribution obtained by laser granulometry for the fresh catalyst.

Table 3.2: Average particle size of the catalyst in its different synthesis phases.

	Average particle size [µm]
Support	150
Fresh catalyst	139
Reduced catalyst	126
Spent catalyst	124

3.2.2 Reduction behaviour.

The reduction behaviour of the catalyst has been studied by Temperature Programmed Reduction (TPR) under H_2 flow and it is shown in Figure 3.3. The phase transition during TPR process for iron oxides is likely to be $Fe_2O_3 \rightarrow Fe_3O_4 \rightarrow FeO \rightarrow Fe$. (Xie et al., 2017; Wan et al.,

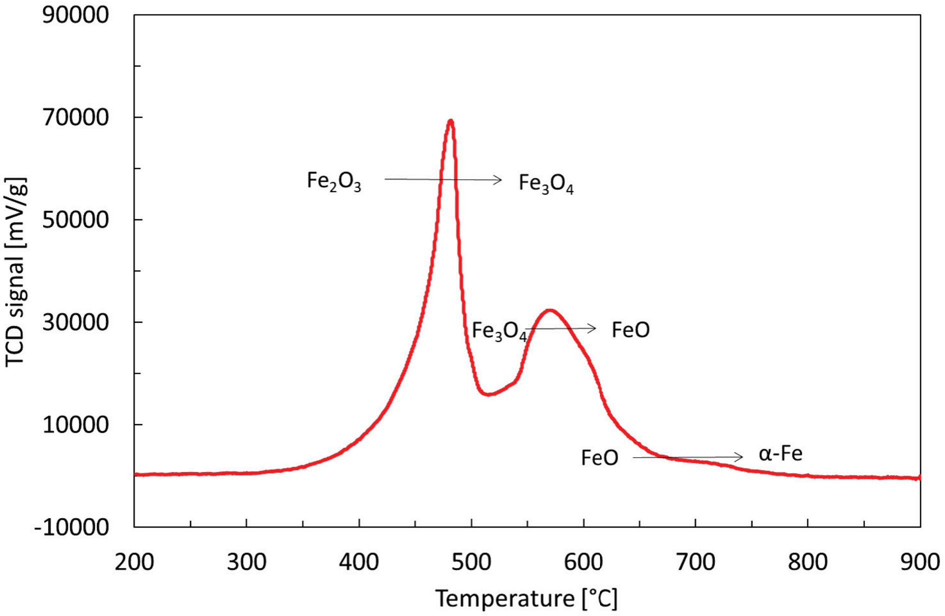

Figure 3.3: H_2-TPR profile of fresh catalyst.

2007) However, interactions of Fe with the alumina support and the presence of K, that has a reduction promoting effect, can influence the reduction peaks. The reduction of hematite (Fe_2O_3) to magnetite (Fe_3O_4) is generally reported at 350-380°C but interactions with the support can shift this peak towards higher temperatures. (Xie et al., 2017; Wan et al., 2007) Thus, the peak at 482°C is attributed to the reduction of Fe_2O_3 to Fe_3O_4, which is probably simultaneous to the reduction of K_2O, generally reported at temperatures between 450 and 500°C. (Xie et al., 2017) The peak at 572°C is attributed to the reduction of magnetite to wustite (FeO), which is generally observed at temperatures over 600°C but that can be shifted to lower temperatures because of interactions with K. (Gálvez et al., 2014) The last broad peak at about 725°C is attributed to the partial reduction of wustite to metallic iron. (Xie et al., 2017)

3.2.3 Thermogravimetric and elemental analysis.

Thermogravimetric analysis and elemental analysis have been performed over the same catalyst sample, before and after the reaction. Figure 3.4 shows the mass loss profile of the samples with increasing temperature.

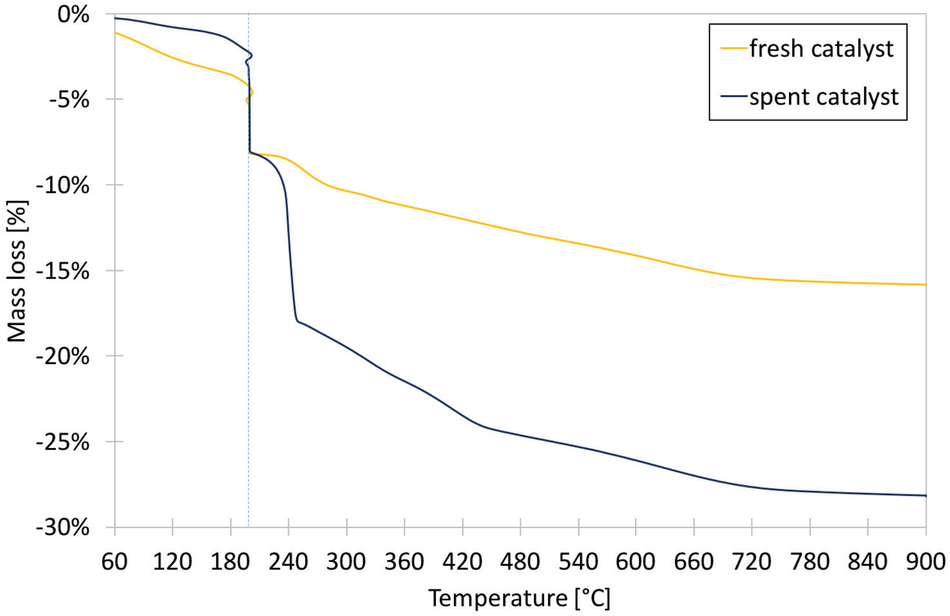

Figure 3.4: Profile of mass loss for a fresh sample (before reaction) and a spent sample (after reaction) measured during thermogravimetric analysis.

The total mass loss of the fresh and the spent samples are 16 and 28%, respectively. Two gradual mass losses are observed for both samples during the two temperature ramps (between 60 and 200°C and then between 250 and 900°C). These losses are probably due to the desorption of water which is in part physisorbed on the sample and easily desorbed at low temperatures and in part more strongly sorbed on the sample and desorbed at higher temperature (>250°C). (Champon et al., 2019) The most important difference between the two samples is observed between 200 and 250°C where an important mass loss occurs for the spent sample, from 8% to 18%. The equipment used for the analysis was not coupled to a mass spectrometer, thus the desorbed species could not be identified. However, we can suppose that this difference derives from the desorption of the carbon adsorbed on the catalyst surface that was formed during the reaction and that was not present on the fresh sample.

This assumption would explain the results obtained with the elemental analysis that allowed the quantification of the elements C, H, N and S adsorbed on the catalyst surface. Figure 3.5

reports the results of the elemental analysis on the fresh and spent samples (N and S were measured in very small quantities, thus they are not reported here). We can observe that more than 18% of the mass of the spent catalyst was represented by adsorbed C, while only 2% was contained by the fresh sample. This is thus in accord with the supposition that the mass loss observed on the spent sample between 200 and 250°C is due to the desorption of C.

We can thus suppose that, during the reaction, carbon was adsorbed on the catalytic surface. To study its chemical nature further analysis are needed.

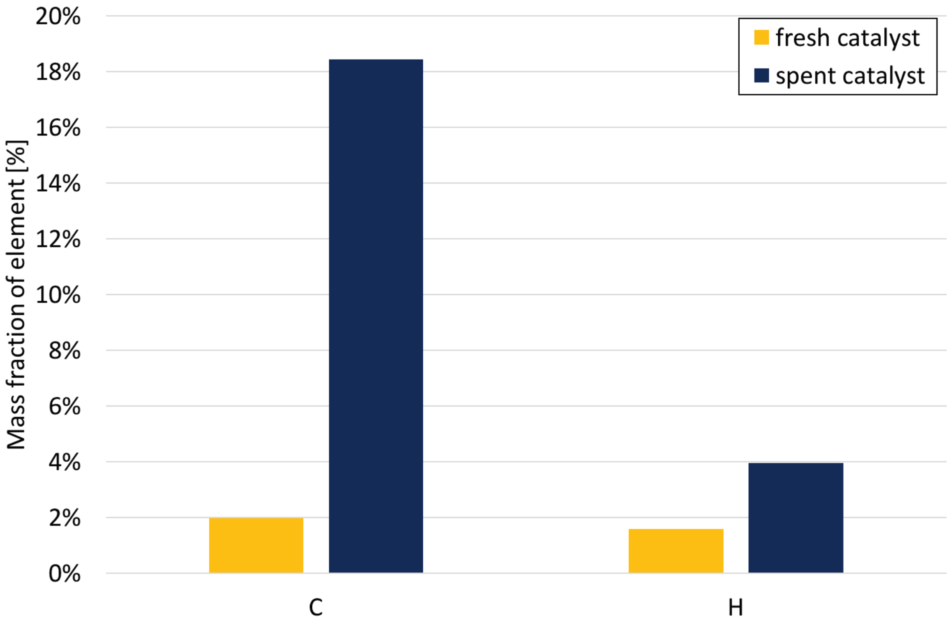

Figure 3.5: Results of the elemental CHNS analysis for a fresh sample (before reaction) and a spent sample (after reaction).

3.2.4 Phase and morphology.

The morphology of the catalyst was studied by X-ray diffraction and Mössbauer spectroscopy.

The patterns obtained by XRD are presented in Figure 3.6 for alumina support and fresh, reduced and spent catalysts. Peaks at 36°, 46° and 67° are typical of the γ-Al_2O_3 phase, used as support, but a possible mixture of γ-Al_2O_3 and η-Al_2O_3 phases cannot be excluded. Anyhow, the crystal phase of the support should not have strong influence on the catalytic activity. The black line in Figure 3.6 shows the XRD pattern for the fresh catalyst. Peaks at 23.6°, 33.2°, 35.7°, 49.1° and 54.2° correspond to a rhomboid hematite phase α-Fe_2O_3. Peaks at 19°, 23°, 29°, 32°, 34° and 41° suggest the presence of a $K(NO_3)$ orthorombic phase. This can seem a bit unlikely, as nitrates should be eliminated during the calcination process. However, it has been already observed before on catalysts with similar pore sizes. (Numpilai et al., 2019) Small pore sizes were suggested to hinder the decomposition of $K(NO_3)$ to K_2O. In our sample, we also observed the presence of the K_2O phase, represented by peaks at 27° and 39°. The blue line in Figure 3.6 shows the XRD pattern for the reduced catalyst. In the reduced catalyst, the main phase observed is cubic metallic α-Fe(0), as demonstrated by the presence of peaks at 44.7° and 64.9°. Finally, the XRD pattern of the used catalyst is characterized by the presence of multiple peaks at 39.6°, 43.9° and 44.5°, typical of the monoclinic Hägg carbide phase χ-Fe_5C_2, often observed in such catalytic processes. (Visconti et al., 2017; Hwang et al., 2019; Xie et al., 2017; Kim et al., 2006) Table 3.3 shows the identified phases and the cell parameters obtained from XRD. Crystallite sizes varies between 3 and 14Å.

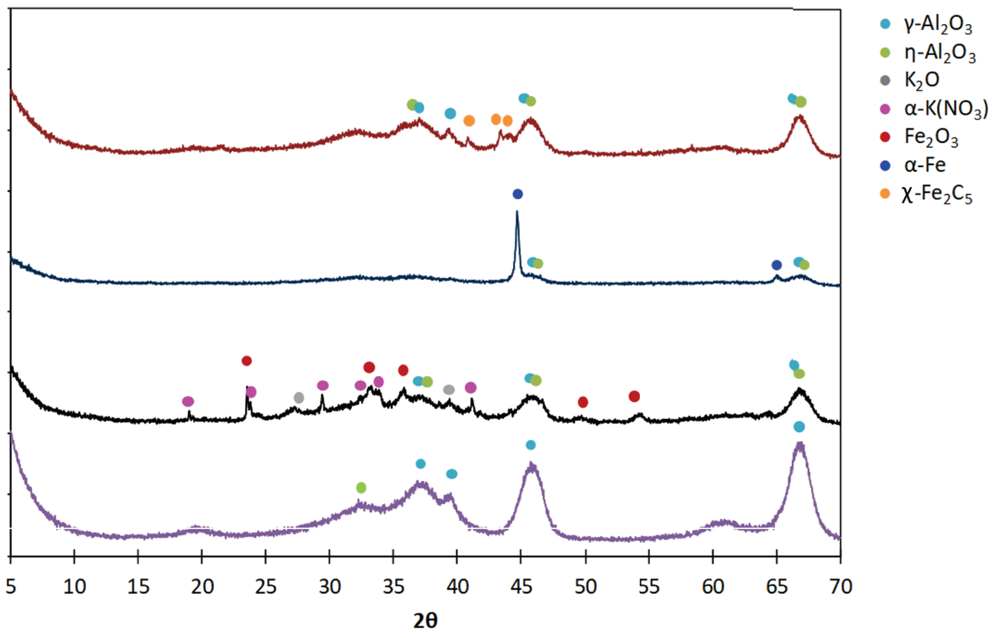

Figure 3.6: Patterns obtained from X-ray diffraction of alumina support (violet line), fresh catalyst after calcination (black line), reduced catalyst (blue line) and spent catalyst (brown line).

Table 3.3: Identified phases and corresponding cell parameters obtained from XRD.

Compound name	**Formula**	**Lattice**	**a** [Å]	**b** [Å]	**c** [Å]	α	β	γ	**Z**
Alumina, γ	Al_2O_3								
Alumina, η	$Al_{2.667}O_4$	Cubic	7.9						8
Hematite	Fe_2O_3	Rhomboid	5.0		13.8				6
Iron, α	Fe	Cubic	2.9						2
Hägg carbide, χ	$Fe_{2.5}C$	Monoclinic	11.6	4.6	5.1		97.7		4
Potassium oxide	K_2O	Cubic	6.4						
Potassium nitrate, α	KNO_3	Orthorombic	10.8	13.4	6.4				

Mössbauer spectroscopy has been simultaneously performed on the catalyst to study its crystallite structure. It allows to detect amorphous phases that could be missed by XRD. The Mössbauer spectra of fresh, reduced and spent catalysts are presented in Figure 3.7, while signal analysis and attributions are reported in Table 3.4.

The fresh catalyst presents a doublet with a chemical shift of 0.442 mm/s and a quadrupole splitting of 0.999 mm/s and a sextet with chemical shift of 0.459 and magnetic field of 513.5 kOe. The sextet can be attributed to the Fe(III) of hematite Fe_2O_3. (Greenwood and Gibb, 1971) The doublet is again attributed to Fe(III) but derives from a Fe_2O_3 superparamagnetic. This is typical of small particles below 50-100 nm. (Greenwood and Gibb, 1971) The two phases are present in the sample almost at the same concentration, indicating that all iron existing at this stage is in Fe(III) form, confirming the observations of XRD.

In the reduced catalyst, we observe the appearance of a new sextet with hyperfine magnetic field of 340.6 kOe and chemical shift of 0.102 mm/s. It is attributed to the metallic iron Fe(0). The two Fe(III) phases observed in the fresh catalyst are still present but in lower quantities. That means that the reduction process leads to a transition of hematite to metallic α-Fe which becomes the dominant phase.

The signal of the spent catalyst is quite hard to elaborate, as different signals appear, meaning

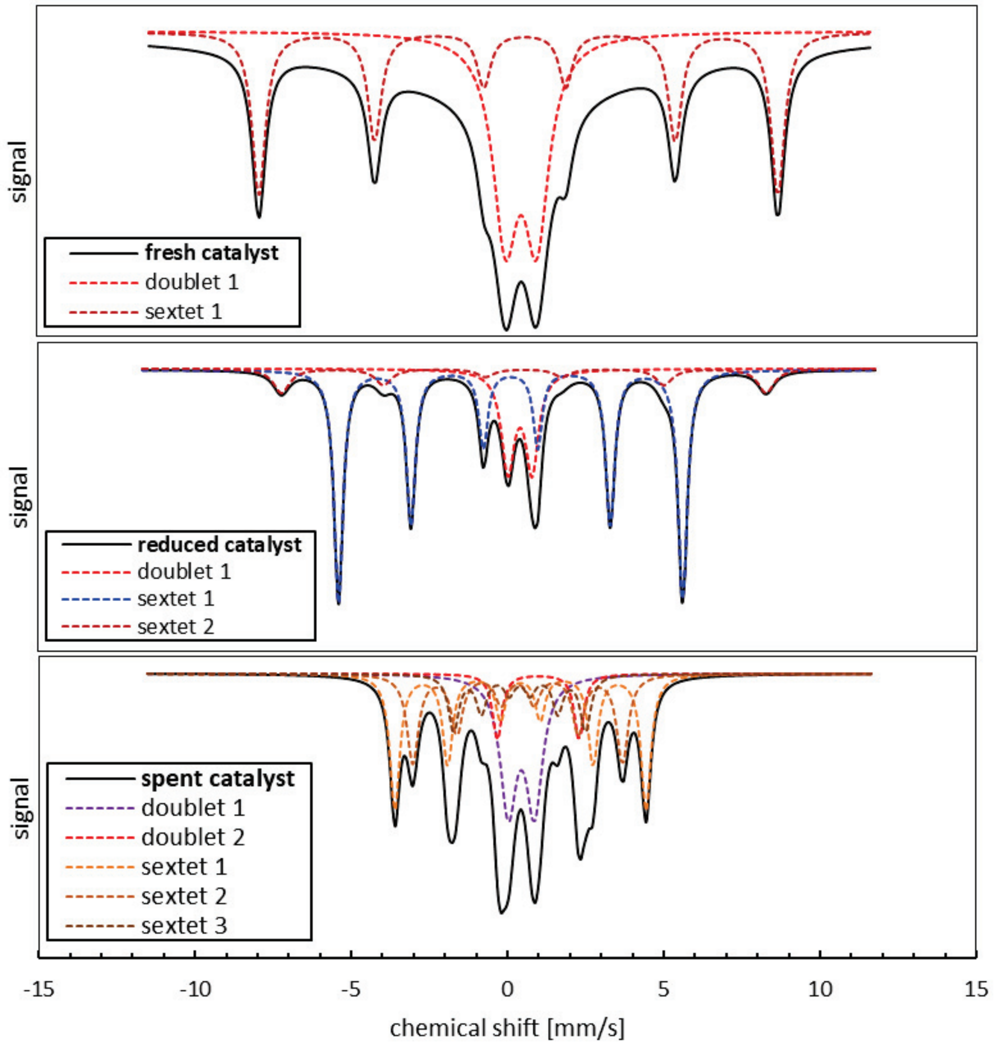

Figure 3.7: Results of Mössbauer spectroscopy for fresh catalyst after calcination (up), reduced catalyst (center) and spent catalyst (down).

that a mixture of iron phases is present in the catalyst. The three sextets with hyperfine magnetic fields at 249.5, 208.2 and 131.0 kOe and chemical shifts at 0.411, 0.322 and 0.384 are attributed to the three different iron sites of the Hägg carbide phase χ-Fe_5C_2, which constitutes the 68% of the sample. The doublet with chemical shift of 0.441 mm/s and quadropole splitting of 0.836 mm/s is attributed to Fe(III), while the doublet with chemical shift of 0.980 mm/s and quadrupole splitting of 2.617 mm/s is attributed to Fe(II), meaning that iron oxides are also present in the spent catalyst, possibly in the Fe_3O_4 species form, as previously reported in literature. (Visconti et al., 2017; Hwang et al., 2019; Xie et al., 2017; Kim et al., 2006)

In conclusion, catalyst characterization by XRD and Mössbauer spectroscopy confirms that different active phases are involved in the CO_2 hydrogenation, as previously reported. (Riedel et al., 2003; Gnanamani et al., 2013; Schulz et al., 2005, 1999; Visconti et al., 2017) It is generally recognised that many types of active sites are involved in the catalysis of the CO_2 hydrogenation over Fe catalyst, as we will discuss later in this Chapter. The catalyst in its fresh form is not active, as it contains only Fe_2O_3 which is believed to be inactive for this reaction. After reduction, the main phase becomes the metallic α-Fe which is believed to be active only for the secondary hydrogenations of olefins. Iron carbides are the active phase for the chain-growth and

Table 3.4: Results of Mössbauer spectroscopy for fresh catalyst after calcination, reduced catalyst and spent catalyst and attribution to the corresponding iron phase.

Signal	δ [mm/s]	ϵ [mm/s]	Δ [mm/s]	H [kOe]	R [%]	Attribution
Fresh catalyst						
doublet 1	0.442		0.999		52%	Fe(III) of superparamagnetic Fe_2O_3
sextet 1	0.459	-0.103		513.5	48%	Fe(III) of Fe_2O_3
Reduced catalyst						
doublet 1	0.401		0.769		21%	Fe(III) of superparamagnetic Fe_2O_3
sextet 1	0.102	0.001		340.6	67%	α-Fe(0)
sextet 2	0.522	0		479.5	12%	Fe(III) of Fe_2O_3
Spent catalyst						
doublet 1	0.441		0.836		25%	Fe(III)
doublet 2	0.980		2.617		7%	Fe(II)
sextet 1	0.411	0		249.5	31%	χ-Fe_5C_2
sextet 2	0.322	0		208.2	24%	χ-Fe_5C_2
sextet 3	0.384	0		131.0	13%	χ-Fe_5C_2

the CO conversion. We have observed this phase only in our spent catalyst and this suggests that iron carbides are formed during the reaction. The catalyst thus needs to undergo a reorganisation phenomenon so that the active phases are formed. We will discuss this phenomenon later in the Chapter.

The morphology of the catalyst has also been studied by transmission electron microscopy. Figure 3.8 shows the TEM images, while Figure 3.9 presents the EDS maps of the fresh, reduced and spent catalysts, showing how K and Fe are dispersed on the catalytic surface. K seems to be well dispersed on the support, while Fe appears in form of bigger agglomerates. Globally, we can observe that the catalyst is extremely inhomogeneous and Fe dispersion is not optimal.

Some areas of the reduced catalyst present the formation of needle-shaped particles mainly made of K, as shown in Figure 3.10. These are probably due to the formation of potassium nitrate crystals, which would confirm the presence of the KNO_3 phase observed by XRD. As the TEM images have been obtained after many months from the catalyst synthesis, we do not know whether these crystals formed during the ex-situ reduction step or later, during their exposure to air for some months. If they are effectively formed during the reduction and thus they are present in the catalyst that is used to catalyse the reaction, this K would not take part to the catalysis of the reaction. Thus, this would explain why, while having a catalyst with higher K content than expected (see next Section), the catalyst performances obtained were similar to those reported in literature over catalysts with lower Fe/K content than ours.

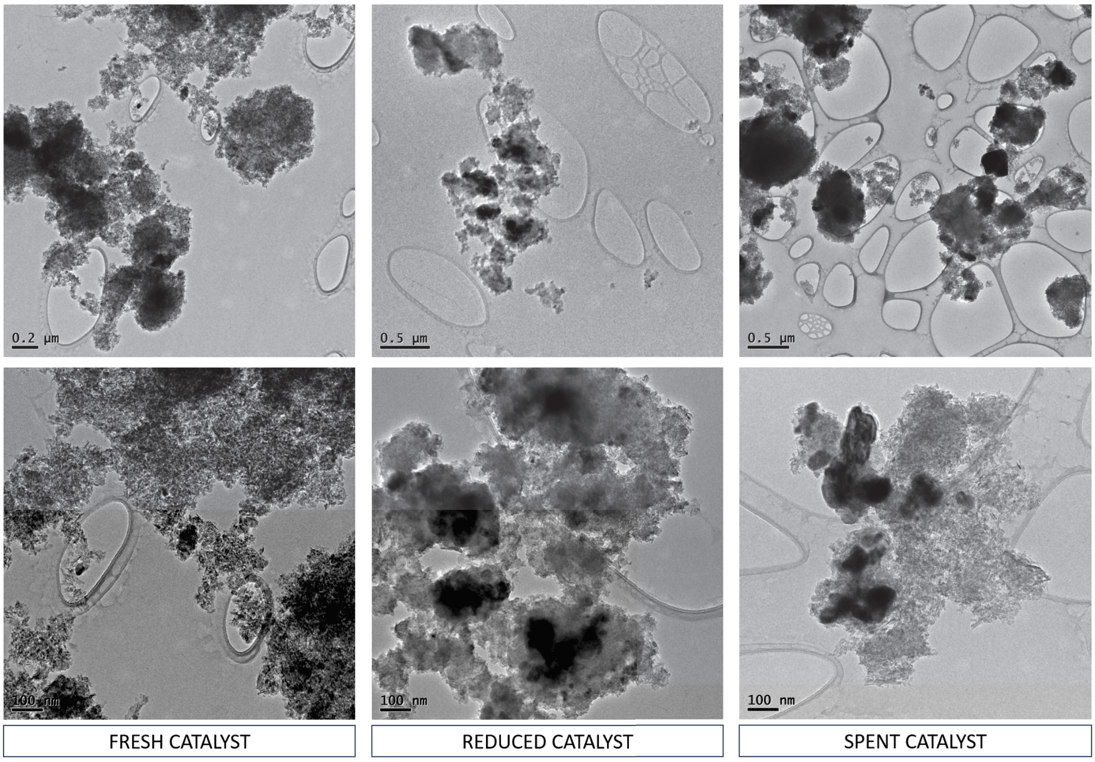

Figure 3.8: TEM images of fresh, reduced and spent catalysts.

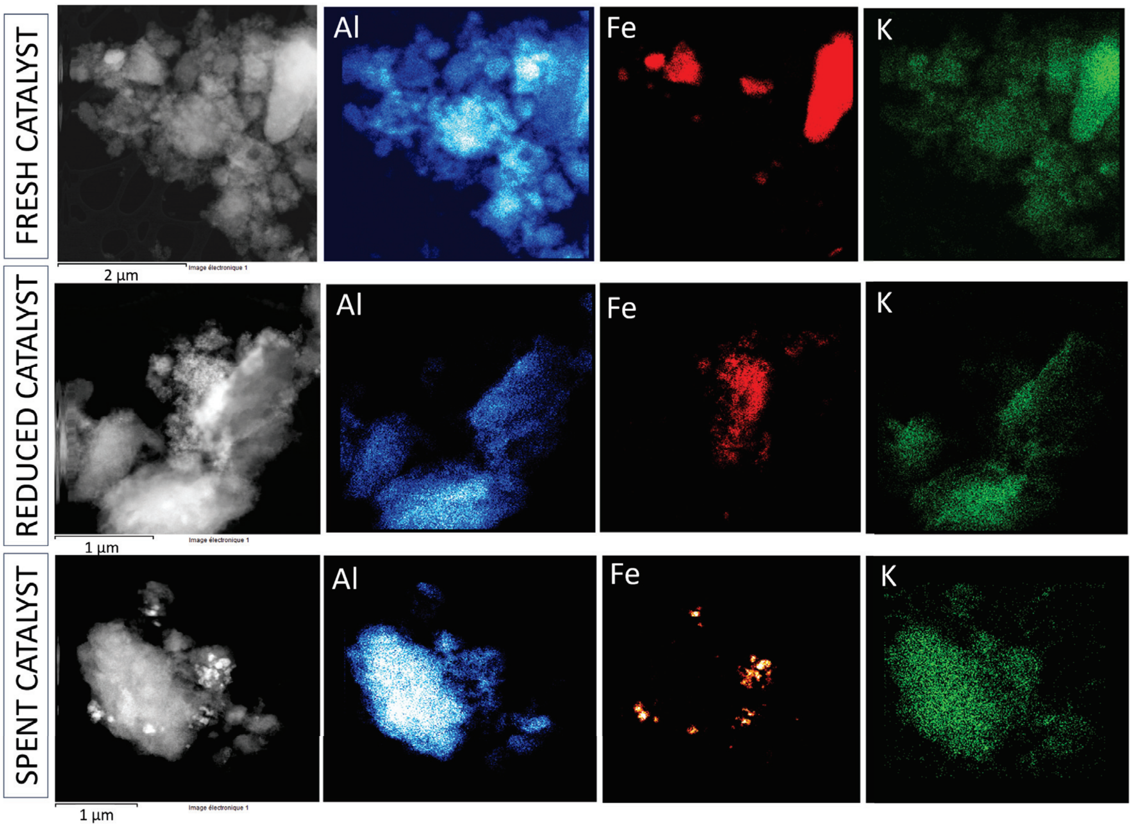

Figure 3.9: EDS maps of fresh, reduced and spent catalysts.

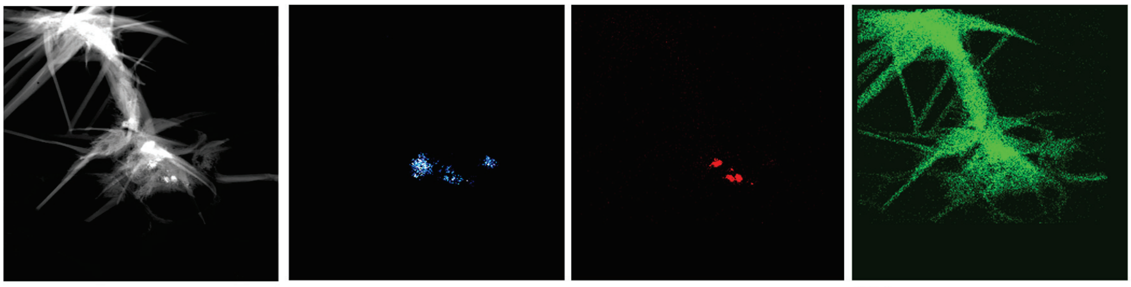

Figure 3.10: EDS maps of the reduced catalyst, showing the formation of K crystals.

3.2.5 Catalyst composition.

Catalyst composition was analysed by ICP-EOS analysis. Results are reported in Table 3.5. According to the synthesis procedure followed, the expected K/Fe mass ratio is 0.35, with 20% of Fe as mass fraction of the total alumina mass (or 16% as fraction of total catalyst mass). Table 3.5 presents the results of the ICP analysis, shown as fraction of total catalyst mass. These results show higher K/Fe mass ratios than expected (higher than 0.75), with higher fractions of K and lower content of Fe lower than expected.

We do not have a certain explication for the observed result. We have analysed via ICP each step of the synthesis protocol, but we have not observed any important losses of Fe during any of the steps. Moreover, we have verified and checked many times the ICP analysis procedure but we could not find any problem and the results were generally very reproducible. We are not aware of eventual problems with this kind of analysis when used with elements such as K and Fe and, on the contrary, this technique is one of the most reliable. However, the authors of the paper whose synthesis procedure we have followed have not reported the results of an ICP analysis of their catalyst (Kim et al., 2006), thus we have no reference to compare. One could say that these results come from the high inhomogeneity of our catalyst, as we have observed with TEM. However, the catalyst has been sieved and mixed before sending it to the ICP analysis and the ICP results are too reproducible to conclude that the inhomogeneity is the cause.

One possible explication can derive from the observation of the significant decrease of specific area after impregnation of the support and the morphology of the structure studied by TEM, XRD and Mössbauer. The observed significant reduction in the specific surface area may indicate the formation of large particles of iron oxide, or even gangue, that obstruct an important fraction of the pores, therefore reducing the specific surface area. Moreover, after the catalyst particles grinding, the material could become heterogeneous and form particles of iron oxide well dispersed on the support, together with larger particles made of iron oxides and smaller particles made of potassium nitrate or potassium oxide. It is possible that after sieving, a part of these larger particles rich in iron are discarded and therefore some of the iron initially introduced in the catalyst is lost. This has not been verified yet and still remains an hypothesis. To verify this hypothesis, ICP of the catalyst before and after sieving is currently ongoing and could contribute to confirm or exclude this hypothesis.

Table 3.5: Bulk composition of calcined and reduced catalysts. Values are intended as weight fractions of the total mass.

	Fe [%wt]	**K** [%wt]	**K/Fe** [-]
Calcined catalyst	11.0	8.4	0.76
Reduced catalyst	13.6	10.5	0.77

We remind that the objective of this work is not to synthesize an optimal catalyst, as a lot of effort has already been dedicated to this aim by different authors. Our purpose here is to synthesize a catalyst that allows us to perform an experimental study, in order to gain enough information to develop detailed models of the kinetics and of the reactor. Thus, we have chosen a catalyst that seemed to have acceptable performances and at the same time to be easy to synthesize. Its synthesis and reduction procedures were not optimized. Future works should dedicate some effort to improve the synthesis procedure, so that better active elements dispersion and homogeneity could be reached.

3.3 Catalyst activation and stability.

The first step of the study of the catalyst performances is to verify its long-term stability, to check if deactivation phenomena occur. We have thus performed some tests where the pre-reduced catalyst is loaded in the reactor and reference operating conditions (2000 Nml/g_{cat}/h, H_2/CO_2 ratio of 3, 15 bars and 300°C) are applied for almost 300 hours.

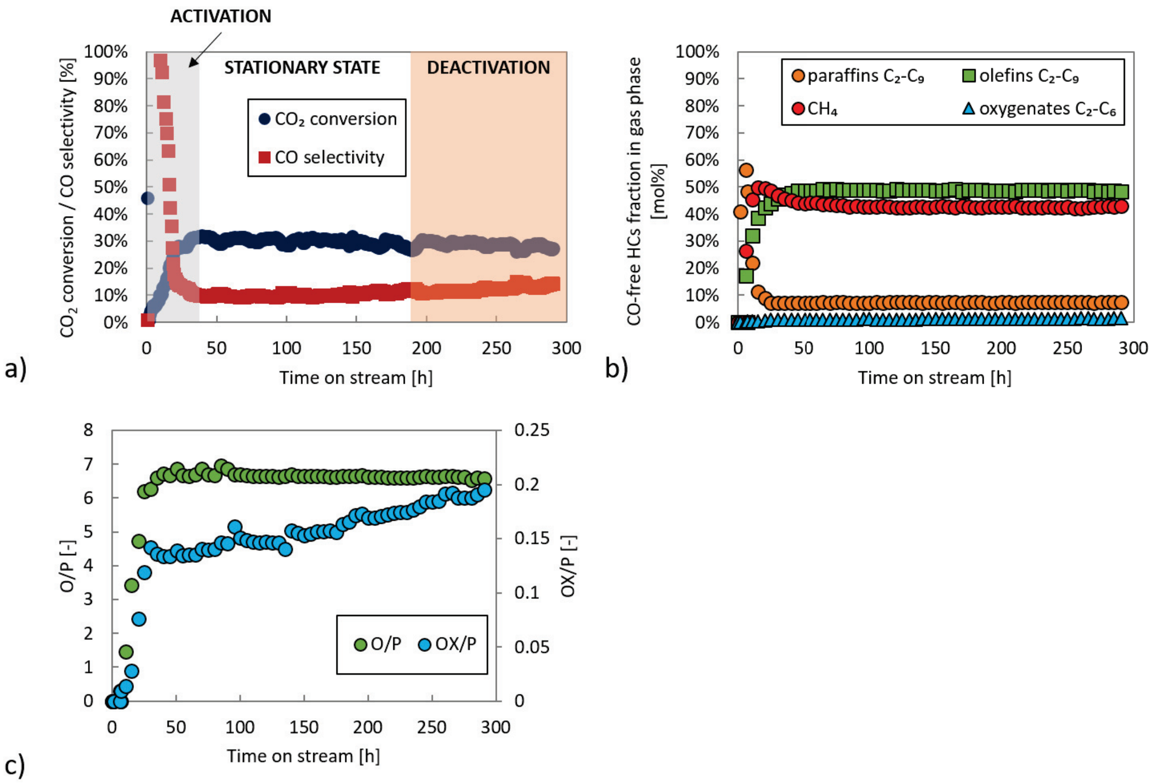

Figure 3.11: a) Evolution of CO_2 conversion and CO selectivity during the reaction. b) Evolution of CH_4, C_2-C_9 paraffins and olefins and C_{2+} oxygenates formation observed in gaseous phase during the reaction. Fractions are calculated as mole fractions of CO-free total hydrocarbons. c) Evolution of O/P and OX/P ratios in gaseous phase during the reaction. Results are referred to reference reaction conditions (2000 Nml/g_{cat}/h, H_2/CO_2 ratio of 3, 15 bars and 300°C).

The catalytic performances of the catalyst during a long run are reported in Figure 3.11. We can observe that during the first 45 hours the catalytic activity progressively increases: CO_2 conversion progressively increases until a value of about 30% is reached at stationary state. At low time on stream, CO results to be the main product, then its selectivity progressively decreases until the value of 10% is reached in stationary conditions. Figure 3.11.b shows the evolution of compounds in the gas phase during time on stream. Only gaseous phase is analysed here, thus only products until 9 C atoms are included. We can observe that CH_4 and paraffins formation decreases with time on stream, while olefins gradually increase until the value of 50% at stationary state, becoming the main product of the reaction. Oxygenates fraction in gas phase is very small, as they are almost completely condensed and thus detected in very small extent in the gaseous phase. Anyway, a slight increase of their fraction in the gas phase is observed during the first hours of reaction. The evolution of the olefins/paraffins and oxygenates/paraffins ratios can give interesting insights about the reaction mechanism. It can be observed that both O/P and OX/P ratios are low at the beginning of the reaction when paraffins are the main product and then they gradually increase. The increase of OX/P ratio is a gradual process and its stationary state is never reached during the experiment time.

These aspects suggest that the catalyst evolves during the reaction and that different active sites are involved in the catalysis. This has been observed before by different authors. (Schulz et al., 1999; Riedel et al., 2003; Schulz et al., 2005; Schulz, 2014) In particular, the "self-organization" phenomenon has been reported as typical of iron catalysts during CO_2 hydrogenation. During this process, the carbiding activity is dominant at the beginning of the reaction and leads to the transition of metal iron into iron carbides, which represent the active phase for the chain-growth reactions. Two other active sites are believed to be involved in the reaction: the Fe_3O_4, responsible for the RWGS activity, and the Fe(0), responsible for the secondary hydrogenation reactions. At the beginning of the reaction, CO is observed to be the main product, suggesting that the catalyst has a strong RWGS activity and thus the Fe_3O_4 is formed. The presence of CO_2 is supposed to reoxide the metallic iron to Fe_3O_4, so that RWGS activity can be developed. The observed decrease of CO selectivity and the increase of hydrocarbons formation indicate that, during the activation, the RWGS active sites are progressively converted into iron carbides, so that the activity towards chain-growth and HCs formation are increased. Moreover, the increase of the O/P ratio and the decrease of paraffins formation suggest that the number of sites for secondary hydrogenation reactions of olefins decreases with time on stream, reducing the formation of paraffins. Similar behaviours have been observed by other authors on similar catalysts. (Visconti et al., 2017; Schulz, 2014)

After activation, stationary state is reached and a constant activity is maintained for another 140 hours. After this working zone, the catalyst starts to present deactivation: the CO_2 conversion is kept almost stable, but the CO selectivity starts to gradually increase. No significant changes are observed in the hydrocarbons products distribution during deactivation. This suggests that iron phases in the catalyst evolve and a re-oxidation of the Hägg carbide into iron oxides is believed to occur and to be the cause of such a deactivation. (Zhang et al., 2019) Thus, the catalyst loses its activity towards the formation of hydrocarbons, but not its activity towards the RWGS and this is the reason why not significant changes are observed on the CO_2 conversion. The reason for such a loss of activity could be the high amount of H_2O at which the catalyst is exposed during the reaction and that favours iron carbides oxidation, but further experiments have to be performed to better understand the catalyst deactivation. Another explication could be the carbon deposition, favoured by the high K content of the catalyst. Moreover, regeneration of the catalyst by re-reducing with H_2 should be tested to see if a recovery of the catalytic activity could be obtained.

Figure 3.12 shows the axial temperature profile measured during a long-time run in reference conditions. The left graph refers to the activation (first 50 hours). The temperature increase observed is due to the increase of the catalytic activity towards the exothermic FT reaction. The graph on the right is referred to the stationary state and shows an almost constant profile until time on stream of 200 hours. After that, we observe a slow shift of the temperature profile towards lower temperatures, sign of a loss of activity for the FT reaction and to an increase of the activity for the RWGS, which is endothermic. This is in agreement with the observed catalyst deactivation previously described.

The catalytic performances obtained during the stationary state are discussed in the following section.

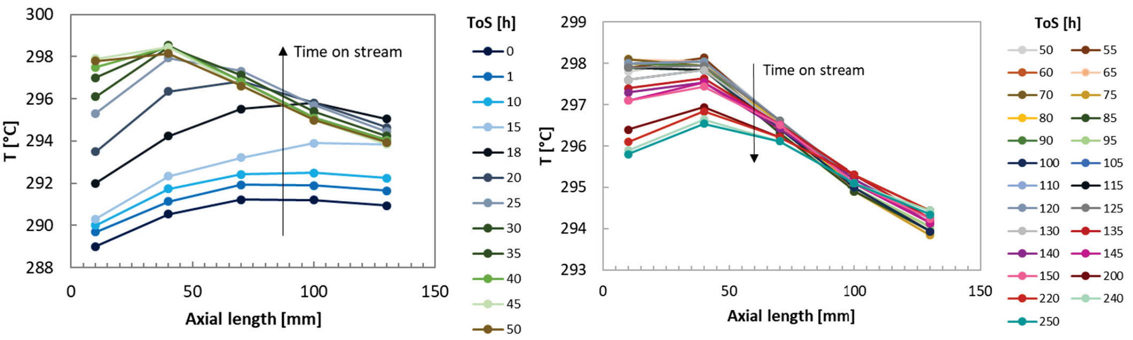

Figure 3.12: Axial temperature profile along the reactor as a function of time on stream (ToS). On the left from 0 to 50 hours, on the right from 50 to 250 hours. Points represent measured temperatures, lines are just for a better visualisation.

3.4 Activity at steady-state.

In the previous section, we have analysed the evolution of the catalytic activity during a reaction of 300 hours, by focusing our attention on the phases of activation and deactivation. Here, we analyse the performances obtained during the stationary state.

Table 3.6: Summary of catalytic performances of CO_2 hydrogenation over a Fe-K/Al_2O_3 catalyst at steady-state in reference conditions (GHSV of 2000 Nml/g_{cat}/h, H_2/CO_2 ratio of 3, 15 bars and 300°C). Distribution of products are given as fractions among all the obtained hydrocarbons, CO and water free.

Parameter	Value	Parameter	Value
CO_2 conversion	32%	CH_4	36%
CO selectivity	12%	Paraffins $C_2 - C_4$	5%
		Paraffins C_{5+}	1%
O/P	6.22	Olefins $C_2 - C_4$	31%
OX/P	2.27	Olefins C_{5+}	8%
		CH_3OH	2%
α_1	0.58	Oxygenates $C_2 - C_6$	14%
α_2	0.78	Others	2%

The catalytic performances obtained in reference conditions (GHSV of 2000 Nml/g_{cat}/h, H_2/CO_2 ratio of 3, 15 bars and 300°C), once the stationary state has been reached, are summarized in Table 3.6. In these conditions a CO_2 conversion of about 30% and a CO selectivity of 12% are obtained. These performances are in accordance with those reported in literature for similar catalysts: CO_2 conversion has been reported in the range of 30-40% and CO selectivity between 7 and 42%. (Riedel et al., 1999; Hwang et al., 2001; Liu et al., 2018; Kim et al., 2006; Xie et al., 2017; Lee et al., 2003) Among hydrocarbons, linear α-olefins are the most abundant product, in particular the short-chains C_2-C_4 olefins fraction that represents the 31% of the obtained hydrocarbons. However, the 36% of products is represented by methane that in these conditions is thermodynamically favoured. Linear paraffins represent only the 6% of total products, while an important fraction of oxygenates (14%) is observed, mainly constituted by alcohols, carboxylic acids and aldehydes until 6 C numbers. The olefins/paraffins and oxygenates/paraffins ratios are significantly higher than 1, indicating a low selectivity towards paraffins formation, in favour of olefins and oxygenates. Methanol is observed in small quantities (<2%). Products labelled as others refer to compounds observed in very small quantities, such as branched olefins, branched paraffins and aromatics.

The distribution of C_1-C_{30} hydrocarbons is shown in Figure 3.13: the logarithm of the mole

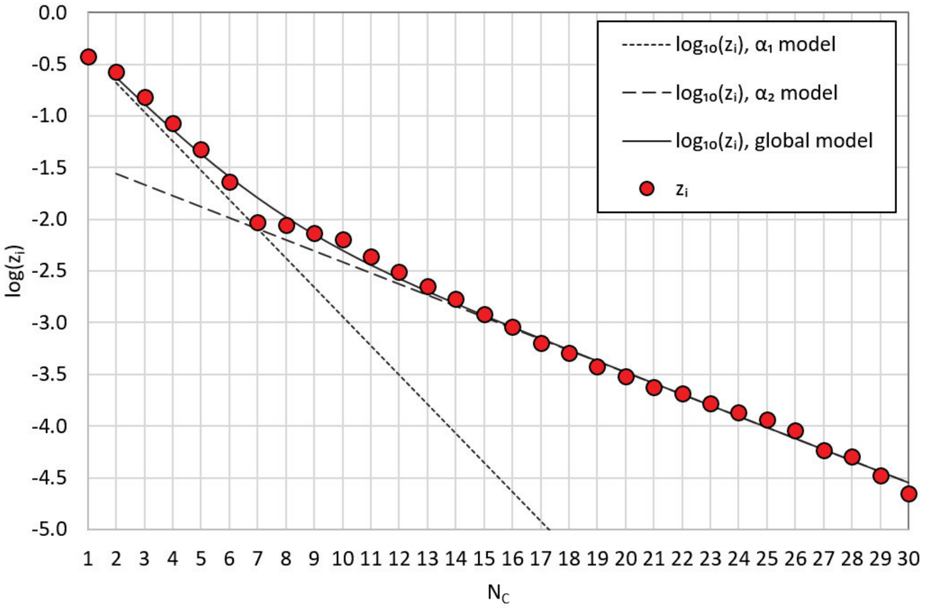

Figure 3.13: ASF distribution of C_1-C_{30} products for the reaction in reference conditions (2000 Nml/g_{cat}/h, H_2/CO_2 ratio of 3, 15 bars and 300°C). z_i is the mole fraction of products with i carbon number among all hydrocarbons.

fraction of compounds with carbon number i is plotted as a function of the carbon number. The ideal ASF distribution expects all the points to be on the same straight line, with slope α, according to:

$$z_i = (1-\alpha)\alpha^{i-1} \tag{3.1}$$

However, we observe that long hydrocarbons (C_{7+}) show a positive deviation from the ideal ASF-distribution. Positive deviations of long hydrocarbons have been already observed for Fischer-Tropsch synthesis over iron catalysts. (Donnelly et al., 1988; Donnelly and Satterfield, 1989; Dictor and Bell, 1986; Schliebs and Gaube, 1985) The cause is still not clear but different interpretations have been given, such as the presence of different active sites (Donnelly et al., 1988; Madon, 1981) or different reaction mechanisms. (Patzlaff et al., 1999) Over Ru and Co catalysts, deviations of long hydrocarbons from the ideal ASF distribution were explained by re-adsoprtion of 1-alkenes and their secondary hydrogenations. (Iglesia et al., 1991; Kuipers et al., 1995; Schulz and Claeys, 1999) However, over iron-based catalysts, secondary hydrogenations of 1-alkenes were observed to be negligible (Patzlaff et al., 1999), thus the most likely interpretation seems to be connected to the co-existence of different active sites and/or reaction mechanisms. (Patzlaff et al., 2002)

The observed distribution can be modelled with a double-α ASF distribution, derived from the superposition of two independent ASF distributions and characterised by two αs, one for short products (C_2-C_7) and one for long-chain products (C_{8+}). (Patzlaff et al., 1999) The obtained values of α_1 and α_2, respectively 0.58 and 0.78, are in the range reported in literature for CO_2 hydrogenation. (Riedel et al., 2001; Kim et al., 2006).

Figure 3.14 shows the ASF distribution of C_1-C_{30} hydrocarbons by product group: olefins, paraffins, alcohols and acids. In this case, for each group, the ideal ASF distribution is used to fit the experimental data (excluding C_1) and a value of chain-growth probability α is estimated for each group. Values of α obtained are reported in Table 3.7. From these values, it can be observed that the chain-growth probabilities of olefins and paraffins are very close, suggesting that their formations are competitive reactions that follow similar mechanisms. On the other

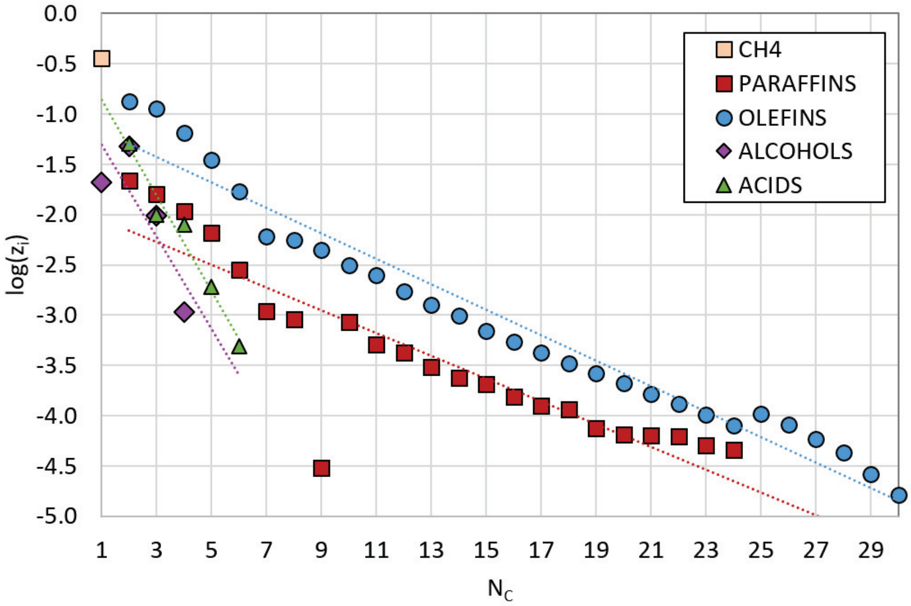

Figure 3.14: ASF distribution of C_1-C_{30} olefins, paraffins, alcohols and acids for the reaction in reference conditions (2000 Nml/g_{cat}/h, H_2/CO_2 ratio of 3, 15 bars and 300°C). z_i is the mole fraction of products with i carbon number among all hydrocarbons. Dashed lines represent the ideal ASF fit of the experimental points.

side, the chain-growth probabilities of oxygenate compounds are significantly lower, indicating that a possible different mechanism is followed for their formation.

Table 3.7: Values of α estimated via the ideal ASF distribution for olefins, paraffins, acids and alcohols.

Group	α
OLEFINS	0.75
PARAFFINS	0.76
ACIDS	0.33
ALCOHOLS	0.15

Once studied the catalytic performances in reference conditions, we performed a parametric study by varying different operating parameters (such as contact time, temperature, pressure and H_2/CO_2 ratio). The results of this study are discussed in the next section.

3.5 Influence of operating parameters.

3.5.1 Effects of contact time.

The effect of contact time has been studied by varying the modified contact time τ_{mod} in the range between 0.5 and 8 g_{cat}.s/Nml. The results of the experiments conducted by varying the contact time are reported in Figure 3.15. Until τ_{mod} of 4 g_{cat}.s/Nml, increasing contact time led to the increase of the CO_2 conversion almost linearly with τ_{mod}, as expected. At the same time, a progressive decrease of the CO selectivity is observed, suggesting that FT is a slow reaction and increasing the contact time favours the conversion of CO towards the hydrocarbons. At higher τ_{mod}, a decline of CO_2 conversion and an increase of the CO selectivity were observed, possibly due to deactivation of the catalyst caused by high water partial pressures, as already

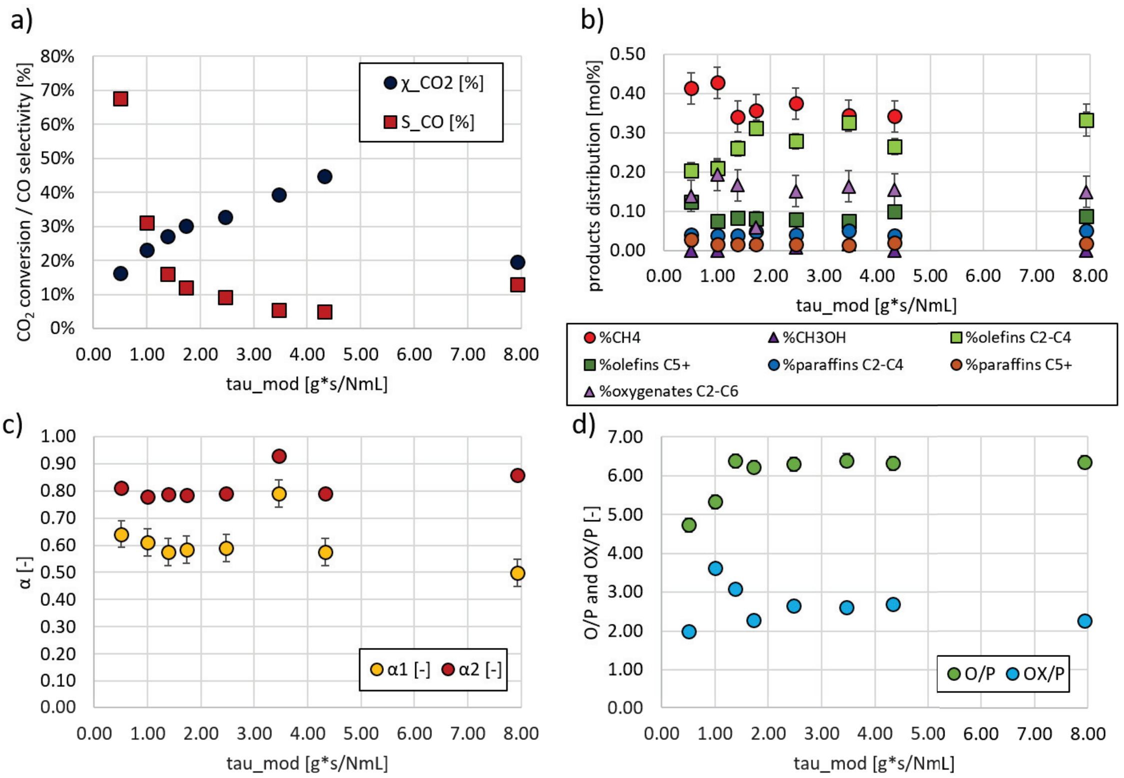

Figure 3.15: Effects of contact time on catalytic performances: a) CO$_2$ conversion and CO selectivity; b) distribution of hydrocarbon products, calculated as fraction of total hydrocarbons obtained (CO-free); c) C$_{2+}$ olefins/paraffins ratio and oxygenates/paraffins ratio; d) values of α_1 and α_2. Points represent experimental data, lines represent model results. Error bars indicate standard deviations. Operating conditions: H$_2$/CO$_2$ ratio of 3, 15 bars, 300°C, GHSV varied between 800 and 7000 Nml/g$_{cat}$/h and mass of catalyst between 1.8 to 3.8 g.

observed by Iglesias et al. (Iglesias Gonzalez et al., 2015)

Concerning the HCs distribution, we observe a gradual increase of the olefins fraction, especially the short chains, with a consequent increase of the O/P ratio when increasing τ_{mod}. For $\tau_{\text{mod}} < 2$ g.s/Nml higher values of OX/P are observed, as well as higher fractions of oxygenates, compared to the values for higher τ_{mod}, probably due to high incertitudes in the experimental measures. No other evident effects of contact time are observed on hydrocarbons distributions neither on the values of αs.

Figure 3.16 represents the evolution of CO and HCs selectivity as functions of the CO$_2$ conversion. Extrapolation of the CO selectivity towards zero CO$_2$ conversion results in values equal to 1, indicating that HCs are mostly secondary products and that direct hydrogenation of CO$_2$ can be neglected, as already observed by Riedel et al. (Riedel et al., 2001) The formation of CO as primary product can also explain the increase of CO selectivity when reducing the contact time.

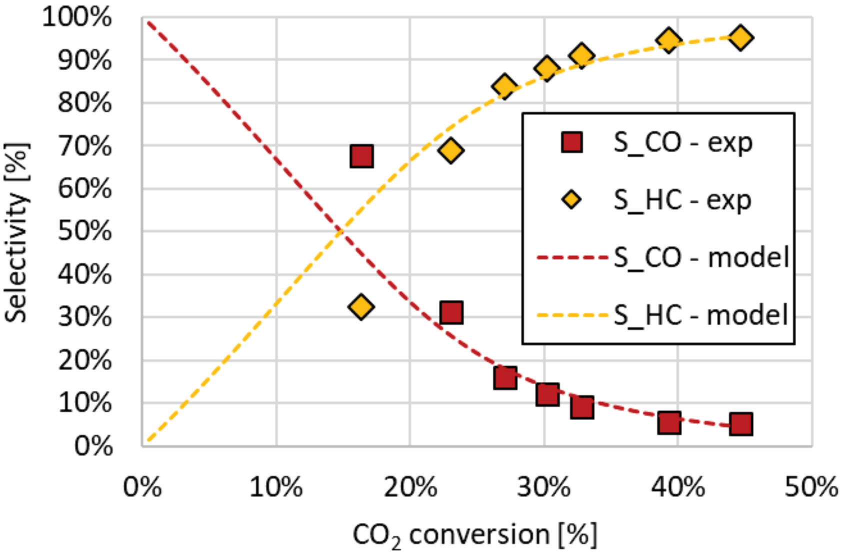

Figure 3.16: Evolution of CO and HCs selectivity with CO_2 conversion. Operating conditions: H_2/CO_2 ratio of 3, 15 bars, 300°C, GHSV varied between 800 and 7000 Nml/g_{cat}/h and mass of catalyst between 1.8 to 3.8 g. The dotted lines represent the predictions of the kinetic model, described in the following chapter.

3.5.2 Effects of temperature.

The effect of temperature has been studied in the interval between 250°C and 350°C. The results of the experiments conducted by varying the temperature are reported in Figure 3.17. At 350°C irreversible catalyst deactivation was observed, leading to important production of CO and no more increase of the CO_2 conversion. The deactivation mechanism at high temperatures has been been ascribed in the literature to 3 common phenomena: coke deposition (favoured by the high K content) and/or re-oxidation of carbides and/or sintering. (Riedel et al., 2001; Iglesias Gonzalez et al., 2015) Further investigations have to be made in order to understand which of those phenomena is involved here.

We can observe that an increase of temperature from 250°C to 325°C leads to a gradual increase of CO_2 conversion from 13% to 39% and to a decrease of CO selectivity from 47% to 9%, as expected. In fact, higher temperatures allow to shift the RWGS equilibrium towards higher CO_2 conversion, leading to higher production of CO. At the same time at high temperatures, the CO dissociation is favoured, resulting in higher rates of FT reaction.

Concerning the HCs distribution, we can observe that methane fraction is slightly decreased when temperature is increased, while short olefins C_2-C_4 formation is increased. Longer chains are formed to a lesser extent, indicating that at high temperatures the formation of long-chain hydrocarbons becomes less important. Paraffinic fractions also decrease with increasing temperature, leading to higher O/P and OX/P ratios at higher temperatures. The higher olefinic content and the decrease of methane fraction when temperature is increased can be explained by the lowering of H_2/CO ratio due to the greater closeness to equilibrium of the RWGS at higher temperatures.

The value of α_2 seems to be less influenced by temperature changes than α_1. This latter gradually decreases when increasing temperature. This suggests that long chains could be formed with a different mechanism than short chains, as previously proposed (Patzlaff et al., 1999; Gaube and Klein, 2008) and as would be in agreement with the observed ASF distribution. The mechanism that dominates the formation of short chains seems to be much more influenced by the temperature.

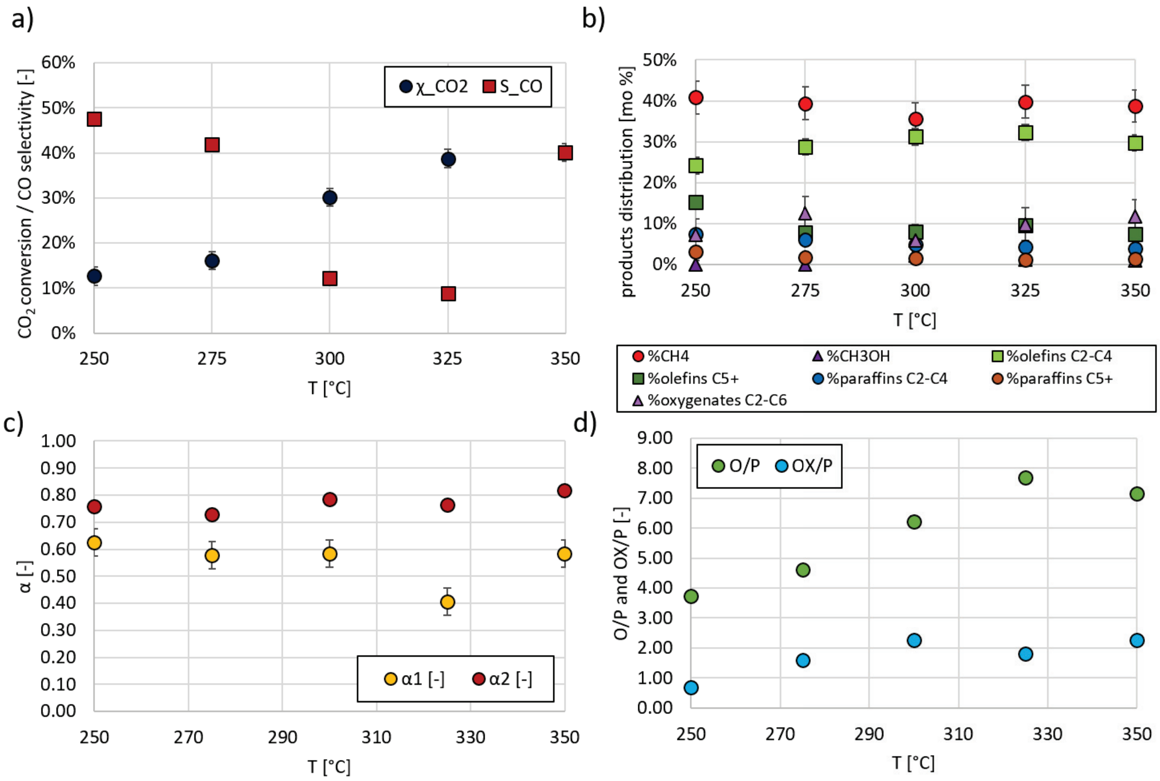

Figure 3.17: Effects of temperature on catalytic performances: a) CO_2 conversion and CO selectivity; b) distribution of hydrocarbon products, calculated as fraction of total hydrocarbons obtained (CO-free); c) C_{2+} olefins/paraffins ratio and oxygenates/paraffins ratio; d) values of α_1 and α_2. Points represent experimental data, lines represent model results. Error bars indicate standard deviations. Operating conditions: H_2/CO_2 ratio of 3, 15 bars, GHSV 2000 Nml/g_{cat}/h and temperature varied between 250 and 350°C.

3.5.3 Effects of inlet H_2/CO_2 molar ratio.

The effect of the stoichiometry of the reaction, expressed as H_2/CO_2 molar ratio at the reactor feed, has been investigated by varying this ratio between 3 and 24. The results reported in Figure 3.18 show that the increase of the H_2/CO_2 ratio leads to an important increase of the CO_2 conversion that reaches a value of 91% for the highest H_2/CO_2 ratio tested. Moreover, a significant reduction of the formation of CO is observed, with values very close to 0 for H_2/CO_2 higher than 15. Thus, a high excess of H_2 in the reactor feed is largely beneficial for the catalytic performances. However, high excess of H_2 in the feed also leads to greater formation of CH_4, which becomes more than 50% of the hydrocarbons products at the highest H_2/CO_2 ratio tested. When H_2/CO_2 ratio is increased, C_2-C_4 olefin fraction slightly drops and oxygenates fraction clearly declines, leading to a decrease of both O/P and OX/P ratios.

The observed increase of CH_4 formation can be explained by the dependence of the hydrogenation rate of CO on the H_2 content in the feed. Increasing the H_2/CO_2 ratio in facts leads to higher H/C ratios at the catalytic surface, resulting in lower chain-growth rate and lower secondary olefins reactions.

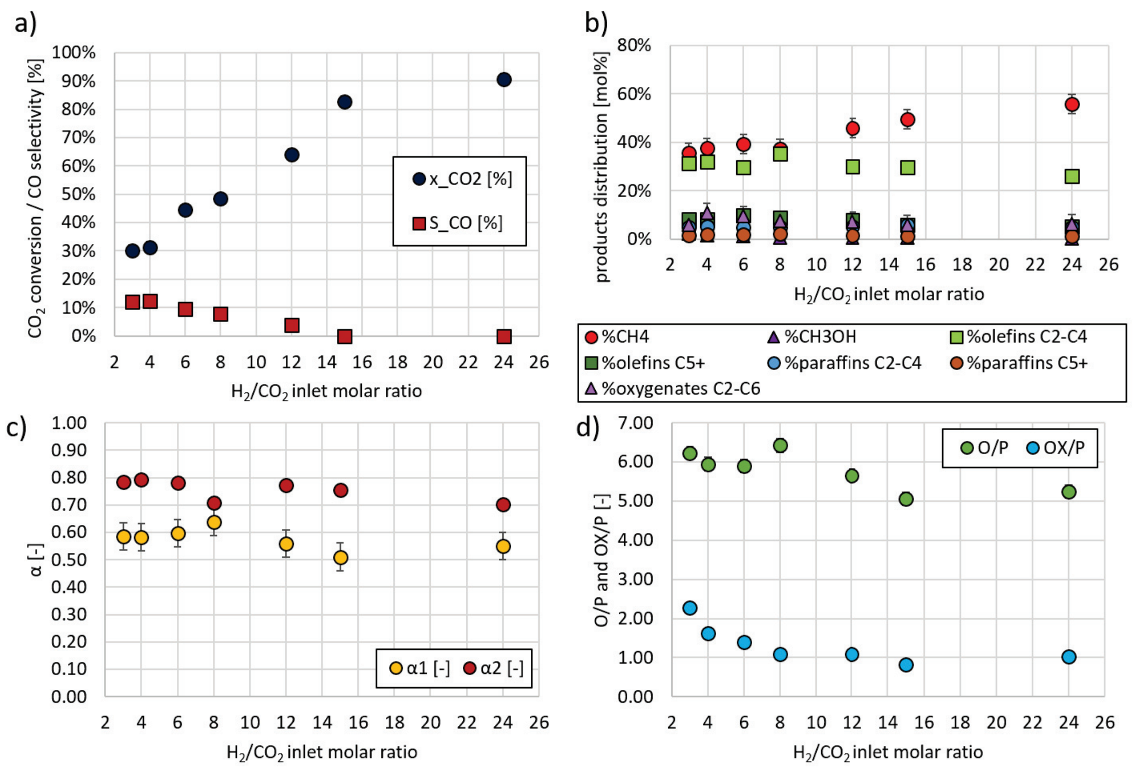

Figure 3.18: Effects of H_2/CO_2 inlet molar ratio on catalytic performances: a) CO_2 conversion and CO selectivity; b) distribution of hydrocarbon products, calculated as fraction of total hydrocarbons obtained (CO-free); c) C_{2+} olefins/paraffins ratio and oxygenates/paraffins ratio; d) values of α_1 and α_2. Points represent experimental data, lines represent model results. Error bars indicate standard deviations. Operating conditions: 15 bars, 300°C, GHSV of 2000 $Nml/g_{cat}/h$ and H_2/CO_2 ratio varied between 3 and 24.

3.5.4 Effects of pressure.

The effect of total pressure has been investigated in the range between 10 and 25 bars. Results reported in Figure 3.19 show that above 15 bars, pressure changes do not significantly influence the catalytic performances. CO_2 conversion increases from 21 to 31% and CO selectivity decreases from 20 to 11% while increasing the pressure from 10 to 15 bars, then minor changes are observed. Only FT thermodynamics depend on reaction pressure, while RWGS does not involve mole changes. Thus, it can be asserted that above 15 bars, CO dissociation rates play a more important role than CO molecules concentrations in influencing the FT reaction rate. (Jiang et al., 2018; Visconti et al., 2017)

Concerning product distribution, the increase of pressure in the range between 10 and 25 bars leads to a slight increase of methane and oxygenates production, at the loss of olefins, resulting in lower O/P ratios. Slight increases of α values are also observed.

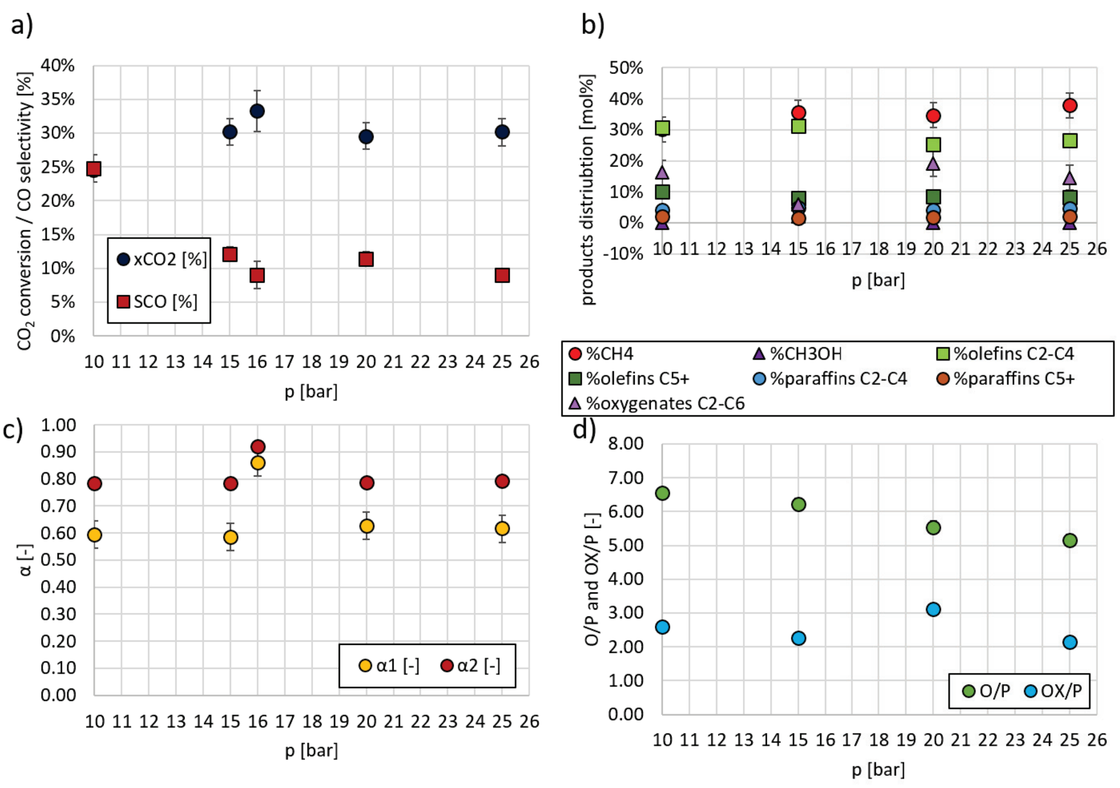

Figure 3.19: Effects of total pressure on catalytic performances: a) CO_2 conversion and CO selectivity; b) distribution of hydrocarbon products, calculated as fraction of total hydrocarbons obtained (CO-free); c) C_{2+} olefins/paraffins ratio and oxygenates/paraffins ratio; d) values of α_1 and α_2. Points represent experimental data, lines represent model results. Error bars indicate standard deviations. Operating conditions: H_2/CO_2 ratio of 3, 300°C, GHSV of 2000 $Nml/g_{cat}/h$ and total pressure varied between 10 and 25 bars.

This parametric study gave us an overall view of the effects of different operating conditions. These data are important to understand how the system could be influenced to increase the yield towards hydrocarbons production. For example, operating at higher temperatures and high excess of H_2 could contribute to increase the CO_2 conversion and to limit the CO formation. Moreover, these data will be used to validate kinetic models that are developed in order to describe the behaviour of the reaction in different operating conditions.

3.6 Co-feeding studies.

In this section, we will focus on the liquid co-feeding studies that have been performed with the aim to study how water and ethanol can influence the catalytic performances. This is very important in order to understand something more about the reaction mechanism and the catalytic deactivation.

Water is in fact believed to be one of the main causes of catalytic deactivation, because of its tendency to re-oxide iron carbides thus leading to a loss of activity towards the hydrocarbons formation. (Pendyala et al., 2010; Satterfield et al., 1986) Some authors observed that ethanol (and higher alcohols) can re-adsorb on the catalytic surface and form long hydrocarbons. The existence of two parallel mechanisms for the formation of shorter and longer hydrocarbon chains has been proposed before and a possible mechanism could pass by the re-adsorption of primary alcohols. (Gaube and Klein, 2008; Kummer and Emmett, 1953) A comprehensive review of the literature information on the role of ethanol and other alcohols, as well as on the role of water, can be found in section 1.3.2.

Thus, it seems interesting to study the roles of water and alcohols, by injecting them in the feed with the reactants. Ethanol has been selected as the alcohol to use in the described experimental set-up, because of its easy availability and its easy manipulation (avoiding health issues connected with the use of methanol for example). The study that we have performed is still at a preliminary stage, as the experimental bench was not optimal and only few experiments could be performed. However, we could obtain some useful information that are presented in the following.

3.6.1 Study of the effects of water in the feed.

The effects of water co-injection were studied with two kinds of experiments:

- 50 hours run where in the first 10.5 hours water is not injected; then a molar fraction of 5% of water is added to the feed (by reducing the fraction of inert gas) and these conditions are kept for a bit less than 15 hours; finally, conditions without water injections are restored and kept for other 20 hours.
- 50 hours run where in the first 20 hours water is not injected; then a molar fraction of 15% of water is added to the feed and these conditions are kept for 25 hours; finally, conditions without water injections are restored and kept for other 5 hours.

The results of these tests are presented in Figure 3.20. For the test at low concentration (left figure), it can be noticed that when water was added to the feed, we immediately observed an increase of the CO selectivity from 20% to >30% accompanied by a lighter decrease of the CO_2 conversion from 20% to 12%. Once water is not fed to the reactor anymore, we observe a gradual restoration of the initial performances, even if activity before water injection is not achieved. Thus, water at these concentrations favours the loss of FT activity and this deactivation is only partially reversible. When water is added in higher concentrations and for longer time (right figure), a complete deactivation of the catalyst is observed, with CO_2 conversion approaching zero and CO selectivity becoming very high. In this case, the deactivation seems irreversible, as restoring initial conditions did not lead to a restoration of the catalytic activity. This has been observed before in the literature during CO-FT reaction over iron catalysts. Previous studies reported that water led to reversible deactivation of iron catalysts when it was fed in low concentration for a short time, while higher concentrations for longer periods caused irreversible catalyst deactivation. (Satterfield et al., 1986) Others reported that only at low temperatures deactivation was observed due to oxidation of the carbides, while at higher temperatures the addition of water had beneficial effects on the conversion, as the higher WGS reaction rate allowed the consumption of the added water, avoiding the surface iron carbides re-oxidation. (Pendyala et al., 2010) Despite these results, authors generally agree when saying that water favours the oxidation of the iron carbides, forming iron oxides, causing a decrease of the hydrocarbons formation rate. (Pendyala et al., 2010; Satterfield et al., 1986)

We have analysed the phase composition of the used catalyst after the first test at low water concentrations by XRD and Mössbauer spectroscopy. Results of XRD and Mössbauer are reported in Figures 3.21 and 3.22 and Table 3.8. The XRD pattern shows the presence of the typical Hägg carbide phase and of another phase, the Fe_3O_4, which is considered to be the active phase for the RWGS. Carbon deposition is also a possible cause of deactivation, as the peak at 21° can be attributed to carbon species. Mössbauer spectroscopy confirmed the presence of the Hägg carbides (the three sextets with magnetic fields of 121, 207 and 249 kOe) and the presence of the Fe_3O_4 (the two sextets with magnetic fields of 466 and 496 kOe). Possible formation of the inactive phase Fe_2O_3 is also considered, as Fe(III) ions of amorphous Fe_2O_3 are observed by Mössbauer spectroscopy. These results are in agreement with what presented before: the presence of water favours the formation of iron oxides at the expense of iron carbides.

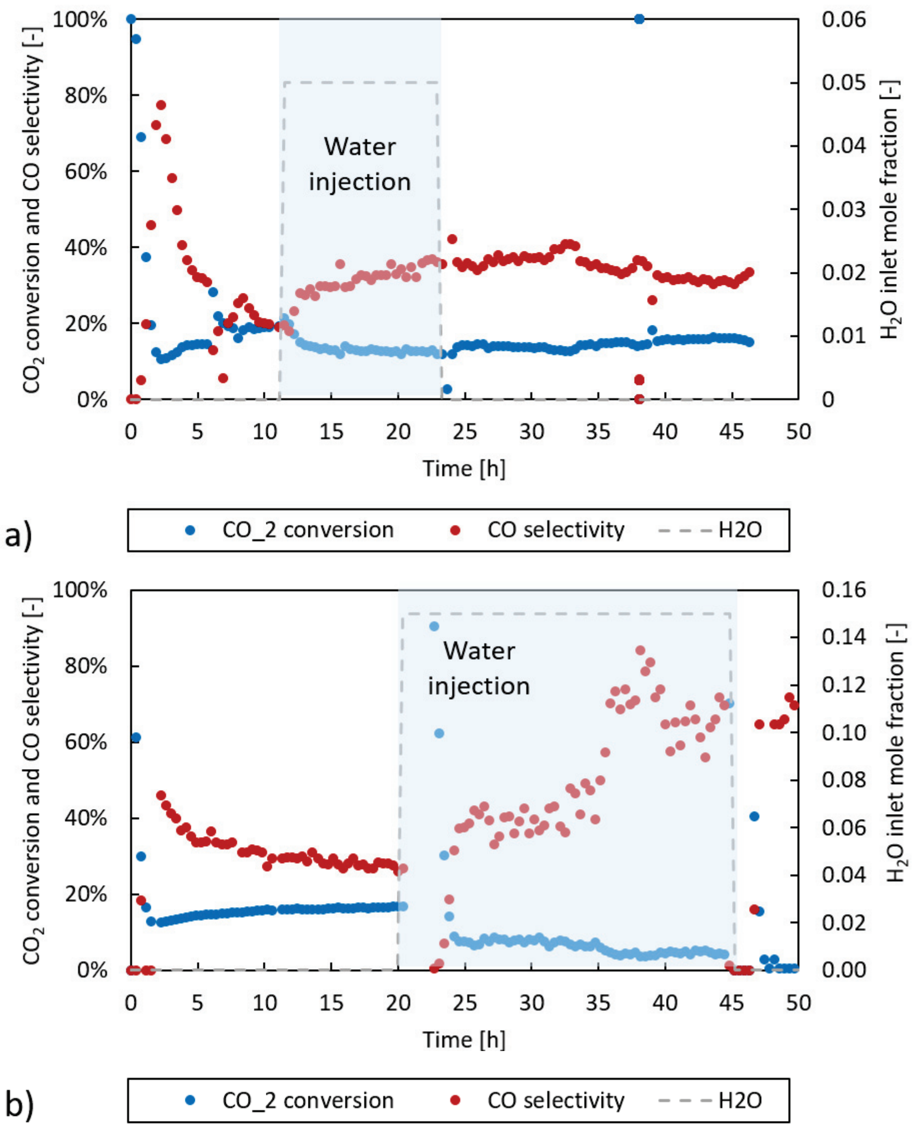

Figure 3.20: Effects of water co-feeding on CO_2 conversion and CO selectivity. a) molar fraction of water in the feed of 5%; b) molar fraction of water in the feed of 15%.

Table 3.8: Results of Mössbauer spectroscopy for spent catalyst after reaction with water at 5% and attribution to the corresponding iron phase.

Signal	δ [mm/s]	ϵ [mm/s]	Δ [mm/s]	**H** [kOe]	**R** [%]	**Attribution**
doublet 1	0.461		0.665		11%	Fe(III) of amorphous Fe_2O_3
doublet 2	1.114		2.730		11%	Fe(II)
sextet 1	0.400	0		495.8	16%	Fe(III) of Fe_3O_4
sextet 2	1.110	0		465.5	5%	Fe(II) of Fe_3O_4
sextet 3	0.425	0		249.3	28%	$\chi - Fe_5C_2$
sextet 4	0.307	0		207.0	17%	$\chi - Fe_5C_2$
sextet 5	0.250	0		121.0	13%	$\chi - Fe_5C_2$

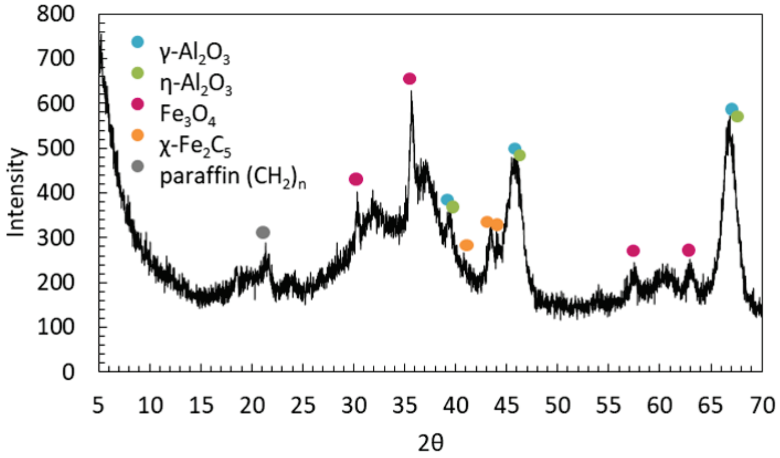

Figure 3.21: XRD pattern of spent catalyst after reaction with water at 5%.

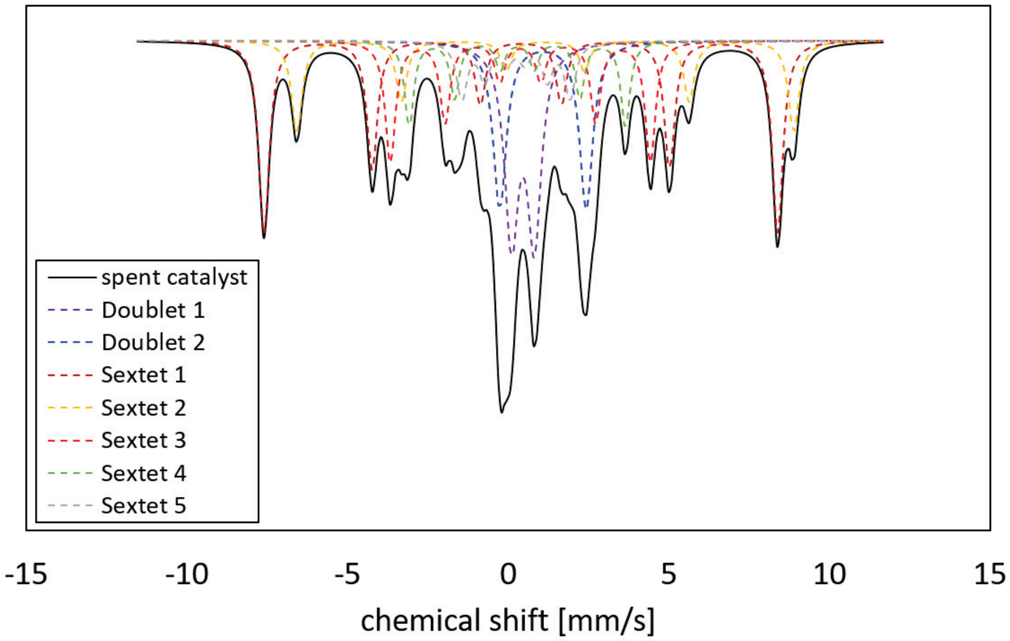

Figure 3.22: Mössbauer spectrum of the spent catalyst after reaction with water at 5%.

3.6.2 Study of the effects of ethanol in the feed.

The effects of ethanol co-feeding have been experimentally studied in a range of EtOH molar inlet fractions from 0 to 5% (corresponding to ethanol partial pressures from 0 to 0.75 bar). As explained in the previous Chapter, results obtained at high concentrations of EtOH have been discarded as the EtOH injection was not uniform and C balances were not respected. Figure 3.23 presents the retained results. We can observe that adding ethanol to the reactants feed did not significantly influence the CO_2 conversion, but on the opposite led to a decrease of the CO selectivity, simultaneously favouring the hydrocarbons production. If we look at the hydrocarbons distribution, we can observe that CH_4 formation is slightly limited when the EtOH content in the feed is increased, while olefins formation is favoured, in particular the short chains C_2-C_4. Ramified chains (included in 'others') are also favoured, while oxygenates production is decreased. The values of α are slightly increased when ethanol fraction in the feed increases.

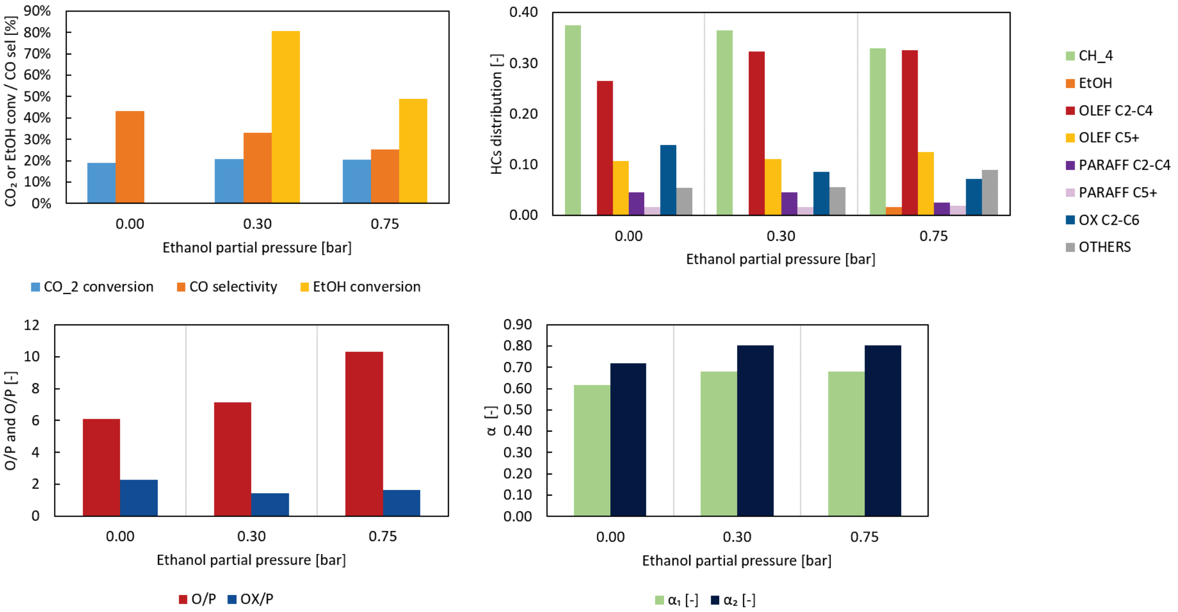

Figure 3.23: Effects of ethanol co-feeding: a) CO_2 conversion, EtOH conversion and CO selectivity; b) hydrocarbons distribution; c) olefins/paraffins and oxygenates/paraffin ratio; d) α.

Thus, from these preliminary results we can conclude that ethanol has an effect in favouring the formation of hydrocarbons. The fraction that was observed to increase more with the increase of ethanol in the feed is the short olefins one. Thus, from these results we can assert that ethanol has a role in the formation of hydrocarbons chains. It is possible that ethanol is dehydrated to ethylene and thus re-adsorbed on the active sites and contributes to the chain-growth. However, we have to consider that ethanol acts as a solvent for hydrocarbons compounds, thus a possible effect of better elution of hydrocarbons due to the presence of ethanol can have an influence in the observed increase of the hydrocarbons fractions. Further investigation is thus needed to completely understand the role of ethanol and higher alcohols in the reaction mechanism.

3.7 Experimental results of the reaction performed in a fixed-bed reactor with cooling system.

Finally, we will focus on the results obtained from the experimental study conduced in the CEA bench. The aim of this section is to present the results obtained in a scaled-up reactor and to compare them with the results obtained in the lab-scaled one.

Figure 3.24 shows the results of the experiments conduced at different contact times (between 0.36 and 1.33 g.s/Nml). As expected, an increase of the CO_2 conversion with τ_{mod} is observed with a simultaneous decrease of the CO selectivity. CH_4 selectivity is increased when τ_{mod} is increased but to a lower extent than CO_2 conversion. These results are close to those obtained in the same operating conditions in the lab-scale reactor at CP2M, as shown in Table 3.9. A slightly higher CO_2 conversion with slightly lower CO selectivity was obtained in the scaled-up reactor.

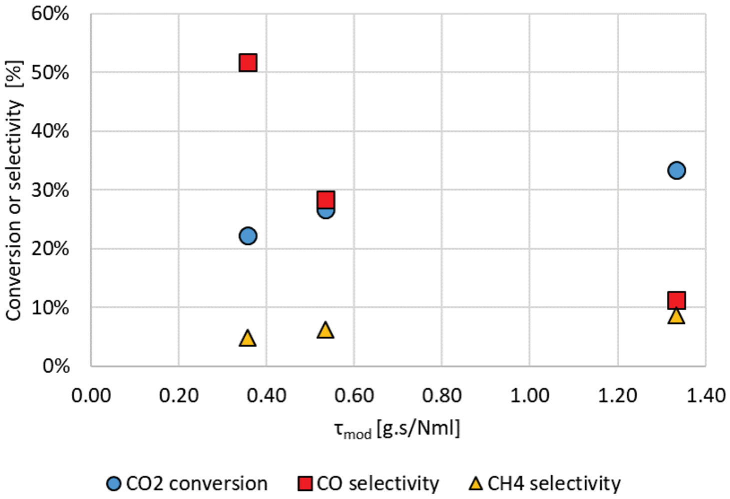

Figure 3.24: Evolution of CO_2 conversion, CO selectivity and CH_4 selectivity with modified contact time.

Table 3.9: Comparison of results obtained in the lab-scale reactor and in the scaled-up one.

Reactor type	τ_{mod} [g.s/Nml]	χ_{CO_2} [%]	S_{CO} [%]
Lab-scale reactor	1.38	27%	16%
Scaled-up reactor	1.33	33%	11%

We have to evidence here that the regulation system of the two reactors is different: in the case of the lab-scale reactor, the regulated temperature is that of the oven that contains the reactor, meaning that the actual temperature inside the reactor is slightly lower than the set value (for oven temperature of 300°C the reactor temperature was measured to be around 298°C). In the case of the cooled reactor, the reactor temperature can be regulated with higher accuracy, as the system of heat-transfer oil circulation allows to regulate the reactor temperature to the set value. Therefore, even if the same operating temperature is applied in the two benches, differences in the actual temperatures of the reactors can occur and this can explain the slightly higher CO_2 conversion obtained in the scaled-up reactor.

We can observe the measured axial temperature profile along the reactor and its evolution during the reaction in Figure 3.25, for the run at τ_{mod} 0.53 g.s/Nml. Points 1 and 5 measure the temperature of the reactor in the zones filled with inert material at the inlet and outlet of the reactor. The inlet temperature inside the reactor is measured to be around 301°C. A maximum $\Delta T < 5°C$ is observed and the maximum temperature is observed next to the catalytic bed entrance (point 2).

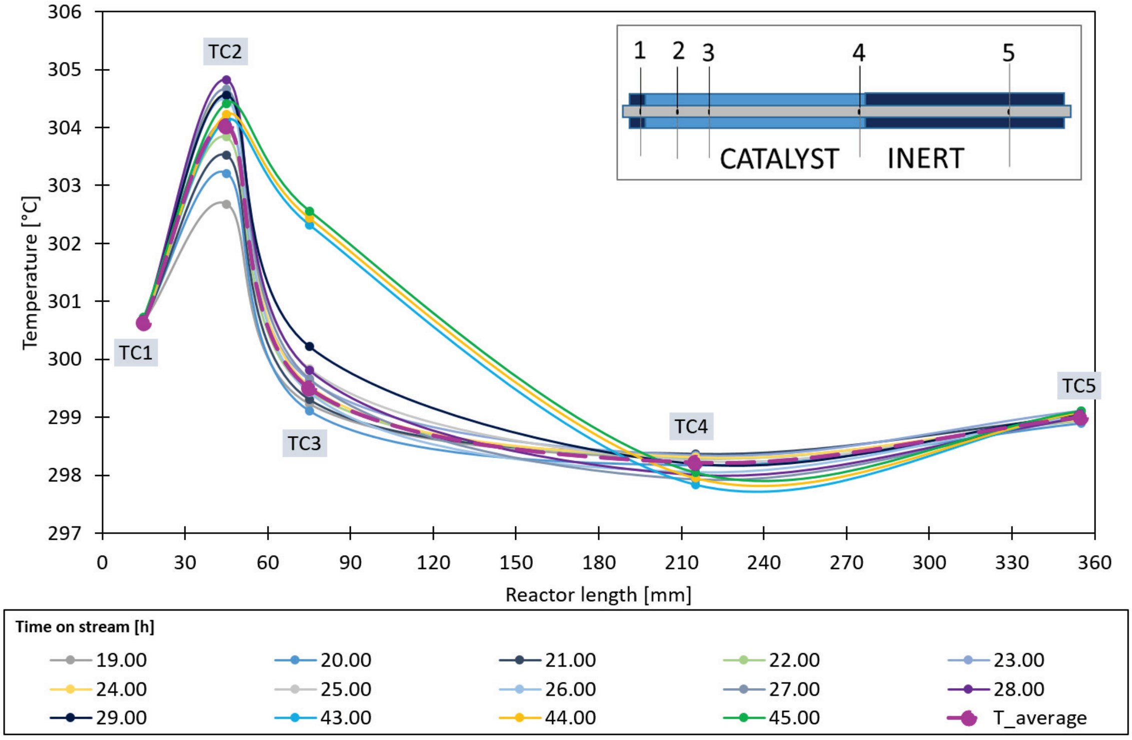

Figure 3.25: Evolution with time on stream of reactor temperature measured at 5 axial positions in the catalytic bed (curves are only given to help visual identification of measurements). Evolution of temperature axial profile along the reactor during the reaction. A scheme of the reactor is also presented with indication of the points of measure. Points 1 and 5 correspond to the inert bed.

3.7.1 CO co-feeding.

We have also performed a preliminary study of the effects of co-injection of CO in the reactor feed. The CO fraction in the feed was varied between 0 and 5% for τ_{mod} =0.53 g.s/Nml and its effects on the catalytic performances have been observed. The results are reported in Figure 3.26. We can observe that for small concentrations of CO in the feed (2%), the CO is observed to be converted in very small amounts (close to 0), but the CO_2 conversion is observed to significantly decrease to a value of 19%. When the CO fraction in the feed further increases, CO conversion rapidly increases until values of 30% for 5% of CO in the feed. A gradual decrease of CO_2 conversion is simultaneously observed. CH_4 selectivity did not have significant changes with the increase of CO in the feed, indicating that HCs formation is favoured.

When performing hydrogenation with CO/CO_2 mixtures, a competitive adsorption between the two species has been observed. CO is observed to gain this competition, resulting in lower CO_2 conversion rates compared to CO_2 only hydrogenations. (Visconti et al., 2016) This is in agreement with the results observed here: when increasing the CO content in the feed, CO_2 is converted to a lower extent, while CO conversion rate rapidly increases. We could not observe in these experiments the hydrocarbons distribution. However, major modifications of the methane fraction were not observed, suggesting that hydrocarbons distribution was probably not affected by the addition of CO, as previously observed by other authors. (Visconti et al., 2016; Riedel et al., 1999)

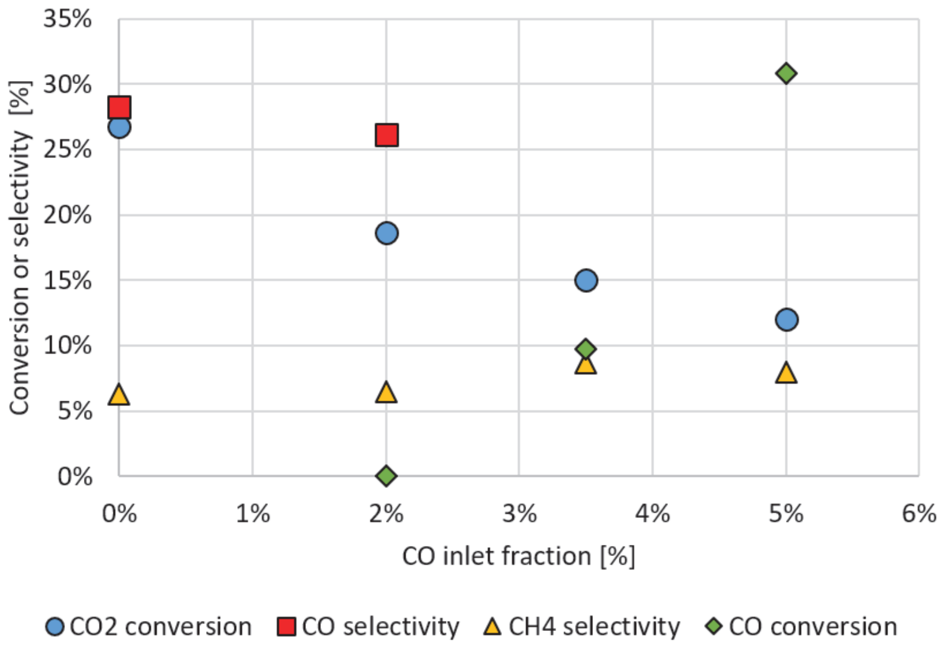

Figure 3.26: Evolution of CO_2 conversion, CO selectivity and CH_4 selectivity with CO molar inlet fraction in the feed.

3.8 Conclusion

In this Chapter we have thus shown and discussed the results of the experimental study. The objectives of this study, the understanding of the catalytic behaviour of the synthesized catalyst and the collection of enough experimental data to develop a mathematical model, have been achieved.

We have studied the catalyst textural and morphologic properties, its iron phases composition and its evolution before and after the reaction. Even if the catalyst appears not to be optimal in terms of homogeneity and surface area, we have observed morphological properties similar to those of the most used iron catalysts for the CO_2 hydrogenation. Moreover, we have shown that it has catalytic performances similar - and even better - to other similar catalysts.

We have also performed the kinetic experimental study, varying different operating parameters and monitoring their effect on CO_2 conversion, CO selectivity and hydrocarbons distribution. That allowed to gain insights about the reaction mechanism and provided some information about how to influence the system towards the production of the desired products. To increase CO_2 conversion and minimize the CO formation for example, operating at high excess of H_2 can be useful. However, if the objective is to maximize the formation of C_2-C_4 olefins, other ways should be adopted, such as working at higher temperatures.

From the results of the experimental kinetic study it seems that the reaction passes by the formation of CO as intermediate, suggesting that hydrocarbons are formed as secondary products from conversion of CO. Direct CO_2 hydrogenation seems negligible from the observed results. These results also showed that the most abundant products are short linear α-olefins and oxygenates (mainly alcohols and acids until 6 carbon atoms), as well as methane. Paraffins were observed in lower quantities. Longer chains, especially olefinic ones, were observed until 30 carbon atoms. We have observed that the longest hydrocarbons chains present deviations from the ideal ASF distribution that could be related to the co-existence of different active sites and mechanism for the formation of hydrocarbons. Thus, a double-α ASF distribution was observed to better describe the HCs distribution. Moreover, it was observed that, while the chain-growth probabilities for olefins and paraffins are very close, those for oxygenates are significantly lower, suggesting that these compounds could be formed by a different mechanism than olefins and paraffins.

To acquire other information about the reaction mechanism, preliminary experiments of co-injection of water and ethanol were performed. We have observed that water could deactivate the catalyst by re-oxidising the iron carbides. Ethanol seems to be involved in the formation of C_{2+} hydrocarbons, via dehydration to ethylene and re-adsorption to give chain-growth reactions. These are only preliminary results that should be confirmed by further investigation. Future works should focus on the study of the role of alcohols, water and eventually 1-alkenes, as many information about the reaction mechanism could be obtained.

We have observed deactivation of the catalyst in different operating conditions: at low residence time, at high temperatures and after 190 hours of working in reaction conditions. The high partial pressure of water at which the catalyst is exposed in these conditions could contribute to the observed loss of activity. Sintering and coke deposition were also considered as possible causes of deactivation. In the following of the manuscript, conditions were the catalyst was deactivated are excluded and the kinetic models will be developed without considering the deactivation. Further work on the investigation of the deactivation's causes and eventual catalyst regeneration should be performed in future studies.

Finally, we have shown that scaling-up the reaction to a fixed-bed reactor at higher scale allows to obtain similar results to those obtained in the lab-scaled one. The co-injection of CO has confirmed that the CO_2 conversion rate is significantly reduced in presence of CO.

The data obtained from the experimental study and presented in this Chapter, besides providing information about the catalytic behaviour and the reaction mechanism, also represent the experimental points that will be used for the validation of the kinetic models that are described in the next Chapters. As already evidenced, the main objective of the thesis is to provide a tool to mathematically model the CO_2 hydrogenation. Thus, the following Chapters will be focused on the developing of such mathematical models, validated on the experimental data described in this Chapter.

References

I. Champon, A. Bengaouer, A. Chaise, S. Thomas, and A.-C. Roger. Carbon dioxide methanation kinetic model on a commercial Ni/Al_2O_3 catalyst. *Journal of CO2 Utilization*, 34:256–265, 2019. ISSN 2212-9820. doi: 10.1016/j.jcou.2019.05.030. URL `http://www.sciencedirect.com/science/article/pii/S2212982019301799`.

R. A. Dictor and A. T. Bell. Fischer-Tropsch synthesis over reduced and unreduced iron oxide catalysts. *Journal of Catalysis*, 97(1):121–136, 1986. ISSN 0021-9517. doi: 10.1016/0021-9517(86)90043-6. URL `https://www.sciencedirect.com/science/article/pii/0021951786900436`.

T. J. Donnelly and C. N. Satterfield. Product distributions of the Fischer-Tropsch synthesis on precipitated iron catalysts. *Applied Catalysis*, 52(1):93–114, 1989. ISSN 01669834. doi: 10.1016/S0166-9834(00)83375-8. URL `https://linkinghub.elsevier.com/retrieve/pii/S0166983400833758`.

T. J. Donnelly, I. C. Yates, and C. N. Satterfield. Analysis and prediction of product distributions of the Fischer-Tropsch synthesis. *Energy & Fuels*, 2(6):734–739, 1988. ISSN 0887-0624. doi: 10.1021/ef00012a003. URL `https://pubs.acs.org/doi/abs/10.1021/ef00012a003`.

J. Gaube and H.-F. Klein. Studies on the reaction mechanism of the Fischer–Tropsch synthesis on iron and cobalt. *Journal of Molecular Catalysis A: Chemical*, 283(1):60–68, 2008. ISSN 1381-1169. doi: 10.1016/j.molcata.2007.11.028. URL `http://www.sciencedirect.com/science/article/pii/S1381116907006711`.

M. K. Gnanamani, G. Jacobs, W. D. Shafer, and B. H. Davis. Fischer–Tropsch synthesis: Activity of metallic phases of cobalt supported on silica. *Catalysis Today*, 215:13–17, 2013. ISSN 09205861. doi: 10.1016/j.cattod.2013.03.004. URL `https://linkinghub.elsevier.com/retrieve/pii/S0920586113000898`.

N. N. Greenwood and T. C. Gibb. *Mössbauer Spectroscopy*. Springer Netherlands, Dordrecht, 1971. ISBN 978-94-009-5699-5 978-94-009-5697-1. doi: 10.1007/978-94-009-5697-1. URL `http://link.springer.com/10.1007/978-94-009-5697-1`.

M. Gálvez, S. Ascaso, P. Stelmachowski, P. Legutko, A. Kotarba, R. Moliner, and M. Lázaro. Influence of the surface potassium species in Fe–K/Al_2O_2 catalysts on the soot oxidation activity in the presence of NO_x. *Applied Catalysis B: Environmental*, 152-153:88–98, 2014. ISSN 09263373. doi: 10.1016/j.apcatb.2014.01.041. URL `https://linkinghub.elsevier.com/retrieve/pii/S0926337314000472`.

J. S. Hwang, K.-W. Jun, and K.-W. Lee. Deactivation and regeneration of Fe-K/alumina catalyst in CO_2 hydrogenation. *Applied Catalysis A: General*, 208:217–222, 2001.

S.-M. Hwang, S. J. Han, J. E. Min, H.-G. Park, K.-W. Jun, and S. K. Kim. Mechanistic insights into Cu and K promoted Fe-catalyzed production of liquid hydrocarbons via CO_2 hydrogenation. *Journal of CO2 Utilization*, 34:522–532, 2019. ISSN 22129820. doi: 10.1016/j.jcou.2019.08.004. URL `https://linkinghub.elsevier.com/retrieve/pii/S2212982019306018`.

E. Iglesia, S. C. Reyes, and R. J. Madon. Transport-enhanced α-olefin readsorption pathways in Ru-catalyzed hydrocarbon synthesis. *Journal of Catalysis*, 129(1):238–256, 1991.

M. Iglesias Gonzalez, C. de Vries, M. Claeys, and G. Schaub. Chemical energy storage in gaseous hydrocarbons via iron Fischer–Tropsch synthesis from H_2/CO_2 —Kinetics, selectivity and process considerations. *Catalysis Today*, 242:184–192, 2015. ISSN 09205861. doi: 10.1016/j.cattod.2014.05.020. URL `https://linkinghub.elsevier.com/retrieve/pii/S0920586114003903`.

F. Jiang, B. Liu, S. Geng, Y. Xu, and X. Liu. Hydrogenation of CO_2 into hydrocarbons: enhanced catalytic activity over Fe-based Fischer–Tropsch catalysts. *Catalysis Science & Technology*, 8(16):4097–4107, 2018. ISSN 2044-4753, 2044-4761. doi: 10.1039/C8CY00850G. URL `http://xlink.rsc.org/?DOI=C8CY00850G`.

J.-S. Kim, S. Lee, S.-B. Lee, M.-J. Choi, and K.-W. Lee. Performance of catalytic reactors for the hydrogenation of CO_2 to hydrocarbons. *Catalysis Today*, 115(1-4):228–234, 2006. ISSN 09205861. doi: 10.1016/j.cattod.2006.02.038. URL `http://linkinghub.elsevier.com/retrieve/pii/S0920586106001179`.

E. W. Kuipers, I. H. Vinkenburg, and H. Oosterbeek. Chain Length Dependence of α-olefin Readsorption in Fischer-Tropsch synthesis. *Journal of Catalysis*, 152:137–146, 1995. doi: https://doi.org/10.1006/jcat.1995.1068. URL `https://www.sciencedirect.com/science/article/pii/S0021951785710688?via%3Dihub`.

J. T. Kummer and P. H. Emmett. Fischer—Tropsch Synthesis Mechanism Studies. The Addition of Radioactive Alcohols to the Synthesis Gas. *Journal of the American Chemical Society*, 75(21):5177–5183, 1953. ISSN 0002-7863. doi: 10.1021/ja01117a008. URL `https://doi.org/10.1021/ja01117a008`.

S.-C. Lee, J.-H. Jang, B.-Y. Lee, M.-C. Kang, M. Kang, and S.-J. Choung. The effect of binders on structure and chemical properties of Fe-K/γ-Al_2O_3 catalysts for CO_2 hydrogenation. *Applied Catalysis A: General*, 253(1):293–304, 2003. ISSN 0926860X. doi: 10.1016/S0926-860X(03)00540-4. URL `http://linkinghub.elsevier.com/retrieve/pii/S0926860X03005404`.

J. Liu, A. Zhang, X. Jiang, M. Liu, Y. Sun, C. Song, and X. Guo. Selective CO_2 Hydrogenation to Hydrocarbons on Cu-Promoted Fe-Based Catalysts: Dependence on Cu–Fe Interaction. *ACS Sustainable Chemistry & Engineering*, 6(8):10182–10190, 2018. ISSN 2168-0485, 2168-0485. doi: 10.1021/acssuschemeng.8b01491. URL `http://pubs.acs.org/doi/10.1021/acssuschemeng.8b01491`.

R. Madon. Fischer-Tropsch synthesis on a precipitated iron catalyst. *Journal of Catalysis*, 69(1):32–43, 1981. ISSN 00219517. doi: 10.1016/0021-9517(81)90125-1. URL `https://linkinghub.elsevier.com/retrieve/pii/0021951781901251`.

T. Numpilai, N. Chanlek, Y. Poo-Arporn, S. Wannapaiboon, C. K. Cheng, N. Siri-Nguan, T. Sornchamni, P. Kongkachuichay, M. Chareonpanich, G. Rupprechter, J. Limtrakul, and T. Witoon. Pore size effects on physicochemical properties of Fe-Co/K-Al_2O_3 catalysts and their catalytic activity in CO_2 hydrogenation to light olefins. *Applied Surface Science*, 483:581–592, 2019. doi: https://doi.org/10.1016/j.apsusc.2019.03.331. URL `https://www.sciencedirect.com/science/article/pii/S0169433219309705?via%3Dihub`.

J. Patzlaff, Y. Liu, C. Graffmann, and J. Gaube. Studies on product distributions of iron and cobalt catalyzed Fischer–Tropsch synthesis. *Applied Catalysis A: General*, 186(1-2):109–119, 1999. ISSN 0926860X. doi: 10.1016/S0926-860X(99)00167-2. URL `https://linkinghub.elsevier.com/retrieve/pii/S0926860X99001672`.

J. Patzlaff, Y. Liu, C. Graffmann, and J. Gaube. Interpretation and kinetic modeling of product distributions of cobalt catalyzed Fischer–Tropsch synthesis. *Catalysis Today*, 71(3-4):381–394, 2002. ISSN 09205861. doi: 10.1016/S0920-5861(01)00465-5. URL `https://linkinghub.elsevier.com/retrieve/pii/S0920586101004655`.

V. R. R. Pendyala, G. Jacobs, J. C. Mohandas, M. Luo, H. H. Hamdeh, Y. Ji, M. C. Ribeiro, and B. H. Davis. Fischer–Tropsch Synthesis: Effect of Water Over Iron-Based Catalysts. *Catalysis Letters*, 140 (3):98–105, 2010. ISSN 1572-879X. doi: 10.1007/s10562-010-0452-7. URL `https://doi.org/10.1007/s10562-010-0452-7`.

T. Riedel, M. Claeys, H. Schulz, G. Schaub, N. Sang-Sung, J. Ki-Won, K. Gurram, and L. Kyu-Wan. Comparative study of Fisher-Tropsch sythesis with H_2/CO and H_2/CO_2 syngas using Fe- and Co-based catalysts. *Applied Catalysis A: General*, 186:201–213, 1999.

T. Riedel, G. Schaub, K.-W. Jun, and K.-W. Lee. Kinetics of CO_2 Hydrogenation on a K-Promoted Fe Catalyst. *Industrial & Engineering Chemistry Research*, 40(5):1355–1363, 2001. ISSN 0888-5885, 1520-5045. doi: 10.1021/ie000084k. URL `http://pubs.acs.org/doi/abs/10.1021/ie000084k`.

T. Riedel, H. Schulz, G. Schaub, K.-W. Jun, J.-S. Hwang, and K.-W. Lee. Fischer–Tropsch on iron with H_2/CO and H_2/CO_2 as synthesis gases: the episodes of formation of the Fischer–Tropsch regime and construction of the catalyst. *Topics in Catalysis*, 26(1-4):41–54, 2003.

C. N. Satterfield, R. T. Hanlon, S. E. Tung, Z. M. Zou, and G. C. Papaefthymiou. Effect of water on the iron-catalyzed Fischer-Tropsch synthesis. *Industrial & Engineering Chemistry Product Research and Development*, 25(3):407–414, 1986. ISSN 0196-4321. doi: 10.1021/i300023a007. URL `https://doi.org/10.1021/i300023a007`.

B. Schliebs and J. Gaube. The Influence of the Promoter K_2CO_3 in Iron Catalysts on the Carbon Number Distribution of Fischer-Tropsch-Products. *Berichte der Bunsengesellschaft für physikalische Chemie*, 89(1):68–73, 1985. ISSN 00059021. doi: 10.1002/bbpc.19850890113. URL `http://doi.wiley.com/10.1002/bbpc.19850890113`.

H. Schulz. Selforganization in Fischer–Tropsch synthesis with iron- and cobalt catalysts. *Catalysis Today*, 228:113–122, 2014. ISSN 09205861. doi: 10.1016/j.cattod.2013.11.060. URL `https://linkinghub.elsevier.com/retrieve/pii/S0920586113006895`.

H. Schulz and M. Claeys. Kinetic modelling of Fischer–Tropsch product distributions. *Applied Catalysis A: General*, 186(1):91–107, 1999. ISSN 0926-860X. doi: 10.1016/S0926-860X(99)00166-0. URL `http://www.sciencedirect.com/science/article/pii/S0926860X99001660`.

H. Schulz, G. Schaub, M. Claeys, and T. Riedel. Transient initial kinetic regimes of Fischer–Tropsch synthesis. *Applied Catalysis A: General*, 186(1-2):215–227, 1999.

H. Schulz, T. Riedel, and G. Schaub. Fischer–Tropsch principles of co-hydrogenation on iron catalysts. *Topics in Catalysis*, 32(3-4):117–124, 2005. ISSN 1022-5528, 1572-9028. doi: 10.1007/s11244-005-2883-8. URL `http://link.springer.com/10.1007/s11244-005-2883-8`.

C. G. Visconti, M. Martinelli, L. Falbo, L. Fratalocchi, and L. Lietti. CO_2 hydrogenation to hydrocarbons over Co and Fe-based Fischer-Tropsch catalysts. *Catalysis Today*, 277:161–170, 2016. ISSN 09205861. doi: 10.1016/j.cattod.2016.04.010. URL `https://linkinghub.elsevier.com/retrieve/pii/S0920586116302632`.

C. G. Visconti, M. Martinelli, L. Falbo, A. Infantes-Molina, L. Lietti, P. Forzatti, G. Iaquaniello, E. Palo, B. Picutti, and F. Brignoli. CO_2 hydrogenation to lower olefins on a high surface area K-promoted bulk Fe-catalyst. *Applied Catalysis B: Environmental*, 200:530–542, 2017. ISSN 09263373. doi: 10.1016/j.apcatb.2016.07.047. URL `https://linkinghub.elsevier.com/retrieve/pii/S0926337316305896`.

H.-J. Wan, B.-S. Wu, C.-H. Zhang, H.-W. Xiang, Y.-W. Li, B.-F. Xu, and F. Yi. Study on Fe–Al_2O_3 interaction over precipitated iron catalyst for Fischer–Tropsch synthesis. *Catalysis Communications*, 8 (10):1538–1545, 2007. ISSN 15667367. doi: 10.1016/j.catcom.2007.01.002. URL `https://linkinghub.elsevier.com/retrieve/pii/S156673670700012X`.

T. Xie, J. Wang, F. Ding, A. Zhang, W. Li, X. Guo, and C. Song. CO_2 hydrogenation to hydrocarbons over alumina-supported iron catalyst: Effect of support pore size. *Journal of CO2 Utilization*, 19:202–208, 2017. ISSN 22129820. doi: 10.1016/j.jcou.2017.03.022. URL `https://linkinghub.elsevier.com/retrieve/pii/S2212982016304760`.

Y. Zhang, C. Cao, C. Zhang, Z. Zhang, X. Liu, Z. Yang, M. Zhu, B. Meng, J. Xu, and Y.-F. Han. The study of structure-performance relationship of iron catalyst during a full life cycle for CO_2 hydrogenation. *Journal of Catalysis*, 378:51–62, 2019. ISSN 0021-9517. doi: 10.1016/j.jcat.2019.08.001. URL `http://www.sciencedirect.com/science/article/pii/S0021951719303872`.

CHAPTER 4

Development of the macro-kinetic model.

4.1 Introduction.

In this first Chapter about modelling, we will focus on the development of a semi-empiric macro-kinetic model. The aim of this part of the work is to develop a simple kinetic model that could be used for more complex simulations, such as reactor modelling and process simulations. We thus need a model that could be detailed enough to describe the formation of all the main species observed and at the same time simple enough to be explicit and easy to code.

Some kinetic models for CO_2 hydrogenation have already been developed and have been comprehensively described in Chapter 1. These models are all very simple and do not take into account the formation of products with different chain length or different chemical moieties. (Riedel et al., 2001; Willauer et al., 2013; Najari et al., 2019; Iglesias Gonzalez et al., 2015)

Here, we present the development of a kinetic model that describes the formation of olefins, paraffins and oxygenates from 1 to 20 carbon atoms. Such a model is based on semi-empirical kinetic rates, thus it does not give enough information about the detailed reaction mechanism. For the study of the reaction mechanism, a more detailed and complex kinetic model has been developed, based on hypothesis on the reaction mechanism and it will be presented in the next Chapter. However, the macro-kinetic model here developed has the purpose to be easily implemented in more complex simulations.

The development of a kinetic model consists in:

1. studying the thermodynamics of the system to understand in which phase the reaction takes place and the properties of such a phase;
2. choosing a reactor model to describe the compounds flows variation along the reactor;
3. choosing the kinetic laws to describe the consumption rates of reactants and the formation rates of products (r_i);
4. choosing a regression method to estimate the relationship between model predictions and experimental data. Kinetic parameters represent this relationships and they need to be estimated.

In the next sections we will presents all the assumptions made for the model and the results of the kinetic parameters optimization.

4.2 Thermodynamic study.

First, we need to study the thermodynamics of the system. The thermodynamic study has been conduced with the aim to verify that in the reaction conditions liquid products are not formed, capillary condensation does not occur in catalytic pores and the gas phase can be considered as ideal. In this Section, we will thus present the procedure followed for the thermodynamic study and the obtained results.

4.2.1 Liquid-vapour equilibrium study.

The liquid-vapour equilibrium study allows to describe the repartition of species between the gas and the liquid phases. Before calculating the compositions at the thermodynamic equilibrium, some preliminary steps are needed: it is necessary to define the thermodynamic models for each species and for the mixtures. In fact, the mixtures involved contain different hydrocarbons whose properties are not easily measurable. Different approaches could be used to estimate the properties of pure compounds or mixtures, but these methods are generally not very precise for heavy hydrocarbons. (Poling et al., 2001) A general approach developed specifically for linear hydrocarbons is the ABC (Asymptotic Behaviour Correlations) method, developed by Marano and Holder. (Marano and Holder, 1997a,b,c) Comparing the behaviour of linear hydrocarbons to that of polymers, the properties of pure corps can be estimated from asymptotic correlations. These correlations relate the thermodynamic property to carbon number and eventually temperature. Marano and Holder's correlations can also be used to estimate mixture properties. Thus, this approach is generally the most used when modelling FT mixtures and it will be adopted in our model.

4.2.1.1 Pure corps properties.

Critical properties and saturated pressure.

Critical properties of compounds until C_{11} are available in literature and were taken from Poling et al. (Poling et al., 2001) For data not available in literature, Marano and Holder's correlations are used (Eqs. 4.1 and 4.2). (Marano and Holder, 1997a)

$$Y = Y_{\infty,0} + \Delta Y_{\infty}\left(n - n_0\right) - \Delta Y_0 exp\left(-\beta\left(n - n_0\right)^{\gamma}\right) \quad for\ T_c,\ p_c,\ ln\left(P_{sat}\right) \tag{4.1}$$

$$Y = \Delta Y_0 + \beta\left(n - n_0\right)^{\gamma} \quad for\ \omega_c \tag{4.2}$$

Saturated pressure is calculated from Marano and Holder's asymptotic correlations (Eq. 4.1). (Marano and Holder, 1997a) Parameters to be used for Eqs. 4.1 and 4.2 are reported in Table D.1.

Molar volume.

The molar volume of gas is calculated from an equation of state. Generally, cubic equations of state are applied for systems containing hydrocarbons. The Soave-Redlich-Kwong (SRK) equation of state is accurate for the estimation of vapour pressure of hydrocarbons, but it is not able to accurately predict molar volumes, especially of the liquid phase. (Soave et al., 2010) Peng-Robinson (PR) equation of state is more accurate in terms of liquid molar volumes prediction. SRK and PR equations of state for pure corps can be written in the form:

$$p = \frac{RT}{(v - b)} - \frac{a}{(v - br_1)(v - br_2)} \tag{4.3}$$

where the attraction parameter is defined as:

$$a = \Omega_A \frac{R^2 T_c^2}{p_c} \alpha \tag{4.4}$$

$$\alpha = \left(1 + m\left(1 - \sqrt{T_r}\right)\right)^2 \tag{4.5}$$

$$m = M_0 + M_1\omega + M_2\omega^2 \tag{4.6}$$

and the co-volume b is defined as:

$$b_i = \Omega_B \frac{RT_c}{p_c} \tag{4.7}$$

Parameters of Eqs. 4.3-4.7 are reported in Table D.7. Here Peng-Robinson equation of state (Peng and Robinson, 1979) is used, as it is the most suitable with this kind of hydrocarbons mixtures.

Liquid molar volumes are calculated according to the asymptotic correlations reported by Marano and Holder. (Marano and Holder, 1997a) For light HCs and non-HCs compounds:

$$V_i^{\infty} = V_{i,0} + n\Delta V_i \quad with \;\; V_{i,0} = A + BT \tag{4.8}$$

and for heavy HCs:

$$Y = Y_{\infty,0} + \Delta Y_{\infty}\left(n - n_0\right) - \Delta Y_0 exp\left(-\beta\left(n + n_0\right)^{\gamma}\right) \tag{4.9}$$

Parameters of the previously reported equations are reported in Tables D.3 and D.5.

4.2.1.2 Mixture properties.

Molar volume of the mixture in vapour phase is calculated from the PR equation of state, defined in vapour phase for a mixture:

$$p = \frac{RT}{\left(v_V - b_V\right)} - \frac{a_V}{\left(v_V - b_V r_1\right)\left(v_V - b_V r_2\right)} \tag{4.10}$$

where a_V and b_V are calculated as follows:

$$a_V = \sum_i \sum_j y_i y_j a_{ij} \tag{4.11}$$

$$b_V = \sum_i y_i b_i \tag{4.12}$$

and

$$a_{ij} = \sqrt{\left(a\alpha\right)_i \left(a\alpha\right)_j}\left(1 - k_{ij}\right) \tag{4.13}$$

$$\left(a\alpha\right)_i = a_i\alpha_i \tag{4.14}$$

$$\alpha_i = \left(1 + m_i\left(1 - \sqrt{T_{ri}}\right)\right)^2 \tag{4.15}$$

$$m_i = M_0 + M_1\omega_i + M_2\omega_i^2 \tag{4.16}$$

Equation 4.10 is solved with a Cardano-type algorithm that is presented in Appendix D. Parameters to use in Eqs. 4.10-4.16 are reported in Table D.7.

Binary interaction parameters k_{ij} are known for compounds until 20 carbon atoms. It is generally recognized that the gaseous phase of an FT mixture behaves as an ideal phase (see section 4.2.3), thus k_{ij} could be set to 0. (Marano and Holder, 1997a) However, for the liquid, the accuracy in the calculation of the parameters k_{ij} is more important, as inaccuracies on these values can lead to high errors in the estimation of the liquid phase properties. Thus, we have followed the Marano and Holder approach to estimate the liquid molar volume for a mixture of linear hydrocarbons. (Marano and Holder, 1997a) This approach considers the hydrocarbons mixture as a pseudo-solvent with $\bar{n}_C$ carbon atoms. The liquid molar volume of the hydrocarbon mixture is calculated as the molar volume of the pure corps that form the pseudo-solvent (Eq. 4.18).

$$\bar{n}_C = \sum_i x_i n_i \tag{4.17}$$

$$v_L = \sum_i x_i v_i^L \tag{4.18}$$

4.2.1.3 Fugacity of vapour and liquid phases.

The fugacity in vapour phase is calculated from the fugacity coefficient ϕ_i^V, obtained from Peng-Robinson equation:

$$ln\Phi_i^V = -ln\frac{p\left(v_V - b_V\right)}{RT} + \frac{b_i}{b_V}\left(Z_V - 1\right) + \frac{a_V}{b_V RT\left(r_1 - r_2\right)}\left(\frac{2\sum_j a_{ij} y_j}{a_V} - \frac{b_i}{b_V}\right) ln\frac{\left(v_V - b_V r_1\right)}{\left(v_V - b_V r_2\right)} \tag{4.19}$$

$$f_i^V = \Phi_i^V y_i p \tag{4.20}$$

Fugacity in liquid phase is estimated by considering each compound as a solute infinitely diluted in the pseudo-solvent. For light HCs and non-HCs compounds, fugacity are calculated from Henry coefficient H_i^∞ by using the Poyinting factor $\mathcal{J}_i$ to adjust the deviation on liquid fugacity due to pressure effects:

$$f_i^L = H_i^\infty \mathcal{J}_i x_i \tag{4.21}$$

$$\mathcal{J}_i = exp\left(\frac{\bar{v_{i,L}}}{RT}\left(P - P^\sigma_{pseudo-solvent}\right)\right) \tag{4.22}$$

Henry coefficient is calculated from empiric correlations proposed by Marano and Holder (Marano and Holder, 1997a):

$$lnH_i^\infty = H_{i,0} - \bar{n}_C \Delta H_i \tag{4.23}$$

with

$$H_{i,0} = A + \frac{B}{T} + Cln(T) + DT^2 + \frac{E}{T^2} \tag{4.24}$$

Parameters of the equation Eq. 4.24 are reported in Table D.6.

For condensable compounds (C_{3+}), fugacity are calculated from the activity coefficient at infinite dilution γ_i^{∞} adjusted with Poyinting factor:

$$f_i^L = \gamma_i^{\infty} \mathcal{J}_i' P_i^{sat} x_i \tag{4.25}$$

$$\mathcal{J}_i' = exp\left(\frac{\bar{v_{i,L}}}{RT}\left(P - P_i^{\sigma}\right)\right) \tag{4.26}$$

Activity coefficients are calculated from empiric correlations proposed by Marano and Holder (Marano and Holder, 1997a):

$$ln\gamma_i^{\infty} = ln\left(\gamma_r^{\infty}\right)\left(\frac{\bar{n}_C - i}{\bar{n}_C - r}\right) \tag{4.27}$$

with

$$\gamma_r^{\infty} = \frac{H_r^{\infty}}{P_r^{\sigma}} \tag{4.28}$$

where r is a reference hydrocarbon, here n-heptane.

4.2.1.4 Liquid-vapour equilibrium.

We can thus now perform the liquid-vapour equilibrium study. From this study we can estimate the value of α_V, representing the vapour fraction. If this value is different than 1, it means that some liquids are formed during the reaction. The numerical procedure is described in the following.

For a simple flash equilibrium problem, from mole balances and definitions of equilibrium ratios, the Rachford-Rice objective equation can be derived (Vidal et al., 2003):

$$F\left(\alpha_V\right) = \sum_{i=1}^{n} \frac{z_i\left(K_i - 1\right)}{1 + \alpha_V\left(K_i - 1\right)} = 0 \tag{4.29}$$

where z_i is the mole fraction of i in the feed and K_i represents the liquid/vapour equilibrium constant. If we know z_i and K_i, we are then able to solve this equation for α_V and then we can calculate all the compositions in liquid and vapour phases (according to Eqs. 4.30-4.32), as well as all the thermodynamics properties in the two phases.

$$y_i = \frac{z_i K_i}{1 + \alpha_V\left(K_i - 1\right)} \tag{4.30}$$

$$x_i = \frac{z_i}{1 + \alpha_V\left(K_i - 1\right)} \tag{4.31}$$

$$K_i = \frac{y_i}{x_i} \tag{4.32}$$

Rachford-Rice objective function is a monotonically decreasing function, thus the Newton-Raphson procedure will guarantee convergence. However, it is not continuous at all points of the domain, thus the solution should be found in the domain $0 < \alpha_V < 1$. Newton-Raphson method is generally an iterative procedure with a fast rate of convergence. It consists in calculating a new estimation of α_V (α_V^{new}), which is closer to the real answer than the previous guess $\left(\alpha_V^{old}\right)$, according to:

$$\alpha_V^{new} = \alpha_V^{old} - \frac{F\left(\alpha_V\right)}{F'\left(\alpha_V\right)} = \alpha_V^{old} + \frac{\sum_{i=1}^{n} \dfrac{z_i\left(K_i-1\right)}{1+\alpha_V\left(K_i-1\right)}}{\sum_{i=1}^{n} \dfrac{z_i\left(K_i-1\right)^2}{1+\alpha_V\left(K_i-1\right)^2}} \tag{4.33}$$

The convergence is achieved when

$$|\alpha_V^{new} - \alpha_V^{old}| < \epsilon$$

where ϵ is a small number ($\epsilon = 10^{-9}$). To solve Eq. 4.29 for α_V with the iterative Newton-Raphson procedure, a first guess of K_i is required. A very commonly used empirical correlation in the oil and gas field is Wilson's empirical correlation (Vidal et al., 2003) that correlates K_i with reduced properties and Pitzer's acentric factor:

$$K_i = \frac{1}{p_{ri}} exp\left(5.37\left(1+\omega_i\right)\left(1-\frac{1}{T_{ri}}\right)\right) \tag{4.34}$$

This equation is only applicable at low pressures, as it is based on Raoult-Dalton's derivation. Thus, it only has to be used as a first estimation of K_i. Then, a more rigorous method is needed to estimate equilibrium ratios. The “fugacity” approach is the most common method for the estimation of equilibrium ratios in the oil and gas field. This approach, combined with the Newton-Raphson procedure for the estimation of α_V, allows us to calculate the fugacity in vapour and liquid phases as shown before (Eqs. 4.20, 4.21, 4.25). The procedure is ended when the equilibrium condition is attained. Equilibrium condition in terms of fugacity can be written as:

$$f_i^V = f_i^L \tag{4.35}$$

Thus, the convergence is attained when:

$$\sum_{i=1}^{n} = \left(\frac{f_i^L}{f_i^V} - 1\right)^2 < 10^{-14} \tag{4.36}$$

If the convergence is not attained, the value of K_i has to be updated and the calculation is repeated. The updating of the value of K_i is formulated with the Successive Substitution Method (SSM). This method is the easiest to implement, but it can be very slow to reach the convergence. The updated value of K_i estimated with the SSM is formulated as follows:

$$K_i^{(n+1)} = \left(\frac{y_i}{x_i}\right)^{(n)} \left(\frac{f_i^L}{f_i^V}\right)^{(n)} \tag{4.37}$$

The detailed algorithm that has been followed is outlined in Figure 4.1.

4.2.1.5 Results of the LVE study.

From the LVE study that we have performed, we could thus estimate the fraction of vapour phase present in the system (α_V). Figure 4.2 shows the evolution of α_V with the system temperature at two pressures (10 and 25 bars). We can observe that for temperatures higher than 180°C for both pressures, the value of α_V is 1, thus the formation of liquid products can be excluded.

In CO-FT traditional conditions, the formation of liquid products is considered as an important aspect of the FT modelling. All kinetic or reactor models include the repartition of

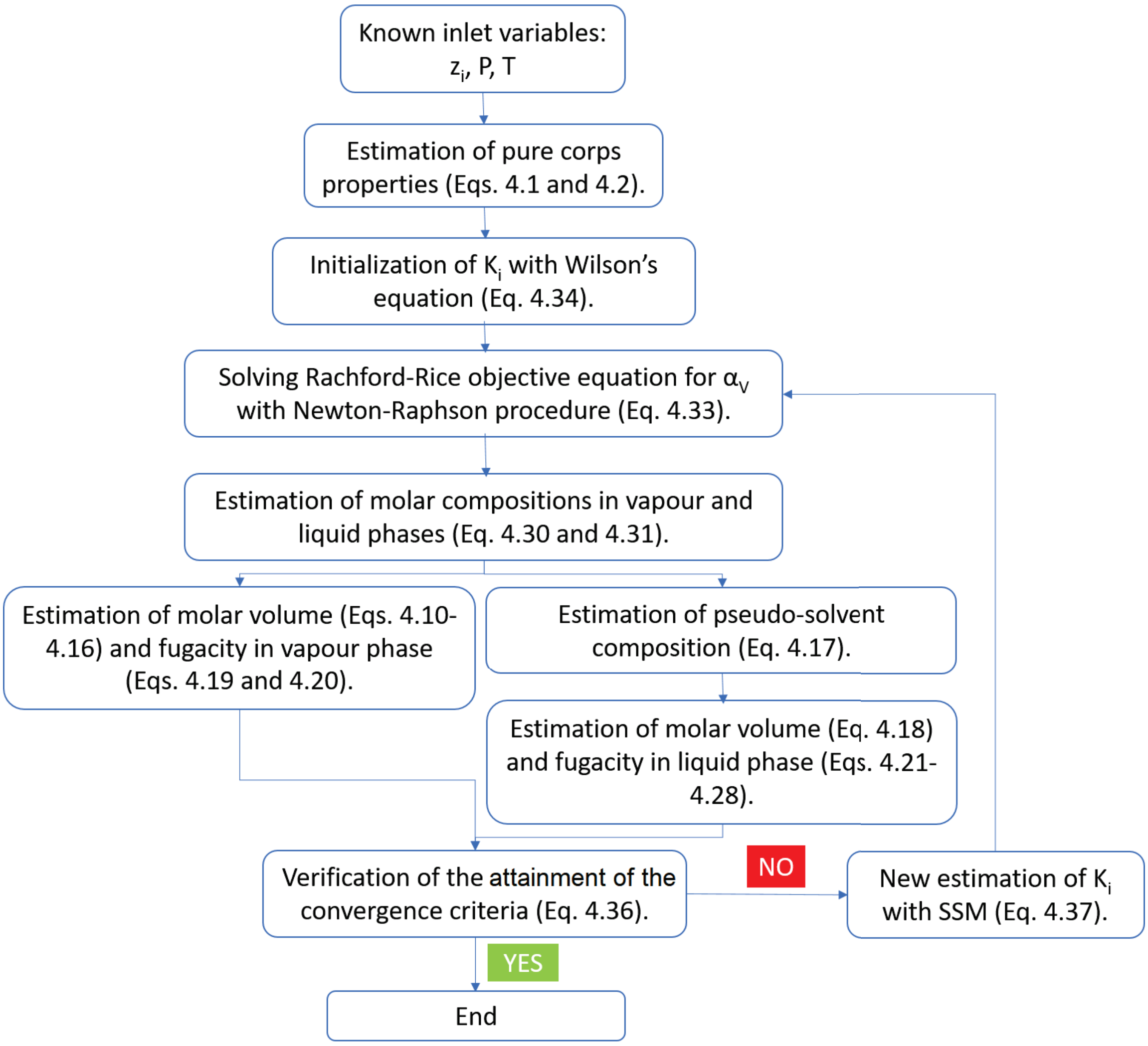

Figure 4.1: Outline of the detailed algorithm followed to solve the LVE study.

compounds between vapour and liquid phases. This is due to the significant production of heavy hydrocarbons in CO-FT conditions. In our system, the production of heavy hydrocarbons is very limited, as the main part of the obtained products is made of C_2-C_4 olefins. Thus, for CO_2-FT liquid-vapour equilibrium has never been considered in the kinetic models available in the literature. We performed this LVE study to verify that this hypothesis is effective.

To completely exclude the presence of a liquid phase in the system, it is also necessary to verify that gaseous reactants and products do not condensate inside the catalyst pores because of capillary condensation. The procedure and the results will be explained in the following section.

4.2.2 Capillary condensation in catalytic pores.

When vapour pressure in small capillaries (pores) is higher than at dew point, capillary forces can lead to the condensation of the vapour in the smallest pores of the catalyst. To study the capillary condensation in catalytic pores, we estimate the Kelvin's critical diameter (Thomson, 1872):

$$d_i = -\frac{4\sigma_i v_i}{RTln\left(\frac{p_i}{P_i^{sat}}\right)} \tag{4.38}$$

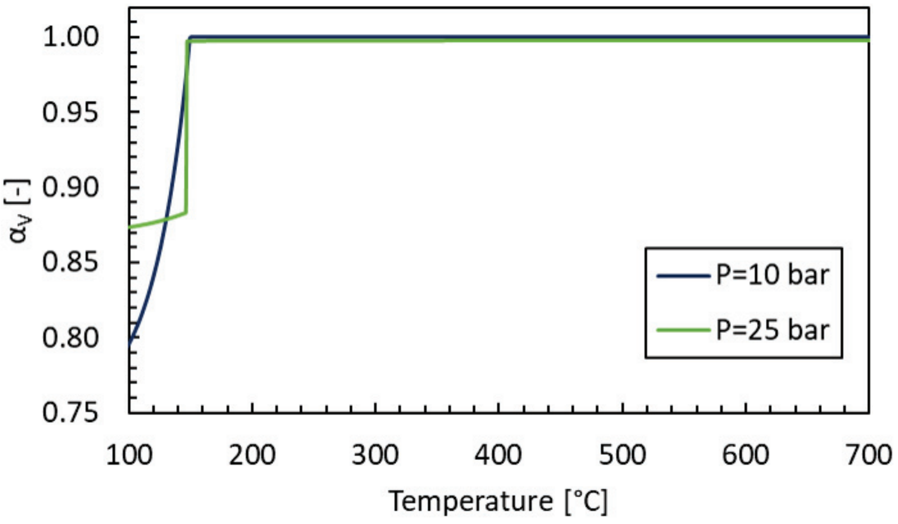

Figure 4.2: Vapour fraction calculated from the LVE study as function of the temperature varied between 100 and 700°C, at two conditions of pressure (10 and 25 bars).

Surface tension is estimated from critical properties according to Pitzer's equation (Poling et al., 2001):

$$\sigma_i = p_{c,i}^{2/3} T_{c,i}^{1/3} \frac{1.86 + 1.18\omega_{c,i}}{19.05} \left[\frac{3.75 + 0.91\omega_{c,i}}{0.291 - 0.08\omega_{c,i}} \right]^{2/3} (1 - T_r)^{11/9} \tag{4.39}$$

The calculation has been performed in reference conditions with partial pressures $\mathrm{p_i}$ corresponding to those experimentally obtained at the reactor outlet. The obtained critical diameters are reported in Figure 4.3 for the species considered. Kelvin's critical diameter is the diameter below which vapour can condensate in catalytic pores because of capillary condensation. Thus, to exclude capillary condensation, the estimated critical diameters have to be lower than the size of the catalyst's pores. We can observe that the critical diameters obtained for our system are all lower than 1 nm, while the pore diameter of our catalyst is around 7 nm and only few pores have diameters close to 1 nm (see Figure 3.1). Thus, the condensation of products in the pores can be neglected.

The capillary condensation in CO-FT is generally observed over both Co and Fe catalysts. (Ermolaev et al., 2010, 2015; Lox et al., 1988; Ma et al., 2013; Asami et al., 2013; Huff Jr and Satterfield, 1985) It is thus important to understand why in the case of CO_2-FT this phenomenon is less important. First of all, we have to consider that in typical CO-FT conditions products with more than 60 carbon atoms are formed and long chains are those that can condense in the pores. For example, Huff and Satterfield (Huff Jr and Satterfield, 1985) reported that over an iron catalyst supported on alumina and at 263°C and 8 bar, C_{65+} products were in liquid phase, C_{35} to C_{60} were distributed between the two phases, while $C_{<30}$ could not condense. In our reaction conditions, much lighter hydrocarbons are produced (not more than 35 C atoms) and in very small concentrations, thus we should not expect them to condense in the pores. Moreover, CO_2-FT is generally performed at higher temperatures compared to traditional CO-FT, contributing to increase the critical diameter and thus to limit the capillary condensation effect. (Huff Jr and Satterfield, 1985)

4.2.3 Ideality of vapour phase.

We have thus shown that the formation of liquid products can be excluded. We have now to understand whether the gas phase can be treated as an ideal phase or another equation of state

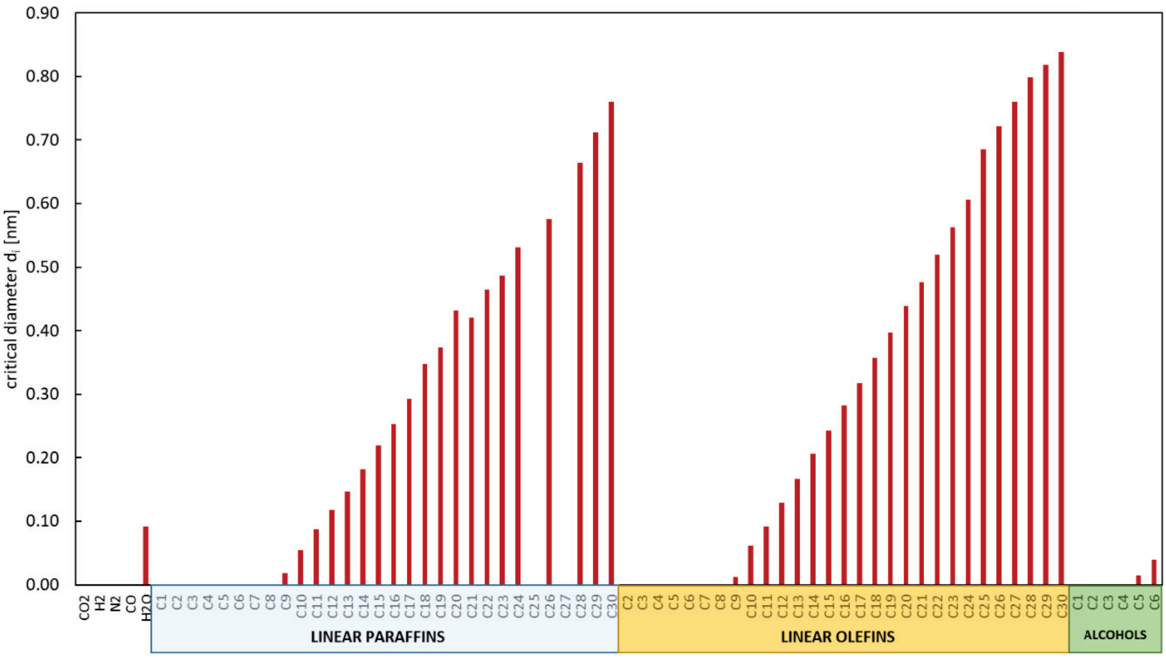

Figure 4.3: Values of critical diameters obtained for non-hydrocarbons, n-paraffins, α-olefins and alcohols for reference conditions (T=300°C, p=15 bar, H_2/CO_2=3 and GHSV=2000 Nml/g/h) and for the composition obtained at the reactor outlet in stationary regime.

would provide a better description. Thus, we assume that the gas phase cannot be treated as an ideal system and we simulate the system by using a different equation of state. We have chosen to use a cubic equation of state, as they are commonly applied for systems with this kind of hydrocarbons. The Soave-Redlich-Kwong (SRK) equation of state is accurate for the estimation of vapour pressure of hydrocarbons, but it is not able to accurately predict molar volumes of the liquid phase. (Soave et al., 2010) Peng-Robinson equation of state is more accurate in terms of liquid molar volumes prediction. (Peng and Robinson, 1979) However, in this case, we are interested in studying only the gas phase, thus both equations of state can be used.

Cubic equations of state (Eq. 4.10) are used instead of the ideal gas law to simulate the model in vapour phase. Eqs. 4.19 and 4.20 are used to estimate fugacity of each compound in vapour phase and fugacity are used in the kinetic laws instead of partial pressures. The compressibility factor Z is calculated for both equations of state:

$$Z = \frac{pv}{nRT} \tag{4.40}$$

Z is a measure of the ideality of the system. The closer it is to 1, the closer the system is to an ideal gas. Table 4.1 presents the values of Z and molar volume obtained for ideal, SRK and PR cases. We can observe that compressibility factors are very close to 1 regardless of the equation of state used. Thus, we can conclude that the ideal gas law can accurately describe the behaviour of the vapour phase in the system in the operative conditions of interest.

We have thus shown that the reaction can be considered to occur only in vapour phase, with a negligible formation of liquid products. Moreover, the vapour phase can be approximated to an ideal phase.

Table 4.1: Obtained compressibility factor Z and molar volumes in the case of ideal phase or SRK and PR equations of state.

	Z [-]	**v** [cm^3/mol]
ideal	1	0.0048
SRK	0.9995	0.0048
PR	0.9971	0.0048

4.3 Reactor modelling.

The lab-scale fixed-bed reactor is mathematically described with a plug-flow reactor model. To use a plug-flow model, typical criteria for fixed-bed reactors need to be verified:

- the system can be considered as isotherm (the axial temperature profile along the reactor shows a maximum $\Delta T < 5$ °C);
- axial dispersion and wall effects are negligible; (Mears, 1971b; Gierman, 1988; Chu and Ng, 1989)
- internal and external mass transfer limitations are not significant; (Froment, 1962; Mears, 1971a)

We have shown the calculations of these criteria in the section 2.3.3.1.

4.3.1 Reactor model equations.

Based on these verifications, a steady-state, one-dimensional and isothermal plug-flow model could be developed for each compound considered (Eq. 4.41). The gas phase is considered as ideal and liquid products formation is neglected.

$$\frac{dF_i}{d\tau_{mod}} = \dot{V}_{IN} \sum_j \nu_{i,j} r_{i,j} \tag{4.41}$$

4.4 Kinetic laws derivation.

We have now to define the kinetic laws $r_{i,j}$ to use in the reactor model. The CO_2 hydrogenation reaction is believed to take place in two steps: the RWGS first converts CO_2 to CO, then CO is further converted to hydrocarbons via FT synthesis. We did not consider direct CO_2 hydrogenation, as early works reported that it is negligible compared to the two-step pathway. (Riedel et al., 2001) Moreover, we have experimentally observed that CO is mainly a primary product and hydrocarbons are formed as secondary products (see section 3.5.1).

We considered the formation of the main hydrocarbons observed as products: CO (Eq. 4.42), 1-alkenes (Eq. 4.43) and n-alkanes (Eq. 4.44) until 20 carbon atoms and alcohols until 6 carbon atoms (Eq. 4.45). Heaviest products and other oxygenates (acids, aldehydes) are not considered, as their concentration is negligible.

$$CO_2 + H_2 \leftrightarrow CO + H_2O \tag{4.42}$$

$$CO + 2H_2 \rightarrow \frac{1}{n} C_nH_{2n} + H_2O \tag{4.43}$$

$$CO + \frac{2n+1}{n}H_2 \rightarrow \frac{1}{n}C_nH_{2n+2} + H_2O \tag{4.44}$$

$$CO + 2H_2 \rightarrow \frac{1}{n}C_nH_{2n+1}OH + \frac{n-1}{n}H_2O \tag{4.45}$$

The FT reaction is defined as the sum of all the reactions that lead to the formation of alkenes, alkanes or oxygenates (Eq. 4.46).

$$r_{FT} = \sum_{i=1}^{N} ir_i = r_1 + \sum_{i=2}^{\xi} ir_i + \sum_{i=\xi+1}^{N} ir_i = r_1\left(1 + \sum_{i=2}^{\xi}\alpha_1^{i-1} + \sum_{i=\xi+1}^{N}\alpha_1^{\xi-1}\alpha_2^{i-\xi}\right) \tag{4.46}$$

We thus need to define the equation rates for RWGS and FT. Previous studies reported that FT reaction rate is generally proportional to H_2 and CO partial pressures. Moreover, the inhibiting effects of CO_2 and water vapour are considered. For RWGS, a kinetic law similar to the one defined for FT was used before. The equations used in our work were taken from the work of Riedel (Riedel et al., 2001) that we modified by including the H_2 inhibition term at denominator. Thus, the reaction rates for RWGS and FT are defined as follows:

$$r_{RWGS} = k_{0RWGS}\, exp\left(-\frac{E_{ARWGS}}{RT}\right)\frac{p_{CO_2}p_{H_2} - \dfrac{p_{CO}p_{H_2O}}{K_{eq}}}{p_{CO} + a_{RWGS}p_{H_2O} + b_{RWGS}p_{CO_2} + c_{RWGS}p_{H_2}} \tag{4.47}$$

$$r_{FT} = k_{0FT}\, exp\left(-\frac{E_{AFT}}{RT}\right)\frac{p_{CO}p_{H_2}}{p_{CO} + a_{FT}p_{H_2O} + b_{FT}p_{CO_2} + c_{FT}p_{H_2}} \tag{4.48}$$

We want our model to be more detailed than those previously reported in literature and to be able to describe not only the global FT reaction rate, but also to distinguish the formation rate of each compound considered in the model. In order to do that, we need to add to the model new parameters that allow to describe the formation rate according to the chain length and to the chemical nature of the product. The kinetic law that we need is in the form:

$$r_{i,k} = S_i\phi_i^k r_{FT} \tag{4.49}$$

where S_i is the selectivity according to the carbon number and ϕ_i^k is the selectivity according to the product type (alkane, alkene, oxygenate).

To describe the carbon number selectivity, a double-α model is used, based on the one described by Patzlaff. (Patzlaff et al., 1999) The carbon number distribution is described by the superposition of two independent ASF distributions, characterized by two different chain-growth probabilities, α_1 and α_2. The point of intersection between the two ASF distributions is named ξ. The overall distribution can be expressed as in Eq. 4.50 and it is dominated by α_1 for low carbon numbers and by α_2 for higher carbon numbers. μ_2 represents the fraction of hydrocarbons formed with growth probability α_2 and is defined by Eq. 4.51.

$$x_i = (1-\mu_2)(1-\alpha_1)\alpha_1^{i-1} + \mu_2(1-\alpha_2)\alpha_2^{i-1} \tag{4.50}$$

$$\mu_2 = \frac{(1-\alpha_1)\alpha_1^{\xi-1}}{(1-\alpha_1)\alpha_1^{\xi-1} + (1-\alpha_2)\alpha_2^{\xi-1}} \tag{4.51}$$

As explained in the previous Chapter, C_1 is not included in this distribution, thus its reaction rate is derived separately. C_1 reaction rate is derived from the definition of r_{FT} and defined according to Eq. 4.52.

$$r_1 = \frac{r_{FT}}{1 + \sum_{i=2}^{\xi} \alpha_1^{i-1} + \sum_{i=\xi+1}^{N} \alpha_1^{\xi-1} \alpha_2^{i-\xi}} \tag{4.52}$$

The formation rates of each compound can finally be derived and are defined as in Eqs. 4.53 and 4.54.

$$r_i = \alpha_1 r_{i-1} = \alpha_1^{i-1} r_1 \qquad for\ 2 \leqslant i \leqslant \xi \tag{4.53}$$

$$r_i = \alpha_2 r_\xi = \alpha_1^{\xi-1} \alpha_2^{i-xi} r_1 \qquad for\ i > \xi \tag{4.54}$$

These rate equations are referred to C_1 reaction rate and those of compounds from C_2 to C_ξ depend on the parameter α_1, while those of $C_{\xi+1}$ to C_N depend on a combination of α_1 and α_2.

The selectivity ϕ_i^k is defined as the fraction of olefin, paraffin or oxygenate for a given carbon number i. Each r_i is thus defined as the sum of the reaction rate that forms the olefin, the paraffin and the oxygenate for the given carbon number i, as defined in Eq. 4.55.

$$r_i = r_{i,O} + r_{i,P} + r_{i,OX} = (O_i + P_i + OX_i) r_i \tag{4.55}$$

At this point, we have defined a kinetic model that is able to describe the formation of CO and olefins, paraffins and alcohols until 20 carbon atoms. We have a model that depends on products and reactants partial pressures and on kinetic parameters that have to be determined. We still need to find the laws that describe the variation of α, ξ and ϕ_i^k with the operating conditions.

Empirical correlations that describe the variation of α with operating conditions are available in literature. (Vervloet et al., 2012; Ermolaev et al., 2015; Ostadi et al., 2016) However, these laws were not able to accurately describe the variation of α_1 and α_2 in our case, thus we proposed a new empirical correlation (Eq. 4.56) which resulted to be the most suitable to describe the changes of these parameters with temperature and partial pressures of CO_2 and H_2.

$$\alpha_i = \frac{1}{1 + k'_{0i}\, exp\left(-\frac{E_{Ai}}{RT}\right) \frac{p_{H_2}^{a_i}}{p_{CO_2}^{b_i}}} \tag{4.56}$$

ξ was experimentally found to be close to 7 for every run, thus it is set constant and equal to 7.

The same procedure was followed to describe the variation of O_i, P_i and OX_i fractions with operating conditions. The empiric laws in Eq. 4.57 and 4.58 were defined for P_i and OX_i, while O_i is calculated from Eq 4.59.

$$P_i = (a_P\, log(i) + b_P(T)) * \left(\frac{p_{CO_2}}{p_{H_2}}\right)^{e_P}; \qquad b_P = b_{P1} T + b_{P2} \tag{4.57}$$

$$OX_i = a_{OX}(T) \left(\frac{p_{CO_2}}{p_0}\right)^{e_{OX}} exp(-b_{OX} i); \qquad a_{OX} = a_{OX1} T^2 + a_{OX2} T + a_{OX3} \tag{4.58}$$

$$O_i = 1 - OX_i - P_i \tag{4.59}$$

We have now determined the reactor model and the kinetic laws. We thus only have to chose the numerical method that allows to solve the system and to determine the values of the kinetic parameters.

4.5 Numeric methods.

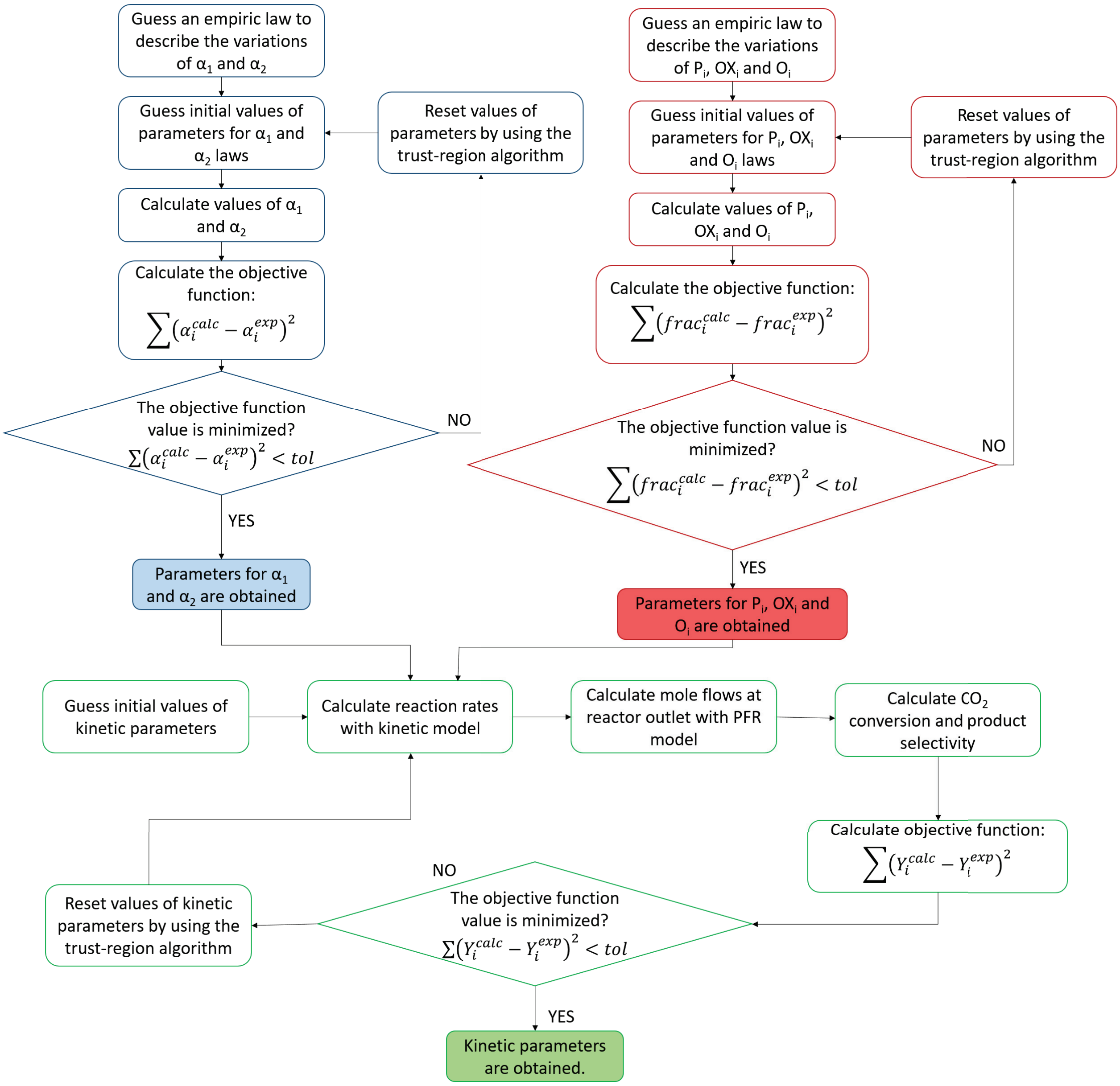

Figure 4.4: Scheme of the algorithm followed for the kinetic parameters optimization.

The objective of the calculation is to find the values of kinetic parameters that better fit the model with the experimental results. For nonlinear parameters estimation problems, least-squares methods are generally used. A least-squares problem consists in finding the vector x that minimizes the value of the function $f(x)$ which is defined as a sum of squares:

$$min_x f(x) = min_x ||F(x)||_2^2 = min_x \sum_i F_i^2(x) \tag{4.60}$$

To solve this problem different algorithms can be used. We have performed the numerical optimization by using the software Matlab and its function *lsqcurvefit*, using the Levenberg-Marquardt algorithm. The objective function to minimize has been defined as the differences between experimental and calculated values of CO_2 conversion and CO and HCs selectivity:

$$F(x) = Y^{exp} - Y^{calc}(x, x_{exp}) \tag{4.61}$$

where Y^{exp} is the vector containing the experimental data observed in x_{exp} and $Y^{calc}(x, x_{exp})$ is the vector containing the evaluated function in x_{exp} with the parameters contained in x.

The system of ordinary differential equations is solved with the Runge-Kutta solver, by using the solver *ode23* that can solve non-stiff differential equations of the type $y' = f(t, y)$.

The algorithm followed to solve the problem is outlined in Figure 4.4. First, the parameters for the empiric laws that describe the variations of αs and fractions are determined. Then, these laws are integrated in the kinetic model and the kinetic parameters are determined.

To improve the convergence of the computation, we have expressed the kinetic constants as follows:

$$k_i = k_{i,0}^* exp\left(\frac{-E_i}{R\left(\frac{1}{T} - \frac{1}{T_{ref}}\right)}\right)$$

where T_{ref} is a reference temperature, here set to 548.15 K. Thus, the $k_{i,0}$ is then derived from:

$$k_{i,0} = k_{i,0}^* exp\left(\frac{E_i}{RT_{ref}}\right)$$

A simulation was run with varying reaction orders of each compound, to check if orders different than 1 could improve the prediction of experimental data. Orders were found to be very close to 1, thus they were all set to 1 and not considered as kinetic parameters to determine. Results of the simulation with varying orders are reported in Figure D.1 in comparison with those obtained when orders are set to 1.

The evaluation of the goodness of the fit is made by estimating the mean average relative residual (MARR) according to Eq. 4.62.

$$MARR\ \% = \frac{1}{n_{exp}} \frac{1}{n_{var}} \sum_{j=1}^{nexp} \sum_{i=1}^{nvar} \frac{|Y_{ij}^{exp} - Y_{ij}^{calc}|}{Y_{ij}^{exp}} \tag{4.62}$$

A good fit represents a model that is able to predict the observed data with little uncertainty and where model coefficients can be evaluated with little uncertainty. Thus, it is necessary to estimate the uncertainty of the obtained parameters. For this purpose, confidence intervals for the fitted coefficients were estimated. They are expressed as:

$$CI = x \pm t\sqrt{S} \tag{4.63}$$

where x are the fitted parameters, t represents a parameter derived from the inverse of the Student's cumulative distribution factor and S represents the values of the covariance matrix of the estimated parameters *cov*. The *cov* matrix is calculated as:

$$cov = \left(J^T J\right)^{-1} MSE \tag{4.64}$$

where MSE is the mean squared error representing the sum of squared error divided by the degree of freedom v

$$MSE = \frac{resnorm}{v} \tag{4.65}$$

and J is the Jacobian matrix for the estimated parameters, defined as:

$$J = \begin{bmatrix} \frac{\delta Y_1^{calc}(x)}{\delta x_1} & \cdots & \frac{\delta Y_1^{calc}(x)}{\delta x_{n_{par}}} \\ \vdots & \ddots & \vdots \\ \frac{\delta Y_{n_{exp}}^{calc}(x)}{\delta x_1} & \cdots & \frac{\delta Y_{n_{exp}}^{calc}(x)}{\delta x_{n_{par}}} \end{bmatrix}$$

The confidence intervals were estimated with the function *nlparci* that gives as output the confidence intervals at 95% for the estimated parameters from the values of residuals and elements of the covariance matrix.

Finally, we have performed a statistical analysis to establish the relationships between the estimated parameters. Correlation coefficients and p-values were estimated. The first tell if there is a correlation between two parameters, while p-values are indication of the statistical significance of the parameter. Pearson's correlation between parameters x_1 and x_2 are defined as:

$$R_{x_1,x_2} = \frac{cov\left(x_1, x_2\right)}{\sigma_{x_1}\sigma_{x_2}} \tag{4.66}$$

where σ_x is the standard deviation of x. We have estimated correlation parameters with the function *corrcov* that converts the covariance to a correlation matrix. The values of correlation parameters are comprised between -1 and 1: -1 represents strong negative correlations, while +1 represents strong positive correlations. 0 represents no correlation.

p-values are defined as the probability of obtaining results at least as extreme as those observed, when making the assumption that the null hypothesis is correct. (Walpole et al., 2017) They are used as a measure of the statistical significance of a result: the lower the p-value, the lower the probability of obtaining that result if the null hypothesis was true. That means that for low values of p-value, the null hypothesis can be rejected, thus the obtained results are statistically significant. The null-hypothesis is rejected when p-value is less than the value of α, known as significance level, which is set by the researcher. We have set $\alpha = 0.05$, as commonly used. To evaluate p-values, we have to consider an unknown distribution T and a statistical test t. The p-value is the probability that the value observed is at least as extreme as t, assuming that the null hypothesis H_0 is true. Mathematically, this can be written as:

$$\begin{aligned} &p = Pr\left(T \geqslant t|H_0\right) \quad for\ a\ one-sided\ test \\ &p = Pr\left(T \leqslant t|H_0\right) \quad for\ a\ one-sided\ test \\ &p = 2min\left[Pr\left(T \leqslant t|H_0\right), Pr\left(T \geqslant t|H_0\right)\right] \quad for\ a\ two-sided\ test \end{aligned} \tag{4.67}$$

If we assume that the distribution is symmetric, the double-sided test becomes:

$$p = Pr\left(|T| \geqslant |t|\ |H_0\right) \tag{4.68}$$

p-values have been estimated by using the function *tcdf* that returns the cumulative distribution function of the Student's distribution evaluated in t. t is estimated as follows:

$$t = R\sqrt{\frac{n_{par} - 2}{1 - R^2}} \tag{4.69}$$

4.6 Results of the kinetic model and validation.

In this section we present the results of the optimization of the kinetic parameters, obtained according to the procedure explained previously.

4.6.1 Fitting of α values.

The correlation of Eq. 4.56 was used to describe the variation of α_1 and α_2 with the operating parameters. As discussed in the previous Chapter, α_1 and α_2 are influenced by reaction temperature and partial pressures of CO_2 and H_2, while contact time and total pressure have less significant effects. Moreover, α_1 variations are more important than those of α_2.

The optimized parameters obtained for the variations of αs are reported in Table 4.2. Figure 4.5 shows the evolution of α values predicted by the model, compared to the experimental data. We can observe that the model can predict the experimental values with quite good accuracy. The most important deviations are for the variation of α_1 with the temperature, as the model overestimates the values compared to the experimental data. Moreover, for high H_2 partial pressures, the model is not able to accurately predict the slight decrease of α_1 that is observed experimentally. Values of α_2 change less and are thus better predicted by the model.

Table 4.2: Parameters obtained for the empiric law that describes the variation of α_1 and α_2 with operating conditions (Eq. 4.56).

		α_1	α_2
Parameter	Unit	Value	Value
$k_{0,i}$	[-]	10.47	5.90
a_i	[-]	0.14	-0.08
b_i	[-]	0.06	0.15
$E_{A,i}$	[J/mol]	18605	0

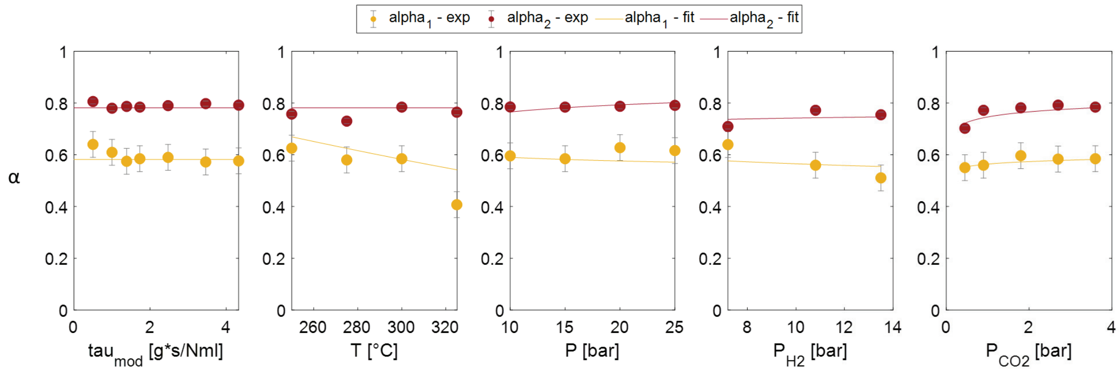

Figure 4.5: Evolution of α_1 and α_2 with operating parameters (contact time, temperature, total pressure and H_2 and CO_2 partial pressures). Lines represent model predictions, points represent experimental data. Error bars are calculated as standard deviations.

4.6.2 Fitting olefins, paraffins and oxygenates fractions.

Correlations in Eqs. 4.57 and 4.58 were used to describe the evolution of paraffins and oxygenates fractions with operating conditions. As for αs, these fractions are functions of the reaction temperature and the partial pressures of CO_2 and H_2 (only CO_2 for oxygenates) and depend on the carbon number of the compound considered. The parameters obtained from the optimization study are reported in Table 4.3. Figure 4.6 presents the predictions of the model compared to the experimental values. It is not possible to fit exactly the experimental values, as many parameters would have to be considered and the incertitude on some experimental points can be significant. However, we can observe that the predictions of the model are quite in agreement with the experimental values: the increase of paraffin formation when reducing temperature and partial pressure of CO_2 are well predicted by the model, as well as the corresponding decrease of oxygenates formation.

Table 4.3: Parameters obtained for the empiric law that describes the variation of P_i and OX_i with operating conditions (Eqs. 4.57 and 4.58).

P_i		OX_i	
Parameter	Value	Parameter	Value
a_P	0.07	a_{OX1}	$-1.03\text{x}10^{-4}$
b_{P1}	$-8.14\text{x}10^{-4}$	a_{OX2}	0.14
b_{P2}	0.05	a_{OX3}	-40.58
e_P	-0.08	b_{OX}	0.84
		e_{OX}	0.34
		p_{ref}	$1.50\text{x}10^6$

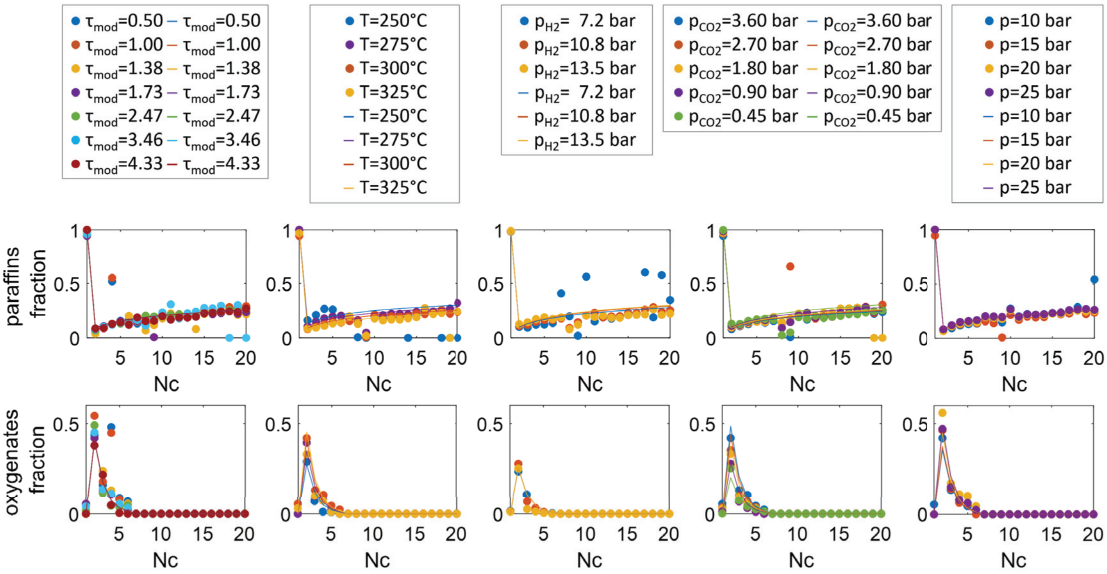

Figure 4.6: Variation of P_i and OX_i with the operating parameters (modified residence time, temperature, p_{H_2}, p_{CO_2} and p_{tot}). Points represent experimental data, lines model predictions.

To resume, the parameters obtained for Eqs. 4.56, 4.57 and 4.58 allow to estimate the values of α_1, α_2, P_i and OX_i corresponding to the operating conditions of interest. Of course, this only allows to predict the hydrocarbon distributions at the outlet of the reactor and the approach is totally empirical and valid in the operating conditions studied.

4.6.3 Kinetic parameters.

The complete kinetic model as described before has been simulated and the optimized values of kinetic parameters are reported in Table 4.4.

The activation energies are in the range reported in literature for RWGS (55-139 kJ/mol), while they are a bit lower for the FT (72-150 kJ/mol). (Riedel et al., 2001; Iglesias Gonzalez et al., 2015; Willauer et al., 2013; Najari et al., 2019) FT activation energy results to be lower than RWGS one. The values of activation energy have to be considered as apparent and representative of the temperature-sensitivity of the reactions, as inhibition terms are considered not dependent on temperature. Pre-exponential factors can hardly be compared to the values reported in literature, as the reported values are in a very wide range and kinetic laws are not

Table 4.4: Kinetic parameters values obtained by non-linear regression for RWGS and FT reactions.

RWGS				
Parameter	Unit	Value	Confidence interval	
$k_{0,\mathrm{RWGS}}$	[mol/kg/s/MPa^2]	2.97x10^3	$-$3.02x10^4	3.62x10^4
E_{RWGS}	[kJ/mol]	72.8	72.8	72.8
a_{RWGS}	[MPa^{-1}]	0		
b_{RWGS}	[MPa^{-1}]	0.207	-2.75	3.17
c_{RWGS}	[MPa^{-1}]	0.004	-0.08	0.09
FT				
Parameter	Unit	Value	Confidence interval	
$k_{0,\mathrm{FT}}$	[mol/kg/s/MPa^2]	3.78x10^5	1.54x10^5	6.02x10^5
E_{FT}	[kJ/mol]	49.6	49.6	49.6
a_{FT}	[MPa^{-1}]	0		
b_{FT}	[MPa^{-1}]	449.2	439.0	459.5
c_{FT}	[MPa^{-1}]	54.8	44.5	65.0

exactly the same. FT pre-exponential factor obtained is two orders of magnitude higher than RWGS one.

The equations of our proposed model take into account the inhibition effects caused by the adsorption of all CO, H_2O, CO_2 and H_2. The values of a_{RWGS} and a_{FT}, representing the inhibition constants of H_2O referred to CO, were found to be very close to 0 and were thus neglected. On the contrary, the inhibition effect of CO_2 in the case of the FT reaction is dominant, as indicated by the high value of b_{FT}. This is in agreement with literature and can be explained by the high content of K of the catalyst, as K favours CO_2 adsorption over iron catalysts. (Riedel et al., 2001) The value of c_{FT} also suggests that the inhibition effect of H_2 adsorption cannot be neglected. For the RWGS, the values of b_{RWGS} and c_{RWGS} are both lower than 1, indicating that the inhibition effect of CO is the most important.

Confidence interval at 95% of each parameter have been estimated. They are reported in Table 4.4. We can observe that for FT the obtained intervals are acceptable, representing variations of less than 20%, except for the $k_{0,FT}$ that has deviations of 60%. For the RWGS, on the contrary, we can observe that the minimum value for all parameters (except the activation energy) is a negative number. This does not have any physical meaning.

Numerically, the problem comes from the Jacobian matrix J that is found to be close to singularity (reciprocal condition number = 7x10^{-21}). When the reciprocal condition number of a matrix is close to 0, the matrix is close to singular or badly scaled and this means that its inverse matrix cannot be calculated. The number of experimental points is probably not sufficient to have robust results, or the quality of the experimental points is not the good one. Thus, providing more experimental points could probably contribute to reduce the confidence intervals of the estimated parameters.

The correlation between parameters is shown in Figure 4.7 that reports the correlations coefficients R_{ij} and the p-values for each couple of parameters. Three couples of parameters present values of R_{ij} very close to 1, indicating strong correlations between them (b_{RWGS} with $k_{0,RWGS}$, b_{FT} with $k_{0,RWGS}$ and b_{FT} with b_{RWGS}). The same three couples of parameters also show p-values lower than the set significance level (< 0.05). For these three couples we can thus say that the results are statistically significant. For the others however we cannot say that they are not significant, just that we do not have enough evidence to understand their significance.

The proposed model within the optimized parameters is able to fit the experimental data with good accuracy (MARR $< 5\%$). Predictions of the model are compared to experimental data in Figure 4.8, while the parity plot of the response variables considered is presented in Figure 4.9.

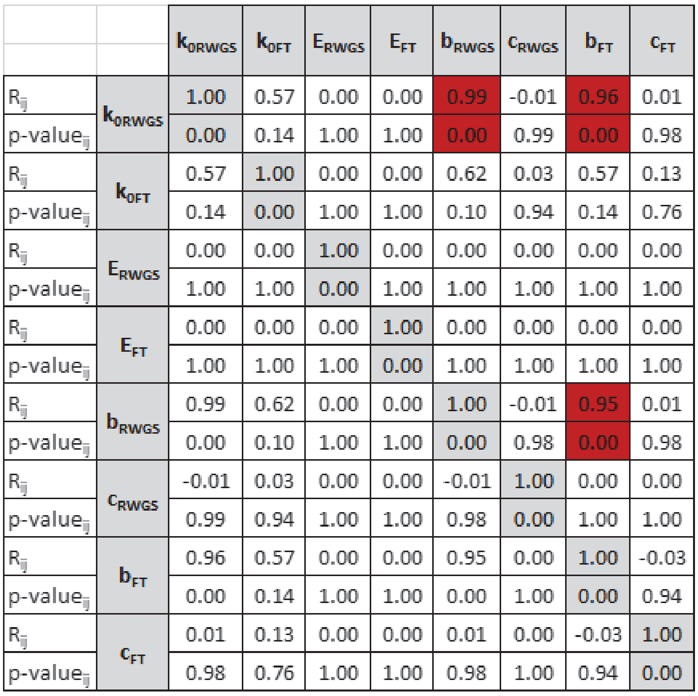

		k_{0RWGS}	k_{0FT}	E_{RWGS}	E_{FT}	b_{RWGS}	c_{RWGS}	b_{FT}	c_{FT}
R_{ij}	k_{0RWGS}	1.00	0.57	0.00	0.00	0.99	-0.01	0.96	0.01
p-value$_{ij}$		0.00	0.14	1.00	1.00	0.00	0.99	0.00	0.98
R_{ij}	k_{0FT}	0.57	1.00	0.00	0.00	0.62	0.03	0.57	0.13
p-value$_{ij}$		0.14	0.00	1.00	1.00	0.10	0.94	0.14	0.76
R_{ij}	E_{RWGS}	0.00	0.00	1.00	0.00	0.00	0.00	0.00	0.00
p-value$_{ij}$		1.00	1.00	0.00	1.00	1.00	1.00	1.00	1.00
R_{ij}	E_{FT}	0.00	0.00	0.00	1.00	0.00	0.00	0.00	0.00
p-value$_{ij}$		1.00	1.00	1.00	0.00	1.00	1.00	1.00	1.00
R_{ij}	b_{RWGS}	0.99	0.62	0.00	0.00	1.00	-0.01	0.95	0.01
p-value$_{ij}$		0.00	0.10	1.00	1.00	0.00	0.98	0.00	0.98
R_{ij}	c_{RWGS}	-0.01	0.03	0.00	0.00	-0.01	1.00	0.00	0.00
p-value$_{ij}$		0.99	0.94	1.00	1.00	0.98	0.00	1.00	1.00
R_{ij}	b_{FT}	0.96	0.57	0.00	0.00	0.95	0.00	1.00	-0.03
p-value$_{ij}$		0.00	0.14	1.00	1.00	0.00	1.00	0.00	0.94
R_{ij}	c_{FT}	0.01	0.13	0.00	0.00	0.01	0.00	-0.03	1.00
p-value$_{ij}$		0.98	0.76	1.00	1.00	0.98	1.00	0.94	0.00

Figure 4.7: Matrix of Pearson correlation coefficients between pairs of parameters and their corresponding p-value. Boxes coloured in red have important correlation and are statistically significant.

We can observe that almost all predicted values agree with experimental data within an error of ±20%. Some exceptions are observed for long chain products (C_{5+}paraffins and olefins fractions) and for oxygenates, but it is necessary to remind that the experimental error on these quantities is very high, due to the uncertainties of the analysis. Residuals plot, shown in Figure 4.10, represents the differences between the experimental data and the fit ($Y^{exp} - Y^{calc}$): almost the same variability for all response variables is observed, except for paraffins fraction that presents higher positive variations. Points appear randomly scattered around zero, indicating that data are well described by the model.

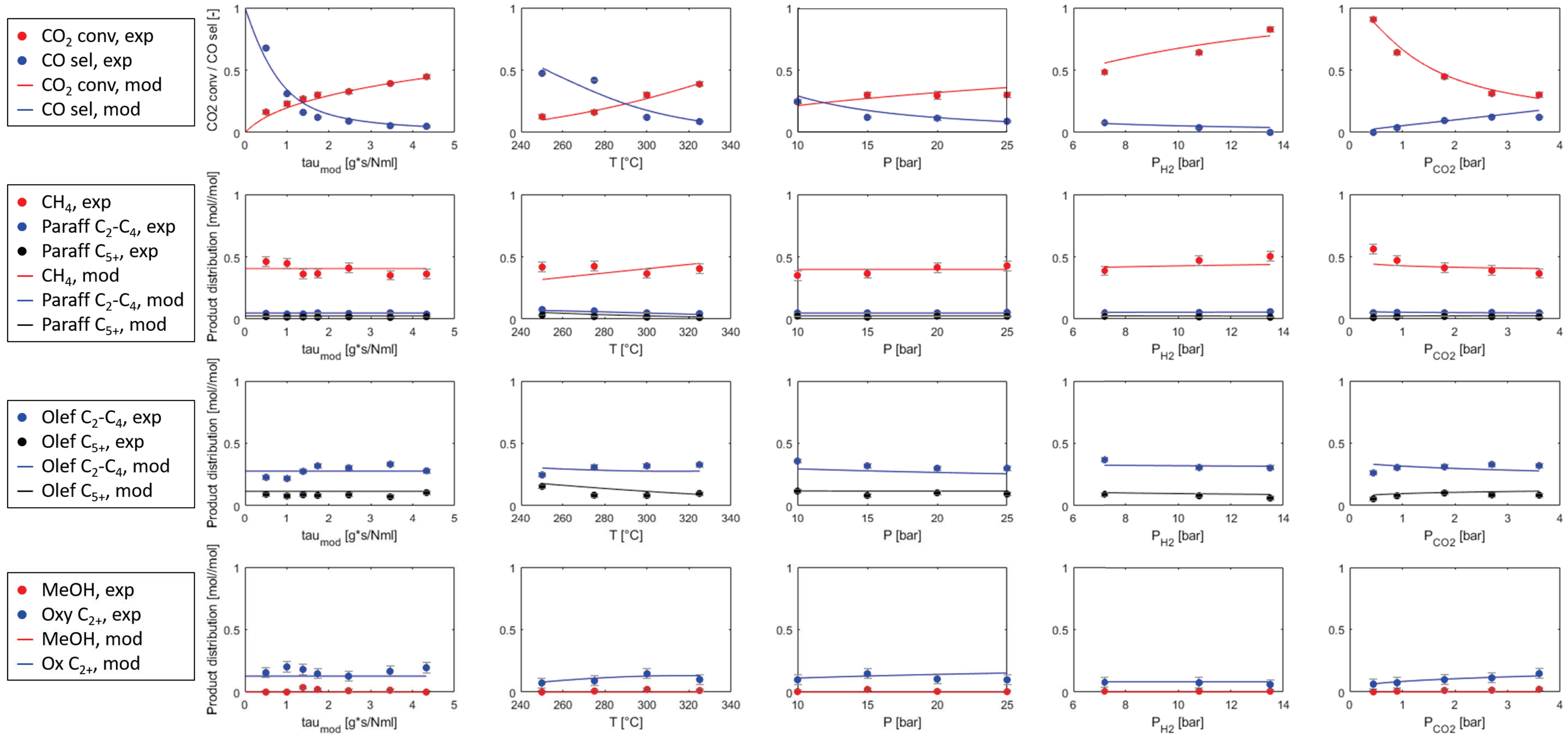

Figure 4.8: Predictions of kinetic model compared to experimental data. Lines represent model predictions, points represent experimental data. Error bars are calculated as standard deviations.

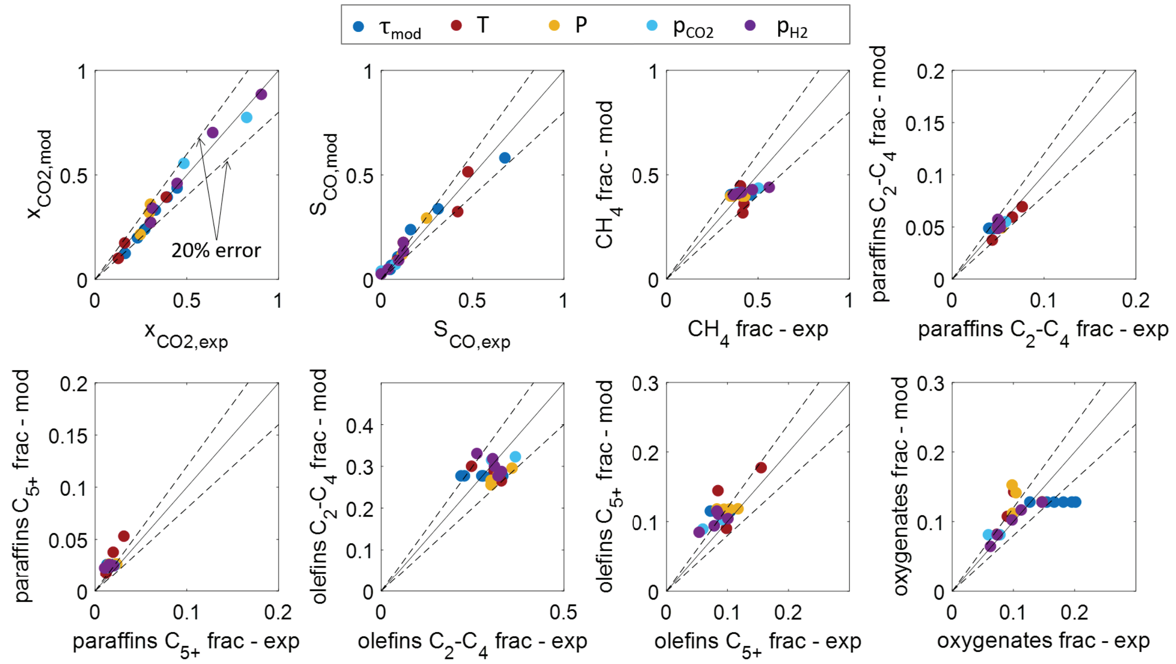

Figure 4.9: Parity plot for calculated values and experimental data of all response variables. Dashed lines represent the 20% error.

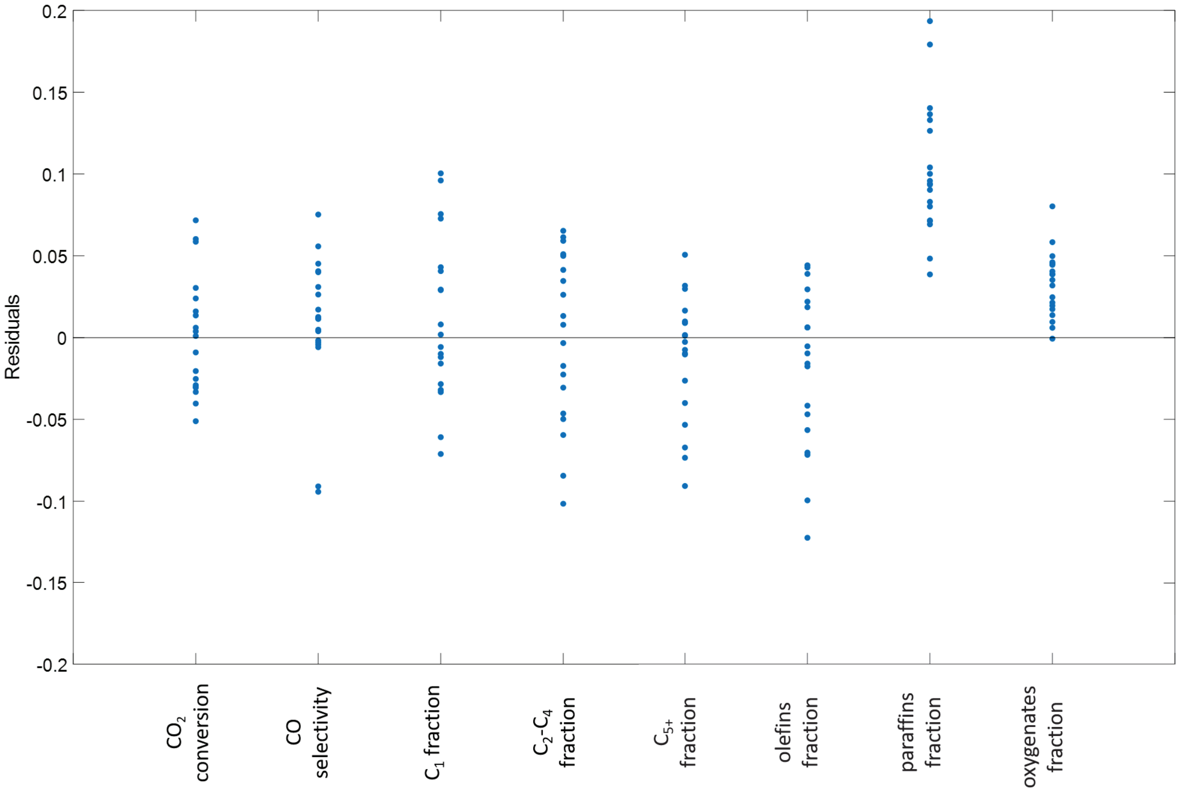

Figure 4.10: Plot of residuals of each response variable considered.

4.7 Conclusion.

In conclusion, we have developed a detailed semi-empirical macro-kinetic model that is able to describe the formation of the main products observed during CO_2 hydrogenation. The model includes empiric laws to describe the variation of the parameters α_1, α_2, P_i and OX_i with operating conditions. These parameters are included in the kinetic model, allowing to describe the distribution of products according to their chain length and their chemical nature.

The model still needs some improvements, especially in the prediction of the methane fraction and the short olefins fraction at low temperature and high H_2/CO_2 ratios. Moreover, the model does not consider the influence of residence time on HCs distribution, which should be taken into account to improve the accuracy of the model. Furthermore, when drawing conclusions about this model, we have to keep in mind that it is mostly empirical and that some of the obtained parameters present high uncertainties.

Thus, this model has to be seen as a useful tool for simulations of kinetics in reactor or process simulations, while for deeper insights about the reaction mechanism, different approaches should be considered. A mechanistic model for this reaction has been developed and provides better understanding of the reaction mechanism. It will be presented in the next Chapter.

References

K. Asami, A. Iwasa, N. Igarashi, S. Takemiya, K. Yamamoto, and K. Fujimoto. Fischer–Tropsch synthesis over precipitated iron catalysts supported on carbon. *Catalysis Today*, 215:80–85, 2013. ISSN 09205861. doi: 10.1016/j.cattod.2013.04.020. URL `https://linkinghub.elsevier.com/retrieve/pii/S0920586113002095`.

C. F. Chu and K. M. Ng. Flow in packed tubes with a small tube to particle diameter ratio. *AIChE Journal*, 35(1):148–158, 1989. ISSN 0001-1541. doi: 10.1002/aic.690350116. URL `https://doi.org/10.1002/aic.690350116`. Publisher: John Wiley & Sons, Ltd.

V. S. Ermolaev, V. Z. Mordkovich, and I. G. Solomonik. Influence of Capillary Condensation on Heat and Mass Transfer in the Grain of a Fischer–Tropsch Synthesis Catalyst. *Theoretical Foundations of Chemical Engineering*, 44(5):660–664, 2010. doi: 10.1134/S0040579510050040. URL `https://link.springer.com/article/10.1134/S0040579510050040`.

V. S. Ermolaev, K. O. Gryaznov, E. B. Mitberg, V. Z. Mordkovich, and V. F. Tretyakov. Laboratory and pilot plant fixed-bed reactors for Fischer-Tropsch synthesis: Mathematical modeling and experimental investigation. *Chemical Engineering Science*, 138:1–8, 2015. doi: https://doi.org/10.1016/j.ces.2015.07.036. URL `https://www.sciencedirect.com/science/article/pii/S0009250915005217?via%3Dihub`.

G. Froment. Design of fixed-bed catalytic reactors based on effective transport models. *Chemical Engineering Science*, 17(11):849–859, 1962. ISSN 00092509. doi: 10.1016/0009-2509(62)87017-1. URL `https://linkinghub.elsevier.com/retrieve/pii/0009250962870171`.

H. Gierman. Design of laboratory hydrotreating reactors: Scaling Down of Trickle-flow Reactors. *Applied Catalysis*, 43(2):277–286, 1988. ISSN 0166-9834. doi: 10.1016/S0166-9834(00)82732-3. URL `https://www.sciencedirect.com/science/article/pii/S0166983400827323`.

G. A. Huff Jr and C. N. Satterfield. Liquid accumulation in catalyst pores in a Fischer-Tropsch fixed-bed reactor. *Industrial & Engineering Chemistry Process Design and Development*, 24(4):986–995, 1985.

M. Iglesias Gonzalez, C. de Vries, M. Claeys, and G. Schaub. Chemical energy storage in gaseous hydrocarbons via iron Fischer–Tropsch synthesis from H_2/CO_2 —Kinetics, selectivity and process considerations. *Catalysis Today*, 242:184–192, 2015. ISSN 09205861. doi: 10.1016/j.cattod.2014.05.020. URL `https://linkinghub.elsevier.com/retrieve/pii/S0920586114003903`.

E. S. Lox, G. B. Marin, E. De Grave, and P. Bussiere. Characterization of a promoted precipitated iron catalyst for Fischer-Tropsch synthesis. *Applied Catalysis*, 40:197–218, 1988.

W. Ma, G. Jacobs, J. Kang, D. E. Sparks, M. K. Gnanamani, V. R. R. Pendyala, W. D. Shafer, R. A. Keogh, U. M. Graham, G. A. Thomas, and B. H. Davis. Fischer–Tropsch synthesis. Effect of alkali, bicarbonate and chloride addition on activity and selectivity. *Catalysis Today*, 215:73–79, Oct. 2013. ISSN 09205861. doi: 10.1016/j.cattod.2013.03.003. URL `https://linkinghub.elsevier.com/retrieve/pii/S0920586113000886`.

J. J. Marano and G. D. Holder. Characterization of Fischer-Tropsch liquids for vapor-liquid equilibria calculations. *Fluid Phase Equilibria*, 138(1-2):1–21, Nov. 1997a. ISSN 03783812. doi: 10.1016/S0378-3812(97)00166-0. URL `https://linkinghub.elsevier.com/retrieve/pii/S0378381297001660`.

J. J. Marano and G. D. Holder. General Equation for Correlating the Thermophysical Properties of n -Paraffins, n -Olefins, and Other Homologous Series. 1. Formalism for Developing Asymptotic Behavior Correlations. *Industrial & Engineering Chemistry Research*, 36(5):1887–1894, May 1997b. ISSN 0888-5885, 1520-5045. doi: 10.1021/ie960511n. URL `https://pubs.acs.org/doi/10.1021/ie960511n`.

J. J. Marano and G. D. Holder. Prediction of Bulk Properties of Fischer-Tropsch Derived Liquids. page 12, 1997c.

D. E. Mears. Diagnostic criteria for heat transport limitations in fixed bed reactors. *Journal of Catalysis*, 20(2):127–131, 1971a. ISSN 0021-9517. doi: 10.1016/0021-9517(71)90073-X. URL `https://www.sciencedirect.com/science/article/pii/002195177190073X`.

D. E. Mears. The role of axial dispersion in trickle-flow laboratory reactors. *Chemical Engineering Science*, 26(9):1361–1366, Sept. 1971b. ISSN 0009-2509. doi: 10.1016/0009-2509(71)80056-8. URL `https://www.sciencedirect.com/science/article/pii/0009250971800568`.

S. Najari, G. Gróf, S. Saeidi, and F. Gallucci. Modeling and optimization of hydrogenation of CO_2: Estimation of kinetic parameters via Artificial Bee Colony (ABC) and Differential Evolution (DE) algorithms. *International Journal of Hydrogen Energy*, 44(10):4630–4649, 2019. ISSN 03603199. doi: 10.1016/j.ijhydene.2019.01.020. URL `https://linkinghub.elsevier.com/retrieve/pii/S036031991930093X`.

M. Ostadi, E. Rytter, and M. Hillestad. Evaluation of kinetic models for Fischer–Tropsch cobalt catalysts in a plug flow reactor. *Chemical Engineering Research and Design*, 114:236–246, Oct. 2016. ISSN 0263-8762. doi: 10.1016/j.cherd.2016.08.026. URL `http://www.sciencedirect.com/science/article/pii/S0263876216302775`.

J. Patzlaff, Y. Liu, C. Graffmann, and J. Gaube. Studies on product distributions of iron and cobalt catalyzed Fischer–Tropsch synthesis. *Applied Catalysis A: General*, 186(1-2):109–119, 1999. ISSN 0926860X. doi: 10.1016/S0926-860X(99)00167-2. URL `https://linkinghub.elsevier.com/retrieve/pii/S0926860X99001672`.

D.-Y. Peng and D. B. Robinson. A New Two-Constant Equation of State. *Industrial & Engineering Chemistry Process Design and Development*, 18(2), 1979.

B. E. Poling, J. M. Prausnitz, and J. P. O'Connell. *The properties of gases and liquids*. McGraw-Hill, New York, 5th ed edition, 2001. ISBN 978-0-07-011682-5.

T. Riedel, G. Schaub, K.-W. Jun, and K.-W. Lee. Kinetics of CO_2 Hydrogenation on a K-Promoted Fe Catalyst. *Industrial & Engineering Chemistry Research*, 40(5):1355–1363, 2001. ISSN 0888-5885, 1520-5045. doi: 10.1021/ie000084k. URL `http://pubs.acs.org/doi/abs/10.1021/ie000084k`.

G. Soave, S. Gamba, and L. A. Pellegrini. SRK equation of state: Predicting binary interaction parameters of hydrocarbons and related compounds. *Fluid Phase Equilibria*, 299(2):285–293, Dec. 2010. ISSN 03783812. doi: 10.1016/j.fluid.2010.09.012. URL `https://linkinghub.elsevier.com/retrieve/pii/S037838121000467X`.

W. Thomson. 4. On the Equilibrium of Vapour at a Curved Surface of Liquid. *Proceedings of the Royal Society of Edinburgh*, 7:63–68, 1872. ISSN 0370-1646. doi: 10.1017/S0370164600041729. URL `https://www.cambridge.org/core/article/4-on-the-equilibrium-of-vapour-at-a-curved-surface-of-liquid/FE2D8D526BD8347E46274E63329AA521`. Edition: 2014/09/15 Publisher: Royal Society of Edinburgh Scotland Foundation.

D. Vervloet, F. Kapteijn, J. Nijenhuis, and J. R. van Ommen. Fischer–Tropsch reaction–diffusion in a cobalt catalyst particle: aspects of activity and selectivity for a variable chain growth probability. *Catalysis Science & Technology*, 2(6):1221–1233, 2012. ISSN 2044-4753. doi: 10.1039/C2CY20060K. URL `http://dx.doi.org/10.1039/C2CY20060K`.

J. Vidal, T. S. Pheney, and M. E. McHugh. *Thermodynamics : applications in chemical engineering and the petroleum industry*. Institut français du pétrole publications. Paris : Editions Technip, paris : editions technip edition, 2003. URL `https://www.worldcat.org/title/thermodynamics-applications-in-chemical-engineering-and-the-petroleum-industry/oclc/912295404`.

R. E. Walpole, R. H. Myers, S. L. Myers, and K. Ye. *Probability & statistics for engineers & scientists: MyStatLab update*. 2017. ISBN 978-1-292-16141-9. URL `http://www.myilibrary.com?id=947904`. OCLC: 1014366070.

H. D. Willauer, R. Ananth, M. T. Olsen, D. M. Drab, D. R. Hardy, and F. W. Williams. Modeling and kinetic analysis of CO_2 hydrogenation using a Mn and K-promoted Fe catalyst in a fixed-bed reactor. *Journal of CO2 Utilization*, 3-4:56–64, 2013. ISSN 22129820. doi: 10.1016/j.jcou.2013.10.003. URL `https://linkinghub.elsevier.com/retrieve/pii/S2212982013000504`.

CHAPTER 5

Development of the micro-kinetic model.

In the previous Chapter, we have shown the derivation of a macro-kinetic model that describes the formation of the main products of the CO_2 hydrogenation. Such a model, as we have already discussed, is very useful for simulations because it is explicit and contains a limited number of parameters. However, this model presents an important limitation: it is semi-empirical, thus it does not give useful information about the reaction pathways followed for the formation of the different species.

Understanding the mechanism of a reaction is very important and can be helpful for the design of a better catalyst for the optimisation of the reaction selectivity. Moreover, the development of a kinetic model based on the reaction mechanism can be applied to predict the changes in hydrocarbons distributions in the case of variation of operating conditions or system type and size. Conversely, these mechanistic models are very complex, not always explicit and can contain a high number of kinetic parameters, especially in the case of a complex reaction such as the CO_2 hydrogenation.

Understanding the CO_2 hydrogenation mechanism is thus not obvious. It is a very complex reaction that involves the formation of many different products. We want in particular to focus on the formation of olefins, paraffins and oxygenates (which are the main groups of products observed during the experimental study) in order to understand how they are formed and which species are involved as active sites. In particular, we want to understand which mechanism is followed for the chain-growth and if eventually multiple mechanisms and active sites co-exist. We also want to investigate the oxygenates formation and to understand on which active sites they are formed, according to which mechanism and if they intervene in the chain-growth of hydrocarbons.

Therefore, in this chapter we present the development of two micro-kinetic models with the aim to understand the reaction mechanism. We start by making hypothesis on the elementary reactions - based on previous works available in the literature and our experimental observations - and we derive the kinetic rates of each compound by following the Langmuir-Hinshelwood-Hougen-Watson procedure. The two models derived differ in the hypothesis on the number of active sites: in the first model we consider that hydrocarbons (intended as olefins and paraffins) and oxygenates (alcohols and acids) are formed over the same kind of active site. In the second model we consider that oxygenates are formed over a different active site than that responsible for the formation of hydrocarbons.

The two models are validated on the data obtained from our experimental study at laboratory-scale and compared to each other. Conclusions about the mechanism of formation of olefins, paraffins and oxygenates and on the possible active sites involved are then drawn.

These models contain much more parameters and are harder to include in complex reactor models, but they can help to give information about the reaction mechanism.

The contents of the Chapter are adapted from our paper that will soon be submitted:

Panzone, C., Philippe, R., Nikitine, C., Vanoye, L., Bengaouer, A., Chappaz, A. and Fongarland, P. 'Development and validation of a detailed micro-kinetic model for the CO_2 hydrogenation reaction towards hydrocarbons over a Fe-K/Al_2O_3 catalyst.',

5.1 Introduction

CO_2 valorization by conversion into value-added products has become an important challenge as a way to reduce CO_2 emissions in the atmosphere, but especially as a way to store renewable electricity surplus under other forms of energy. In particular, CO_2 hydrogenation towards hydrocarbons via Fischer-Tropsch route can represent a versatile way to make different kind of gaseous and liquid hydrocarbons, with possible applications as fuels or in the chemical industry. (Centi et al., 2013; Centi and Perathoner, 2009; Styring et al., 2015; Li et al., 2018)

The CO_2 hydrogenation reaction is believed to occur in two steps, the RWGS and the FT synthesis. Iron-based catalysts have been widely applied for this reaction because of their activity for both reaction steps. (Visconti et al., 2017; Rodemerck et al., 2013) Generally, K is added as promoter to enhance the RWGS and chain-growth activity. (Weatherbee and Bartholomew, 1984; Martinelli et al., 2014; Amoyal et al., 2017; Visconti et al., 2016)

Although many advancements have been made in the catalyst synthesis optimization, few information is available about the mechanism of this reaction, which would be very important in order to understand how the different products are formed and how to optimize the selectivity towards the desired products. Some simple macro-kinetic models, useful for use in simulations and reactor models, have been developed. (Riedel et al., 2001; Willauer et al., 2013; Iglesias Gonzalez et al., 2015; Brübach et al., 2022) We have previously developed a more detailed macro-kinetic model that is able to describe the formation of the main species observed as products. (Panzone et al., 2021) However, this model is based on semi-empirical hypothesis and does not comprehensively explain the reaction mechanism.

The purpose of this work is to develop a micro-kinetic model, based on hypothesis about the reaction mechanism and aiming at understanding the formation of the different groups of products observed.

5.1.1 Mechanistic background

Detailed mechanistic studies of the CO_2 hydrogenation reaction do not exist in the literature. Lee et al. (Lee et al., 2004) proposed a mechanism for the direct CO_2 hydrogenation to hydrocarbons, based on a formic mechanism. Najari et al. (Najari et al., 2019) proposed a mechanistic model based on a hydroxyl-methylene mechanism, but only considered the formation of species until 4 carbon atoms. The reaction is generally believed to occur in two steps, by passing for the formation of CO via RWGS and then converting CO to hydrocarbons via FT synthesis, while the role of the direct reaction is generally recognized as minor. (Riedel et al., 2001) Activation energies for RWGS over iron catalysts are generally found to be lower than those for the FT reaction, as the RWGS is a fast reaction especially over iron oxides. (Spencer, 1995) Values of activation energies reported in literature for the two reactions can be found in Table 5.1. The mechanisms of these two reactions have been and still are widely debated in literature and the most important points are discussed in the following.

A variety of mechanisms have been proposed in literature for the FT synthesis. They have recently been reviewed by different authors. (Mousavi et al., 2015; Saeidi et al., 2017) The FT synthesis is a polymerization reaction that occurs with stepwise chain-growth and needs a monomer and an initiator. (Dry, 1996) The main discussions are focused on the CO dissociation mechanism and on the species that act as monomer and initiator for the chain-growth reaction. The carbide mechanism is based on the assumption that the $CH_2 - s$ surface species acts as monomer and it is formed from reduction reactions of carbides that are formed from adsorbed CO. (Fischer and Tropsch, 1926) Different hypotheses exist about the polymerization initiator of the FT synthesis. The alkyl mechanism proposes an alkyl species $CH_3 - s$ that can react with $CH_2 - s$ leading to chain-growth reactions. (Brady and Pettit, 1980, 1981) Although this mechanism easily describes the formation of linear alkanes and alkenes, it is not able to describe the formation of branched chains or oxygenates, thus more complex mechanisms have

Table 5.1: Values published in literature for apparent activation energies of the FT and RWGS reactions over iron catalysts.

Catalyst		E_i [kJ/mol]	**Reference**
FT			
Fe-Si-Cu-K-Na	PARAFFINS	94.5	(Lox and Froment, 1993)
	OLEFINS	132.3	
Fe-Cu-K	METHANE	92.9	(Wang et al., 2003)
	PARAFFINS	87.0	
	OLEFINS	111.0	
Fe-Mn	CHAIN-GROWTH	75.5	(Yang et al., 2003)
	METHANE	97.4	
	PARAFFINS	111.5	
	OLEFINS	97.4	
Fe-Cu-K-Si	CHAIN-GROWTH	73.5	(Chang et al., 2007)
	METHANE	79.6	
	PARAFFINS	77.0	
	OLEFINS	84.1	
Fe-Mn	CHAIN-GROWTH	76.9-79.9	(Teng et al., 2005a, 2006, 2007)
	METHANE	86.3-86.8	
	PARAFFINS	94.5-97.9	
	OLEFINS	87.4-87.6	
Fe-Cu	METHANE	68	(Nakhaei Pour et al., 2014)
	PARAFFINS	76-102	
	OLEFINS	72-148	
RWGS			
FeSi		67.7	(Kaspar et al., 1994)
FeSi-H		81.9	(Kaspar et al., 1994)
FeSi-K		69	(Kaspar et al., 1994)
Fe_3O_4/Cr_2O_3		80	(Spencer, 1995)
Fe_3O_4		80	(Spencer, 1995)

been proposed, such as the alkenyl mechanism (Maitlis, 2004) (that considers as initiator a vinyl surface species) or the alkylidene-hydride-methylidyne mechanism (Ciobıcă et al., 2002) (that considers as monomer $CH - s + H - s$). These two mechanisms can describe the formation of branched chains, but not the formation of oxygenates products.

To explain the formation of oxygenates during the FT reaction, the CO insertion mechanism is generally adopted. It is based on the hypothesis that $CO - s$ is the monomer for chain-growth that leads to the formation of acyl intermediates $R - C = O - s$. (Pichler and Schulz, 1970) Alcohols are formed by hydrogenation of the acyl intermediates, while acids are formed by reaction between the acyl intermediates and hydroxyl groups adsorbed on the catalytic surface.

Other mechanisms have been proposed, such as the enolic and the formate mechanisms, but none of them is considered very accurate for the reaction over Fe catalysts.

Some mechanisms have also been proposed to explain the formation of all the products observed (paraffins, olefins and oxygenates) by combining two different reaction pathways that lead to the formation of two different reaction intermediates. The CO insertion-carbide mechanism, proposed by Gaube and Klein (Gaube and Klein, 2010), assumes that CO insertion and alkyl mechanism take place simultaneously. This mechanism has been previously adopted over Fe catalysts to explain the formation of paraffins, olefins, acids and alcohols. (Teng et al., 2006,

2007) Another proposed mechanism is the H-assisted CO dissociation, based on the assumption that CO dissociation is mediated by H, allowing to reduce the energetic barrier that would otherwise be very high and limiting. This model proposes as monomer the $CH - s$, according to the alkylidene-hydride-methylidyne mechanism. (Ojeda et al., 2010)

For the RWGS mechanism, the redox mechanism is commonly considered as the most accurate for the reaction over metal oxides. (Amoyal et al., 2017; Saeidi et al., 2017; Daza and Kuhn, 2016; Chou et al., 2019) Alternatively, the associative mechanism can be assumed. It involves the formation of a formate species as intermediate ($COOH - s$) and it is considered as the most accurate to describe the WGS reaction mechanism under FT-conditions over iron catalysts. (Lox and Froment, 1993; Wang et al., 2013; Van der Laan and Beenackers, 2000) It has also been adopted in different works to describe the RWGS mechanism over iron catalysts. (Loiland et al., 2016; Nakhaei Pour and Housaindokht, 2017)

Concerning the CO_2 hydrogenation reaction mechanism, the main contributions to the understanding of the reaction mechanism have been provided by the works of Schulz and Visconti and their collaborators. (Visconti et al., 2017; Martinelli et al., 2014; Schulz et al., 2005; Schulz, 2014) Over Fe catalysts, it has been found that at least three different active sites exist: (Visconti et al., 2017; Martinelli et al., 2014; Schulz, 2014)

- Fe_3O_4, responsible for the RWGS activity;
- Fe carbides, responsible for the chain-growth activity and thus the formation of primary products;
- metallic Fe, responsible for the olefin re-adsorption and secondary hydrogenations.

Over alkalized Fe catalysts, an alkyl mechanism is generally adopted and CO dissociation is assumed to occur by passing for the formation of a $C - s$ intermediate. K has a role in controlling the rate of formation of the C monomer, as it strengthens the Fe-C interactions and simultaneously weakens the C-O bond. (Visconti et al., 2017; Amoyal et al., 2017; Schulz, 2014; Jiang et al., 2018) The $C - s$ intermediate that is formed can undergo different kind of reactions and form either the $CH - s$ monomer responsible for the chain-growth, iron carbides that are the active phase for the chain-growth, or C phases that depose on catalytic surface and lead to its deactivation. The right content of K in the catalyst can favour the formation of $CH - s$ monomer, accordingly enhancing chain-growth reactions. However, too high content of K can favour the C deposition and thus the catalyst deactivation. (Schulz, 2014; Jiang et al., 2018)

The chain-growth reaction has been explained by Schulz according to two mechanisms, the linear chain prolongation and the chain branching, both addressed as primary reactions. (Schulz et al., 2005; Schulz, 2014) Linear chain prolongation is explained as the reaction between an alkylene and a methyl species to form an alkyl intermediate, attached to the active site with its α-C atom. Branching reactions follow the same mechanism but the alkyl intermediate is attached with its β-C atom and a further growth of these intermediates leads to the formation of a branched chain. The branching probability has been observed to decrease when increasing carbon number. This is due to spatial constraints that are stronger for branching reactions and depend on the size of the intermediate species. (Schulz et al., 2005; Schulz, 2014; Riedel et al., 2003)

Olefins and paraffins formation is generally considered as a primary reaction. Dissociative desorption of the alkyl intermediate to form α-olefins and its associative desorption to form n-paraffins are considered as competitive reactions that occur on the same active sites, but the formation of α-olefins under CO_2 hydrogenation conditions appears to be dominant. (Schulz et al., 2005; Schulz, 2014; Riedel et al., 2003; Schulz and Claeys, 1999) α-olefins can also undergo secondary hydrogenation, isomerization or double bond shift reactions, which are believed to occur over metallic Fe sites. (Schulz, 2014) The tendency of the olefins to undergo secondary hydrogenation reactions depends on their carbon number: the longer the olefin chain, the slower the diffusion rate of the molecule thus the higher the conversion to the corresponding paraffin. (Visconti et al., 2017) Exceptions to this tendency have been observed for ethene which is very reactive for secondary hydrogenations. (Schulz, 2014; Riedel et al., 2003)

Oxygenates are frequent by-products of the FT process and they can be formed both as primary or secondary products. Oxygenates formation seems to occur over iron oxides active sites. A mechanism proposed for the alcohols formation is related to the dissociation of CO over iron, followed by the reaction between adsorbed oxygen and hydrogen, which would create OH groups, chemisorbed on the catalytic surface and available for the reaction to hydrocarbon species. (Riedel et al., 2003) Other mechanisms have been proposed, such as the CO insertion (in analogy to what happens with cobalt) and secondary olefin hydroformylation, followed by reduction of the formed aldehyde. (Schulz et al., 1999) Among alcohols, methanol is generally produced in very low quantities, as iron catalysts are not active for methanol production and it is thermodynamically not favoured in the conditions generally used for the CO_2 hydrogenation towards hydrocarbons. Oxygenates with 2 C atoms are, on the contrary, very abundant, because of the high reactivity of ethene. (Schulz et al., 1999)

Understanding the mechanism of such a complex reaction is thus not evident. Many active sites can have a role and parallel mechanisms can be involved. The most part of the mechanistic kinetic models that have been developed in the literature are focused on the description of the formation of only paraffins and olefins, while few can describe the formation of oxygenates, and even fewer consider the formation of both oxygenates and paraffins and olefins. In this work, we have developed the first detailed mechanistic kinetic model for the CO_2 hydrogenation reaction. The model takes into consideration the formation of olefins, paraffins and oxygenates formed over a Fe-K/γ-Al_2O_3 catalysts. In particular, we have investigated the formation of oxygenates with the aim to understand the mechanism of their formation and whether they are formed over the same active sites as for olefins and paraffins.

5.2 Experimental

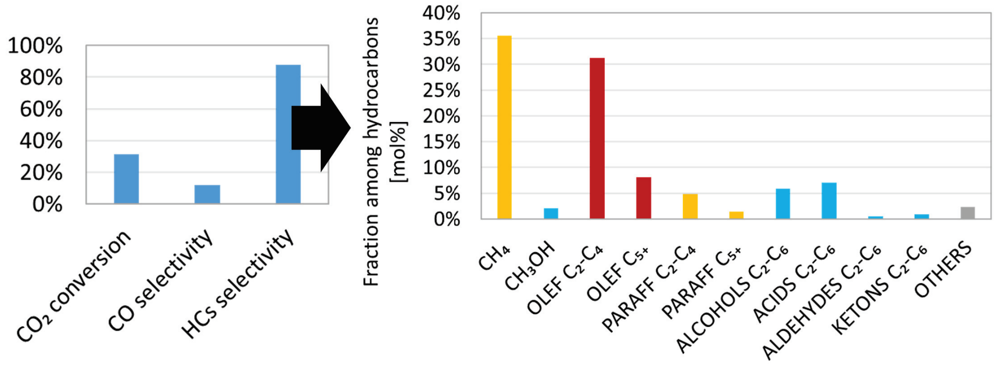

Figure 5.1: Experimental results obtained in reference conditions (H_2/CO_2 molar inlet ratio of 3, 15 bars, 300°C, GHSV of 2080 Nml/g_{cat}/h). CO_2 conversion and CO and HCs selectivity are represented on the left, HCs distribution as mole fraction among all hydrocarbons obtained are represented on the right. Products labelled as “others” represent branched chains or aromatic compounds. Refer to (Panzone et al., 2021) for more details.

The reaction has been studied in a laboratory-scale fixed-bed reactor over a Fe-K/γ-Al_2O_3 catalyst. The reactor consists in a stainless steel tube with inner diameter of 6 mm and filled with about 3 g of catalyst. Products are collected in three phases, gaseous, organic and water, which are all analysed by gas chromatography. The catalyst synthesis and the experimental protocol have been described in our previous work. (Panzone et al., 2021) Tests have been performed

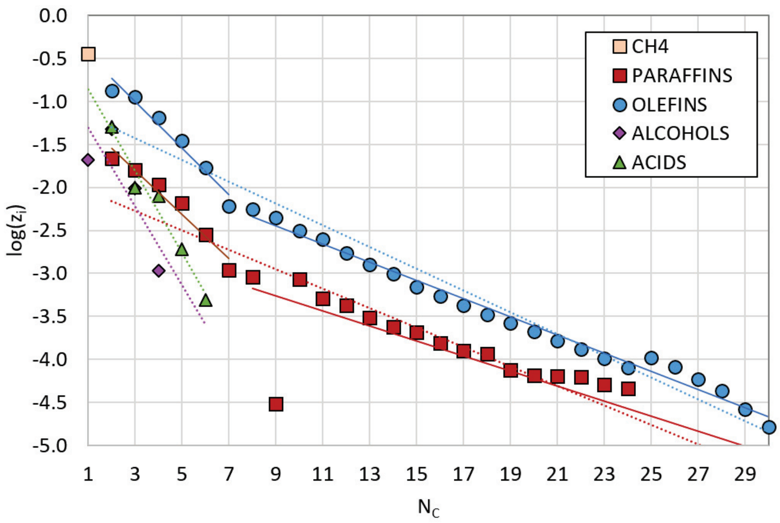

Figure 5.2: ASF distribution of products from C_1 to C_{30} for olefins, paraffins, acids and alcohols for the reference conditions (H_2/CO_2 molar inlet ratio of 3, 15 bars, 300°C, GHSV of 2080 Nml/g_{cat}/h). Methane is excluded from this distribution. Points represent experimental data, dotted lines represent the fitted model according to ideal ASF distribution, while solid lines represent the fitted model according to a double-α distribution.

Table 5.2: Experimental values of α obtained for olefins, paraffins, alcohols and acids in reference conditions (H_2/CO_2 molar inlet ratio of 3, 15 bars, 300°C, GHSV of 2080 Nml/g_{cat}/h).

	Ideal ASF	**Double-α ASF**	
	α	α_1	α_2
olefins	0.75	0.55	0.78
paraffins	0.76	0.56	0.79
acids	0.33		
alcohols	0.15		

in different operating conditions, by varying reactor temperature, total pressure, GHSV and H_2/CO_2 molar inlet ratio, in the ranges reported in our previous work. (Panzone et al., 2021) All the experimental conditions tested were under chemical regime, as phenomena of internal and external mass and heat transfer limitations were excluded through the calculation of typical criteria used for fixed beds (see reference (Panzone et al., 2021)).

The results obtained during a typical run in reference conditions (H_2/CO_2 molar inlet ratio of 3, 15 bars, 300°C, GHSV of 2080 Nml/g_{cat}/h) are reported in Figure 5.1. It can be observed that olefins, especially short chains C_2-C_4, are the prevalent product, while paraffins are produced in lower quantity. Methane also represents a very important fraction of the products pool. Oxygenates represent as well a significant fraction of the products, in particular carboxylic acids and alcohols.

Figure 5.2 shows the ASF distribution of olefins, paraffins, acids and alcohols and Table 5.2 reports the corresponding obtained values of the experimental chain-growth probability α. Experimental data have been fitted with an ideal ASF model (dotted lines), to derive the value of α, according to Eq. 5.1:

$$z_i = (1-\alpha)\,\alpha^{i-1} \tag{5.1}$$

It can be observed that the α of olefins and paraffins are very close, suggesting that they are parallel competitive reactions. The slope of acids and alcohols distribution is significantly different from that of olefins and paraffins, indicating that these species are probably formed according to a different mechanism. Values of α of Table 5.2 and distributions shown in Figure 5.2 do not consider methane, which is observed to have positive deviations from the ideal ASF distribution. Positive deviations of methane from the ideal ASF distribution are common especially over Co and Ru catalysts and their reason is still discussed in literature. It could be due to special active sites, to an increased termination probability or to a different reaction mechanism. (Förtsch et al., 2015) For CO_2 hydrogenation preferential formation of methane has been attributed to the low C/H ratio on the catalyst surface that favours the hydrogenation of adsorbed species, leading to formation of methane. (Saeidi et al., 2017) On paraffins and olefins distributions, a deviation of high C numbers ($n_C > 7$) from the ideal ASF can be observed. This is typical of Fe-K catalysts (Donnelly et al., 1988; Donnelly and Satterfield, 1989; Dictor and Bell, 1986; Schliebs and Gaube, 1985) and can be explained by assuming the co-existence of different active sites and eventually reaction mechanisms for short and long chains, as we have already discussed in our previous work. (Panzone et al., 2021) Thus, experimental data for paraffins and olefins have also been fitted with a double-α ASF distribution, derived from the superposition of two independent ASF distributions (see solid lines in Figure 5.2) and characterized by two α values (α_1 and α_2). (Patzlaff et al., 1999) The double-α model is shown in Eq. 5.2:

$$z_i = (1-\mu_2)(1-\alpha_1)\,\alpha_1^{i-1} + \mu_2(1-\alpha_2)\,\alpha_2^{i-1} \tag{5.2}$$

where ξ is the point of intersection between the two ASF distributions and μ_2 is the fraction of hydrocarbons formed with growth probability α_2, defined by Eq. 5.3:

$$\mu_2 = \frac{(1-\alpha_1)\,\alpha_1^{\xi-1}}{(1-\alpha_1)\,\alpha_1^{\xi-1} + (1-\alpha_2)\,\alpha_2^{\xi-1}} \tag{5.3}$$

5.3 Kinetic model development

Based on the obtained experimental data, the kinetic model should be able to predict the formation of the main categories of products observed, namely olefins and paraffins, as well as oxygenates.

5.3.1 Establishment of detailed kinetic models

The model takes into account the formation of all the main species observed as products: CO (Eq. 5.4), 1-alkenes (Eq. 5.5), n-alkanes (Eq. 5.6), alcohols (Eq. 5.7) and acids (Eq. 5.8) until 20 C atoms. In the following, we will refer to equations 5.5-5.7 when talking about FT. Branched chains and aromatics are neglected, as well as aldehydes and ketones which are present in the product pool in very small quantities.

$$CO_2 + H_2 \leftrightarrow CO + H_2O \tag{5.4}$$

$$CO + 2H_2 \rightarrow \frac{1}{n}C_nH_{2n} + H_2O \tag{5.5}$$

$$CO + \frac{2n+1}{n}H_2 \rightarrow \frac{1}{n}C_nH_{2n+2} + H_2O \tag{5.6}$$

$$CO + 2H_2 \rightarrow \frac{1}{n}C_nH_{2n+1}OH + \frac{n-1}{n}H_2O \tag{5.7}$$

$$CO + \frac{2(n-1)}{n}H_2 \rightarrow \frac{1}{n}C_nH_{2n-1}OOH + \frac{n-2}{n}H_2O \tag{5.8}$$

The following assumptions are made in order to develop the model:

1. the CO_2 hydrogenation reaction is considered to occur in two steps, the RWGS followed by the FT synthesis. Direct formation of hydrocarbons from CO_2 is thus neglected, as previously observed. (Riedel et al., 2001; Panzone et al., 2021)
2. RWGS and FT are considered to take place on two different types of active sites. Fe_5C_2 and Fe_3O_4 are assumed as the active sites for FT and RWGS, respectively.
3. Secondary hydrogenations of olefins are neglected, as it has been previously observed that this reaction is not dominant over alkalised catalysts. (Schulz, 2014; Riedel et al., 2003; Schulz et al., 1999)
4. Formation of C_1 products is considered separately, as they have been observed not to follow the ideal ASF distribution (see Figure 5.2). Formic acid formation is not included, as it was not observed as product.

For the RWGS, a redox mechanism is assumed, based on the simple redox mechanism previously proposed by Saeidi et al. (Saeidi et al., 2017) A schematic representation of the mechanism is shown in Figure 5.3. Adsorbed CO_2 is considered to directly form CO by reacting with H_2.

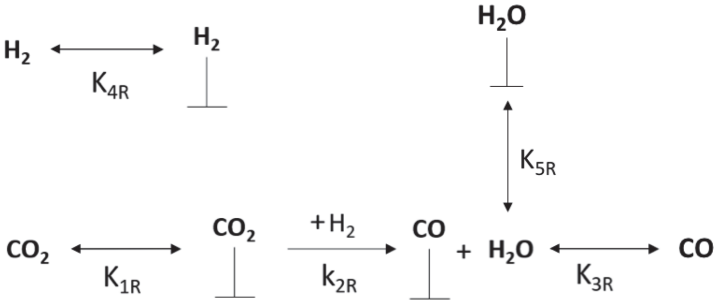

Figure 5.3: Reaction mechanism assumed for the formation of CO via RWGS.

For the FT synthesis, two kinetic models are derived, based on different assumptions:

1. The first is a mono-site model (model FT-A), where the hypothesis that all species considered are formed on the same active sites is made. A combination of alkyl mechanism and CO insertion mechanism is assumed to explain the formation of the different species, based on the previous work of Teng et al. (Teng et al., 2006) The alkyl mechanism is assumed to explain the chain-growth and the formation of alkanes and alkenes. It considers $CH_2 - s$ as monomer and $CH_3 - s$ as initiator. $CH_2 - s$ is formed from CO, via H-mediated CO dissociation that yields to $C - s$. The adsorbed carbon then forms $CH_2 - s$ by reacting with H_2. Chain-growth occurs through consecutive insertion of the $CH_2 - s$ species. Products termination can occur via β-hydride elimination to form 1-alkenes or via H_2 addition to form n-alkanes. The alkyl adsorbed intermediate can also react with adsorbed CO and form oxygenated intermediates: $C_nH_{2n-1}O - s$ that can react with $OH - s$ and be desorbed as an acid, or $C_nH_{2n}OH - s$ that can react with $H - s$ and be desorbed as an alcohol. This mechanism is illustrated in Figure 5.4.

2. The second model (FT-B) is developed with the assumption that oxygenates are formed on different active sites then alkanes and alkenes. For type I (s) sites (where alkanes and alkenes are formed, iron carbides presumably) the same alkyl mechanism explained before is assumed, but no oxygenates are considered to be formed over these sites. For the type II (x) sites (where oxygenates are formed), a CO-insertion mechanism is assumed. CO is considered as the monomer, while a surface methyl species is considered as the chain initiator. The chain-growth occurs via reaction of the adsorbed CO with the methyl surface species $C_{n-1}H_{2n-1} - x$. Chain termination leads to the formation of alcohols or acids according to the mechanism explained before. This mechanism is illustrated in Figure 5.5.

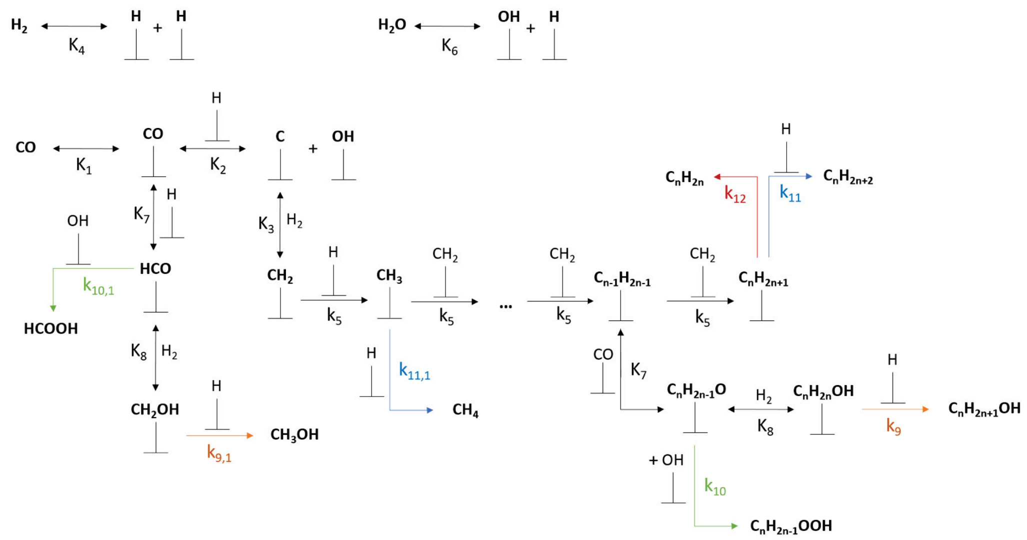

Figure 5.4: Reaction mechanism assumed for the formation of olefins, paraffins, alcohols and acids via FT when the presence of only one type of active site is assumed (FT-A).

5.3.1.1 Derivation of kinetic laws

To derive the equations for the kinetic model the Langmuir-Hinshelwood-Hougen-Watson procedure was followed. Elementary reaction steps are derived according to the hypothesis made on the reaction mechanism. Some of the elementary steps are supposed as kinetically relevant, while for the others a pseudo-equilibrium condition is assumed. Adsorption constants are considered as independent of temperature, thus adsorption enthalpies are not included. Kinetic constants are expressed according to the Arrhenius law.

In the following, the rate equations obtained for RWGS and FT are shown and discussed. Derivation of the FT-A model (mono-site) is explained in detail. For the other models, the same procedure has been considered.

FT-A model: mono-site

Elementary steps assumed for the mono-site model are reported in Table 5.3. Step *5* represents the chain-growth and it is assumed as kinetically relevant step. Termination reactions (*9, 10, 11* and *12*) are also assumed as kinetically relevant. The concentration of the adsorbed species can thus be derived from the pseudo-equilibrium condition:

$$[CO - s] = K_1 p_{CO} \, [s] \tag{5.9}$$

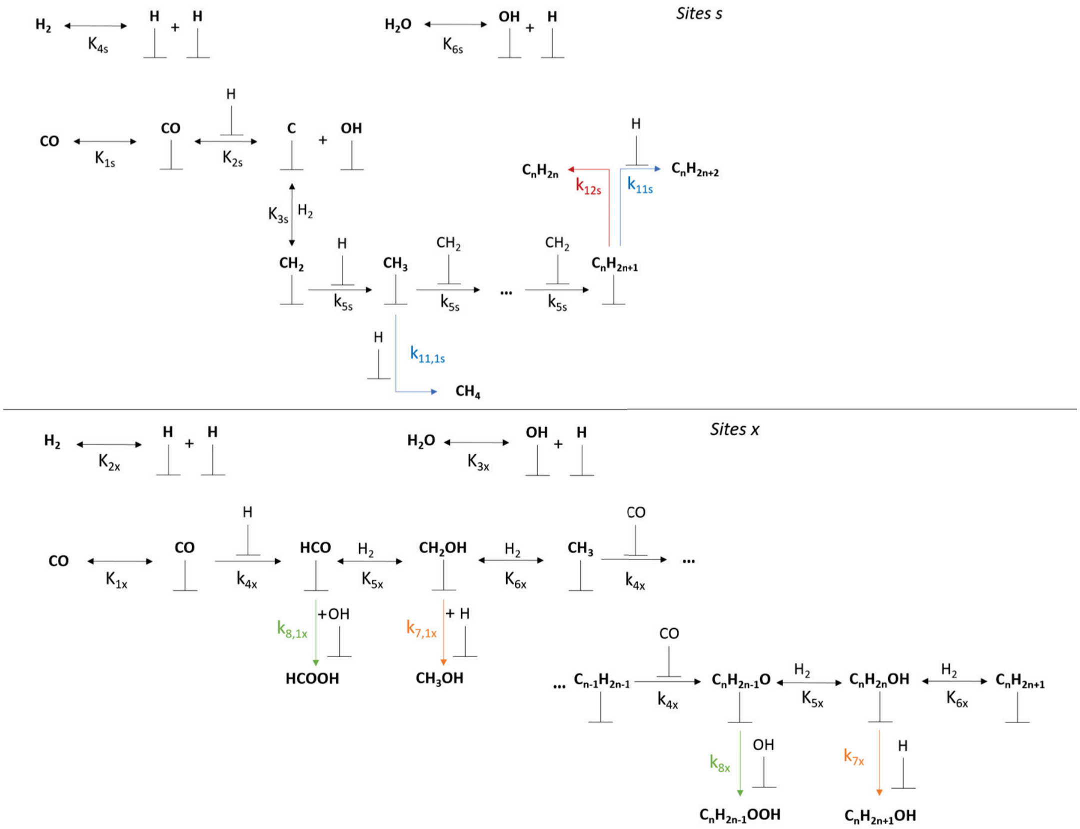

Figure 5.5: Reaction mechanism assumed for the formation of olefins, paraffins, alcohols and acids via FT when the presence of two types of active site is assumed (FT-B).

$$[C-s] = \frac{K_1K_2K_4}{K_6}\frac{p_{CO}p_{H_2}}{p_{H_2O}}\,[s] \tag{5.10}$$

$$[CH_2-s] = \frac{K_1K_2K_3K_4}{K_6}\frac{p_{CO}p_{H_2}^2}{p_{H_2O}}\,[s] \tag{5.11}$$

$$[H-s] = \sqrt{K_4p_{H_2}}\,[s] \tag{5.12}$$

$$[OH-s] = \frac{K_6p_{H_2O}}{\sqrt{K_4p_{H_2}}}\,[s] \tag{5.13}$$

$$[C_nH_{2n-1}O-s] = K_1K_7p_{CO}\,[C_{n-1}H_{2n-1}-s] \tag{5.14}$$

$$[HCO-s] = K_1K_7p_{CO}\sqrt{K_4p_{H_2}}\,[s] \tag{5.15}$$

$$[C_nH_{2n}OH-s] = K_1K_7K_8p_{CO}p_{H_2}\,[C_{n-1}H_{2n-1}-s] \tag{5.16}$$

Table 5.3: Elementary reaction steps for FT — mono-site model.

Step	Elementary reaction	Constant
1	$CO + s \leftrightarrow CO - s$	K_1
2	$CO - s + H - s \leftrightarrow C - s + OH - s$	K_2
3	$C - s + H_2 \leftrightarrow CH_2 - s$	K_3
4	$H_2 + 2s \leftrightarrow 2H - s$	K_4
5	$CH_2 - s + H - s \rightarrow CH_3 - s + s$ $CH_2 - s + C_{n-1}H_{2n-1} - s \rightarrow C_nH_{2n+1} - s + s$	k_5
6	$H_2O + 2s \leftrightarrow HO - s + H - s$	K_6
7	$H - s + CO - s \leftrightarrow HCO - s + s$ $C_{n-1}H_{2n-1} - s + CO - s \leftrightarrow C_nH_{2n-1}O - s + s$	K_7
8	$HCO - s + H_2 \leftrightarrow CH_2OH - s$ $C_nH_{2n-1}O - s + H_2 \leftrightarrow C_nH_{2n}OH - s$	K_8
9.1	$CH_2OH - s + H - s \rightarrow CH_3OH + 2s$	$k_{9,1}$
9.n	$C_nH_{2n}OH - s + H - s \rightarrow C_nH_{2n+1}OH + 2s$	k_9
10.1	$HCO - s + OH - s \rightarrow HCOOH + 2s$	$k_{10,1}$
10.n	$C_nH_{2n-1}O - s + OH - s \rightarrow C_nH_{2n-1}OOH + 2s$	k_{10}
11.1	$CH_3 - s + H - s \rightarrow CH_4 + 2s$	$k_{11,1}$
11.n	$C_nH_{2n+1} - s + H - s \rightarrow C_nH_{2n+2} + 2s$	k_{11}
12.n	$C_nH_{2n+1} - s \rightarrow C_nH_{2n} + H - s + s$	k_{12}

$$[CH_2OH - s] = K_1K_7K_8p_{CO}p_{H_2}\sqrt{K_4p_{H_2}}\,[s] \tag{5.17}$$

Reaction rates for methane and methanol are defined as follows:

$$r_{CH_4} = r_{11,1} = k_{11,1}\,[CH_3 - s]\,[H - s] \tag{5.18}$$

$$r_{CH_3OH} = r_{9,1} = k_{9,1}\,[CH_2OH - s]\,[H - s] \tag{5.19}$$

while reaction rates for C_{2+} compounds are defined as follows:

$$r_{paraffins,n} = r_{11} = k_{11}\,[C_nH_{2n+1} - s]\,[H - s] \tag{5.20}$$

$$r_{olefins,n} = r_{12} = k_{12}\,[C_nH_{2n+1} - s]\,[s] \tag{5.21}$$

$$r_{alcohols,n} = r_9 = k_9\,[C_nH_{2n}OH - s]\,[H - s] \tag{5.22}$$

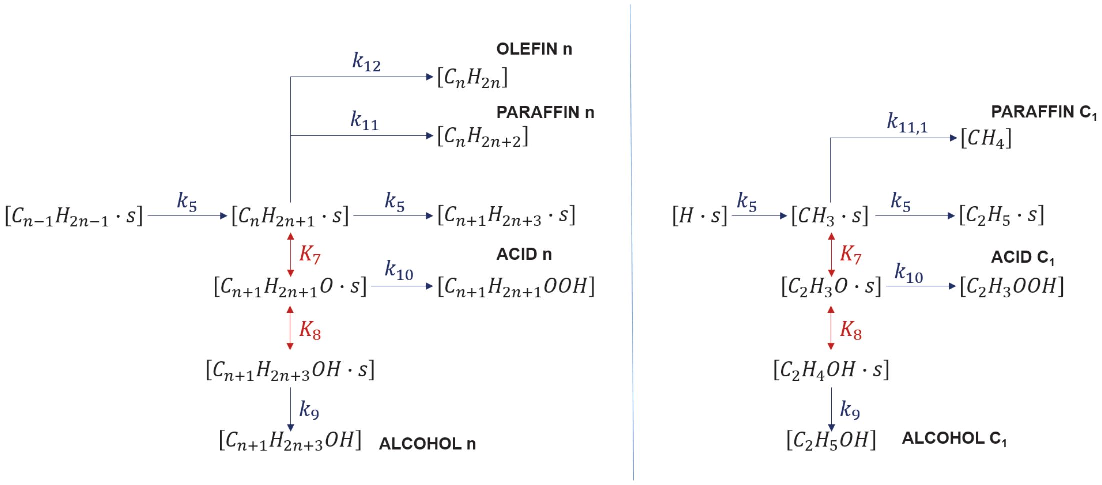

Figure 5.6: Possible reaction pathways for $[C_nH_{2n+1} - s]$ and $[CH_3 - s]$.

$$r_{acids,n} = r_{10} = k_{10}\left[C_nH_{2n-1}O - s\right]\left[OH - s\right] \tag{5.23}$$

Those rate equations are all functions of concentrations of surface intermediates, which are not object of measure. Thus, correlations between the intermediate concentrations and measurable concentrations (products or reactants) have to be found. To derive the concentrations of $CH_3 - s$ and $C_nH_{2n+1} - s$, steady-state approximation can be applied. The intermediate $C_nH_{2n+1} - s$ is formed by $C_{n-1}H_{2n-1} - s$ and can form $C_{n+1}H_{2n+3} - s$ following the reaction *5*. Alternatively, it can undergo termination reactions (*11.n* or *12.n*) to give the corresponding paraffin (C_nH_{2n+2}) or olefin (C_nH_{2n}). Moreover, it can undergo further reactions with $CO - s$ and eventually with H_2 and then be desorbed as the corresponding acid ($C_{n+1}H_{2n+1}OOH$) or alcohol ($C_{n+1}H_{2n+3}OH$). A graphical description of the reaction routes for the $C_nH_{2n+1} - s$ intermediate is given in Figure 5.6. Thus, we obtain:

$$\begin{aligned}\frac{d\left[C_nH_{2n+1} - s\right]}{dt} &= k_5\left[C_{n-1}H_{2n-1} - s\right]\left[CH_2 - s\right] - k_5\left[C_nH_{2n+1} - s\right]\left[CH_2 - s\right] + \\ &- k_9\left[C_{n+1}H_{2n+2}OH - s\right]\left[H - s\right] - k_{10}\left[C_{n+1}H_{2n+1}O - s\right]\left[OH - s\right] + \\ &- k_{11}\left[C_nH_{2n+1} - s\right]\left[H - s\right] + -k_{12}\left[C_nH_{2n+1} - s\right]\left[s\right] = 0\end{aligned} \tag{5.24}$$

and from Eq. 5.24, an expression for $[C_nH_{2n+1} - s]$ is derived:

$$\left[C_nH_{2n+1} - s\right] = \frac{k_5\left[CH_2 - s\right]\left[C_{n-1}H_{2n-1} - s\right]}{\left(\begin{aligned}k_5\left[CH_2 - s\right] + k_9K_1K_7K_8p_{CO}p_{H_2}\left[H - s\right] + \\ + k_{10}K_1K_7p_{CO}\left[OH - s\right] + k_{11}\left[H - s\right] + k_{12}\left[s\right]\end{aligned}\right)} \tag{5.25}$$

The parameter α can thus be introduced. It represents the chain-growth probability and it is defined as the ratio between the concentration of the intermediate with n carbon atoms and that of the intermediate with n-1 carbons atoms:

$$\alpha = \frac{\left[C_nH_{2n+1} - s\right]}{\left[C_{n-1}H_{2n-1} - s\right]} = \frac{k_5\frac{K_1K_2K_3K_4}{K_6}\frac{p_{H_2}^2p_{CO}}{p_{H_2O}}}{\left(\begin{aligned}k_5\frac{K_1K_2K_3K_4}{K_6}\frac{p_{H_2}^2p_{CO}}{p_{H_2O}} + k_9K_1K_7K_8p_{CO}p_{H_2}\sqrt{K_4p_{H_2}} + \\ + k_{10}\frac{K_1K_6K_7}{\sqrt{K_4p_{H_2}}}p_{CO}p_{H_2O} + k_{11}\sqrt{K_4p_{H_2}} + k_{12}\end{aligned}\right)} \tag{5.26}$$

The same procedure can be applied to $CH_3 - s$ to derive the expression that correlates its concentration to measurable concentrations. Steady-state conditions are applied to $CH_3 - s$, giving:

$$\begin{aligned}\frac{d\,[CH_3 - s]}{dt} &= k_5\,[H - s]\,[CH_2 - s] - k_5\,[CH_3 - s]\,[CH_2 - s] + \\ &- k_9\,[C_2H_4OH - s]\,[H - s] - k_{10}\,[C_2H_3O - s]\,[OH - s] + \\ &- k_{11,1}\,[CH_3 - s]\,[H - s] = 0\end{aligned} \tag{5.27}$$

Similarly to α, a chain-growth probability for C_1 compounds is defined:

$$\alpha_1 = \frac{[CH_3 - s]}{[H - s]} = \frac{k_5 \frac{K_1K_2K_3K_4}{K_6} \frac{p_{H_2}^2 p_{CO}}{p_{H_2O}}}{\left(\begin{aligned} k_5 \tfrac{K_1K_2K_3K_4}{K_6} \tfrac{p_{H_2}^2 p_{CO}}{p_{H_2O}} + k_9 K_1 K_7 K_8 p_{CO} p_{H_2} \sqrt{K_4 p_{H_2}} + \\ + k_{10} \tfrac{K_1K_6K_7}{\sqrt{K_4 p_{H_2}}} p_{CO} p_{H_2O} + k_{11,1} \sqrt{K_4 p_{H_2}} \end{aligned}\right)} \tag{5.28}$$

Finally, the concentrations of $CH_3 - s$, $C_nH_{2n+1} - s$, $C_nH_{2n}OH - s$ and $C_nH_{2n-1}O - s$ can be defined as follows:

$$[CH_3 - s] = \alpha_1\,[H - s] = \alpha_1 \sqrt{K_4 p_{H_2}}\,[s] \tag{5.29}$$

$$[C_nH_{2n+1} - s] = \alpha\,[C_{n-1}H_{2n-1} - s] = \alpha^{n-1} \alpha_1 \sqrt{K_4 p_{H_2}}\,[s] \tag{5.30}$$

$$[C_nH_{2n}OH - s] = \alpha^{n-2} \alpha_1 K_1 K_7 K_8 p_{CO} p_{H_2} \sqrt{K_4 p_{H_2}}\,[s] \tag{5.31}$$

$$[C_nH_{2n-1}O - s] = \alpha^{n-2} \alpha_1 K_1 K_7 p_{CO} \sqrt{K_4 p_{H_2}}\,[s] \tag{5.32}$$

The concentration of free active sites $[s]$ is derived from normalization of the concentration of all the intermediates adsorbed on the catalytic surface:

$$\begin{aligned}&[s] + [CO - s] + [H - s] + [C - s] + [OH - s] + \\ &\quad + [CH_2 - s] + [CH_3 - s] + [HCO - s] + [CH_2OH - s] + \\ &\quad + \sum_{i=2}^{N} \Big([C_iH_{2i+1} - s] + [C_iH_{2i+1}O - s] + [C_iH_{2i+2}OH - s] \Big) = 1\end{aligned} \tag{5.33}$$

Thus $[s]$ is expressed as follows:

$$\begin{aligned}[s] = \Bigg[& 1 + K_1 p_{CO} + \sqrt{K_4 p_{H_2}}\,(1 + \alpha_1 + K_1 K_7 p_{CO} + K_1 K_7 K_8 p_{CO} p_{H_2}) + \\ & + \frac{K_1K_2K_4}{K_6} \frac{p_{CO} p_{H_2}}{p_{H_2O}} + \frac{K_6 p_{H_2O}}{\sqrt{K_4 p_{H_2}}} + \frac{K_1K_2K_3K_4}{K_6} \frac{p_{CO} p_{H_2}^2}{p_{H_2O}} + \\ & + \alpha_1 \sqrt{K_4 p_{H_2}}\,(1 + K_1 K_7 p_{CO} + K_1 K_7 K_8 p_{CO} p_{H_2}) \sum_{i=2}^{N} \alpha^{i-1} \Bigg]^{-1}\end{aligned} \tag{5.34}$$

Finally, rate equations are obtained for each compound:

$$r_{CH_4} = r_{11,1} = k_{11,1}\alpha_1 K_4 p_{H_2} [s]^2 \tag{5.35}$$

$$r_{CH_3OH} = r_{9,1} = k_{9,1} K_1 K_4 K_7 K_8 p_{CO} p_{H_2}^2 [s]^2 \tag{5.36}$$

$$r_{paraffins,n} = r_{11} = \alpha^{n-1}\alpha_1 k_{11} K_4 p_{H_2} [s]^2 \tag{5.37}$$

$$r_{olefins,n} = r_{12} = \alpha^{n-1}\alpha_1 k_{12}\sqrt{K_4 p_{H_2}} [s]^2 \tag{5.38}$$

$$r_{alcohols,n} = r_9 = \alpha^{n-2}\alpha_1 k_9 K_1 K_4 K_7 K_8 p_{CO} p_{H_2}^2 [s]^2 \tag{5.39}$$

$$r_{acids,n} = r_{10} = \alpha^{n-2}\alpha_1 k_{10} K_1 K_6 K_7 p_{CO} p_{H_2O} [s]^2 \tag{5.40}$$

All model equations obtained are summarized in Table 5.6.

This first model thus describes the formation of all the species considered assuming that the chain-growth probability is the same for each category of product and differentiating only the termination mechanism. However, we observed that our experimental results showed a difference between the value of α for oxygenates and that for olefins and paraffins. Thus, it is worth to further investigate the mechanism hypothesis and consider two different mechanisms for the formation of oxygenates and olefins and paraffins.

FT-B model: multi-site

Elementary steps assumed for the FT multi-site model are reported in Table 5.4. Model derivation is not reported here, the same procedure as for the mono-site model was followed. Sites I (s) are referred to the formation of olefins and paraffins, sites II (x) are those where oxygenates are formed. Again, chain-growth reaction (step *5s* and *4x*) and termination reactions (*7s*, *8s* and *7x*, *8x*) are considered as kinetically relevant.

The rate equations derived are reported in Table 5.6. In this case, two different chain-growth probabilities are defined, one for each site, allowing the differentiation of oxygenates formation from that of olefins and paraffins, as experimentally observed.

RWGS model

The elementary steps of the redox mechanism assumed for the RWGS are reported in Table 5.5. Step *2-R*, representing the CO_2 dissociation, is assumed as the kinetically relevant step.

The reaction rate equation obtained for the RWGS reaction rate is reported in Table 5.6. It includes equilibrium constant K_{eq} to take into account the thermodynamics of the reaction and adsorption constants for all reactants and products.

5.3.2 Numerical methods

The derived kinetic model for RWGS is combined with each of the models derived for FT and integrated in an ideal reactor model. In our previous work, we verified that the reactor can be described with an isothermal plug-flow behaviour, that no liquid is formed during the reaction

Table 5.4: Elementary reaction steps for FT — multi-site model.

Step	**Elementary reaction**	**Constant**
Sites I		
1s	$CO + s \leftrightarrow CO - s$	K_{1s}
2s	$CO - s + H - s \leftrightarrow C - s + OH - s$	K_{2s}
3s	$C - s + H_2 \leftrightarrow CH_2 - s$	K_{3s}
4s	$H_2 + 2s \leftrightarrow 2H - s$	K_{4s}
5s	$CH_2 - s + H - s \rightarrow CH_3 - s + s$ $CH_2 - s + C_{n-1}H_{2n-1} - s \rightarrow C_nH_{2n+1} - s + s$	k_{5s}
6s	$HO - s + H - s \leftrightarrow H_2O + 2s$	K_{6s}
7.1,s	$CH_3 - s + H - s \rightarrow CH_4 + 2s$	$k_{7,1s}$
7.n,s	$C_nH_{2n+1} - s + H - s \rightarrow C_nH_{2n+2} + 2s$	k_{7s}
8.n,s	$C_nH_{2n+1} - s \rightarrow C_nH_{2n} + H - s + s$	k_{8s}
Sites II		
1x	$CO + x \leftrightarrow CO - x$	K_{1x}
2x	$H_2 + 2x \leftrightarrow 2H - x$	K_{2x}
3x	$H_2O + 2x \leftrightarrow HO - x + H - x$	K_{3x}
4x	$H - x + CO - x \rightarrow HCO - x + x$ $C_{n-1}H_{2n-1} - x + CO - x \rightarrow C_nH_{2n-1}O - x + x$	k_{4x}
5x	$HCO - x + H_2 \leftrightarrow CH_2OH - x$ $C_nH_{2n-1}O - x + H_2 \leftrightarrow C_nH_{2n}OH - x$	K_{5x}
6x	$CH_2OH - x + H_2 \leftrightarrow CH_3 - x + H_2O$ $C_nH_{2n}OH - x + H_2 \leftrightarrow C_nH_{2n+1} - x + H_2O$	K_{6x}
7.1,x	$CH_2OH - x + H - x \rightarrow CH_3OH + 2x$	$k_{7,1x}$
7.n,x	$C_nH_{2n}OH - x + H - x \rightarrow C_nH_{2n+1}OH + 2x$	k_{7x}
8.1,x	$HCO - x + OH - x \rightarrow HCOOH + 2x$	$k_{8,1x}$
8.n,x	$C_nH_{2n-1}O - x + OH - x \rightarrow C_nH_{2n-1}OOH + 2x$	k_{8x}

Table 5.5: Elementary reaction steps for RWGS.

Step	**Elementary reaction**	**Constant**
1R	$CO_2 + \sigma \leftrightarrow CO_2 - \sigma$	K_{1R}
2R	$CO_2 - \sigma + H_2 \rightarrow CO - \sigma + H_2O$	k_{2R}
3R	$CO - \sigma \leftrightarrow CO + \sigma$	K_{3R}
4R	$H_2 + \sigma \leftrightarrow H_2 - \sigma$	K_{4R}
5R	$H_2O + \sigma \leftrightarrow H_2O - \sigma$	K_{5R}

and that the gas phase can be treated as an ideal phase. (Panzone et al., 2021) The system is thus simulated as 1D steady-state isothermal plug-flow model:

$$\frac{dF_i}{d\tau_{mod}} = \dot{V}_{IN} \sum_j \nu_{i,j} r_{i,j} \tag{5.41}$$

where $r_{i,j}$ are the kinetic laws derived in the previous sections.

The system of ordinary differential equation is solved with a Runge-Kutta method, by using the Matlab function *ode23*. The optimization is performed with a non-linear curve fitting with minimization of least-square, based on the trust-region-reflective algorithm. The Matlab solver *lsqcurvefit* is used. The objective function is defined as the sum of squared deviations of model predictions compared to experimental values of CO_2 conversion and product selectivities (Eq. 5.42).

$$F = \sum_{j=1}^{nexp} \sum_{i=1}^{nvar} f_{ij}^2 = \sum_{j=1}^{nexp} \sum_{i=1}^{nvar} \left(Y_{ij}^{exp} - Y_{ij}^{calc} \right)^2 \tag{5.42}$$

Initial values of kinetic parameters were taken from the work of Teng et al. (Teng et al., 2006). First, all parameters are considered independent of temperature. Then, variation with temperature is introduced and kinetic constants are expressed according to the Arrhenius law referred to a reference temperature:

$$k_i = k_{i0} exp \left(\frac{E_i}{R} \left(\frac{1}{T} - \frac{1}{T_{ref}} \right) \right) \tag{5.43}$$

The mean average relative residual (MARR) is estimated according to Eq. 5.44 as an evaluation of the accuracy of the fit:

$$MARR\ \% = \frac{1}{n_{exp}} \frac{1}{n_{var}} \sum_{j=1}^{nexp} \sum_{i=1}^{nvar} \frac{|Y_{ij}^{exp} - Y_{ij}^{calc}|}{|Y_{ij}^{exp}|} \tag{5.44}$$

The sum of squares due to error SSE is also calculated to estimate the accuracy of the fit:

$$SSE = \sum_{i=1}^{nexp} \sum_{i=1}^{nvar} \left(Y_{ij}^{exp} - Y_{ij}^{calc} \right)^2 \tag{5.45}$$

In total, 160 experimental data ($n_{exp} = 20, n_{var} = 8$) were used to determine the values of respectively 27 and 32 kinetic parameters.

Table 5.6: Equations derived for each proposed mechanism.

Model	**Equations**
RWGS model	$r_{RWGS} = \dfrac{K_{1,R}k_{2,R}\left(p_{CO_2}p_{H_2} - p_{CO}p_{H_2O}/K_{eq}\right)}{1 + K_{1,R}\,p_{CO_2} + K_{3,R}\,p_{CO} + K_{4,R}\,p_{H_2} + K_{5,R}\,p_{H_2O}}$
FT - model A	$r_{CH_4} = k_{11,1}\alpha_1 K_4 p_{H_2}\left[s\right]^2$ $r_{CH_3OH} = k_{9,1}K_1K_4K_7K_8p_{CO}p_{H_2}^2\left[s\right]^2$ $r_{paraffins,n} = \alpha^{n-1}\alpha_1 k_{11}K_4p_{H_2}\left[s\right]^2$ $r_{olefins,n} = \alpha^{n-1}\alpha_1 k_{12}\sqrt{K_4p_{H_2}}\left[s\right]^2$ $r_{alcohols,n} = \alpha^{n-2}\alpha_1 k_9K_1K_4K_7K_8p_{CO}p_{H_2}^2\left[s\right]^2$ $r_{acids,n} = \alpha^{n-2}\alpha_1 k_{10}K_1K_6K_7p_{CO}p_{H_2O}\left[s\right]^2$ $\alpha_1 = \dfrac{\frac{k_5K_1K_2K_3K_4}{K_6}\frac{p_{H_2}^2p_{CO}}{p_{H_2O}}}{\frac{k_5K_1K_2K_3K_4}{K_6}\frac{p_{H_2}^2p_{CO}}{p_{H_2O}} + k_9K_1K_7K_8p_{CO}p_{H_2}\sqrt{K_4p_{H_2}} + k_{10}K_1K_7K_6\frac{p_{CO}p_{H_2O}}{\sqrt{K_4p_{H_2}}} + k_{11,1}\sqrt{K_4p_{H_2}}}$ $\alpha = \dfrac{k_5\frac{K_1K_2K_3K_4}{K_6}\frac{p_{H_2}^2p_{CO}}{p_{H_2O}}}{k_5\frac{K_1K_2K_3K_4}{K_6}\frac{p_{H_2}^2p_{CO}}{p_{H_2O}} + k_9K_1K_7K_8p_{CO}p_{H_2}\sqrt{K_4p_{H_2}} + k_{11}\sqrt{K_4p_{H_2}} + k_{10}K_1K_6K_7\frac{p_{CO}p_{H_2O}}{\sqrt{K_4p_{H_2}}} + k_{12}}$ $[s] = \Bigg[1 + K_1p_{CO} + \sqrt{K_4p_{H_2}}\left(1 + \alpha_1 + K_1K_7p_{CO} + K_1K_7K_8p_{CO}p_{H_2}\right) + \dfrac{K_1K_2K_4}{K_6}\dfrac{p_{CO}p_{H_2}}{p_{H_2O}} + \dfrac{K_6p_{H_2O}}{\sqrt{K_4p_{H_2}}} +$ $+ \dfrac{K_1K_2K_3K_4}{K_6}\dfrac{p_{CO}p_{H_2}^2}{p_{H_2O}} + \alpha_1\sqrt{K_4p_{H_2}}\left(1 + K_1K_7p_{CO} + K_1K_7K_8p_{CO}p_{H_2}\right)\sum_{i=2}^{N}\alpha^{i-1}\Bigg]^{-1}$
FT - model B	$r_{CH_4} = k_{7,1s}\alpha_{HC,1}K_{4s}p_{H_2}\left[s\right]^2$ $r_{paraffins,n} = \alpha_{HC}^{n-1}\alpha_{HC,1}k_{7s}K_{4s}p_{H_2}\left[s\right]^2$ $r_{olefins,n} = \alpha_{HC}^{n-1}\alpha_{HC,1}k_{8s}\sqrt{K_{4s}p_{H_2}}\left[s\right]^2$ $\alpha_{HC,1} = \dfrac{k_{5s}K_{1s}K_{2s}K_{3s}K_{4s}/K_{6s}\frac{p_{H_2}^2p_{CO}}{p_{H_2O}}}{k_{5s}K_{1s}K_{2s}K_{3s}K_{4s}/K_{6s}\frac{p_{H_2}^2p_{CO}}{p_{H_2O}} + k_{7,1s}\sqrt{K_{4s}p_{H_2}}}$ $\alpha_{HC} = \dfrac{k_{5s}K_{1s}K_{2s}K_{3s}K_{4s}/K_{6s}\frac{p_{H_2}^2p_{CO}}{p_{H_2O}}}{k_{5s}K_{1s}K_{2s}K_{3s}K_{4s}/K_{6s}\frac{p_{H_2}^2p_{CO}}{p_{H_2O}} + k_{7s}\sqrt{K_{4s}p_{H_2}} + k_{8s}}$ $[s] = \Bigg[1 + K_{1s}p_{CO} + \dfrac{K_{1s}K_{2s}K_{4s}}{K_{6s}}\dfrac{p_{CO}p_{H_2}}{p_{H_2O}} + \dfrac{K_{6s}p_{H_2O}}{\sqrt{K_{4s}p_{H_2}}} + \dfrac{K_{1s}K_{2s}K_{3s}K_{4s}}{K_{6s}}\dfrac{p_{CO}p_{H_2}^2}{p_{H_2O}} +$ $+ \sqrt{K_{4s}p_{H_2}}\left(1 + \alpha_{HC,1} + \alpha_{HC,1}\sum_{i=2}^{N}\alpha_{HC}^{i-1}\right)\Bigg]^{-1}$ $r_{CH_3OH} = \alpha_{OX,1}k_{7,1x}K_{2x}/K_{6x}p_{H_2O}\left[x\right]^2$ $r_{alcohols,n} = \alpha_{OX}^{n-1}\alpha_{OX,1}k_{7x}K_{2x}/K_{6x}p_{H_2O}\left[x\right]^2$ $r_{acids,n} = \alpha_{OX}^{n-1}\alpha_{OX,1}k_{8x}K_{3x}/K_{5x}/K_{6x}\dfrac{p_{H_2O}^2}{p_{H_2}^2}\left[x\right]^2$ $\alpha_{OX,1} = \dfrac{k_{4x}K_{1x}p_{CO}}{k_{4x}K_{1x}p_{CO} + k_{7,1x}\frac{\sqrt{K_{2x}p_{H_2}}p_{H_2O}}{K_{6x}p_{H_2}} + k_{8,1x}\frac{K_{3x}p_{H_2O}^2}{K_{5x}K_{6x}p_{H_2}^2\sqrt{K_{2x}p_{H_2}}}}$ $\alpha_{OX} = \dfrac{k_{4x}K_{1x}p_{CO}}{k_{4x}K_{1x}p_{CO} + k_{7x}\frac{\sqrt{K_{2x}p_{H_2}}p_{H_2O}}{K_{6x}p_{H_2}} + k_{8x}\frac{K_{3x}p_{H_2O}^2}{K_{5x}K_{6x}p_{H_2}^2\sqrt{K_{2x}p_{H_2}}}}$ $[x] = \Bigg[1 + K_{1x}p_{CO} + \sqrt{K_{2x}p_{H_2}} + \dfrac{K_{3x}p_{H_2O}}{\sqrt{K_{2x}p_{H_2}}} +$ $+ \alpha_{OX,1}\sqrt{K_{2x}p_{H_2}}\left(1 + \dfrac{p_{H_2O}}{K_{6x}p_{H_2}} + \dfrac{p_{H_2O}}{K_{5x}K_{6x}p_{H_2}^2}\right)\left(1 + \sum_{i=2}^{N}\alpha_{OX,1}^{i-1}\right)\Bigg]^{-1}$

5.4 Results and discussion

5.4.1 Mono-site model

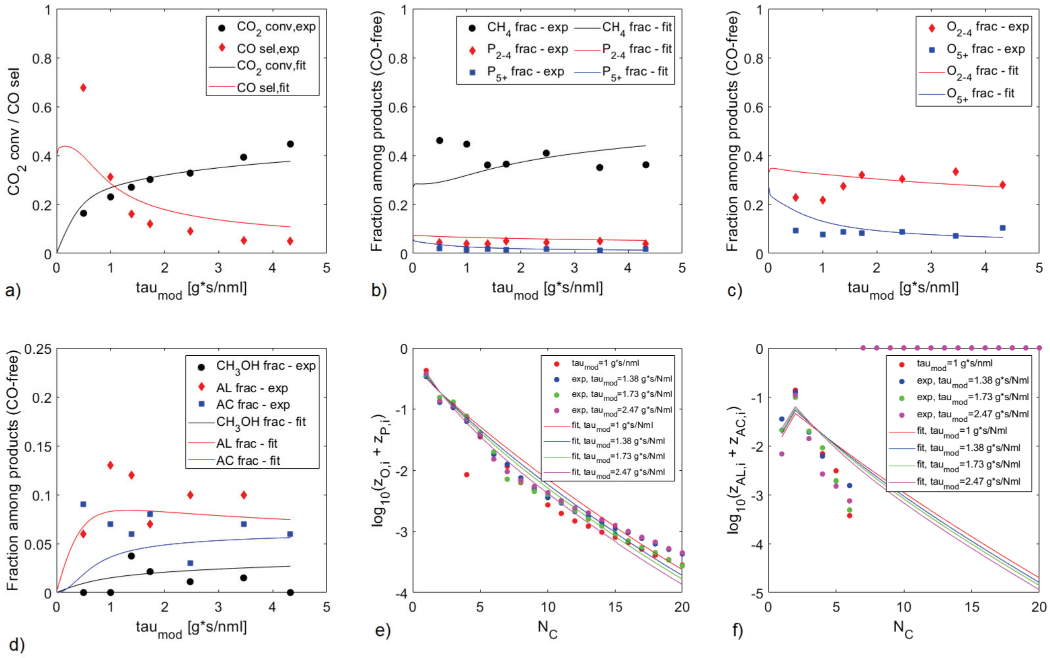

Figure 5.7: Results of the mono-site kinetic model as function of τ_{mod}. Evolution of: a) CO_2 conversion and CO selectivity; b) fractions of CH_4, C_2-C_4 paraffins and C_{5+} paraffins; c) fractions of C_2-C_4 olefins and C_{5+} olefins; d) fractions of methanol, C_2-C_6 alcohols and C_2-C_6 acids; e) ASF distribution for olefins and paraffins; f) ASF distribution for alcohols and acids. Model predictions are represented by solid lines, points represent experimental data.

Values of kinetic parameters estimated for the mono-site model are reported in Table 5.8. All kinetically relevant reactions were considered temperature-dependant, except for the acid termination reaction (step 10) because its activation energy E_{10} was observed to be irrelevant to the model, no matter its value, thus it was set to 0. For each reaction step, pre-exponential factors and activation energies were estimated, then the value of the kinetic constant at 300°C is calculated according to the Arrhenius law.

The methane termination reaction ($k_{11,1}$) results faster than the termination of longer hydrocarbons, as its kinetic constant is significantly larger than that of reactions 11 and 12. This is in accord with the important methane formation experimentally observed. The kinetic constants obtained for the oxygenated products ($k_{9,1}$, k_9, k_{10}) are on the contrary higher, of the same order of magnitude of the chain-growth reaction (k_5), suggesting an important production of oxygenates.

With these values of kinetic parameters, the model is able to describe with good accuracy the experimental data. The parity plot is presented in Figure S.1 and shows that the main part of the model results agree with the experimental data within an absolute error of 20%. The most important deviations are observed for variables that have small values, such as the long olefins, methanol, alcohols and acids fractions. The evaluation of the goodness of the fit is made by estimating the MARR and the SSE of the model, which are 3.5% and 0.38, respectively. These values are relatively low, considering the high number of parameters involved, and suggest a good quality of the fit.

Results of the mono-site model compared with experimental data are reported in Figures 5.7-5.11. The variation of CO_2 conversion, CO selectivity and hydrocarbons distribution with τ_{mod},

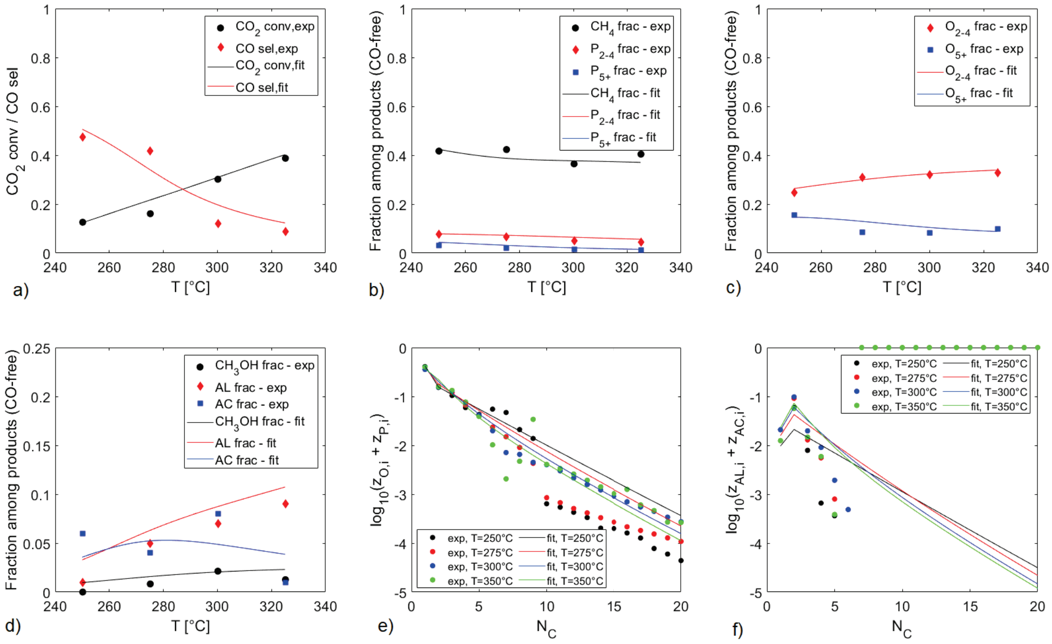

Figure 5.8: Results of the mono-site kinetic model as function of temperature. Evolution of: a) CO_2 conversion and CO selectivity; b) fractions of CH_4, C_2-C_4 paraffins and C_{5+} paraffins; c) fractions of C_2-C_4 olefins and C_{5+} olefins; d) fractions of methanol, C_2-C_6 alcohols and C_2-C_6 acids; e) ASF distribution for olefins and paraffins; f) ASF distribution for alcohols and acids. Model predictions are represented by solid lines, points represent experimental data.

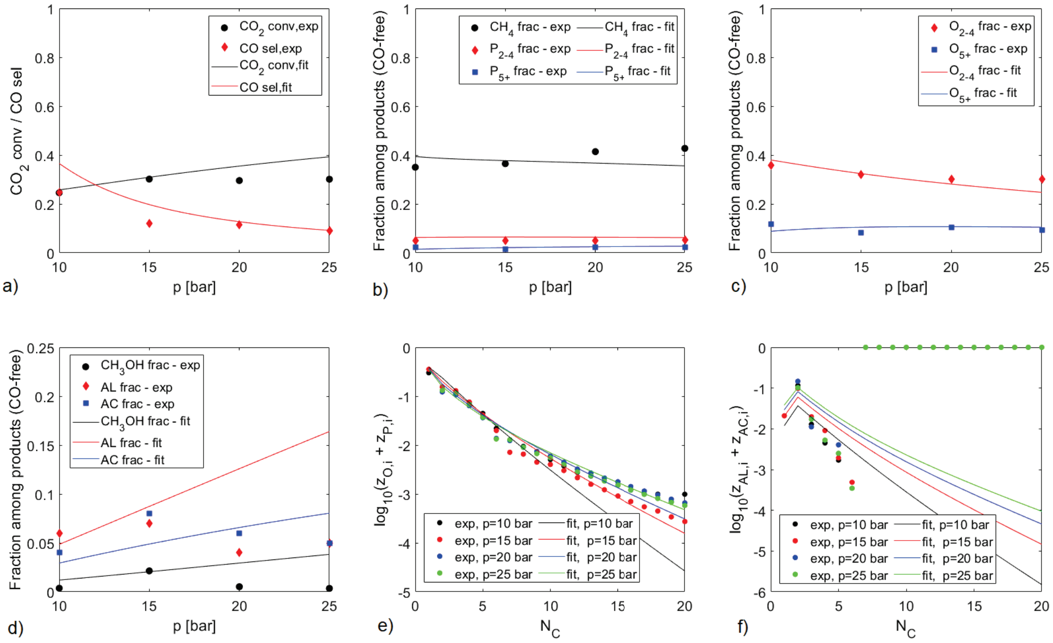

Figure 5.9: Results of the mono-site kinetic model as function of total pressure. Evolution of: a) CO_2 conversion and CO selectivity; b) fractions of CH_4, C_2-C_4 paraffins and C_{5+} paraffins; c) fractions of C_2-C_4 olefins and C_{5+} olefins; d) fractions of methanol, C_2-C_6 alcohols and C_2-C_6 acids; e) ASF distribution for olefins and paraffins; f) ASF distribution for alcohols and acids. Model predictions are represented by solid lines, points represent experimental data.

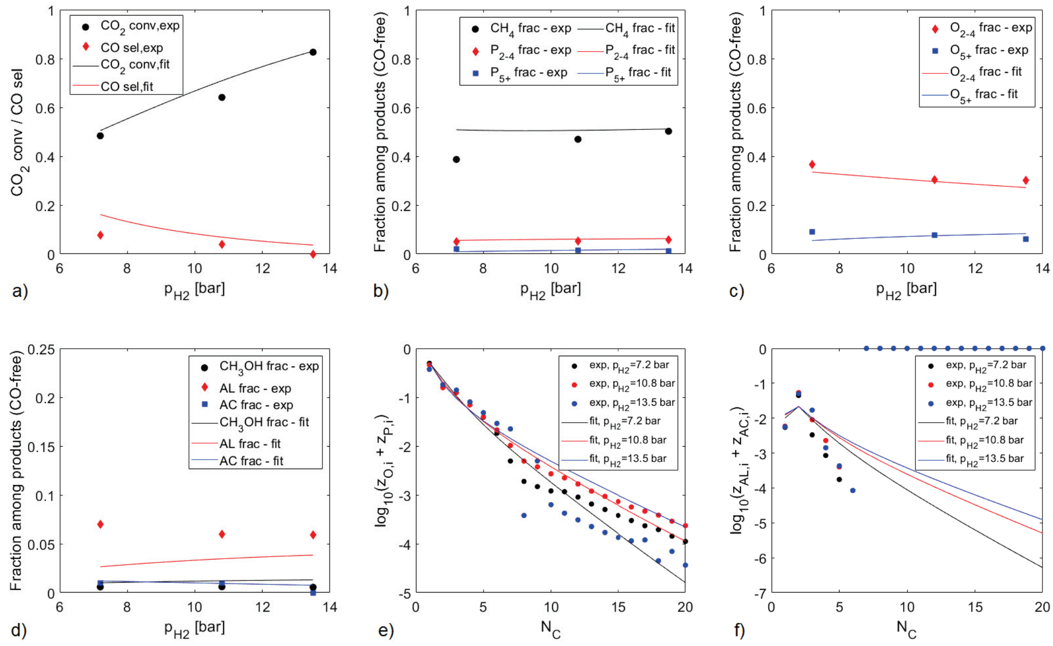

Figure 5.10: Results of the mono-site kinetic model as function of p_{H_2}. Evolution of: a) CO_2 conversion and CO selectivity; b) fractions of CH_4, C_2-C_4 paraffins and C_{5+} paraffins; c) fractions of C_2-C_4 olefins and C_{5+} olefins; d) fractions of methanol, C_2-C_6 alcohols and C_2-C_6 acids; e) ASF distribution for olefins and paraffins; f) ASF distribution for alcohols and acids. Model predictions are represented by solid lines, points represent experimental data.

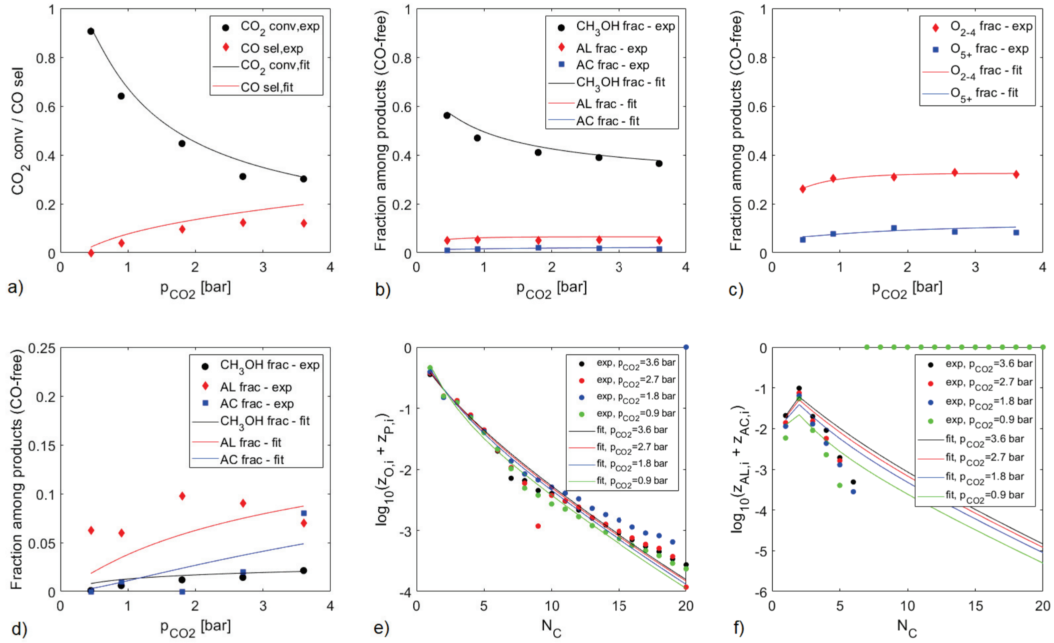

Figure 5.11: Results of the mono-site kinetic model as function of p_{CO_2}. Evolution of: a) CO_2 conversion and CO selectivity; b) fractions of CH_4, C_2-C_4 paraffins and C_{5+} paraffins; c) fractions of C_2-C_4 olefins and C_{5+} olefins; d) fractions of methanol, C_2-C_6 alcohols and C_2-C_6 acids; e) ASF distribution for olefins and paraffins; f) ASF distribution for alcohols and acids. Model predictions are represented by solid lines, points represent experimental data.

T, p, p_{H_2} and p_{CO_2} are compared with the experimental data, as well as the ASF distribution for olefins+paraffins and alcohols+acids. It is observed that the mono-site model can predict with good accuracy the evolution of CO_2 conversion, the CO selectivity and the formation of olefins and paraffins from 1 to 20 C atoms with the different operating parameters. However, it presents higher deviations in the prediction of oxygenates compounds. This is particularly clear when the ASF distribution of hydrocarbons is analysed (see Figures 5.7-5.11.e,f). The model properly fits the experimental values for olefins and paraffins, but it does not fit those obtained for oxygenates. The average values of chain-growth parameters predicted by the model in reference conditions are reported in Table 5.7. It has to be evidenced here that the chain-growth α defined for $C \geqslant 2$ in Eq. 5.26 does not depend on the C number and it is referred to the ratio of reaction rates:

$$\alpha = \frac{r_{C_n}}{r_{C_{n-1}}} \tag{5.46}$$

The parameter represented by the slope of the ASF distribution curve is on the contrary dependent on the C number and refers to the chain-growth probability obtained when the reaction rates are integrated in the plug-flow model to calculate mole flows. We thus define this parameter α' as:

$$\alpha' = \frac{F_{C_n}}{F_{C_{n-1}}} \tag{5.47}$$

The chain-growth probability predicted by the model thus varies with C number, allowing to predict the deviations of longer chains from the ideal distribution, as discussed before. It can also be observed that for olefins and paraffins the chain-growth probability is well predicted by the model, while for oxygenates the values is significantly overestimated. The different α' value of oxygenates compared to olefins and paraffins has already been observed. (Teng et al., 2006, 2007, 2005b) Such a difference in the decrease of alcohols and acids formation rates compared to that of olefins and paraffins was attributed by Teng et al. to the re-adsorption of alcohols and acids over the catalyst surface. (Teng et al., 2007) Re-adsorbed acids and alcohols can take part to chain-growth reactions and be hydrogenated to paraffins and olefins. This hypothesis is supported by experimental results that showed that co-feeding alcohols to the inlet of the reaction leads to the formation of more hydrocarbons and higher carbon number species. (Gaube and Klein, 2008; Kokes et al., 1957; Kummer and Emmett, 1953) Another explanation can be that oxygenates are formed on different active sites than those where olefins and paraffins are formed. (Anderson and Ekerdt, 1985) In this study, as already explained, we have chosen to consider this second hypothesis, but the assumption of oxygenates re-adsorption should also be investigated.

Table 5.7: Values of α' predicted by the two models.

	FT-A model	**FT-B model**
	α'	α'
olefins + paraffins	0.68	0.69
acids + alcohols	0.68	0.31

Table 5.8: Values of optimized kinetic parameters obtained for the two models investigated.

Parameter	Value	Unit	k$_{\mathrm{i}}$ at 300°C	Unit	Parameter	Value	Unit	k$_{\mathrm{i}}$ at 300°C	Unit
Mono-site model									
$k_{5,0}$	8.42x10^{9}	mol/kg/s	6.90	mol/kg/s	K_1	0.069	MPa^{-1}		
E_5	99.70	kJ/mol			K_2	619.54	-		
$k_{9,1,0}$	4.57x10^{6}	mol/kg/s	1.91	mol/kg/s	K_3	6.54x10^{-3}	MPa^{-1}		
$E_{9,1}$	69.98	kJ/mol			K_4	9.98x10^{-3}	MPa^{-1}		
$k_{9,0}$	1.02x10^{10}	mol/kg/s	6.61	mol/kg/s	K_6	0.15	MPa^{-1}		
E_9	100.82	kJ/mol			K_7	0.39	-		
$k_{10,0}$	5.10	mol/kg/s	5.10	mol/kg/s	K_8	3.53	MPa^{-1}		
E_{10}	0	kJ/mol			$k_{2R,0}$	8.00x10^{5}	mol/kg/s/MPa	5.02x10^{-3}	mol/kg/s/MPa
$k_{11,1,0}$	2.39x10^{4}	mol/kg	0.15	mol/kg/s	E_{2R}	90.00	kJ/mol		
$E_{11,1}$	56.98	kJ/mol			K_{1R}	9812.52	MPa^{-1}		
$k_{11,0}$	6.81x10^{4}	mol/kg/s	2.40x10^{-2}	mol/kg/s	K_{3R}	3668.67	MPa		
E_{11}	70.80	kJ/mol			K_{4R}	5.14	MPa^{-1}		
$k_{12,0}$	1.44x10^{6}	mol/kg/s	1.18x10^{-2}	mol/kg/s					
E_{12}	88.72	kJ/mol			K_{5R}	760.85	MPa^{-1}.		
MARR	3.5	%							
SSE	0.38								
Multi-site model									
K_{1s}	2.67	MPa^{-1}			K_{5x}	1.71	MPa^{-1}		
K_{2s}	29.97	-			K_{6x}	3.33	MPa^{-1}		
K_{3s}	1.62	MPa^{-1}			$k_{4,0,x}$	4.43x10^{7}	mol/kg/s	0.39	mol/kg/s
K_{4s}	0.25	MPa^{-1}			E_{4x}	88.40	kJ/mol		
K_{6s}	17.17	MPa^{-1}			$k_{7,1,0,x}$	1.40x10^{7}	mol/kg/s	6.02x10^{-2}	mol/kg/s
$k_{5,0,s}$	1.18x10^{8}	mol/kg/s	0.29	mol/kg/s	$E_{7,1x}$	91.80	kJ/mol		
E_{5s}	94.42	kJ/mol			$k_{7,0,x}$	2.40x10^{8}	mol/kg/s	0.87	mol/kg/s
$k_{7,1,0,s}$	1.93x10^{6}	mol/kg/s	0.21	mol/kg/s	E_{7x}	92.62	kJ/mol		
$E_{7,1s}$	76.41	kJ/mol			$k_{8,0,x}$	. 2.64x10^{7}	mol/kg/s	0.13	mol/kg/s
$k_{7,0,s}$	9.07x10^{6}	mol/kg/s	4.56x10^{-2}	mol/kg/s	E_{8x}	91.32	kJ/mol		
E_{7s}	91.05	kJ/mol			K_{1R}	2.20	MPa^{-1}		
$k_{8,0,s}$	4.59x10^{7}	mol/kg/s	0.11	mol/kg/s	K_{3R}	9.90	MPa		
E_{8s}	94.64	kJ/mol			K_{4R}	1.09	MPa^{-1}		
K_{1x}	0.37	MPa^{-1}			K_{5R}	1.90	MPa^{-1}		
K_{2x}	0.09	MPa^{-1}			$k_{2,0,R}$	1.52x10^{8}	mol/kg/s/MPa	0.88	mol/kg/s/MPa
K_{3x}	2.86	MPa^{-1}			E_{2R}	90.40	kJ/mol		
MARR	4.5	%							
SSE	0.53								

5.4.2 Multi-site model

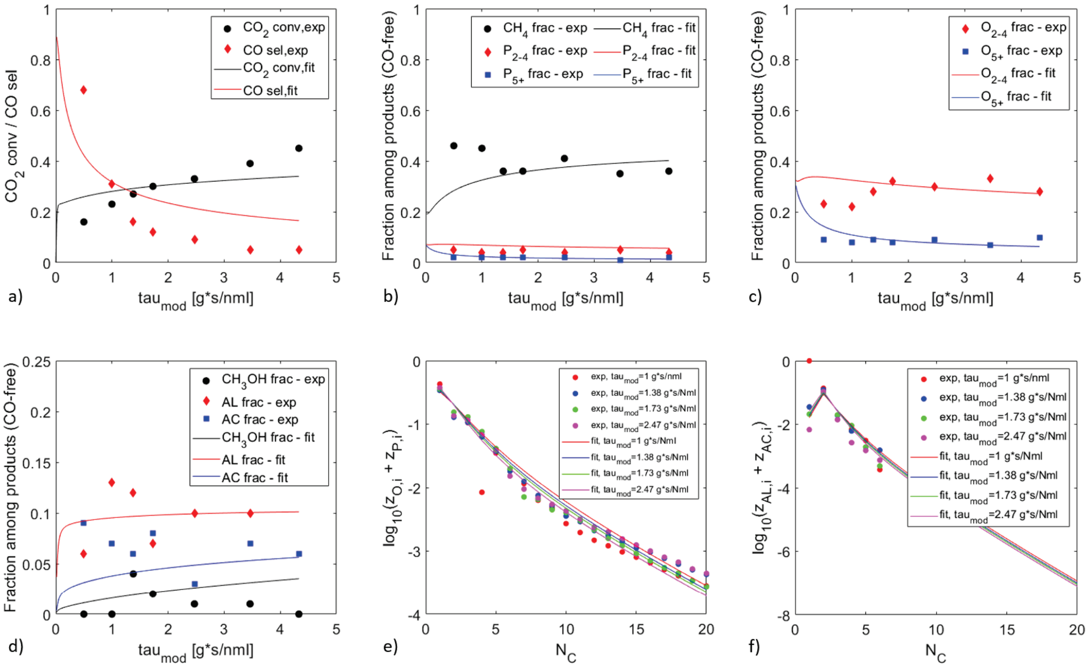

Figure 5.12: Results of the multi-site kinetic model as function of τ_{mod}. Evolution of: a) CO_2 conversion and CO selectivity; b) fractions of CH_4, C_2-C_4 paraffins and C_{5+} paraffins; c) fractions of C_2-C_4 olefins and C_{5+} olefins; d) fractions of methanol, C_2-C_6 alcohols and C_2-C_6 acids; e) ASF distribution for olefins and paraffins; f) ASF distribution for alcohols and acids. Model predictions are represented by solid lines, points represent experimental data.

Values of kinetic parameters estimated for the multi-site model are reported in Table 5.8. The value of activation energy for the RWGS is close to that obtained for the mono-site model (E_{2R} = 90.4 kJ/mol), while the value of the activation energy for the chain-growth step over sites s is only slightly lower than that obtained for the chain-growth reaction with the mono-site model (E_{5s} = 94.4 kJ/mol). The activation energy obtained for the CO insertion step over sites x is lower compared to the activation energy obtained for the chain-growth reaction over sites s (E_{4x} = 88.4 kJ/mol). The comparison of the kinetic constants at 300°C confirms that over the s sites the methane formation is faster compared to the formation of longer hydrocarbons and show a faster formation of olefins compared to paraffins. Over x sites, the formation of alcohols results faster than that of acids.

A question raises about the nature of these different active sites. The sites where the RWGS occurs are generally reported to be iron oxides, Fe_3O_4 in particular. (Visconti et al., 2017) The sites s responsible for the formation of the hydrocarbons and for the chain-growth are likely to be identified as iron carbides. (Visconti et al., 2017) In our previous work, we have observed the formation of the Hägg carbide phase on the spent catalyst, pointing out the role of this phase in the catalysis of this reaction. (Panzone et al., 2021) Concerning the nature of sites x, the discussion is still more open. Some authors reported that oxygenates formation occurs over iron oxides sites (Biloen and Sachtler, 1981; Yang, 2004), however their exact nature is not known. Some authors have reported that oxygenates formation and CO formation via RWGS both occur over the same active sites Fe_3O_4. (Visconti et al., 2017) However, deeper investigation is needed to understand where the oxygenates formation takes place. In this study, we have not considered the formation of oxygenates to occur over the same active sites as the RWGS, even if this is a hypothesis that has to be verified in future works.

The results of the multi-site model compared with experimental data are shown in Fig-

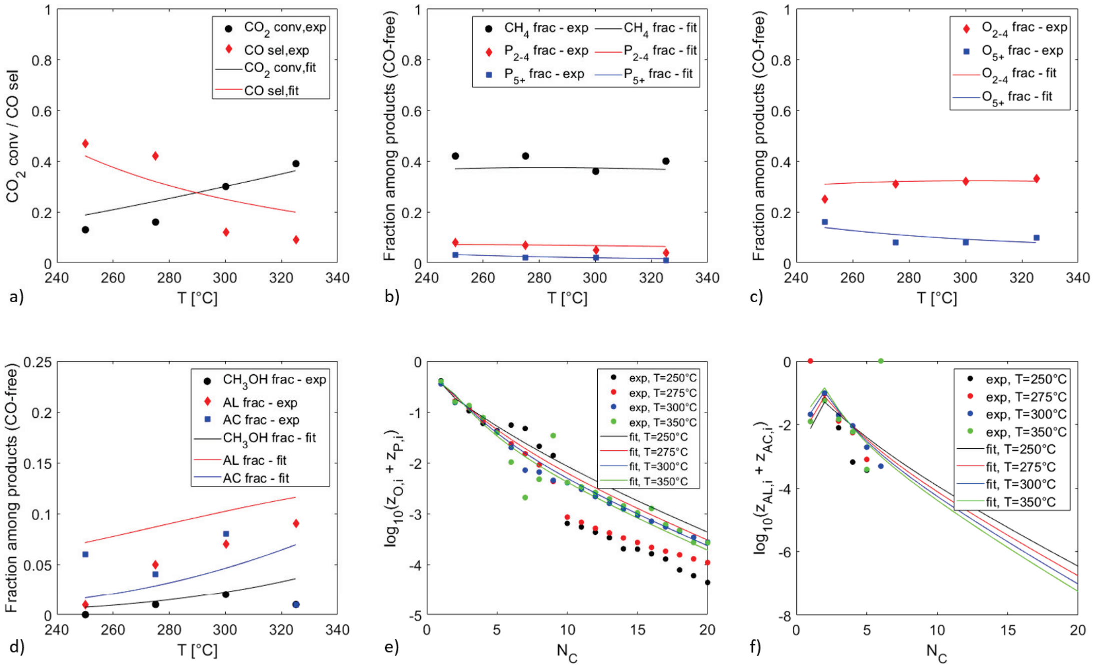

Figure 5.13: Results of the multi-site kinetic model as function of T. Evolution of: a) CO_2 conversion and CO selectivity; b) fractions of CH_4, C_2-C_4 paraffins and C_{5+} paraffins; c) fractions of C_2-C_4 olefins and C_{5+} olefins; d) fractions of methanol, C_2-C_6 alcohols and C_2-C_6 acids; e) ASF distribution for olefins and paraffins; f) ASF distribution for alcohols and acids. Model predictions are represented by solid lines, points represent experimental data.

ures 5.12-5.16. It can be noticed that this model better fits the experimental data of oxygenates formation (see Figures 5.12-5.16.f) and predicts values of α for oxygenates significantly closer to the experimental values than those predicted by the mono-site model (see Table 5.7). However, the obtained MARR and SSE (respectively 4.5% and 0.53) are slightly higher than those estimated for the mono-site model, suggesting a slightly worse fit.

Both these models, especially the multi-site one, probably suffer from the large number of kinetic parameters involved that lead to large confidence intervals. To improve the models, two solutions can be proposed: performing other experiments and improve the analytic protocol in order to have more robust data with lower experimental error; simplify the model and reduce the number of parameters to determine by fixing the value of some of them to an arbitrary value. To do this, a sensitivity analysis of the influence of the parameters on the kinetic rate can be performed to identify the most important parameters. Moreover, a DFT study can help in estimating the values of some kinetic parameters. Furthermore, other hypothesis on the mechanism could be made and tested. As RWGS is globally believed to take place over iron oxides as well, the hypothesis that oxygenates formation is a competitive reaction with the RWGS cannot be excluded, and on the contrary should be investigated by future works. Moreover, performing co-feeding experiments with alcohols and olefins could help to verify if alcohols and olefins adsorption effectively occur. The hypothesis of alcohols re-adsorption and their involvement in chain-growth reactions and formation of olefins and paraffins could not be excluded and should as well be investigated.

Therefore, from the results obtained in this study, we should currently consider the mono-site micro-kinetic model developed as the most reliable one. However, based on the evidence reported in the literature and on what observed experimentally in our work, the hypothesis of a multi-site mechanism cannot be excluded either. The existence of a different mechanism and/or a different active site for the formation of oxygenates has been largely evidenced in the literature. Similarly

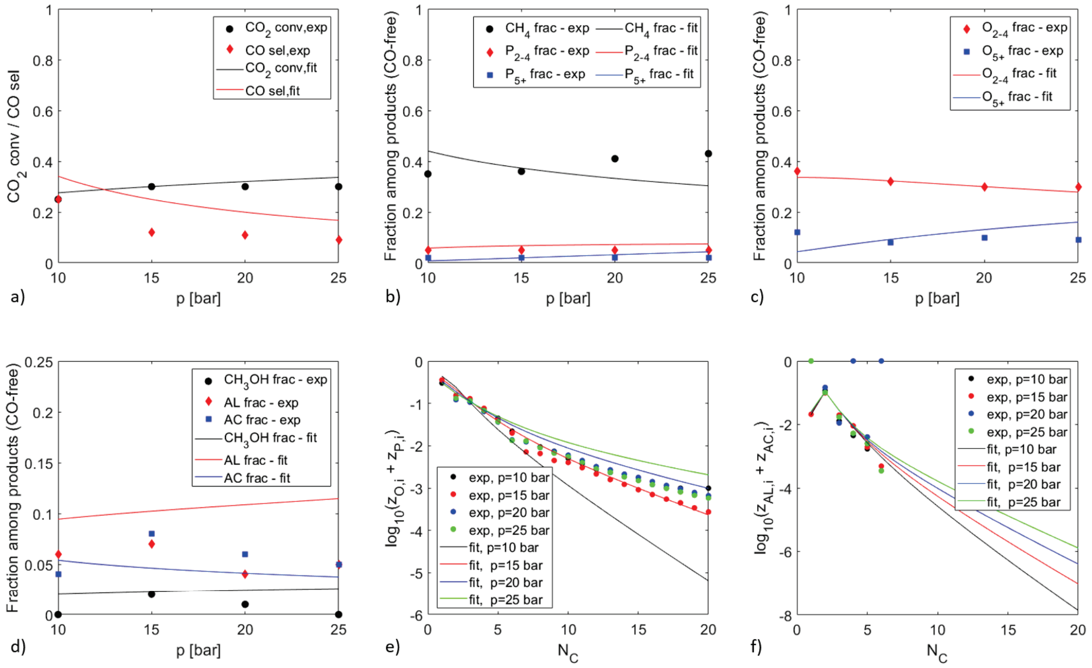

Figure 5.14: Results of the multi-site kinetic model as function of total pressure. Evolution of: a) CO_2 conversion and CO selectivity; b) fractions of CH_4, C_2-C_4 paraffins and C_{5+} paraffins; c) fractions of C_2-C_4 olefins and C_{5+} olefins; d) fractions of methanol, C_2-C_6 alcohols and C_2-C_6 acids; e) ASF distribution for olefins and paraffins; f) ASF distribution for alcohols and acids. Model predictions are represented by solid lines, points represent experimental data.

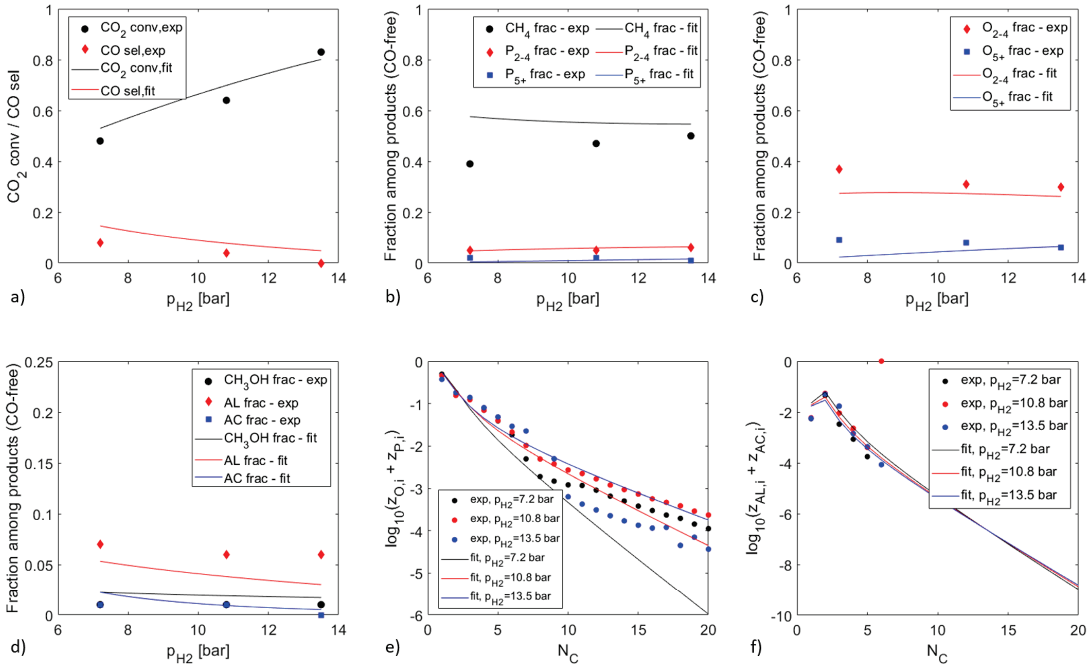

Figure 5.15: Results of the multi-site kinetic model as function of p_{H_2}. Evolution of: a) CO_2 conversion and CO selectivity; b) fractions of CH_4, C_2-C_4 paraffins and C_{5+} paraffins; c) fractions of C_2-C_4 olefins and C_{5+} olefins; d) fractions of methanol, C_2-C_6 alcohols and C_2-C_6 acids; e) ASF distribution for olefins and paraffins; f) ASF distribution for alcohols and acids. Model predictions are represented by solid lines, points represent experimental data.

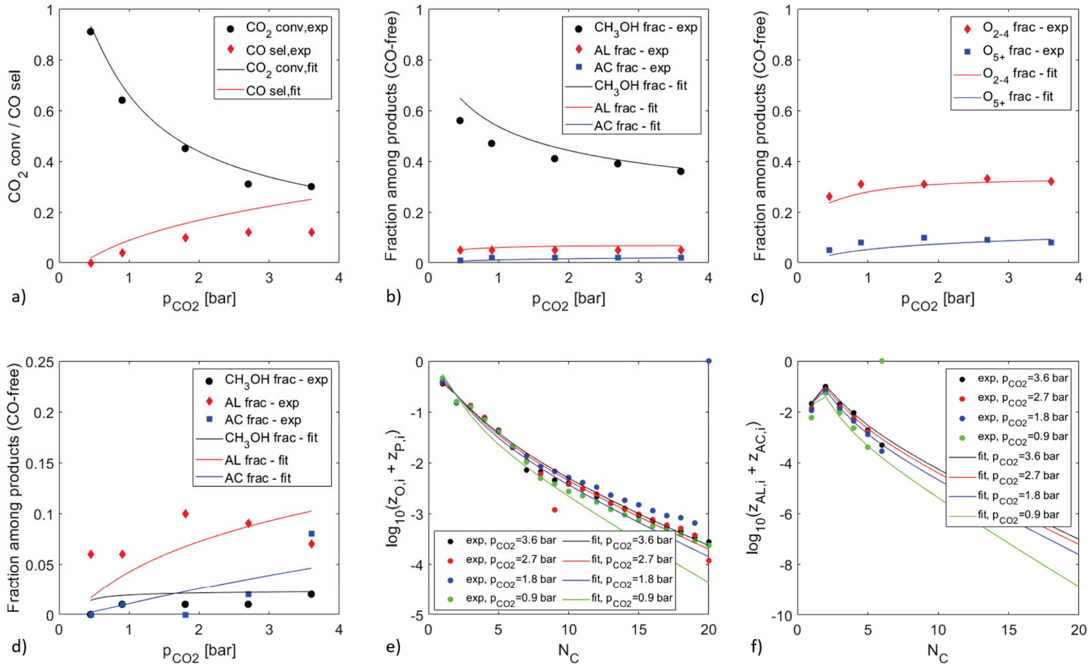

Figure 5.16: Results of the multi-site kinetic model as function of p_{CO_2}. Evolution of: a) CO_2 conversion and CO selectivity; b) fractions of CH_4, C_2-C_4 paraffins and C_{5+} paraffins; c) fractions of C_2-C_4 olefins and C_{5+} olefins; d) fractions of methanol, C_2-C_6 alcohols and C_2-C_6 acids; e) ASF distribution for olefins and paraffins; f) ASF distribution for alcohols and acids. Model predictions are represented by solid lines, points represent experimental data.

to the results obtained by our work, other experiments performed over iron catalysts have shown that the chain-growth probability of oxygenates is lower than that for hydrocarbons. (Teng et al., 2006, 2007) This is an indication that two different mechanisms are involved. Moreover, it has been reported that the active sites responsible for the formation of oxygenates are iron oxides sites. (Biloen and Sachtler, 1981; Yang, 2004; Visconti et al., 2017; de Smit and Weckhuysen, 2008) As it is widely recognized that iron carbides (in particular the Hägg phase Fe_5C_2) are the sites responsible for the chain-growth and the formation of hydrocarbons, this is another indication of the existence of a different active site for the oxygenates formation and eventually a different mechanism.

5.5 Conclusions

A detailed kinetic model has been derived for the CO_2 hydrogenation reaction to describe the formation of CO, paraffins, olefins, alcohols and acids until 20 C atoms. An alkyl mechanism was assumed for paraffins and olefins, while oxygenates were considered to be formed via CO insertion. A redox mechanism was supposed for the CO formation via RWGS. Two mechanisms were derived: the first one, the mono-site model, based on the hypothesis that both hydrocarbons and oxygenates are formed over the same active sites; the second one, the multi-site model, based on the hypothesis that oxygenates and hydrocarbons are formed over different active sites.

From the results obtained by this study, it has been observed that the mono-site model better fits the experimental data, showing slightly lower statistical error. However, the mono-site model is not able to predict with accuracy the formation of oxygenates, giving a value of the chain-growth probability significantly far from the experimental value. The multi-site model on the contrary better describes the oxygenates formation but has higher error and confidence intervals. To better understand how the formation of oxygenates occurs, an improvement of the models is thus necessary, by reducing the number of parameters to determine and by providing a larger number of experimental data.

Beside the need to improve the models fit, this work presents a first investigation of the comprehensive mechanism of the CO_2 hydrogenation over Fe catalysts, including the formation of both hydrocarbons and oxygenates. It has been shown that a complex mechanism is involved, including the chain-growth via an alkyl mechanism combined with a CO-insertion mechanism to form the oxygenates products. However, other hypothesis have to be considered in future works in order to better study the mechanism, especially the formation of oxygenates. They might in fact be formed over the same sites where CO is formed via RWGS or have a role in the formation of long-chain hydrocarbons.

References

M. Amoyal, R. Vidruk-Nehemya, M. V. Landau, and M. Herskowitz. Effect of potassium on the active phases of Fe catalysts for carbon dioxide conversion to liquid fuels through hydrogenation. *Journal of Catalysis*, 348:29–39, 2017. ISSN 00219517. doi: 10.1016/j.jcat.2017.01.020. URL https://linkinghub.elsevier.com/retrieve/pii/S0021951717300325.

K. G. Anderson and J. G. Ekerdt. Study of Fischer-Tropsch synthesis over FeSiO$_2$: Effect of diethylamine on hydrocarbon and alcohol production. *Journal of Catalysis*, 95(2):602–604, 1985. ISSN 0021-9517. doi: 10.1016/0021-9517(85)90138-1. URL http://www.sciencedirect.com/science/article/pii/0021951785901381.

P. Biloen and W. Sachtler. Mechanism of Hydrocarbon Synthesis over Fischer-Tropsch Catalysts. In D. Eley, H. Pines, and P. B. Weisz, editors, *Advances in Catalysis*, volume 30, pages 165–216. Academic Press, 1981. ISBN 0360-0564. doi: 10.1016/S0360-0564(08)60328-4. URL https://www.sciencedirect.com/science/article/pii/S0360056408603284.

R. C. Brady and R. Pettit. Reactions of diazomethane on transition-metal surfaces and their relationship to the mechanism of the Fischer-Tropsch reaction. *Journal of the American Chemical Society*, 102 (19):6181–6182, 1980. ISSN 0002-7863. doi: 10.1021/ja00539a053. URL https://doi.org/10.1021/ja00539a053.

R. C. Brady and R. Pettit. Mechanism of the Fischer-Tropsch reaction. The chain propagation step. *Journal of the American Chemical Society*, 103(5):1287–1289, 1981. ISSN 0002-7863. doi: 10.1021/ja00395a081. URL https://doi.org/10.1021/ja00395a081.

L. Brübach, D. Hodonj, and P. Pfeifer. Kinetic Analysis of CO $_2$ Hydrogenation to Long-Chain Hydrocarbons on a Supported Iron Catalyst. *Industrial & Engineering Chemistry Research*, 61(4): 1644–1654, Feb. 2022. ISSN 0888-5885, 1520-5045. doi: 10.1021/acs.iecr.1c04018. URL https://pubs.acs.org/doi/10.1021/acs.iecr.1c04018.

G. Centi and S. Perathoner. Opportunities and prospects in the chemical recycling of carbon dioxide to fuels. *Catalysis Today*, 148(3-4):191–205, 2009. ISSN 09205861. doi: 10.1016/j.cattod.2009.07.075. URL https://linkinghub.elsevier.com/retrieve/pii/S0920586109004416.

G. Centi, E. A. Quadrelli, and S. Perathoner. Catalysis for CO$_2$ conversion: a key technology for rapid introduction of renewable energy in the value chain of chemical industries. *Energy & Environmental Science*, 6:1711–1731, 2013. doi: 10.1039/c3ee00056g. URL https://pubs.rsc.org/en/content/articlelanding/2013/ee/c3ee00056g#!divAbstract.

J. Chang, L. Bai, B. Teng, R. Zhang, J. Yang, Y. Xu, H. Xiang, and Y. Li. Kinetic modeling of Fischer–Tropsch synthesis over Fe-Cu-K-SiO$_2$ catalyst in slurry phase reactor. *Chemical Engineering Science*, 62(18-20):4983–4991, 2007. ISSN 00092509. doi: 10.1016/j.ces.2006.12.031. URL https://linkinghub.elsevier.com/retrieve/pii/S0009250906008219.

C.-Y. Chou, A. J. Loiland, and F. R. Lobo. Reverse Water-Gas Shift Iron Catalyst Derived from Magnetite. *Catalysts*, 9(9), 2019. ISSN 2073-4344. doi: 10.3390/catal9090773.

I. Ciobıcă, G. Kramer, Q. Ge, M. Neurock, and R. van Santen. Mechanisms for Chain Growth in Fischer–Tropsch Synthesis over Ru(0001). *Journal of Catalysis*, 212(2):136–144, 2002. ISSN 0021-9517. doi: 10.1006/jcat.2002.3742. URL http://www.sciencedirect.com/science/article/pii/S0021951702937425.

Y. A. Daza and J. N. Kuhn. CO$_2$ conversion by reverse water gas shift catalysis: comparison of catalysts, mechanisms and their consequences for CO$_2$ conversion to liquid fuels. *RSC Advances*, 6(55): 49675–49691, 2016. ISSN 2046-2069. doi: 10.1039/C6RA05414E. URL http://xlink.rsc.org/?DOI=C6RA05414E.

E. de Smit and B. M. Weckhuysen. The renaissance of iron-based Fischer–Tropsch synthesis: on the multifaceted catalyst deactivation behaviour. *Chemical Society Reviews*, 37(12):2758, 2008. ISSN 0306-0012, 1460-4744. doi: 10.1039/b805427d. URL http://xlink.rsc.org/?DOI=b805427d. Number: 12.

R. A. Dictor and A. T. Bell. Fischer-Tropsch synthesis over reduced and unreduced iron oxide catalysts. *Journal of Catalysis*, 97(1):121–136, 1986. ISSN 0021-9517. doi: 10.1016/0021-9517(86)90043-6. URL https://www.sciencedirect.com/science/article/pii/0021951786900436.

T. J. Donnelly and C. N. Satterfield. Product distributions of the Fischer-Tropsch synthesis on precipitated iron catalysts. *Applied Catalysis*, 52(1):93–114, 1989. ISSN 01669834. doi: 10.1016/S0166-9834(00)83375-8. URL https://linkinghub.elsevier.com/retrieve/pii/S0166983400833758.

T. J. Donnelly, I. C. Yates, and C. N. Satterfield. Analysis and prediction of product distributions of the Fischer-Tropsch synthesis. *Energy & Fuels*, 2(6):734–739, 1988. ISSN 0887-0624. doi: 10.1021/ef00012a003. URL https://pubs.acs.org/doi/abs/10.1021/ef00012a003.

M. E. Dry. Practical and theoretical aspects of the catalytic Fischer-Tropsch process. *Applied Catalysis A: General*, 138(2):319–344, 1996. ISSN 0926860X. doi: 10.1016/0926-860X(95)00306-1. URL https://linkinghub.elsevier.com/retrieve/pii/0926860X95003061.

F. Fischer and H. Tropsch. Über die direkte Synthese von Erdöl-Kohlenwasserstoffen bei gewöhnlichem Druck. (Erste Mitteilung). *Berichte der deutschen chemischen Gesellschaft (A and B Series)*, 59(4):830–831, 1926. ISSN 03659488. doi: 10.1002/cber.19260590442. URL https://onlinelibrary.wiley.com/doi/10.1002/cber.19260590442.

D. Förtsch, K. Pabst, and E. Groß-Hardt. The product distribution in Fischer–Tropsch synthesis: An extension of the ASF model to describe common deviations. *Chemical Engineering Science*, 138:333–346, 2015. ISSN 00092509. doi: 10.1016/j.ces.2015.07.005. URL https://linkinghub.elsevier.com/retrieve/pii/S0009250915004893.

J. Gaube and H.-F. Klein. The promoter effect of alkali in Fischer-Tropsch iron and cobalt catalysts. *Applied Catalysis A: General*, 350(1):126–132, 2008. doi: 10.1016/j.apcata.2008.08.007. URL https://www.scopus.com/inward/record.uri?eid=2-s2.0-52949093496&doi=10.1016%2fj.apcata.2008.08.007&partnerID=40&md5=2c3e6588591724ea2540c1e206054bec.

J. Gaube and H.-F. Klein. Further support for the two-mechanisms hypothesis of Fischer-Tropsch synthesis. *Applied Catalysis A: General*, 374(1-2):120–125, 2010. doi: 10.1016/j.apcata.2009.11.039. URL https://www.scopus.com/inward/record.uri?eid=2-s2.0-74049106279&doi=10.1016%2fj.apcata.2009.11.039&partnerID=40&md5=4302b37e105b313c89d742162625111d.

M. Iglesias Gonzalez, C. de Vries, M. Claeys, and G. Schaub. Chemical energy storage in gaseous hydrocarbons via iron Fischer–Tropsch synthesis from H_2/CO_2 —Kinetics, selectivity and process considerations. *Catalysis Today*, 242:184–192, 2015. ISSN 09205861. doi: 10.1016/j.cattod.2014.05.020. URL https://linkinghub.elsevier.com/retrieve/pii/S0920586114003903.

F. Jiang, B. Liu, S. Geng, Y. Xu, and X. Liu. Hydrogenation of CO_2 into hydrocarbons: enhanced catalytic activity over Fe-based Fischer–Tropsch catalysts. *Catalysis Science & Technology*, 8(16):4097–4107, 2018. ISSN 2044-4753, 2044-4761. doi: 10.1039/C8CY00850G. URL http://xlink.rsc.org/?DOI=C8CY00850G.

J. Kaspar, M. Graziani, A. Rahman, A. Trovarelli, E. Vichi, and E. da Silva. Carbon dioxide hydrogenation over iron containing catalysts. *Applied Catalysis A: General*, 117:125–137, 1994.

R. J. Kokes, W. K. Hall, and P. H. Emmett. Fischer-Tropsch Synthesis Mechanism Studies. The Addition of Radioactive Ethanol to the Synthesis Gas. *Journal of the American Chemical Society*, 79(12):2989–2996, 1957. ISSN 0002-7863. doi: 10.1021/ja01569a002. URL https://doi.org/10.1021/ja01569a002.

J. T. Kummer and P. H. Emmett. Fischer—Tropsch Synthesis Mechanism Studies. The Addition of Radioactive Alcohols to the Synthesis Gas. *Journal of the American Chemical Society*, 75(21):5177–5183, 1953. ISSN 0002-7863. doi: 10.1021/ja01117a008. URL https://doi.org/10.1021/ja01117a008.

S.-B. Lee, J.-S. Kim, W.-Y. Lee, K.-W. Lee, and M.-J. Choi. Product Distribution Analysis for Catalytic Reduction of CO_2 in a Bench Scale Fixed Bed Reactor. *Studies in Surface Science and Catalysis*, 153:73–78, 2004. doi: 10.1016/S0167-2991(04)80222-2. URL https://www.sciencedirect.com/science/article/pii/S0167299104802222.

W. Li, H. Wang, X. Jiang, J. Zhu, Z. Liu, X. Guo, and C. Song. A short review of recent advances in CO_2 hydrogenation to hydrocarbons over heterogeneous catalysts. *RSC Advances*, 8(14):7651–7669, 2018. ISSN 2046-2069. doi: 10.1039/C7RA13546G. URL `http://xlink.rsc.org/?DOI=C7RA13546G`.

J. A. Loiland, M. J. Wulfers, N. S. Marinkovic, and R. F. Lobo. Fe/γ-Al_2O_3 and Fe–K/γ-Al_2O_3 as reverse water-gas shift catalysts. *Catalysis Science & Technology*, 6(14):5267–5279, 2016. ISSN 2044-4753. doi: 10.1039/C5CY02111A. URL `http://dx.doi.org/10.1039/C5CY02111A`.

E. S. Lox and G. F. Froment. Kinetics of the Fischer-Tropsch reaction on a precipitated promoted iron catalyst. 2. Kinetic modeling. *Industrial & Engineering Chemistry Research*, 32(1):71–82, 1993.

P. Maitlis. Fischer-Tropsch, organometallics, and other friends. *Journal of Organometallic Chemistry*, 689(24 SPEC. ISS.):4366–4374, 2004. doi: 10.1016/j.jorganchem.2004.05.037. URL `https://www.scopus.com/inward/record.uri?eid=2-s2.0-9944229887&doi=10.1016%2fj.jorganchem.2004.05.037&partnerID=40&md5=e590b86c11e5128a9ff986d2582d4f12`.

M. Martinelli, C. G. Visconti, L. Lietti, P. Forzatti, C. Bassano, and P. Deiana. CO_2 reactivity on Fe–Zn–Cu–K Fischer–Tropsch synthesis catalysts with different K-loadings. *Catalysis Today*, 228:77–88, 2014. ISSN 09205861. doi: 10.1016/j.cattod.2013.11.018. URL `https://linkinghub.elsevier.com/retrieve/pii/S0920586113006226`.

S. Mousavi, A. Zamaniyan, M. Irani, and M. Rashidzadeh. Generalized kinetic model for iron and cobalt based Fischer–Tropsch synthesis catalysts: Review and model evaluation. *Applied Catalysis A: General*, 506:57–66, 2015. ISSN 0926-860X. doi: 10.1016/j.apcata.2015.08.020. URL `http://www.sciencedirect.com/science/article/pii/S0926860X15301150`.

S. Najari, G. Gróf, S. Saeidi, and F. Gallucci. Modeling and optimization of hydrogenation of CO_2: Estimation of kinetic parameters via Artificial Bee Colony (ABC) and Differential Evolution (DE) algorithms. *International Journal of Hydrogen Energy*, 44(10):4630–4649, 2019. ISSN 03603199. doi: 10.1016/j.ijhydene.2019.01.020. URL `https://linkinghub.elsevier.com/retrieve/pii/S036031991930093X`.

A. Nakhaei Pour and M. R. Housaindokht. A new kinetic model for direct CO_2 hydrogenation to higher hydrocarbons on a precipitated iron catalyst: Effect of catalyst particle size. *Journal of Energy Chemistry*, 26(3):359–367, 2017. ISSN 20954956. doi: 10.1016/j.jechem.2016.12.006. URL `https://linkinghub.elsevier.com/retrieve/pii/S2095495616301607`.

A. Nakhaei Pour, H. Khodabandeh, M. Izadyar, and M. R. Housaindokht. Detailed kinetics of Fischer–Tropsch synthesis on a precipitated iron catalyst. *Reaction Kinetics, Mechanisms and Catalysis*, 111(1):29–44, 2014. ISSN 1878-5204. doi: 10.1007/s11144-013-0640-8. URL `https://doi.org/10.1007/s11144-013-0640-8`.

M. Ojeda, R. Nabar, A. U. Nilekar, A. Ishikawa, M. Mavrikakis, and E. Iglesia. CO activation pathways and the mechanism of Fischer–Tropsch synthesis. *Journal of Catalysis*, 272(2):287–297, 2010. ISSN 00219517. doi: 10.1016/j.jcat.2010.04.012. URL `https://linkinghub.elsevier.com/retrieve/pii/S0021951710001399`.

C. Panzone, R. Philippe, C. Nikitine, L. Vanoye, A. Bengaouer, A. Chappaz, and P. Fongarland. Catalytic and kinetic study of the CO_2 hydrogenation reaction over a Fe-K/Al_2O_3 catalyst towards liquid and gaseous hydrocarbons production. *Industrial & Engineering Chemistry Research*, 2021. doi: https://doi.org/10.1021/acs.iecr.1c02542.

J. Patzlaff, Y. Liu, C. Graffmann, and J. Gaube. Studies on product distributions of iron and cobalt catalyzed Fischer–Tropsch synthesis. *Applied Catalysis A: General*, 186(1-2):109–119, 1999. ISSN 0926860X. doi: 10.1016/S0926-860X(99)00167-2. URL `https://linkinghub.elsevier.com/retrieve/pii/S0926860X99001672`.

H. Pichler and H. Schulz. Neuere Erkenntnisse auf dem Gebiet der Synthese von Kohlenwasserstoffen aus CO und H_2. *Chemie Ingenieur Technik - CIT*, 42(18):1162–1174, 1970. ISSN 0009-286X, 1522-2640. doi: 10.1002/cite.330421808. URL `http://doi.wiley.com/10.1002/cite.330421808`.

T. Riedel, G. Schaub, K.-W. Jun, and K.-W. Lee. Kinetics of CO_2 Hydrogenation on a K-Promoted Fe Catalyst. *Industrial & Engineering Chemistry Research*, 40(5):1355–1363, 2001. ISSN 0888-5885, 1520-5045. doi: 10.1021/ie000084k. URL http://pubs.acs.org/doi/abs/10.1021/ie000084k.

T. Riedel, H. Schulz, G. Schaub, K.-W. Jun, J.-S. Hwang, and K.-W. Lee. Fischer–Tropsch on iron with H_2/CO and H_2/CO_2 as synthesis gases: the episodes of formation of the Fischer–Tropsch regime and construction of the catalyst. *Topics in Catalysis*, 26(1-4):41–54, 2003.

U. Rodemerck, M. Holeňa, E. Wagner, Q. Smejkal, A. Barkschat, and M. Baerns. Catalyst Development for CO_2 Hydrogenation to Fuels. *ChemCatChem*, 5(7):1948–1955, 2013. ISSN 18673880. doi: 10.1002/cctc.201200879. URL http://doi.wiley.com/10.1002/cctc.201200879.

S. Saeidi, S. Najari, F. Fazlollahi, M. K. Nikoo, F. Sefidkon, J. J. Klemeš, and L. L. Baxter. Mechanisms and kinetics of CO_2 hydrogenation to value-added products: A detailed review on current status and future trends. *Renewable and Sustainable Energy Reviews*, 80:1292–1311, 2017. ISSN 1364-0321. doi: 10.1016/j.rser.2017.05.204. URL http://www.sciencedirect.com/science/article/pii/S1364032117308390.

B. Schliebs and J. Gaube. The Influence of the Promoter K_2CO_3 in Iron Catalysts on the Carbon Number Distribution of Fischer-Tropsch-Products. *Berichte der Bunsengesellschaft für physikalische Chemie*, 89(1):68–73, 1985. ISSN 00059021. doi: 10.1002/bbpc.19850890113. URL http://doi.wiley.com/10.1002/bbpc.19850890113.

H. Schulz. Selforganization in Fischer–Tropsch synthesis with iron- and cobalt catalysts. *Catalysis Today*, 228:113–122, 2014. ISSN 09205861. doi: 10.1016/j.cattod.2013.11.060. URL https://linkinghub.elsevier.com/retrieve/pii/S0920586113006895.

H. Schulz and M. Claeys. Kinetic modelling of Fischer–Tropsch product distributions. *Applied Catalysis A: General*, 186(1):91–107, 1999. ISSN 0926-860X. doi: 10.1016/S0926-860X(99)00166-0. URL http://www.sciencedirect.com/science/article/pii/S0926860X99001660.

H. Schulz, G. Schaub, M. Claeys, and T. Riedel. Transient initial kinetic regimes of Fischer–Tropsch synthesis. *Applied Catalysis A: General*, 186(1-2):215–227, 1999.

H. Schulz, T. Riedel, and G. Schaub. Fischer–Tropsch principles of co-hydrogenation on iron catalysts. *Topics in Catalysis*, 32(3-4):117–124, 2005. ISSN 1022-5528, 1572-9028. doi: 10.1007/s11244-005-2883-8. URL http://link.springer.com/10.1007/s11244-005-2883-8.

M. S. Spencer. On the activation energies of the forward and reverse water-gas shift reaction. *Catalysis Letters*, 32(1-2):9–13, 1995.

P. Styring, E. A. Quadrelli, and K. Armstrong. *Carbon Dioxide Utilisation: Closing the Carbon Cycle*. Elsevier, Amsterdam, 2015. ISBN 978-0-444-62746-9. doi: 10.1016/B978-0-444-62746-9.05001-5. URL http://www.sciencedirect.com/science/article/pii/B9780444627469050015.

B. Teng, J. Chang, H. Wan, J. Lu, S. Zheng, Y. Liu, Y. Liu, and X. Guo. A Corrected Comprehensive Kinetic Model of Fischer–Tropsch Synthesis. *Chinese Journal of Catalysis*, 28(8):687–695, 2007. ISSN 1872-2067. doi: 10.1016/S1872-2067(07)60060-6. URL http://www.sciencedirect.com/science/article/pii/S1872206707600606.

B.-T. Teng, J. Chang, J. Yang, G. Wang, C.-H. Zhang, Y.-Y. Xu, H.-W. Xiang, and Y.-W. Li. Water gas shift reaction kinetics in Fischer–Tropsch synthesis over an industrial Fe–Mn catalyst. *Fuel*, 84(7):917–926, 2005a. ISSN 0016-2361. doi: 10.1016/j.fuel.2004.12.007. URL http://www.sciencedirect.com/science/article/pii/S0016236105000104.

B.-T. Teng, C.-H. Zhang, J. Yang, D.-B. Cao, J. Chang, H.-W. Xiang, and Y.-W. Li. Oxygenate kinetics in Fischer–Tropsch synthesis over an industrial Fe–Mn catalyst. *Fuel*, 84(7):791–800, 2005b. ISSN 0016-2361. doi: 10.1016/j.fuel.2004.12.008. URL http://www.sciencedirect.com/science/article/pii/S001623610500013X.

B.-T. Teng, J. Chang, C.-H. Zhang, D.-B. Cao, J. Yang, Y. Liu, X.-H. Guo, H.-W. Xiang, and Y.-W. Li. A comprehensive kinetics model of Fischer–Tropsch synthesis over an industrial Fe–Mn catalyst. *Applied Catalysis A: General*, 301(1):39–50, 2006. ISSN 0926-860X. doi: 10.1016/j.apcata.2005.11.014. URL `http://www.sciencedirect.com/science/article/pii/S0926860X05008732`.

G. P. Van der Laan and A. A. Beenackers. Intrinsic kinetics of the gas–solid Fischer–Tropsch and water gas shift reactions over a precipitated iron catalyst. *Applied Catalysis A: General*, 193(1-2):39–53, 2000.

C. G. Visconti, M. Martinelli, L. Falbo, L. Fratalocchi, and L. Lietti. CO_2 hydrogenation to hydrocarbons over Co and Fe-based Fischer-Tropsch catalysts. *Catalysis Today*, 277:161–170, 2016. ISSN 09205861. doi: 10.1016/j.cattod.2016.04.010. URL `https://linkinghub.elsevier.com/retrieve/pii/S0920586116302632`.

C. G. Visconti, M. Martinelli, L. Falbo, A. Infantes-Molina, L. Lietti, P. Forzatti, G. Iaquaniello, E. Palo, B. Picutti, and F. Brignoli. CO_2 hydrogenation to lower olefins on a high surface area K-promoted bulk Fe-catalyst. *Applied Catalysis B: Environmental*, 200:530–542, 2017. ISSN 09263373. doi: 10.1016/j.apcatb.2016.07.047. URL `https://linkinghub.elsevier.com/retrieve/pii/S0926337316305896`.

J. Wang, Z. You, Q. Zhang, W. Deng, and Y. Wang. Synthesis of lower olefins by hydrogenation of carbon dioxide over supported iron catalysts. *Catalysis Today*, 215:186–193, 2013. ISSN 09205861. doi: 10.1016/j.cattod.2013.03.031. URL `https://linkinghub.elsevier.com/retrieve/pii/S0920586113001442`.

Y.-N. Wang, W.-P. Ma, Y.-J. Lu, J. Yang, Y.-Y. Xu, H.-W. Xiang, Y.-W. Li, Y.-L. Zhao, and B.-J. Zhang. Kinetics modelling of Fisher-Tropsh synthesis over an industrial Fe-Cu-K catalyst. *Fuel*, 82: 195–213, 2003.

G. D. Weatherbee and C. H. Bartholomew. Hydrogenation of CO_2 on group VIII metals: IV. Specific activities and selectivities of silica-supported Co, Fe, and Ru. *Journal of Catalysis*, 87(2):352–362, 1984.

H. D. Willauer, R. Ananth, M. T. Olsen, D. M. Drab, D. R. Hardy, and F. W. Williams. Modeling and kinetic analysis of CO_2 hydrogenation using a Mn and K-promoted Fe catalyst in a fixed-bed reactor. *Journal of CO2 Utilization*, 3-4:56–64, 2013. ISSN 22129820. doi: 10.1016/j.jcou.2013.10.003. URL `https://linkinghub.elsevier.com/retrieve/pii/S2212982013000504`.

J. Yang, Y. Liu, J. Chang, Y.-N. Wang, L. Bai, Y.-Y. Xu, H.-W. Xiang, Y.-W. Li, and B. Zhong. Detailed Kinetics of Fischer-Tropsch Synthesis on an Industrial Fe-Mn Catalyst. *Industrial & Engineering Chemistry Research*, 42(21):5066–5090, 2003. ISSN 0888-5885. doi: 10.1021/ie030135o. URL `https://doi.org/10.1021/ie030135o`.

Y. Yang. Effect of potassium promoter on precipitated iron-manganese catalyst for Fischer?Tropsch synthesis. *Applied Catalysis A: General*, 266(2):181–194, July 2004. ISSN 0926860X. doi: 10.1016/j.apcata.2004.02.018. URL `https://linkinghub.elsevier.com/retrieve/pii/S0926860X04001437`.

CHAPTER 6

Reactor modelling and process optimization.

6.1 Introduction.

This last Chapter is focused on the modelling of the reactor and on the optimisation of the process.

First, we will present a comparison between a heterogeneous reactor model and a pseudo-homogeneous one, applied to a fixed bed reactor with a cooling system, that will be validated with the experimental data obtained on the experimental bench used in CEA. Until now in this work, all the reactor models developed did not consider the heat exchange, because of the assumption of isothermal conditions, verified by experimental measurements. However, in the phase of scaling-up of the reactor and the catalyst, the heat and mass transfer limitations may not be negligible anymore. To gain insights about these phenomena, we have developed a heterogeneous model that takes into account the presence of the fluid bulk phase and of the solid catalytic phase and we have compared it with a pseudo-homogeneous model. This comparison allows to verify whether the hypothesis of negligible limitations of mass and heat transport are effectively appropriate. Moreover, the scaling-up to a bigger reactor allows to verify that the macro-kinetic model developed in Chapter 4 is still accurate when applied to a different reactor size.

Then, we will analyse the possible options to optimize the process and maximize the hydrocarbons yield. As we have already discussed (see Sections 1.3.2.2 and 3.6), one of the problems of this reaction is its sensitivity to water, that can lead to fast deactivation of the catalyst. (Satterfield et al., 1986; Pendyala et al., 2010) Therefore, the adoption of a membrane reactor can be beneficial. We have thus simulated a membrane reactor and studied the effects of water removal during the reaction.

Finally, we have considered the process scale and simulated the reaction and the downstream products separation. We propose a possible process configuration that allows the production of valuable products that can have applications in the current economic sector. Moreover, we estimate the carbon and the energy efficiency to compare this process to other hydrocarbons synthesis technologies and to understand its feasibility in view of eventual future industrial applications.

6.2 Reactor modelling.

The results of the experimental study described in section 3.7 are here used to validate the reactor model, developed to describe the behaviour of the reaction. In the previous Chapters, we have developed kinetic models, by making the assumptions that the laboratory-scale reactor could be modelled as an isothermal plug-flow reactor, as we have verified that all the criteria for excluding mass and heat transfer limitations were satisfied. Now, we are considering a bigger reactor with a cooling system that allows a better management of the heat produced by the reaction. We want to verify:

1. if the macro-kinetic model developed in Chapter 4 can be adapted to reactors of other sizes;
2. if the hypothesis of excluding mass and heat transfer limitations is justified;
3. if the model is still able to predict the reactor behaviour when CO/CO_2 mixtures are fed. The eventual recirculation of unreacted gases to the reactor inlet would in fact lead to the presence of variable contents of CO in the reactor feed.

For these purposes, we have modelled the reactor with non-isothermal plug-flow and heterogeneous models, both in one-dimension. A brief description of the possible approaches to model reactors with heterogeneously-catalysed reactions is given in the next section.

6.2.1 The problem of modelling reactors with heterogeneously-catalysed reactions.

The modelling of fixed-bed reactors with heterogeneously-catalysed reactions involves phenomena coupled at different scales, as shown in Figure 6.1. The feeding of reactants and the circulation of the cooling fluid occur at macroscopic scale. The transport of the fluid around the catalytic particles is a mesoscopic-scale phenomenon. Finally, the chemical reaction and the thermal and mass transfer occur at microscopic scale, inside the particle's pores. Given the number of physical-chemical phenomena involved in packed beds, their precise description requires very complex mathematical problems that are highly demanding in terms of computation times. Thus, simplifications are generally employed to describe heterogeneous media. The most common simplification is the continuum approach based on the identification of a "representative elementary volume" (REV). (Biot, 1941; Coussy, 1991; Hsu, 2005; Quintard and Whitaker, 2005) This approach consists in considering the actual porous medium as the superposition of two continuum phases, the solid phase - representing the catalytic particles - and the gas phase. For a given geometric coordinate of the porous medium, the two phases coexist and the local structural and physical properties of the porous medium are averaged in the control volume considered. The REV has to be big enough to avoid the inhomogeneity of the porous medium, but little enough to maintain a local behaviour in the description of the variations of the physical

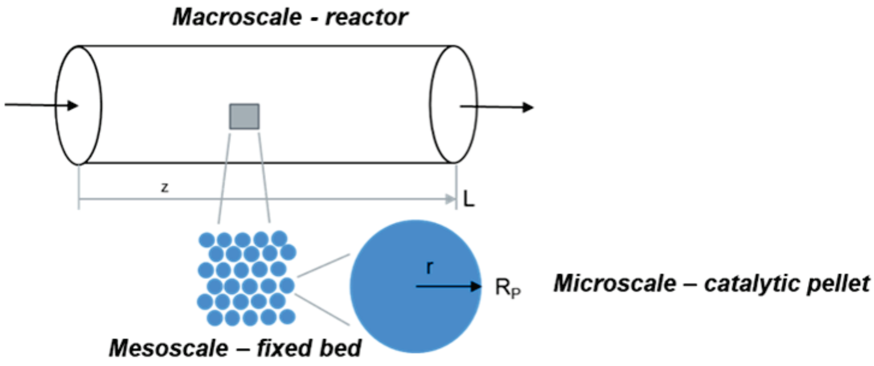

Figure 6.1: Representation of different scales involved in the modelling of a reactor with heterogeneous-catalysed reaction.

properties. Therefore, the REV scale has to be chosen much bigger than the pore size and much lower than the reactor size. These criteria are easily satisfied at the industrial scale, given the big size of the reactors, while this is not the case for laboratory-scale reactors. (Rolland, 2014) Despite the controvert applicability of this approach for lab-scale reactors, this simplification is the best in terms of precision/simplicity ratio and the only one actually accessible and applicable and thus the one commonly adopted.

Indubitably, this method of homogenisation via a representative elementary volume generates a loss of information about the porous medium, in particular about the phenomena of mass, heat and momentum transfer in the medium. To represent these phenomena, parameters are introduced as representative of several phenomena grouped. These parameters are determined from correlations, generally based on empirical derivation.

In the common applications, two approaches exist to model reactors with heterogeneously-catalysed reactions: the heterogeneous and the pseudo-homogeneous approaches. If the REV method is applied to the catalytic bed, the heterogeneous model is derived. It distinguishes the two scales of the porous medium - the catalytic pores where the reaction takes place and the bulk phase - and describes the transfers of mass and heat within the catalyst. The pseudo-homogeneous model is based on the hypothesis that transfers between the two scales are at the equilibrium, thus assumes that the temperature and the composition of the fluid in the catalytic pores are equal to those of the fluid surrounding the catalytic particles.

To model the behaviour of our reactor, we have used both approaches and compared them. In the following sections the equations of the models are described.

6.2.2 Equations of the 1D pseudo-homogeneous plug-flow model.

The 1D plug-flow model is described by the following equations. For the variation of mole flow of compound i in the bulk (F_i) (Perry et al., 1997):

$$\frac{dF_i}{dz} = \rho_{bed} S_r \sum_j \nu_{i,j} r_j \tag{6.1}$$

where ρ_{bed} is the catalytic bed density, S_r is the cross-sectional surface of the reactor, r_j is the rate of the reaction j, described by the macro-kinetic model shown in Chapter 4.

For the variation of the bed temperature T_{bed} along the reactor (Perry et al., 1997):

$$c_P F_0 \frac{dT_{bed}}{dz} = \rho_{bed} S_r \sum_j r_j \Delta H_j^r - \frac{4}{d_r} S_r h_{OV} \left(T_{bed} - T_C\right) \tag{6.2}$$

where c_P is the heat capacity at constant pressure, F_0 is the gas total flow at the reactor inlet, ΔH_j^r is the enthalpy of reaction j, d_r is the reactor diameter and h_{OV} is the overall heat transfer coefficient, defined in the next section, according to equations 6.38-6.46. T_C represents the temperature of the cooling fluid.

6.2.3 Equations of the 1D heterogeneous model.

The 1D heterogeneous model in stationary state includes equations for the mass, heat and momentum transfer in the bulk and in the catalyst's pores. The equations of the model are presented in the following.

6.2.3.1 Momentum balance.

The momentum balance in the bulk phase, for a 1D stationary model, is described by the Darcy equation (Perry et al., 1997):

$$-\frac{dp}{dz} = \frac{\mu_{mix}}{\kappa} u_b \tag{6.3}$$

where μ_{mix} is the viscosity of the gas mixture and κ is the permeability of the porous medium. The value of μ_{mix} used in the work, as well as values of other parameters of the model can be found in Table 6.2. The permeability κ is estimated from the Carman-Kozeny equation for fixed beds (Rushton et al., 2000):

$$\kappa = \frac{(2R_P)^2 \epsilon_{bed}^3}{180\,(1-\epsilon_{bed})^2} \tag{6.4}$$

where ϵ_{bed} is the porosity of the packed bed which is estimated from the apparent bed density ($\rho_{bed} = 1.13\ g/cm^3$) and the density of the catalyst pellet measured with a gas pycnometer ($\rho_{cat} = 3.22\ g/cm^3$):

$$\epsilon_{bed} = 1 - \frac{\rho_{bed}}{\rho_{cat}} \tag{6.5}$$

The obtained ϵ_{bed} is thus estimated to be 0.63.

The boundary conditions of Eq 6.3 are:

- At the reactor entrance ($z = 0$) the mass flux is imposed equal to N_0:

$$-\rho_{mix} u = N_0 = F_0 M_{mix}/S_r \tag{6.6}$$

- At the reactor outlet ($z = L_{bed}$) the total pressure is imposed:

$$p = p_{out} \tag{6.7}$$

6.2.3.2 Mass balance.

Mass balance in the catalytic bed.

The equation of mass balance of the species i, for a 1D stationary model, in bulk phase is (Perry et al., 1997):

$$u_b \rho_{mix} \frac{d\omega_i}{dz} + \frac{dJ_i}{dz} = R_i \tag{6.8}$$

where the term on the left represents the variation of the convective mass flux of the species i, J_i represents the mass diffusion flux and R_i the mass source term. Only CO_2, H_2, CO, H_2O and C_4H_8 are considered as compounds. C_4H_8 has been chosen as compound representative of all the hydrocarbons obtained as its molar mass is close to the averaged molar mass of the pool of products obtained.

The boundary conditions for equations in the bulk phase are:

- At the reactor entrance ($z = 0$) the composition is set equal to that of the feed:

$$\omega_i = \omega_{i0} \tag{6.9}$$

- At the reactor outlet ($z = L_{bed}$) the diffusive flow is null:

$$J_i = 0 \tag{6.10}$$

Diffusion flux.

The diffusion flux J_i can be expressed with the Fick's law (Perry et al., 1997), as a function of the mass fraction gradient of the compound i and the corresponding diffusion coefficient:

$$J_i = -\rho_{mix} D_{i,m} \frac{d\omega_i}{dz} \tag{6.11}$$

The estimation of the diffusion coefficient $D_{i,m}$ is not evident for this kind of concentrated mixtures, where none of the species is predominant. Generally, correlations for the estimation of diffusion coefficients are defined for diluted mixtures and as functions of the molar fraction gradient of compound i. Thus, we can define a molar diffusion flux J_i^* (Perry et al., 1997; Delgado, 2006):

$$J_i^* = -M_i c D_{i,m}^* \frac{dx_i}{dz} \tag{6.12}$$

In the case of multi-components mixtures, $D_{i,m}^*$ and $D_{i,m}$ are not the same. Thus, we have to define the mass diffusion flux J_i as function of the molar diffusion flux J_i^*, so that we can use the existing correlations for the estimation of diffusion coefficients. For this purpose, the mixture-averaged approximation can be used. (Kee et al., 2017) The diffusion coefficient of each compound is calculated by approximating the other gases to a single corps with averaged properties and thus considering the mixture as a binary mixture. Therefore, the mass and molar diffusion fluxes can be correlated with the following expression:

$$J_i = \left(\frac{1-\omega_i}{1-x_i}\right) J_i^* \tag{6.13}$$

and

$$J_i = -\rho_i \left(\frac{1-\omega_i}{1-x_i}\right) D_{i,m}^* \frac{dx_i}{dz} \tag{6.14}$$

For non-diluted mixtures, the diffusion coefficients are estimated from the correlations derived from Maxwell equations by Fairbanks and Wilke (Fairbanks and Wilke, 1950):

$$D_{i,m}^* = \frac{1-x_i}{\sum_{j\neq i} \frac{x_j}{D_{i,j}}} \tag{6.15}$$

where $D_{i,j}$ are the binary diffusion coefficients, calculated from Fuller equation (Fuller and Giddings, 1965; Fuller et al., 1966):

$$D_{i,j} = \frac{0.00143 T^{1.75}}{p M_{ij}^{0.5} \left(\left(\nu_i^{1/3} + \nu_j^{1/3}\right)^2\right)} \tag{6.16}$$

where $M_{ij} = 2\left(M_i^{-1} + M_j^{-1}\right)^{-1}$ in kg/mol; ν_i are the Fuller's diffusion volumes reported in Table 6.1; T in K, p in bar, $D_{i,j}$ in cm^2/s.

Table 6.1: Values of Fuller's volumes ν calculated from atomic contributions given in Poling et al. (2001).

Compound	ν_i
CO_2	26.9
CO	18
H_2	6.1
N_2	18.5
H_2O	13.1
C_4H_8	86.7

When the mixture-averaged approximation is used, the mass conservation equation is not respected anymore, because the sum of all the diffusive fluxes is not null. The solution proposed by Kee et al. (2017) consists in omitting the resolution of the mass balance equation of one species, whose composition is derived from those of the other species. In our model, we omitted the resolution of mass balance of carbon dioxide.

Axial dispersion is not considered in these models, as it was found to be negligible. Preliminary simulations have been run by including the effect of the axial dispersion coefficients, estimated with the correlation of Edward and Richardson (Edwards and Richardson, 1968):

$$\frac{D^*_{i,ax}}{D^*_{i,m}} = \gamma_1 \epsilon_{bed} + \gamma_2 Re_P Sc_i \tag{6.17}$$

where $\gamma_1 = 0.73$ and $\gamma_2 = 0.5 \left(1 + \frac{13\gamma_1 \epsilon_{bed}}{Re_p Sc_i}\right)^{-1}$. From this simulations we obtained a value of $\frac{D^*_{i,ax}}{D^*_{i,m}}$ close to 0.6, resulting in a $D^*_{i,ax}$ of the same magnitude order of $D^*_{i,m}$ that did not show any effects on the compositions in the reactor. The results of these preliminary simulations are not shown here. In the following, axial dispersion will be neglected.

Mass source.

The mass source term R_i for an heterogeneous model is represented by the mass exchange between the bulk phase and the catalyst pellet surface and it is expressed as follows:

$$R_i = -\left(1 - \epsilon_{bed}\right) M_i a_S k_{G,i} \left(C^b_i - C^S_{i,P}\right) \tag{6.18}$$

where ϵ_{bed} is the bed porosity and C^b_i and C^S_{iP} represent the concentration of i in the bulk phase and at the particle's surface, respectively. a_S is the external specific surface that for spherical particles forming a bed of porosity ϵ_{bed} is estimated as follows:

$$a_S = \frac{6}{d_P}\left(1 - \epsilon_{bed}\right) \tag{6.19}$$

The obtained value of a_S can be found in Table 6.2. $k_{G,i}$ is the mass transfer coefficient between bulk phase and catalyst particle, that can be estimated from the Sherwood number:

$$k_{G,i} = \frac{D_{i,m} Sh_i}{d_P} \tag{6.20}$$

Sh_i is calculated from Satterfield's correlation for fixed bed reactors (Satterfield et al., 1978):

$$Sh_i = \frac{0.357}{1 - \epsilon_{bed}} Re_P^{0.641} Sc_i^{1/3} \tag{6.21}$$

with

$$Re_P = \frac{\rho_{mix} u_b d_P}{\mu_{mix}} \tag{6.22}$$

$$Sc_i = \frac{\mu_{mix}}{\rho_{mix} D_{i,m}} \tag{6.23}$$

Mass conservation inside the catalytic pellet.

Inside the catalytic particle, the equation of mass conservation for the species i in stationary conditions in 1D is:

$$\frac{1}{r^2}\frac{d}{dr}\left(-D_{i,eff} r^2 \frac{dC_{i,P}}{dr}\right) = \sum_{j=1}^{N_r} \nu_{ij} r^*_j \tag{6.24}$$

where the first term represents the internal diffusion flux and the second is the mass source, due to the chemical reaction.

The boundary conditions for mass conservation equations in the catalyst's particle are:

- Mass flow at the particle center ($r = 0$) is null:

$$\left.\frac{dC_{i,P}}{dr}\right|_{r=0} = 0 \tag{6.25}$$

- Mass flow at the particle surface ($r = R_P$) is represented by the mass exchange with the bulk phase:

$$-D_{i,eff}\left.\frac{dC_{i,P}}{dr}\right|_{r=R_P} = k_{G,i}\left(C_{i,b} - C_{i,P}^{S}\right) \tag{6.26}$$

The diffusion coefficient $D_{i,eff}$ takes into account all the diffusion phenomena that can occur in the catalytic pores. Diffusion in the pores can be due to two mechanisms: the Knudsen diffusion and the molecular gas diffusion. The first is dominant when the pores diameter is much smaller than the mean free path of the gas molecules. The mean free path of a gas molecule λ can be calculated according to the approximate equation based on Brown et al. (Brown et al., 1946):

$$\lambda = \left(\frac{2\mu}{p}\right)\sqrt{\frac{8RT}{\pi M}} \tag{6.27}$$

The Knudsen number is defined as the ratio of the mean free path to the pore size:

$$Kn = \frac{\lambda}{d_{pores}} \tag{6.28}$$

The average pore diameter of the catalyst used in this work is about 10 nm. In the operating conditions, the Knudsen number obtained has a value of 1.5, indicating that the flow is dominated by the molecular diffusion inside the catalytic pores. Thus, we have neglected here the Knudsen diffusion and considered only the molecular diffusion in the catalytic pores. The diffusion coefficient in the catalyst pores has to be modified due to the solid material that makes the effective diffusion in the catalyst pores lower than the bulk diffusion. The diffusion coefficient in the catalytic pores is thus estimated by considering the catalyst porosity and tortuosity:

$$D_{i,eff} = D_{i,m}\frac{\epsilon_{pores}}{\tau_{pores}} \tag{6.29}$$

where ϵ_{pores} is estimated to be 0.66, from the volume of pores measured by BJH analysis ($V_{pores} = 0.21\ cm^3/g$) and the density of the catalyst pellet measured with a gas pycnometer ($\rho_{cat} = 3.22\ g/cm^3$). The tortuosity of the catalytic particle τ_{pores} is set to 4, as suggested by Satterfield. (Satterfield, 1991)

The kinetic laws r_j^* derive from the macro-kinetic model previously described in Chapter 4. r_j^* are expressed in $\mathrm{mol/m^3_{cat}/s}$ and as function of the concentrations of i in the particle, in the form:

$$r_j^* = \frac{m_{cat}}{V_{cat}}r_j = \frac{m_{cat}}{V_{cat}}k_jRT\frac{C_Ac_B - C_CC_D/K_{eq,j}}{C_C + a_jC_D + b_jC_A + c_jC_B} \tag{6.30}$$

6.2.3.3 Heat transfer.

In the bulk phase, the equation of heat conservation for the species i in stationary conditions in 1D is (Perry et al., 1997):

$$S_r\rho_{mix}c_{p,mix}u_b\frac{dT_{bed}}{dz} + \frac{dq}{dz} = S_rQ + \pi d_rh_{OV}\left(T_{bed} - T_C\right) \tag{6.31}$$

where the first term represents the convective heat flux, the q is the conductive flux and Q is the heat source.

The boundary conditions for equations in the bulk phase are:

- At the reactor entrance ($z = 0$) the bed temperature is set equal to that of the feed:

$$T_{bed} = T_{bed,0} \tag{6.32}$$

- At the reactor outlet ($z = L_{bed}$) the conductive flow is null:

$$q = 0 \tag{6.33}$$

Conductive flux.

The conductive heat flux is expressed according to the Fourier's law. (Bird et al., 1960) It is proportional to the temperature gradient:

$$q = -A_r k_{ax} \frac{dT_{bed}}{dz} \tag{6.34}$$

k_{ax} is the axial thermal conductivity of the packed bed, calculated from the following correlation (VDI, 2010):

$$\frac{k_{ax}}{\lambda_{mix}} = 7 + 0.5 Re_P Pr \tag{6.35}$$

Heat source.

The heat source term, in analogy to the mass transfer, is represented by the heat exchange between the bulk phase and the catalyst pellet surface and it is expressed as follows:

$$Q = -\left(1 - \epsilon_{bed}\right) a_S k_t \left(T_{bed} - T_P^S\right) \tag{6.36}$$

where T_{bed} and T_P^S are the bed temperature and the temperature of the catalyst pellet at the external surface, respectively. k_t is the heat transfer coefficient between bulk phase and pellet and it is estimated from Satterfield's correlation derived in the case of fixed beds (Trambouze and Euzen, 2004):

$$k_t = \frac{0.43}{1 - \epsilon_{bed}} \rho_{mix} c_{P,mix} u_b Re_P^{-0.36} Pr^{-0.67} \tag{6.37}$$

Overall heat transfer coefficient.

The h_{OV} represents the overall heat transfer coefficient next to the reactor wall. It is estimated as the combination of difference resistances in series (see Fig. 6.2):

$$\frac{1}{h_{OV}} = \frac{1}{\alpha_{bed}} + \frac{1}{\alpha_{w,out}} + \frac{1}{h_C} \tag{6.38}$$

where α_{bed} represents the heat transfer coefficient through the catalytic bed, $\alpha_{w,out}$ the heat transfer coefficient through the reactor wall and h_C the heat transfer coefficient with the cooling fluid. $1/\alpha_{bed}$ is the combination of two elements, one representing the thermal resistance of the packed bed $1/\alpha_{rad}$ and one representing the thermal resistance to heat transfer on the bed side of the wall $1/\alpha_{w,int}$:

$$\frac{1}{\alpha_{bed}} = \frac{1}{\alpha_{rad}} + \frac{1}{\alpha_{w,int}} \tag{6.39}$$

The term $1/\alpha_{rad}$ derives when passing from a two-dimensional model to a one-dimensional one. When passing to the 1D model, in fact, we consider a mean temperature of the bed and we assume that the radial temperature profile has a parabolic curvature between the center of the reactor and the internal wall. (Rothenberg, 2013) By making this assumption, we derive that:

$$\frac{1}{\alpha_{rad}} = \frac{d_r}{8\lambda_{rad}} \tag{6.40}$$

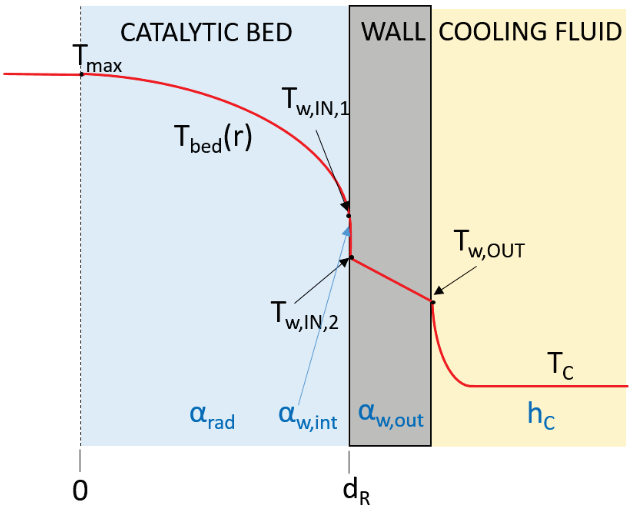

Figure 6.2: Radial temperature profile in a cooled packed-bed reactor according to the simplified one-dimensional model with α_{bed}.

The radial effective heat conductivity in the bed λ_{rad} can be estimated from the following equation (Bauer, 1978a,b):

$$\frac{\lambda_{rad}}{\lambda_{mix}} = \frac{\lambda_{bed}}{\lambda_{mix}} + \frac{Re_P Pr}{7\left[2 - \left(1 - 2\dfrac{d_P}{d_r}\right)^2\right]} \tag{6.41}$$

Eq. 6.41 is valid only for $d_r/d_P > 5$. λ_{bed} is the effective thermal conductivity of the bed without flow. For $\lambda_P/\lambda_{mix} > 10$, $\lambda_{bed}/\lambda_{mix}$ is generally in the range 2-10. For modelling wall-cooled reactors, a value of $\lambda_{bed}/\lambda_{mix}$ of 4 can be used. (Westerterp et al., 1991; Jess and Kern, 2012; Chabot et al., 2015; Rothenberg, 2013)

The internal wall heat transfer $\alpha_{w,int}$ can be estimated from the correlation of Martin and Nilles (Martin and Nilles, 1993):

$$Nu_w = \frac{\alpha_{w,int} d_P}{\lambda_{mix}} = \left(1.3 + 5\frac{d_P}{d_r}\right)\frac{\lambda_{bed}}{\lambda_{mix}} + 0.19 Re_P^{3/4} Pr^{1/3} \tag{6.42}$$

The external wall heat transfer $\alpha_{w,out}$ can be estimated as follows:

$$\frac{1}{\alpha_{w,out}} = \frac{e_w}{\lambda_s} \tag{6.43}$$

where e_w is the wall thickness and λ_s is the thermal conductivity of the wall material. In this case, as the stainless steel has high thermal conductivity (17 W/m/K), the wall heat transfer resistance results to be very small and can thus be neglected.

The external heat transfer coefficient h_C can be estimated from the Nusselt number:

$$h_C = \frac{Nu_C \lambda_C}{L_c} \tag{6.44}$$

Nusselt numbers can reasonably be estimated from correlations of the form:

$$Nu = C Re^m Pr^n \tag{6.45}$$

The Nusselt number that characterises the heat transfer by forced convection from a fluid to the surface of a cylinder in the range of $4 \text{x} 10^4 < Re < 4 \text{x} 10^5$ can be estimated with the following correlation (Rothenberg, 2013):

$$Nu_C = 0.027 Re_C^{0.805} Pr_C^{1/3} \tag{6.46}$$

where Re_C and Pr_C are the Reynolds and Prandtl numbers of the heat-transfer fluid. Their values, as well as the heat-transfer fluid properties, are reported in Table 6.2. The obtained h_{OV} is around 200 W/m^2/K.

Table 6.2: Values of parameters used in the model.

Parameter	Description	Value
Bulk phase		
d_r	Reactor diameter	10.2 mm
ϵ_{bed}	Bed porosity	0.63
u_b	Surface velocity	0.017 m/s
ρ_{mix}	Density	4.65 kg/m^3
μ_{mix}	Viscosity	0.024 mPa.s
λ_{mix}	Thermal conductivity	0.16 W/m/K
$c_{p,mix}$	Heat capacity	31.4 J/mol/K
Re_P	Reynolds number	0.53
Pr	Prandtl number	0.32
Pe	Peclet number	0.17
Particle phase		
d_P	Particle diameter	160 µm
λ_P	Thermal conductivity of the particle	0.65 W/m/K
d_{pores}	Diameter of catalyst pores	10 nm
ϵ_{pores}	Porosity of catalyst pores	0.66
τ_{pores}	Tortuosity of catalyst pores	4
λ_P/λ_{mix}		4.01
d_r/d_P		63.9
Cooling fluid		
u_C	Surface velocity	4.4 m/s
ρ_C	Density	824.1 kg/m^3
μ_C	Viscosity	0.4 mPa.s
λ_C	Thermal conductivity	0.10 W/m/K
$c_{p,C}$	Heat capacity	2.45 kJ/mol/K
L_C	Characteristic length	15 mm
Re_C	Reynolds number	1.4x10^5
Pr_C	Prandtl number	10

Heat transfer equation in the catalytic pellet.

Inside the catalytic particle, the equation of heat conservation in stationary conditions in 1D is:

$$\frac{1}{r^2}\frac{d}{dr}\left(-\lambda_P r^2 \frac{dT_P}{dr}\right) = \sum_{j=1}^{N_r} r_j^* \Delta H_{ij}^r \tag{6.47}$$

where the first term represents the internal diffusion flux and the second is the heat source, due to the chemical reaction.

The boundary conditions for heat transfer equations in the catalyst's particle are:

- Heat flow at the particle center ($r = 0$) is null:

$$\left.\frac{dT_P}{dr}\right|_{r=0} = 0 \tag{6.48}$$

- Heat flow at the particle surface ($r = R_P$) is represented by the heat exchange with the bulk phase:

$$-\lambda_P \frac{dT_P}{dr}\bigg|_{r=R_P} = k_t \left(T_{bed} - T_P^S\right) \tag{6.49}$$

λ_P is the thermal conductivity of the catalytic particle and it depends on the internal porosity of the catalyst. It can be estimated as follows (Rothenberg, 2013):

$$\lambda_P = 4\lambda_{mix} \tag{6.50}$$

6.2.4 Numerical methods.

The heterogeneous model was implemented and solved with the software COMSOL Multiphysics. The momentum conservation is described by using the Darcy's equation module. The module Transport of Concentrated Species Interface is used to describe the mass transport at the fixed bed level. The Heat Transfer module is used to describe the heat transport at the fixed bed level. Transports at the catalytic pellet level were described by adding equations in weak form. The numeric model is solved by the software with a finite element method.

The module Thermodynamic Properties of Liquid and Gases is used for the estimation of different thermodynamic and thermophysical properties of single compounds and mixtures (ρ, μ, λ and c_p). The ideal gas law is adopted to describe the gas phase, as it was previously shown that it is appropriate to describe the fluid as a vapour phase in the reaction conditions considered (see section 4.2). The kinetic theory is used to evaluate thermal conductivities, while the Brokaw model is adopted for the estimation of viscosities.

The plug-flow (PFR) model was implemented and solved with the software COMSOL Multiphysics, as well. EDP modules were used to implement model equations.

6.2.5 Validation of the reactor model.

In the following, the results of the pseudo-homogeneous and the heterogeneous models are discussed and compared to experimental data for validation.

6.2.5.1 Concentration and temperature profiles along the bed.

Figure 6.3 presents the results of the heterogeneous model (dotted lines) and the plug-flow model (solid lines) compared to the experimental results. On the left, CO_2 conversion and CO selectivity are shown. First of all, we observe that the two models do not show any differences in the prediction of the composition in the bulk phase. This suggests that limitations to the mass transport, internal and external, can be excluded. The trends of both variables are well predicted by the models, but they show an overestimation of CO formation and an underestimation of CO_2 conversion compared to the experimental data. We have to remark that in the experimental conditions adopted, with τ_{mod} between 0 and 1.5 g.s/Nml, the kinetic model developed in Chapter 4 is not very accurate: for low τ_{mod}, in fact, the kinetic model predicts CO_2 conversions slightly lower than the experimental ones, with slightly higher CO selectivity. This can explain the gap between models predictions and experimental data, at least in part.

The lower conversion of CO_2 is reflected in the bed temperature profile. The right plot in Figure 6.3 shows the maximum temperature reached in the bed as a function of τ_{mod}: we observe that temperatures experimentally obtained are 1 to 5°C higher than those predicted by the model. This is in agreement with the observed lower CO_2 conversion. Lower conversion comports lower heat produced by the reaction and thus lower reactor temperatures. The temperature measured at $\tau_{mod} = 1.27$ g.s/Nml can be the result of a local hot point of the reactor.

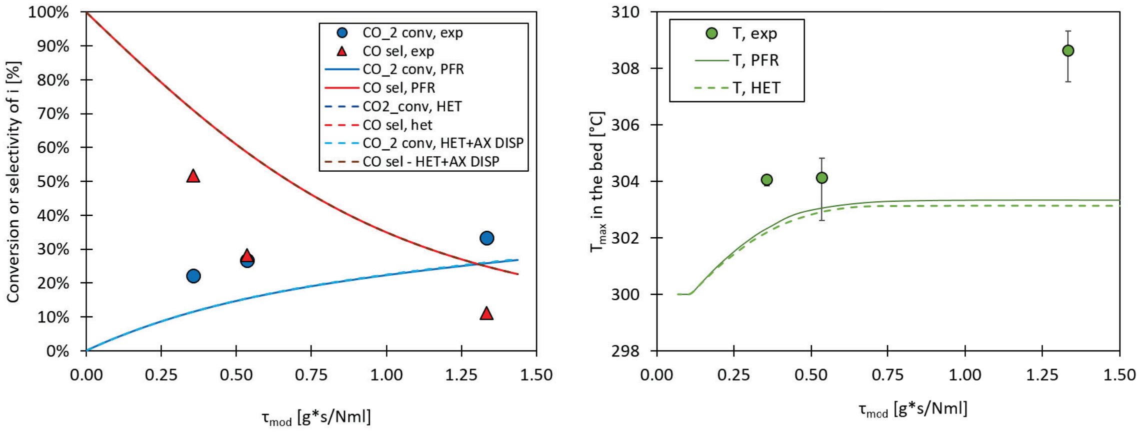

Figure 6.3: Left: Evolution of CO_2 conversion and CO selectivity with τ_{mod} at 300°C, 15 bar and H_2/CO_2 ratio of 3. Right: Evolution of maximum temperature along the bed with τ_{mod}. Points represent experimental data, dashed lines the predictions of the heterogeneous model, solid lines the predictions of the PFR model.

Figure 6.4 reports the parity plot of CO_2 conversion and CO selectivity. Most of the points agree with experimental data within an error of 50%. Definitely, the experimental points are not enough and not in the right range so that the model could be completely validated. We have previously discussed the reasons that led us to work in these conditions. For a complete validation of the model, data at higher values of τ_{mod} should be collected.

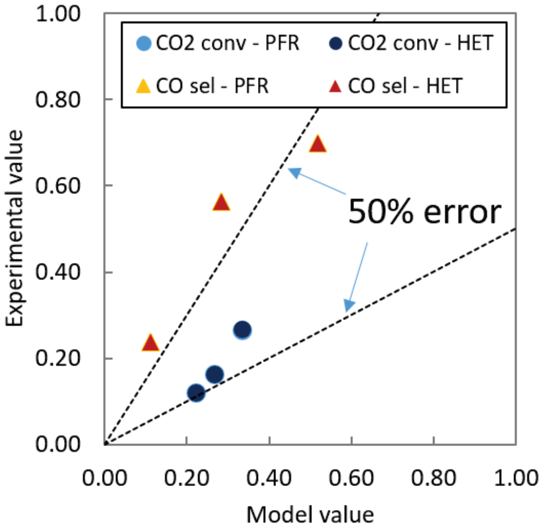

Figure 6.4: Parity plot for CO_2 conversion and CO selectivity.

Figure 6.5 shows the axial profile along the reactor for τ_{mod}= 1.33 g.s/Nml predicted by the heterogeneous and the pseudo-homogeneous models, in comparison with the corresponding experimental measured profile. We can observe that the temperatures predicted next to the reactor outlet are higher than the experimental one. This latter is lower than the inlet temperature and that could be an indication of a defective isolation of the reactor in the experimental bench. The temperature next to the reactor entrance is well predicted by the models, while the intermediate one is much lower than the experimental one. We have not enough information to conclude if this is due to the model hypothesis or to possible hot points in the fixed bed.

When comparing the results of the heterogeneous model with those of the pseudo-homogeneous

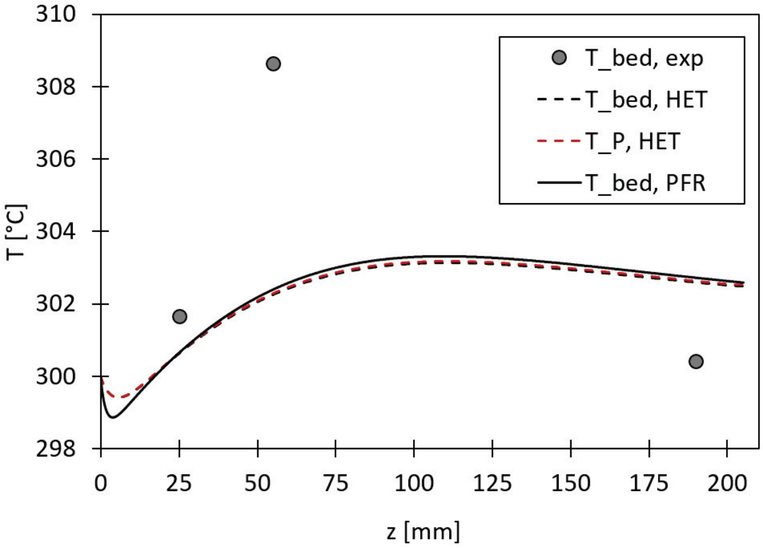

Figure 6.5: Axial temperature profile along the reactor for 300°C, 15 bar, H_2/CO_2 ratio of 3 and 1.33 g.s/Nml. Points represent experimental data, dashed lines the predictions of the heterogeneous model, solid lines the predictions of the PFR model.

one, we observe that next to the reactor entrance the PFR model (solid line) predicts a lower minimum temperature compared to the heterogeneous one (black dashed line). The difference between the two models can be explained by taking into account the effects of the axial thermal conductivity k_{ax}. Figure 6.6 shows the effects of decreasing k_{ax} on the bed temperature profile. We can observe that decreasing the heat transfer coefficient k_{ax} leads to deeper endothermic peaks and to a shift of the curve representing the T_{bed} axial profile of the heterogeneous model towards that of the PFR model. k_{ax} represents the axial thermal conductivity in the bed. This parameter is not taken into account by the PFR model, thus decreasing the value of k_{ax} allows to reduce the effects of this parameter, approaching the heterogeneous model to a pseudo-homogeneous model.

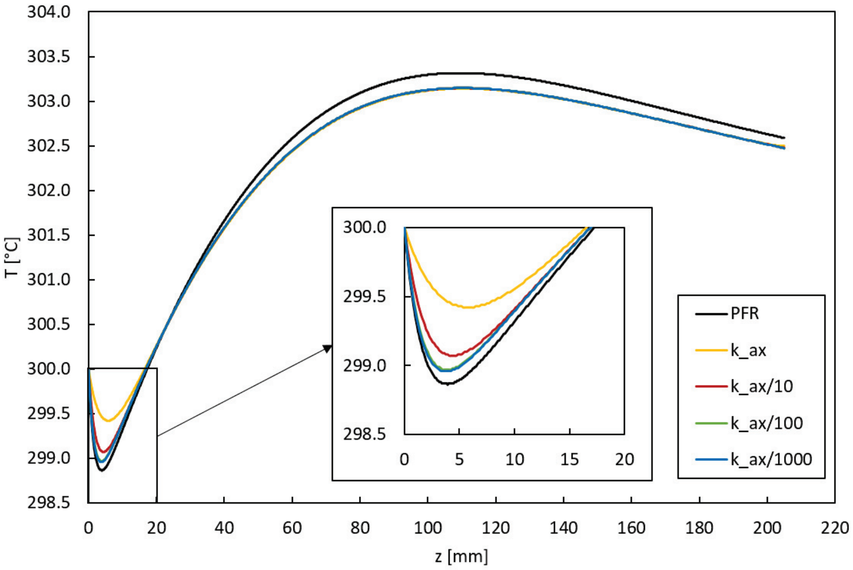

Figure 6.6: Effects of the parameter k_{ax} on bed temperature.

Figure 6.5 also shows the particle temperature profile at the surface along the reactor (red dashed line). This temperature is very close to the bed temperature, an indication that external heat transfer limitations can be considered negligible.

Figure 6.7 shows the profiles along the catalytic particle of CO_2 and CO concentrations and of particle temperature at the inlet and outlet of the reactor. We observe that CO_2 diffuses towards the particle center ($r = 0$) where it reacts, as expected. On the contrary, CO acts as a product at the reactor inlet, diffusing from the particle center ($r = 0$) towards the particle surface, while at the reactor outlet it acts as reactant, diffusing from the surface towards the center. The temperature in the particle decreases towards the particle center at the reactor inlet, when the endothermic RWGS prevails and thus the heat is required by the reaction; at the reactor outlet, when the FT reaction prevails, the heat is generated by the reaction and thus the particle temperature is higher at the particle center. However, all these profiles are almost flat, indicating that internal transport limitations are negligible.

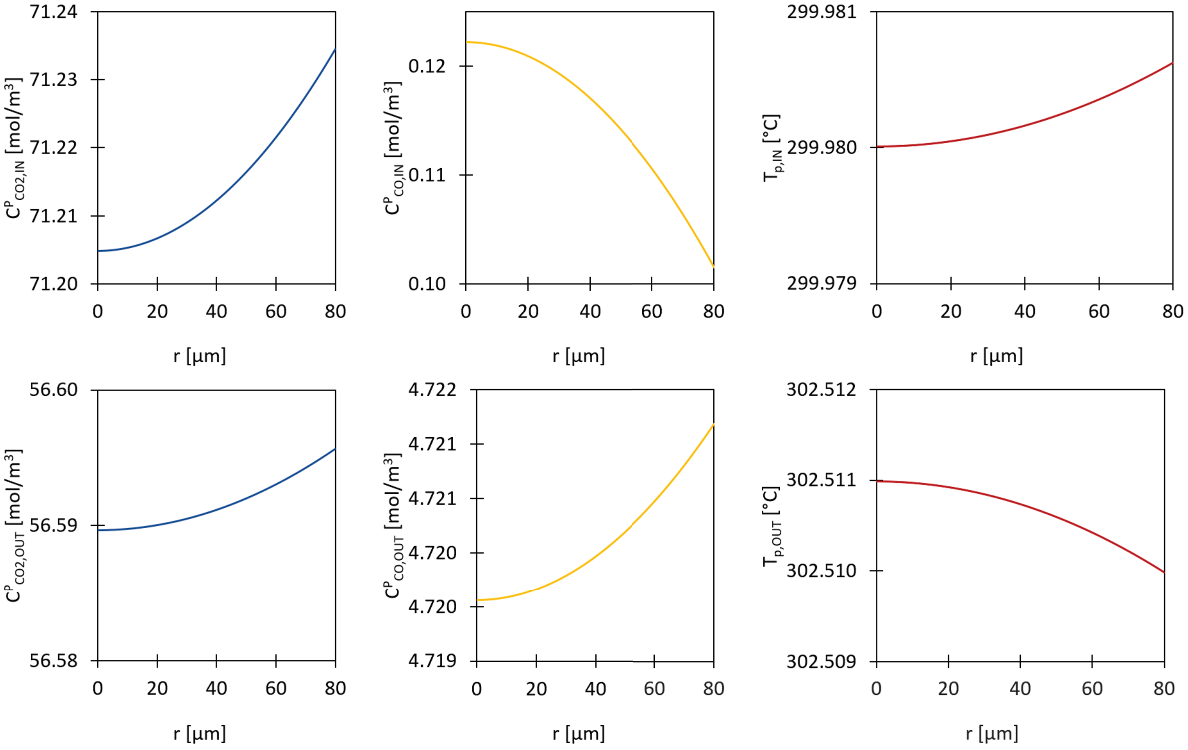

Figure 6.7: Profiles of concentration of CO_2 and CO and of temperature in the catalytic pellet, predicted by the heterogeneous model at the reactor inlet (top line) and at the reactor outlet (bottom line).

We have thus shown that, in these conditions, limitations of internal and external mass and heat transfer limitations can be neglected and the pseudo-homogeneous model is enough to describe the behaviour of the reactor with acceptable accuracy. Some investigations are still needed to verify the hypothesis on the heat exchange.

6.2.5.2 CO influence.

The predictions of the models when CO fraction is increased in the feed are reported in Figure 6.8 in comparison to the experimental data. The model is able to predict accurately the CO_2 and the total C conversion variations. However, it clearly overpredicts the CO conversion for CO fractions $> 2\%$. The kinetic model has been developed for pure CO_2/H_2 mixtures, thus it is expected that, when CO is added to the feed, it is not able anymore to predict the results with good accuracy. For applications to CO/CO_2 mixtures, experimental data should be collected in the lab-scale reactor with CO/CO_2 mixtures and then new kinetic model parameters should be estimated.

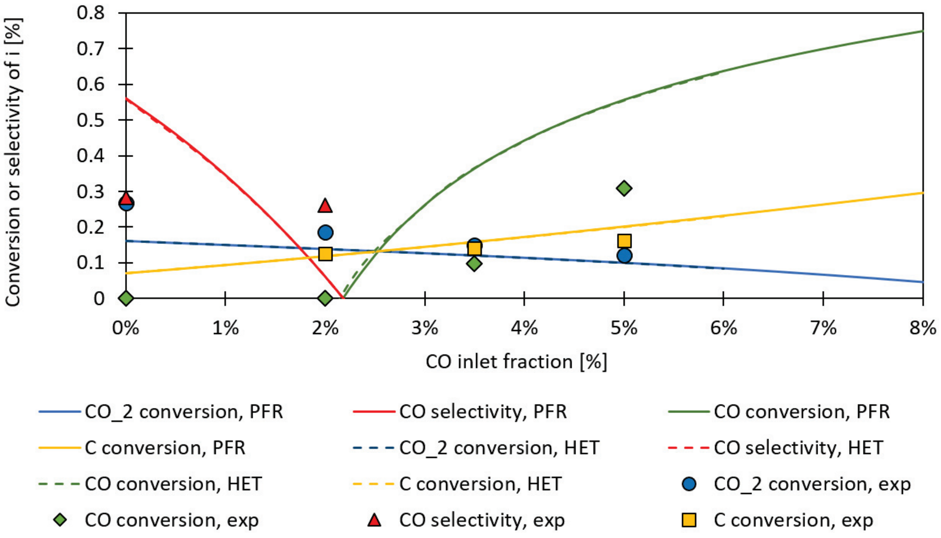

Figure 6.8: Evolution of CO_2 and CO conversions, CO selectivity and total C conversion with CO molar inlet fraction in the feed. Points represent experimental data, dashed lines the predictions of the heterogeneous model, solid lines the predictions of the PFR model. Conditions tested: 300°C, 15 bar, H_2/C ratio of 3 and 1.33 g.s/Nml.

6.2.6 Conclusion and perspectives on the reactor modelling.

In conclusion, we have developed a heterogeneous model to describe the scaled-up reactor behaviour and we have compared it with a pseudo-homogeneous one and validated them on the experimental data previously obtained.

The complete validation of the model was not possible because of the low number of available experimental points. We are able to predict the composition of the gas with an acceptable accuracy, while the temperature predictions present higher deviations.

We have also shown that the heterogeneous model in these conditions does not provide more useful informations than the pseudo-homogeneous one, indicating that the mass and heat transfer limitations at this scale are still a negligible phenomenon.

Therefore, we have presented a first scale-up stage, but more experimental points are needed to finally validate the model.

Finally, we have shown that our kinetic model, described in Chapter 4, overpredicts the CO conversion when it is applied for $CO/CO_2/H_2$ mixtures. This was expected as the model has not been developed for this kind of mixtures. Experimental tests at the lab-scale with $CO/CO_2/H_2$ mixtures would allow to adjust the kinetic parameters of the model developed in Chapter 4 so that it becomes able to accurately predict the CO conversion.

6.3 Enhancement of the CO_2 hydrogenation performances by using a membrane reactor for water removal.

We have already discussed about the role of water on the reaction performances. Water is believed to be the cause of catalyst deactivation, because of its tendency to favour iron carbides oxidation, thus leading to a loss of activity towards the formation of long-chain hydrocarbons.

(Dry, 1990) Moreover, high H_2O partial pressures contribute to shift the RWGS equilibrium towards the consumption of CO and the formation of CO_2, leading to lower conversion and inhibition of the FT reaction rate. (Rohde et al., 2008) Selective removal of water during CO_2 hydrogenation could increase the process performances by reducing catalyst inhibition and deactivation.

In this section, a membrane reactor model is presented, with the aim to observe the effects of water removal through a membrane and the benefits that this can cause to the reactants conversion. A 1D plug-flow model is developed and presented in the following. Then results of the model are shown and discussed.

6.3.1 Equations of the membrane reactor model.

The reactor configuration is shown in Figure 6.9 and its properties are summarized in Table 6.3. The internal tube is filled up with catalyst particles and constitutes the reactive zone. The tube wall is coated with a water perm-selective membrane. Water permeates through the membrane due to the partial pressure gradient between reactive and permeation zones. The shell side is the permeate zone where a gas is fed to sweep the permeated water. N_2 and H_2 have been considered as sweep gases, in order to investigate the effects of the sweep gas nature on the overall performances of the membrane. The membrane considered in this work is a ZSM-5 (MFI type zeolite) membrane, permeable to H_2O and partially to H_2, whose performances are summarized in Table 6.4. (Bernal et al., 2000) The performances of this membrane significantly decline when temperature is increased from 200 to 300°C. However, we have chosen this membrane because it is the one that presents the best performances in terms of permeability and perm-selectivity at 300°C.

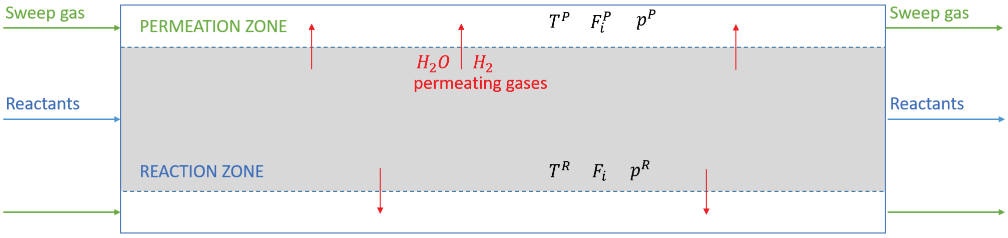

Figure 6.9: Configuration of the fixed-bed reactor with water removal via perm-selective membrane.

Reactive zone.

The mass balance for the reactive zone is written as:

$$\frac{1}{S_r}\frac{dF_i}{dz} = \rho_{bed}\sum_j \nu_{i,j} r_j - \frac{A_r}{V_r} J_i \tag{6.51}$$

with $S_r = \frac{\pi}{4} d_r^2$ the cross-sectional area of the tube, $A_r = \pi d_r L$ the lateral area of the tube and $V_r = S_r L$ the reactor volume. $\sum_{j=1}^{N_r} \nu_{ij} r_j$ represents the mass source, due to the chemical reaction, and J_i is the flux that permeates through the membrane. J_i is expressed as the product of the permeability Q_i and the difference of partial pressures between the reactor and the permeate sides:

$$J_i = Q_i \left(p_i^R - p_i^P\right) \tag{6.52}$$

The heat balance for the reactive zone is written as:

$$u^R c^R_{p,mix} \rho^R_{mix} \frac{dT^R}{dz} = -Q_0 + Q_r - Q_m \tag{6.53}$$

Table 6.3: Values of parameters used in the model.

Parameter	Description	Value
d_r	Reaction zone diameter (tube)	10.2 mm
d_{sh}	Permeation zone diameter (shell)	12.7 mm
L	Reactor length	205 mm
e_m	Membrane thickness	6 μ
e_w	Wall thickness	2 mm
d_P	Particle diameter	160 μ
ϵ_{bed}	Porosity of the catalytic bed	0.63
ρ_{bed}	Density of the catalytic bed	822.4 kg/m^3
λ_m	Thermal conductivity of the membrane	1.17 W/m/K
λ_w	Thermal conductivity of the wall	17 W/m/K
Reaction side		
H_2/CO_2	Inlet molar ratio in the reactor side	3
T^R_{IN}	Inlet temperature in the reactor side	300°C
p^R_{IN}	Inlet pressure in the reactor side	15 bar
F^R_{IN}	Inlet flow in the reactor side	0.021 mol/min
Permeation side		
T^P_{IN}	Inlet temperature in the permeation side	300°C
p^P_{IN}	Inlet pressure in the permeation side	$= \phi\ p^R_{IN}$
F^P_{IN}	Inlet flow in the permeation side	$= SW\ F^R_{IN}$
ϕ	Ratio between pressure in permeation and reaction sides	0.9
SW	Ratio between flows in permeation and reaction sides	3

Table 6.4: Permeabilities and perm-selectivity of the ZSM-5 (MFI type zeolite) membrane at different temperatures. (Bernal et al., 2000)

Temperature [°C]	Q_{H_2O} [mol/(m^2.s.Pa)]	Q_{H_2O}/Q_{H_2} [-]
200	5x10^{-7}	50
250	4x10^{-7}	30
300	1.5x10^{-7}	6

where Q_r is the heat source due to the reaction, Q_m is the heat removed with the permeation of compounds and Q_0 is the heat exchanged with the permeation zone:

$$Q_r = \sum_j r_j \left(-\Delta H^r_j\right) \tag{6.54}$$

$$Q_m = \frac{A_r}{V_r} \left(\sum_j J_i c_{pi}\right) \left(T^R - T^P\right) \tag{6.55}$$

$$Q_0 = U_{perm} \frac{A_r}{V_r} \left(T^R - T^P\right) \tag{6.56}$$

The heat transfer coefficient U_{perm} is estimated as:

$$\frac{1}{U_{perm}} = \frac{1}{\alpha_{rad}} + \frac{A_r}{A_{log}} \frac{1}{\lambda_m} + \frac{A_r}{A_{sh}} \frac{1}{h_{perm}} \tag{6.57}$$

where α_{rad} is estimated according to Eq. 6.40, λ_m is set equal to 1.17 W/m/K and h_{perm} is estimated as follows (Najari et al., 2019):

$$h_{perm} = \frac{Nu^P \lambda^P}{d_{sh} - d_m} \tag{6.58}$$

with

$$Nu^P = 0.0256 \left(Re^P\right)^{0.8} \left(Pr^P\right)^{0.3} \tag{6.59}$$

A_{log} is the logarithmic mean area between the reactor and the membrane:

$$A_{log} = \frac{ln \dfrac{d_m}{d_r}}{2\pi L} \tag{6.60}$$

$A_{sh} = \pi d_{sh} L$ is the lateral area of the shell.

Pressure drops are described with the Ergun's equation:

$$\frac{dp^R}{dz} = -\frac{u^R}{d_P} \left(\frac{1 - \epsilon_{bed}}{\epsilon_{bed}^3}\right) \left(150 \frac{(1 - \epsilon_{bed})\, \mu_{mix}^R}{d_P} + 1.75 \rho_{mix}^R u^R\right) \tag{6.61}$$

Permeation zone.

The mass balance for the permeation zone is written as:

$$\frac{1}{S_r} \frac{dF_i^P}{dz} = \frac{A_r}{V_r} J_i \tag{6.62}$$

The heat balance for the permeation zone is written as:

$$u^P c_p^P \rho^P \frac{dT^P}{dz} = Q_0 + Q_m - Q_c \tag{6.63}$$

where Q_c is the heat exchanged with the outside:

$$Q_c = h_C \frac{\pi d_{out}}{S_r} \left(T^R - T^C\right) \tag{6.64}$$

Supposing that the reactor is placed into an isolated box where a ventilator allows the uniform distribution of the heat, the heat transfer coefficient estimated for the forced conduction of air is 238.5 W/m^2/K.

Pressure drops in the permeation zone are considered negligible.

The model includes two important parameters that have high influence on the membrane reactor performances. The pressure ratio ϕ is defined as the ratio between total pressure in the permeate zone and that in the reactor:

$$\phi = \frac{p^P}{p^R} \tag{6.65}$$

and the sweep ratio SW is defined as the ratio of molar flows in the permeate and in the reactor:

$$SW = \frac{F_{SW}}{F_0^R} \tag{6.66}$$

For the simulation in the base case ϕ is set to 0.9 and the SW is set to 3.

6.3.2 Results of the simulation of a membrane reactor model.

Figure 6.10 shows the results of the simulation of a membrane reactor with H_2 or N_2 as sweep gases compared with a traditional plug-flow reactor without membrane. The CO_2 conversion and the CO and total HCs selectivity are analysed.

We can observe that, when adding the membrane, the CO_2 conversion distinctly increases without major modifications of the products selectivity. In the case where H_2 is used as sweep gas, the increase of CO_2 conversion is more significant.

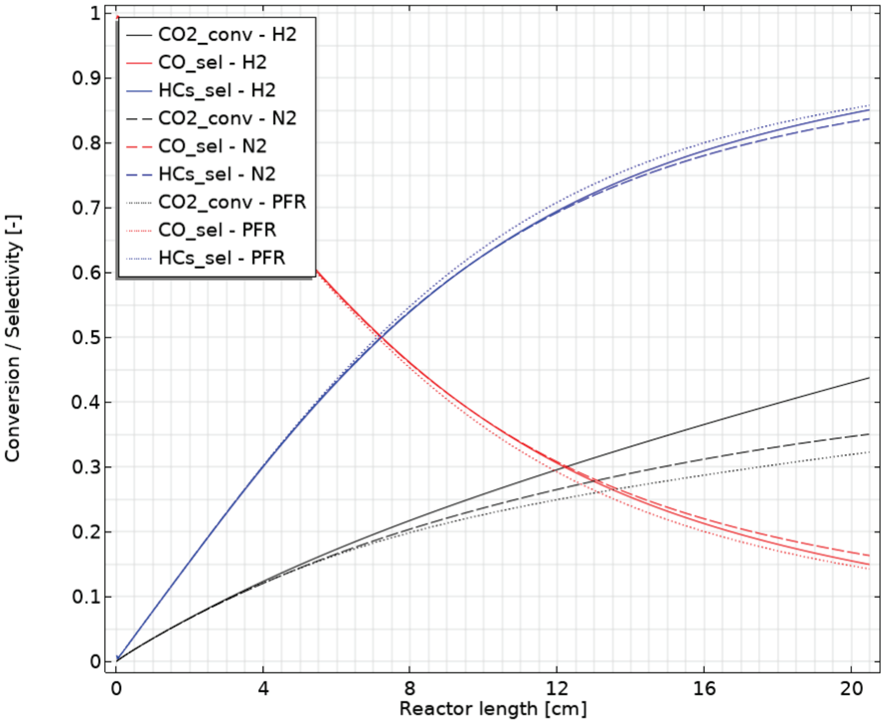

Figure 6.10: Evolution of CO_2 conversion, CO selectivity and HCs selectivity along the reactor. Simulations performed for a membrane reactor with H_2 or N_2 as sweep gas and for a traditional PFR without membrane.

To understand the reason why this happens, we have to consider the flows that permeates the membrane that are presented in Figure 6.11. When N_2 is used as sweep gas, both H_2O and H_2 pass through the membrane from the reactive side towards the permeation side. Thus, water is removed from the reactor, but there is also a loss of the reactant H_2. On the contrary, when H_2 is used as sweep gas, water is removed almost at the same extent, but H_2 flows on the opposite direction, from the permeation to the reaction zone, avoiding the loss of reactants and contributing to create over-stoichiometric conditions in the reaction side.

We have simulated a case where only H_2 can permeate the membrane, in order to verify that the increase of CO_2 conversion that we observe when H_2 is used as sweep gas is mainly due to water removal and not to the continuous feed of hydrogen through the membrane. Figure 6.12 shows the results of this simulation compared with the case with H_2 as sweep gas. Without water removal but with H_2 permeation, an increase of conversion compared to the traditional PFR case is observed, but this increase is limited compared to the case with water removal. We can thus conclude that the use of H_2 as sweep gas allows to increase the CO_2 conversion in higher extent than when N_2 is used because it avoids the loss of reactants, at the same time granting the removal of water.

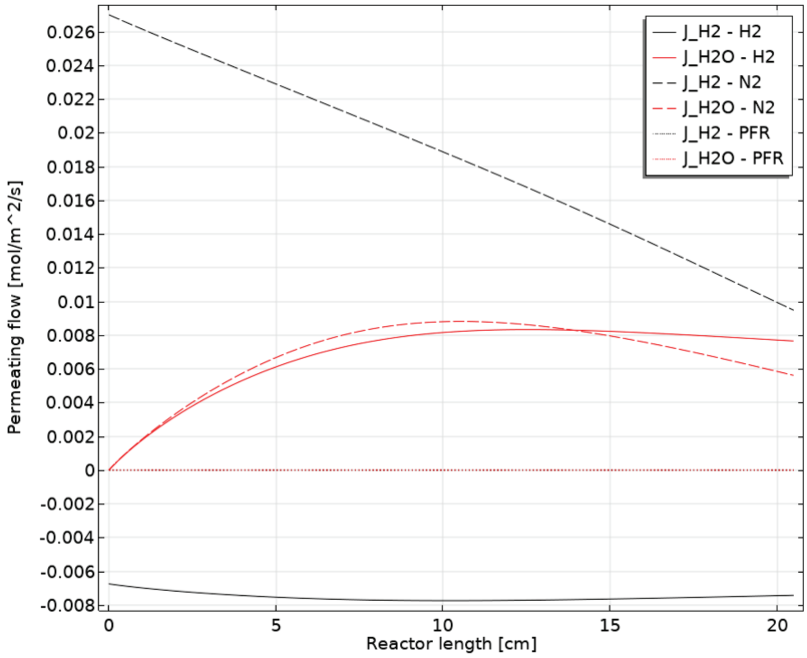

Figure 6.11: Evolution of permeation flows J_i of water and hydrogen along the reactor. Simulations performed for a membrane reactor with H_2 or N_2 as sweep gas and for a traditional PFR without membrane.

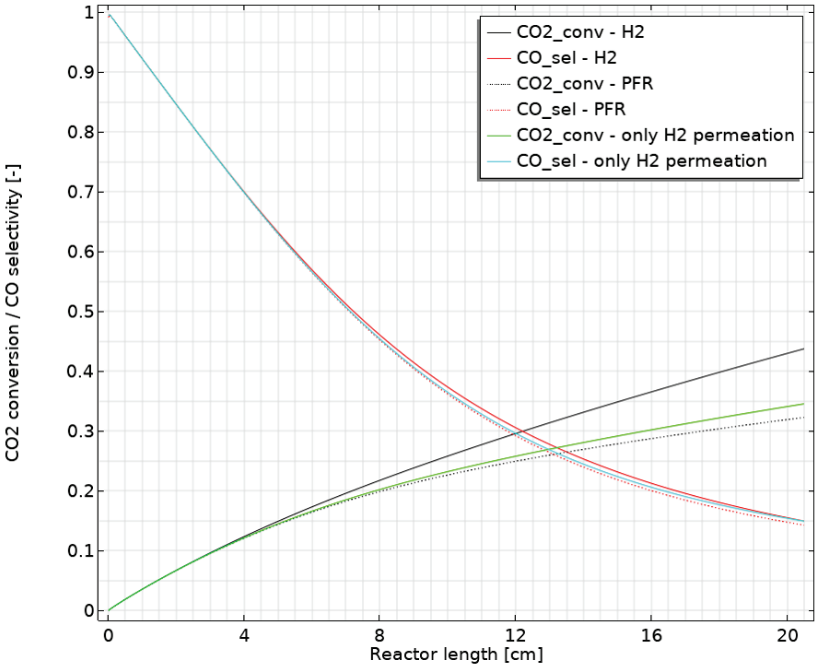

Figure 6.12: Evolution of CO_2 conversion and CO selectivity along the reactor. Simulations performed for a membrane reactor with H_2 as sweep gas with a membrane permeable only to H_2 or to both H_2 and H_2O and for a traditional PFR without membrane.

Figure 6.13 shows the axial profile of the bed temperature T_{bed} along the reactor. We can observe that the maximum temperature reached in the membrane reactor with H_2 as sweep gas is slightly higher than in the case without membrane (about 1°C higher). This is due to the fact that the heat produced by the reaction from the increase of CO_2 conversion Q_R is only partially compensated by the increase of the heat exchanged with the shell side Q_P (see

Figure 6.14), resulting in higher temperatures in the bed. In the case of N_2 only slight differences compared to the traditional PFR case are observed. The heat exchanged through the membrane by permeation of compounds is negligible.

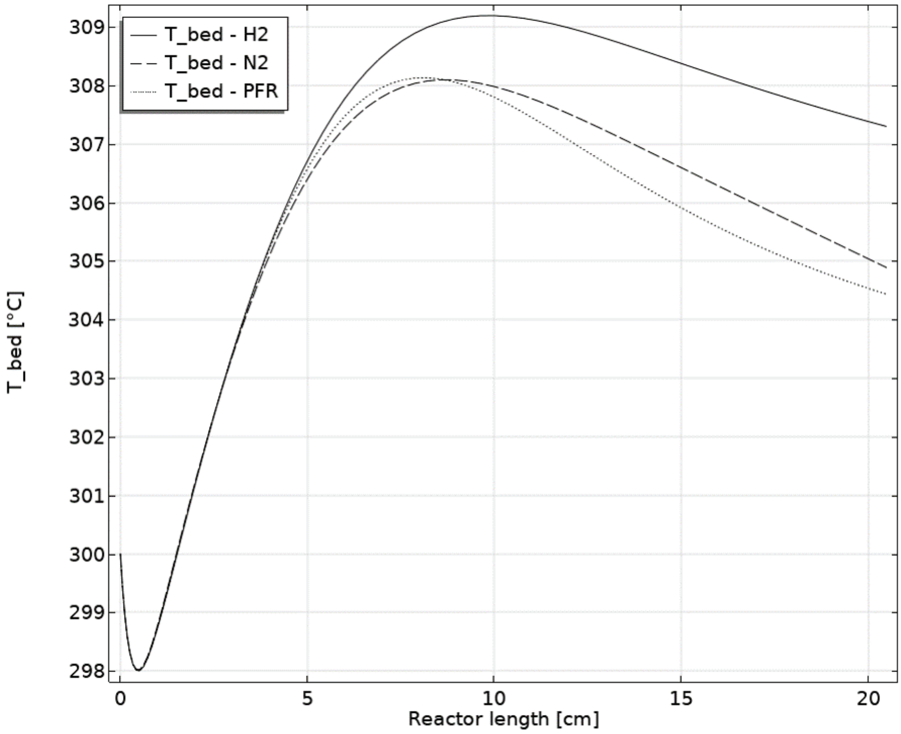

Figure 6.13: Axial profile of bed temperature along the reactor. Simulations performed for a membrane reactor with H_2 or N_2 as sweep gas and for a traditional PFR without membrane.

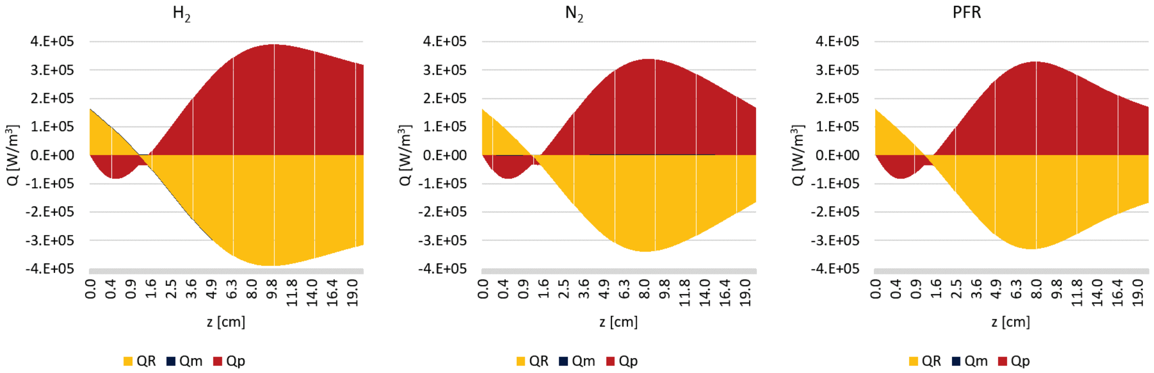

Figure 6.14: Contributions to heat exchanged between the reactor and the shell for a membrane reactor with H_2, with N_2 and for a traditional PFR without membrane.

To optimize the water removal, we have performed a parametric study by varying the values of the parameters ϕ and SW. Their effects are shown in Figure 6.15. The first line is referred to the case where H_2 is used as sweep gas. To maximize the conversion of CO_2, high values of ϕ are required. Increasing the ϕ value however leads to an increase of the CO selectivity at the expense of hydrocarbons. Values of ϕ of about 0.8 allows to reach selectivity towards HCs higher than 83%, maximizing their yield. The SW has less important effects on CO_2 conversion and products selectivity. However, the sweep ratio significantly influences the efficiency of heat removal: high values of SW are necessary to reduce the maximum ΔT in the reactor (see Figure 6.16). Values of *SW* higher than 10 allows to keep the maximum ΔT below 6°C, allowing an efficient cooling of the reactor.

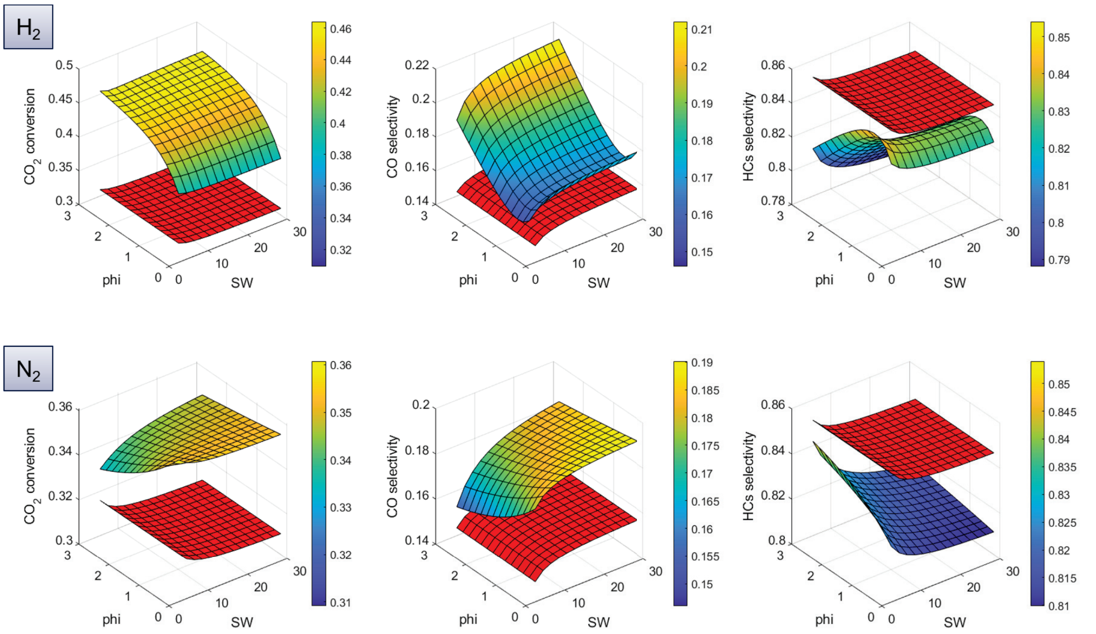

Figure 6.15: Effects of variation of ϕ and *SW* on the CO_2 conversion, CO selectivity and HCs selectivity. Red surfaces refer to the base case without membrane. First line is referred to the case with H_2 as sweep gas and the bottom line is referred to the case with N_2 as sweep gas.

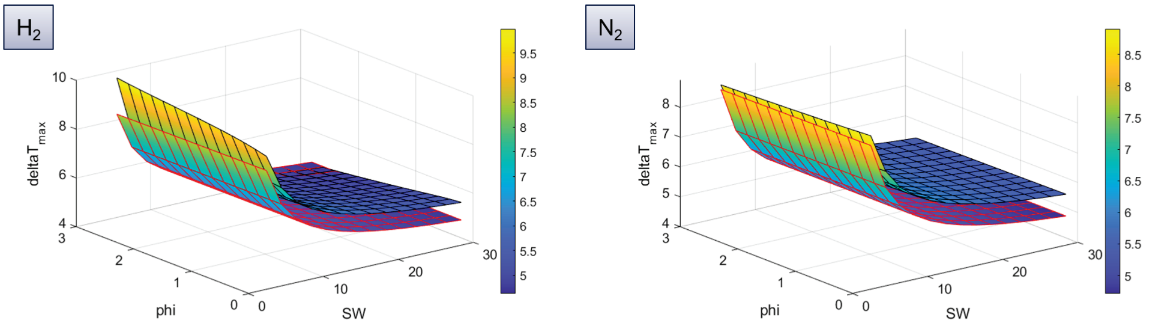

Figure 6.16: Effects of variation of ϕ and *SW* on the ΔT_{max} in the bed. Surface with red edges refers to the base case without membrane. Figure on the left is referred to the case with H_2 as sweep gas and figure on the right is referred to the case with N_2 as sweep gas.

In the case of N_2, we observe that small values of ϕ and high values of *SW* allow the increase of the CO_2 conversion to values up to 35%. In these conditions however, the formation of CO is favoured over that of hydrocarbons. High values of ϕ and low values of *SW* are required to maximize the selectivity towards hydrocarbons. These variations are however quite small, with conversions varying between 0.33 to 0.35 and HCs selectivity varying between 0.81 and 0.84. The *SW* again influences the maximum ΔT in the reactor, thus high values of flows in permeation size are required to provide a good cooling of the reactor.

6.3.3 Final considerations and perspectives on the membrane reactor.

In conclusion, we have shown that removing the water formed during the reaction via a membrane reactor has in general positive effects on the HCs yields. In particular, the sweep gas used has a very important influence: when using an inert gas such as nitrogen, the performances are only slightly increased because of the loss of the reactant across the membrane. Membranes able to separate water selectively at high temperatures, keeping a good mechanical stability, have not been developed yet. The loss of reactant, due to the hydrogen permeation through the membrane, makes the increase of performances very slight. On the contrary, when using hydrogen as sweep gas, the loss of reactants is avoided and the observed increase of performances is more evident. Performing the process in a membrane reactor with H_2 as sweep gas and with ϕ around 0.8 and SW around 10 can thus allow to obtain good HCs selectivity. Moreover, the configuration that we have chosen, with the internal tube filled of catalyst, allows to the feed in the shell side to play both the roles of sweep gas and cooling fluid. This configuration avoids the need to add an additional system for cooling, as high sweep flows will provide a sufficient cooling, at least in the operating conditions tested.

The main limit of these simulations is that they showed that the global HCs yield can be increased, but they do not allow to show how the hydrocarbons distribution changes when the membrane is added. Future work should be focused on experimental studies of membrane reactors, so that experimental data could be collected and used to make the model able to predict the product distribution. Alternatively, a kinetic model based on mechanistic assumptions could be used in this kind of simulations. However, these models, such as the one that we have developed (in Chapter 5), generally contain a large number of parameters and are harder to code.

6.4 Process simulation.

This final section deals with process simulations that we have performed in order to estimate the energy efficiency of the process and to analyse possible ways for its optimisation.

As we have already shown, the main part of the obtained products is represented by methane and short alkenes. The CO_2 conversion achieved, at least in reference conditions, is only about 30%. The aim of these simulations has thus to be the maximization of the recovery of the obtained products from the unreacted gases and the increase of the total CO_2 conversion. In order to increase the CO_2 conversion, the unreacted gases could be recirculated to the reactor inlet, but this requires their separation from the hydrocarbons products. Separation of CO_2 and H_2 from light hydrocarbons can be performed by using selective polymeric membranes that allow a good separation of CO_2 and H_2 from CH_4 and light hydrocarbons. Polyimide membranes are currently used in different industrial applications, especially for the purification of natural gas, because they present high CO_2 permeability and high CO_2/CH_4 selectivity (>30). (Sanders et al., 2013; Baker, 2002; He, 2018; Ungerank and Baumgartner, 2010)

In this work, we will present two different process configurations:

1. the first configuration includes two traditional tubular reactors for the CO_2 hydrogenation to increase the CO_2 total conversion, followed by a separation system made of three flash units at 5, 0.1 and -30°C.

2. the second configuration includes separation of unreacted gases and their recirculation to the reactor inlet. The separation is made of two flashes, one at 5°C and one at 0.1°C, followed by two membrane separation units containing polyimide membranes that can separate with high selectivity CO_2 and H_2 from the light hydrocarbons.

6.4.1 Methodology.

Process simulations were performed with the software ProSimPlus for process simulation and optimization.

The system considers as compounds the reactants CO_2 and H_2, the co-products CO and H_2O and the products n-alkanes and 1-alkenes from C_1 to C_{20} and alcohols from C_1 to C_6. The thermodynamic properties and the phase equilibrium of pure components and mixtures are estimated with a thermodynamic model. In this work, the Peng-Robinson (PR) equation of state coupled with the Boston-Mathias function is used to describe the phase behaviour of the system. The PR equation of state is widely applied in the field of refining and synthetic hydrocarbons production (Peng and Robinson, 1979; Elia et al., 2010; Sudiro and Bertucco, 2009; König et al., 2015a), while the Boston-Mathias function allows a better description of the light hydrocarbons behaviour. (Boston and Mathias, 1980)

The reactor units are simulated as plug-flow reactors where kinetic laws are described. The macro-kinetic model derived in Chapter 4 is implemented via a script. Pressure drops in the reactors are calculated with the Darcy equation, while for the estimation of the axial temperature profile the heat exchange coefficient is provided.

Flash units are simulated as flash at specified temperature and pressure. The recovery ratio of each compound in a specified phase is estimated as:

$$Recovery\ of\ i\ in\ phase\ x\ = \frac{F_i\ in\ phase\ x}{F_i\ in\ inlet\ stream} \tag{6.67}$$

Separation via membrane is simulated by using the Membrane filter module where the permeances of each compound are specified, as well as the temperature of operation. The recovery of each compound at the membrane outlet is estimated as:

$$Recovery\ of\ i\ = \frac{F_i\ in\ permeate}{F_i\ in\ inlet\ stream\ tube\ side\ + F_i\ in\ inlet\ stream\ shell\ side} \tag{6.68}$$

SPEC modules are used to add specifications and constraints.

Lower (LHV) and Higher (HHV) heating values are estimated for each stream via the scriptlet option in ProSimPlus. Energy efficiency η_{PtX} and the carbon conversion η_C are estimated according to the following equations:

$$\eta_{PtX} = \frac{\sum_i LHV_i \dot{m}_i}{LHV_{H_2}\dot{m}_{H_2} + \dot{P}_u} \tag{6.69}$$

$$\eta_C = \frac{\sum_i \dot{m}_{C,i}}{\dot{m}_{C,IN}} \tag{6.70}$$

where $\dot{P}_u$ is the power needed for the utilities and it is calculated as the absolute value of the sum of the heat to provide or released by each unit.

The Wobbe index, that is commonly used to evaluate fuel interchangeability in terms of heat release rate (Borman and Ragland, 1998; Zhao et al., 2019), is defined as:

$$WI = \frac{HHV_{fuel}}{\sqrt{d_{fuel}}} \tag{6.71}$$

where d_{fuel} is the density of the fuel relative to the density of air (at 25°C and 1 atm). WI is estimated from ProSimPlus with the scriptlet function.

6.4.2 First configuration: two reactors in series.

This first configuration, shown in Figure 6.17, includes two reaction steps to increase the CO_2 total conversion. The reactants H_2 and CO_2 are fed to the reactor R-1 after pre-heating at 300°C (E-1). H_2 is considered to be derived directly from an electrolyser and to have the pressure of 15 bar. CO_2 is first compressed to 15 bar via the compressor C-1 and then mixed

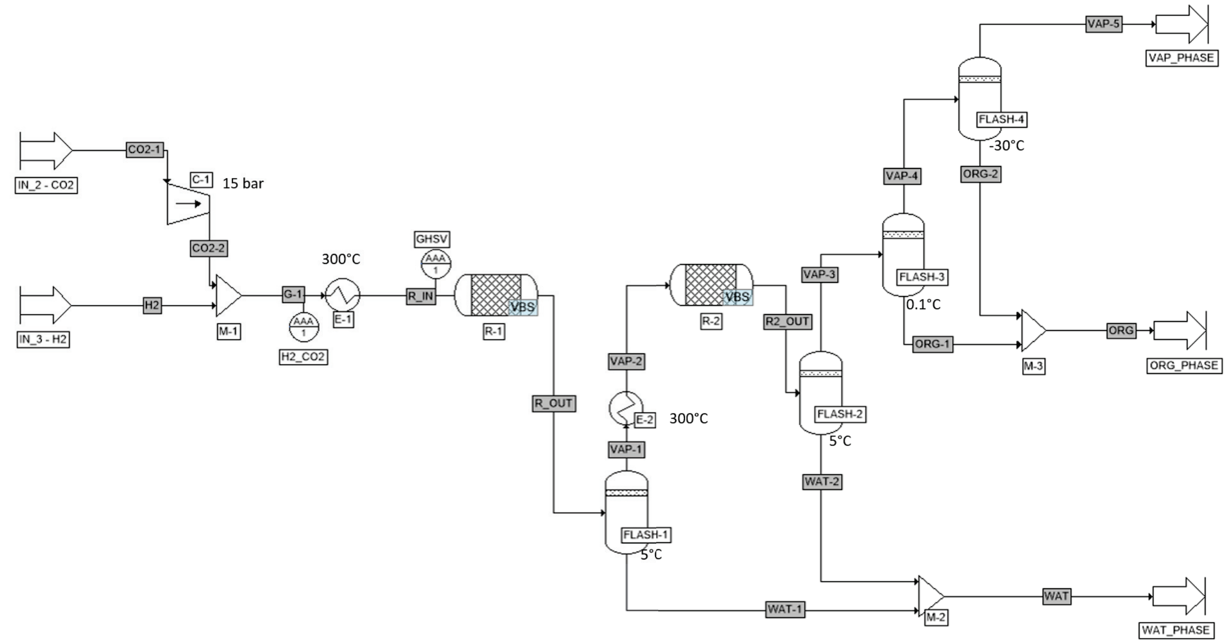

Figure 6.17: Schematic diagram of the process configuration with two reactors in series.

Table 6.5: Summary of properties of each simulated unit in configuration 1.

Compressor C-1		**Flash FLASH-2**	
Pressure	15 bar	Temperature	5°C
Isoentropic efficiency	0.65	Pressure	of stream R2_OUT
Exchanger E-1		**Flash FLASH-3**	
Temperature	300°C	Temperature	0.1°C
Exchanger E-2		Pressure	of stream VAP-3
Temperature	300°C	**Flash FLASH-3**	
Flash FLASH-1		Temperature	-30°C
Temperature	5°C	Pressure	of stream VAP-4
Pressure	of stream R_OUT		
Reactors R-1 and R-2			
Inner reactor diameter $d_{r,in}$		1.11 m	
Reactor length L_r		22.2 m	
Particle diameter d_P		160 μ	
Diameter of shell d_C		2.5 m	
Temperature of cooling fluid T_C		300°C	
Mass flow of cooling fluid $\dot{m}_C$		43500 kg/s	
Heat capacity of the cooling fluid $c_{P,C}$		2.45 kJ/kg/K	
Heat exchange coefficient catalytic bed side h_{int}		470 W/m^2/K	
Heat exchange coefficient outlet side h_{ext}		4000 W/m^2/K	

with the H_2 stream. Reactors R-1 and R-2 are simulated as fixed-bed reactors with catalytic reactions and kept at 300°C thanks to a cooling fluid circulation. Between the two reaction steps, the gas is passed through a flash unit at 5°C (FLASH-1) to remove the formed water and then through an heater (E-2) to heat it up to 300°C. After the second reactor (R-2), the gas is passed through a separation unit that consists in three flashes in series: FLASH-2 operates at

5°C and allows the separation of water, FLASH-3 operates at 0.1°C and allows the separation of most of the heaviest products and finally FLASH-4 operates at -30°C and allows further separation of short-chain products. The properties of each unit are summarized in Table 6.5.

The results obtained from this simulation are discussed in the following. The mass flow diagram of the simulated process is shown in Figure 6.18.

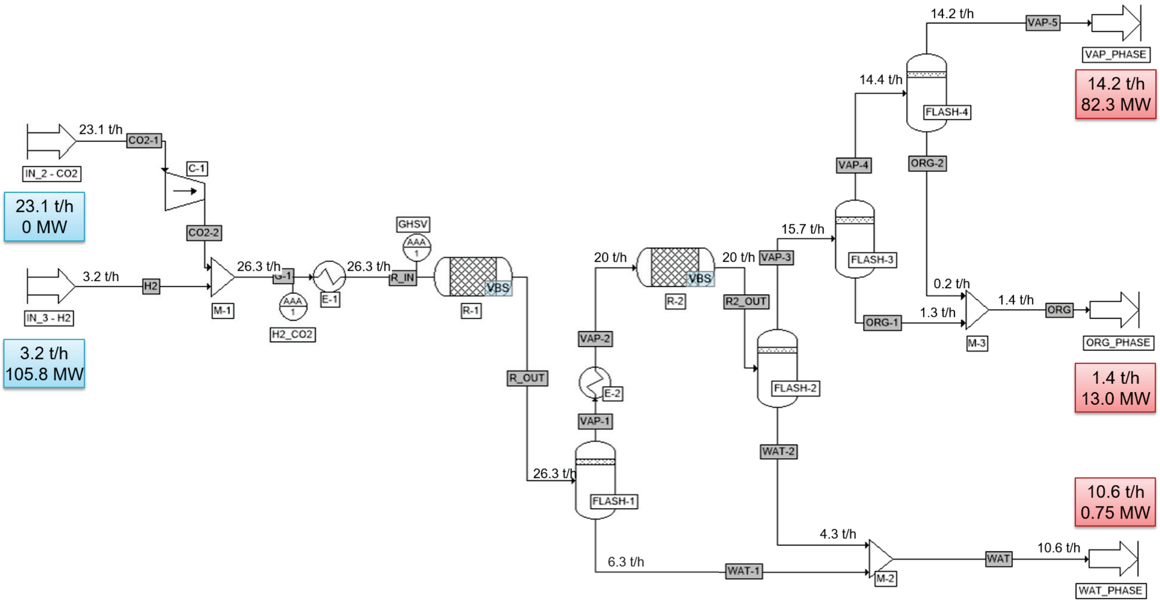

Figure 6.18: Mass flow diagram of the simulated process with configuration 1.

In both reactors CO_2 is converted to an extent close to 35%, with 12% of selectivity to CO in R-1 and 45% of CO conversion in R-2, as shown in Figure 6.19. The FLASH-1 allows the separation of almost all water and some ethanol, while all other products stay in gaseous phase, as shown in Figure 6.19 (right).

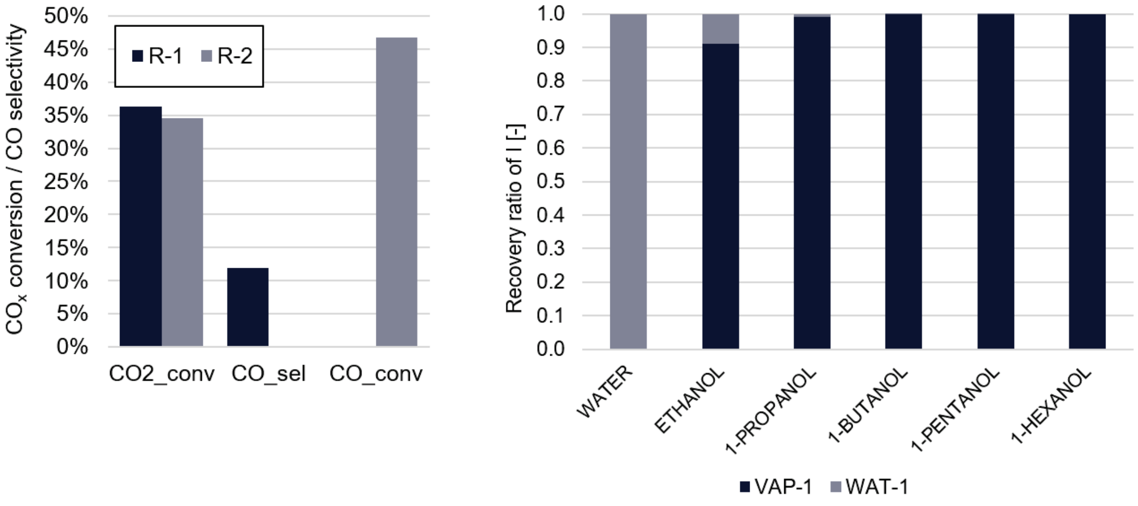

Figure 6.19: Conversion and selectivity in reactors R-1 and R-2 (on the left) and recovery ratios of water and oxygenated compounds in FLASH-1 (on the right). Results obtained for configuration 1.

The three flashes FLASH-2, FLASH-3 and FLASH-4 allow the separation of the heaviest products from the light ones. Figure 6.20 reports the recovery ratio of each compound in the liquid streams (WAT-2, ORG-1 and ORG-2) and shows that cooling to -30°C allows to separate almost completely all the C_{7+} products and the main part of the C_{5+}. However, C_2-C_4 products, that represent the main part of the products formed within methane, stay in vapour phase. The obtained vapour phase thus has a high content of H_2 (59%) and also contains CO_2 (22%), CH_4 (12%) and small fractions of C_2-C_2 hydrocarbons, as shown in Figure 6.21.

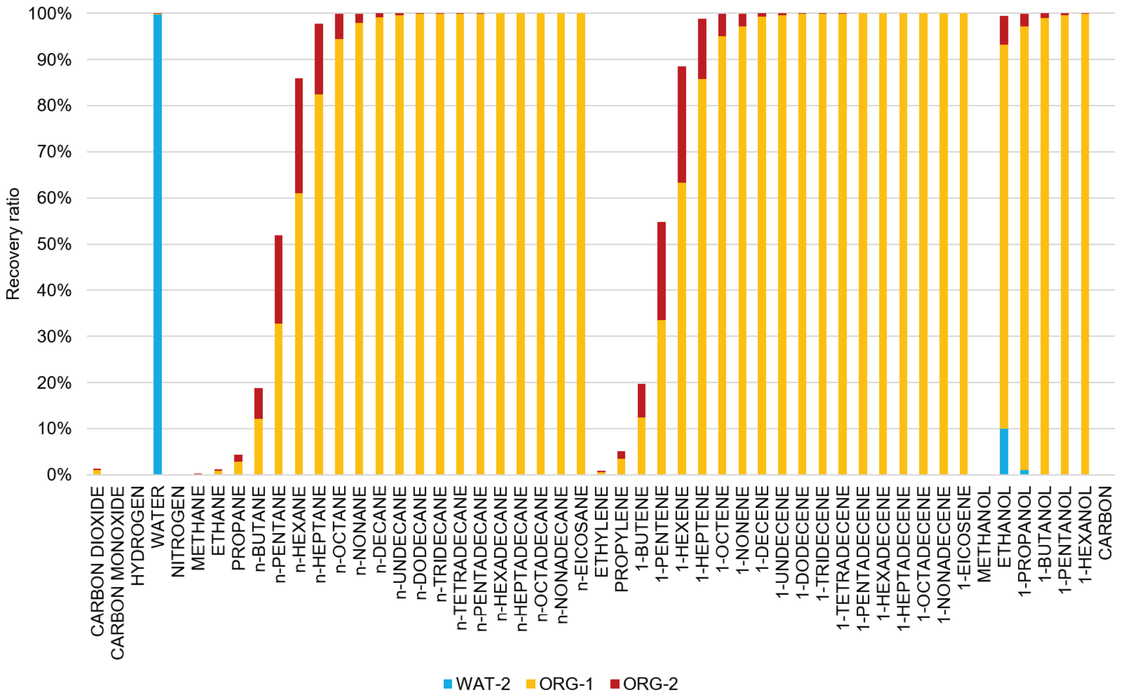

Figure 6.20: Recovery ratios of each compound in WAT-2, ORG-1 and ORG-2. Results obtained for configuration 1.

This vapour phase can thus hardly be exploited, because of its high content of H_2 and CO_2. Specifications for the injection of natural gas in the grid are reported in Table 6.6, while the values of these properties calculated for the vapour product VAP-5 are reported in Table 6.7. It can be observed that none of these requirements is fulfilled; the value of the WI is much lower than required because of the high content of H_2 that contributes to reduce the energy content per unit of volume.

Table 6.6: Specifications for natural gas, according to the Common Business Practice 2005-001/01 of the European Association for the Streamlining of Energy Exchange. (EASEE-gas, 2005)

Parameter	Unit	Min value	Max value
Wobbe index	kWh/m^3	13.4	15.7
Higher heating value	kWh/m^3	10.7	12.8
CO_2 content	mol%		2.5
H_2 content	mol%		6

We have thus estimated an energy efficiency and a carbon conversion, considering that the only exploitable product is the organic phase. We have obtained $\eta_{PtX} = 11\%$ and $\eta_C = 15\%$. These values are very low, as expected, due to the fact that the main part of the products is not exploited.

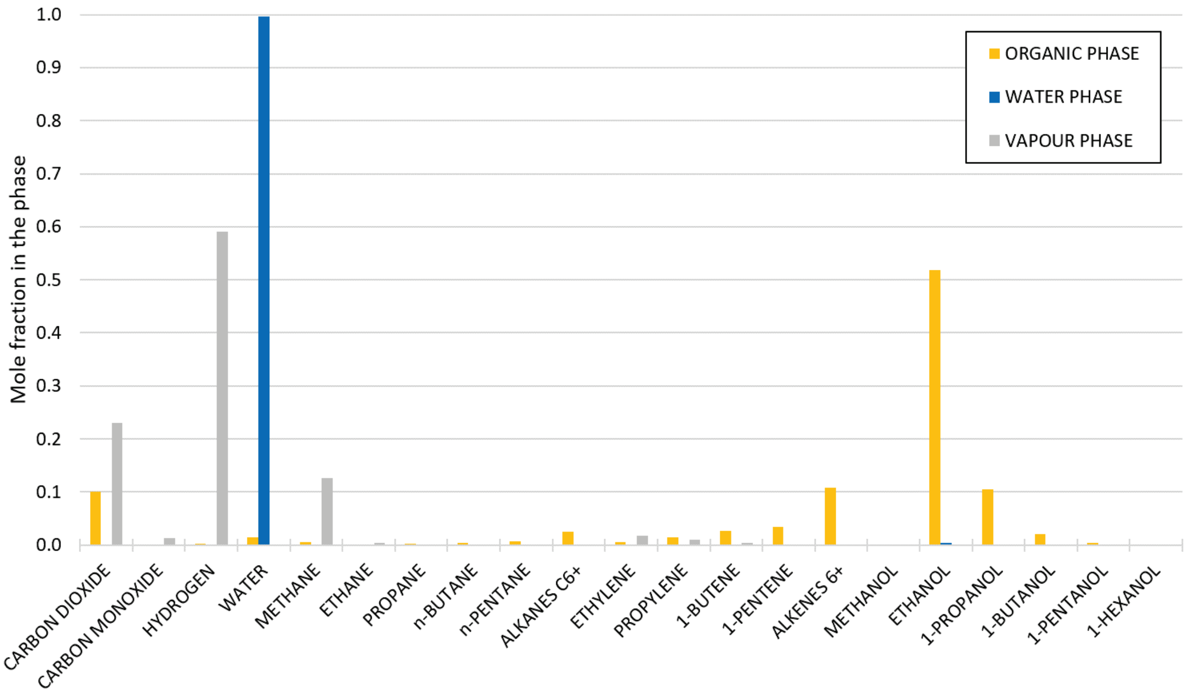

Figure 6.21: Composition of organic, vapour and water phases. Results obtained for configuration 1.

Table 6.7: Properties of vapour phase VAP-5 obtained from simulation of configuration 1.

Parameter	Unit	Value
Wobbe index	kWh/m^3	9.5
Higher heating value	kWh/m^3	4.1
CO_2 content	mol%	23
H_2 content	mol%	59

In order to increase this energy efficiency, it is necessary to recover the products that we have collected in vapour phase, by separating them from CO_2 and H_2. To do that, we have added a separation system that allows the separation of the unreacted gases from light hydrocarbons, via membrane separation. This configuration is discussed in the next section.

6.4.3 Second configuration: two reactors in series, separation of unreacted gases and recycle to the reactor inlet.

This second configuration, shown in Figure 6.22, as the previous one, includes the two reaction steps (R-1 and R-2) followed by water condensation (FLASH-1 and FLASH-2) and a first step of separation, FLASH-3, operating at 0.1°C, whose liquid product is recuperated as liquid phase (ORG_PHASE). Products that did not condense (VAP-4) are sent to a membrane separation unit that allows the separation of unreacted gases from light hydrocarbons. The adopted membranes are polyimide membranes with the properties reported in Table 6.8. MS-1 operates at 25°C and contains a CO_2 selective membrane, while MS-2 operates at 75°C and contains an H_2 selective membrane. A sweep gas is needed at the permeate side to guarantee the separation. A mixture (SW-1) of H_2 and CO_2 at the same molar ratio of the reactor inlet is fed to the MS-1, after mixing with the recirculated flow at the MS-2 shell outlet (PERM-2). In order to maximize the recovery of CO_2 and H_2, the pressure of the inlet sweep was set to 1 bar and its flow to 10

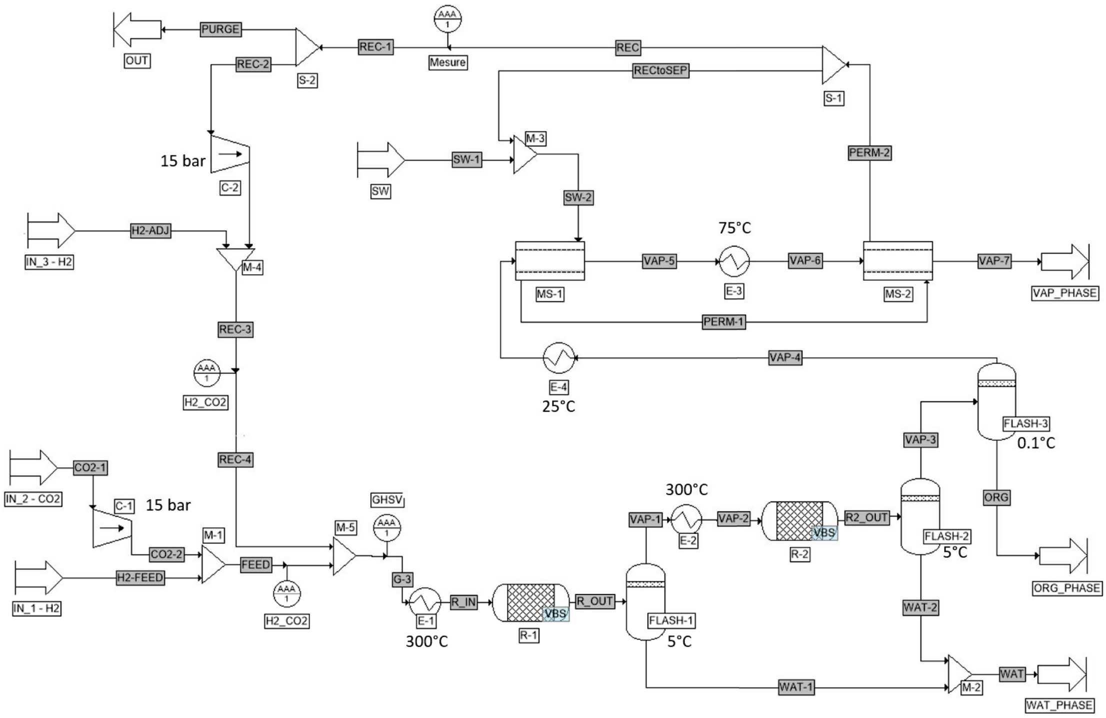

Figure 6.22: Schematic diagram of the process configuration with two reactors in series and separation of unreacted gases from light hydrocarbons via membrane filters.

mol/s (ratio of pressures=15, ratio of flows=0.13). The permeate flow at the outlet of MS-1's shell is sent as sweep gas to MS-2, while the outlet gas of MS-1's tube is sent to the MS-2's tube side, after heating to 75°C (E-3). PERM-2 is partially recirculated to the shell side of MS-1 (split ratio of S-1 to RECtoSEP=0.2) and the remaining gas is re-compressed to 15 bar and recirculated to the reactor inlet. Parameters used for each equipment are summarised in Table 6.9.

Table 6.8: Membrane permeance. (Huang et al., 2020)

Compound	**Gas permeance** [mol/(m^2.s.Pa)]	
	MS-1	MS-2
H_2	6.44x10^{-8}	2.38x10^{-7}
CO_2	5.22x10^{-7}	6.61x10^{-8}
CO	2.15x10^{-8}	8.59x10^{-9}
H_2O	9.91x10^{-7}	4.96x10^{-7}

Table 6.9: Summary of properties of each simulated unit in configuration 2. (We have specified here only parameters for units that were not in configuration 1. For those that were already used in configuration 1 see Table 6.5).

Compressor C-2		**Membrane filter MS-1**	
Pressure	15 bar	Temperature	25°C
Isoentropic efficiency	0.65	Ratio of pressures	15
		Ratio of flows	0.13
Exchanger E-3		**Membrane filter MS-2**	
Temperature	75°C	Temperature	75°C
		Ratio of pressures	15
		Ratio of flows	3.7
Exchanger E-4			
Temperature	25°C		

The mass flow diagram of the simulated process is shown in Figure 6.23. As in the previous configuration, CO_2 conversion in the reactors R-1 and R-2 are respectively 35 and 34%. Water is almost completely condensed between the two reactors, and then after the second reactor. The organic phase is collected after further condensation at 0.1°C (ORG). The compounds that do not condense are sent to the membrane separation units: MS-1 allows the separation of 97% of CO_2 and 91% of H_2, while after MS-2 the 99% of CO_2 and the 98% of H_2 are separated from the light hydrocarbons. Some CO and H_2O are separated as well within CO_2 and H_2. The

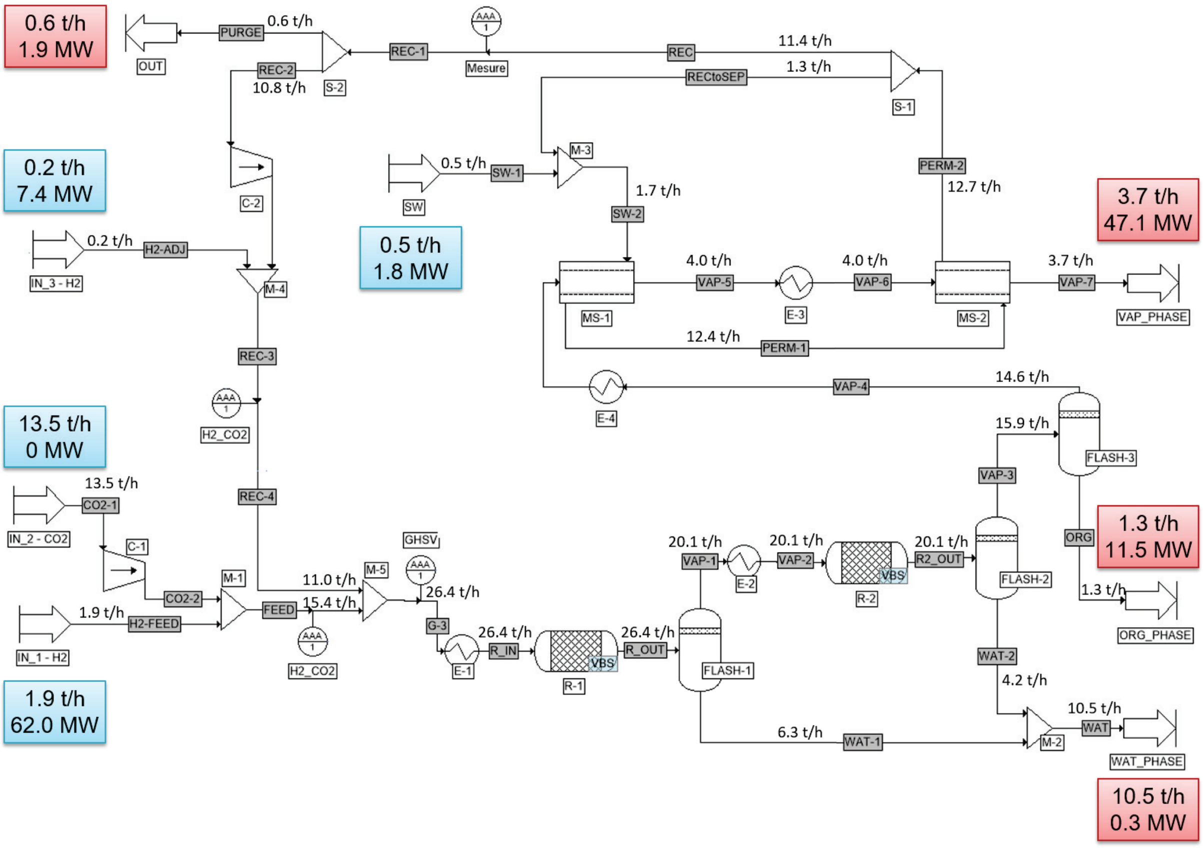

Figure 6.23: Mass flow diagram of the simulated process. Results obtained for configuration 2.

recovery of each compound in the two separation steps are reported in Table 6.10.

Table 6.10: Recovery ratio of each compound in the membrane separation units. Results obtained for configuration 2.

Compound	MS-1	MS-2
Carbon dioxide	0.97	0.99
Carbon monoxide	0.79	0.89
Hydrogen	0.91	0.98
Water	0.98	0.99

The compositions of the obtained products fractions are shown in Figure 6.24. The obtained organic phase is rich in hydrocarbons, especially alkenes. It has however a high content of ethanol (more than 50% mol) and contains 10% of CO_2 that condensed in the FLASH-3 unit, favoured by the high content of alcohol. Ethanol can be separated from the mixture of hydrocarbons via distillation or liquid-liquid extraction with liquid ammonia. (de Klerk, 2008, 2009, 2011; Fenske, 1951) Ethanol is widely used as feedstock for the food and beverage industry, for the chemicals industry (solvents, paints...) and for the cosmetics and pharmaceutical fields. It can also be blended into the motor-gasoline or dehydrated to olefins. (de Klerk, 2011) Olefins are largely used in the chemical industry, especially for the production of polymers. Suitable refining of the organic phase can therefore lead to valorization of the organic product with possible applications as feedstock in the chemical industry or as fuels.

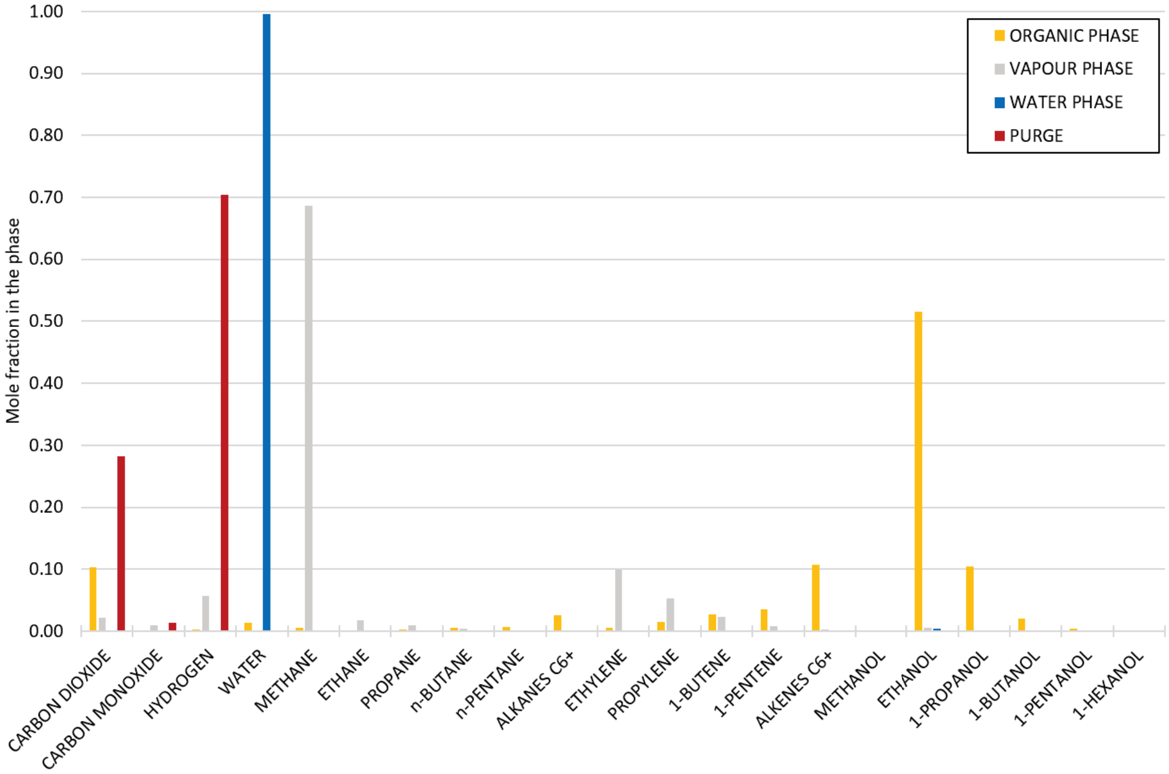

Figure 6.24: Composition of organic, vapour, water and purge phases. Results obtained for configuration 2.

The obtained vapour phase in this case follows the specifications required for the injection of natural gas in the grid. The properties of the vapour phase VAP-7 are reported in Table 6.11.

The contents of H_2 and CO_2 are lower than the maximum values allowed, 6% and 2.5% respectively. The WI is equal to 14.1 kWh/m^3 and in the range allowed from the legislation.

Table 6.11: Properties of vapour phase VAP-7 obtained from simulation of configuration 2.

Parameter	Unit	Value
Wobbe index	kWh/m^3	14.1
Higher heating value	kWh/m^3	12.1
CO_2 content	mol%	2.1
H_2 content	mol%	5.7

Thus, both vapour and organic phases can be valorized and therefore both can be considered in the estimation of the energy efficiency and the carbon conversion of the process. The energy efficiency and carbon conversion obtained are $\eta_{PtX} = 66\%$ and $\eta_C = 95\%$. The heat needed for the utilities is estimated to be around -18 MW. This is a heat released from the system. The heat required by each unit is shown in Figure 6.25. The system thus creates an availability of heat energy that is released from the system. This energy is taken into account in the energy efficiency, by considering its absolute value. A rigorous procedure would require an energy integration study and the incorporation of a coefficient to consider that the energy is required for the cooling, thus it is energetically less expensive than the energy required for the heating. In our work, we have not performed an energy integration and we have considered that the energy required for the cooling is still an energy that needs to be provided to the system, thus we consider its absolute value and we include it in the estimation of the energy efficiency. The energy efficiency obtained in this case is thus higher compared to the previous case, because the separation of unreacted gases and their recirculation at the reactor inlet allows at the same time to 1) valorize the obtained vapour phase and 2) increase the global reactants conversion of the process.

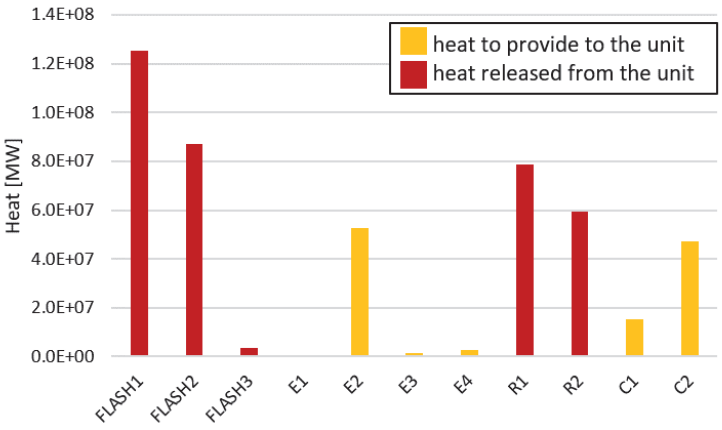

Figure 6.25: Heat required from each unit. Results obtained for configuration 2.

6.4.4 Final considerations and perspectives on process simulation.

This work wanted to investigate whether the direct CO_2 hydrogenation, intended as the process where RWGS and FT are performed in the same reactor, could be comparable and even better than the indirect way (RWGS and FT performed in two different reactors) in terms of energy efficiency. In this last section we have tried to answer this question. We have shown that the energy efficiency of a possible process configuration for the direct CO_2 hydrogenation is around 66%.

Comparing this estimated value with values reported in literature is not obvious. Each study in fact takes into account different hypothesis which are not always comparable. Some values that have been reported in the literature are summarised in Table 6.12 and are referred to various studies conduced on the two-step synthesis. We can observe that the energy efficiencies reported varies between 47 and 66%, while the carbon conversions varies between 74 and 94%, according to the hypothesis of the study. Many of the energy efficiencies reported include the step of hydrogen production via water electrolysis and the CO_2 capture that we have not considered in our simulations.

Table 6.12: Energy efficiency for various Power-to-Liquid plants.

Source	Energy efficiency [%]	Carbon conversion [%]	Description
König et al. (2015b)	66%	74%	RWGS unit followed by FT unit
Vázquez et al. (2018)	47%	94%	DAC, electrolysis, RWGS unit followed by FT unit
Fasihi et al. (2016)	58%		co-electrolysis followed by FT synthesis
Schmidt et al. (2016)	60-62%		HT electrolysis, CO_2 capture, RWGS unit and FT unit
Sunfire (2019)	60%		CO_2 capture, co-electrolysis, FT synthesis and product refining

The value reported by König et al. (2015b) for a Power-to-Liquid plant via indirect route derives from hypothesis similar to those that we have made in our study. The plant efficiency and the carbon conversion are referred to the conversion of CO_2 to hydrocarbons, without considering the H_2 production neither the liquid products refining. We can thus compare their value with ours and we observe that the estimated energy efficiencies are very close. The carbon conversion obtained in our case is significantly higher than that obtained by König et al. (2015b). This is in agreement with the fact that in that paper the short products were reformed and recycled to the reactor inlet and only heavier compounds are thus valorised as products.

However, our simulations did not take into account the hydrogen production, the CO_2 capture and the product refining and upgrading. Including these steps in the process simulation would lead to the estimation of more realistic efficiencies that could be compared with those of other processes such as Power-to-Methane, Power-to-Hydrogen or Power-to-Methanol.

Furthermore, we can suggest some ways to improve the energy efficiency of the process. For example, we have previously shown that the use of a membrane reactor could be beneficial to increase the hydrocarbons yield. Simulation of the global process with membrane reactors instead of traditional would thus allow to estimate the eventual improvement in energy efficiency when membrane reactors are used. The current ProSimPlus software version did not allow us to simulate this case, but future effort should be dedicated to this aim. Moreover, we have shown previously that the use of large excesses of H_2 at the reactor inlet could increase the CO_2 conversion and reduce the formation of CO as co-product. Reaction with high H_2/CO_2 ratio followed by separation of the unreacted H_2 from the hydrocarbons mixture and its recirculation to the reactor inlet could potentially further improve the energy efficiency, even if that would mean to increase the methane fraction obtained.

In conclusion, on one side many improvements can still be made in the optimisation of the process (energy integration, membrane reactors, large hydrogen excess...), but on the other side more detailed process simulation have to be made, including the H_2 generation and the CO_2 capture, as well as the product refining.

Despite that, we have shown the potential of the direct CO_2 hydrogenation process that could become part of the energetic mix of the future for possible applications in the chemical industry and eventually in the energy and transports field. Indubitably, before asserting that industrial applications are possible for this reaction, an economic evaluation needs to be done, to estimate the final cost of the obtained hydrocarbons, including the steps of H_2 production and CO_2 capture, as well as product upgrading and investment costs, that were not considered in our simulations.

References

R. W. Baker. Future Directions of Membrane Gas Separation Technology. *Industrial & Engineering Chemistry Research*, 41(6), 2002. doi: https://doi.org/10.1021/ie0108088. URL https://pubs.acs.org/doi/10.1021/ie0108088.

R. Bauer. Effective Radial Thermal Conductivity of Packings in Gas Flow. Part II. Thermal conductivity of the packing fraction without gas flow. *International Journal of Chemical Engineering*, 18:181–204, 1978a. URL https://ci.nii.ac.jp/naid/10003393839/en/.

R. Bauer. Effective Radial Thermal Conductivity of Packings in Gas Flow. Part I. Convective transport coefficient. *International Journal of Chemical Engineering*, 18:181–204, 1978b. URL https://ci.nii.ac.jp/naid/10003393839/en/.

M. Bernal, E. Piera, J. Coronas, M. Menéndez, and J. Santamarıa. Mordenite and ZSM-5 hydrophilic tubular membranes for the separation of gas phase mixtures. *Catalysis Today*, 56(1-3):221–227, 2000. ISSN 09205861. doi: 10.1016/S0920-5861(99)00279-5. URL https://linkinghub.elsevier.com/retrieve/pii/S0920586199002795.

M. A. Biot. General Theory of Three-Dimensional Consolidation. *Journal of Applied Physics*, 12(2): 155–164, 1941. ISSN 0021-8979, 1089-7550. doi: 10.1063/1.1712886. URL http://aip.scitation.org/doi/10.1063/1.1712886.

R. B. Bird, W. E. Stewart, and E. N. Lightfoot. *Transport phenomena*. New York: John Wiley & Sons, Inc., 1960.

G. Borman and K. Ragland. *Combustion Engineering*. McGraw Hill, Boston, 1998.

J. Boston and P. Mathias. PHASE EQUILIBRIA IN A THIRD-GENERATION PROCESS SIMULATOR. *EFCE Publication Series (European Federation of Chemical Engineering)*, (11):823–849, 1980. URL https://www.scopus.com/inward/record.uri?eid=2-s2.0-0019243035&partnerID=40&md5=c21730cc93cdf94082023b1e6e1f414e.

G. P. Brown, A. DiNardo, G. K. Cheng, and T. K. Sherwood. The Flow of Gases in Pipes at Low Pressures. *Journal of Applied Physics*, 17(10):802–813, 1946. ISSN 0021-8979, 1089-7550. doi: 10.1063/1.1707647. URL http://aip.scitation.org/doi/10.1063/1.1707647.

G. Chabot, R. Guilet, P. Cognet, and C. Gourdon. A mathematical modeling of catalytic milli-fixed bed reactor for Fischer–Tropsch synthesis: Influence of tube diameter on Fischer Tropsch selectivity and thermal behavior. *Chemical Engineering Science*, 127:72–83, 2015. ISSN 00092509. doi: 10.1016/j.ces.2015.01.015. URL https://linkinghub.elsevier.com/retrieve/pii/S0009250915000305.

O. Coussy. *Mecanique des milieux poreux*. Paris : Editions Technip, Paris, 1991.

A. de Klerk. Hydroprocessing peculiarities of Fischer–Tropsch syncrude. *International Symposium on Advances in Hydroprocessing of Oils Fractions (ISAHOF 2007)*, 130(2):439–445, 2008. ISSN 0920-5861. doi: 10.1016/j.cattod.2007.10.006. URL http://www.sciencedirect.com/science/article/pii/S0920586107005883.

A. de Klerk. Can FischerTropsch Syncrude Be Refined to On-Specification Diesel Fuel? *Energy & Fuels*, 23(9):4593–4604, 2009. ISSN 0887-0624. doi: 10.1021/ef9005884. URL https://doi.org/10.1021/ef9005884.

A. de Klerk. Fischer–Tropsch fuels refinery design. *Energy & Environmental Science*, 4(4):1177–1205, 2011. ISSN 1754-5692. doi: 10.1039/C0EE00692K. URL http://dx.doi.org/10.1039/C0EE00692K.

J. M. P. Q. Delgado. A critical review of dispersion in packed beds. *Heat and Mass Transfer*, 42(4): 279–310, 2006. ISSN 0947-7411, 1432-1181. doi: 10.1007/s00231-005-0019-0. URL http://link.springer.com/10.1007/s00231-005-0019-0.

M. E. Dry. Fischer-Tropsch synthesis over iron catalysts. *Catalysis Letters*, 7(1):241–251, 1990. ISSN 1572-879X. doi: 10.1007/BF00764506. URL https://doi.org/10.1007/BF00764506.

EASEE-gas. Common Business Practice - Harmonisation of Natural Gas Quality. Technical Report 2005-001/02, 2005. URL https://easee-gas.eu/uploads/kcFinder/files/cbp-2005-001-02-harmonisation-of-natural-gas-quality%20%281%29.pdf.

M. F. Edwards and J. F. Richardson. Gas dispersion in packed beds. *Chemical Engineering Science*, 23:109–123, 1968.

J. A. Elia, R. C. Baliban, and C. A. Floudas. Toward Novel Hybrid Biomass, Coal, and Natural Gas Processes for Satisfying Current Transportation Fuel Demands, 2: Simultaneous Heat and Power Integration. *Industrial & Engineering Chemistry Research*, 49(16):7371–7388, 2010. ISSN 0888-5885, 1520-5045. doi: 10.1021/ie100064q. URL https://pubs.acs.org/doi/10.1021/ie100064q.

D. F. Fairbanks and C. R. Wilke. Diffusion Coefficients in Multicomponent Gas Mixtures. *Industrial & Engineering Chemistry*, 42(3):471–475, 1950. ISSN 0019-7866, 1541-5724. doi: 10.1021/ie50483a022. URL https://pubs.acs.org/doi/abs/10.1021/ie50483a022.

M. Fasihi, D. Bogdanov, and C. Breyer. Techno-Economic Assessment of Power-to-Liquids (PtL) Fuels Production and Global Trading Based on Hybrid PV-Wind Power Plants. *Energy Procedia*, 99:243–268, 2016. ISSN 18766102. doi: 10.1016/j.egypro.2016.10.115. URL https://linkinghub.elsevier.com/retrieve/pii/S1876610216310761.

M. R. Fenske. Separation of alcohols from hydrocarbons, 1951. URL https://patents.google.com/patent/US2848503.

E. N. Fuller and J. C. Giddings. A Comparison of Methods for Predicting Gaseous Diffusion Coefficients. *Journal of Chromatographic Science*, 3(7):222–227, 1965. ISSN 0021-9665. doi: 10.1093/chromsci/3.7.222. URL https://doi.org/10.1093/chromsci/3.7.222.

E. N. Fuller, P. D. Schettler, and J. C. Giddings. New method for prediction of binary gas-phase diffusion coefficients. *Industrial & Engineering Chemistry*, 58(5), 1966.

X. He. A review of material development in the field of carbon capture and the application of membrane-based processes in power plants and energy-intensive industries. *Energy, Sustainability and Society*, 8(1):34, 2018. ISSN 2192-0567. doi: 10.1186/s13705-018-0177-9. URL https://energsustainsoc.biomedcentral.com/articles/10.1186/s13705-018-0177-9.

C.-T. Hsu. Dynamic Modeling of Convective Heat Transfer in Porous Media. In *Handbook of Porous Media*, page 42. Kambiz Vafai, 2nd edition, 2005. URL https://doi.org/10.1201/9780415876384.

W. Huang, X. Jiang, G. He, X. Ruan, B. Chen, A. K. Nizamani, X. Li, X. Wu, and W. Xiao. A Novel Process of $HCO_2/COCO_2$ Membrane Separation of Shifted Syngas Coupled with Gasoil Hydrogenation. *Processes*, 8(5):590, 2020. ISSN 2227-9717. doi: 10.3390/pr8050590. URL https://www.mdpi.com/2227-9717/8/5/590.

A. Jess and C. Kern. Influence of Particle Size and Single-Tube Diameter on Thermal Behavior of Fischer-Tropsch Reactors. Part II. Eggshell Catalysts and Optimal Reactor Performance. *Chemical Engineering & Technology*, 35(2):379–386, 2012. ISSN 09307516. doi: 10.1002/ceat.201100616. URL http://doi.wiley.com/10.1002/ceat.201100616.

R. J. Kee, M. E. Coltrin, P. Glarborg, and H. Zhu. *Chemically Reacting Flow: Theory, Modeling, and Simulation*. Wiley, 2017. ISBN 978-1-119-18630-4 978-1-119-18487-4. doi: 10.1002/9781119186304. URL http://doi.wiley.com/10.1002/9781119186304.

D. H. König, N. Baucks, R.-U. Dietrich, and A. Wörner. Simulation and evaluation of a process concept for the generation of synthetic fuel from CO_2 and H_2. *Energy*, 91:833–841, 2015a. ISSN 0360-5442. doi: 10.1016/j.energy.2015.08.099. URL http://www.sciencedirect.com/science/article/pii/S0360544215011767.

D. H. König, M. Freiberg, R.-U. Dietrich, and A. Wörner. Techno-economic study of the storage of fluctuating renewable energy in liquid hydrocarbons. *Fuel*, 159:289–297, 2015b. ISSN 00162361. doi: 10.1016/j.fuel.2015.06.085. URL https://linkinghub.elsevier.com/retrieve/pii/S0016236115006651.

H. Martin and M. Nilles. Radiale Wärmeleitung in durchströmten Schüttungsrohren: Radiale Wärmeleitung in durchströmten Schüttungsrohren. *Chemie Ingenieur Technik*, 65(12):1468–1477, 1993. ISSN 0009286X. doi: 10.1002/cite.330651206. URL `http://doi.wiley.com/10.1002/cite.330651206`.

S. Najari, G. Gróf, and S. Saeidi. Enhancement of hydrogenation of CO_2 to hydrocarbons via In-Situ water removal. *International Journal of Hydrogen Energy*, 44(45):24759–24781, 2019. ISSN 0360-3199. doi: 10.1016/j.ijhydene.2019.07.159. URL `http://www.sciencedirect.com/science/article/pii/S0360319919327491`.

V. R. R. Pendyala, G. Jacobs, J. C. Mohandas, M. Luo, H. H. Hamdeh, Y. Ji, M. C. Ribeiro, and B. H. Davis. Fischer–Tropsch Synthesis: Effect of Water Over Iron-Based Catalysts. *Catalysis Letters*, 140 (3):98–105, 2010. ISSN 1572-879X. doi: 10.1007/s10562-010-0452-7. URL `https://doi.org/10.1007/s10562-010-0452-7`.

D.-Y. Peng and D. B. Robinson. A New Two-Constant Equation of State. *Industrial & Engineering Chemistry Process Design and Development*, 18(2), 1979.

R. H. Perry, D. W. Green, and J. O. Maloney, editors. *Perry's chemical engineers' handbook*. McGraw-Hill, New York, 7th ed edition, 1997. ISBN 978-0-07-049841-9.

B. E. Poling, J. M. Prausnitz, and J. P. O'Connell. *The properties of gases and liquids*. McGraw-Hill, New York, 5th ed edition, 2001. ISBN 978-0-07-011682-5.

M. Quintard and S. Whitaker. Coupled, Nonlinear Mass Transfer and Heterogeneous Reaction in Porous Media. In *Handbook of Porous Media*, page 36. Kambiz Vafai, 2nd edition, 2005. URL `https://doi.org/10.1201/9780415876384`.

M. Rohde, G. Schaub, S. Khajavi, J. Jansen, and F. Kapteijn. Fischer–Tropsch synthesis with in situ H_2O removal – Directions of membrane development. *Microporous and Mesoporous Materials*, 115(1-2):123–136, 2008. ISSN 13871811. doi: 10.1016/j.micromeso.2007.10.052. URL `https://linkinghub.elsevier.com/retrieve/pii/S1387181108000772`.

M. Rolland. *Des limites à la réduction d'échelle en réacteur de test catalytique en lit fixe?* PhD thesis, Lyon 1, 2014.

G. Rothenberg. Chemical Technology. An Integral Textbook. By Andreas Jess and Peter Wasserscheid. *Angewandte Chemie International Edition*, 52(33):8501–8502, 2013. ISSN 1433-7851. doi: 10.1002/anie.201305324. URL `https://doi.org/10.1002/anie.201305324`. Publisher: John Wiley & Sons, Ltd.

A. Rushton, A. Ward, and R. Holdich. *Solid-Liquid Filtration and Separation Technology*. Wiley-VCH, 2000. ISBN 978-3-527-28613-3. URL `https://onlinelibrary.wiley.com/doi/book/10.1002/9783527614974`.

D. F. Sanders, Z. P. Smith, R. Guo, L. M. Robeson, J. E. McGrath, D. R. Paul, and B. D. Freeman. Energy-efficient polymeric gas separation membranes for a sustainable future: A review. *Polymer*, 54(18):4729–4761, 2013. ISSN 00323861. doi: 10.1016/j.polymer.2013.05.075. URL `https://linkinghub.elsevier.com/retrieve/pii/S0032386113005399`.

C. N. Satterfield. *Heterogeneous catalysis in industrial practice. 2nd edition*. McGraw Hill, New York, NY (United States), 2nd edition, 1991. URL `https://www.osti.gov/biblio/5495428`.

C. N. Satterfield, M. W. Van Eek, and G. S. Bliss. Liquid-solid mass transfer in packed beds with downward concurrent gas-liquid flow. *AIChE Journal*, 24(4):709–717, 1978. ISSN 0001-1541, 1547-5905. doi: 10.1002/aic.690240421. URL `http://doi.wiley.com/10.1002/aic.690240421`.

C. N. Satterfield, R. T. Hanlon, S. E. Tung, Z. M. Zou, and G. C. Papaefthymiou. Effect of water on the iron-catalyzed Fischer-Tropsch synthesis. *Industrial & Engineering Chemistry Product Research and Development*, 25(3):407–414, 1986. ISSN 0196-4321. doi: 10.1021/i300023a007. URL `https://doi.org/10.1021/i300023a007`.

P. Schmidt, W. Weindorf, A. Roth, V. Batteiger, and F. Riegel. Power-to-Liquids. Potentials and Perspectives for the Future Supply of Renewable Aviation Fuel. Technical report, German Environment Agency, 2016.

M. Sudiro and A. Bertucco. Production of synthetic gasoline and diesel fuel by alternative processes using natural gas and coal: Process simulation and optimization. *Energy*, 34(12):2206–2214, 2009. ISSN 03605442. doi: 10.1016/j.energy.2008.12.009. URL `https://linkinghub.elsevier.com/retrieve/pii/S0360544208003186`.

P. Trambouze and J.-P. Euzen. *Chemical reactors : from design to operation*. Institut français du pétrole publications. Ed. Technip, Paris, 2004. ISBN 2-7108-0845-5.

M. Ungerank and G. Baumgartner. Polyimide membranes made of polymerization solutions, 2010.

VDI. *Heat Atlas*. Springer, Berlin, Heidelberg, Düsseldorf, Germany, 2nd edition, 2010. ISBN 978-3-540-79999-3. URL `https://link.springer.com/referencework/10.1007%2F978-3-540-77877-6#about`.

F. V. Vázquez, J. Koponen, V. Ruuskanen, C. Bajamundi, A. Kosonen, P. Simell, J. Ahola, C. Frilund, J. Elfving, M. Reinikainen, N. Heikkinen, J. Kauppinen, and P. Piermartini. Power-to-X technology using renewable electricity and carbon dioxide from ambient air: SOLETAIR proof-of-concept and improved process concept. *Journal of CO2 Utilization*, 28:235–246, 2018. ISSN 22129820. doi: 10.1016/j.jcou.2018.09.026. URL `https://linkinghub.elsevier.com/retrieve/pii/S2212982018305213`.

K. R. Westerterp, W. Van Swaaij, and A. A. Beenackers. *Chemical Reactor Design and Operation, 2nd Edition*. Wiley, 2nd edition edition, 1991. ISBN 978-0-471-91730-4.

Y. Zhao, V. McDonell, and S. Samuelsen. Influence of hydrogen addition to pipeline natural gas on the combustion performance of a cooktop burner. *International Journal of Hydrogen Energy*, 44(23):12239–12253, 2019. ISSN 03603199. doi: 10.1016/j.ijhydene.2019.03.100. URL `https://linkinghub.elsevier.com/retrieve/pii/S0360319919311061`.

Conclusions et perspectives

This work was focused on the study and the optimisation of the CO_2 hydrogenation reaction and is included in the framework of the Power-to-X technologies that aim at using renewable power to form H_2 and then hydrogenate CO_2 into gaseous and liquid hydrocarbons. The feasibility of this technology at the industrial scale can be constrained by the limited conversion and selectivity of this reaction and by the fast deactivation of the catalyst due to the formation of water as co-product. The aim of this work was thus to understand the behaviour of the reaction and to find solutions to improve its efficiency. The reaction was thus experimentally studied at laboratory-scale and an analytic protocol was developed to quantify all the products obtained. A macro-kinetic model was then developed to describe the formation of these products and a micro-kinetic model was developed to understand their mechanism of formation. The macro-kinetic model was then integrated into a reactor model, developed to study the heat and mass transfer at higher scale, and into a membrane reactor model, developed to simulate the effects of water removal. Finally, a process configuration was proposed to optimise the energy efficiency and to valorise the most part of the obtained products.

The first chapter was focused on the analysis of the previous work on the subject available in the literature. The CO_2 hydrogenation reaction is a catalysed reaction that occurs in two steps: first, CO_2 is converted into CO via the reverse water-gas shift, then the obtained CO is converted into hydrocarbons via the Fischer-Tropsch synthesis. These two reactions, the first an endothermic reaction, the second an exothermic one, are optimised in different operating conditions and with different catalysts. Thus, an optimisation of the catalyst composition and of the operating parameters is necessary. The first part of the state-of-the-art study is an analysis of the performances obtained with different types of catalysts in different operating conditions. Iron-based catalysts are generally recognised as the most suitable ones. Fe is in fact active for the catalysis of both RWGS and FT. Moreover, the addition of alkali metals, such as potassium, to Fe-based catalysts has been proven to favour the formation of long hydrocarbons and to limit the formation of methane. The supported form of Fe-K catalysts gives better stability and better dispersion of the active metals. With Fe-K catalysts, CO_2 conversions between 30 and 40% and CO selectivity between 16 and 40% can be obtained, according to the catalyst composition and the operating conditions. Generally, the reaction is performed at relatively low temperature and pressures (T=300-400°C, p=5-20 bar) and with H_2/CO_2 molar ratios of 3.

The second part of the state-of-the-art study is focused on the understanding of the reaction mechanism. First of all, different active sites are involved in the catalysis of the reaction over Fe catalysts: iron carbides are believed to be the active phase for the chain-growth and thus responsible for the formation of the hydrocarbons chains; Fe_3O_4 is recognised as the species responsible for the RWGS activity and thus for the formation of CO; finally, metallic iron is considered as responsible for the secondary reactions of olefins, such as their hydrogenation. The relative amount of these sites during the reaction evolves, as it is influenced by the operating conditions and the gas composition. The relative amount of these sites also influences the final composition of the product. The RWGS that takes place over iron oxide sites can either follow a redox mechanism, with direct reduction of CO_2 to CO, or an associative mechanism, passing by the formation of a formate species intermediate. The FT reaction is a polymerization reaction and its mechanism passes by the reaction between an initiator and a monomer. The mechanism followed is much harder to describe. The main mechanisms generally accepted for the FT reaction are the carbide mechanism (or its variant, the alkyl mechanism), that considers CH_2 as the monomer, and the CO-insertion mechanism, that considers CO as the monomer. K can be involved in the mechanism, by promoting - according to its content in the catalyst - either the formation of the monomer or the formation of adsorbed C that leads to deactivation.

The second chapter describes the experimental procedures followed for the experimental studies. We have performed three different kinds of experiments:

1. first, we have performed an experimental kinetic study in a laboratory-scale in conditions where the heat and mass transfer limitations could be excluded;
2. secondly, we have modified the experimental bench for the co-injection of liquids, such as water and ethanol, in the reactor inlet;
3. finally, we have performed some tests in a scaled-up reactor with a cooling system.

An important contribution of our work is the development of an analytic protocol that allows the analysis of all the main products obtained. Products are collected in three phases: the gaseous phase contains the lightest products and the unreacted gases; the liquid organic phase contains the heaviest hydrocarbons; and the liquid water phase contains water and oxygenates products. All these three phases were analysed by gas-chromatography and the main products were all quantified. The protocol developed allows to close the C mass balance with an error below 10%.

The third chapter consists in an extensive experimental study of the reaction. First, we describe the synthesis and the characterisation of an iron-based catalyst, promoted with K and supported on alumina. We have chosen this catalyst as it is a good compromise between the simplicity of the synthesis procedure and the good performances. Characterisation of the catalyst via different techniques showed that the distribution of the active metals was not optimal and that it was highly inhomogeneous. Despite that, the catalytic performances obtained during the experimental tests were comparable to those obtained over similar catalysts by other authors, with CO_2 conversion close to 30% and CO selectivity of 11%. We have observed that in the reference conditions the reaction leads to formation of methane and short olefins as main products, with lower - but not negligible - quantities of paraffins and oxygenates.

An experimental kinetic study was conduced by varying different operating parameters (pressure, temperature, contact time and H_2/CO_2 inlet ratio). We have observed that in some conditions (typically with high H_2/CO_2 ratios at the inlet) the formation of CO as co-product can be minimized and the CO_2 conversion maximized, but in all conditions the formation of methane is always very important. It is thus clear that if the production of longer hydrocarbons wants to be maximized, it is necessary to reduce the formation of methane and this is not possible only by changing the operating conditions. A better formulation of the catalyst is thus required.

We have also performed some preliminary tests with co-injection of water and ethanol as reactants. We have observed that exposure to high partial pressures of water for long time could lead to the irreversible deactivation of the catalyst, probably due to the reoxidation of the iron carbides caused by water. The ethanol co-feeding study led to the conclusion that ethanol may have a role in the formation of long hydrocarbons, but further investigations are needed to verify this observation.

Finally, we have shown that the scale-up of the reactor allows to obtain very similar results to those obtained in the lab-scale reactor.

In the fourth chapter we have developed a macro-kinetic model that describes the behaviour of the reaction in different operating conditions. The model is based on semi-empirical correlations for the reaction rates and includes additional empirical laws to estimate the parameters that describe the distribution of hydrocarbons by carbon number and by product type. The model has been validated on the experimental data obtained in the laboratory-scale reactor and is able to predict them with a good accuracy. The main contribution of this part of the work is that it provides a model that is detailed enough to describe the distribution of hydrocarbons from 1 to 20 carbon atoms and belonging to the groups of alkanes, alkenes and alcohols. Moreover, this is a useful tool to simulate the kinetic behaviour of this reaction in more complex reactor models or in process simulations.

In the fifth chapter we have investigated the mechanism of the reaction. In particular, we aimed at understanding how oxygenates are formed compared to alkanes and alkenes and on which active sites. To do that, we have made assumptions about the elementary reactions of the reaction pathway and we have developed a micro-kinetic model via the Langmuir-Hinshelwood-Hougen-Watson procedure. We have assumed an alkyl mechanism for alkanes and alkenes and a CO-insertion mechanism for the formation of oxygenates. We have then made two different hypothesis: in one case we considered that oxygenates are formed on the same active sites as alkanes and akenes (here referred as hydrocarbons); in the other case, we considered that two different active sites are involved, one for oxygenates and one for hydrocarbons. We thus derived two complex models (containing 27 and 32 kinetic parameters, respectively).

The results of this study showed that the hypothesis that oxygenates are formed over different active sites allowed to better predict their distribution. However, the statistical error of the model is very high, due to the high number of kinetic parameters involved. Some useful insights on the reaction mechanism were still gained. We observed that the hypothesis that iron carbides are involved in the formation of hydrocarbons via an alkyl mechanism allows to well predict the experimental data. Conversely, the CO-insertion mechanism seems to be the suitable one to describe the oxygenates formation.

Indubitably, an improvement of both models is needed, as well as further investigations, in order to better understand the oxygenates formation mechanism.

In the sixth and last chapter we have studied the reaction in a scaled-up reactor and we have simulated the global process. First, we have developed a heterogeneous and a pseudo-homogeneous reactor model for the scaled-up reactor. We have shown that, at the scale tested, mass and heat transfer limitations can still be neglected. Thus, the pseudo-homogeneous approach could be adopted for the description of the reactor behaviour in the conditions tested.

Then, we have proposed a solution for the catalyst deactivation problem related to the formation of high quantities of water during the reaction. As we have reported previously, water can oxidise carbide sites, responsible for the chain-growth, leading to a loss of activity. The use of membrane reactors seems a promising solution for the water removal during the reaction. In fact, perm-selective membranes allow the selective separation of water during the reaction and that leads to beneficial effects for the CO_2 conversion and eventually for the catalyst lifetime. We have shown that using a membrane reactor with H_2 as sweep gas can lead to an increase of the CO_2 conversion, without important losses in the HCs yield. Moreover, if high flows of sweep gas are applied, the cooling of the reactor could be granted without the need for an additional cooling system.

Finally, we have proposed a process configuration that allows to reach acceptable energy and carbon efficiencies and the valorisation of the main part of products. We have simulated a system where two reactors in series are employed, with intermediate water condensation.

The obtained products are separated via a multi-step condensation system; CO_2, H_2 and CO unreacted are then separated from the lightest products via a membrane separation system and recirculated to the reactor inlet. The products are collected as organic phase and vapour phase. The organic phase is rich in hydrocarbons, especially olefins, and could be refined and used in the chemical industry or in the transport field. The vapour phase is rich in CH_4 and could be injected in the natural gas grid. This configuration allows to obtain an energy efficiency of 66% and a carbon efficiency of 95%. These values are very close to those estimated for the indirect pathway, indicating the feasibility of such a process.

In conclusion, with this work, we have provided preliminary contributions to the understanding of the reaction mechanism that can be useful for the design of an optimal catalyst for the maximization of the yield towards the desired products. We have also provided the tools needed for the modelling of this reaction which are useful for the design of reactors and processes and would thus allow to study the reaction at higher scale or in different process configurations. We have also suggested possible ways to further improve the process efficiency and to avoid one of the typical issues of this reaction, the deactivation due to high partial pressure of water.

This work opens up many perspectives.

We have shown that the catalyst that we have synthesised presents a high level of inhomogeneity and it does not have exactly the desired composition, even if the catalytic performances obtained are not far from those obtained in the literature. The synthesis process should be optimised, for example by varying the conditions applied during the evaporation and the calcination steps to reach a better distribution of the active elements. A more homogeneous catalyst with the right K/Fe ratio could have a longer lifetime, as deactivation due to the C deposition promoted by the high alkalisation degree would be avoided or at least reduced.

Moreover, based on the advancements on the reaction mechanism, a better catalyst formulation could be designed. To optimize the selectivity towards the long-chain hydrocarbons, the iron carbides content should be increased, while the presence of Fe_2O_3 should be minimized.

The macro-kinetic model developed in this work is quite accurate in the description of the products formation and the reactants consumption. However, it slightly over-predicts the methane formation and under-predicts the short olefins formations. These aspects could be improved by performing experiments in other conditions to increase the number and the quality of the data ensemble.

The model does not work in presence of CO/CO_2 mixtures. A model that predicts the kinetic behaviour of the reaction in presence of CO/CO_2 mixtures could be useful for the simulation of systems with recirculation of unreacted gases or in presence of non-pure sources of CO_2, such as syngas from co-electrolysis or biomass gasification. Therefore, an experimental study with CO/CO_2 feeds should be performed at laboratory-scale and data should be used to adjust the kinetic model for the presence of CO as reactant.

This works also provides some insights about the reaction mechanism. We have shown that the mechanism of formation of oxygenates could follow the CO-insertion mechanism and that their formation seems to be related to the presence of an active site different than the one where hydrocarbons are formed. However, it was not possible to draw accurate conclusions about the oxygenates formation. Moreover, many other questions can be raised. Is the site where oxygenates are formed the same where RWGS occurs? Are alcohols somehow involved in the formation of long-chains hydrocarbons? Is the deviation of long-chains hydrocarbons from ideal ASF distribution due to the re-adsorption of alcohols and their subsequent reaction? Or is it due to the re-adsorpion of olefins?

To answer these questions first a micro-kinetic model based on the hypothesis that RWGS and oxygenates formation occur on the same active sites should be developed. Metallic Fe, in fact, responsible for the RWGS activity, has been previously reported to have a role in the formation of oxygenates. Then, the role of alcohols and olefins should be investigated with an experimental study.

We have started to investigate these problems by experimental co-feeding studies of alcohols. However, our experimental system was not optimal for this kind of tests and thus our results are only preliminary. Co-injection of ethanol in a range of concentration larger than those that we have tested could help to confirm the hypothesis of reincorporation of ethanol into longer-chain hydrocarbons. The co-injection of higher alcohols, such as propanol or butanol, could also clarify if the eventual role of ethanol in the formation of long-chain hydrocarbons is only due to the high reactivity of ethene, or if longer alcohols are still involved in the formation of long hydrocarbons. Moreover, studies with C^{14} radiolabeled alcohols, as those that were conducted for the traditional FT synthesis, could provide more detailed information about the mechanism of alcohol re-adsorption and incorporation into growing chains.

In the same way, the co-injection of olefins within the reactants can provide informations about their tendency to re-adsorb and eventually contribute to the formation of longer hydrocarbons. Experiments with short and long olefins should be performed to investigate their tendency to readsorb as a function of their chain length.

Concerning the reactor model, we have shown that the scale-up of the reactor to the tested scale did not lead to the occurrence of heat and mass transfer limitations. A study at higher scales would be interesting, in order to identify until which scale these phenomena are negligible and what happens when they cannot be neglected anymore.

The application of membrane reactors for the CO_2 hydrogenation was shown in this work as a promising way to improve the CO_2 conversion and the formation of hydrocarbons. However, our model is not able to predict the eventual changes in the hydrocarbons distribution that could be caused by the shift of the equilibrium and the increase of H_2 content in the feed along the reactor. An experimental study with a membrane reactor should be performed in order to investigate the influence of the water removal on the hydrocarbons distribution and to collect experimental data for the validation of the model.

Finally, the simulation of the process showed that acceptable carbon and energy efficiencies could be reached. Many improvements have to be made on these preliminary estimations. First of all, an energy integration of the process should be performed in order to estimate with more accuracy the energy needed for the utilities and thus the energy efficiency. Moreover, some questions have to be answered. How much does the energy efficiency decrease when the H_2 generation via electrolysis and the CO_2 capture are considered? How much liquid product can effectively be recovered if the refining process of liquid compounds is considered?

Other ways to optimize the process should also be investigated. For example the integration of membrane reactors instead of traditional tubular reactors. Another possibility to investigate is the application of high H_2/CO_2 ratios, so that the conversion of CO_2 is increased and the hydrocarbons yield maximised.

APPENDIX A

Chemicals.

Table A.1: Summary of chemicals used and their properties.

Injector

Chemical	**Supplier**	**Product properties**
$\gamma - Al_2O_3$	SASOL	Puralox SCCa 150-200
$Fe(NO_3)_3 9H_2O$	Sigma-Aldrich	⩾98%
K_2CO_3	Acros Organics	⩾99%
SiC	Alfa-Aesar	120 grit (100 µm)
Methyl-ciclohexane	Fischer Chemical	Extra pur
Acetonitrile	Sigma-Aldrich	⩾99.9%
CO_2	Air Liquide	Alphagaz 1, ⩾99.9%
H_2	Air Liquide	⩾99.999%
N_2	Air Liquide	⩾99.999%
He	Air Liquide	Alphagaz 1, ⩾99.999%

APPENDIX B

Analytic protocol.

B.1 Analytic protocol for experiments in lab-scale reactor.

B.1.1 Analytic methods.

B.1.1.1 Method for analysis of gaseous compounds.

The analysis of gaseous compounds is made by on-line GC at atmospheric pressure at the reactor outlet, after condensation of heaviest products. The parameters of the analysis are the following:

Injector	
Injected volume	0.5 µl
Vector gas	He
Split ratio	200
Temperature	150°C
Pressure	1.214 bar
Total flow	493 ml/min

Columns	
Column 1	Supelco Carboxen-1010 plot
Flow column 1	1.0 ml/min
Average velocity column 1	28 cm/s
Column 2	Agilent JW CP-Porabond Q
Flow column 2	1.4 ml/min
Average velocity column 2	37 cm/s

Oven temperature profile	
Initial temperature	50°C, hold 2 min
Ramp	40°C/min
Final temperature	240°C, hold 10 min

Detectors	
Detector 1 (TCD)	

Temperature	150°C
Reference flow	12.0 ml/min
Detector 2 (FID)	
Temperature	250°C
Hydrogen flow	40 ml/min
Air flow	450 ml/min

B.1.1.2 Method for analysis of compounds in organic phase.

The parameters of the analysis are the following:

Injector	
Injected volume	1 µl
Vector gas	H2
Split ratio	50
Temperature	340°C
Pressure	1.549 bar
Total flow	49.0 ml/min

Columns	
Column	Optima 5-HT
Pressure	1.551 bar
Flow	0.4 ml/min
Average velocity	50 cm/s

Oven temperature profile	
Initial temperature	40°C, hold 2 min
Ramp	40°C/min
Final temperature	340°C, hold 2.5 min

Detectors	
Detector (FID)	
Temperature	280°C
Hydrogen flow	40 ml/min
Air flow	400 ml/min

B.1.1.3 Method for analysis of compound in water phase.

The parameters of the analysis are the following:

Injector	
Injected volume	0.5 µl
Vector gas	H2
Split ratio	500
Temperature	250°C

Pressure	1.522 bar
Total flow	436 ml/min

Columns	
Column	Agilent JW DB-Heavy Wax
Pressure	1.522 bar
Flow	0.4 ml/min
Average velocity	50 cm/s

Oven temperature profile	
Initial temperature	30°C, hold 1 min
Ramp	40°C/min
Final temperature	290°C, hold 0.50 min

Detectors	
Detector (FID)	
Temperature	250°C
Hydrogen flow	40 ml/min
Air flow	450 ml/min

B.1.2 Estimation of response coefficients.

B.1.2.1 Estimation of response coefficients of gaseous compounds.

For gaseous compounds detected with TCD, response coefficients are calculated from a direct calibration of the GC with a reference bottle having the following composition:

Compound	Composition [%vol]
CO	5
CH_4	10
N_2	10
CO_2	20
H_2	55

The split ratio of the GC has been varied in the range 100 to 400, in order to have different compositions of the gas. For each value of split, a response factor referred to N_2 is calculated from Eq. B.1 and a standard deviation is evaluated (values are reported in Table B.4).

$$MRF_{i,N2} = \frac{F_{i,OUT}/F_{N_2,IN}}{A_i/A_{N_2}} \tag{B.1}$$

For light hydrocarbons the Equivalent Carbon Number (ECN) method is used. A molar reference response factor is calculated referred to the methyl octanoate, used as the ISTD compound, from Eq. B.2, then the response factor is passed to a referred to nitrogen one through the ratio of the pick areas of methane detected from FID and TCD ($A_{CH_4,FID}/A_{CH_4,TCD}$), according to Eq. B.3.

$$MRF_{i,ISTD} = 10^3(-61.3 + 88.8n_C + 18.7n_H - 41.3n_O + 6.4n_N)^{-1} \tag{B.2}$$

$$MRF_{i,N2} = \frac{MRF_{i,ISTD}}{MRF_{CH4,ISTD}} \frac{A_{CH4,FID}}{A_{CH4,TCD}} \tag{B.3}$$

Table B.4: Values of MRF obtained for CO_2, CO, CH_4 and H_2.

Split ratio:	**200**	**100**	**400**	Average	Standard deviation
MRF_{H_2/N_2}	17.649	235.397	89.391	114.1455	79.4%
MRF_{CO/N_2}	1.034	0.998	1.009	1.0136	1.5%
MRF_{CH_4/N_2}	1.094	1.071	1.016	1.0601	3.1%
MRF_{CO_2/N_2}	0.834	0.812	0.804	0.8168	1.6%

B.1.2.2 Estimation of response coefficients of compounds in organic phase.

Organic phase compounds were calibrated by using a solution of heptane, nonane and 1-dodecene in different compositions diluted in methyl-cyclohexane. Mass response factors of the other compound have been calculated from the ECN method (Eq. B.2 and Eq. B.3), using heptane as reference for all linear paraffins and 1-dodecene for all 1-olefins (instead of CH_4). For branched chains and non identified products the RF of the 1-olefin with the closest C number has been used. The values of RF obtained are reported in Table B.5.

Table B.5: Values of RF obtained for 1-olefins and n-paraffins from C_5 to C_{33}.

C number	RF (1-olefin)	RF (n-paraffin)
5	1.15831	
6	1.13790	1.01254
7	1.12376	1.00450
8	1.11338	0.99852
9	1.10544	0.99389
10	1.09917	0.99021
11	1.09410	0.98721
12	1.08990	0.98472
13	1.08637	0.98262
14	1.08337	0.98082
15	1.08078	0.97926
16	1.07853	0.97790
17	1.07654	0.97671
18	1.07479	0.97564
19	1.07322	0.97469
20	1.07181	0.97384
21	1.07055	0.97307
22	1.06939	0.97237
23	1.06835	0.97173
24	1.06739	0.97114
25	1.06650	0.97060
26	1.06569	0.97011
27	1.06494	0.96965
28	1.06425	0.96922
29	1.06360	0.96882
30	1.06299	0.96845
31	1.06243	0.96811

32	1.06190	0.96778
33	1.06141	

B.1.2.3 Estimation of response coefficients of compounds in water phase.

Water phase compounds were calibrated by using a water solution of acetone, methanol, ethanol, 1-butanol, acetic acid, propanoic acid, hexanoic acid, acetaldehyde and butyraldehyde. Mass response factors of the other compounds have been calculated again from the ECN method (Eq. B.2 and Eq. B.3), using ethanol as reference for all alcohols, acetic acid for all acids and acetaldehyde for all aldehydes. The values of RF obtained are reported in Table B.6.

Table B.6: Values of RF obtained for alcohols, acids and aldehydes from C_1 to C_6.

C number	RF for alcohols	RF for acids	RF for aldehydes
1	1.62060		
2	1.14692	2.43190	1.62856
3	0.89358	1.47167	1.16515
4	0.80910	1.07231	0.99255
5	0.72594	0.92089	
6	0.68798	0.91675	

B.2 Analytic protocol for two-dimensional GC analysis.

Equipment	GC Agilent 6890 + MS 5975
Vector gas	He
Injection volume	0.2 µl
Injection temperature	300°C
Split ratio	10
Vector gas flow	2 ml/min
Oven temperature	50°C for 5 min 1.75°C/min until 300°C
Columns	VB1701MS, 30m x 0.25mm x 0.25 µm DB-1, 3m x 0.1mm x 0.1 µm
MS detection	scan mode, $33 < m/z < 280$ (22 Hz)

Samples were injected pure, without dilution.

B.3 Analytic protocol for experiments in SynToMe set-up.

B.3.1 Method for µGC.

The method used for the analysis in the µ-GC is detailed in the following:

Injector temperature	90°C
Pressure	28 psi
Column temperature	90°C
Analysis time	300 s

B.3.2 Estimation of response coefficients of products detected with μGC.

Response coefficients for compounds detected in gaseous phase were estimated from calibration. Calibration was performed by using the gas flow-meters for CO_2, H_2, CO, CH_4 and N_2. For ethylene and ethane a mixture calibration bottle is used. Response coefficients for C_3 have been estimated with the ECN method. The obtained response coefficients referred to N_2 are reported in Table B.7.

Table B.7: Values of RF obtained for compounds analysed with μ-GC.

Compound	RF
H_2	0.0852
CH_4	0.4036
CO	0.9491
CO_2	0.0068
C_2H_4	0.5531
C_2H_6	0.6016
C_3H_6	0.4996
C_3H_8	0.5684

APPENDIX C

Requirements for measurements of intrinsic kinetics in fixed-bed reactors.

Table C.1 reports the values of criteria calculated for different operating conditions to verify the absence of diffusional limitations of mass and heat and that the pattern is a plug-flow one.

Table C.1: Calculated values of criteria used to verify that kinetic regime is dominant for CO_2 in different operating conditions. The condition number refers to Table 2.2.

	Condition:	1	3	9	10	13	20	22	14	
Criterion					Values					Limit
External mass transfer	Ca	$2.01x10^{-4}$	$2.63x10^{-4}$	$6.99x10^{-5}$	$8.51x10^{-5}$	$5.81x10^{-4}$	$1.57x10^{-4}$	$2.21x10^{-4}$	$8.50x10^{-3}$	< 0.16
Internal mass transfer	Φ	$1.81x10^{-4}$	$1.33x10^{-4}$	$8.69x10^{-5}$	$7.16x10^{-5}$	$5.25x10^{-4}$	$1.91x10^{-4}$	$1.41x10^{-4}$	$8.82x10^{-3}$	< 0.08
Axial dispersion	L_{bed}/d_p	731.71	731.71	731.71	731.71	731.71	731.71	731.71	731.71	
		>	>	>	>	>	>	>	>	
	Limit value	1.12	3.78	0.39	0.36	3.27	0.85	1.17	9.70	
External heat transfer	ΔT_{film}	$1.03x10^{-1}$	$1.20x10^{-1}$	$3.54x10^{-2}$	$4.29x10^{-2}$	$2.42x10^{-1}$	$7.97x10^{-2}$	$1.08x10^{-1}$	$4.55x10^{-2}$	
Internal heat transfer	ΔT_{int}	$6.14x10^{-4}$	$4.19x10^{-4}$	$2.80x10^{-4}$	$2.51x10^{-4}$	$1.55x10^{-3}$	$4.65x10^{-4}$	$6.64x10^{-4}$	$2.35x10^{-4}$	< 8.64
Radial heat transfer	ΔT_{rad}	$7.90x10^{-4}$	$5.46x10^{-4}$	$3.61x10^{-4}$	$3.26x10^{-4}$	$1.95x10^{-3}$	$6.04x10^{-4}$	$8.71x10^{-4}$	$3.03x10^{-4}$	

Diffusion coefficients.

Molecular diffusion coefficients $D_{i,m}$ are estimated from the mixture average approximation, according to Eq. C.1:

$$D_{i,m} = \frac{1-\omega_i}{\sum_{k\neq i}^{N} \frac{z_k}{D_{ik}}} \tag{C.1}$$

where D_{ik} is the binary diffusion coefficient of i in k, estimated from Fuller method, according to Eq. C.2. (Fuller et al., 1966; Fuller and Giddings, 1965)

$$D_{ik} = \frac{0.00143T^{1.75}}{pM_{ik}^{0.5}\left(\left(\nu_i^{1/3}+\nu_k^{1/3}\right)^2\right)} \tag{C.2}$$

Effective diffusion coefficients $D_{i,eff}$ are defined as in Eq. C.3:

$$D_{i,eff} = \frac{\epsilon_{pores}}{\tau_{pores}} \frac{1}{\frac{1}{D_{i,m}}+\frac{1}{D_{i,Kn}}} \tag{C.3}$$

where $D_{i,Kn}$ is the Knudsen diffusion coefficient, calculated from Eq. C.4:

$$D_{i,Kn} = \frac{2}{3} r_{pores}\sqrt{\frac{8RT}{\pi M_i}} \tag{C.4}$$

Mass transfer coefficient.

$k_{G,i}$ is estimated from the definition of Sherwood number Sh (Eq. C.5):

$$Sh_i = \frac{k_{G,i}d_P}{D_{i,m}} \tag{C.5}$$

Sherwood number can be estimated with the empirical correlation by Wakao (Wakao et al., 1979) (Eq. C.6):

$$Sh_i = 2 + 1.1Re_P^{0.6}Sc_i^{1/3} \tag{C.6}$$

where Re_P is the Reynolds number defined as:

$$Re_P = \frac{\rho_{mix}u_0 d_P}{\mu_{mix}} \tag{C.7}$$

and Sc_i is the Schmidt number, defined as:

$$Sc_i = \frac{\mu_{mix}}{\rho_{mix}D_{i,m}} \tag{C.8}$$

Heat transfer coefficients.

The heat transfer coefficient between particle and bulk α_p is estimated from the Nusselt number, estimated from the empirical correlation in Eq. C.9 (Wakao et al., 1979):

$$Nu = 2 + 1.1Re_P^{0.6}Pr^{1/3} \tag{C.9}$$

with Nusselt number defined as:

$$Nu = \frac{c_{p,mix}\mu_{mix}}{\lambda_{mix}} \tag{C.10}$$

The thermal conductivity of the catalyst particle λ_P is estimated from Eq. C.11:

$$\lambda_P = 4\lambda_{mix} \tag{C.11}$$

The effective radial thermal conductivity in the bed α_{bed} is estimated as in Eq. C.12:

$$\alpha_{bed} = \left(\frac{1}{\alpha_{rad}} + \frac{1}{\alpha_w} \right)^{-1} \tag{C.12}$$

where α_{rad} is defined as:

$$\alpha_{rad} = \frac{d_R}{8\lambda_{rad}} \tag{C.13}$$

$$\lambda_{rad} = (4 + Re_P Pr/7)\lambda_{mix} \tag{C.14}$$

and α_w is calculated from its Nusselt number, estimated according to the empiric correlation in Eq. C.15:

$$Nu_w = 4(1.3 + 5d_P/d_R) + 0.19 Re_P^{3/4} Pr^{1/3} \tag{C.15}$$

Tables C.2 and C.3 report the values of parameters used for the estimation of criteria.

Table C.2: Values of parameters (not depending on the operating conditions) used for the calculation of criteria.

Property	Unit	Value
d_r	[m]	0.006
L_{bed}	[m]	0.12
d_P	[m]	0.000164
a_s	[1/m]	36585.37
ϵ_{bed}	[-]	0.40
τ_{bed}	[-]	1.58
n_{CO_2}	[-]	0.3164
E_a	[J/mol]	15804.08
ΔH^r	[J/mol]	2.45x10^{-5}

Table C.3: Values of parameters (depending on operating conditions) used for the calculation of criteria. The condition number refers to Table 2.2.

	Condition:	1	3	9	10	13	20	22	14
Property	Unit	Values							
R^{obs}_{v,CO_2}	[mol$_{\mathrm{CO_2}}$/(m$^3_{\mathrm{cat}}$.s)]	3.30	1.95	1.75	1.50	6.50	2.67	3.27	1.57
$C_{CO_2,bulk}$	[mol/m^3]	57.50	46	65	74	36	40	86	0.5
ρ_{mix}	[kg/m^3]	4.65	4.95	4.25	4.65	4.9	2.97	8.1	3.21
μ_{mix}	[Pa.s]	2.28x10^{-5}	2.20x10^{-5}	2.35x10^{-5}	2.19x10^{-5}	2.34x10^{-5}	2.31x10^{-5}	2.24x10^{-5}	2.29x10^{-5}
Re_P	[-]	0.300	0.125	0.488	0.313	0.292	0.296	0.305	0.223
Sc_{CO_2}	[-]	1.150	1.000	1.400	1.450	0.950	1.245	1.050	1.015
k_{G,CO_2}	[m/s]	0.0078	0.0044	0.0105	0.0065	0.0085	0.0116	0.0047	0.0101
$D_{CO_2,m}$	[m^2/s]	4.30x10^{-6}	4.45x10^{-6}	3.96x10^{-6}	3.30x10^{-6}	5.10x10^{-6}	6.40x10^{-6}	2.65x10^{-6}	7.02x10^{-6}
$D_{CO_2,eff}$	[m^2/s]	1.56x10^{-7}	1.57x10^{-7}	1.52x10^{-7}	1.39x10^{-7}	1.69x10^{-7}	1.72x10^{-7}	1.32x10^{-7}	1.75x10^{-7}
h_P	[W/m^2/K]	214	109	330	234	180	224	202	231
λ_P	[W/m/K]	0.590	0.510	0.685	0.655	0.460	0.630	0.540	0.735
α_{bed}	[W/m/K]	690	590	800	760	550	730	620	857

References

E. N. Fuller and J. C. Giddings. A Comparison of Methods for Predicting Gaseous Diffusion Coefficients. *Journal of Chromatographic Science*, 3(7):222–227, 1965. ISSN 0021-9665. doi: 10.1093/chromsci/3.7.222. URL `https://doi.org/10.1093/chromsci/3.7.222`.

E. N. Fuller, P. D. Schettler, and J. C. Giddings. New method for prediction of binary gas-phase diffusion coefficients. *Industrial & Engineering Chemistry*, 58(5), 1966.

N. Wakao, S. Kaguei, and T. Funazkri. Effect of fluid dispersion coefficients on particle-to-fluid heat transfer coefficients in packed beds. *Chemical Engineering Science*, 34(3):325–336, 1979. ISSN 00092509. doi: 10.1016/0009-2509(79)85064-2. URL `https://linkinghub.elsevier.com/retrieve/pii/0009250979850642`.

APPENDIX D

Thermodynamic study.

D.1 Parameters used for the estimation of pure corps and mixture properties according to Marano and Holder correlations.

Table D.1: Parameters to use in Eqs. 4.1 and 4.2 for the estimation of pure compounds critical properties and saturated pressure. (Marano and Holder, 1997)

	$\mathbf{T_C}$ **[K]**		$\mathbf{p_C}$ **[bar]**		ω_c [-]		$\mathbf{ln(P_{sat})}$ **[-]**	
Compound	n-paraffin	α-olefin	n-paraffin	α-olefin	n-paraffin	α-olefin	n-paraffin	α-olefin
Equation	4.1		4.1		4.2		4.1	
$\mathbf{n_0}$	0.896021	0.980154	-3.625581	-3.039461	-23.608415	-23.174122	1.126231	1.281405
ΔY_0	892.82		-1336.74		-6.5597		from Eq. D.1	
$\mathbf{Y_{\infty,0}}$	1020.71		0				2.72709	
ΔY_∞	0		0				from Eq. D.1	
β	0.198100		2.111827		3.383261		0.619226	
γ	0.629752		0.258439		0.208770		0.416321	

$$\Delta Y = A + \frac{B}{T} + ClnT + DT^2 + \frac{E}{T^2} \tag{D.1}$$

Table D.2: Temperature-dependent parameters to use in Eq. D.1. (Marano and Holder, 1997)

	ΔY_0	ΔY_∞
ΔT [°C]	0-300	0-300
A	-5.75509	15.8059
B	-7.56568	-1496.56
C	0.0857734	-2.17342
D	$-1.41964\text{x}10^{-5}$	$7.27763\text{x}10^{-7}$
E	$2.67209\text{x}10^{5}$	37876.2

Table D.3: Parameters to use in Eqs. 4.9 for the estimation of liquid molar volume of heavy hydrocarbons. (Marano and Holder, 1997)

	$\mathbf{v_L}$ [cm^3/mol]	
Compound	n-paraffin	α-olefin
Equation	4.9	
$\mathbf{n_0}$	-1.388524	-1.061318
ΔY_0	from Eq. D.2	
$\mathbf{Y_{\infty,0}}$	0	
ΔY_∞	from Eq. D.2	
β	5.519846	
γ	0.0570632	

$$\Delta Y = A + BT + CT^2 + DT^3 \tag{D.2}$$

Table D.4: Temperature-dependent parameters to use in Eq. D.2. (Marano and Holder, 1997)

	ΔY_0	ΔY_∞
ΔT [°C]	0-300	0-300
A	8592.30	12.7924
B	-85.7292	0.0150627
C	0.280284	$-1.30794\text{x}10^{-5}$
D	$-4.48451\text{x}10^{-4}$	$1.59611\text{x}10^{-8}$

Table D.5: Parameters to use in Eqs. 4.8 for the estimation of liquid molar volume of non-hydrocarbons and light hydrocarbons. (Marano and Holder, 1997)

	$\mathbf{H_2}$	$\mathbf{CO_2}$	**CO**	$\mathbf{CH_4}$	$\mathbf{C_2H_4}$	$\mathbf{C_2H_6}$
Solvent $\mathbf{n_C}$	20-36	20-44	20-36	20-44	20-36	20-44
ΔT [**K**]	323-423	313-573	323-573	323-573	323-573	373-573
ΔV_i	0.704424	5.50000	1.50538	2.47603	5.08308	8.02413
A	-64.9424	-124.328	-18.3528	-7.41354	93.6738	66.4657
B	0.237301	0.250075	0.160773	0.169051	0	0

Table D.6: Parameters to use in Eqs. 4.23 and 4.24 for the estimation of Henry coefficient of non-hydrocarbons and light hydrocarbons. (Marano and Holder, 1997)

	$\mathbf{N_2}$	$\mathbf{H_2}$	$\mathbf{CO_2}$	**CO**	$\mathbf{CH_4}$	$\mathbf{C_2H_4}$
Solvent $\mathbf{n_C}$	16-36	16-36	16-44	16-36	16-44	16-36
ΔT [**K**]	298-475	300-553	298-573	298-573	298-573	298-573
ΔH_i	0.0181705	0.0200959	0.0211	0.0173238	0.0190354	0.0246608
A	8.44317	12.9353	6.6525	5.79833	0.300209	6.61084
B	49.5974	22.9058	15.2964	19.5937	-114.655	15.2170
C	-0.278896	-0.974709	-0.0761	0.152199	1.02385	-0.0751183
D	-1.30377x10^{-6}	-1.20408x10^{-6}	-2.56x10^{-7}	-1.89733x10^{-6}	-2.53913x10^{-6}	-2.56655x10^{-7}
E	4378.02	2244.61	-144960.00	2031.63	-4257.18	-183928

	$\mathbf{C_2H_6}$	$\mathbf{C_3H_6}$	$\mathbf{C_3H_8}$	$\mathbf{C_6H_{14}}$	$\mathbf{H_2O}$
Solvent $\mathbf{n_C}$	16-44	16-36	16-36	16-36	16-28
ΔT [**K**]	298-573	298-413	298-519	298-525	413-525
ΔH_i	0.0226055	0.0202632	0.0214924	0.0173970	0.0605329
A	6.66047	6.33671	5.22622	5.03841	7.88232
B	15.1525	15.0950	7.43296	102.049	14.4370
C	-0.0745718	-0.0743429	0.0598087	0.0782713	-0.0648305
D	-2.55981x10^{-7}	-2.54569x10^{-7}	6.02721x10^{-7}	-2.31129x10^{-7}	0
E	-239557	-314944	-291596	-650347	-465952

Table D.7: Parameters of cubic equations of state (Peng-Robinson and Soave-Redlich-Kwong).

	SRK	**PR**
$\mathbf{r_1}$	0	$-1-\sqrt{2}$
$\mathbf{r_2}$	0	$-1+\sqrt{2}$
Ω_A	0.4275	0.4572
Ω_B	0.0866	0.0778
$\mathbf{M_0}$	0.4800	0.3746
$\mathbf{M_1}$	1.5740	1.5423
$\mathbf{M_2}$	-0.1760	-0.2699

D.2 Cardano-type algorithm to solve cubic polynomial equations.

A Cardano-type algorithm is used to solve the PR equation of state for the mole volume. (noa) Given a cubic polynomial in the form:

$$x^3 + ax^2 + bx + c = 0$$

we define:

$$Q = \frac{a^2 - 3b}{9}$$

and

$$R = \frac{2a^3 - 9ab + 27c}{54}$$

where $M = R^2 - Q^3$ is the discriminant. Thus, we can have two situations:

1. $M < 0$, the polynomial has 3 real roots:

$$x_1 = -\left(2\sqrt{Q}cos\frac{\theta}{3}\right) - \frac{a}{3}$$

$$x_2 = -\left(2\sqrt{Q}cos\frac{\theta + 2\pi}{3}\right) - \frac{a}{3}$$

$$x_3 = -\left(2\sqrt{Q}cos\frac{\theta - 2\pi}{3}\right) - \frac{a}{3}$$

with

$$\theta = arccos\left(\frac{R}{\sqrt{Q^3}}\right)$$

2. $M > 0$, the polynomial has only one real root:

$$x_1 = S + T - \frac{a}{3}$$

with

$$S = \sqrt[3]{-R + \sqrt{M}}$$

$$T = \sqrt[3]{-R - \sqrt{M}}$$

D.3 Variation of reaction orders - results.

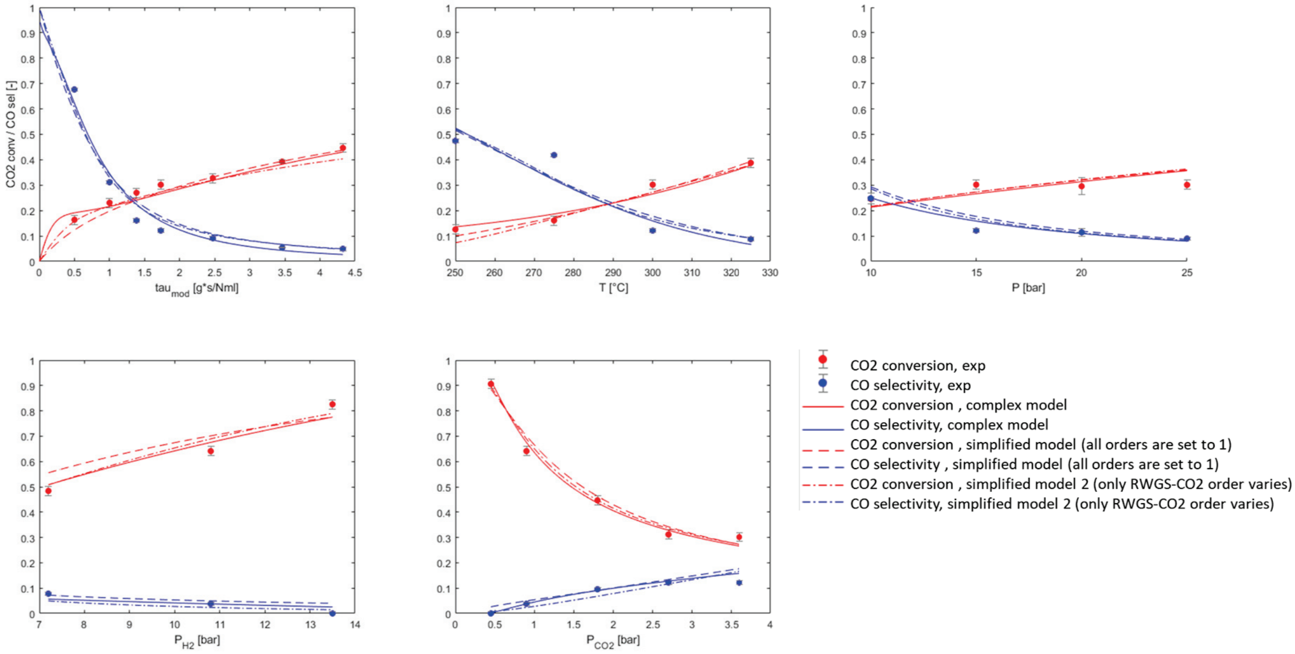

Figure D.1: CO_2 conversion and CO selectivity predicted by the model in comparison with the experimental data (points) in the case of: 1) complex model where all reaction orders are considered as variables (solid lines); 2) simplified model where all reaction orders are set to 1 (dashed lines); 3) variation of the simplified model where only CO_2 order in the RWGS reaction rate is considered as variable (dash-dot lines).

References

Phase Relations in Reservoir Engineering. URL https://www.e-education.psu.edu/png520/node/1405.

J. J. Marano and G. D. Holder. Characterization of Fischer-Tropsch liquids for vapor-liquid equilibria calculations. *Fluid Phase Equilibria*, 138(1-2):1–21, Nov. 1997. ISSN 03783812. doi: 10.1016/S0378-3812(97)00166-0. URL https://linkinghub.elsevier.com/retrieve/pii/S0378381297001660.